Strain-induced precipitation during the thermomechanical processing of AA6111 alloy

Yinggang Song

Thesis submitted for the degree of Doctor of Philosophy

The Department of Engineering Materials
The University of Sheffield
December 2007

Abstract

It is well known that the finishing temperature of 6xxx alloys determines the resultant texture, which clearly has a strong effect on formability. Specifically, the texture is determined by whether the finishing temperature is above or below the β transus. This study was initiated in order to directly determine the mechanisms that take place during the hot deformation of AA6111 to directly explain these observations. Accordingly, the effect of inter-pass time during thermomechanical processing of AA61111 on flow behaviour and microstructure evolution has been investigated. This was achieved using plane strain compression testing undertaken on the Sheffield Thermomechanical Compression (TMC) facility, using the hit-hold-hit-quench approach at temperatures of 320°C, a strain rate of 85 s^{-1} to an initial strain of 0.5, unloaded and held for delay times of 0, 6, 60, 600 and 6000 seconds, followed by the second deformation. Hardening of the alloy was observed, the extent of which was dependent on the hold time. Electron backscatter diffraction (EBSD) and transmission electron microscopy (TEM) were used in the investigation and a comparison of the substructural characteristics obtained by these techniques was made. TEM identified precipitation, predominantly β and Q phases, on dislocation lines, the size of which was a function of the hold time. In contrast to conventional ageing studies, the Q phase was found to be the majority precipitate phase. The coarsening rate of the Q during the hold period of the precipitates was considerably faster than for coarsening following a conventional precipitation treatment. The size of the microband structure at the end of the double deformation was a function of the hold time, suggesting that coarsening of the precipitates during the hold had altered the Zener pinning potential. Texture analysis through EBSD revealed that the texture was mainly composed of the α and β fibres, indicating a classic hot deformation texture with no evidence of a recrystallisation texture. This, the EBSD maps themselves, optical and transmission electron microscopy indicated that no recrystallisation had occurred for any inter-pass delay time. Small changes in deformation texture were observed with changes in inter-pass delay time, however, such differences were believed to be small. Deformation substructure increased in size (e.g. microband width) with increased inter-pass time, as expected, which with the increase in precipitate size led to the softening observed at 600 and 6000 seconds. The implications of these observations are discussed.

Contents

1. INTRODUCTION

The demands for weight reduction in automotive construction have led to increasing interest in the use of aluminum alloys for autobody applications. Indeed several high value cars now utilize this technology. For skin sheet material the emphasis is on achieving a good balance of formability, strength after the paint-bake, and a high surface quality after pressing and paint finish. Consequently, the bake hardening 6xxx alloys are the primary choice for outer panel applications. Compared to other Al-alloys, 6xxx sheets stand out by a combination of good formability, good corrosion resistance and satisfactory strengthening potential during paint-bake cycles at sufficiently high temperature.

The main alloys of interest are the Al-Mg-Si-Cu alloys AA6016, which has reasonable strength and high formability, and AA6111, which has high final strength, e.g. [1, 2]. The alloy AA6111 was developed as an addition to the 6000 series of aluminium alloys, with the addition of copper to improve mechanical properties. In this alloy some transition element dispersoids containing Mn and Cr are generally used to control grain growth during thermomechanical processing, because of the stability of the dispersoids during heat treatment.

The production route can be split into three stages: 1, the breakdown of cast ingot to solutionised thin sheet via thermomechanical processing; 2, shaping of the product and 3, age hardening of the final product at temperatures of approximately 150-200°C. The microstructure/precipitation response during stage 3 has been relatively well studied and has been shown to be complex due to the occurrence of many intermediate phases [3-5] though a general precipitation sequence has been widely described as [1, 3-5]

$$\text{SSS} \rightarrow \text{GP zones/clusters} \rightarrow \beta'' + \text{Q}' \rightarrow \text{equilibrium } \beta + \text{Q}$$

where SSS refers to supersaturated solid solution. The copper-rich Q-phase is common to all Al-Mg-Si-Cu alloys, and is found as an equilibrium phase, co-existing with β (Mg_2Si) in nearly all compositions [4]. The exact composition and structure of the Q-phase is a much debated issue, however it is believed to have a hexagonal structure [4], appearing as laths, with a composition of either $Al_4Cu_2Mg_8Si_7$, $Al_5Cu_2Mg_8Si_6$ or $Al_4CuMg_5Si_4$ [3, 6]. In comparison, the microstructure evolution during stage 1 has received much less attention though its impact is critical for achieving successful stage 2 forming via control of grain size and crystallographic texture.

Engler and Hirsch [7] suggest the key factor in controlling texture, and hence formability in 6xxx sheets, is control of the state of β precipitation during the entire chain of thermomechanical processing so as to achieve a weak final recrystallisation texture which produces good formability and good final surface appearance.

Recent work at Sheffield has suggested that AA6111 exhibits strain-induced precipitation in much the same way as found for microalloyed steels, but confirmation of this phenomenon was required. The current work was undertaken using plane strain compression testing on the thermomechanical compression (TMC) machine, using the hit-hold-hit-quench approach, with the specific objective to explore the extent and mechanisms of strain-induced precipitation during the hot working of this alloy.

2. OBJECTIVES

The objectives of the work were specifically:

- Determine the stress-strain curves for a series of plane strain compression (PSC) tests and evaluate the flow behaviour of this alloy for indications of strain-induced precipitation and recrystallisation.

- Quantitatively characterise the type, size and location of precipitates formed under the double hit deformation conditions. Further, measure the coarsening rates as a function of precipitate hold time.

- Determine the deformation substructure using TEM and EBSD to understand the effect of precipitation on the deformation mechanisms.

- Identify the evolution of crystallographic texture developed in this alloy and the relationship between the texture and corresponding microstructure, such as, microband, deformation banding, misorientation, stored energy etc, with various hold time. Thereby elucidate the effect that strain induced precipitation has on the deformation behaviour.

- Elucidate the mechanisms for inhibiting recrystallisation.

3. LITERATURE REVIEW

The heat treatable 6xxx (Al-Mg-Si) series aluminum alloys have received considerable interest from the automotive industry as potential autobody sheet material due to their ability to be shaped in the solution treated state and then age hardened during the paint-bake cycle [7]. Alloys of 6xxx series contain magnesium and silicon, both with and without additions of copper. Copper additions generally increase the kinetics of precipitation during artificial aging, as well as reduce the deterioration in the age-hardening response arising from natural aging of the Al-Mg-Si alloy [8, 9]. Additionally, the addition of copper to Al-Mg-Si alloys improves their mechanical properties, especially their ductility [10]. Increasing Si in 6xxx type alloys increases strength in the T4 and T8X tempers. Whilst the tensile elongations of these alloys are very similar, bendability and also Erichsen dome height deteriorate with increasing Si level [11]. Excess Si reduces the time to initiate strengthening, and increases strength in both the T4 and artificially aged tempers. Excess Si also reduces the Mg/Si ratio in the zones/clusters and β'' precipitates and reduces the peak strength stability in over-aged conditions [12]. These alloys can be shaped, their low density, their very good corrosion-and surface-properties and good weld-ability are factors that together with a low price make them commercially very attractive [13-16].

Heat treatable aluminium alloys are being used increasingly for automotive skin sheet, both in North America and Europe [8, 11, 12, 14, 17-19]. The main alloys of interest are the Al-Mg-Si-Cu alloys AA6016, which has reasonable strength and high formability, and AA6111, which has high final strength [1, 2]. In North America, where the outer skin gauge is about 1 mm or less, the alloy AA6111 is generally preferred. This alloy has a T4 strength of around 150 MPa, which increases to approximately 220 MPa in the painted, T8X temper. In Europe, the skin panel gauges are generally thicker and the lower strength alloy, AA6016 is used, which has a T4 strength of about 120 MPa, and a T8X strength of around 190 MPa [11]. The properties of aluminium alloys for car applications are largely controlled by microstructure and crystallographic texture of the final sheets. Heat treatable 6xxx alloys achieve their final strength only during the paint-bake cycle of the final automotive construction [14]. The typical paint-bake cycle in the automobile manufacturing process is 30 minutes heating at 175°C. Al-Mg-Si alloys reach a peak hardness condition after 10-20 hours at 175°C, thus the paint-baked body

sheet aluminium alloys must be used in an underaged condition [20].

Strain-induced precipitation is a key phenomenon that controls the microstructure evolution during the finish rolling stages of microalloyed steels [21]. The process is based on the assumption that heterogeneous nucleation of precipitates on dislocations (in deformation bands, microbands and other sub-grain structures) and on grain boundaries leads to major changes in the recrystallisation kinetics to the point where, if the temperature, prior strain and hold time are correct, recrystallisation is entirely prevented. However, the high dislocation density leads to enhanced coarsening of the precipitates due to pipe diffusion [22]. The microalloying elements, which remain in solution (partially or completely) during roughing deformation, start precipitating following the finishing deformations at low temperatures. Nb, Ti and V are the most commonly used microalloying elements and upon cooling they combine with C and/or N to form carbide, nitride and/or carbonitride precipitates. These fine precipitates play an effective role by retarding recrystallisation (thereby, increasing the recrystallisation-stop temperature) [21-23] that usually follows the deformation and thus helps to retain the accumulated strain and deformed structures of austenite grains. Prior deformation enhances the precipitation kinetics significantly. The presence of precipitates in austenite increases the flow stress of the material and hence the rolling loads [22].

Work at Sheffield using a model Fe–30 wt% Ni, 0.1 C, 1.61 Mn, 0.1 Nb microalloyed steel confirmed that the precipitation occurred entirely on dislocations, present principally as microband walls but also as a rudimentary cell structure within the microbands. No evidence was found for NbC precipitation in the matrix, which therefore remains supersaturated with Nb. The effect of dense strain-induced precipitation on microband walls is expected to pin them, so that their behaviour in the second and subsequent deformation passes is severely modified. The matrix within the microband cores remains supersaturated with Nb, which is therefore available for strain-induced precipitation during subsequent inter-pass delay times [24]. Also, in a Fe-30wt%Ni alloy, the retardation of austenite recovery and recrystallisation during finishing rolling inter-pass delay times results in a heavily deformed structure that result in the formation of a fine transformation product upon cooling. These processes are known to be controlled by the strain-induced precipitation of microalloy carbides and nitrides onto the austenite structure [25].

3.1 Precipitation

3.1.2 The precipitation/transformation sequence

In an Al-Mg-Si alloy, the aging sequence is generally accepted as: GP zones→ metastable β'→ equilibrium β phase [13, 20, 26, 27]. Also, large insoluble Al (Fe, Mn, Cu, Cr) Si particles, which typically have an average diameter of ~80 nm, are observed for all conditions. The particles are dispersoids, which formed during the solidification/homogenisation treatment, and the solution treatment and aging processes were found to have no effect on these particles [17]. The precipitation in Cu-containing Al-Mg-Si alloys has been traditionally considered, Q and its metastable precursor, Q' [26].

The automobile manufacturing process can be split into three stages: 1, the breakdown of cast ingot to solutionised thin sheet via thermomechanical processing; 2, shaping of the product and 3, age hardening of the final product at temperatures of approximately 150-200°C. The microstructure/precipitation response during stage 3 has been shown to be complex due to the occurrence of many intermediate phases [3-5] though a general precipitation sequence has been widely described as [1, 3-5]

$$SSS \rightarrow GP\ zones/clusters \rightarrow \beta'' + Q' \rightarrow equilibrium\ \beta + Q$$

where SSS refers to supersaturated solid solution. The copper rich Q-phase is common to all Al-Mg-Si-Cu alloys, and is found as an equilibrium phase, co-existing with β (Mg_2Si) in nearly all compositions [4]. During ageing at 180°C, the precipitation sequence in AA6111 can be presented as: Clusters / GP zones → β''+Q'→euqilibrium Q+Mg_2Si [17, 28, 29]. The metastable phase β'' has been identified as the main strengthening phase in AA6111 alloy [29]. Miao and Laughlin [9] suggested that Cu induces the formation of Q and its precursor metastable phases. For the alloy with 0.07 wt% Cu, the precipitation sequence is

GP zones→needle-like β'' →rod-like β' +lath-like Q′ →β+Si.

The precipitation sequence in the alloy with 0.91 wt pct Cu is

GP zones→ needle-like β'' →lath-like Q′ →Q+Si [9]

In AA6022, the Q' precipitates are more likely to form by heterogeneous nucleation processes. Therefore, instead of the sequence Clusters/GP zones→β''→β'+Q' for the metastable phases in the undeformed condition, the following sequence for precipitation of metastable phases in the pre-deformed samples is proposed: Clusters/GP

zones→β'+Q'→Q' [30]. Table 3.1 summarises the type of Mg-Si precipitates observed.

Table 3.1 The evolution of Mg-Si phases [26, 31]

Transformation/precipitation sequence	Crystal type	Size (nm)	Composition
Clusters of Si and fewer of Mg	Unknown	unknown	Si (Mg)
Clusters containing Si and Mg	unknown	unknown	Mg/Si<1
Coherent spherical GP-I zones	unknown	~1-3	Mg/Si~1
Semi-coherent GP-II zones (β" needles)	monoclinic	~4×4×50	Mg/Si ≤1
β' rods	hexagonal	~20×20×500	Mg/Si~1.7
β -Mg_2Si plates	cubic	microns	Mg/Si=2

3.1.2.1 Atomic clusters

In Al-Mg-Si alloys, separate Mg- and Si-clusters are present in the as-quenched condition, but Mg and Si atoms aggregate during natural aging to form Mg-Si co-clusters [20]. Marioara et al. [13] also suggested that in a 6082 alloy, the atomic clusters are created during storage at room temperature. Subsequently, spherical GP zones are formed, the chemical nature of which is similar to the co-clusters. GP zones give contrast in TEM images but the co-clusters do not, because the former has a higher solute concentration than the latter [20]. However, 3D Atom Probe analysis clearly revealed segregation of both Mg and Si into a high number density of small particles [32]. The clusters appear spherical and the Si/Mg-ratio of about 2 was found, quite similar to the alloy composition [32].

3.1.2.2 GP zones and the β" phase

The precipitation of the GP zones are not very effective in hardening and provide heterogeneous nucleation sites for the β" precipitates [20]. The spherical GP zones have an atomic ratio of Mg:Si atoms of close to 1:1 with uncertain structure. Copper does not associate with the formation of the GP zones [8, 9]. In an AA6111 alloy, the differential scanning calorimetry (DSC) revealed that for short aging time, the microstructure is comprised of small (pre-β") GP zones and β" for the very early stages of aging, while Q' precipitates appears later. It is evident that while β" and Q' precipitate simultaneously, the small GP zones gradually disappear during the ageing period over which β" precipitation approaches completion [29].

β" precipitates, roughly circular in cross section, are needle-shaped and is clearly

visible by strain field contrast. The needles are aligned along the <100> directions of aluminium matrix and are coherent with the matrix along their length [9, 14-17, 26, 27, 29-33]. The atomic unit cell contains two units of Mg_5Si_6. It has a C-centred monoclinic structure with space group C2/m, a=1.516±0.002 nm, b=0.405 nm, c=0.674±0.002 nm, β=105.3±0.5°. The aluminium content of the precipitates increases with the degree of coherency in the Al matrix [15, 26, 31]. The atomic packing may be regarded as a hard ball packing using clusters, the clusters being (1) centred tetrahedrons of Mg atoms and (2) so-called twin 'icescapes' where Mg atoms are centred above and below pentagonal rings of four Si atoms and one Mg atom. A growth-related stacking fault in the structure is explained by a deficiency of Mg atoms. The following relationship between the phases can be found: $(001)_{Al} \parallel (010)_{\beta''}$, $[-310]_{Al} \parallel [001]_{\beta''}$, $[230]_{Al} \parallel [100]_{\beta''}$ [7]. Matsuda et al. [27] also suggested that the formed β'' phase is a monoclinic lattice with the lattice parameters a=0.77±0.02 nm, b=0.67±0.01 nm, c=0.203 nm, and γ=75°±0.5°, with space group P2/m. The crystallographic orientation relationship is as follows: $(001)_{\beta''} \parallel (001)_m$ and $[100]_{\beta''} \parallel [310]_m$. The chemical composition of the β'' phase is Si:Al:Mg=6:3:1 [27].

3.1.2.3 The β' and β phase

In Al-Mg-Si-Cu alloy at the early stage of aging, the predominant precipitates are in the transition phase. There is also β' phase, but this is not the main metastable phase. The Q' phase dramatically increases with increasing aging time after these transitions while the β' phase becomes a major phase in an early stage of aging in the balanced alloy [10]. The rod-shaped β' phase has the hexagonal axis along the needle direction with lattice parameters a=0.705 nm and c=0.405 nm. The end-on section of these precipitates revealed a sphere-shape [9]. The a-axis therefore fits well with the phase intergrown with β''. It may be expected that much of the β' particles nucleate on β'' [9, 26, 31]. Additionally, Cayron et al. [34] suggested that the space group of the β' is found to be hexagonal P-62m and a=0.71 nm.

The β phase (Mg_2Si) is usually formed as platelets on {100} of Al having the CaF_2 structure with a=0.639 nm [9].

3.1.2.4 The Q' phase

The exact composition and structure of the Q' phase is a much debated issue, however it is believed to have a hexagonal structure [4], appearing as laths, with a

composition of either $Al_4Cu_2Mg_8Si_7$, $Al_5Cu_2Mg_8Si_6$ or $Al_4CuMg_5Si_4$ [3, 6]. Generally, Q' precipitates have a lath morphology with a rectangular cross-section when viewed end-on, and its crystal lattice is a hexagonal of a=1.04 nm and c=0.405 nm. The orientation relationship between the Q' phase and the matrix is $[0001]_{Q'} \| [001]_m$ and $[1\text{-}210]_{Q'} \| [130]_m$ [9, 10, 17].

In 6xxx series alloy, in an under-aged condition, large, lath-shaped particles of the copper containing Q' phase were observed at grain boundaries. In the over-aged condition, Q' phase was the main matrix phase [35]. The formation of Q' precipitates up to the peak-aged condition does not involve any reduction in the β'' volume fraction. Also, the slow hardening as well as the small aging response is related to the slow rate of precipitation of the Q' phase [29].

3.1.2.5 The Q phase

The composition of the Q phase, as determined by a detailed EDX analysis in a overaged AA6111 alloy, was 20% Al, 21% Cu, 32% Mg, and 31% Si (in wt%) [26]. The Mg/Si ratio was ~1.1. Q phase forms as laths lying along $<100>_{Al}$. In cross section, the laths show a prominent (flat) habit plane, $\{510\}_{Al}$, and irregular side facets [26]. Q phase has a hexagonal structure with a unit cell a =1.04 nm and c=0.405 nm [33]. In AA6111 alloy aged 10 minutes at 315°C, lath-shaped Q phase about 8.0×23.0 nm^2 in cross section and more than 600 nm in length are visible. Many of the laths observed in cross-section have their longer axis at an angle of 11° with respect to $<100>_{Al}$ [26].

The Q phase grows into the grain with which it has a preferred orientation relationship. If the grain boundary plane contains a <100> direction, the precipitate grows with a faceted morphology along that direction and maintains a $\{510\}_{Al}$ facet plane. If the grain boundary does not contain a <100> direction, the morphology of the Q phase is more equiaxed, but still maintains the preferred orientation relationship with one of the two grains. The first precipitation of the Q phase in the matrix occurs heterogeneously on dislocations where it is parallel to the long axis of the laths [26].

3.1.3 Volume fraction

On ageing at 180 °C, the number density of β'' is much higher than that for Q'. The equivalent radius for β'' and Q' in the directly aged material start at very similar values and increase at the same rate during artificial aging. On the other hand, for the case of natural aging, the radius of Q' precipitates is considerably larger than for β'' precipitates.

This difference remains constant as the aging time increases [17].

Both β" and Q' phases are coherent along the longitudinal direction of precipitates, reflecting a low energy coherent interface. However, during growth and coarsening, the length of the precipitates increases at a substantially higher rate than the diameter of precipitates. The width of the size distribution increases in proportion to the mean precipitate size.

On aging at 180°C, the total volume fraction comes mainly form the β" precipitate and the contribution of the Q' is lower. However, the relative amount of Q' increases with aging time. After aging at 250°C, the structure is much coarser. The volume fraction of β" is similar, but the volume fraction of Q' is approximately 5 times higher after aging at 250°C compared to 180°C [17].

3.1.4 Strengthening reaction

In 6xxx alloys the strengthening due to precipitates will be a function of the spacing and strength of the obstacles lying on the glide plane that the dislocation encounters. In addition, for these alloys where multiple sets of obstacles may be present: e.g. precipitates, GP zones, solute atoms or clusters and forest dislocations [28]. Solid solution additions, e.g. magnesium, may lower the fault energy (SFE) of aluminium, which is high for commercial purity aluminium, and therefore enhance planer slip [36]. Also, the large constituent particles tend to weaken the recrystallisation texture and refine the grain size in the final T4 state by providing nucleation sites for particle stimulation nucleation (PSN: nucleation in the deformation zones around these particles) [14].

The magnitude of the strengthening depends on the microstructural morphology of the precipitates, which in turn is governed by the interfacial and strain energies of the precipitate/matrix system. These interfacial and strain energies are sensitive to the nature of the crystal structure of the precipitate phases, the matrix phase, and the interface between them [18]. However, the shearing of strengthening precipitates by dislocations is the prevalent mechanism that controls the plastic deformation of the material. By-passing of particles, assisted by cross-slip, is an additional process whose effects are enhanced when the temperature increases consistently with the correlated decrease of the flow stress and the hardening rate. This non-planar mechanism leads to a work hardening of the alloy that limits the effect of internal stress and results in a high mechanical strength [37, 38].

Considering the effect of individual precipitate types, the high hardening rate, as well as the large aging response, is related to the rapid nucleation and growth of β'' precipitates. The slow hardening as well as the small aging response is related to the slow rate of precipitation of the Q′ phase [29].

3.2 Microstructural evolution during deformation processing

3.2.1 Substructure evolution

Microstructural characterisation and modelling of a variety of metals deformed by different thermomechanical processes have shown a universal structural evolution [39-45]. For materials with a medium or high stacking fault energy the earliest microstructures develop with strain from "tangled" dislocations to a structure consisting of cells or subgrains. Especially in polyslip, a number of significant heterogeneities also characterize the deformed state, for example dense dislocation walls, microbands, transition bands and shear bands [46, 47].

Generally in fcc metals for rolled polycrystals or deformed single crystals, TEM studies have characterised the following typical stages of dislocation sub-structure evolution: (i) $\epsilon<0.2$, a first decomposition of the grains into cell blocks occurs; (ii) $0.2<\epsilon<1$ the average geometrically necessary boundary (GNB) misorientation, θ, increases while the cell size decreases and the cell walls collapse into sub-boundaries; (iii) $0.5<\epsilon<2$ microshear bands appear and (iv) $\epsilon>2$ the cell and micro-band structure evolves into a lamellar structure [48]. During low strain plastic deformation, individual grains are subdivided into crystallites rotating independently of one another to accommodate the imposed strain. The reason for grain fragmentation is that the number and selection of simultaneously acting slip systems differs between neighbouring volume elements within a grain. This leads to differences in lattice rotations between neighbouring elements within a grain when the material is strained. Depending upon the crystal lattice orientation of the grain and its interaction with near neighbours, grains could develop a well-defined cell-block structure of similar lattice orientation but rotating at differing rates and sometimes in differing directions. In some instances the lattice rotation rate within a grain changes in a continuous fashion, thus developing long-range orientation gradients [44, 45]. With increasing strain, the width of cells or subgrains hardly changes, while the length of cells or subgrains and the ratio of length-to-width of subgrains decrease [49]. This result is similar with hot deformed 316L steel

[50]. At the lower strain level, the deformation substructure appeared to be rather poorly developed. At the larger strain, the substructure within most grains became well developed and the corresponding misorientations increased. With increased strain level, the mean subgrain size became finer, the corresponding mean misorientation angle increased and both these characteristics became less dependent on a particular grain orientation [50]. On the other hand, for deformation at constant strain rate, the subgrain size decreases with strain until a steady-state size is reached. Associated with this, the misorientation between microbands and subgrains increases with strain to a steady-state value. The dislocation density within the grains also increases with strain until a steady-state value is reached. Under transient conditions of a reducing strain rate to a strain of 1.0, the subgrain size and misorientation are smaller than in steady state. During deformation at constant strain rate after the transient, the subgrains grow by a process of dissociation of subgrain boundaries, which produces a larger number of dislocations in the subgrains until the values characteristic of steady state [51].

Some authors [52, 53] suggested that in deformed fcc metals, in the macroscopic system defined by the deformation axes, boundaries lie close to the macroscopically most stressed planes. In the crystallographic system, the boundary plane depends on the grain/crystal orientation. The more the slip is concentrated on a slip plane, the closer the boundaries lie to this. Winther et al. [54] also confirmed that in a 25% cold rolled AA1050 alloy, the grain orientation-dependent dislocation boundary planes are a general phenomenon. Some grain orientations have boundaries aligned with slip planes while others do not. In addition, Hurley et al. [55] suggested that in a rolled Al-0.13%Mg alloy, there was no evidence for alignment of the substructural boundaries with slip planes or any other simple crystallographic element, and it seems that the substructure is orientated primarily with respect to the macroscopic or mesoscopic straining state.

3.2.1.1 Dislocation boundaries

Deformed polycrystalline metals are subdivided by grain boundaries and dislocation boundaries which are arranged in a lamellar or subgrain structure. The frequency and distribution of these boundaries determines the properties of the deformed metal, including the flow stress, texture, recrystallisation behaviour and the formability [56].

Dislocations are generated during deformation and they accumulate in dislocation boundaries; large-scale, long, typically extended dense dislocation walls and

microbands, considered as geometrically necessary boundaries (GNBs) and short cell boundaries termed incidental dislocation boundaries (IDBs) [39]. GNBs and IDBs are typically low-to-medium angle dislocation boundaries and have characteristics typical of low energy dislocation structures (LEDs). For any given dislocation population, such structures nearly minimize their free energy per unit length of dislocation line among all configurations in principle accessible to the dislocations [41].

The misorientation across GNBs should typically be much larger than across IDBs and should rise faster with increasing strain, and the influence on the flow stress should be different for the two types of boundaries. The relative change in angle and spacing is smaller for IDBs than for GNBs. This indicates that the dislocations formed during deformation may have a stronger tendency to be accommodated in GNBs rather than in IDBs. This behaviour may be related to a decreasing rate of increase in energy of a dislocation boundary with increasing angle. As a consequence, less energy is stored per unit length of dislocation line for dislocations accommodated in GNBs when compared with dislocations positioned in IDBs [57]. Hughes also confirmed that in heavily cold worked metals, these dislocation boundaries have a large angular spread and that the misorientation across many boundaries is of the magnitude characteristic of ordinary high angle boundaries [56].

GNBs play an important role in the deformation process; to accommodate the strain imposed during deformation, additional dislocations arrange to form geometrically necessary high-disorientation regions associated with dislocations, interactions and slip patterns that develop within a deforming grain. Thus, during deformation grains subdivide into crystallites whose orientation is rotated with respect to that of their neighbours [40]. Although most of the GNBs have a macroscopic orientation (defined by the deformation axes), e.g. inclined about 45° with the rolling plane at small-to-medium rolling reductions, the boundary orientation in the crystallographic lattice strongly depends on the grain orientation [39]. During cold rolling to small strains (ϵ<0.5), regular arrays of the cell wall boundaries oriented is approximately 30-40° to the rolling direction. As the strain level increases (0.5<ϵ<1), these boundaries are intersected by microshear bands (or S-bands), consisting of fine-scale cells linked up to form thin two-dimensional planar structures within grains, within which strain may become localized, leading to increasing misorientations across these boundaries. However, in grains of metastable orientation, such bands of higher misorientation may not form until very

large strains. At high levels of strain (ϵ>1), the original grain boundaries, together with the higher angle boundaries generated during the deformation, become progressively aligned to within ~10° of the rolling direction [58]. An increase in the number of slip systems caused an increasing deviation of the dislocation boundaries from the slip plane. Cross slip may contribute to the formation of crystallographic boundaries. Slip planes with no or only one active slip system may receive additional sets of dislocations from other slip planes through cross slip and thereby become candidates for crystallographic boundary formation. Cross slip may also contribute additional dislocations to a slip plane which already has two sets of dislocations. Cross slip is relatively frequent in materials with high stacking fault energy. In fcc crystals secondary slip produces dislocations which form stable Lomer-Cottrell networks with the primary dislocations as long as the boundary plane stays within 25° of the primary slip plane [43, 59].

During severe deformation processing, at low strains the presence of coarse second-phase particles has been shown to reduce the characteristic length scale of grain subdivision to that of the inter-particle spacing. New high misorientation boundaries are rapidly developed within deformation zones surrounding the second-phase particles, which leads to an acceleration in both the density and misorientation of the new HAGBs formed in a particle-containing alloy, relative to a single-phase material. At higher strains, submicron grains are rapidly formed in regions of high local particle volume fraction and particles cause heterogeneities in plastic flow, which disrupt any regions with regular lamellar boundary structures and increase their rate of refinement to submicron grains. At very high strains the deformation structures of both materials tended to converge. However, a slightly higher level of refinement was still seen in the particle-containing alloy even after deformation to a strain of ten [60].

3.2.1.2 Microbands

The deformation can occur within a grain by the activation of volume elements (or cell blocks). Each cell block, comprising a number of smaller cells, is bounded by dense dislocation walls (DDWs) or microbands (MB) (i.e. sets of two parallel bands of DDWs), aligned at 30-40° to the rolling plane [42, 43, 51, 61, 62]. Microband formation has been attributed to the asymmetry of slip for certain grain orientations, where double the amount of slip has to occur on the two co-planar (CP) systems compared with the two co-directional (CD) systems. The localisation of slip on the CP planes is thought to cause microbands to form parallel to the CP slip systems [63]. During the initial stages of

deformation, dislocation cells and, later, dense dislocation walls (DDWs) develop. Long DDWs are the boundaries between cell blocks (CBs) in which different combinations of slip systems operate. As consequence, larger misorientations develop across DDWs than across ordinary cell walls, which leads to the formation of a "hierarchical" dislocation cell structure. A gradual increase in the misorientation angles, as well as a decrease in the mean cell block size, occurs during deformation. In addition, some suitably oriented DDWs progressively increase their misorientation and misorientation axis vectors (MA vectors) across them gradually rotate toward a common orientation which facilitates "macroscopic" rigid body rotation of one part of a grain with respect to another [64].

DDW/MBs as planar structures in fcc single crystals have been reported to conincide with {111} planes [43, 59, 65]. However, DDW/MBs which are not aligned with a {111} plane have also been observed. A DDW/MBs is normally taken to be crystallographic if its trace in the plane of observation deviates less than 5° from that of a {111} plane. It was observed that crystallographic DDW/MBs formed if the high Schmid factors were concentrated in two slip planes. If the high Schmid factors were distributed over several slip planes, the DDW/MBs were non-crystallographic [33]. Winther et al. [43] also suggested that at low and medium strain, dense dislocation walls (DDWs), microbands (MBs) and ordinary cell boundaries are dominating, whereas at high strain lamellar boundaries and subgrain boundaries develop. These dislocation structures, together with the crystallographic textures are key elements controlling important material properties.

With increasing deformation, the width of the microbands becomes greatly reduced. At the highest deformation it attains nanometric dimensions. The microbands are subjected to contraction, and a substantial misorientation appears between the bands, indicating considerable rotation of the blocks of material. At the same time the concentration of deformation in the nanometric microbands produces local softening of the material, which leads to stabilization of the alloy properties in the range of the highest deformations [66]. Richert et al. [67] also suggested that with large degrees of deformation, dense dislocation walls and microbands cutting randomly distributed tangles of dislocations, were observed. After a true shear strain γ=16, mutual crossing of microbands led to a 'subgrain like' microstructure. Large disorientation angles up to 60° were found between some neighbouring 'subgrains', but generally angles were lower (below 15°) [67, 68].

3.2.1.3 Deformation banding

Deformation banding (DB) is the process by which certain grains in a polycrystalline material subdivide into regions that rotate in different directions [64]. Deformation bands were separated by either narrow sharp boundaries or rather wide diffuse regions, in which the misorientations change significantly. The boundaries or regions separating deformation bands are called transition bands [69]. Fig. 3.1 illustrates schematically different types of deformation bands. Deformation banding clearly results from ordinary glide dislocation motions on account of misfit stresses due to slip system selections which within any one region cannot produce homogeneous deformation; and occurs on account of remarkably small energy differentials, i.e. between a structure in which slip system differences are accommodated by means of some irregularly shaped volume elements as compared to the patterns of primary, secondary and even tertiary bands that have been observed. The banding does not significantly depend on strain rates between 0.05 and 100%/s, nor on temperature between ambient to cryogenic (-193°C) [70].

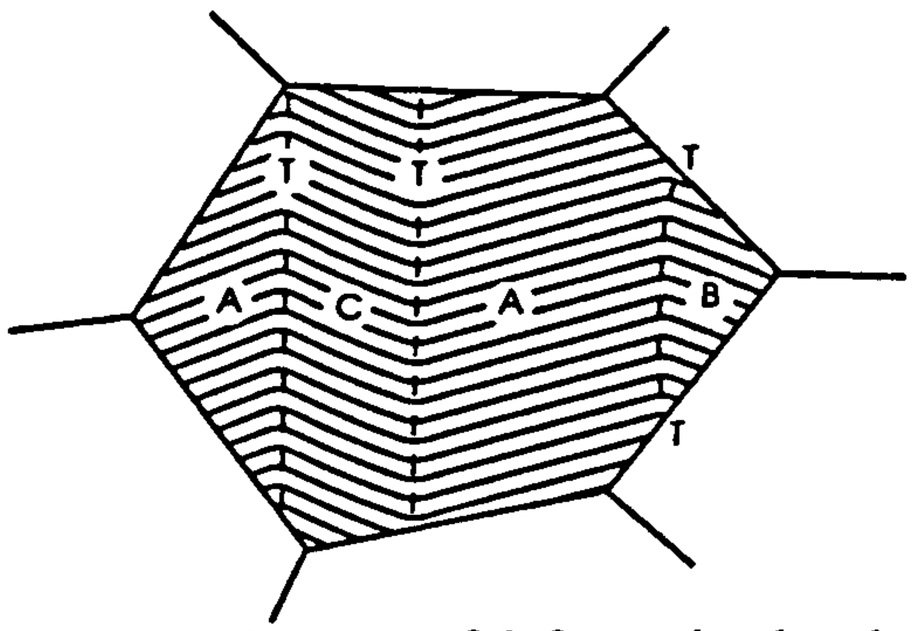

Fig. 3.1 Schematic diagram of deformation bands, transition bands [69].

Some fragments of cube-oriented material must be left over from, or generated by, the previous large strain deformation, probably in the form of thin cube-oriented transition bands (TBs) between volume elements with typical rolling orientations. By virtue of the nature of the slip systems and their highly symmetrical nature, the cube orientation is metastable during room temperature compression and can exhibit heterogeneous deformation bands. The plane strain compression, channel-die or rolling of cube and near-cube oriented fcc crystals is generally highly heterogeneous, leading of a splitting of the grains into deformation bands. In the case of aluminium, copper and nickel the first formed bands are characterized by large and alternating TD rotations. During subsequent deformation the bands undergo further TD and RD rotations. In

copper, and to a lesser extent in nickel, secondary micro-shear bands develop within the coarse deformation bands and lead to additional rotations about RD (and some ND) [71]. Another example is the development of deformation bands in (001)[110] textured aluminium polycrystalline sheet material deformed in tension at room temperature. Individual grains rotate at different rates despite the very strong starting texture and macroscopically homogeneous deformation. A majority of these grains gradually split into two complementary orientation groups during straining by rotations about an axis close to the transverse direction. These orientations finally approach the two symmetrical stable copper texture components. [72].

3.2.1.4 Shear bands

During cold rolling of a single-phase Al-0.1Mn alloy, at low strains, bands of elongated cells are formed. As the applied strain increases, intersecting thinner and more widely spaced bands form within many grains, flow becomes localised within these new bands and they develop into microshear bands, which shear the original elongated cell structures [61]. The shear bands occur at a variety of angles to the rolling plane, with a typical range between 20° and 40°, while an average value of 35° is generally reported [61, 63, 73]. In materials with low stacking fault energy (SFE) like brass or austenitic steels, the onset of mechanical twinning gives rise to the massive formation of so-called brass-type shear bands that extend basically over the entire sample thickness. In contrast, materials with medium to high SFE may form the so-called copper-type shear bands, which are generally restricted to one or, at the most, a few contiguous grains. Shear bands are thought to affect the recrystallisation behaviour that occurs during subsequent annealing, and thus have a very important effect on properties such as recrystallised grain size and texture [63]. Fig. 3.2 shows shear band formation mapped out as a function of both deformation temperature and strain.

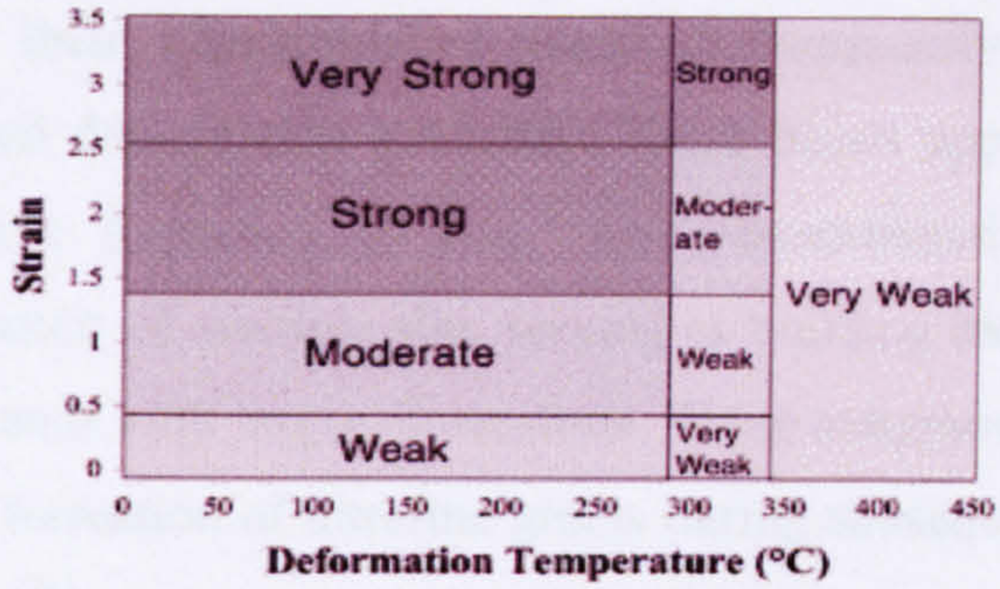

Fig. 3.2 Shear band formation mapped out as a function of both deformation temperature and strain (for a constant strain rate of $\dot{\varepsilon} = 1\ s^{-1}$) [63].

Copper-type shear bands are generally categorized as forming at medium-to-high strains but have been observed for strain as low as ϵ=0.3 (25% reduction). At low strains they are often observed to be restricted to single grains whereas at higher strains they appear to cross grain boundaries and are observed over several adjacent grains. The tendency for shear banding to occur has not only been linked to composition but also to initial grain size, temperature of deformation and grain orientation [63]. In an S-orientated grain, the shear banding occurs along a {111} plane containing the TD axis. The influence of localization on texture evolution is that the shear bands stabilize the Brass texture component [65].

There are theories based on continuum mechanics that attempt to predict the formation of shear bands and in particular the angle to the rolling plane at which they form. Plasticity is described mathematically from continuum shear flows that occur along the various slip systems of a crystal and discrete dislocation motion is therefore not explicitly modelled. One is that groupings of parallel microbands forming a lamellae structure cause long-range internal stresses that lead to the co-operative movement of dislocations, and that this results in shear processes. Groups of microbands generate large stress concentrations at their tips and emit an elasto-plastic impulse on meeting a grain boundary, and are thus able to penetrate a neighbouring grain. Consequently, the crystallographic nature of the microbands is lost and non-crystallographic shear bands form. Microbands act as obstacles to dislocation glide on slip systems that intersect the microbands, and therefore glide is restricted to slip systems parallel to them. This restricted glide then leads to strong shear in the vicinity of the microbands [63].

Shear bands have also been observed in two austenitic steels. During hot deformation, the shear bands formed at moderate strains within a matrix composed of

microbands and that their characteristics were predominantly governed by the macroscopically imposed deformation geometry. These bands appeared to be created through the co-operative formation of fine, highly-misoriented subgrains, largely resulting from the operation of multiple slip, serving as building blocks for the gradual development of shear bands with larger dimensions. These subgrains appeared to act as potential nuclei for the formation of ultrafine grains during subsequent recrystallisation or phase transformation [74].

3.2.1.5 Recovery

It has been suggested that microband formation is essentially a form of dynamic recovery during deformation. A normal recovered cell structure is prevented from forming by pinning of dislocations by alloying element atoms and hence microbands form due to the co-operative movement of pinned dislocations [63]. Dynamic recovery involves dislocation dipole annihilation and dislocation rearrangements into more stable (low energy) configurations such as low-angle boundaries in subgrain formation. These processes are facilitated by dislocation movement in the form of glide, climb and cross-slip [63, 75, 76]. Higher deformation temperatures and lower strain rates provide more thermal energy and time for this dislocation movement. The addition of magnesium to aluminium alloy results in the pinning of otherwise mobile dislocations. It could be that microbands form instead by the co-operative movement of these pinned dislocations. Once the dislocations are unpinned then normal subgrain formation can take place during dynamic recovery [63].

3.2.1.6 Recrystallisation

Recrystallisation is split into two distinct cases, namely, dynamic and static. The latter recrystallisation occurs during plastic deformation and is similar to static recrystallisation where relatively strain-free grains grow and "consume" deformed grains. Small dislocation–free regions are produced by dislocation rearrangement at grain boundaries. These small dislocation–free regions, called nuclei, can grow into the surrounding material containing dislocations. Such recrystallized regions are separated from the surrounding material by high angle boundaries [77]. Materials deformed to very large strains may be stable against conventional discontinuous recrystallisation because a large fraction of the boundaries are of high angle, but may, on subsequent annealing,

evolve relatively equiaxed fine-grained microstructures by continuous recrystallisation mechanisms [75].

Channel die plane strain compression of single-phase Al-Si crystals of orientation {110}(001) confirmed that this orientation is stable to reductions of up to 95% ($\epsilon = 3$). The deformation microstructure contains neither large orientation gradients nor heterogeneities, thus making the crystals resistant to recrystallisation. On annealing at temperatures greater than 250°, a small number of subgrains grow rapidly and discontinuously to diameters of over 100μm. The rapidly growing subgrains are those at the edge of the orientation spread of the local subgrain assembly [78]. In direct chill (DC) cast and strip cast (SC) AA 5182 aluminum alloys, it was difficult to obtain a strong cube texture in annealed SC hot bands. Recrystallisation occurred more easily in cold rolled DC hot bands than in cold rolled SC hot bands. The DC hot bands have a fully recrystallized structure and a strong cube texture, while the SC hot bands have a typical deformation structure and a strong β fiber rolling texture. When DC and SC hot bands are annealed at 454°C, the recrystallisation textures of DC AA 5182 aluminum alloy are significantly stronger than those of SC AA 5182 aluminum alloy, especially the cube component. The grains in SC AA 5182 aluminum alloy are slightly elongated along the rolling direction, while nearly equiaxed grains are developed in DC cast AA 5182 aluminum alloy [79]. The recrystallisation temperature of cold rolled CC AA 5182 aluminum alloy without pre-treatment is about 24◦C higher than that of cold rolled CC AA 5182 aluminum alloy with pre-treatment, and the former shows slightly finer and more elongated recrystallized grains than the latter. In the deformed and recovered states, CC AA 5182 aluminum alloy without pre-treatment possesses a significantly higher 45◦ earing (undesirable undulations of the rim of cups may form during the deep drawing operation, this being called earing) value than CC AA 5182 aluminum alloy with pre-treatment. Recrystallisation decreases the 45◦ earing value. After complete recrystallisation, the 45◦ earing value of CC AA 5182 aluminum alloy without pre-treatment is slightly lower than that of the alloy with pre-treatment [80].

In Al-alloys that contain large second-phase particles (>1μm) prior to deformation, recrystallisation is generally strongly accelerated in comparison to single-phase materials. During the first stages of a subsequent annealing, the dislocations are able to recover rapidly and to form subgrains that are substantially smaller than the subgrains in the matrix well away from the particles. In the next stages of annealing, subgrain

growth takes place in this very fine local subgrain structure, until finally one or a few large subgrains consume the complete deformation zone and form high-angle grain boundaries. Finally, if their size exceeds the critical diameter of ~1μm, some of the enlarged subgrains will be able to grow out of the deformation zone into the surrounding deformed matrix [81]. Humphreys also suggested that an Al single crystals with a dispersion of small Al_2O_3, after deformation and annealing, the single phase region recrystallizes readily, but in general the recrystallisation front is halted at the single/two-phase interface. At intermediate strains, grains with misorientations of -40° about axes close to (111) with respect to the deformed matrix may penetrate the two-phase region [82].

3.2.1.7 Stored energy

A portion of the mechanical energy expended in plastically deforming a solid is elastic and recoverable, while the remainder is the plastic work. Generally most, but not all, of the plastic working is converted into heat. The plastic work not converted into heat is the stored energy of cold work and, at least in crystalline metals, is the energy stored in an evolving defect structure [83]. The stored energy of plastically strained metals, mostly in the form of their dislocation substructures, is one of the keys to controlling and improving the properties of metallic alloys. Apart from providing a direct strengthening mechanism it also provides the driving force for subsequent microstructural evolution on heating by recovery and recrystallisation [84, 85]. After hot plane strain compression, the S texture component has the highest stored energy compared to the Brass, Goss and Cube orientations, which are practically equal. During recrystallisation, it is shown that the S orientation, associated with the highest values of stored energy, is preferentially consumed by the recrystallisation [84]. In warm plane-strain deformed aluminium, the observed high frequency of cube nucleation arose directly from the stability of the deformed cube bands under large strains and their possession of low stored energies [86]. Also, Cube oriented bands in heavily rolled copper showed lower than average stored energy. They suggested that easier recovery was possible in cube oriented fcc metals, deformed by plane-strain compression, since the active slip systems had orthogonal, and thus elastically non-interacting, Burgers vectors [86].

3.2.2 The evolution of crystallographic texture in FCC metals

Engler and Hirsch [7] suggest the key factor in controlling texture, and hence formability in 6xxx sheets, is control of the state of β precipitation during the entire chain of thermomechanical processing so as to achieve a weak final recrystallisation texture which produces good formability and good final surface appearance. Evolution of the deformation texture with increasing strain was characterized by gradual crystallite rotations towards the stable-end texture components located along both the α and the β fibres in Euler space [87] (The Goss {011}<100> and Brass {011}<112> component composed the α fibre. The Brass {011}<112>, Copper {112}<111> and S {123}<634> composed the β fibre. See the Fig. 3.3). In particular, the characteristics of the deformation structure play a central role in determining the processes of nucleation and growth during recrystallisation and thus the resulting recrystallisation structure [70].

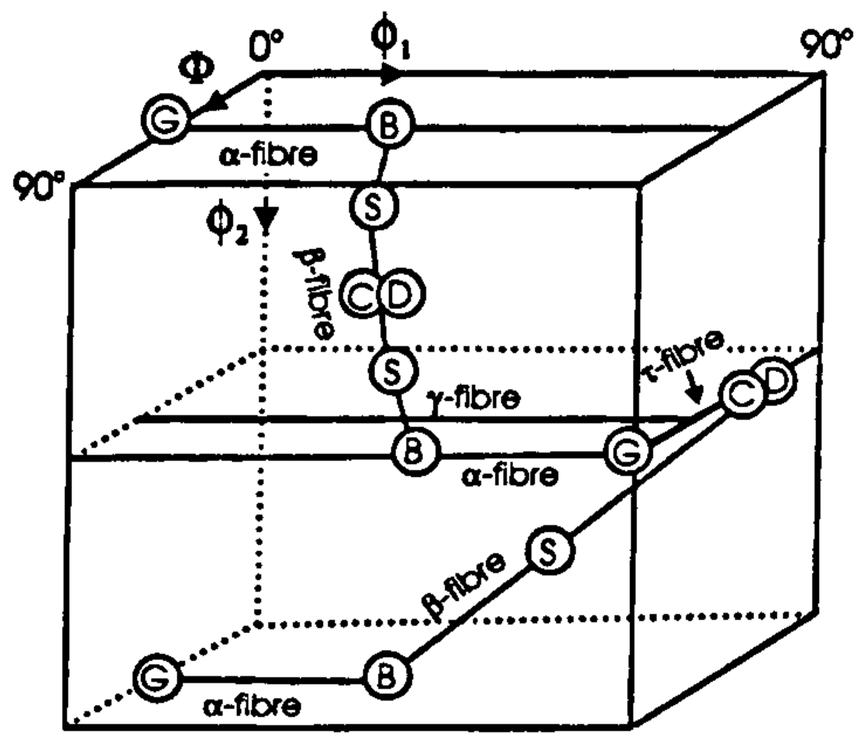

Fig. 3.3 schematic representation of important fibres for f.c.c metals in three-dimensional Euler angle space [69].

3.2.2.1 Deformation texture

During plastic deformation, substructure characteristics (such as cell/subgrain size, shape and misorientation) that evolve within a given fcc metal grain, embedded in a polycrystalline metal, depend strongly on the grain orientation. The values of deformation energy stored within individual grains also display orientation dependence [87]. Crystallographic texture of fcc metals is typically concentrated on orientations lying along a β fibre, between the Brass, Copper and S orientation. The names, symbols and Euler angles of the above orientations are listed in Table 3.2 and Fig. 3.3.

Table 3.2 Texture components often found in rolling texture of fcc metals [69].

Component, Symbol	{hkl}	<uvw>	ϕ_1	Φ	ϕ_2
Copper, C	112	111	90	35	45
S	123	634	59	37	63
Goss, G	011	100	0	45	90
Brass, B	011	211	35	45	90
Cube	001	100	0	0	0

In high stacking fault energy metals such as aluminum, the orientation densities along that fibre are relatively uniform. When the stacking fault energy is low, the "Brass" component dominates, especially at relatively high strain [88]. Also, as the cold rolling reduction increases, the volume fractions of the cube, rotated cube (r-cube), rotated Goss (r-Goss) and remainder components decrease, whereas the volume fraction of the β fibre component increases. The volume fraction of the Goss component first increases with increasing reduction, and then decreases [71, 89, 90]. Volume fractions of Brass and S components are double the amount of that for Cu as depicted in the intensity variations in β-fibre. The random texture component decreases with the degree of rolling; the rate becomes slower rate at medium strain level and after ϵ>1.5 it again starts decreasing [91].

Liu et al. [89] also gave the detail that hot and cold deformation affects the lattice rotation of crystallites and thus the distribution of orientation intensities along the β fibre. Initial orientations are more easily rotated to the S orientation than to the Brass and Cube orientations during cold rolling. During hot rolling, however, initial orientations are uniformly rotated to the β fibre at a low strains. As hot rolling continues, a few more orientations are rotated to the Brass orientation, leading to the strongest Brass component. The increase in the Brass component has been attributed to the increase of the strain-rate sensitivity index, to the additional activation of other, non-octahedral slip systems at very high deformation temperatures, and differential dynamic grain growth [89].

By channel die compression tests, polycrystals and oriented single crystals in the temperature range 200–400°C a substantial increase in the $110\langle 1\bar{1}2\rangle$ Brass component at higher temperatures together with a small but significant amount of near-Cube

orientations. These texture variations with temperature occur in the absence of recrystallisation. The near-Cube orientations tend to be stabilized by slip on 110 planes while the Brass orientation undergoes a substantially reduced ε_{12} (in-plane) shear [92]. In commercial purity aluminum cold-rolled to a reduction of 40%, the results demonstrate the different behaviour of grains with different orientations: (i) Grains oriented close to the cube {001}<100> and RD-rotated cube {025}<100> components develop orientation gradients over distances of 10-20μm. (ii) Grains with orientations near TD-rotated cube {205}<502> form fragments with relatively large misorientations, and (iii) grains within the β-fibre (S, Copper and Brass orientations) form fragments with relatively small misorientations [93]. In another cold rolled alloy, the essential features of the texture evolution can be summarized as follows: (i) The Brass orientation is anisotropic. It scatters in two directions: one part is extended towards S with an auxiliary component Brass/S; the other part leads to the Goss orientation forming the Brass/G component. (ii) Cu orientation increases with strain except for a little softening at the strain level of ϵ=0.77. (iii) S orientation is scattered from Φ=28 to 36.7°. Volume of S orientations increases from the beginning of rolling; it does not show any tendency for softening [91].

Single crystals of {001}<110> orientation are very unstable during rolling deformation, undergoing large rotations strongly about TD [91]. The (011)[01-1] orientation in a single Al crystal deformed in plane strain compression shows decreasing stability with increasing deformation temperature. Deformation produces high angle boundaries at ~45° to the ND which correspond to the {100} planes, implying the operation of non-octahedral slip processes [94].

In an Al-1%Mn alloy, the Brass orientation has the largest sub-grains whose dimensions tend to be relatively little influenced by temperature and strain rate (as for the U orientation). The S orientation is particularly sensitive to the Zener-Hollomon parameter, Z, so that much smaller sub-grains are found at high strain rates. Sub-grain misorientations evolve with strain in the classical manner; the average value increases rapidly then approximate stabilisation thereafter. There is, however, a tendency for the small, non-TD misorientation components to increase continuously. The average misorientations of all crystal orientations increase with the temperature corrected strain rate, many of the size effects can be attributed to an enhanced rate of sub-boundary generation in the case of the unstable grain orientations [95].

In a fcc metals on rolled polycrystals or single crystals deformed in channel-die compression, low rates of dislocation accumulation in some stable orientations like {110}<112> and 'S' {123}<412>, high rates in the 'Goss' orientation which displays high work hardening capacity and also high rates in some unstable orientations which break up during deformation to form transition bands separating rotated deformation bands. Low dislocation accumulation rates are favoured by stable texture components, full constraints boundary conditions and tilt boundaries. On the contrary, crystallites of unstable orientations deformed under boundary conditions with few imposed strain rate components and bounded by a twist boundary will generally develop high dislocation densities within the GNBs [48].

3.2.2.2 Recrystallisation texture

Recrystallisation texture has long been a subject of research by metallurgists since it is one of the main factors responsible for the mechanical anisotropy of properties of final sheet products. The recrystallisation texture of most aluminum alloys is characterized by the cube orientation with some scatter about the rolling direction towards the Goss orientation [80, 96-98]. The volume fractions of the cube, Goss and R components increase with increasing hot rolling strain, whereas the volume fractions of the r-Cube, r-Goss and the remainder components decrease. Further cold deformation after hot deformation suppresses the formation of the Cube component. Hot deformation promotes the Cube and Goss components at the expense of the r-Cube and remainder components. The formation of the R component does not appear to be affected by hot and cold deformation [97]. Also, the S orientation, associated with the highest values of stored energy, is preferentially consumed by the recrystallisation [99]. The major decrease through recrystallisation is in the strength of the β fibre component. Moreover, recrystallisation also decreases the Goss component, but increases the Cube, r-Cube, r-Goss, and remainder components [80].

Recrystallisation texture depends on the competition of the nucleation sites at the Cube bands, grain boundaries, shear bands and second-phase particles [75, 97, 100]. The Cube-orientation is favoured because of two opposite effects: (i) its rapid nucleation due to its preferred recovery, and (ii) its optimum growth conditions [102]. Cube-oriented grains evolve from band-like structures, which are already present in the deformed microstructure [96, 102, 103]. The Cube possibly did not form by transition banding as no definite orientation relationship existed between Cube and its immediate neighbours [104,

[105]. The cube orientation has a fast growing 40° <111> orientation relationship with respect to the S orientation. The formation of the Cube recrystallisation texture depends on deformation temperature [96, 106-108]. Also, the compositions of aluminum alloys affect the formation of the cube texture [109]. The cube orientation is unstable during large cold-rolling reductions. Cube-oriented grains remain orientation metastable during hot deformation. The origin of the Cube-oriented bands appearing in the hot deformed samples is "old" Cube grains (present in the starting material), which survive the deformation process. These Cube bands have a unique subgrain size distribution with a long tail of large subgrains, making them very potent as nucleation sites for recrystallized grains. Nucleation of recrystallized Cube grains takes place preferentially from those bands which are surrounded by the S deformation texture component [110]. In recrystallized Al-Mg alloys, the frequency of Cube oriented grains and the Σ1 boundary significantly increased at an early stage and then decreased. In the second stage a small amount of isolated large grains with the non-Cube component grew and consumed the surrounding cube grains. In contrast, the frequency of Cube oriented grains and the grain boundary character distribution showed no significant change during grain growth [111].

Concurrent precipitation plays a significant role in altering the behaviour of recrystallisation in aluminum alloys. Precipitation resulted in relatively strong P {011}<455> and ND-rotated Cube {001}<310> textures. The formation of the P texture depends strongly on annealing temperature. The strength of the P texture decreases with increasing annealing temperature. The formation of the P texture can be attributed to the effect of Zener-particle pinning caused by concurrent precipitation. Hot deformation strongly promotes the formation of the P texture [96]. This enhanced recrystallisation kinetics is caused by the additional nucleation in the deformation zones around these particles (particle stimulated nucleation, PSN). The deformation zones form due to deformation incompatibilities at the matrix/particle interface where very high dislocation densities and strong lattice rotations are being built-up [81].

Shear bands are believed to offer alternative nucleation sites to cube oriented nucleation sites; that is they effectively reduce the relative frequency of Cube oriented nuclei. Additionally but less significantly, they are also believed to destroy Cube oriented nucleation sites [112]. The impact of nucleation at shear bands on recrystallisation texture is two-fold. (i) Shear bands are known to cut through the Cube-

bands, thus reducing the nucleation sites available for nucleation of the Cube orientation. (ii) Furthermore, nucleation at shear bands may give rise to the formation of new orientations that are not usually observed in the recrystallisation textures of Al-alloys. Shear bands generate large stress concentrations at their tips which may eventually enable them to penetrate a neighboring grain. Nucleation at the intersection of shear bands and grain boundaries leads to the R orientation in the recrystallisation texture [113].

During recrystallisation, the boundary velocities are found to be directly proportional to the driving pressure and the activation energy for boundary migration is consistent with a process of boundary migration controlled by lattice diffusion of the solute [114]. High angle tilt boundaries which are misoriented to the recovered matrix are found to have a higher mobility than other boundaries [115].

4. EXPERIMENTAL PROCEDURE

4.1. Materials

The material used in this study was precipitation hardenable AA6111 alloy, the generic composition shown in table 4.1, supplied by Alcan Technology & Management AG. The supplied material was from a 70 mm thick quarter section of a commercial DC ingot, taken perpendicular to the casting direction. From this quarter section, a sample of 200×200×70 mm was taken for further testing. The positioning of the sample in the DC ingot was selected to minimize microstructural variation. Before rolling, the samples were individually homogenised for 10 hours at 560°C, with a heating rate of 50°C/minute as recommended by Alcan. This treatment was designed to replicate a typical industrial homogenisation cycle. The slow heating rate of 50°C/minute was selected. At the end of the treatment the samples were left to air cool. To generate a hot rolled microstructure the samples were heated to 540°C at 20°C/minute, held for 20 minutes to attain a uniform temperature, and rolled to 12 mm thick plate in a 3-pass schedule. The samples were reheated to 540°C after each pass for 5 minutes to promote static recrystallisation and refine the grain structure.

4.2. Deformation testing

The hot plane strain compression tests were conducted using a Servotest Thermomechanical Compression Simulator (TMC) in the University of Sheffield, which is computer-controlled, equipped with servohydraulic test and motion simulation systems.

4.2.1 Samples

The samples for PSC deformation testing were cut perpendicular to the rolling direction. A thermocouple hole, 0.5 mm in diameter and 5 mm deep, was drilled into the centre of 60×10 mm^2 face, 10 mm away from the centre of deformation zone. The specimens were all hard chromium plated to minimize surface oxidation and interaction with glass lubricant prior to the tests. DAG2626 glass was painted on the deformation zones of the specimens as lubricant and allowed to dry before deformation. Before testing, the samples were painted with a single coat of water-based graphite lubricant, to minimize the effect of friction at the interface between the specimen and tools.

4.2.2 Plane strain compression testing

Prior thermal cycle and test conditions for plane strain compression were chosen to simulate the last stages of industrial tandem mill rolling, as suggested by Alcan. PSC specimens were reheated to a temperature of 560°C for 1200 seconds, and then water mist quenched to test temperature 320°C, deformed at a constant true strain rate of 85 s^{-1} to an initial strain of 0.5, unloaded and held for delay times of 0.019, 6, 60, 600 and 6000 seconds, then second deformed to a strain of 0.5, followed by an immediate water quench to room temperature (quench time <1s) (as shown in Fig. 4.1). The actual PSC testing was performed by Mr D Manville, the technician responsible for the machine, as is the standard practice in the Department. A final year project was run in parallel with the current work at the start of the project, with the objective of analyzing the constitutive equations for the hot deformation of this alloy. The output of this project, by Mr M Cross, is briefly summarized in the Appendix. Thus, the microstructural analysis performed in the current work can be used directly in combination with the constitutive analysis undertaken by Mr Cross.

4.3 Microscopic techniques

Investigation of the grain structure, crystallographic texture, dislocation substructure and precipitation was undertaken in the deformed areas of PSC specimens, using light microscopy, electron backscattered diffraction (EBSD) and transmission electron microscopy (TEM) techniques. All samples were cut from the PSC specimen using a Struers Accutom-5 cutting machine.

4.3.1 Optical metallography and Electron Backscattered Diffraction

The specimens for optical metallography and EBSD were polished using the diamond paste with particle size 6 μm then 1 μm and then given a final polishing with colloidal silica suspension. The sample was prepared by the electropolishing method, using 30% nitric and 70% methanol at 12 volts and -15°C cooled by liquid nitrogen.

- **Optical microscopy**

The image grabbing and analysis were performed on a POLYVAR and standard image analysis routines were undertaken on digitised images using commercial software KS Run 3.0 Analyser.

- **EBSD**

The sample for EBSD was prepared from the PSC specimens, the dimensions of which were about 10×10×5 mm^3. High resolution EBSD was acquired using an FEI Sirion field emission gun FEGSEM equipped with a HKL Nordlys camera.

- **EBSD software**

The corresponding data acquisition and processing were carried out using the HKL Channel 5 software. Crystallographic texture was represented using the orientation distribution function (ODF) in the Euler space. This function was calculated in the Channel 5 software via superimposing Gaussian spreads of half-width of 10° on the measured individual orientations. Some post-processing of the data was also performed using the VMAP software package, kindly provided by Professor Humphreys from the University of Manchester, which includes a modified Kuwahara filter routine for orientation averaging. Using this software, five Kuwahara filter passes were systematically applied on a given orientation map and both the mean subgrain diameter and the misorientaion angle values were determined using a linear intercept method, disregarding all the boundaries having misorientations below 0.5°. Note that unrealistically low subgrain dimensions were generally obtained without the application of the Kuwahara filter routine owing to a relatively high orientation noise. The VMAP software also provided a rough estimate of the stored energy values, based on a calculation of the overall sub-boundary energy. As the above calculation simultaneously takes into account both the subgrain size and the misorientation angle data, it was convenient to use stored energy values for illustrating relative differences between selected regions in the microstructure.

4.3.2 Transmission Electron Microscopy

4.3.2.1 Specimen preparation

Thin slices were cut off from transverse plane of the deformed PSC specimen of thickness approximately 4mm. The slices were ground to a thickness of less than 0.5mm and then punched to get 3 mm diameter discs. The discs were ground on a sequence of abrasive papers from coarse-to-fine, finalizing on 1200 grit until the thickness was less than 100 um and thoroughly cleaned using acetone solution. Finally the clean discs were electro-polished using a Struers Tenupol-2 electropolisher operating at a voltage of

15V. The electrolyte used was a 25vol.% nitric acid and 75vol.% methanol solution cooled with liquid nitrogen to a temperature of -15°C. The electropolished specimens were then washed in methanol. Conventional TEM was undertaken using a Philips 420 operating at 120 kV. High Resolution Electron Microscopy (HREM) was performed on a Jeol 2010F with an accelerating voltage of 200 kV and a Field Emission Gun, also equipped with a GATAN Imaging Filter (GIF) and the images were recorded with a Gatan the slow-scan CCD camera included with the GIF.

5. RESULTS

5.1 The evaluation of stress-strain curves

The flow stress curves of the interrupted deformation test ID1-ID5 are shown in Fig. 5.1, in which the double hit deformation conditions were at 320°C and a constant true strain rate of $85s^{-1}$ to a strain of 0.5. The only variable between each test is the deformation interruption time. The test ID1, with an almost instantaneous interruption time of 0.019 seconds, was taken as the reference test, from which the other tests and their associated interruption behaviour are compared. All of the flow stress curves revealed no peak stress with increasing strain. On reloading at a strain of 0.5, significant hardening was observed for delay times of 6 and 60 seconds samples, whilst minimal hardening was observed for the instantaneous and 600 seconds samples. The 6000 seconds delayed sample showed appreciable softening. Fig. 5.2 shows the corresponding softening curve as a function of deformation interruption time. The plot shows that with an instantaneous interruption time there is no softening or hardening, as expected. Maximum hardening was after a 6 seconds delay, decreasing only slightly for the test with a 60 seconds interruption. Hardening is negligible for a 600 seconds interruption, and at the longer time of 6000 seconds substantial softening is observed. The true ultimate strains for the double hit deformation shown in Fig. 5.1 are listed in Table 4.3.

5.2 Grain structure and crystallographic texture after the single deformation

5.2.1 Grain structure

The optical micrographs of the deformed structure in the rolling plane and transverse planes after the single deformation, which was deformed at a constant strain rate of 85 s^{-1} to an initial strain 0.5, are shown in Fig. 5.3a and b. There are homogeneously distributed spherical Al/Si/Cu/Mn-constituent particles formed within the grains and rod-shaped coarse particles at the grain boundaries, in which the length of some particles is over 1 μm. Also present were particles formed in the matrix which were smaller than those formed at grain boundaries. Fig. 5.3b shows some boundaries formed within the particle-free zones (PFZs) with the block structure. Meanwhile, the zones cross the grain boundaries, indicating that the boundaries moved after the PFZs was formed, but apparently without influencing the shape of the rod-shaped particles at

the grain boundaries. The morphology of the particle-free zones indicated that they were formed before the single deformation.

5.2.2 Crystallographic texture

Fig. 5.4 gives the EBSD orientation and texture maps, with an area of 5140μm×2540μm (as shown in Table 5.1), generated by the Channel 5 software. Fig. 5.4a shows an orientation map of the single deformed sample, in which boundaries have been drawn in different colours, according to the disorientation angle. The colours green, red and black denote the boundaries with the misorientation angle ranges of 5-10°, 10-15° and above 15° respectively, shown in the figure legend. If not otherwise specified, all the following orientation maps generated using EBSD will all utilize the same legend throughout the thesis. The texture components directly related to the microstructure are shown in Fig. 5.4b. Different grain colours represent different texture components, as shown in the legend of this figure. Brown, red, yellow, blue, green, and white indicate the grains with orientations close to texture components S, Brass, Cube, Copper, Goss and Random, respectively. Subsequent texture maps will all use this same legend. Fig. 5.5a shows orientation distribution functions (ODF) maps. ODF representation was confined to the familiar subset of the Euler space with $0° \leq (\psi_1, \phi, \psi_2) \leq 90°$ and ψ_2=constant. The texture changed from Brass {011}<112> and Goss {011}<100> ($\Phi 2=0°$), i.e. the α fibre, to Copper {112}<111>($\Phi 2=45°$), then S {123}<634>($\Phi 2=65°$), i.e. the β fibre with the Brass component, finally to the α fibre ($\Phi 2=90°$). They are all rolling texture components. Fig. 5.5b shows the misorientation angle distribution, which indicates that the misorientation angles concentrate in lower angle region.

The EBSD orientation and texture maps, with an area of 5328μm×1672μm, generated from the transverse plane, as shown in Figs. 5.6a and b. Fig 5.7a shows orientation distribution functions (ODF) maps. The texture changed from the α fibre, to the β fibre, finally to the α fibre. The same is true in Fig. 5.5, for the normal plane. Also, the rotated Cube component was observed. Fig. 5.7b shows the misorientation angle distribution, which indicates that the misorientation angles concentrate in lower angle region.

Fig. 5.8a and b show the orientation intensity of the α and β fibres within the normal and transverse planes. In the α fibre, the density of the Goss and Brass components within the normal plane is higher than from the transverse plane. In the β

fibre the intensity within the normal plane is higher than that within the transverse plane. The intensity of the S component is higher than the other components. The changes in the intensity in the normal plane are larger than in the transverse plane. Fig. 5.8c compares the misorientation angle distribution from the normal and transverse planes. The volume of low angle boundaries in the normal plane is higher than that in the transverse plane.

5.2.2.1 Random-oriented grain

The boundary map and ODF for a randomly-oriented grain is presented in Fig. 5.9. The rotation axes in both the sample and crystal lattice coordinates for the randomly-oriented grain are shown in Fig. 5.9e and f respectively. When expressed in the sample coordinates (Fig. 5.9e), misorientation axes display some tendency to cluster around the transverse direction. Conversely, the misorientation axis distributions in the crystal lattice coordinate system (Fig. 5.9f) appear essentially random.

The randomly-oriented grains largely contained two families of approximately parallel extended large angle sub-boundaries, bounding elongated microbands subdivided into slightly elongated subgrains by shorter lower-angle transverse sub-boundaries (as shown in Fig. 5.10a and b). The sub-boundaries in the C direction are systematically aligned close to the {111} crystallographic slip plane traces and those in the D direction are about 30° to the {111} trace. Line scans were performed along lines C and D, which are parallel to each family of dislocation walls, indicated in Fig. 5.10a and the corresponding relative and cumulative misorientation distributions are shown in Fig. 5.10e f-j respectively. In the D direction the relative angular distributions also show the presence of large angle dislocation boundaries and the misorientation angles show a strong tendency to cumulate across the grain. The randomly-oriented grains observed in the single deformed sample largely showed no tendency to split into shear bands. Deformation banding is shown in Fig. 5.10b (arrowed). The line scans performed along the A and B showed that in these two regions the deformation bands were separated by some single high-angle boundaries (red boundaries in Fig. 5.10b) with the misorientation angles larger than 22° and 11°, respectively. The cumulative misorientation angle profile showed that two deformation bands rotated about 16° and 20° away from matrix as a result of the deformation. Regions b and B have a Cube orientation.

5.2.2.2 Copper-oriented grain

The texture component, boundary map and ODF for a Copper-oriented grain are presented in Fig. 5.11a and b. The rotation axes in both the sample and crystal lattice coordinates are shown in Fig. 5.11e and f respectively. When expressed in the sample coordinates (Fig. 5.11e) misorientation axes display some tendency to the transverse direction. Conversely, the misorientation axis distributions in the crystal lattice coordinate system (Fig. 5.11f) appear essentially random.

The Copper-oriented grains contained two families of approximately parallel extended large angle sub-boundaries, bounding elongated microbands (as shown in Fig. 5.12a and b). The sub-boundaries were aligned close to the {111} crystallographic slip plane traces. Line scans were performed along lines A and B, indicated in Fig. 5.12a and the corresponding relative and cumulative misorientation distributions are shown in Fig. 5.12d and f respectively. The Copper-oriented grains observed in the single deformed sample largely showed no tendency to split into shear bands. Deformation banding is shown in Fig. 5.12b (the arrows). The line scan performed along the line C showed that in this region the deformation bands were separated by some single high-angle boundaries (red boundaries in Fig. 5.12b) with the misorientation angles lager than 5°. The cumulative misorientation angle profile showed a rotation of about 7° away from the matrix as a result of the deformation.

5.2.2.3 S-oriented grain

The texture component and boundary map for an S-oriented grain are presented in Fig. 5.13a. This map was Kuwahara filtered, in which only the boundaries with misorientation angles larger than 7° are shown. The ODF map for this particular grain (as shown in Fig. 5.13b) shows an S texture characterized by a rather small orientation scatter. Pole figures and inverse pole figures are shown in Figure 5.13c and d respectively. The distributions of rotation axes in both sample and crystal lattice coordinates are shown in Fig. 5.13e and f respectively. When expressed in the sample coordinates, misorientation axes display some tendency to the transverse direction. Conversely, the misorientation axis distributions in the crystal lattice coordinate system appear essentially random.

The S-oriented grains contained one family of approximately parallel extended large angle sub-boundaries, bounding elongated microbands (as shown in Fig. 5.14a).

The sub-boundaries were aligned close to the {111} crystallographic slip plane traces. Line scans were performed along lines A and B, indicated in Fig. 5.14a and the corresponding relative and cumulative misorientation distributions are shown in Fig. 5.14b-e respectively. The S-oriented grains observed in the single deformed sample largely showed no tendency to split into shear bands. And three high angle boundaries showed in the A direction. The misorientation is larger than 5° and about 8° away from the matrix.

5.2.2.4 P-oriented grain

Similar to the case of the S-oriented grain, the texture component and boundary map for a P-oriented grain are presented in Fig. 5.15a. The boundary map was Kuwahara filtered. The ODF map for this grain (as shown in Fig. 5.15b) shows a P texture characterized by a rather small orientation scatter. Pole figures and inverse pole figures are shown in Fig. 5.15c and d respectively. The distributions of rotation axes in both sample and crystal lattice coordinates are shown in Fig. 5.15e and f respectively. When expressed in the sample coordinates, misorientation axes display some tendency to cluster around the sample transverse direction. Conversely, the misorientation axis distributions in the crystal lattice coordinate system appear essentially random. The arrangements of sub-boundaries show random and subdivided into equiaxed subgrains The P-oriented grain observed in the single deformed sample largely showed no tendency to split into microbands. Some randomly-oriented regions are shown in Fig. 5.15a.

Fig. 5.16a shows the relative map of the P-oriented grain. Line scans were performed along lines A and B, indicated in Fig. 5.16a. Fig. 5.16b-f show the relative and cumulative misorientation distributions of line scans performed along A and B in (a).

5.2.2.5 Brass-oriented grain

The texture component and boundary map for a Brass-oriented grain are presented in Fig. 5.17a. The ODF map for this grain (as shown in Fig. 5.17b) shows a typical Brass texture characterized by a rather small orientation scatter. Pole and inverse pole figures are shown in Fig. 5.17c and d respectively. The distributions of rotation axes in both sample and crystal lattice coordinates are shown in Fig. 5.17e and f respectively. When expressed in the sample coordinates, misorientation axes display some tendency to cluster around the sample transverse direction. Conversely, the misorientation axis

distributions in the crystal lattice coordinate system appear essentially random. A randomly-oriented region is shown in Fig. 5.17a.

The Brass-oriented grain contained one family of approximately parallel extended large angle sub-boundaries, bounding elongated microbands (as shown in Fig. 5.18a). The sub-boundaries in the B direction were about 15° to the {111} crystallographic slip plane traces. Line scans were performed along lines A and B, indicated in Fig. 5.18a and the corresponding relative and cumulative misorientation distributions are shown in Fig. 5.18b-e respectively. In the A direction, the relative angular distributions also show the presence of large angle dislocation boundaries and the misorientation angles show a strong tendency to cumulate with the distance. The Brass-oriented grains observed in the single deformed sample largely showed no tendency to split into shear bands.

5.2.2.6 Cube-oriented grain

The texture component and boundary map for a Cube-oriented grain is presented in Fig. 5.19a. The ODF for this grain (as shown in Fig. 5.19b) shows a typical Cube texture. Pole and inverse pole figures are shown in Fig. 5.19c and d respectively. The rotation axes in both the sample and crystal lattice coordinates are shown in Fig. 5.19e and f respectively. When expressed in the sample coordinates (Fig. 5.19e), misorientation axes display some tendency to the transverse direction. Conversely, the misorientation axis distributions in the crystal lattice coordinate system (Fig. 5.19f) appear essentially random. A randomly-oriented region was present in the centre of the Cube grain.

Fig. 5.20a shows the relative map of the Cube-oriented grain. Line scans were performed along lines A and B, indicated in Fig. 5.20a. Fig. 5.20b- f show the relative and cumulative misorientation distributions of line scans performed along A and B in (a). The arrangements of sub-boundaries show random and subdivided into equiaxed subgrains. Deformation banding is shown in Fig. 5.20a (arrowed) and the corresponding line scan performed along the C showed that in this region the deformation bands were separated by some single high-angle boundaries (black boundaries in Fig. 5.20a) with the misorientation angles larger than 25°. The cumulative misorientation angle profile showed the rotation of about 25° away from the matrix as a result of the deformation. A random oriented region exhibits in this band.

5.2.2.7 Goss-oriented grain

UNIVERSITY OF SHEFFIELD LIBRARY

The texture component and boundary map for a Goss-oriented grain is presented in Fig. 5.21a. The ODF for this grain (as shown in Fig. 5.21b) shows a typical Goss texture. Pole and inverse pole figures are shown in Fig. 5.21c and d respectively. The rotation axes in both the sample and crystal lattice coordinates are shown in Fig. 5.21e and f respectively. When expressed in the sample coordinates (Fig. 5.21e), misorientation axes display some tendency to the transverse direction. Conversely, the misorientation axis distributions in the crystal lattice coordinate system (Fig. 5.21f) appear essentially random.

The Goss-oriented grains largely contained two families of approximately parallel extended large angle sub-boundaries, bounding elongated microbands (as shown in Fig. 5.22a). The sub-boundaries in the B direction were about 15° to the {111} crystallographic slip plane traces. Line scans were performed along lines A and B, indicated in Fig. 5.22a and the corresponding relative and cumulative misorientation distributions are shown in Fig. 5.22b-e respectively. The Goss-oriented grains observed in the single deformed sample largely showed no tendency to split into shear bands. The region near the grain boundary was Goss oriented, while the lattice curvature away from the boundary resulted in the area being marked as randomly oriented by the software from the texture component.

5.2.2.8 Deformation banding

Fig. 5.23 shows a grain split into deformation bands, separated by two transition bands. A line scan performed along the line D showed that in this region the deformation bands were separated by some single high-angle boundaries with the misorientation angles lager than 40° (Fig. 5.23c). The cumulative misorientation angle profile showed the rotation of about 45° away from the matrix as a result of the deformation (see Fig. 5.23d). Fig. 5.23 e shows a {100} pole figure for the deformation bands and matrix. The misorientation axes with angle ranges of 10-65° is expressed in sample coordinates, shown in Fig. 5.23 f. The misorientation axes tend to cluster around the transverse direction. The deformation bands contained elongated micobands. The sub-boundaries were all found to be systematically aligned close to the {111} crystallographic slip plane traces.

Table 5.3 shows the mean subgrain size (D), misorientation angle (°) and Θ/d in the single deformed condition. The highest misorientation of the oriented grains is the Cube

and the lowest is the Goss grain.

5.2.3 TEM of deformation structure

Fig. 5.24 gives the bright and dark field TEM images that show a cell-block structure with dislocation boundaries, imaged with the beam close to [110]. Fig. 5.25a shows the dislocation structure within the block, resolving individual dislocations with in the boundary and a dislocation network formed near the triple junctions region. Fig. 5.25b shows the Al/Si/Cu/Mn particles.

5.3 Instantaneous deformation

5.3.1 Grain structure

Fig. 5.26a shows optical micrographs of the deformed structure after the instantaneous deformation. There are homogeneously distributed sphere-shaped particles formed within the grains and rod-shaped coarse particles at the grain boundaries, with the length of some particles over 1 μm. As expected, the average particle size of those formed in matrix was smaller than those formed at grain boundaries. Fig. 5.26a shows particle-free zones (PFZs), with the block structure. As with the sample deformed in one step, the PFZs cross the grains boundaries, indicating that the boundaries moved after the PFZ was formed, but apparently without influencing the shape of the rod-shaped particles at the grain boundaries. Fig. 5.26b shows the structure from the transverse plane.

5.3.2 Crystallographic texture

Fig. 5.27a shows an orientation map obtained from a central area of the longitudinal section of the PSC sample which received instantaneous double hit deformed at 85 s^{-1} to a strain of 0.5. Fig. 5.27a shows the same microstructural character as shown in the optical micrograph (see Fig. 5.26a) but for a larger area, where greater detail of the boundary structures can be seen. A distribution of grain areas corresponding to the main texture components, highlighted by different colours on the map from Fig. 5.27a, is shown in Fig. 5.27b. These observed crystallographic texture components are also illustrated in Fig. 28a, expressed by the ODF. The texture changed from Brass {011}<112> and Goss {011}<100> ($\Phi 2=0°$), i.e. the α fibre, to Copper {112}<111>($\Phi 2=45°$), then S {123}<634>($\Phi 2=65°$), i.e. the β fibre with Brass component, finally to the α fibre ($\Phi 2=90°$). They are all rolling texture components. Fig.

5.28b shows the misorientation angle distribution, which indicates that the misorientation angles concentrate in lower angle region.

The EBSD orientation map, with an area of 5520μm×2024μm, generated from the transverse direction in Fig. 5.29. Fig. 5.30a shows orientation distribution functions (ODF) maps. The texture changed from an α fibre, to a β fibre, finally to an α fibre. The same is true in Fig. 5.27, for the normal direction. Fig. 5.30b shows the misorientation angle distribution, which indicates that the misorientation angles concentrate in lower angle region.

Fig. 5.31a and b show the orientation intensity of the α and β fibres within the normal and transverse planes. In the α fibre, the intensity of the Goss and Brass components within the transverse plane is higher than from the normal plane. In the β fibre the intensity within the transverse plane is almost on the same level. The intensity of the S component is higher than the other components in the normal plane. The changes in the intensity in the normal plane are larger than in the transverse plane. Fig. 5.31c compares the misorientation angle distribution from the normal and transverse planes. The volume of low angle boundaries in the transverse plane is higher than in the normal plane.

5.3.2.1 Random-oriented grain

The boundary map and ODF for a randomly-oriented grain are presented in Fig. 5.32a and b. The rotation axes in both the sample and crystal lattice coordinates for the randomly-oriented grain are shown in Fig. 5.32e and f respectively. When expressed in the sample coordinates (Fig. 5.32e), misorientation axes display some tendency to cluster around the rolling direction. Conversely, the misorientation axis distributions in the crystal lattice coordinate system (Fig. 5.32f) appear essentially random.

The randomly-oriented grains contained one family of approximately parallel extended large angle sub-boundaries, bounding elongated microbands (as shown in Fig. 5.33a). The sub-boundaries were found to be aligned close to the {111} crystallographic slip plane traces. Line scans were performed along lines A and B, indicated in Fig. 5.33a the corresponding relative and cumulative misorientation distributions are shown in Fig. 5.33b-e respectively. The relative angular distributions also show the presence of large angle dislocation boundaries and the misorientation angles do not show strong tendency to cumulate across the grain. The randomly-oriented grains observed in the

instantaneous deformed sample largely showed no tendency to split into shear bands or deformation banding.

5.3.2.2 S-oriented grain

The texture component and boundary map for an S-oriented grain is presented in Fig. 5.34a. The ODF for this grain (as shown in Fig. 5.34b) shows a typical S texture characterized by a relatively small orientation scatter. Pole and inverse pole figures are shown in Fig. 5.34 c and d respectively. The rotation axes in both the sample and crystal lattice coordinates are shown in Fig. 5.34e and f respectively. When expressed in the sample coordinates (Fig. 5.34e), misorientation axes display some tendency to the rolling direction. Conversely, the misorientation axis distributions in the crystal lattice coordinate system (Fig. 5.34f) appear essentially random.

The S-oriented grains contained one family of approximately parallel extended large angle sub-boundaries, bounding elongated microbands (as shown in Fig. 5.35a). The sub-boundaries in the B direction were about 5° to the {111} crystallographic slip plane traces. Line scans were performed along lines A and B, indicated in Fig. 5.35a and the corresponding relative and cumulative misorientation distributions are shown in Fig. 5.35b-e respectively. The S-oriented grains observed from the instantaneous deformed sample largely showed no tendency to split into shear bands or deformation banding.

5.3.2.3 P-oriented grain

The texture component and boundary map for a P-oriented grain is presented in Fig. 5.36a. The ODF for this grain (as shown in Fig. 5.36b) shows a P texture characterized by a relatively small orientation scatter. Pole and inverse pole figures are shown in Fig. 5.36c and d respectively, while the rotation axes in both the sample and crystal lattice coordinates are shown in Fig. 36e and f. When expressed in the sample coordinates (Fig. 5.36e), misorientation axes display some tendency to the rolling direction. Conversely, the misorientation axis distributions in the crystal lattice coordinate system (Fig. 5.36f) appear essentially random.

The P-oriented grains contained one family of approximately parallel extended large angle sub-boundaries, bounding elongated microbands (as shown in Fig. 5.37a). The sub-boundaries in the B direction were about 8° to the {111} crystallographic slip plane traces. Line scans were performed along lines A and B, indicated in Fig. 5.37a and

the corresponding cumulative misorientation distributions in Fig. 5.37b-e respectively. In the A direction, the relative angular distributions also show the presence of large angle dislocation boundaries and the misorientation angles show a strong tendency to cumulate with the distance. The P-oriented grains observed in the instantaneous deformed sample largely showed no tendency to split into shear bands or deformation banding.

5.3.2.4 Brass-oriented grain

The texture component and boundary map for a Brass-oriented grain is presented in Fig. 5.38a. The ODF for this grain (as shown in Fig. 5.38b) shows a typical Brass texture characterized by a relatively small orientation scatter. Pole and inverse pole figures are shown in Fig. 5.38c and d respectively. The rotation axes in both the sample and crystal lattice coordinates are shown in Fig. 5.38e and f respectively. When expressed in the sample coordinates (Fig. 5.38e), misorientation axes display some tendency to cluster around the rolling direction. Conversely, the misorientation axis distributions in the crystal lattice coordinate system (Fig. 5.38f) appear essentially random.

The Brass-oriented grains contained one family of approximately parallel extended large angle sub-boundaries, bounding elongated microbands (as shown in Fig. 5.39a). The sub-boundaries in the B direction were about 8° to the {111} crystallographic slip plane traces. Line scans were performed along lines A and B, indicated in Fig. 5.39a and the corresponding relative and cumulative misorientation distributions are shown in Fig. 5.39b-e respectively. The Brass-oriented grains observed in the instantaneous deformed sample largely showed no tendency to split into shear bands or deformation banding.

5.3.2.5 Cube-oriented grain

The texture component and boundary map for a Cube-oriented grain is presented in Fig. 5.40a. The ODF map for this grain (as shown in Fig. 5.40b) shows a Cube texture. Pole and inverse pole figures are shown in Fig. 5.40c and d respectively. The distributions of rotation axes in both sample and crystal lattice coordinates are shown in Fig. 5.40e and f respectively. When expressed in the sample coordinates, misorientation axes display some tendency to the rolling direction. Conversely, the misorientation axis distributions in the crystal lattice coordinate system appear essentially random.

Fig. 5.41a shows the relative map of the Cube-oriented grain. Line scans were performed along lines A and B, indicated in Fig. 5.41a. Fig. 5.41b-f show the relative and cumulative misorientation distributions of line scans performed along A and B in (a).

5.3.2.6 Goss-oriented grain

The texture component and boundary map for a Goss-oriented grain are presented in Fig. 5.42a. The ODF for this grain (as shown in Fig. 5.42b) shows a typical Goss texture. Pole and inverse pole figures are shown in Fig. 5.42c and d respectively. The rotation axes in both the sample and crystal lattice coordinates are shown in Fig. 5.42e and f respectively. When expressed in the sample coordinates (Fig. 5.42e), misorientation axes display some tendency to the rolling direction. Conversely, the misorientation axis distributions in the crystal lattice coordinate system (Fig. 5.42f) appear essentially random.

The Goss-oriented grains contained one family of approximately parallel extended large angle sub-boundaries, bounding elongated microbands (as shown in Fig. 5.43a). The sub-boundaries in the A direction were about 15° to the {111} crystallographic slip plane traces. Line scans were performed along lines A and B, indicated in Fig. 5.43a and the corresponding relative and cumulative misorientation distributions in Fig. 5.43b-e respectively. The Goss-oriented grains observed from the instantaneous deformed sample largely showed no tendency to split into shear bands or deformation banding, but the grain did contain some regions with a random orientation.

5.3.2.7 Deformation banding

Fig. 5.44 shows two grains containing deformation bands near the grain boundaries, separated by transition bands, composed of either narrow high-angle or wide diffuse low-angle boundaries, of widths that varied from region-to-region. Along the transition region between the deformation bands labelled A, larger-angle boundaries (above 5°) can be seen, locally even exceeding 60° (black line) and the corresponding line scan performed along the A showed that in this region the deformation bands were separated by a single high-angle boundary with the misorientation angles larger than 10° (see Fig. 5.44c). The cumulative misorientation angle profile showed a rotation of about 20° away from the matrix as a result of the deformation (see Fig. 5.44d). A line scan performed along the B showed that in this region the deformation bands were separated by some single high-angle boundaries with the misorientation angles larger than 10°

(Fig. 5.44d). The cumulative misorientation angle profile showed that two deformation bands rotated about 20° away from the matrix as a result of the deformation (see Fig. 5.44e).

Another example of deformation bands is shown in Fig. 5.45a, separated by the regions having large angle (>50°) boundaries. Relative misorientation angle profile of a line scan performed along the A (Fig. 5.45c) reveals these larger-angle boundaries in both transition regions. Cumulative misorientation angle profile of line scan performed along the A (Fig. 5.45d) shows that the misorientation angles are accumulated across the first transition region and decrease back to the angle nearly equal to the starting point when across the second transition region. The misorientation axes with angle ranges of 10-65° are expressed in sample coordinate respectively, shown in Fig. 5.45e. The misorientation axes tend to cluster around the rolling direction. The transition regions exhibit a P texture with a random orientation in the matrix.

Table 5.4 shows the mean subgrain size (D), misorientation angle (°) and Θ/d in the instantaneous deformed sample. The highest misorientation of the oriented grains is the Cube and the lowest is the S grain.

5.3.3 TEM of the substructure

5.3.3.1 Deformation substructure

Figs. 5.46 and 5.47 show the microband structure. Fig. 5.49 shows a well-developed cell-block structure delineated by the dense dislocation walls (DDWs) and microbands (MBs) which have a preferential direction parallel with the trace of (111) plane. Fig. 5.48 shows the grain boundary offsets at DDW/MB-grain boundary intersections, imaged with the beam close to [110]. Fig. 5.50 shows the cell-structure with dense tangled dislocation between DDWs. imaged with the beam close to [110] and g=(00-1).

5.3.3.2 Precipitates

Fig. 5.51 shows the particle size analysis in the instantaneous sample. The mean length of the particles is 340±80 nm, mean width is 130±50 nm. The EDS spectrum indicated the presence of Al/Si/Cu/Mn particles, and the particles were believed to have formed before the double hit deformation. Fig. 5.52, imaged with g=(001) shows some small phases formed on dislocations within the grain, considering the shape, they are likely to be coherent β'' and small Q phases, although the fine dimensions prevented a

positive identification.

5.4 6 seconds delay sample

5.4.1 Grain structure

Figs. 53a and b show optical micrographs of the deformed structure in the 6 seconds interruption time sample. There are homogeneously distributed particles formed within the grains and at the grain boundaries, with the length of some particles > 1 μm. Also shows that the particles formed in matrix are smaller than those formed at grain boundaries. Fig. 53b shows the grain structure from the transverse plane.

5.4.2 Crystallographic texture

Fig. 5.54 shows an orientation and texture map within the normal plane after the 6 seconds delay double hit deformation. Fig. 5.55a shows ODF maps. The texture is Brass {011}<112> and Goss {011}<100> (Φ2=0°), i.e. the α fibre, to Copper {112}<111>(Φ2=45°), then S {123}<634>(Φ2=65°), i.e. the β fibre with the Brass component, finally to the α fibre (Φ2=85°). Fig. 5.55b shows the misorientation angle distribution, which indicates that the misorientation angles concentrate at lower angles.

Fig. 5.56 shows the EBSD orientation and texture maps, with an area of 5520μm×1840μm, which were generated from the transverse direction. Fig 5.57a shows orientation distribution functions (ODF) maps. The texture changed from the α fibre to the β fibre, finally to the α fibre. The same is true in Fig. 5.54, for the normal direction. Fig. 5.57b shows the misorientation angle distribution, which indicates that the misorientation angles concentrate in lower angle region.

Figs. 5.58a and b show the orientation intensity of the α and β fibres within the normal and transverse planes. In the α fibre, the density of the Goss component within the normal plane is higher than in the transverse plane. In the β fibre, the intensity within the normal plane is higher than within the transverse plane. The changes in the intensity in the transverse plane is larger than in the normal plane. Fig. 5.58c compares the misorientation angle distribution from the normal and transverse planes. The number of low angle boundaries in the transverse plane is higher than in the normal plane.

5.4.2.1 Random-oriented grain

The texture component and boundary map for a randomly-oriented grain is presented in Fig. 5.59a. The ODF map for this particular grain (as shown in Fig. 5.59b)

shows a random texture. Pole and inverse pole figures are shown in Fig. 5.59c and d respectively. The distributions of rotation axes in both sample and crystal lattice coordinates for the randomly-oriented grain are shown in Fig. 5.59e and f respectively. When expressed in the sample coordinates, misorientation axes display some tendency to about 10° to the sample transverse direction. Conversely, the misorientation axis distributions in the crystal lattice coordinate system appear essentially random.

The randomly-oriented grains contained two families of approximately parallel extended large angle sub-boundaries, bounding elongated microbands (as shown in Fig. 5.60a). Line scans were performed along lines A and B, which are parallel to each family of dislocation walls, indicated in Fig. 5.60a and the corresponding relative and cumulative misorientation distributions are shown in Fig. 5.60b-e respectively. The relative angular distributions also show the presence of large angle dislocation boundaries and the misorientation angles show a strong tendency to cumulate across a grain. The randomly-oriented grains observed in the 6 seconds delayed sample showed no tendency to split into shear bands.

5.4.2.2 Copper-oriented grain

The texture component and boundary map for a Copper-oriented grain is presented in Fig. 5.61a. The ODF map for this grain (as shown in Fig. 5.61b) shows a Copper texture. Pole and inverse pole figures were shown in Fig. 5.61c and d respectively. The distributions of rotation axes in both sample and crystal lattice coordinates are shown in Fig. 5.61e and f respectively. When expressed in the sample coordinates, misorientation axes display some tendency to about 10° to the transverse direction. Conversely, the misorientation axis distributions in the crystal lattice coordinate system appear essentially random.

The Copper-oriented grains contained one family of approximately parallel extended large angle sub-boundaries, bounding elongated microbands (as shown in Fig. 5.62a). Line scans were performed along lines A and B, indicated in Fig. 5.62a and the corresponding relative and cumulative misorientation distributions are shown in Fig. 5.62b-e respectively. The Copper-oriented grains observed in the 6 seconds delayed sample largely showed no tendency to split into shear bands.

5.4.2.3 S-oriented grain

The texture component and boundary map for an S-oriented grain is presented in Fig. 5.63a. The ODF map for this grain (as shown in Fig. 5.63b) shows an S texture. Pole and inverse pole figures are shown in Fig. 5.63c and d respectively. The distributions of rotation axes in both sample and crystal lattice coordinates for the S-oriented grain are shown in Fig. 5.63e and f respectively. When expressed in the sample coordinates, misorientation axes display some tendency to the transverse direction. Conversely, the misorientation axis distributions in the crystal lattice coordinate system appear essentially random.

The S-oriented grains contained one family of approximately parallel extended large angle sub-boundaries, bounding elongated microbands (as shown in Fig. 5.64a). Line scans were performed along lines A and B, indicated in Fig. 5.64a and the corresponding relative and cumulative misorientation distributions are shown in Fig. 5.64b-e respectively. The S-oriented grains observed in the 6 seconds delayed sample largely showed no tendency to split into shear bands.

5.4.2.4 P-oriented grain

The texture component and boundary map for a P-oriented grain is presented in Fig. 5.65a. The ODF map for this grain (as shown in Fig. 5.65b) shows a P texture. Pole and inverse pole figures are shown in Fig. 5.65c and d respectively. The distributions of rotation axes in both sample and crystal lattice coordinates are shown in Fig. 5.65e and f respectively. When expressed in the sample coordinates, misorientation axes display some tendency to about 15° to the sample transverse direction. Conversely, the misorientation axis distributions in the crystal lattice coordinate system appear essentially random.

The P-oriented grains largely contained two families of approximately parallel extended large angle sub-boundaries, bounding elongated microbands (as shown in Fig. 5.66a). Line scans were performed along lines A and B, indicated in Fig. 5.66a and the corresponding relative and cumulative misorientation distributions are shown in Fig. 5.66b-e respectively. The relative angular distributions also show the presence of large angle dislocation boundaries and the misorientation angles show a strong tendency to cumulate across a grain. The P-oriented grains observed in the 6 seconds delayed deformed sample largely showed no tendency to split into shear bands.

5.4.2.5 Brass-oriented grain

The texture component and boundary map for a Brass-oriented grain is presented in Fig. 5.67a. The ODF map for this grain (as shown in Fig. 5.67b) shows a Brass texture. Pole and inverse pole figures are shown in Fig. 5.67c and d respectively. The distributions of rotation axes in both sample and crystal lattice coordinates are shown in Fig. 5.67e and f respectively. When expressed in the sample coordinates, misorientation axes display some tendency to cluster around the sample transverse direction. Conversely, the misorientation axis distributions in the crystal lattice coordinate system appear essentially random.

Fig. 5.68a shows the relative map of the Brass-oriented grain. Line scans were performed along lines A and B, indicated in Fig. 5.68a. Fig. 5.68b-f show the relative and cumulative misorientation distributions of line scans performed along A and B in (a).

5.4.2.6 Cube-oriented grain

The texture component and boundary map for a Cube-oriented grain is presented in Fig. 5.69a. The ODF map for this grain (as shown in Fig. 5.69b) shows a Cube texture. Pole and inverse pole figures are shown in Fig. 5.69c and d respectively. The distributions of rotation axes in both sample and crystal lattice coordinates are shown in Fig. 5.69e and f respectively. When expressed in the sample coordinates, misorientation axes display some tendency to cluster around the sample transverse direction. Conversely, the misorientation axis distributions in the crystal lattice coordinate system appear essentially random.

Fig. 5.70a shows the relative map of the Cube-oriented grain. Line scans were performed along lines A and B, indicated in Fig. 5.70a. Figure b-f show the relative and cumulative misorientation distributions of line scans performed along A and B in (a).

5.4.2.7 Deformation banding

A sample of deformation bands, as shown in Fig. 5.71a and b, separated by the regions having large angle (>35°) boundaries. Relative misorientation angles profile of a line scan performed along the A and B (Fig. 5.71c and e) reveals these larger-angle boundaries in both transition regions. The cumulative misorientation angle profile of line scan performed along the A and B (Fig. 5.71d and f) shows that the misorientation angles are accumulated across the first transition region and decrease back to the angle nearly equal to the starting point after crossing the second transition region. The

misorientation axes with angle ranges of 10-65° are expressed in sample coordinate respectively, shown in Fig. 5.71e. The misorientation axes tend to cluster around the transverse direction. The transition regions exhibit a random oriented region with an S texture in the matrix.

Table 5.5 shows the mean subgrain size (D), misorientation angle (°) and Θ/d in the 6 seconds delay sample. The misorientation of the oriented grains is no big different.

5.4.3 TEM of the substructure

5.4.3.1 Deformation substructure

Fig. 5.72 and 5.73 shows the microband structure bounded by the geometrically necessary boundaries (GNBs) which have a preferential direction close to parallel with the trace of (001) plane. The mean distance of the microbands is about 280±40 nm. Imaged with the beam close to [110]. Fig. 5.74 and 5.77 shows the dense tangled dislocations within the microbands. Imaged with the beam close to [110].

5.4.3.2 Precipitates

Figure 5.75 and 5.76 show some β' phases with rod-like shape in length direction and sphere-shape end-on views in the bright and dark field TEM micrograph and the corresponding $[110]_{Al}$ selected area diffraction pattern. The rods were typically 20 and 40nm long. The dark field image showed that the diameter of the round dots were in the range of 2 to 5 nm.

5.5 60 seconds delay sample

5.5.1 Grain structure

Fig. 5.78a shows optical micrographs of the deformed structure from the normal plane from the 60 seconds interrupted sample. There are homogeneously distributed sphere-shaped particles formed within grain and irregularly-shaped particles at the grain boundaries, with the length of some particles >1 μm. Also the particles formed in the matrix are smaller than those formed at grain boundaries. Fig. 5.78a shows some boundaries formed within particle-free zones. The PFZs show the block structure. Meanwhile, as with the previous samples, the zones cross the grains boundaries and apparently without influencing the shape of the rod-shaped particles at the grain boundaries. Fig. 5.78b shows the structure from the transverse plane.

5.5.2 Crystallographic texture

Fig. 5.79 shows the orientation and texture maps from the normal plane after the 60 seconds delay double hit deformation. Fig. 5.80a shows ODF maps. The texture changed from Brass {011}<112> and Goss {011}<100> ($\Phi 2=0°$), i.e. the α fibre, to Copper {112}<111>($\Phi 2=45°$), then S {123}<634>($\Phi 2=65°$), i.e. the β fibre with Brass component, finally to the α fibre ($\Phi 2=85°$). They are all rolling texture components. Fig. 5.80b shows the misorientation angle distribution, which indicates that the misorientation angles concentrate in lower angle region.

The EBSD orientation and texture maps, with an area of 5334μm×1864μm, generated from the transverse direction. Fig. 5.82a shows orientation distribution functions (ODF) maps. The texture changed from an α fibre, to a β fibre, finally to an α fibre. The same is true in Fig. 5.79, for the normal direction. Fig. 5.82 b shows the misorientation angle distribution, which indicates that the misorientation angles concentrate in the lower angle region.

Fig. 5.83a and b show the orientation intensity of the α and β fibres within the normal and transverse planes. In the α fibre, the density of the Goss component within the normal plane is higher than from the transverse plane. In the β fibre, the intensity within the normal plane is almost same as within the transverse plane. The intensity of the Brass component is higher than the other component. The changes in the intensity in the transverse plane is larger than in the normal plane. Fig. 5.83c compares the misorientation angle distribution from the normal and transverse planes. The volume of low angle boundaries in the normal plane is higher than in the transverse plane.

5.5.2.1 Random-oriented grain

The boundary and texture and ODF maps for a randomly-oriented grain are presented in Fig. 5.84a and b. The rotation axes in both the sample and crystal lattice coordinates for the randomly-oriented grain are shown in Fig. 5.84e and f respectively. When expressed in the sample coordinates (Fig. 5.84e), misorientation axes display some tendency to the transverse direction. Conversely, the misorientation axis distributions in the crystal lattice coordinate system (Fig. 5.84f) appear essentially random.

The randomly-oriented grains contained one family of approximately parallel

extended large angle sub-boundaries, bounding elongated microbands (as shown in Fig. 5.85a). The sub-boundaries were found to be aligned close to the {111} crystallographic slip plane traces. Line scans were performed along lines A and B, indicated in Fig. 5.85a and the relative and cumulative misorientation distributions are shown in Fig. 5.85b-e respectively. In the A direction, the relative angular distributions also show the presence of large angle dislocation boundaries and the misorientation angles do not show a strong tendency to cumulate across a grain. The randomly-oriented grains observed in the 60 seconds delayed sample largely showed no tendency to split into shear bands.

5.5.2.2 Copper-oriented grain

The texture component and boundary map for a Copper-oriented grain is presented in Fig. 5.86a. The ODF for this grain (as shown in Fig. 5.86b) shows a Copper texture characterized by a relatively small orientation scatter. Pole and inverse pole figures were shown in Fig. 5.86c and d respectively. The rotation axes in both the sample and crystal lattice coordinates are shown in Fig. 5.86e and f respectively. When expressed in the sample coordinates (Fig. 5.86e), misorientation axes display some tendency to 5° to the transverse direction. Conversely, the misorientation axis distributions in the crystal lattice coordinate system (Fig. 5.86f) appear essentially random.

The Copper-oriented grains contained two families of approximately parallel extended large angle sub-boundaries, bounding elongated microbands (as shown in Fig. 5.87a and b). The sub-boundaries were aligned close to the {111} crystallographic slip plane traces. Line scans were performed along lines A and B, indicated in Fig. 5.87 and the corresponding relative and cumulative misorientation distributions are shown in Fig. 5.87c-f respectively. The relative angular distributions also show the presence of large angle dislocation boundaries and the misorientation angles show strong tendency to cumulate across a grain. The Copper-oriented grains observed in the 60 seconds delayed sample largely showed no tendency to split into shear bands.

5.5.2.3 S-oriented grain

The texture component and boundary map for an S-oriented grain is presented in Fig. 5.88a. The ODF map for this grain (as shown in Fig. 5.88b) shows an S texture characterized by a rather small orientation scatter. Pole and inverse pole figures are shown in Fig. 5.88c and d respectively. The distributions of rotation axes in both sample and crystal lattice coordinates are shown in Fig. 5.88e and f respectively. When

expressed in the sample coordinates, misorientation axes display some tendency to the sample the transverse direction. Conversely, the misorientation axis distributions in the crystal lattice coordinate system appear essentially random.

The S-oriented grains contained one family of approximately parallel extended large angle sub-boundaries, bounding elongated microbands (as shown in Fig. 5.89a). The sub-boundaries were aligned close to the {111} crystallographic slip plane traces. Line scans were performed along lines A and B, indicated in Fig. 5.89a and the corresponding relative and cumulative misorientation distributions are shown in Fig. 5.89b-e respectively. The S-oriented grains observed in the 60 seconds delayed sample largely showed no tendency to split into shear bands.

5.5.2.4 P-oriented grain

The texture component and boundary map for a P-oriented grain is presented in Fig. 5.90a. The ODF for this grain (as shown in Fig. 5.90b) shows a P texture characterized by a relatively small orientation scatter. Pole and inverse pole figures are shown in Fig. 5.90c and d respectively. The rotation axes in both the sample and crystal lattice coordinates are shown in Fig. 5.90e and f respectively. When expressed in the sample coordinates (Fig. 5.90e), misorientation axes display some tendency to cluster around the transverse direction. Conversely, the misorientation axis distributions in the crystal lattice coordinate system (Fig. 5.90f) appear essentially random.

The P-oriented grains contained one family of approximately parallel extended large angle sub-boundaries, bounding elongated microbands (as shown in Fig. 5.91a). The sub-boundaries were all about 30° to the {111} crystallographic slip plane traces. Line scans were performed along lines A and B, indicated in Fig. 5.91a and the corresponding relative and cumulative misorientation distributions are shown in Fig. 5.91b-e respectively. The relative angular distributions also show the presence of large angle dislocation boundaries and the misorientation angles show strong tendency to cumulate with the distance. The P-oriented grains observed in the 60 seconds delayed sample largely showed no tendency to split into shear bands.

5.5.2.5 Brass-oriented grain

The texture component and boundary map for a Brass-oriented grain is presented in Fig. 5.92a. The ODF for this grain (as shown in Fig. 5.92b) shows a Brass texture

characterized by a relatively small orientation scatter. This scatter of orientations around the Brass texture components is also obvious from the corresponding pole and inverse pole figures, which are shown in Fig. 5.92c and d respectively. The rotation axes in both the sample and crystal lattice coordinates are shown in Fig. 5.92e and f respectively. When expressed in the sample coordinates (Fig. 5.92e), misorientation axes display some tendency to the transverse direction. Conversely, the misorientation axis distributions in the crystal lattice coordinate system (Fig. 5.92f) appear essentially random.

The Brass-oriented grains largely contained two families of approximately parallel extended large angle sub-boundaries, bounding elongated microbands (as shown in Fig. 5.93a). The sub-boundaries were aligned close to the {111} crystallographic slip plane traces. Line scans were performed along lines A and B, indicated in Fig. 5.93a and the corresponding relative and cumulative misorientation distributions are shown in Fig. 5.93b-e respectively. The Brass-oriented grains observed in the 60 seconds delayed sample largely showed no tendency to split into shear bands.

5.5.2.6 Cube-oriented grain

The texture component and boundary map for a Cube-oriented grain is presented in Fig. 5.94a. The ODF for this grain (as shown in Fig. 5.94b) shows a Cube texture. Pole and inverse pole figures are shown in Fig. 5.94c and d respectively. The rotation axes in both the sample and crystal lattice coordinates are shown in Fig. 5.94e and f respectively. When expressed in the sample coordinates (Fig. 5.94e), misorientation axes display some tendency to cluster around the transverse direction. Conversely, the misorientation axis distributions in the crystal lattice coordinate system (Fig. 5.94f) appear essentially random.

Fig. 5.95a shows the relative map of the Cube-oriented grain. Line scans were performed along lines A and B, indicated in Fig. 5.95a. Fig. 5.95b-f show the relative and cumulative misorientation distributions of line scans performed along A and B in (a).

5.5.2.7 Goss-oriented grain

The texture component and boundary map for a Goss-oriented grain is presented in Fig. 5.96a. The ODF for this grain (as shown in Fig. 5.96b) shows a Goss texture. Pole and inverse pole figures are shown in Fig. 5.96c and d respectively. The rotation axes in

both the sample and crystal lattice coordinates are shown in Fig. 5.96e and f respectively. When expressed in the sample coordinates (Fig. 5.96e), misorientation axes display some tendency to cluster around the transverse direction. Conversely, the misorientation axis distributions in the crystal lattice coordinate system (Fig. 5.96f) appear essentially random.

The Goss-oriented grains contained one family of approximately parallel extended large angle sub-boundaries, bounding elongated microbands (as shown in Fig. 5.97a and b). The sub-boundaries were aligned close to the {111} crystallographic slip plane traces. Line scans were performed along lines A and B, indicated in Fig. 5.97 and the corresponding relative and cumulative misorientation distributions are shown in Fig. 5.97c-f respectively. The Goss-oriented grains observed in the 60 seconds delayed sample largely showed no tendency to split into shear bands. A deformation banding labeled C and the corresponding relative and cumulative misorientation distributions are shown in Fig. 5.97g and h.

5.5.2.8 Deformation bands

Fig. 5.98 shows deformation bands, separated by the regions having large angle (>50°) boundaries. The relative misorientation angles profile of a line scan performed along the A (Fig. 5.98c) reveals these large angle boundaries in both transition regions and the corresponding cumulative misorientation angle profile of line scan performed along the A (Fig. 5.98d) shows that the misorientation angles are accumulated across the first transition region and decrease back to the angle nearly equal to the starting point when cross the second transition region. Fig. 5.98e shows the pole figure of the deformation banding.

Another sample of Fig. 5.99 also shows deformation bands, separated by the regions having large angle (>10°) boundaries. The relative misorientation angles profile of a line scan performed along the A (Fig. 5.99c) reveals these large angle boundaries in both transition regions and the corresponding cumulative misorientation angle profile of line scan performed along the A (Fig. 5.99d) shows that the misorientation angles are accumulated across the first transition region and decrease back to the angle nearly equal to the starting point when cross the second transition region.

Table 5.6 shows the mean subgrain size (D), misorientation angle (°) and Θ/d in the 60 seconds delay sample. The highest misorientation of the oriented grains is the Cube

and the lowest is the P grain.

5.5.3 TEM of the microstructure

5.5.3.1 Deformation substructure

Figs. 5.100 and 5.101 show a well-developed microband structure bounded by the geometrically necessary boundaries (GNBs) which have a preferential direction close to parallel with the trace of (1-11) plane. The mean distance of the microbands was measured at 280±40 nm. Imaged with the beam close to [110] (Fig. 5.101). Fig. 5.102 shows the dense tangled dislocations within the microbands. Imaged with the beam close to [001]. Fig. 5.103 show the lath shaped Q phases and dense dislocation within microbands. Imaged with g=(001).

5.5.3.2 Precipitates

Fig. 5.104 shows the coarser precipitates formed within the grains. Corresponding selected area diffraction pattern and the EDS spectrum confirm that the coarser precipitates were Q phase. Fig. 5.105 a and b show two types of precipitates formed on dislocation, lath-shaped and small rod-shaped, aligned along $<100>_{Al}$. The lath-shaped precipitates are identifiable by their rectangular end-on and long face-on views. Considering the shape and orientation, the small rod-shaped with sphere-shape end-on views and lath-shaped with rectangle-shape cross sections precipitates are identified as β' and small Q′ phases. Using only conventional TEM, no evidence for GP zones has been found. Fig. 5.106 and 5.107 show the small laths Q′ phase formed on subgrain boundary and in matrix, imaged with the g=(001).

5.6 600 seconds delay sample

5.6.1 Grain structure

Figs. 5.108a and b show optical micrographs of the deformed structure in the 600 seconds interruption time sample. There are homogeneously distributed sphere-shaped particles formed within grain and irregularly-shaped particles at the grain boundaries, with the length of some particles is over 1 μm. As expected, the particles formed in the matrix are smaller than those formed at grain boundaries.

5.6.2 Crystallographic texture

Fig. 5.109a and b show orientation and texture maps after the 600 seconds delay double hit deformation. Fig. 5.110a shows ODF maps. The texture is mainly composed

of Brass {011}<112> and Goss {011}<100> ($\Phi2=0°$) components, i.e. the α fibre, to Copper {112}<111>($\Phi2=45°$), then S {123}<634>($\Phi2=65°$), i.e. the β fibre with the Brass component, finally to the α fibre ($\Phi2=85°$). They are all rolling texture components. Fig. 5.110b shows the misorientation angle distribution, which indicates that the misorientation angles concentrate in the lower angle region.

The EBSD orientation map was generated from an area of 5328μm×1856μm of the transverse direction. Fig. 5.112a shows orientation distribution functions (ODF) maps. The texture changed from the α fibre, to the β fibre, finally to the α fibre. The same is true in Fig. 5.109, for the normal direction. Fig. 5.112b shows the misorientation angle distribution, which indicates that the misorientation angles concentrate in lower angle region.

Fig. 5.113a and b show the orientation intensity of the α and β fibres within the normal and transverse planes. In the α fibre, the intensity within the normal plane is significant match to that from the transverse plane. In the β fibre, the intensity within the transverse plane is higher than within the normal plane. Fig. 5.113c compares the misorientation angle distribution from the normal and transverse planes. The volume of low angle boundaries in the normal plane is higher than in the transverse plane.

5.6.2.1 Random-oriented grain

The texture component and boundary maps for a randomly-oriented grain are presented in Fig. 5.114a. The ODF for this grain (as shown in Fig. 5.114b) shows a random texture. Pole and inverse pole figures are shown in Fig. 5.114c and d respectively. The rotation axes in both the sample and crystal lattice coordinates for the randomly-oriented grain are shown in Fig. 5.114e and f respectively. When expressed in the sample coordinates (Fig. 5.114e), misorientation axes display some tendency to the transverse direction. Conversely, the misorientation axis distributions in the crystal lattice coordinate system (Fig. 5.114f) appear essentially random.

The randomly-oriented grains contained one family of approximately parallel extended large angle sub-boundaries, bounding elongated microbands (as shown in Fig. 5.115a). The sub-boundaries were aligned close to the {111} crystallographic slip plane traces. Line scans were performed along lines A and B, indicated in Fig. 5.115a and the corresponding relative and cumulative misorientation distributions are shown in Fig. 5.115b-e respectively. The randomly-oriented grains observed in the 600 seconds

delayed sample largely showed no tendency to split into shear bands.

5.6.2.2 Copper-orientated grain

The texture component and boundary map for a Copper-oriented grain is presented in Fig. 5.116a. The ODF for this grain (as shown in Fig. 5.116b) shows a Copper texture characterized by a relatively small orientation scatter. Pole and inverse pole figures are shown in Fig. 5.116c and d respectively. The rotation axes in both the sample and crystal lattice coordinates are shown in Fig. 5.116e and f respectively. When expressed in the sample coordinates (Fig. 5.116e), misorientation axes display some tendency to about 5° to the transverse direction. Conversely, the misorientation axis distributions in the crystal lattice coordinate system (Fig. 5.116f) appear essentially random.

The Copper-oriented grains contained one family of approximately parallel extended large angle sub-boundaries, bounding elongated microbands (as shown in Fig. 5.117a). The sub-boundaries were aligned close to the {111} crystallographic slip plane traces. Line scans were performed along lines A and B, indicated in Fig. 5.117a and the corresponding relative and cumulative misorientation distributions are shown in Fig. 5.117b-e respectively. The Copper-oriented grains observed in the 600 seconds delay sample largely showed no tendency to split into shear bands.

5.6.2.3 S-orientated grain

The texture component and boundary map for an S-oriented grain is presented in Fig. 5.118a. The ODF for this grain (as shown in Fig. 5.118b) shows an S texture characterized by a relatively small orientation scatter. Pole and inverse pole figures are shown in Fig. 5.118c and d respectively. The rotation axes in both the sample and crystal lattice coordinates are shown in Fig. 5.118e and f respectively. When expressed in the sample coordinates (Fig. 5.118e), misorientation axes display some tendency to about 5° to the transverse direction. Conversely, the misorientation axis distributions in the crystal lattice coordinate system (Fig. 5.118f) appear essentially random.

The S-oriented grains contained two families of approximately parallel extended large angle sub-boundaries, bounding elongated microbands (as shown in Fig. 5.119a). The sub-boundaries were aligned close to the {111} crystallographic slip plane traces. Line scans were performed along lines A and B, which are parallel to each family of dislocation walls, indicated in Fig. 5.119a and the corresponding relative and

cumulative misorientation distributions are shown in Fig. 5.119b-e respectively. The S-oriented grains observed in the 600 seconds delayed sample largely showed no tendency to split into shear bands. Another deformation banding is shown in Fig. 5.119a. Along the transition region between deformation bands labelled C, larger-angle boundaries (above 6°) can be seen, locally even exceeding 9°.

5.6.2.4 P-orientated grain

The texture component and boundary map for a P-oriented grain is presented in Fig. 5.120a. The ODF for this grain (as shown in Fig. 5.120b) shows a P texture characterized by a relatively small orientation scatter. Pole and inverse pole figures are shown in Fig. 5.120c and d respectively. The rotation axes in both the sample and crystal lattice coordinates are shown in Fig. 5.120e and f respectively. When expressed in the sample coordinates (Fig. 5.120e), misorientation axes display some tendency to cluster around the transverse direction. Conversely, the misorientation axis distributions in the crystal lattice coordinate system (Fig. 5.120f) appear essentially random.

The P-oriented grains contained one family of approximately parallel extended large angle sub-boundaries, bounding elongated microbands (as shown in Fig. 5.121a). The sub-boundaries were aligned close to the {111} crystallographic slip plane traces. Line scans were performed along lines A and B, indicated in Fig. 5.121a and the corresponding relative and cumulative misorientation distributions are shown in Fig. 5.121b-e respectively. In the A direction, the relative angular distributions also show the presence of large angle dislocation boundaries and the misorientation angles do not show strong tendency to cumulate across a grain. The P-oriented grains observed in the 600 seconds delay sample largely showed no tendency to split into shear bands.

5.6.2.5 Brass-orientated grain

The texture component and boundary map for a Brass-oriented grain is presented in Fig. 5.123a. The ODF for this grain (as shown in Fig. 5.123b) shows a Brass texture. Pole and inverse pole figures are shown in Fig. 5.123c and d respectively. The rotation axes in both the sample and crystal lattice coordinates are shown in Fig. 5.123e and f respectively. When expressed in the sample coordinates (Fig. 5.123e), misorientation axes display some tendency to about 5° to the transverse direction. Conversely, the misorientation axis distributions in the crystal lattice coordinate system (Fig. 5.123f) appear essentially random.

The Brass-oriented grains contained one family of approximately parallel extended large angle sub-boundaries, bounding elongated microbands (as shown in Fig. 5.124a). The sub-boundaries were aligned close to the {111} crystallographic slip plane traces. Line scans were performed along lines A and B, indicated in Fig. 5.124a and the corresponding relative and cumulative misorientation distributions are shown in Fig. 5.124b-e respectively. The Brass-oriented grains observed in the 600 seconds delay sample largely showed no tendency to split into shear bands.

5.6.2.6 Cube-orientated grain

The texture component and boundary map for a Cube-oriented grain is presented in Fig. 5.125a. The ODF for this grain (as shown in Fig. 5.125b) shows a Cube texture. Pole and inverse pole figures are shown in Fig. 5.125c and d respectively. The rotation axes in both the sample and crystal lattice coordinates are shown in Fig. 5.125e and f respectively. When expressed in the sample coordinates (Fig. 5.125e), misorientation axes display some tendency to cluster around the transverse direction. Conversely, the misorientation axis distributions in the crystal lattice coordinate system (Fig. 5.125f) appear essentially random.

The Cube-oriented grains largely contained one family of approximately parallel extended large angle sub-boundaries, bounding elongated microbands (as shown in Fig. 5.126a). The sub-boundaries were aligned about 15° to the {111} crystallographic slip plane traces. Line scans were performed along lines A and B, indicated in Fig. 5.126a and the corresponding relative and cumulative misorientation distributions are shown in Fig. 5.126b-e respectively. The Cube-oriented grains observed in the 600 seconds delay sample largely showed no tendency to split into shear bands.

5.6.2.7 Goss-orientated grain

The texture component and boundary map for a Goss-oriented grain is presented in Fig. 5.127a. The ODF for this grain (Fig. 5.127b) shows a Goss texture. Pole and inverse pole figures are shown in Fig. 5.127c and d respectively. The rotation axes in both the sample and crystal lattice coordinates are shown in Fig. 5.127e and f respectively. When expressed in the sample coordinates (Fig. 5.127e), misorientation axes display some tendency to cluster around the transverse direction. Conversely, the misorientation axis distributions in the crystal lattice coordinate system (Fig. 5.127f) appear essentially random.

The Goss-oriented grains largely contained two families of approximately parallel extended large angle sub-boundaries, bounding elongated microbands (as shown in Fig. 5.128a). The sub-boundaries were all found to be systematically aligned close to the {111} crystallographic slip plane traces. Line scans were performed along lines A and B, which are parallel to each family of dislocation walls, indicated in Fig. 5.128a and the corresponding relative and cumulative misorientation distributions are shown in Fig. 128b-e respectively. The Goss-oriented grains observed in the 600 seconds delay sample largely showed no tendency to split into shear bands.

5.6.2.8 Deformation banding

Fig. 5.129 shows a grain containing deformation bands separated by transition bands of widths that varied from region to region, which were composed of either narrow high-angle or wide diffuse low-angle boundaries. Along the transition region between deformation bands labelled A, larger-angle boundaries (above 40°) can be seen, locally even exceeding 50°. The Fig. 5.129d and e show the sample coordinate and 100 pole figure.

Table 5.7 shows the mean subgrain size (D), misorientation angle (°) and Θ/d in the 600 seconds delay sample. The highest misorientation of the oriented grains is the Cube and the lowest is the Brass grain.

5.7 6000 seconds delay sample

5.7.1 Grain structure

Fig. 5.130a and b show optical micrographs of the deformed structure in the 6000 seconds interruption time sample. There are homogeneously distributed sphere-shaped particles formed within grain and irregularly-shaped particles at the grain boundaries, with the length of some particles >1 μm. Also the particles formed in the matrix are smaller than those formed at grain boundaries. Fig. 5.130a shows some particle-free zones. The zones cross the grains boundaries indicating that the boundaries moved after the PFZs was formed as with previous samples, but apparently without influencing the shape of the rod-shaped particles at the grain boundaries.

5.7.2 Crystallographic texture

Fig. 5.131 shows orientation and texture maps after 6000 seconds delay double hit deformation. Fig. 5.132a shows ODF maps. The texture is mainly composed of Brass

{011}<112> and Goss {011}<100> (Φ2=0°), i.e. the α fiber, to Copper {112}<111>(Φ2=45°), then S {123}<634>(Φ2=65°), i.e. the β fiber with Brass component, finally to the α fiber (Φ2=85°). They are all rolling texture components. Fig. 5.132b shows the misorientation angle distribution, which indicates that the misorientation angles concentrate in lower angle region.

Fig. 5.134 gives an EBSD orientation map, with an area of 5328μm×1856μm, generated from the transverse direction. Fig. 5.134a shows orientation distribution functions (ODF) maps. The texture changed from the α fiber, to the β fiber, finally to the α fiber. The same is true in Fig. 5.131, for the normal direction. Fig. 5.134b shows the misorientation angle distribution, which indicates that the misorientation angles concentrate in lower angle region.

Fig. 5.135a and b show the orientation intensity of the α and β fibers within the normal and transverse planes. In the α fiber, the intensity of the Brass components within the transverse plane is higher than from the normal plane. In the β fiber, the intensity within the transverse plane is higher than within the normal plane. The changes in the intensity in the transverse plane is larger than in the normal plane. Fig. 5.135c compares the misorientation angle distribution from the normal and transverse planes. The volume of low angle boundaries in the normal plane is higher than in the transverse plane.

5.7.2.1 Random-oriented grain

The texture component and boundary map for a randomly-oriented grain is presented in Fig. 5.136a. The ODF map for this grain (as shown in Fig. 5.136b) shows a random texture. Pole and inverse pole figures are shown in Fig. 5.136c and d respectively. The distributions of rotation axes in both sample and crystal lattice coordinates for the randomly-oriented grain are shown in Fig. 5.136e and f respectively. When expressed in the sample coordinates, misorientation axes display some tendency to the sample transverse direction. Conversely, the misorientation axis distributions in the crystal lattice coordinate system appear essentially random.

The randomly-oriented grains contained one family of approximately parallel extended large angle sub-boundaries, bounding elongated microbands (as shown in Fig. 5.137a). The sub-boundaries were aligned close to the {111} crystallographic slip plane traces. Line scans were performed along lines A and B, indicated in Fig. 5.137a and the

corresponding relative and cumulative misorientation distributions are shown in Fig. 5.137b-e respectively. The randomly-oriented grains observed in the 6000 seconds delay sample largely showed no tendency to split into shear bands.

5.7.2.2 Copper-oriented grain

The texture component and boundary map for a Copper-oriented grain is presented in Fig. 5.138a. The ODF for this grain (as shown in Fig. 5.138b) shows a Copper texture characterized by a relatively small orientation scatter. Pole and inverse pole figures are shown in Fig. 5.138c and d respectively. The rotation axes in both the sample and crystal lattice coordinates are shown in Fig. 5.138e and f respectively. When expressed in the sample coordinates (Fig. 5.138e), misorientation axes display some tendency to the transverse direction. Conversely, the misorientation axis distributions in the crystal lattice coordinate system (Fig. 5.138f) appear essentially random.

The Copper-oriented grains contained one family of approximately parallel extended large angle sub-boundaries, bounding elongated microbands (as shown in Fig. 5.139a). The sub-boundaries were aligned close to the {111} crystallographic slip plane traces. Line scans were performed along lines A and B, indicated in Fig. 5.139a and the corresponding relative and cumulative misorientation distributions are shown in Fig. 5.139b-e respectively. The Copper-oriented grains observed in the 6000 seconds delay sample largely showed no tendency to split into shear bands.

5.7.2.3 S-orientated grain

The texture component and boundary map for an S-oriented grain is presented in Fig. 5.140a. The ODF for this grain (as shown in Fig. 5.140b) shows an S texture characterized by a relatively small orientation scatter. Pole and inverse pole figures are shown in Fig. 5.140c and d respectively. The rotation axes in both the sample and crystal lattice coordinates are shown in Fig. 5.140e and f respectively. When expressed in the sample coordinates (Fig. 5.140e), misorientation axes display some tendency to the transverse direction. Conversely, the misorientation axis distributions in the crystal lattice coordinate system (Fig. 5.140f) appear essentially random.

The S-oriented grains largely contained two families of approximately parallel extended large angle sub-boundaries, bounding elongated microbands (as shown in Fig. 5.141a). The sub-boundaries in the B direction were about 30° to the {111}

crystallographic slip plane traces. Line scans were performed along lines A and B, indicated in Fig. 5.141a and the corresponding relative and cumulative misorientation distributions are shown in Fig. 5.141b-e respectively. The S-oriented grains observed in the 6000 seconds delay sample largely showed no tendency to split into shear bands.

5.7.2.4 P-orientated grain

The texture component and boundary map for a P-oriented grain is presented in Fig. 5.142a. The ODF for this grain (as shown in Fig. 5.142b) shows a P texture characterized by a relatively small orientation scatter. Pole and inverse pole figures are shown in Fig. 5.142c and d respectively. The rotation axes in both the sample and crystal lattice coordinates are shown in Fig. 5.142e and f respectively. When expressed in the sample coordinates (Fig. 5.142e), misorientation axes display some tendency to cluster around the transverse direction. Conversely, the misorientation axis distributions in the crystal lattice coordinate system (Fig. 5.142f) appear essentially random.

The P-oriented grains largely contained two families of approximately parallel extended large angle sub-boundaries, bounding elongated microbands (as shown in Fig. 5.143a). The sub-boundaries were aligned close to the {111} crystallographic slip plane traces. Line scans were performed along lines A and B, indicated in Fig. 5.143a and the corresponding relative and cumulative misorientation distributions are shown in Fig. 5.143b-e respectively. The P-oriented grains observed in the 6000 seconds delay sample largely showed no tendency to split into shear bands.

5.7.2.5 Brass-orientated grain

The texture component and boundary map for a Brass-oriented grain is presented in Fig. 5.144a. The ODF for this grain (as shown in Fig. 5.144b) shows a Brass texture. Pole and inverse pole figures are shown in Fig. 5.144c and d respectively. The rotation axes in both the sample and crystal lattice coordinates are shown in Fig. 5.144e and f respectively. When expressed in the sample coordinates (Fig. 5.144e), misorientation axes display some tendency to the transverse direction. Conversely, the misorientation axis distributions in the crystal lattice coordinate system (Fig. 5.144f) appear essentially random.

The Brass-oriented grains contained one family of approximately parallel extended large angle sub-boundaries, bounding elongated microbands (as shown in Fig. 5.145a).

The sub-boundaries were aligned close to the {111} crystallographic slip plane traces. Line scans were performed along lines A and B, indicated in Fig. 5.145a and the corresponding relative and cumulative misorientation distributions are shown in Fig. 5.145b-e respectively. The Brass-oriented grains observed in the 6000 seconds delay sample largely showed no tendency to split into shear bands.

5.2.7.6 Cube-oriented grain

The texture component and boundary map for a Cube-oriented grain is presented in Fig. 5.146a. The ODF map for this grain (as shown in Fig. 5.146b) shows a Cube texture. Pole and inverse pole figures are shown in Fig. 5.146c and d respectively. The distributions of rotation axes in both sample and crystal lattice coordinates are shown in Fig. 5.146e and f respectively. When expressed in the sample coordinates, misorientation axes display some tendency to cluster around the sample transverse direction. Conversely, the misorientation axis distributions in the crystal lattice coordinate system appear essentially random.

The Cube-oriented grains largely contained two families of approximately parallel extended large angle sub-boundaries, bounding elongated microbands (as shown in Fig. 5.147a). The sub-boundaries were aligned close to the {111} crystallographic slip plane traces. Line scans were performed along lines A and B, indicated in Fig. 5.147a and the corresponding relative and cumulative misorientation distributions are shown in Fig. 5.147b-e respectively. The Cube-oriented grains observed in the 6000 seconds delay sample largely showed no tendency to split into shear bands.

5.7.2.7 Goss-oriented grain

The texture component and boundary map for a Goss-oriented grain is presented in Fig. 5.148a. The ODF map for this grain (as shown in Fig. 5.148b) shows a Goss texture. Pole and inverse pole figures are shown in Fig. 5.148c and d respectively. The distributions of rotation axes in both sample and crystal lattice coordinates are shown in Fig. 5.148e and f respectively. When expressed in the sample coordinates, misorientation axes display some tendency to cluster around the sample transverse direction. Conversely, the misorientation axis distributions in the crystal lattice coordinate system appear essentially random.

The Goss-oriented grains contained one family of approximately parallel extended

large angle sub-boundaries, bounding elongated microbands (as shown in Fig. 5.149a). The sub-boundaries were aligned close to the {111} crystallographic slip plane traces. Line scans were performed along lines A and B, indicated in Fig. 5.149a and the corresponding relative and cumulative misorientation distributions are shown in Fig. 5.149b-e respectively. The Goss-oriented grains observed in the 6000 seconds delay sample largely showed no tendency to split into shear bands.

Table 5.8 shows the mean subgrain size (D), misorientation angle (°) and Θ/d in the 6000 seconds delay sample. The highest misorientation of the oriented grains is the Brass oriented grain.

5.7.3 TEM of the microstructure

5.7.3.1 Deformation structure

Fig. 5.150 shows a well-developed micorband structure delineated by the GNBs that have two preferential directions and the angle between two direction and the traces of {111} planes is about 40°and 30°, respectively. The mean width of the microbands was measured at 610±160 nm. Imaged with the beam close to [011], Fig. 5.151 shows the dense dislocation cells structure within the microbands. Imaged with the beam close to [112], Fig. 5.152 shows the network dislocation structure.

5.7.3.2 Precipitates

Fig. 5.153 shows the coarser precipitation. The corresponding EDS spectrum confirms the presence of Q phase. Fig. 5.154 shows the coarser laths Q formed on dislocation. Imaged with the beam close to [111], Fig. 5.155 shows the coarser laths Q phase formed on microband walls and in matrix. Imaged with g=(1-1-1), the mean length of the coarser Q phases is 300±80 and 500±140 nm in the 60 and 6000 seconds delayed samples, respectively. The mean widths of the coarser Q phases are 80±30 and 90±20 nm in the 60 and 6000 seconds delayed samples, respectively.

6. DISCUSSION

6.1 Flow stress

The flow curve for the double hit deformation at 320°C and strain of 0.5, given in Fig. 5.1, exhibits similar behaviour to a microalloyed steel [24], namely a time dependent hardening during the inter pass hold. Thus, the interruption time resulted in significant strain-induced precipitation that controls the microstructure evolution during the deformation so that grain elongation and accumulated strain enhance the precipitates nucleation. A consequence of the accumulated strain is an increase in flow stress by retained work hardening, also direct strengthening by the precipitation occurs. It can be seen from Fig. 5.1, the 6 and 60 seconds delayed samples showed the greatest hardening. The 6000 seconds delayed sample showed a little softening that indicated that dynamic recovery occurred during straining. The above results are in accordance with that for microalloyed steels reported in the literature [24, 117] that the strengthening increment increases to a maximum and thereafter rapidly decreases with hold time.

The shape of the flow curve was different for the first and second deformations. The first hit gave a characteristic flow curve, with yielding followed by gradual hardening up to a peak in flow stress, with a possible small decrease thereafter. The curves shown in Fig. 5.1 are the raw curves and have not been corrected for deformational heating. Cross [116] developed the 2nd order constitutive equations for the tests presented in this thesis (see Appendix 1). The data allowed the determination of the activation energy for deformation (201kJ/mol). He also was able to correct the single hit deformation curves for deformational heating which showed that although deformation heating was small, the corrected curves did not exhibit any evidence of dynamic recrystallisation, consistent with the microstructural observations, discussed below. However, Cross's analysis did not allow the correction for double hit curves. Nevertheless, the indications from both Cross' analysis of single hit deformation, and the microstructural observations is that no dynamic recrystallisation occurred, and any softening was attributable to dynamic recovery.

The shape of the flow curve for the second hit was rather different from the first hit. Yielding was followed by very little evidence of work hardening, rather a saturation flow stress was observed, again with some evidence of a small decrease in flow stress with strain. The shape of the curve appeared to be relatively independent of the hold

time, although clearly the absolute level of the flow stress was strongly dependent on the inter pass hold time. The extensive serrations in the flow curve are believed to be associated with the temperature behaviour of the TMC machine. It is perhaps surprising that more hardening was not observed on the second hit as a result of the extensive strain-induced precipitation. Thus, the precipitation appears to have had more effect on yield than on subsequent dislocation flow and work hardening.

6.2 Precipitation

The deformed microstructure of the Al-Mg-Si-Cu alloy was observed at different magnifications. Optical microscopy (Figs. 5.3, 5.26, 5.53, 5.78, 5.108, 5.130) revealed homogeneously distributed sphere-shaped particles formed within grains and irregularly-shaped coarser particles at the grain boundaries. These particles had an average length of 320±80 nm and were observed for all conditions examined in this work. Their composition was found to be Al/Cu/Si/Mn by EDS analysis in the TEM (Fig. 5.51c), and therefore the most likely phase was Al(Fe,Mn,Cu,Cr)Si as mentioned by Wang et al. [17]. These particles were formed during the solidification treatment and were not responsible for the precipitation hardening, rather they are generally used to control grain growth during thermomechanical processing, since such dispersoids are relatively stable during heat treatment [5].

The presence of precipitates and precipitate-free zones (PFZ) away from the grain boundaries suggests considerable grain boundary migration after the formation of the precipitate-free zones. Moreover, this suggests that the precipitates observed on the boundaries had formed after this grain boundary migration.

The largest effect of strain on the kinetics of precipitation is in increasing nucleation sites [117]. Nucleation and growth of precipitates at dislocations is energetically favoured if the particles eliminate part of the energy of the dislocation lines. Nodes in the three-dimensional network of dislocations and in the subgrain boundaries generated by deformation should therefore be especially favoured nucleation sites for precipitation. In the 60 seconds delayed sample, Fig. 5.105, small precipitates formed both on dislocations and apparently homogeneously nucleated in the matrix. TEM studies showed that three types of precipitates viewed along $[001]_{Al}$, i.e., rod-shaped β' (Fig. 5.105) with the circular end-on view and lath-shaped Q' (Fig. 5.105) with rectangular end-on and long face-on views and coarser Q phase (Fig. 5.104)

contribute to the precipitation process during the deformation of the alloy at 320°C. The precipitation sequence for such alloys under standard solution treatment, quench and age occurs by the formation of various complex metastable phases:

$$\text{SSS-Clusters/GP zones-}\beta''\rightarrow \beta'+Q'\rightarrow Q \ ^{[17,29]}$$

In the current work, clusters/GP zones were not observed using conventional TEM in any of the samples, irrespective of delay time. This is not surprising given the high dislocation density offered easy heterogeneous nucleation sites, and the deformation temperature was above the GP zone solvus. This result is consistent with some authors [16, 29] who used in artificial ageing processing and at a heating rate of 10 °C/min for a 6xxx alloys that no GP zones were observed by TEM. However, high angle annular dark field (HAADF) STEM (which is sensitive to atomic number contrast) and energy filtered TEM (EFTEM) (which gives chemical distribution images) results from Hasting et al. [32] indicated needle-like GP zones surrounding the strain field in the matrix aligned in the Al<100> directions, which were not visible in conventional TEM. Several attempts were made in the current work to use both EFTEM and HAADF STEM imaging to determine the location of the precipitates within the deformation substructure. EFTEM proved difficult as the requirements of a very thin sample (<30nm) meant that oxide contamination from specimen preparation obscured the finest detail, and therefore any possible presence of GP zones. However, HAADF STEM proved rather more informative (e.g. Fig. 6.14b) and this did not show any evidence of GP zones, as expected. Moreover, high resolution TEM images (e.g. Fig. 6.14a) also failed to indicate the presence of GP zones.

The flow curves (as seen in Fig. 5.1) indicated that, as expected, there was no hardening response for the instantaneous sample, either between hits or during the second deformation. However, as noted above, TEM indicated that there was strain-induced precipitation (i.e. precipitates lying on dislocations). The strain rate of 85 s^{-1} was too rapid to allow precipitates to form during deformation. Moreover, had precipitates formed during deformation, significant hardening would have been seen. Therefore, the precipitates observed must have formed during cooling after the completion of the second deformation. While the thermomechanical test machine provides as fast a quench as could be expected for the PSC samples, there would nevertheless be at least 2 seconds before the sample cooled to a temperature at which

the precipitation kinetics would have been too slow to expect any hardening.

A significant hardening response was observed after 6 and 60 seconds delay times between deformations, as shown on the stress-strain plot (Fig. 5.1). This indicates that significant strain-induced precipitation occurred at 320°C within 6 seconds. The first deformation introduced a high dislocation density, which resulted in a microband structure, which is characteristic of the deformation of all aluminum alloys [43, 46]. The substantial dislocation density would have offered extensive heterogeneous nucleation sites for precipitation. In the holding time, the nucleation of strain-induced precipitates on all dislocation nodes, followed by growth and coarsening involving both volume diffusion and accelerated pipe diffusion [119]. On further deformation the original dislocations will be moved and new dislocations created to produce a new distribution of nodes. A second nucleation and growth of new precipitates may also occur during the cooling.

In the 60 seconds delayed sample, the bright and dark field TEM images (Figs. 5.102-107) showed three types of precipitates: coarse Q phase within grains, β' and small lath-shaped Q' phase formed on dislocations and microband walls. This result is similar to the work of Esmaeili et al. [29] who observed β'' and Q′ precipitate to form simultaneously at the samples age for 1 and 7 hours at 180°C. Also, while β'' and Q' precipitate simultaneously, the small GP zones gradually disappear during the aging period over which β'' precipitation approaches completion.

The flow curve of the second hit after a 6000 seconds delay showed softening. TEM showed that the precipitate type was the same as in the 60 seconds delayed sample, namely coarse Q phase within grains, β' and small lath-shaped Q' phase formed on dislocations and microband walls. Particularly, the β' is not the main phase rather the Q' and Q phase dramatically increase as shown in Fig. 5.155. Yassar et al. [30] explained that the dislocations are favourable energy sites for precipitates and short circuit path for solute diffusion in a pre-deformed AA6022 alloy. This promotes the precipitation of β' and Q' phases. Matsuda et al. [10] also suggested that the β' phase was not dissolved, but more likely transformed to Q' phase. Fig. 5.153-155 show that these precipitates were substantially coarser than for a 60 seconds delay and therefore the Zenner pinning pressure was too low to pin the dislocations. The increase in precipitate size through coarsening was substantial and much greater than would be expected in conventional

ageing of a supersaturated solid solution. Dutta et al. [117] have explained the flow stress data as a function of inter-pass hold time in an austenitic steel. The bulk diffusion was shown to be too slow to account for the increase in the precipitate radius. The changes in precipitate numbers and size with time indicated that following nucleation on dislocations, rapid coarsening could occur via the pipe diffusion along the dislocation cores. As the coarsening proceeds, the Zenner pinning pressure decreases to the point where the dislocation or grain boundaries could tear away from the pinning precipitates. The kinetics of this process is clearly enhanced by the diffusion of solute along the dislocation and grain boundaries [5].

The composition of the Q phase has been proposed between $Al_4CuMg_5Si_4$ to $Al_4Cu_2Mg_8Si_7$ depending on whether the precipitate is coherent or semi-coherent, has been suggested [3, 6]. The precipitates grow with a lath-shape along <100> directions in the matrix. Fig. 5.104d and 5.153b show the frequency distributions of the equivalent width and length of the coarser Q precipitates for the 60 and 6000 seconds delayed samples. For the 60 seconds sample, the length ranges from 200 to 600 nm with an average of 300 nm. In contrast, the equivalent length for the 6000 seconds sample is larger and ranges from 300 to 1100 nm with an average of 500 nm. And the width is 80 and 90 nm for 60 and 6000 seconds delayed sample. This indicated the growth of Q phase is along the length direction as a function of the delay time. Wang et al. [17] suggested that the Q phase has an identical lattice parameter to Al along the lath axis and is therefore coherent along the longitudinal direction of precipitates, reflecting a low energy coherent interface. However, during growth and coarsening the length of the precipitates increases at a substantially higher rate than the diameter of precipitates. This may be related to the importance of kinetic factors relating to growth such as the migration of ledges.

The coarsening kinetics were analysed using the Lifshitz-Slyozov-Wagner equation [118].

$$R_t^{-3} - R_0^{-3} = Kt \qquad (1)$$

Where R is the radius, K is a rate constant, and t is the time. This yields a coarsening rate of the coarser Q phase of 70 nm^3/s. The size of the Q phase is larger than is reported for static coarsening studies, for example sizes of ~8.0×23.0 nm^2 in cross-

section and ~600 nm in length for AA6111 samples aged 10 minutes at 315°C were observed by Perovic et al. [17, 29], which is an order of magnitude smaller than in the current study. This indicates the strong effect from pipe diffusion along dislocation cores within the microband walls and results in a relatively short time for the growth phase and the early onset of coarsening. Growth is therefore completed quickly due to the short diffusion distance required.

The degree of strengthening is highly dependent on the inter-pass delay time, which controls the nature of the precipitates, the volume fraction, the average size, the size distribution of the precipitates, and also the nature of the interaction of the precipitates with dislocation. When dislocation slip in deformed zones is hindered by the second phase particles, local lattice rotations of the matrix adjacent to these particles may occur to reduce deformation incompatibilities [81]. Cheng et al. [45] suggested that the Q phase is not sheared by dislocations and therefore provide an obstacle to dislocation motion that can only be circumvented by Orowan bowing.

6.3 Microstructure evolution during deformation

During plastic deformation a small fraction of the mechanical energy is stored in the metal, mostly in the form of dislocations. These dislocations are not randomly distributed. They accumulate in dislocation boundaries, which separate regions with a relatively low dislocation density. Large-area EBSD orientation maps and TEM images showed the evolution of the deformation banding, microband, deformation texture and stored energy with increasing inter pass delay time.

6.3.1 Deformation banding

Deformation bands occur with approximately parallel sides and involve a double orientation change A to C and then C back to A (see Fig. 3.1). The regions with finite widths, separating deformation bands, are often called transition bands, the misorientation across which is usually significant. Deformation bands have been studied systematically by many researchers, on either single crystals [71, 119] or polycrystalline [64, 70], due to their profound influence on deformation textures and the subsequent recrystallisation. Deformation bands are different from the microbands. Microbands appear as plate-like features that form initially on the {111} planes, superimposed on the background of cellular-arranged dislocation structures. They have dislocation wall

boundaries with typical misorientations of 2-10°, generally aligned approximately at 35° to the rolling direction. At increased strains, these structures will disappear to be replaced by equiaxed sub-grains [69].

Deformation bands were observed in all double hit deformation samples. The transition areas separating the same pair of deformation bands varied from region-to-region (see Fig. 5.10, 5.12, 5.38), either comprising one single sharp high angle boundary only (e.g. deformation band A in Fig. 5.38, >40°) or a few large angle boundaries (deformation band B in Fig. 5.38). From the line scans performed across different regions of the same transition band, a similar amount of lattice rotation can be obtained. The misorientation axes of the large-angle dislocation walls in the transition bands tended to cluster around either the transverse direction on RD-ND sections, when expressed in sample coordinates (see Fig. 5.11e). The low-angle dislocation boundaries were normally present in the interior regions of the deformation bands, the misorientation of which generally displayed a strong tendency to accumulate along the deformation band length (see Fig. 5.12 b).

Some well-developed deformation bands were separated by single high-angle boundaries with misorientation angles larger than 40° and rotated about 45° away from the matrix. These bands almost cross the whole grain (Fig. 5.43). Some small band regions have about 10-20° misorientation angle boundaries and rotated about 20° away from the matrix. They formed near the grain boundary (Fig. 5.38) as well as inside the grain (Fig. 5.67). In this case, the deformation bands tended to form in the Copper (Fig. 5.12), S (Fig. 5.71) and random (Fig. 5.10) oriented grains. Individual deformation bands never crossed grain boundaries.

In the 6000 seconds delayed sample, the EBSD images (Fig. 5.136-149) revealed few deformation bands. It only shows some high angle sub-boundaries (red) inside the random (Fig. 5.136) and Cube (Fig. 5.146) oriented grains. The misorientation angles are between 10° and 15°. The deformation banding clearly results from ordinary glide dislocation motion due to slip system selections which within any one region cannot produce the homogeneous deformation.

6.3.2 Microband evolution

The TEM results showed the deformation microstructure develops from a tangled dislocation structure to equiaxed cells, as shown in the single deformed sample (as seen

in Fig. 5.24, 5.25). With this structure, dense dislocation walls are formed as the grains are subdivided into cell blocks bounded by geometrically necessary boundaries (GNBs) and incidental dislocation boundaries (IDBs) [125, 126]. These boundaries are typically low-to-medium angle dislocation boundaries and have characteristics typical of low energy dislocation structures [41]. The single DDWs then split into two or more walls.

In the 60 seconds delayed sample, a well-developed microband structure was observed with a width of 350±50 nm, as shown in Figs. 5.100 and 5.101. In the 6000 seconds delayed sample, Fig. 5.150 shows microbands with a width of about 520±240 nm, with both first and second generation microbands being observed. The increase in microband width is consistent with the coarsening of the precipitates to the point that they were shown to be too large to pin the dislocation structure, as discussed in the last section. The angle of misorientation across the GNBs is larger than across IDBs [57].

The value of the average microband width for the instantaneous, 6, 60 and 6000 seconds delayed samples are shown in Fig. 6.1. With the increase in microbands spacing, the 6000 seconds delayed sample shows softening, consistent with coarsening giving a precipitate size too large to pin the dislocations, as discussed earlier. From the TEM images, a significant difference in GNB morphology was observed, in that the GNBs in the instantaneous (Fig. 5.46), 6 (Fig. 5.72) and 60 seconds samples (Fig. 5.100, 5.101) are almost of a single direction and nearly parallel to the trace of {111} whereas the GNBs in the 6000 seconds sample (Fig. 5.150) have two preferential directions. The angles between the two directions and the traces of the nearest (1-11) and (1-1-1) planes are about 40° and 30°, respectively. A general consideration is that single or coplanar slip tends to produce the planar dislocation boundaries on the slip plane and that multiple-slip tends to form the noncrystallographic dislocation boundaries [41].

The results of EBSD showed that the misorientation vectors displayed a clear tendency to cancel each other across the consecutive larger-angle extended microband walls when crossing the microbands in the transverse direction, but misorientation angles were frequently observed to accumulate locally across the low-angle transverse subboundaries in the longitudinal direction. For the observed configuration as a family of parallel dislocation walls characterized by the alternating plus-minus-plus misorientation pattern, the extended microband boundaries are expected to achieve very effective mutual screening of the elastic stress fields [120]. The above microband

characteristics seemed generally consistent with this study.

The EBSD results showed the frequency of microband angle with respect to the rolling direction concentrated around +30° and -30° (as seen in Fig. 6.9 and table 6.1). The result is the same as has been widely published, that the angle is about 30°~40° to the rolling plane [42, 43, 51, 61, 62]. Indeed, this is becoming a universal observation. In the single deformed sample, the angles exhibit the reference distribution about +26° and -35°. From table 6.1, the mean and median angles showed almost the same characteristics. From the single deformation to the instantaneous and 6 seconds delayed sample, the angles show a small increase. The highest angle is +34° in the 60 seconds sample and -36° in the 600 seconds sample. From the 60 to 600 and 6000 seconds delayed sample, the angle had a tendecy to decrease marginally to values of +28, -35° in the 6000 seconds sample. While clearly the measurement of angle through EBSD was reasonably accurate (with errors mainly coming from cutting the sample with respect to the deformation axis), the statistics of the measurments was relatively poor. Furthermore, small variations from grain-to-grain would be expected because of the differences in grain orientation. Therefore, the variations in microband angle with hold time were not believed to be significant. Microbands clearly form during the first and second deformations (sometimes referred to as first and second generation microbands). Thus, the implication of the current findings is that the precipitates pinned the first order microbands and the subsequent coarsening during the inter-pass hold did not appreciably alter the dislocation dynamics that led to the formation of the second order microbands. Again, such an observation appears to be entirely consistent with the observations on microalloyed austentitic stainless steels [24].

The misorientation axis vectors across sub-boundaries preferentially clustered around the sample transverse direction. Nevertheless, in the crystal lattice coordinate system, misorientation axis vectors generally remained widely scattered. These results are similar to the reports of Winther et al. [52,121] and Bai et al. [69]. It has been suggested that the macroscopic preference of dislocation boundaries is attributed to a tendency for all the grains to slip in highly stressed planes, which are determined by the macroscopic deformation mode, while a specific selection of slip systems in individual grains determines the exact boundary orientation. As sub-boundaries tend to align themselves approximately parallel to the active slip planes, the sub-boundary planes must therefore

also lie close to the macroscopically most stressed planes, which appears to be consistent with the observations made in the present study.

Alexander et al. [122] also suggested that the microbands were the result of a local softening caused by co-operative motion of unpinned dislocations. During the inter-pass hold time, when mobile dislocations are pinned by obstacles in the glide plane, Mg migrates towards the dislocations cores. The longer a dislocation is at rest, the more Mg is located in its vicinity, and the greater the stress required to free the dislocation from the solute atoms. A mobile dislocation that recently has been in motion is more likely to be activated again.

6.3.3 Texture evolution

Figs. 6.2-6.8 illustrate the observed evolution of the crystallographic texture, determined using the EBSD technique and expressed by the ODF in Euler space. The deformation texture evolution with increasing delay time, as shown by the ODFs, was largely composed of orientations clustered around the Goss, Brass, S, Copper components. Comparatively fewer orientations were situated in the vicinity of the rotated Goss and Cube components. Thus, the texture was the typical hot rolling texture for all conditions, characterized by gradual crystallite rotations towards the stable end texture components located along both the α and β fibres, as expected for the PSC deformation of fcc materials in the absence of recrystallisation [123]. Thus, the strain induced precipitation had two effects, namely preventing recrystallisation, but also not modifying the dislocation motion to the extent that the global lattice rotation was the same as if there had been no precipitation, as discussed above.

The textures of the deformed material could all be described in terms of components lying along the α and β fibres typical of fcc metals deformed in plane strain compression testing. Representative sections through the ODFs of the deformed samples and orientation densities along the α and β fibres are shown in Fig. 6.2-6.6. In high stacking fault energy metals such as aluminium, the orientation densities along that fibre are relatively uniform [88]. In the normal plane, the orientation density of the single deformed sample is the highest. The orientation density of the 600 and 6000 seconds delayed samples is the lowest, followed by the 6 seconds and then the instantaneous and 60 seconds delayed samples. Compared to the single deformed sample, the α fibre density of the instantaneous and 6000 seconds delayed sample is lower than the single

deformed sample. The others samples exhibit densities close to the single deformed sample.

In the transverse plane, the α fibre initial density of the instantaneous sample was essentially the same as the single deformed sample, as expected. With the increase in delay time, other samples exhibited a higher density than the single deformed sample. The β fibre density of the instantaneous and 6000 seconds delayed samples are higher than the single deformed sample. Densities for the other hold times are close to the single deformed sample. Therefore, the value of texture of the double hit deformation processing match the value of single deformed sample. However, as with the microband angles, the differences in the strength of the texture densities is not great and it is not believed that they represent real differences in deformation mechanisms, consistent with the TEM observations that showed the only major change with hold time was in the microband thickness. Increases in the β fibre are associated with increases in strain, particularly in cold rolling [71] but since the strain was constant, a constant density of the β fibre component would be expected, unless the precipitates significantly altered the deformation mechanism in the second 'hit', which they appear to not have done.

Although there was no significant change in the overall texture, the measured texture data also provided important information on both the approximate relative densities of the individual texture components and the spatial distribution of these components in the orientation maps. Fig. 6.8 plots the orientation density of the major texture components. As seen in the normal plane (Fig. 6.8a), an increase in the delay time reduced the S, Copper and Goss components fraction but increased the fraction of the Brass component. This trend is also shown in Fig. 6.8b. Such texture changes, i.e. an increase in the Brass component with increasing delayed time results in a decrease in the β fibre and increase in the α fibre. In the 60 seconds delay sample, the peak orientation density value of the Brass component, {011}<211> began to dominate the texture. The development of such a texture has often been observed previously in aluminium alloys [88, 89, 92]. Maurice et al. [92] suggested that the increase in the Brass component has been attributed to the additional activation of other, non-octahedral slip systems at very high deformation temperatures.

6.3.4 Orientation dependence of substructure development

The substructures formed through double hit deformation within the grains of each

texture component, namely Goss, Brass, Copper and S texture components showed a very different character. There were no noticeable shear bands, but certainly evidence of some high misoriented deformation bands (as seen in Fig. 5.19, which shows values over 40°). One or two prominent families of approximately parallel extended larger-angle sub-boundaries were generally observed within the above grains, delineating elongated microbands subdivided into slightly elongated subgrains by shorter lower-angle transverse sub-boundaries. The traces of extended sub-boundaries appeared to be aligned approximately parallel with the {111} planes, i.e. they were defined as crystallographic in nature. Also, the EBSD analysis shows the equiaxed substructure in Cube oriented grains. The misorientation axis vectors across sub-boundaries preferentially clustered around the sample elongation direction, for the remaining major components these vectors displayed a tendency to cluster around the sample transverse direction. In the crystal lattice coordinate system misorientation axis vectors generally remained widely scattered.

Cube-oriented grains displayed a totally different substructure characteristics contrasting with those obtained for the rest of the texture components studied. The present results show that during plane-strain compression, the Cube oriented material is largely stable (as seen in Fig. 5.37). These grains were reported to undergo splitting into well-defined macroscopic deformation bands characterized by large rotations of alternating sign occurring predominantly about the sample transverse direction. The observations made in the present study indicate that these grains have no pronounced subdivision into deformation bands. Rather, it shows deformation band with about 25° misorientation angle in the single deformed sample (Fig. 5.20). The EBSD investigation also revealed the presence of extended large-angle dislocation walls within some of the Cube oriented grains, characterized by varying misorientations along their lengths. As some segments of these walls displayed misorientation angles exceeding 15°, their presence indicated a tendency of these grains to split into deformation bands (Figs. 5.70, 5.98, 5.116, 5.138). For all conditions, the sample exhibits some random oriented regions and almost equiaxed substructure appeared in the grains. No microband structure formed in the single deformed, instantaneous, 6 and 60 seconds samples. The 600 and 6000 seconds delayed samples, show some weak microbands parallel to {111} slip plane. The formation of small, low-misoriented substructure might be attributed to a lower recovery of the Cube-orientated regions.

The Brass oriented grains show some random oriented regions and no deformation bands. Particularly in the 6 seconds delayed sample, the Brass grains exhibit an equiaxed substructure. Also, some random oriented region exhibits in Goss component grains; P oriented region exhibits in Copper oriented grains; Copper oriented regions exhibits in S grains. The Goss oriented grains showed almost no deformation bands, as with the Brass oriented grains. Hansen [120] suggested that the grain rotation takes place not by rotation of an entire grain, but by the rotation of individual parts of a grain toward different orientations, which compose the texture.

6.3.5 Stored energy

The quantification of substructure by EBSD revealed a noticeable dependence of substructural characteristics on grain orientation (Tables 5.4-5.8). Mean subgrain diameter values show about 1 μm for all of the grains and the corresponding mean misorientation angles show that the highest value (6.41°) is in the single deformed sample and others is around 4°.

A ratio of the mean misorientation angle to the mean subgrain size for a given texture component might be taken as an approximate indication of the corresponding level of stored deformation energy due to the presence of sub-boundaries [124]. From the value of stored energy given in all of the conditions that the Cube oriented grains seemed to display the relatively highest stored energy levels in the double hit deformation processing. This is different from the work of Cizek et al. [87] and Samajdar et al. [86] that the Cube oriented grains in heavily rolled copper and an austenitic steel showed lower than average stored energy. This means that the recovery is insufficient to lower the stored energy. Fig. 6.13 plots the stored energy of the major texture components. The single deformed and instantaneous samples displayed the highest values, 6 and 60 seconds delayed samples show the lowest values and the 600 and 6000 seconds show the gradually increasing tendency. In the instantaneous, 60 and 600 seconds delayed samples, the Goss oriented grains show the lowest stored energy values. Compared to the S component, only in 6000 seconds delayed sample, the energy is the lowest.

7. CONCLUSION

1. The flow curves corresponding to the double hit deformation at temperatures of 320°C and strain rates of 85 s^{-1} to strain levels of 1 with varying inter-pass hold time resulted in significant strain induced precipitation and hardening characteristics. The greatest hardening was observed for holds of 6 and 60 seconds, while a hold of 6000 seconds displayed softening flow behaviour. For all inter-pass hold times, recrystallisation was suppressed by the strain induced precipitation.

2. Two types precipitates, β and Q, formed heterogeneously on dislocations, principally in microband walls, indicating strain induced precipitation had occurred. The precipitation sequence followed that expected for this alloy, except GP zones were not observed. The Q phase became more dominant than the β with increase in hold time, which is contrary to observations in the literature for conventional solution treat, quench and age, where the β phase was found to be dominant. The coarsening rate constant of the Q phase was estimated at 70 nm^3/s, which is substantially greater than observed in conventional coarsening experiments, indicating a strong contribution from pipe diffusion along dislocation cores.

3. The deformation structure comprised a mixture of deformation bands and microbands, with other more irregular structures observed. EBSD and optical measurements indicated no evidence of recrystallisation for any samples. The misorientation axes of the large-angle dislocation walls in deformation bands tended to cluster around either the transverse direction on RD-ND section, when expressed in sample coordinates. The low-angle dislocation boundaries were normally present in the interior regions of deformation bands, the misorientation of which generally displayed a strong tendency to accumulate along the deformation band length. Individual bands never cross grain boundaries and they resist against dislocation motion. The deformation bands were seen in all samples. But in the 6000 seconds delayed sample, the EBSD images revealed few deformation bands. It only shows some high angle sub-boundaries (red) inside the random and Cube oriented grains. The misorientation angles are between 10° and 15°.

4. TEM analysis of the 60 seconds delayed sample, which exhibited maximum hardening, revealed a well-developed microband structure with an average width of 350±50 nm. In the 6000 seconds delayed sample, microbands were observed in two orientations, with an average width of 520±240 nm width microbands structure with two directions. The microband walls had a tendency to align along the {111} planes, but many microband walls were found to be non crystallographic. EBSD analysis indicated that the angle the microbands made to the rolling direction was distributed between +34° and -36°, with no statistically meaningful variation with inter pass hold time. The misorientation axis vectors across subboundaries preferentially clustered around the sample transverse direction. Nevertheless, in the crystal lattice coordinate system, misorientation axis vectors generally remained widely scattered.

5. The quantification of substructure by EBSD revealed a noticeable dependence of substructural characteristics on grain orientation with respect to the deformation axes. Mean subgrain diameter values were measured at ~1 μm from all of the grains. The corresponding mean misorientation angles show that the highest (6.4°) is in the single deformed sample and all others was around 4°. 6 and 60 seconds delayed samples show the lowest values and the 600 and 6000 seconds show the gradually increasing tendency. The Cube oriented grains displayed the relatively highest stored energy levels in the double hit deformation processing. In the instantaneous, 60 and 600 seconds delayed samples, the Goss oriented grains show the lowest stored energy values. Compared to the S component, only in 6000 seconds delayed sample, the energy is the lowest.

6. The texture was characteristic of a hot worked aluminium alloy without recrystallisation, irrespective of inter-pass hold time. The texture evolution with increasing inter-pass delay time was characterised by gradual crystallite rotations towards the stable end texture components located along both the α and β fibres in Euler space. The ODF was largely composed of orientations clustered around the Goss {011}<100>, Brass {011}<211>, S {123}<634> and Copper {112}<111> texture components. Comparatively fewer orientations were situated in the vicinity of the rotated Goss and Cube components. No recrystallisation texture components were observed. Although differences in texture components with

inter-pass delay time were small, from the orientation density of the major texture components, an increase in delayed time reduced the S, Copper and Goss components fraction but increased the fraction of Brass.

8. FUTURE WORK

Substantial results on the strain-induced precipitation and deformation structural evolution in AA6111 alloy during double hit deformation were obtained from present work. However, there is still further work that needs to be undertaken, namely:

Analyze the 600 seconds delayed samples in TEM.

Undertake more extensive HAADF STEM work to identified the type of the precipitates and calculate the size distribution.

A direct comparison of the double hit specimens with single hit followed by 6s, 60s, 600s and 6000s delay times and then quench would allow a determination of which aspects of the microstructure evolved during the first hit and what changed during the second hit. Unfortunately, insufficient material was available in the current work to undertake these important tests.

Since strain-induced precipitation has clearly been identified in this alloy, it would be appropriate to investigate other precipitation hardening aluminum alloys where there is precipitation potential at the hot working temperature.

ACKNOWLEDGEMENTS

Firstly, I would like to express my sincere gratitude to my supervisor Professor W. Mark Rainforth and Dr B. P. Wynne for the opportunity to do my Ph.D under their supervision and the finance support for my life.

I would like to express my appreciation to Dr Pavel Cizek, Dr Zhaoxia Zhou, Dr Magdalena Lopez-Pedrosa and Dr Matthew Thomas for giving me the invaluable knowledge and help. I thank for the technical staff for their assistance, in particular Dr Peter Korgul, Dr Heath Bagshaw, Mr Keith Penny and Mr Alan Walker for training the microscopes. Thanks are also given to my friends in the Department of Engineering Materials. Without their kind help, I would not be able to finish my Ph.D smoothly.

Finally, I would like to thank my parents and my wife, Hongxia Zhao for giving me endless support and spiritual encouragement.

REFERENCES

1. G.B. Burger, A.K. Gupta, P.W. Jeffery and D.J. Lloyd, *Microstructural control of alouminium sheet used in automotive applications*. Materials Characterization, 1995, Vol 35: pp.23-39

2. W.S. Miller, L. Zhuang, J. Bottema, A.J. Witterbrood, P. De. Smet, A. Haszler and A. Vieregge, *Recent development in aluminium alloy for the automotive industry*. Materials Science Engineer A, 2000, Vol. A280: pp.37-49

3. D.J. Lloyd and A.K. Gupta, *Aluminum alloys and the thermal processing associated with automotive sheet.* THERMEC'97, International conference on thermomechanical processing of steels and other metals, 1997: 99-107.

4. D.J. Chakrabarti and E. Laughlin, *Phase relations and precipitation in Al-Mg-Si alloy with Cu additions*. Progress in Materials Science, 2004, Vol. 49: pp.389-410.

5. S.J. Lilywhite, P.B. Prangnell and F.J. Humphreys, *Interactions between precipitation and recrystallisation in an Al–Mg–Si alloy*. Materials Science and Technology, 2000, Vol. 16: pp.1112-1120

6. G.E. Totten and D.S. MacKenzie, *Handbook of aluminium - Volume 1: Physical metallurgy and processes*, 2003, Marcel Dekker, NY.

7. O. Engler and J. Hirsch, *Texture control by thermomechanical processing of AA6xxx Al-Mg-Si sheet alloy for automotive applications-a review.* Materials Science Engineer A, 2002, 366A: pp.249-262

8. M. Murayama, K. Hono, W.F. Miao and D.E. Laughlin, *The effect of Cu additions on the precipitation kinetics in an Al-Mg-Si alloy with excess Si.* Metallurgical and Materials Transactions A, 2001, Vol.32A: pp.239-246

9. W.F. Miao and D.E. Laughlin, *Effects of Cu Content and Preaging on Precipitation Characteristics in Aluminum Alloy 6022.* Metallurgical and Materials Transactions A, 2000, Vol. 31A: pp.361-371

10. K. Matsuda, Y. Uetani, T. Sato and S. Ikeno, *Metastable Phase in an Al-Mg-Si Alloy Containing Copper.* Metallurgical and Materials Transactions A, 2001, Vol.32A: pp.1293-1299

11. S.M. Hirth, G.J. Marshall, S.A. Court and D.J. Lloyd, *Effects of Si on the aging behaviour and formability of aluminium alloys based on AA6016.* Materials Science and Engineering A, December 2001, Volumes 319-321: pp.452-456,

12. A.K. Gupta, D.J. Lloyd and S.A. Court, *Precipitation hardening in Al–Mg–Si alloys with and without excess Si.* Materials Science and Engineering A, 15 November 2001, Volume 316, Issues 1-2: pp.11-17

13. C.D. Marioara, S.J. Andersen, J. Jansen and H.W. Zandbergen, *The influence of temperature and storage time at RT on nucleation of the β" phase in a 6082 Al-Mg-Si alloy.* Acta Materialia, 2003, 51: pp.789-796

14. S. Esmaeili, D.J. Lloyd and W.J. Poole, *Modeling of precipitation hardening for the naturally aged Al-Mg-Si-Cu alloy AA6111.* Acta Materialia, 2003, 51: pp.3467–3481

15. C.D. Marioara, S.J. Andersen, J. Jansen and H.W. Zandbergen, *Atomic model for GP-zones in A 6082 Al–Mg–Si system.* Acta Materialia, 2001, 49: pp.321–328,

16. W.F. Miao and D.E. Laughlin, *Precipitation hardening in aluminium alloy 6022.* Scripta Materialia, 1999, Vol. 40, No. 7: pp.873–878

17. X. Wang, W.J. Poole, S. Esmaeili, D.J. Lloyd and J.D. Embury, *Precipitation Strengthening of the Aluminum Alloy AA6111.* Metallurgical and Materials Transactions A, 2003, Vol.34A: pp.2913-2924

18. C. Ravi, C. Wolverton, *First-principles study of crystal structure and stability of Al–Mg–Si–(Cu) precipitates.* Acta Materialia, 2004, 52: pp.4213–4227

19. D.J. Chakrabarti and D.E. Laughlin, *Phase relations and precipitation in Al–Mg–Si alloys with Cu additions.* Progress in Materials Science, 2004, 49: pp.389–410

20. M. Murayama and K. Hono, *Pre-precipitate clusters and precipitation processes in Al-Mg-Si alloys.* Acta Materialia, 1999, Vol.47, No.5: pp.1537-1548

21. B. Dutta, E.J. Palmiere and C.M. Sellars, *Modelling the kinetics of strain induced precipitation in Nb microalloyed steels.* Acta Materialia, 2001, 49: pp.785–794

22. A. Pandit, A. Murugaiyan, A.S. Podder, A. Haldar, D. Bhattacharjee, S. Chandra

and R.K. Ray, *Strain induced precipitation of complex carbonitrides in Nb–V and Ti–V microalloyed steels*. 2005, Scripta Materialia, 53: pp.1309–1314

23. S. F. Medina, A. Quispe and M. GoÂmez, *Strain induced precipitation effect on austenite static recrystallisation in microalloyed steels*. Materials Science and Technology, January 2003, Vol. 19: pp.99-108

24. W.M. Rainforth, M.P. Black, R.L. Higginson, R.L. Higginson, E.J. Palmiere, C.M. Sellars, I. Pabst, P. Warbichler & F. Hofer, *Precipitation of NbC in a model austenitic steel*. Acta Materialia, 2002, 50: pp.735-747

25. R. M. Poths, W.M. Rainforth and E.J. Palmiere, *Strain Induced Precipitation in Model and Conventional Microalloyed Steels during Thermomechanical Processing*. Material Science Forum, 2005, Vols. 5001-501: pp.139-146

26. A. Perovic, D.D. Perovic, G.C. Weatherly and D.J. Lloyd, *Precipitation in Aluminum Alloys AA6111 and AA6016*. Scripta Materialia, 1999, Vol.41, No.7: pp.703-708

27. K. Matsuda, Tsutomu Naoi, Kaname Fujii, Yasuhiro Uetani, Tatsuo Sato, Akihiko Kamio and Susumu Ikeno, *Crystal structure of the β" phase in an Al-1.0 mass % Mg_2Si-0.4 mass % Si alloy*. Materials Science and Engineering, 1999, A262: pp.232-237

28. S. Esmaeili, L.M. Cheng, A. Deschamps, D.J. Lloyd and W.J. Poole, *The deformation behaviour of AA6111 as a function of temperature and precipitation state*. Materials Science and Engineering, 2001, A319-321: pp.461-465

29. S. Esmaeili, X. Wang, D.J. Lloyd and W.J. Poole, *On the Precipitation-Hardening Behavior of the Al-Mg-Si-Cu Alloy AA6111*. Metallurgical and Materials Transactions A, 2003, Vol. 34A: pp.751-763

30. R. S. Yassar, D. P. Field and H. Weiland, *The effect of predeformation on the β" and β' precipitates and the role of Q' phase in an Al-Mg-Si alloy. AA6022*. Scripta Materialia, 2005, 53: pp.299-303

31. S.J. Andersen, H.W. Zandbergen, J. Jansen, C. Traeholt, U. Tundal and O. Reiso, *The Crystal Structure of the β" Phase in Al-Mg-Si Alloys*. Acta Materials, 1998, Vol.46, No.9: pp.3283-3298

32. H. Hasting, J. Walmsley, C. Marioara, ATJ. V. Helvoort, R. Holmestad, F.

Danoix and W. Lefebvre, *Characterisation of early precipitation stages in 6xxx series aluminium alloys.* Journal of Physics, Conference Series, 2006, 26: pp.99-102

33. G.C. Weatherly, A. Perovic, N.K. Mukhopadhyay, D.J. Lloyd and D.D. Perovic, *The Precipitation of the Q phase in an AA6111 Alloy.* Metallurgical and Materials Transactions A, February 2001, Vol. 32A: pp.213-218

34. C. Cayron and P.A. Buffat, *Transmission electron microscopy study of the β' phase (Al-Mg-Si alloys) and QC phase (Al-Cu-Mg-Si alloys): ordering mechanism and crystallographic structure.* Acta Materialia, 2000, 48: pp.2639-2653

35. H.S. Hasting, J.C. Walmsley, A.T.J.Van Helvoort, C.D. Marioara, S.J. Andersen and R. Holmestad, *Z-contrast imaging of the arrangement of Cu in precipitates in 6xxx-series Aluminum alloys.* Philosophical Magazine and Philosophical Magazine Letters, in press

36. E. Hornbogen and E.A. Starke JR, *Overview: Theory assisted design of high strength low alloy aluminium.* Acta Metallurgical Materialia, 1993, Vol.41, No.1: pp.1-16

37. F. Delmas, M. Vivas, P. Lours, Marie-Jose Casanove, A. Couret and A. Coujou, *Straining mechanisms in aluminium alloy 6065. In-situ investigation by transmission electron microscopy.* Materials science and Engineering, 2003, A340: pp.286-291

38. A.W. Zhu and E.A. Starke JR, *Strengthening effect of unshearable particles of finite size: a computer experimental study.* Acta Materialia, 1999, Vol.47, No.11: pp.3263-3269

39. G. Winther, X. Huang, A. Godfrey and N. Hansen, *Critical comparison of dislocation boundary alignment studied by TEM and EBSD: technical issues and theoretical consequences.* Acta Materialia, 2004, 52: pp.4437-4446

40. M. Cabibbo, E. Evangelista and C. Scalabroni, *EBSD FEG-SEM, TEM and XRD techniques applied to grain study of a commercially pure 1200 aluminum subjected to equal-channel angular-pressing.* Micron, 2005, 36: pp.401-414

41. J.A. Wert, Q. Liu and N. Hansen, *Dislocation boundaries and active slip systems.* Acta Metallurgica Materialia, 1995, Vol.43, No.11: pp.4153-4163

42. P.J. Hurley, and F.J. Humphreys, *The application of EBSD to the study of substructural development in a cold rolled single-phase aluminium alloy*. Acta Materialia, 2003, 51: pp.1087-1102

43. G. Winther, D. Juul Jensen and N. Hansen, *Dense dislocation walls and microbands aligned with slip planes-theoretical considerations*. Acta Materialia, 1997, Vol.45, No.12: pp.5059-5068

44. D.P. Field, P.B. Trivedi, S.I. Wright and M. Kumar, *Analysis of local orientation gradients in deformed single crystals*. Ultramicroscopy, April 2005, Vol. 103, Issue 1: pp.33-39

45. D.A. Hughes, S.M.A. Khan, A. Godfrey and H.M. Zbib, *Internal structures of deformation induced planar dislocation boundaries*. Materials Science and Engineering A, 15 July 2001, Vol.309-310: pp.220-226

46. B. Bay, N. Hansen, D.A. Hughes and D. Kuhlmann-wilsdorf, *Evolution of FCC deformation structures in polyslip-overview No.96*. Acta Metallurgical Materialia. 1992, Vol.40, No.2: pp.205-219

47. J.A. Wert, Q. Liu and N. Hansen, *Dislocation boundary formation in a cold-rolled cube-oriented Al single crystal*. Acta Materialia, 1997, Vol.45, No.6: pp.2565-2576

48. F. Basson and J.H. Driver, *Modelling the evolution of geometrically necessary boundaries at large plastic strains*. Materials Science and Engineering A, 15 November 1998, Vol.256, Issues 1-2: pp.243-255

49. W.C. Liu, D.J. Jemsem and J.G. Morris, *Effect of grain orientation on microstructures during hot deformation of AA 3104 aluminium alloy by plane strain compression*. Acta materialia, 2001, 49: pp.3347–3367,

50. P. Cizek, J.A. Whiteman, W.M. Rainforth and J.H. Beynon, *EBSD and TEM investigation of the hot deformation substructure characteristics of a type 316L austenitic stainless steel*. 3 March 2004, Journal of Microscopy, Vol.213: pp.285-295

51. G.J. Baxter, T. Furu, Q. Zhu, J.A. Whiteman and C.M. Sellars, *The influence of transient strain-rate deformation conditions on the deformed microstructure of aluminium alloy Al±1% Mg*. Acta Materialia, 1999, Vol. 47, No. 8: pp.2367-2376,

52. G. Winther, *Slip patterns and preferred dislocation boundary planes.* Acta Materialia, 22 January 2003, Vol.51, Issue 2: pp.417-429

53. G. Winther, X. Huang and N. Hansen, *Crystallographic and macroscopic orientation of planar dislocation boundaries-correlation with grain orientation.* Acta Materialia, 29 May 2000, Vol.48, Issue 9: pp.2187-2198

54. G. Winther, X. Huang, A. Godfrey and N. Hansen, *Critical comparison of dislocation boundary alignment studied by TEM and EBSD: technical issues and theoretical consequences*. Acta Materialia, 6 September 2004, Vol.52, Issue 15: pp.4437-4446

55. P.J. Hurley, P.S. Bate and F.J. Humphreys, *An objective study of substructural boundary alignment in aluminium*. Acta Materialia, 15 September 2003, Vol.51, Issue 16: pp.4737-4750

56. D.A. Hughes and N. Hansen, *High angle boundaries formed by grain subdivision mechanisms*. Acta Materialia, 1997, Vol.45, No.9: pp.3871-3886

57. Q. Liu and N. Hansen, *Geometrically necessary boundaries and incidental dislocation boundaries formed during cold deformation*. Scripta Metallurgica et Materialia, 1995, Vol.32, No.8: pp.1289-1295

58. F.J. Humphreys and P.S. Bate, *Measuring the alignment of low-angle boundaries formed during deformation*. Acta Materialia, Vol.54, No.3. 2006, pp.817-829

59. X. Huang and N. Hansen, *Grain orientation dependence of microstructure in alumuinium deformed in tension*. Scripta Materialia, 1997, Vol.37, No.1: pp.1-7

60. P.J. Apps, J.R. Bowen and P.B. Prangnell, *The effect of coarse second-phase particles on the rate of grain refinement during severe deformation processing*. Acta Materialia, 2003, 51: pp.2811-2822

61. P.J. Hurley and F.J. Humphreys, *The application of EBSD to the study of substructural development in a cold rolled single-phase aluminium alloy*. Acta Materialia, 25 February 2003, Vol.51, Issue 4: pp.1087-1102

62. P. Cizek, *Characteristics of the equiaxed cell block structure formed within cube-textured grains during tensile deformation of aluminium*. Scripta Materialia, 10 October 2001, Volume 45, Issue 7: pp.815-822

63. A. Duckham, R.D. Knutsen and O. Engler, *Influence of deformation variables on the formation of copper-type shear bands in Al-Mg*. Acta Materialia, 2001, 49: pp.2739-2740

64. P. Cizek, B.A. Parker and B.J. Wynne, *Dense dislocation walls and deformation banding in commercial purity aluminium*. Scripta Metallurgica et Materialia, 1995, Vol.32, No.3: pp.319-323

65. D. Chapelle and M. Darrieulat, *The occurrence of shear banding in a millimeter scale (-1-23)[634] grain of an Al-4.5% Mg alloy during plane strain compression*. Materials Science and Engineering, A347: 32-/41, 2003

66. M. Richert' and B. Leszczyska, *Structure and properties of dynamically compressed Al99.5 and AlCuZr alloy*. Proceedings of the European Materials Research Society Fall Meeting, Symposium B, Journal of Alloys and Compounds, 17 November 2004, Volume 382, Issues 1-2: pp.305-310

67. M. Richert, H.P. Stüwe, J. Richert, R. Pippan and Ch. Motz, *Characteristic features of microstructure of ALMg5 deformed to large plastic strains*. Materials Science and Engineering A, 31 March 2001, Volume 301, Issue 2: pp.237-243

68. M. Richert, H.J. Mcqueen and J. Richert, *Microband formation in cyclic extrusion compression of aluminium*. Canadian Metallurgical Quarterly, 1 June 1998, Volume 37, Issue 5: pp.449-457

69. F. Bai, *Microstructural evolution in a model Fe-30Ni alloy during plane strain compression*. PhD Thesis, University of Sheffield, 2004

70. S.S. Kulkarni, E.A. Starke JR and D. Kuhlmann-Wilsdorf, *Some observations on deformation banding and correlated microstructures of two aluminium alloys compressed at different temperatures and strain rates*. Acta Materialia, 1998, Vol.46, No.15: pp.5283-5301

71. F. Basson and J.H. Driver, *Deformation banding mechanisms during plane strain compression of cube-orientated F.C.C. crystals*. Acta Materialia, 2000, 48: pp.2101-2115

72. P. Cizek, B.P. Wynne, Hong Lu, and B.A. Parker, *Deformation banding in (001)[110] textured aluminium sheet deformed in tension*. Materials Science and Engineering, 1996, A219: pp.44- 55

73. D. Chapelle, and M. Darrieulat, *The occurrence of shear banding in a millimeter scale* $(\bar{1}\bar{2}3)[634]$*grain of an Al-4.5% Mg alloy during plane strain compression.* Materials Science and Engineering A, 25 April 2003, Volume 347, Issues 1-2: pp.32-41

74. P. Cizek, F. Bai, W.M. Rainforth and J.H. Beynon, *Fine structure of shear bands formed during hot deformation of two austenitic steels.* Materials Transactions, 2004, Vol.45, No.7: pp.2157-2164

75. H H. Jazaeri and F.J. Humphreys, *The transition from discontinuous to continuous recrystallization in some aluminium alloys II-annealing behaviour.* Acta Materialia, 2004, 52: pp.3251-3262

76. H.J. McQueen, W. Blum, *Dynamic recovery: sufficient mechanism in the hot deformation of Al (B99.99).* Materials Science and Engineering, 2000, A290: pp.95–107,

77. M.E. Kassner and S.R. Barrabes, *New developments in geometric dynamic recrystallization.* The Langdon Symposium: Flow and forming of Crystalline Materials, Materials Science and Engineering: A, 25 November 2005, Volumes 410-411: pp.152-155

78. M. Ferry and F.J. Humphreys, *Discontinuous subgrain growth in deformed and annealed {110} (001) aluminium single crystals.* Acta Materialia, 1996, Vol. 44, No. 4: pp.1293-1308

79. W. C. Liu and J. G. Morris, *Comparison of the texture evolution in cold rolled DC and SC AA 5182 aluminum alloys.* Materials Science and Engineering A, 2 January 2003, Volume 339, Issues 1-2: pp.183-193

80. W.C. Liu and J.G. Morris, *Effect of pre-treatment on recrystallization and recrystallizationtextures of cold rolled CC AA 5182 aluminum alloy.* Materials Science and Engineering, 2003, A363: pp.253–262,

81. O. Engler, X.W. Kong and P. Yang, *Influence of particle stimulated nucleation on the recrystalliztion textures in cold deformed Al-alloys part I-experimental observations.* Scripta Materialia, 1997, Vol.37, No.11: pp.1665-1674

82. F.J. Humphreys and M.G. Ardakani, *Grain boundary migration and zener pinning in particle-containing copper crystals.* Acta Materialia, 1996, Vol. 44, No. 7: pp.2711-2121

83. A.A. Benzerga, Y. Bréchet, A. Needleman and E. Van der Giessen, *The stored energy of cold work: Predictions from discrete dislocation plasticity.* Acta Materialia, October 2005, Volume 53, Issue 18: pp.4765-4779

84. G. Guiglionda, A. Borbély and J. H. Driver, *Orientation-dependent stored energies in hot deformed Al–2.5%Mg and their influence on recrystallization.* Acta Materialia, 12 July 2004, Volume 52, Issue 12: pp.3413-3423

85. N. Hansen, R.F. Mehl and A. Medalist, *New Discoveries in Deformed Metals.* The 2001 Institute of Metals Lecture The Minerals, Metals & Materials Society, Metallurgical and Materials Transactions A, December 2001, Vol. 32A: pp.2917-2935

86. I. Samajdar and R.D. Doherty, *Cube recrystallization texture in warm deformed aluminum: understanding and prediction.* Acta Materialia, 22 May 1998, Volume 46, Issue 9: pp.3145-3158,

87. P. Cizek, F. Bai, E.J. Palmiere and W.M. Rainforth, *EBSD study of the orientation dependence of substructure characteristics in a model Fe-30wt%Ni alloy subjected to hot deformation.* Journal of Microscopy, February 2005, Vol.217, Pt 2: pp.138-151

88. P.S. Bate, Y. Huang and F.J. Humphreys, *Development of the "brass" texture component during the hot deformation of Al-6Cu-0.4Zr.* Acta Materialia, 2004, 52: pp.4281-4289

89. W.C. Liu and J.G. Morris, *Effect of hot and cold deformation on the β fiber rolling texture in continuous cast AA 5052 aluminum alloy.* Scripta Materialia, June 2005, Volume 52, Issue 12: pp.1317-1321

90. I. Samajdar, P. Ratchev, B. Verlinden and E. Aernoudt, *Hot working of AA1050—relating the microstructural and textural developments.* Acta Materialia, 13 June 2001, Volume 49, Issue 10: pp.1759-1769

91. Z.J. Li, A. Godfrey and Q. Liu, *Evolution of microstructure and local crystallographic orientations in rolled Al-1%Mn single crystals of {001}<110> orientation.* Acta Materialia, 2004, 52: pp.149-160

92. Cl. Maurice and J.H. Driver, *Hot rolling textures of f.c.c. metals—Part I. Experimental results on Al single and polycrystals.* Acta Materialia, November 1997, Volume 45, Issue 11: pp.4627-4638

93. L. Delannay, O.V. Mishin, D. Juul Jensen and P. Van Houtte, *Quantitative analysis of grain subdivision in cold rolled aluminium*. Acta Materialia, 2001, 49: pp.2441-2451

94. N. Stanford, D. Dunne and M. Ferry, *Deformation and annealing of (011)[01-1] oriented Al single crystals*. Acta Materialia, 2003, 51: pp.665-676

95. J.Ch. Glez and J.H. Driver, *Substructure development in hot plane strain compressed Al-1%Mn crystals*. Acta Materialia, 2003, 51: pp.2989-3003

96. W.C. Liu and J.G. Morris, *Effect of hot and cold deformation on the P {011}<455> recrystallization texture in a continuous cast Al–Mn–Mg aluminum alloy*. Scripta Materialia, June 2006, Volume 54, Issue 12: pp.2095-2099

97. W.C. Liu, C.-S. Man, D. Raabe and J.G. Morris, *Effect of hot and cold deformation on the recrystallization texture of continuous cast AA 5052 aluminum alloy*. Scripta Materialia, December 2005, Volume 53, Issue 11: pp.1273-1277

98. M.C. Theyssier, J.H. Driver, *Recrystallization nucleation mechanism along boundaries in hot deformed Al bicrystals*. Materials Science and Engineering, 1999, A272: pp.73–82,

99. G. Guiglionda, A. Borb_ely, J.H. Driver, *Orientation-dependent stored energies in hot deformed Al–2.5%Mg and their influence on recrystallization*. Acta Materialia, 2004, 52: pp.3413–3423,

100. K. Marthinsen and N. Ryum, *Transformation kinetics and microstructure for grain boundary nucleated recrystallization in two dimensions*. Acta Materialia, 1997, Vol.45, No.3: pp.1127-1136

101. O. Engler, H.E. Vatne, E. Nes, *The roles of oriented nucleation and oriented growth on recrystallization textures in commercial purity aluminium*. Materials Science and Engineering, 1996, A205: pp.187-198,

102. I. Samajdar and R.D. Doherty, *Cube recrystallization texture in warm defromed aluminium: understanding and prediction*. Acta Materialia, 1998, Vol. 46, No. 9: pp.3145-3158,

103. S. Zaefferer, T. Baudin and R. Penelle, *A study on the formation mechanisms of the cube recrystallization texture in cold rolled Fe–36%NI alloys*. Acta

Materialia, 2001, 49: pp.1105–1122,

104. N. Stanford, D. Dunne, M. Ferry, *Effect of orientation stability on recrystallization textures of deformed aluminium single crystals*. Materials Science and Engineering, 2003, A348: pp.154-/162,

105. I. Samajdar, B. Verlinden, L. Rabet, and P. Van Houtte, *Recrystallization texture in a cold rolled commercial purity aluminum: on the plausible macro- and micro-mechanisms*. Materials Science and Engineering, 1999, A266: pp.146–154,

106. O. Daaland and E. Nes, *Recrystallization texture development in commercial Al-Mn-Mg alloys*. Acta Materialia, April 1996, Volume 44, Issue 4: pp.1413-1435

107. M. Feffy and F.J. Humphreys , *The deformation and recrystallization ofparticle-containing {011} (100) aluminium crystals*. Acta Materialia, 1996, Vol. 44, No. 8: pp.3089-3103

108. G. B. Sarma, and B. Radhakrishnan, *Modeling microstructural effects on the evolution of cube texture during hot deformation of aluminium*. Materials Science and Engineering A, 15 November 2004, Volume 385, Issues 1-2: pp.91-104

109. W. C. Liu and J. G. Morris, *Kinetics of the formation of the β fiber rolling texture in continuous cast AA 5xxx series aluminum alloys*. Scripta Materialia, 2 December 2002, Volume 47, Issue 11: pp.743-748

110. H.E. Vatne, R. Shahani and E. Nes, *Deformation of cube-oriented grains and formation of recrystallized cube grains in a hot deformed commercial AlMgMn aluminium alloy*. Acta Materialia, 1996, Vol.44, No.11: pp.4447-4462

111. K. Matsumoto, T. Shibayanagi and Y. Umakoshi, *On the role of grain boundary character distribution in grain growth of Al-Mg alloys*. Acta Materialia, 1997, Vol.45, No.2: pp.439-451

112. A. Duckham, O. Engler, R.D. Knutsen, *Moderation of the recrystallization texture by nucleation at copper-type shear bands in Al-1Mg*. Acta Materialia, 2002, 50: pp.2881–2893,

113. O. Engler, *An EBSD local texture study on the nucleation of recrystallization at shear bands in the alloy Al-3%Mg*. Scripta Materialia, 2001, 44: pp.229–236,

114. Y. Huang, F.J. Humphreys and M. Ferry, *The annealing behaviour of deformed cube-oriented aluminium single crystals*. Acta Materialia, 2000, 48: pp.2543-2556,

115. Y. Huang and F.J. Humphreys, *Measurements of grain boundary mobility during recrystallization of a single-phase aluminium alloy*. Acta Materialia, 1999, Vol. 47, No. 7: pp.2259-2268,

116. Matthew Cross, *The Thermomechanical Processing of Age Hardenable Aluminium Alloy AA6111*. MEng Project Thesis, 2004, The University of Sheffield

117. B. Dutta, E. Valdes and C.M. Sellars, *Mechanism and kinetics of strain induced precipitation of Nb(C, N) in austenite*. Acta Metallurgica et Materialia, 1992, 40: pp.653-662

118. I. Barlow, *Evolution of Microstructure and Thermal Stability of Al-Ti-O and Al-Li-Mg Based Materials*. PhD Thesis, 2001, Sheffield University

119. K.C. Lee, Y.P. Zeng, and C.S. Lee, Influence *of external constraint on deformation banding of copper single crystals of {110} <uvw> orientations.* Scripta Materialia, 1999. Vol. 40(2): pp.197-202.

120. N. Hansen, *New discoveries in deformed metals*. Metallurgical and Materials Transactions, 2001, 32A: pp.2917-2935,

121. G. Winther, D.J. Jensen, and N. Hansen, *Dense dislocation walls and microbands aligned with slip planes-Theoretical considerations*. Acta Materialia, 1997, 45: pp.5059-5068

122. A. Fjeldly, A. Soreng, H. J. Roven, *Strain localisation in solution heat treated Al–Zn–Mg alloys*. Materials Science and Engineering, 2001, A300: pp.165–170

123. V. Randle and O. Engler, "Introduction to Texture Analysis: Macrotexture, Microtexture and Orientation Mapping", Amsterdam: Gordon and Breach Science Publishers, 2000

124. F.J. Humphreys, and M. Hatherly, *Recrystallisation and Related Annealing Phenomena*. Pergamon, Oxford, 1996

125. B. Bay, N. Hansen, D.A. Hughes, and D. Kuhlmann-Wilsdorf, *Evolution of f.c.c.*

deformation structures in polyslip. Acta Metallurgica et Materialia (USA), 1992. Vol. 40(2): pp.205-219.

126. D. Kuhlmann-Wilsdorf and N. Hansen, *Geometrically necessary, incidental and subgrain boundaries.* Scripta Metallurgica et Materialia, 1991. Vol. 25: pp.1557-1562.

APPENDIX

The Mr. M. Cross's project serves as a wide-ranging preliminary experimental and modelling investigation into the thermomechanical processing of AA6111 alloy.

Utilising Sheffield University's TMC testing machine to stimulate industrial deformation conditions, with controlled deformation at a constant strain rate of $85s^{-1}$. The machines FTTU unit has been optimised for the temperature control of aluminium alloys, with controlled heating rates of up to $10.3°Cs^{-1}$, and controlled quenching at up to $30°Cs^{-1}$. Strain-induced precipitation has been observed in AA6111 in the solution treated condition at 320°C. The kinetics of this precipitation is very rapid, with extensive precipitation hardening being observed after 6 seconds at 320°C.

Q_{def} for AA6111 in the solution treated condition has been determined to be 201kJ/mol between the temperatures of 300-500°C. The calculated value shows a good fit over the range of conditions tested, indicating that there are no significant changes in the fundamental mechanisms of deformation between 300-500°C. First and second stage flow behaviour constitutive equations have been successfully derived for AA6111 in the solution treated condition within the temperature range of 300-500°C.

- Constitutive equations

1. Temperature *correction*

First stage constitutive equations do not require temperature correction as they are plotted in terms of instantaneous Z, hence any variations in temperature and strain rate can be sufficiently accounted for in the final equations. Second stage constitutive equations however depend on the individual determination of several characteristic points on a given flow stress curve. Therefore, any deviation in the flow stress curves due to temperature change must be corrected for to enable consistency in the determination of the characteristic points.

2. Determination of Q_{def}

The sensitivity of flow stress to strain rate can be described by an equation of the form:

$$\sigma_{(\varepsilon)} = B_{(\varepsilon)} f\left(\dot{\varepsilon} \exp \frac{Q_{def}}{RT}\right) = B_{(\varepsilon)} f(Z) \qquad (1)$$

where: $\sigma_{(\varepsilon)}$=Flow stress at equivalent true strain ε

$B_{(\varepsilon)}$ =Material constant at equivalent true strain ε

Q_{def} =Activation energy for the deformation mechanism

Z=Zener-Hollomon parameter

Hence the values for $B_{(\varepsilon)}$ and Q_{def} can be found by analysing the experimental flow stress data.

3. Second stage constitutive equations

Second stage constitutive equations describe an extrapolated flow stress curve with the equation:

$$\sigma = \sigma_0 + (\sigma_{ss} - \sigma_0)[(1 - \exp(-\varepsilon/\varepsilon_r)]^{1/2} \qquad (2)$$

where σ_0, σ_1, and σ_{ss} are the characteristic points on a flow stress curve as described above, and ε_r is the transient strain constant, which describes the curvature of the flow stress curve between σ_0 and σ_{ss}, after which point the curve maintains a steady state value.

ε_r is given by the equation:

$$\varepsilon_r = -0.1(\ln\{1 - [(\sigma_{0.1} - \sigma_0)/(\sigma_{ss} - \sigma_0)]^{1/m}\}) \qquad (3)$$

where m = 0.5.

Equation 2 can be approximated to:

$$\sigma = f_1(Z) + (f_2(Z) - f_1(Z))[1 - \exp(-\varepsilon / f_3(Z))]^{1/2} \qquad (4)$$

where $f_1(Z)$, $f_2(Z)$ and $f_3(Z)$ are functions of Z.

Each function can be found from the equation of a linear line of best fit through a plot of log Z v's σ_0, σ_1, and σ_{ss}, as shown in the project. Hence the final equation is:

$$\begin{aligned}\sigma = {} & (16.424 \log Z - 176.18) + ((16.281 \log Z - 177.66) \\ & - (16.424 \log Z - 176.18))[1 - \exp(-\varepsilon / f_3(Z))]^{1/2}\end{aligned} \qquad (5)$$

From this final second stage constitutive equation it is possible to calculate flow stress curves for the tested material in terms of constant and instantaneous Z.

PICTURES AND TABLES

Table 4.1 Chemical Composition of AA6111 alloy

Element	Mg	Si	Cu	Fe	Mn	Cr	Ti	Al
Wt%	0.79	0.60	0.70	0.25	0.20	0.05	0.06	Base

Table 4.2 Precipitates: β'', Q [26]

Phase	Crystal type	Size (nm)	Composition
β″	Monoclinic	~2.5×2.5×8-15	Mg/Si
Q	Hexagonal	~2.0×5.0×100.0	Al/Mg/Si/Cu

Table 4.3 The true ultimate strains for the double hit deformation

Condition	0	6	60	600	6000
Strain	0.86	0.95	0.91	0.89	0.83

Table 5.1. Size of the EBSD images

Condition	Normal plane		Transverse plane	
	μm×μm	mm2	μm×μm	mm2
Single	5140 ×2540	13.05	5328×1672	8.90
0	3624×2120	7.68	5520×2024	11.17
6	4770×3610	17.21	5520×1840	10.15
60	5710×3790	21.64	5334×1864	9.94
600	5704×1120	6.38	5328×1856	9.88
6000	5330×3810	20.30	5328×1856	9.88

Table 5.2 Grain Number from EBSD images.

Condition	Normal Plane		Transverse plane	
	Grain No.	Mini. D.	Grain No.	Mini. D.
Single	766	22.57	1225	18.05
0	691	18.05	2380	18.05
6	1371	22.57	1571	18.05
60	1497	22.57	1497	18.05
600	526	18.05	1538	18.05
6000	1053	22.57	1524	18.05

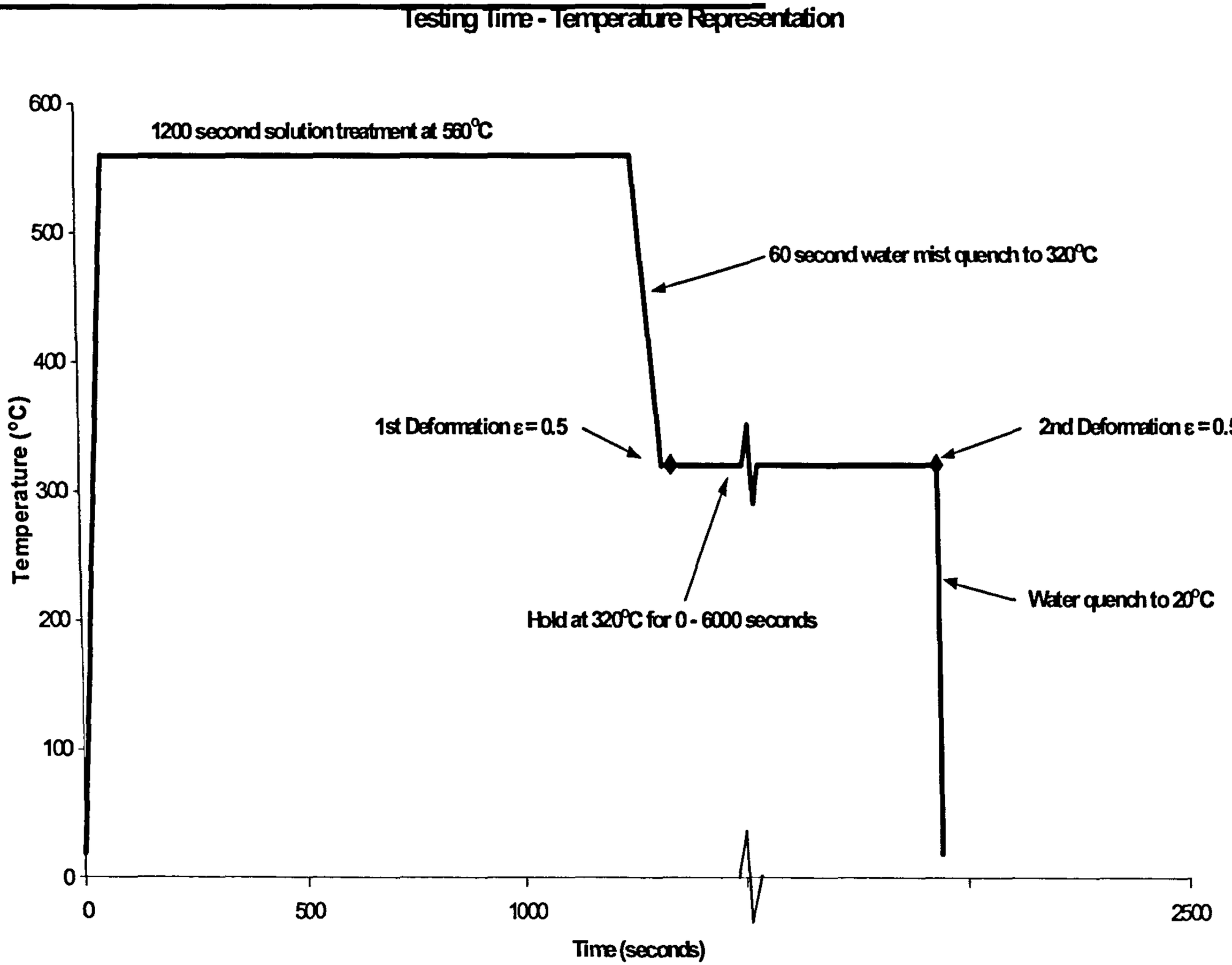

Fig. 4.1 Prior thermal cycle and test conditions for plane strain compression undertaken by Matt Cross, 2004, Master's thesis.

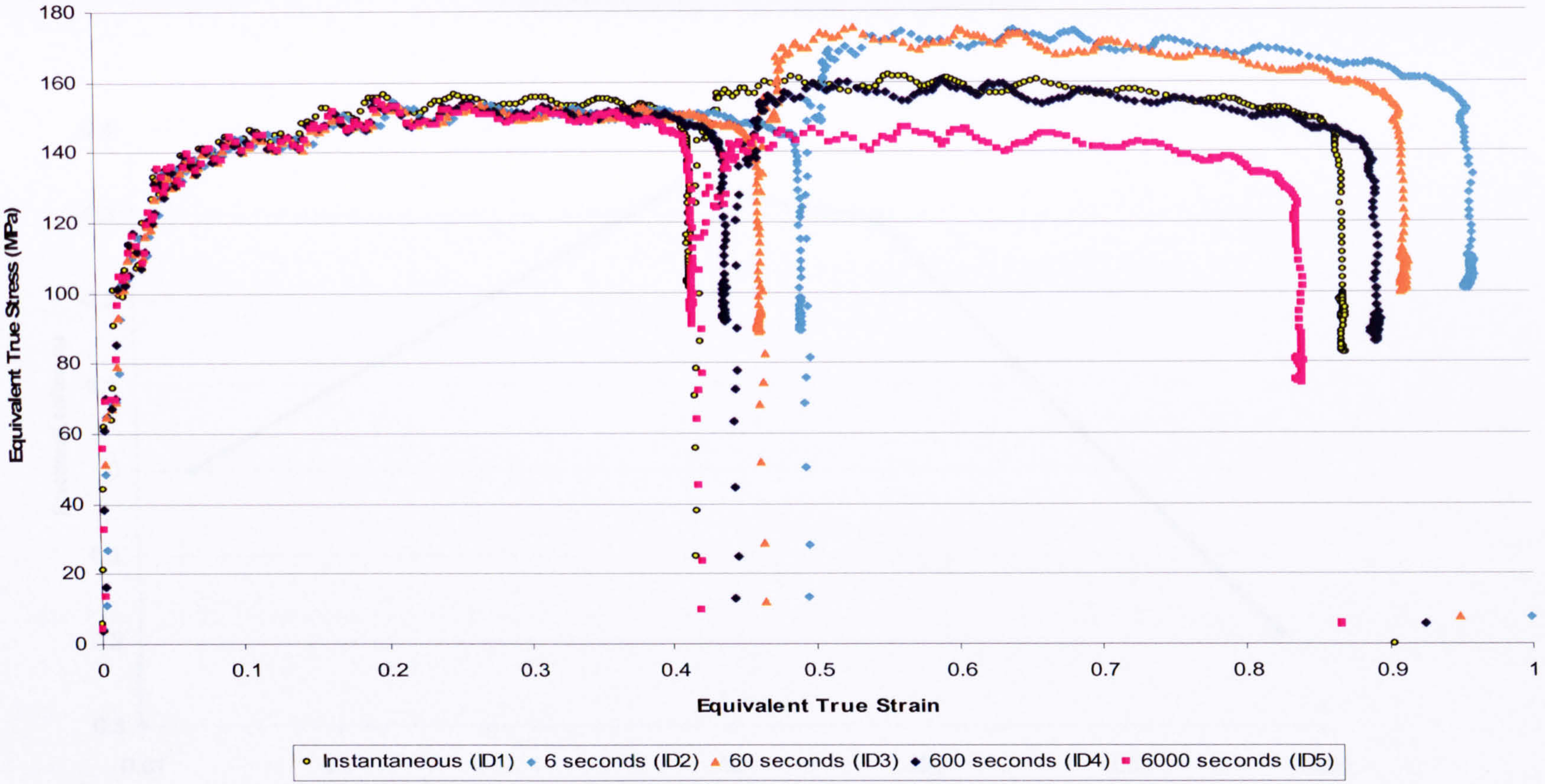

Fig. 5.1 True stress-true strain curves for the AA6111 alloy used in this study. Data from Matt Cross, 2004, Master's thesis.

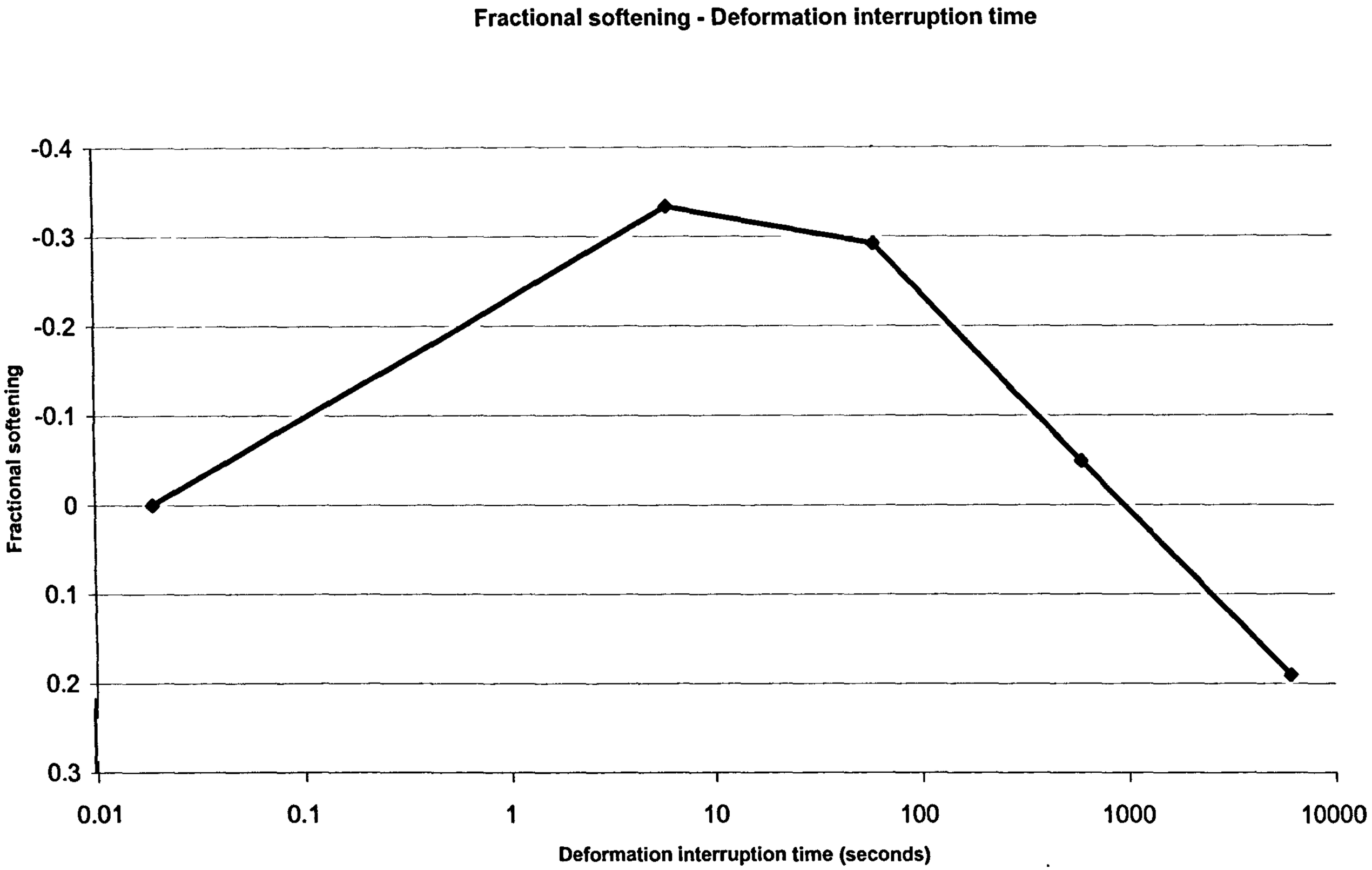

Fig. 5.2 Fractional softening-deformation interruption time plot. Data from Matt Cross, 2004, Master's thesis.

a

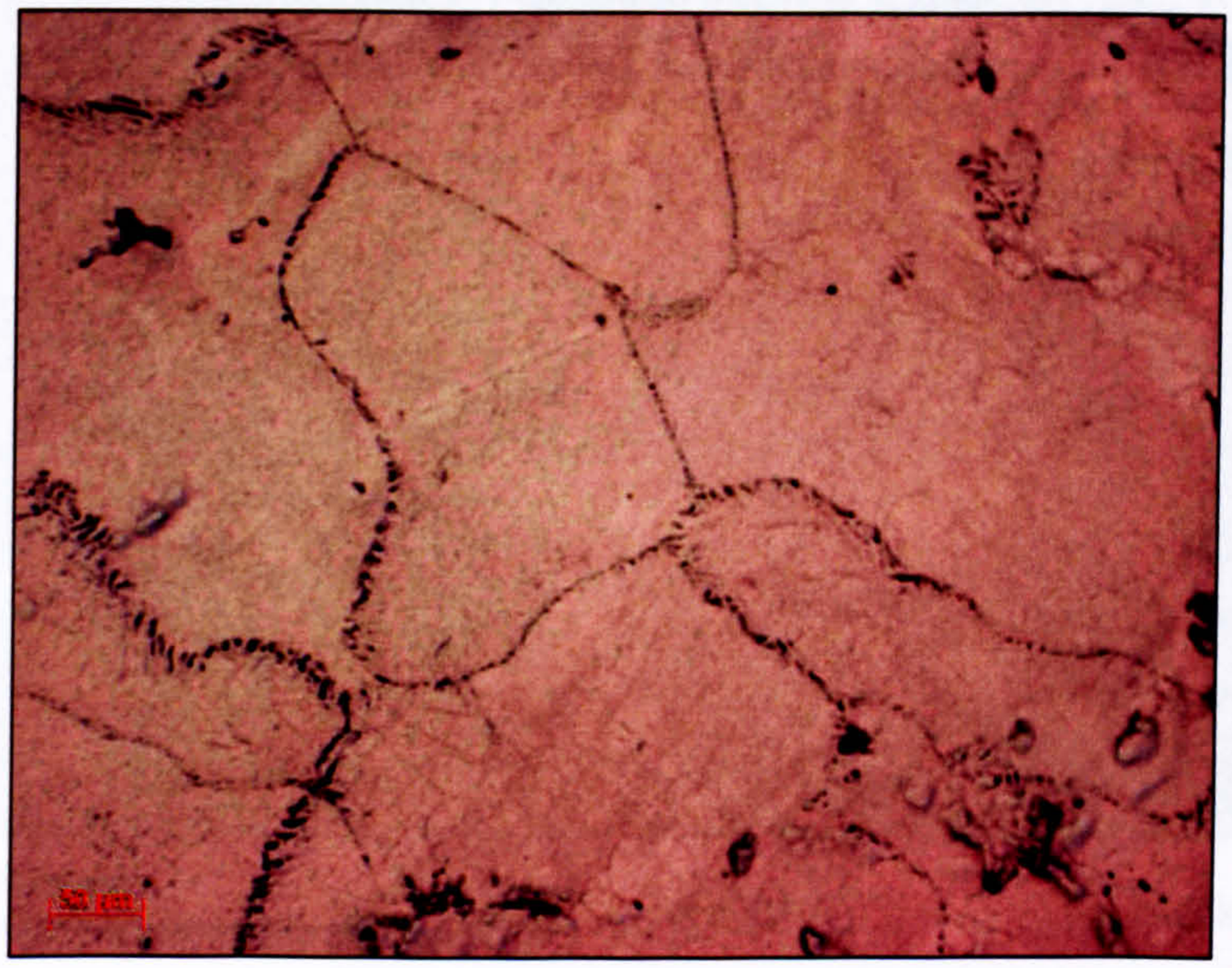

b

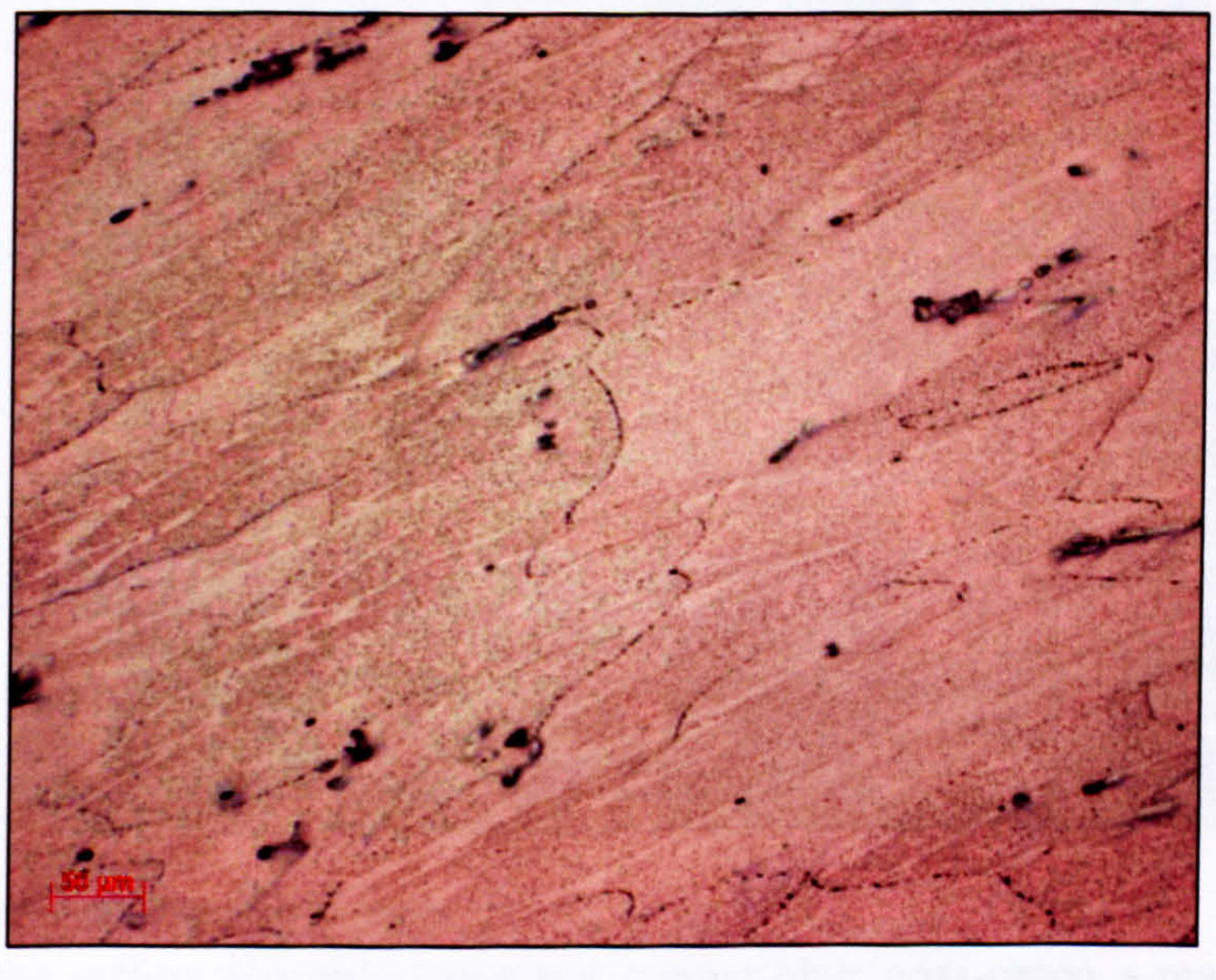

Fig. 5.3 Optical micrographs of deformed structure after the single deformation: (a) normal plane, (b) transverse plane.

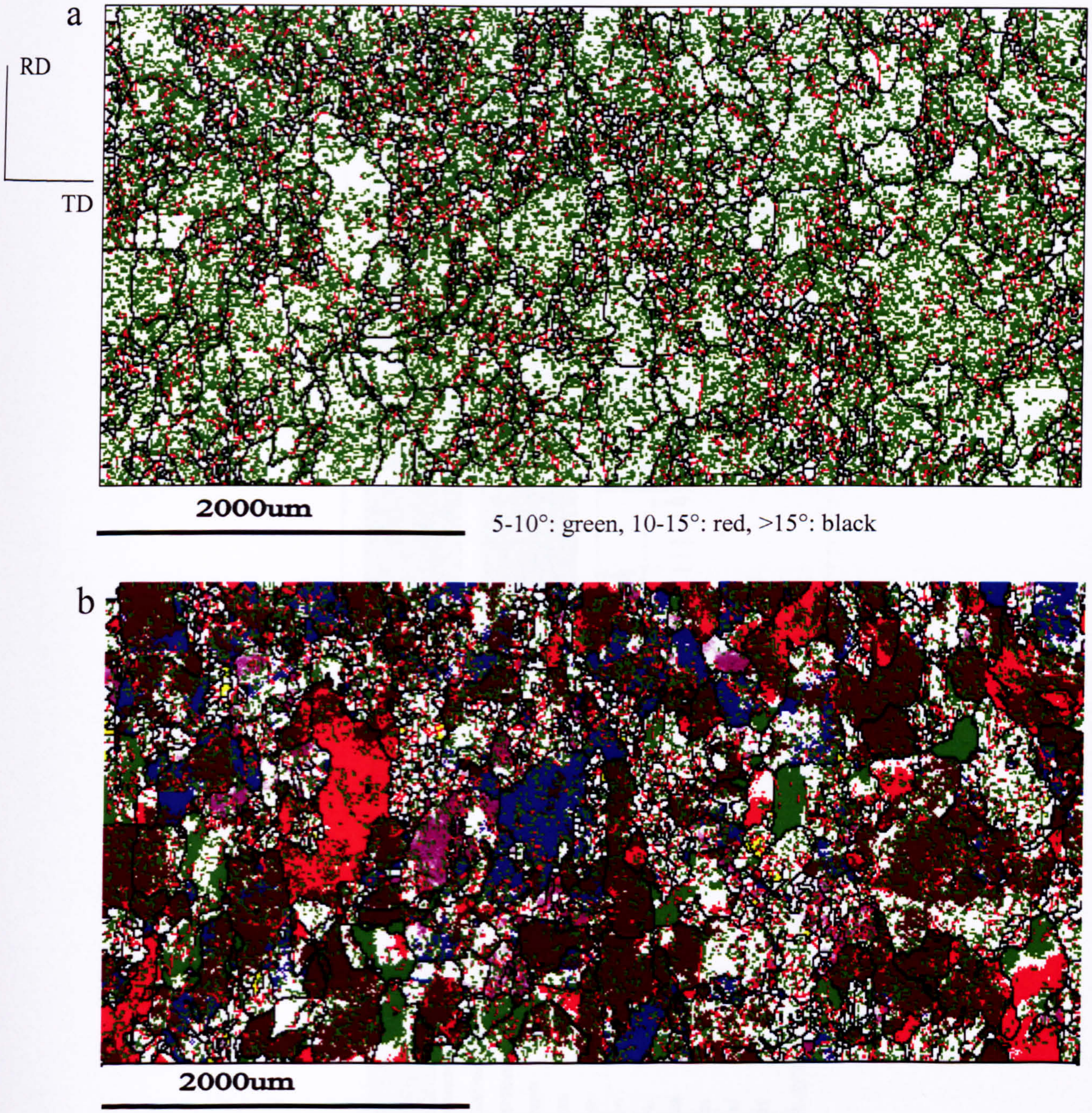

Fig. 5.4 (a) Orientation map and (b) texture components to the microstructure for the single deformed sample (normal plane).

a

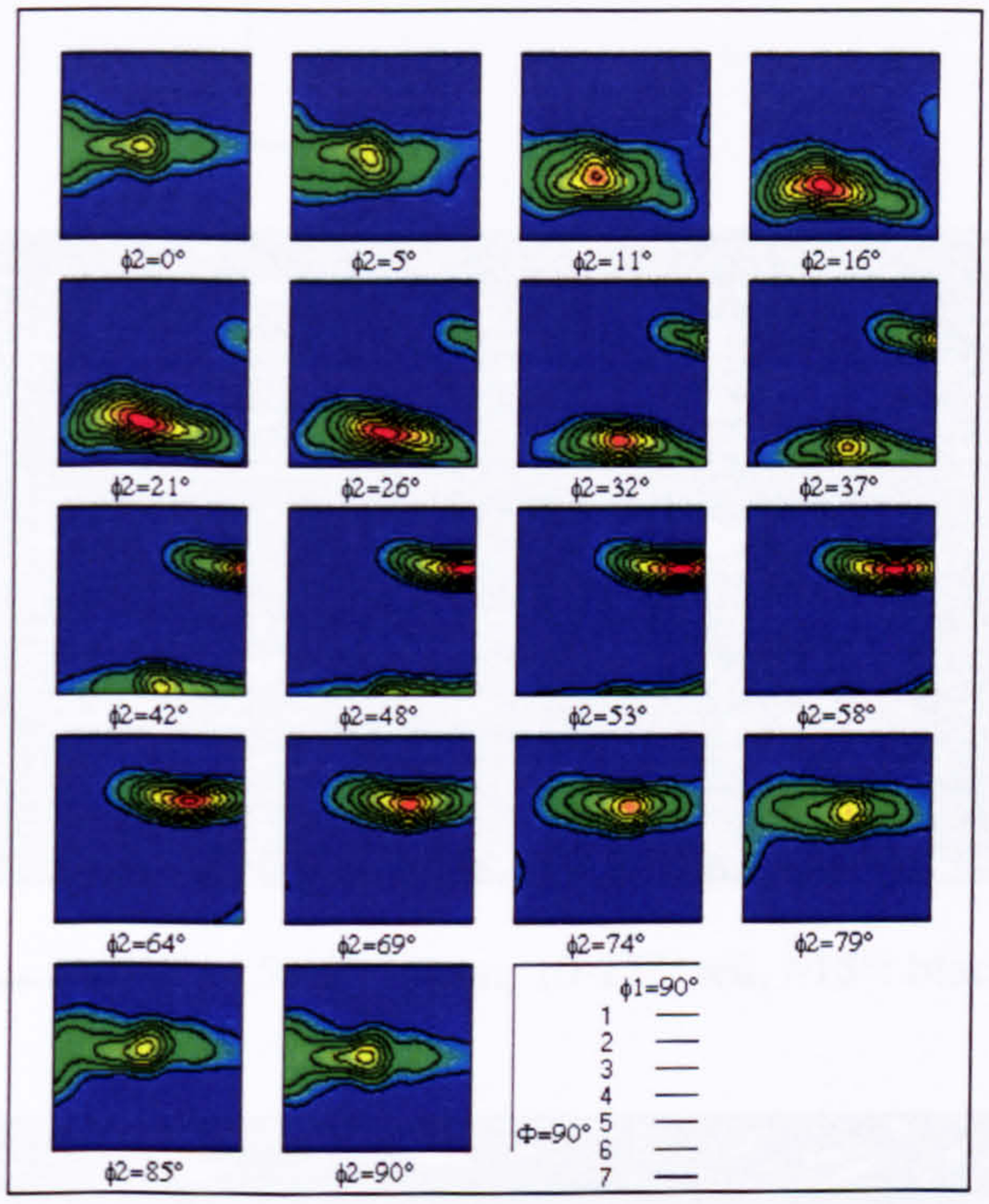

b

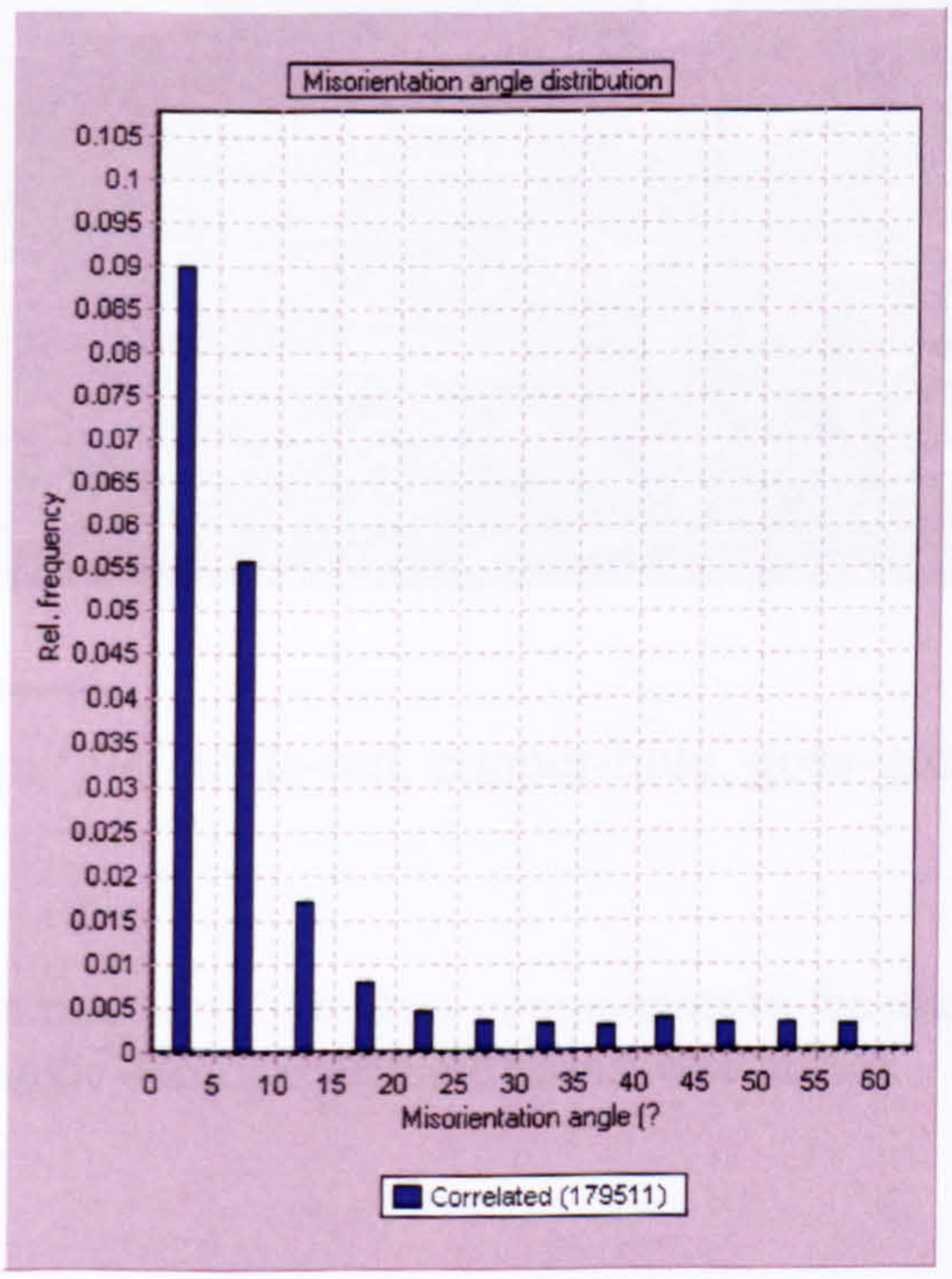

Fig. 5.5 EBSD results of the single deformed sample: (a) orientation distribution functions (ODF) maps, (b) misorientation angle distribution.

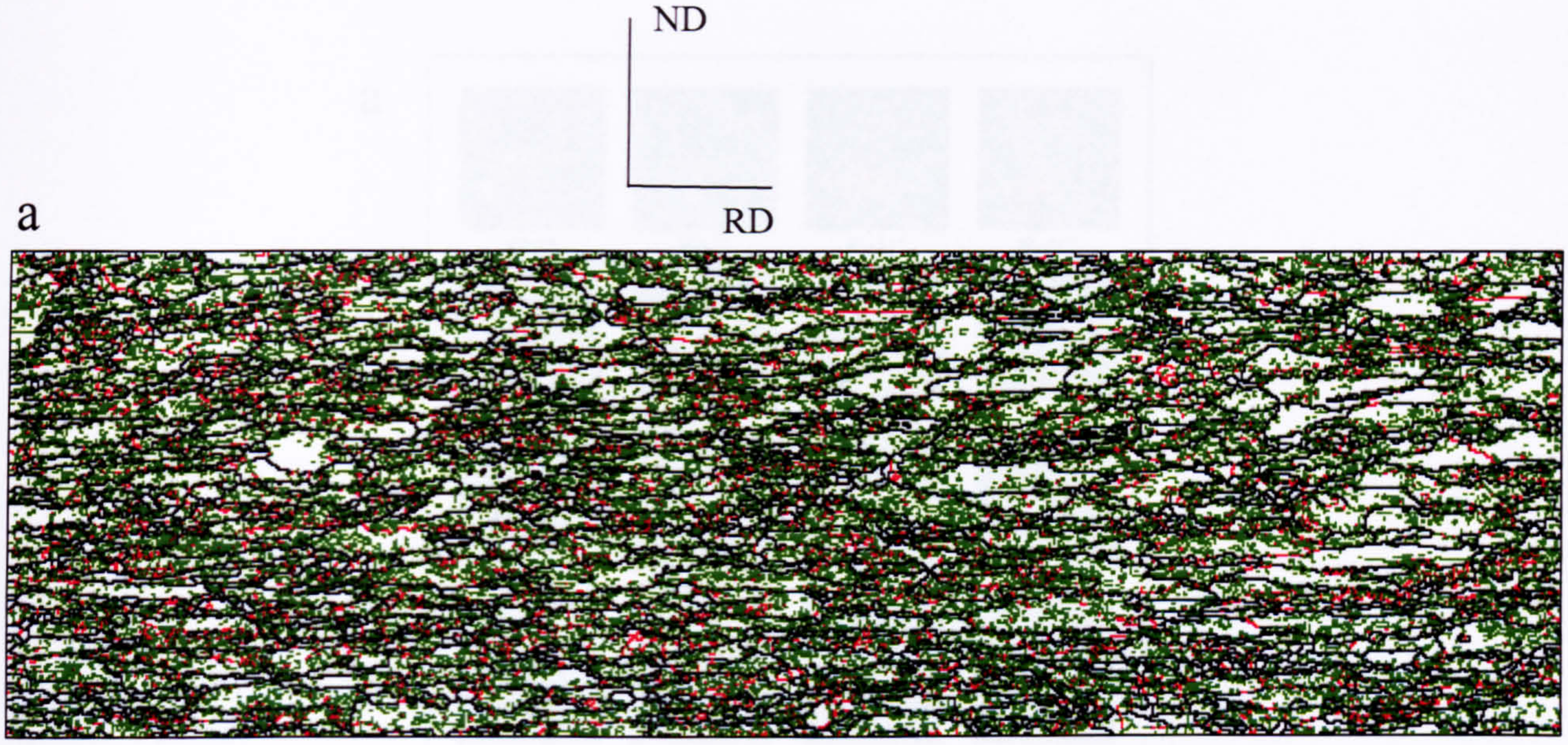

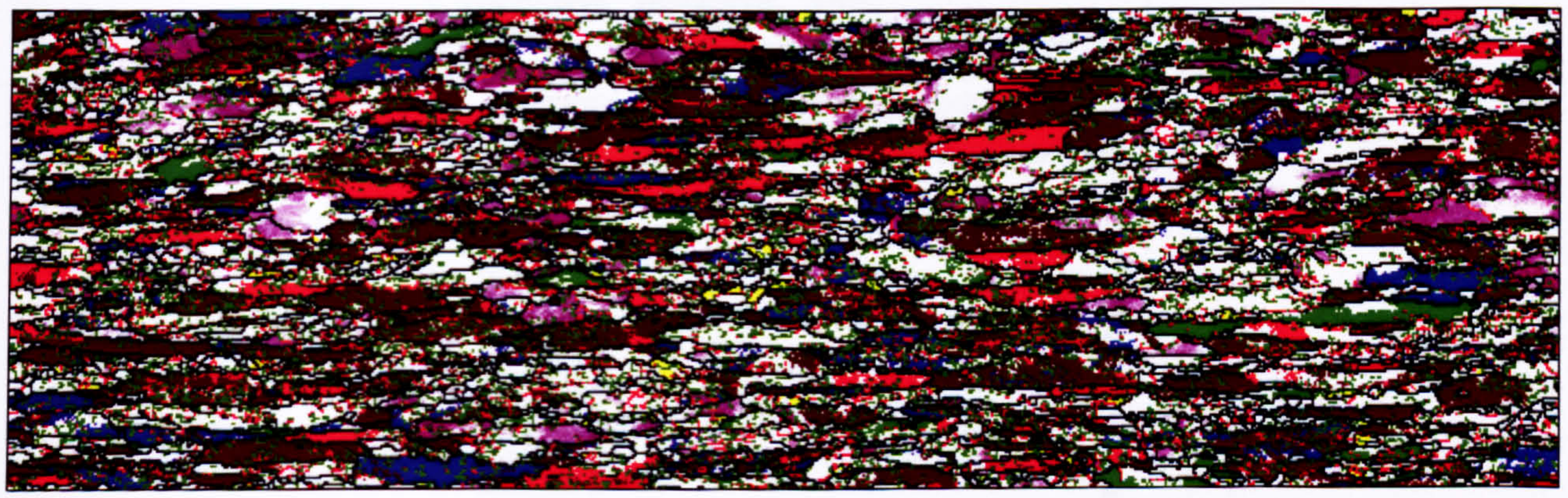

Fig. 5.6 (a) Orientation map and (b) texture components to the microstructure for the single deformed sample (transverse plane).

a

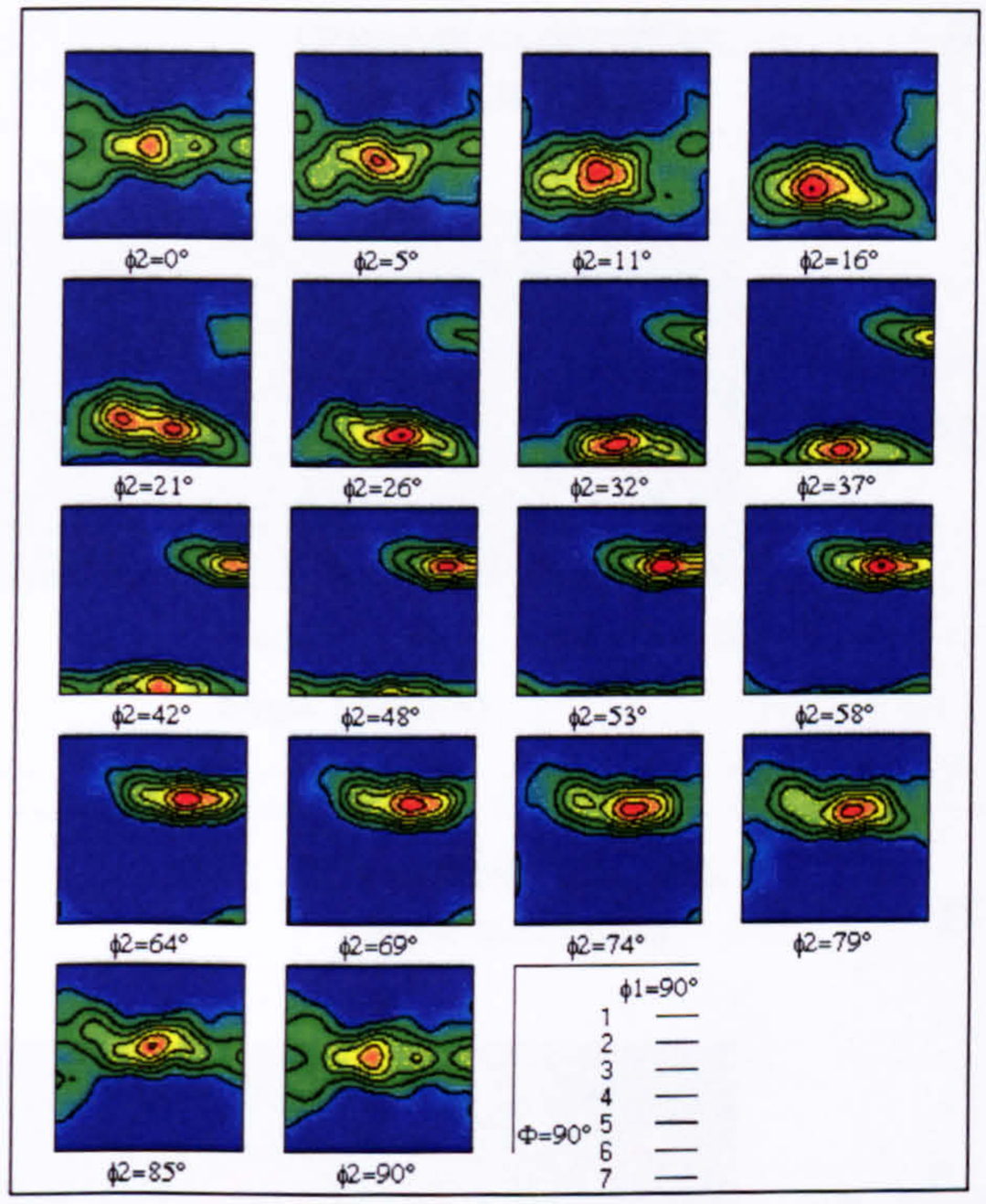

b

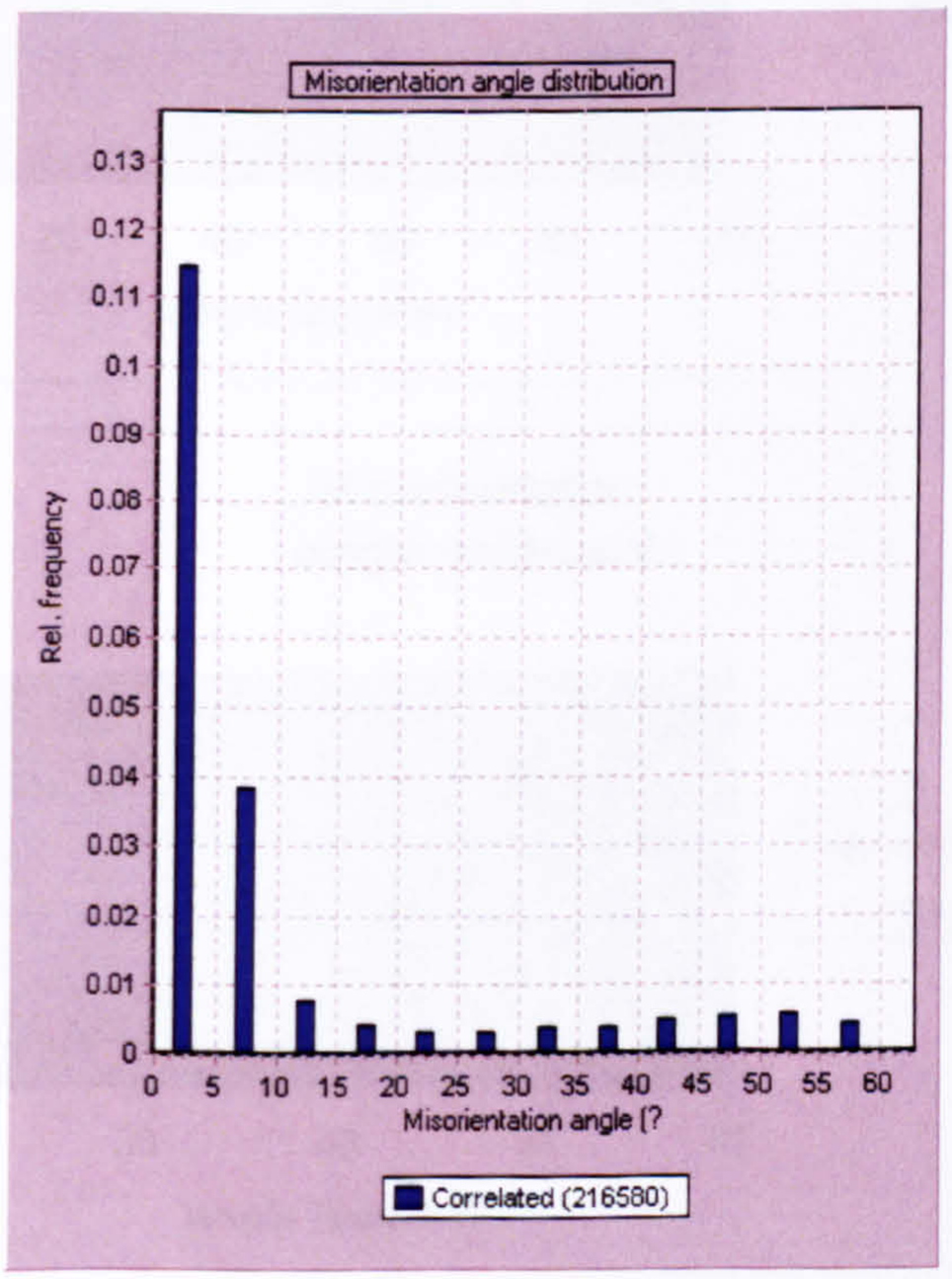

Fig. 5.7 EBSD results of the single deformed sample: (a) orientation distribution functions (ODF) maps, (b) misorientation angle distribution.

a

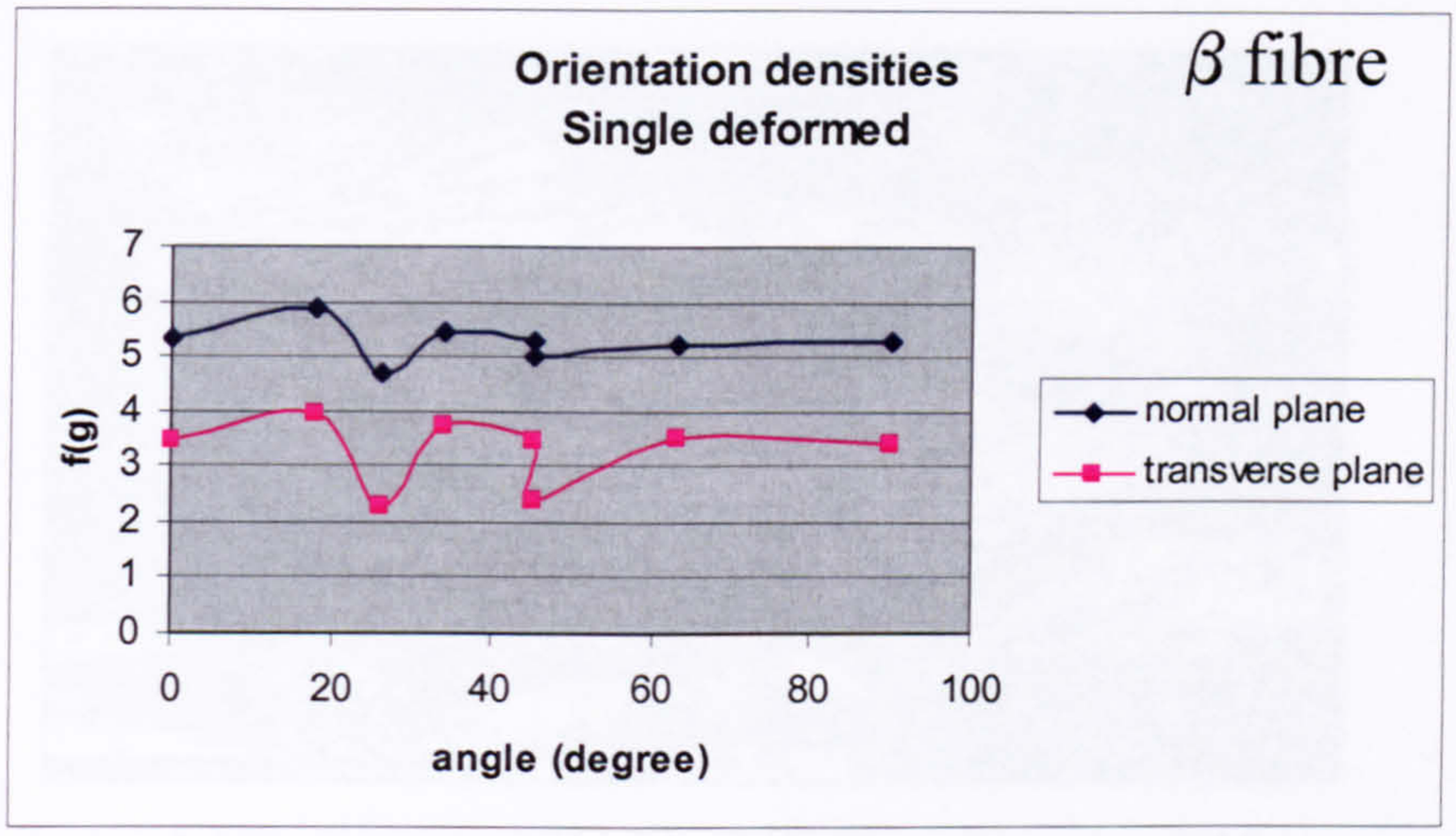

b

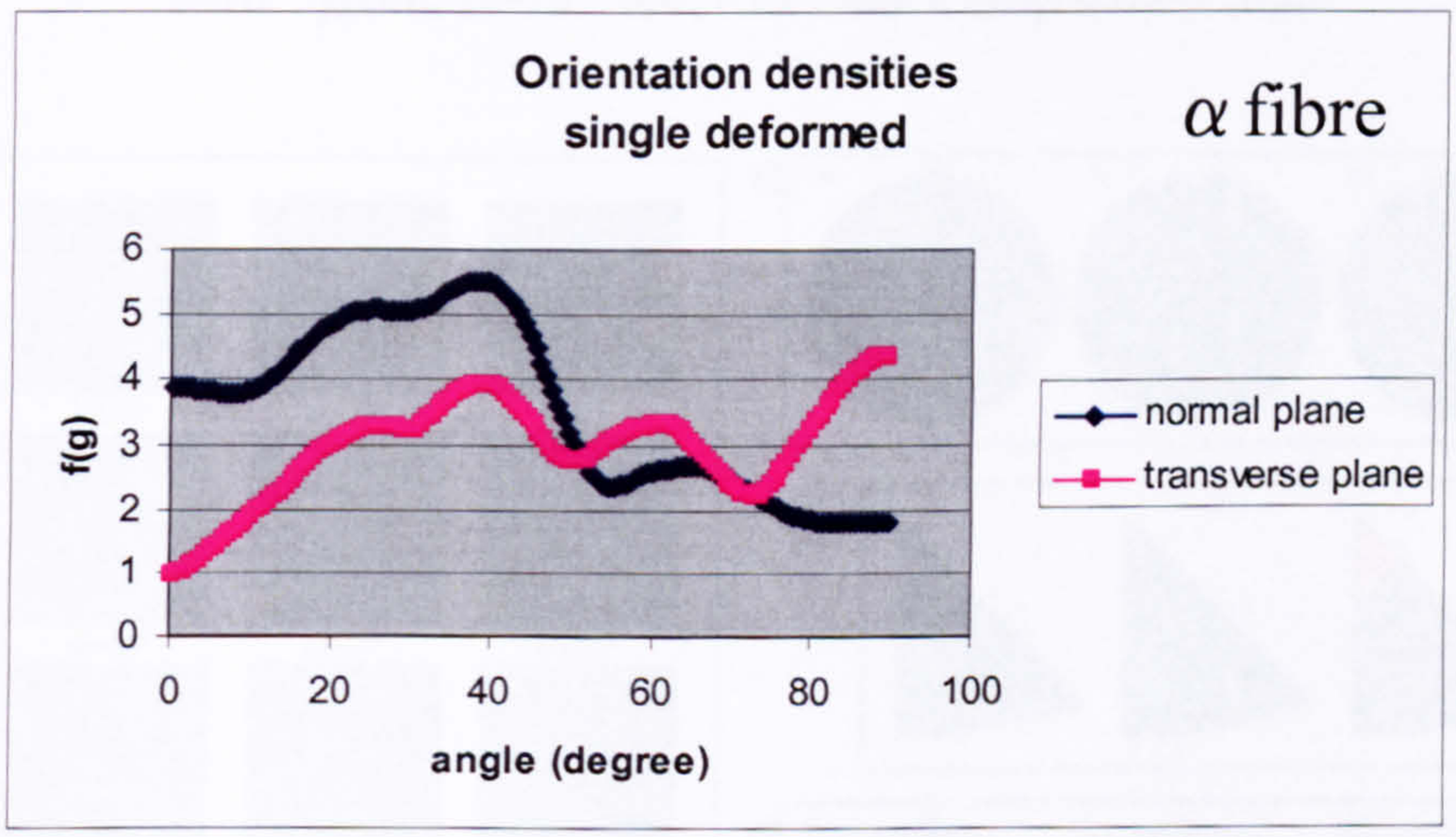

c

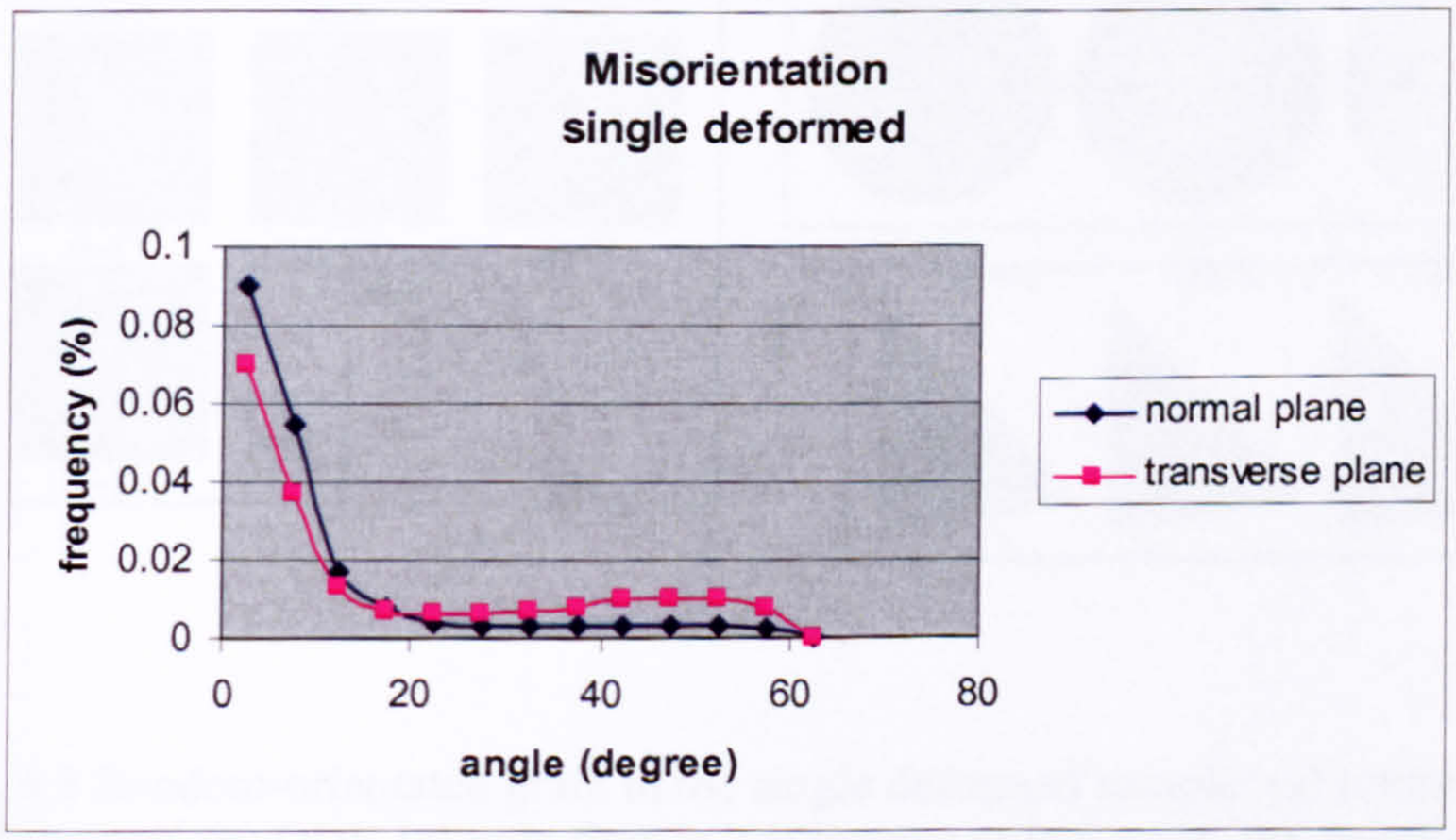

Fig. 5.8 (a) density distribution of β fibre, (b) density distribution of α fibre, (c) misorientaiton distribution for the single deformed sample.

a

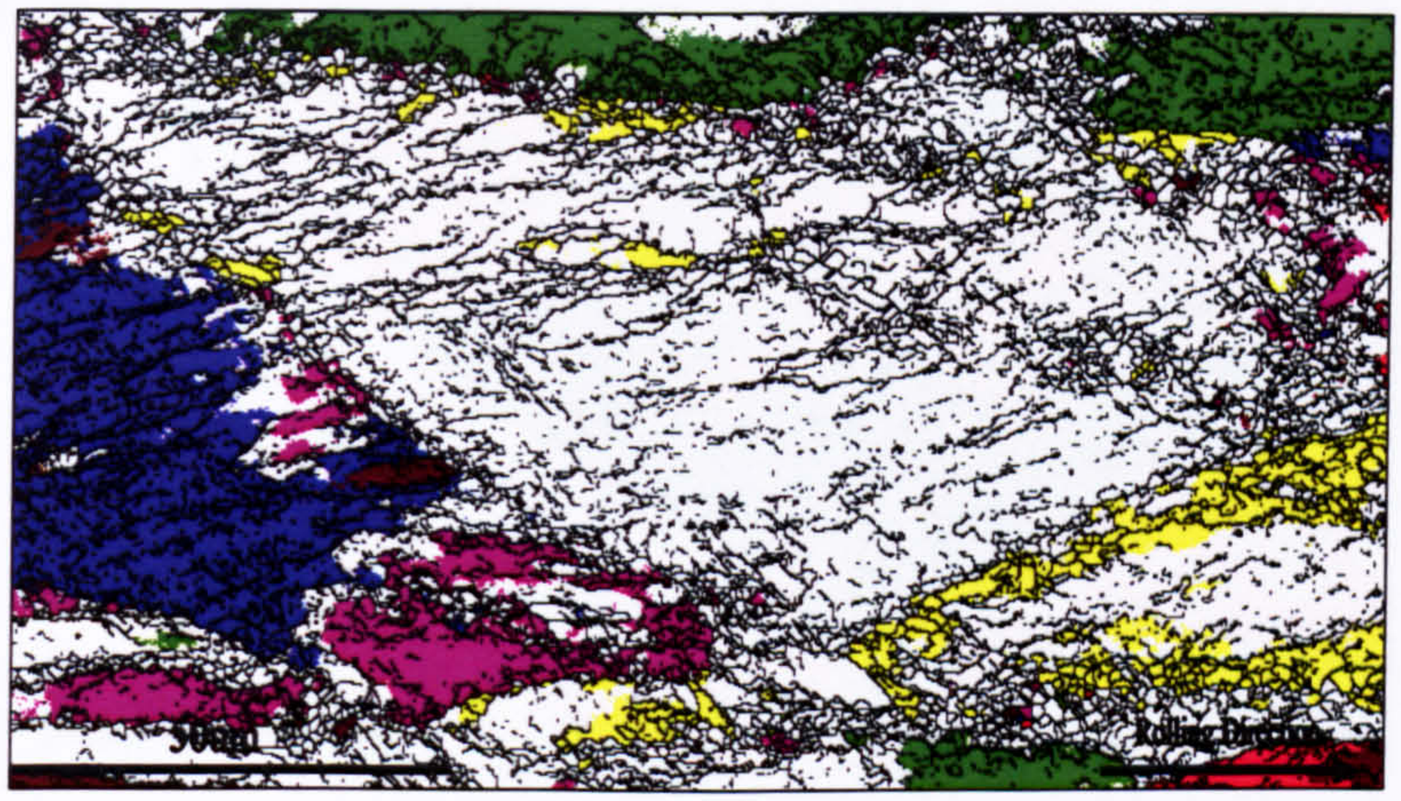

5-10°: green, 10-15°: red, >15°: black Step size=0.25μm

b

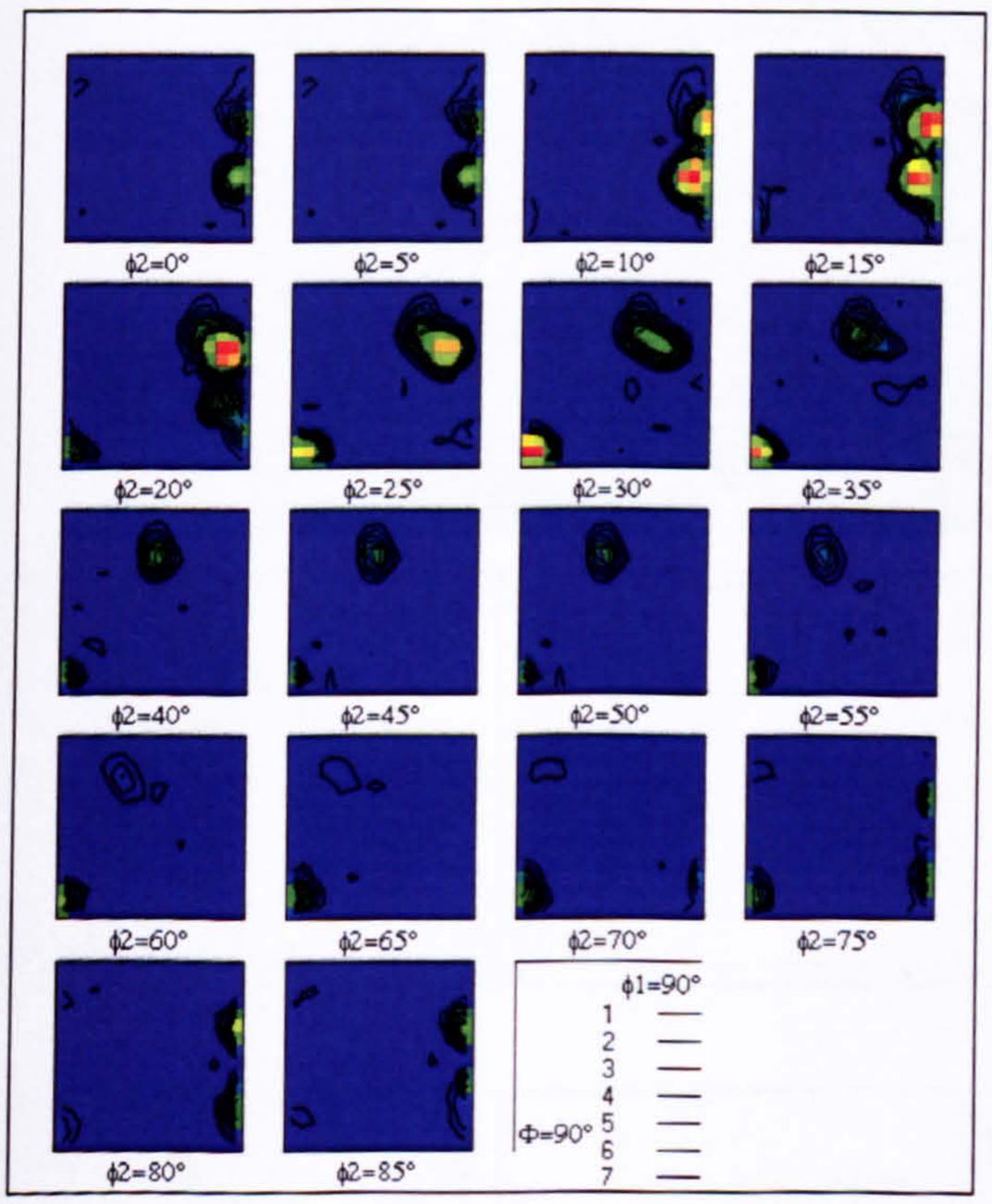

c

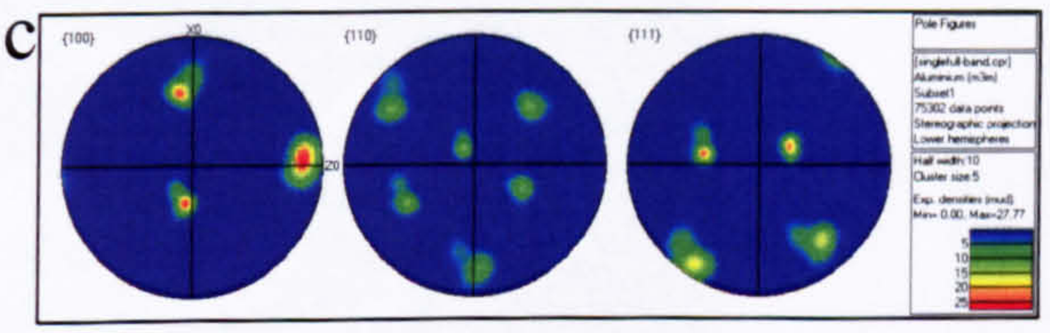

d

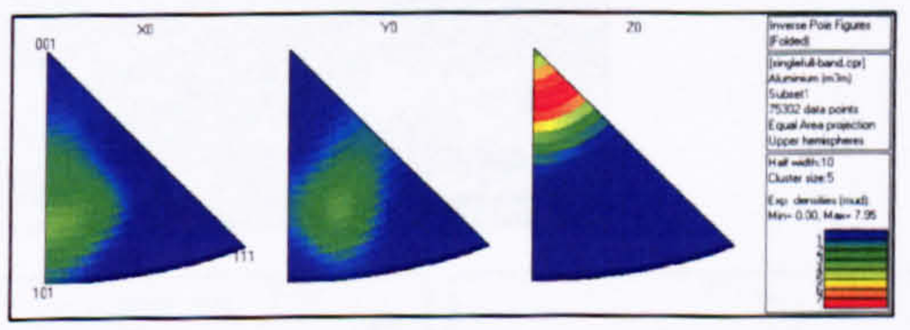

e

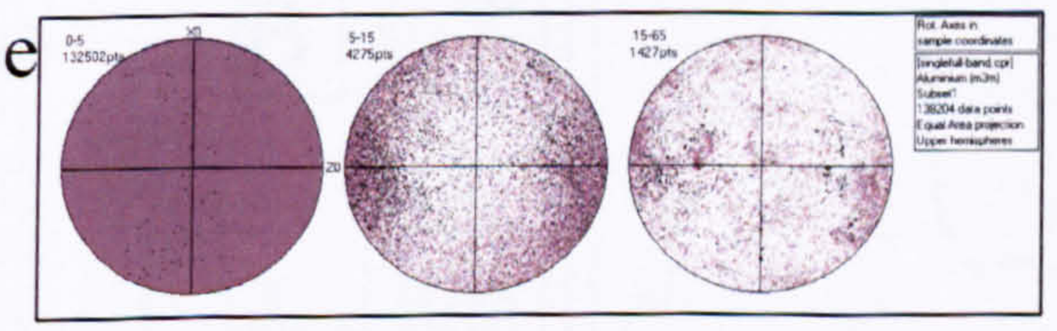

f

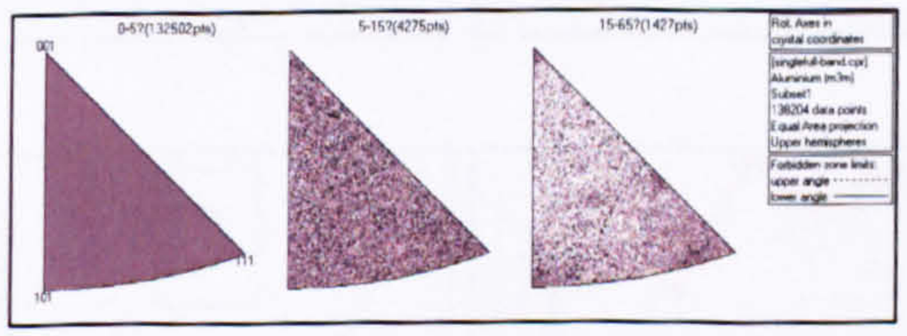

Fig. 5.9 Random-orientated grain in the single deformed sample: (a) texture and boundary map, (b) ODF, (c) pole figures, (d) inverse pole figures, the distribution of misorientation axis vectors in (e) sample and (f) crystal lattice coordinates.

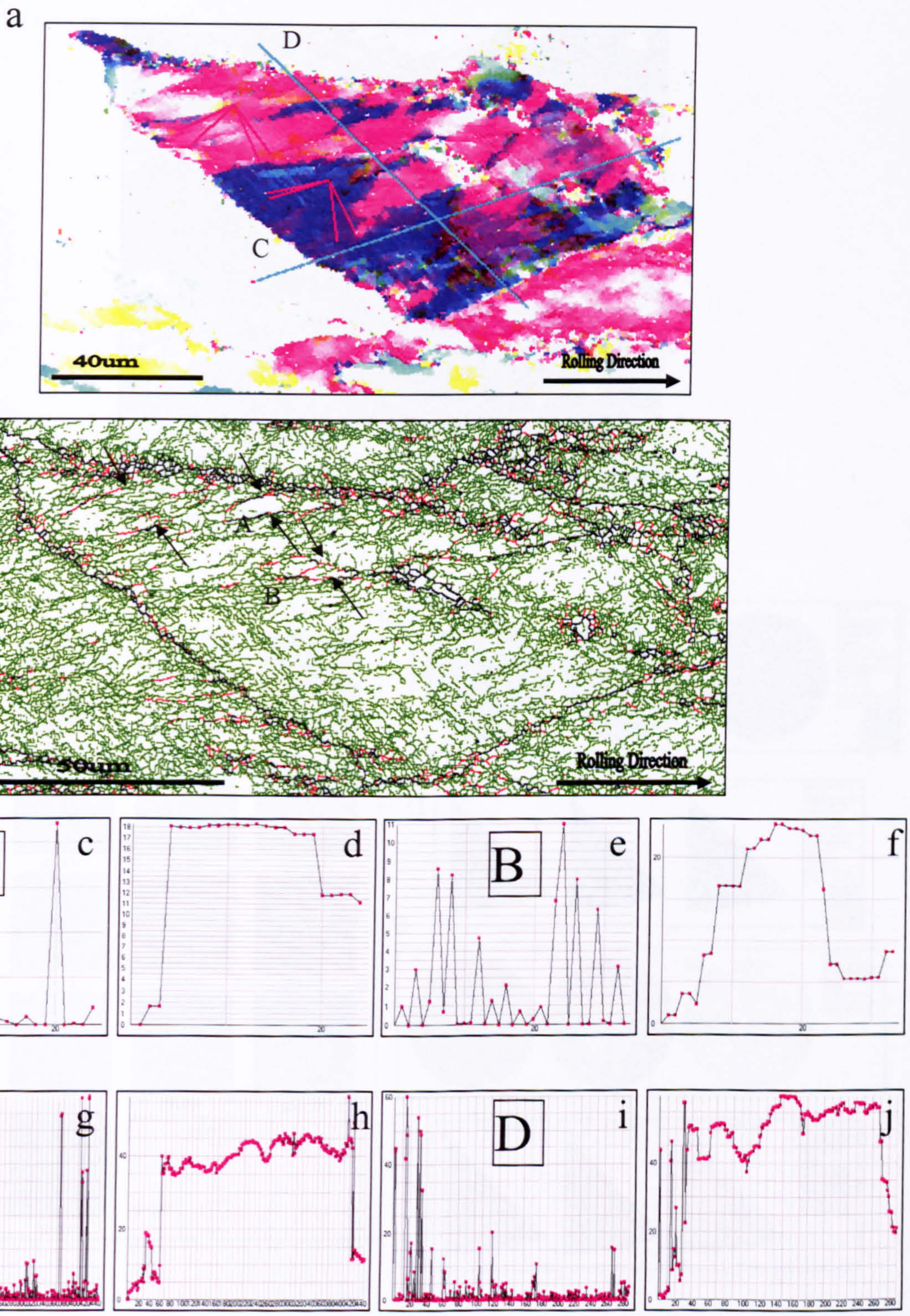

Fig. 5.10 Random-orientated grain in the single deformed sample: (a) relative map, (b) orientation map, (c) (e) (g) (i) relative and (d) (f) (h) (j) cumulative misorientation distributions of line scans performed along A and B in (b), C and D in (a).

a

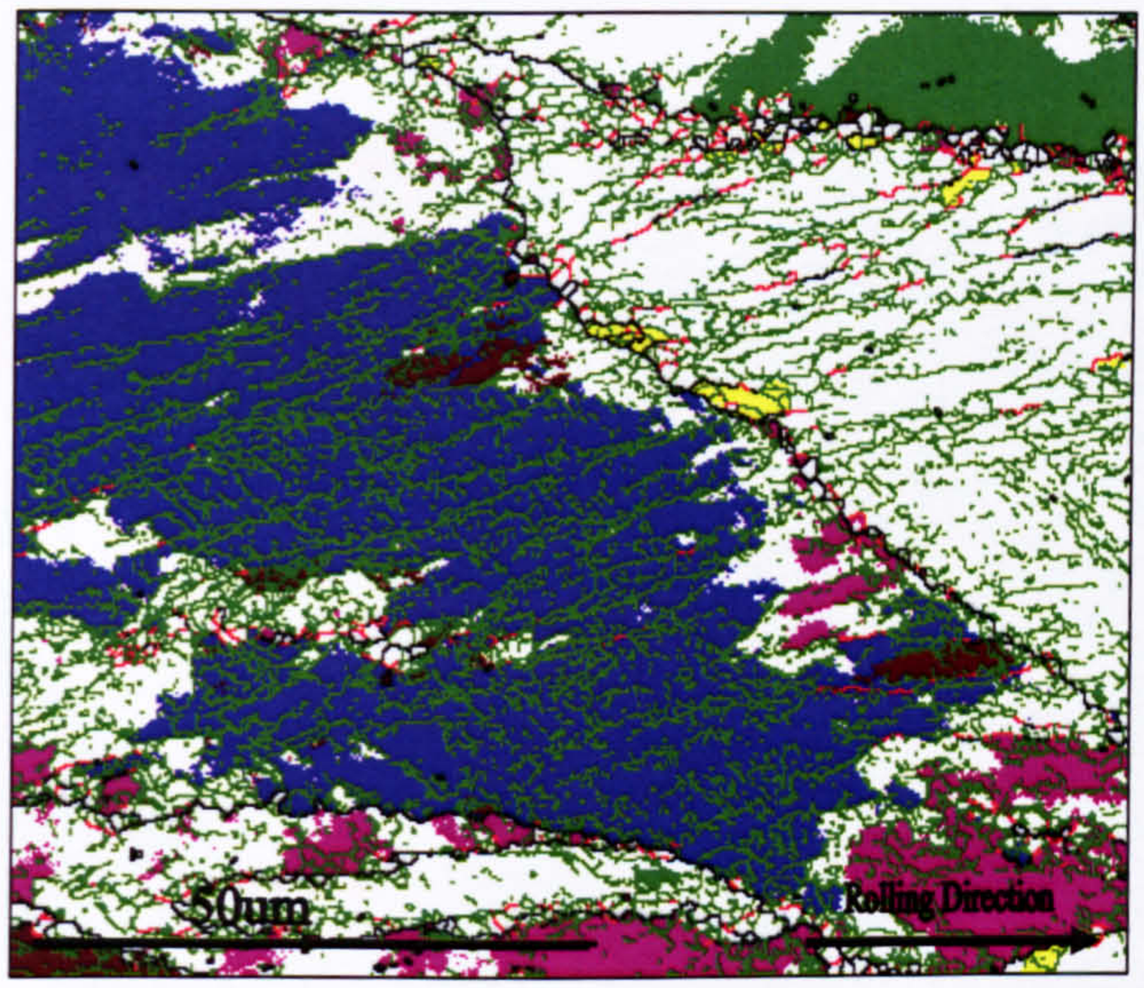

5-10°: green, 10-15°: red, >15°: black step size=0.25μm

b

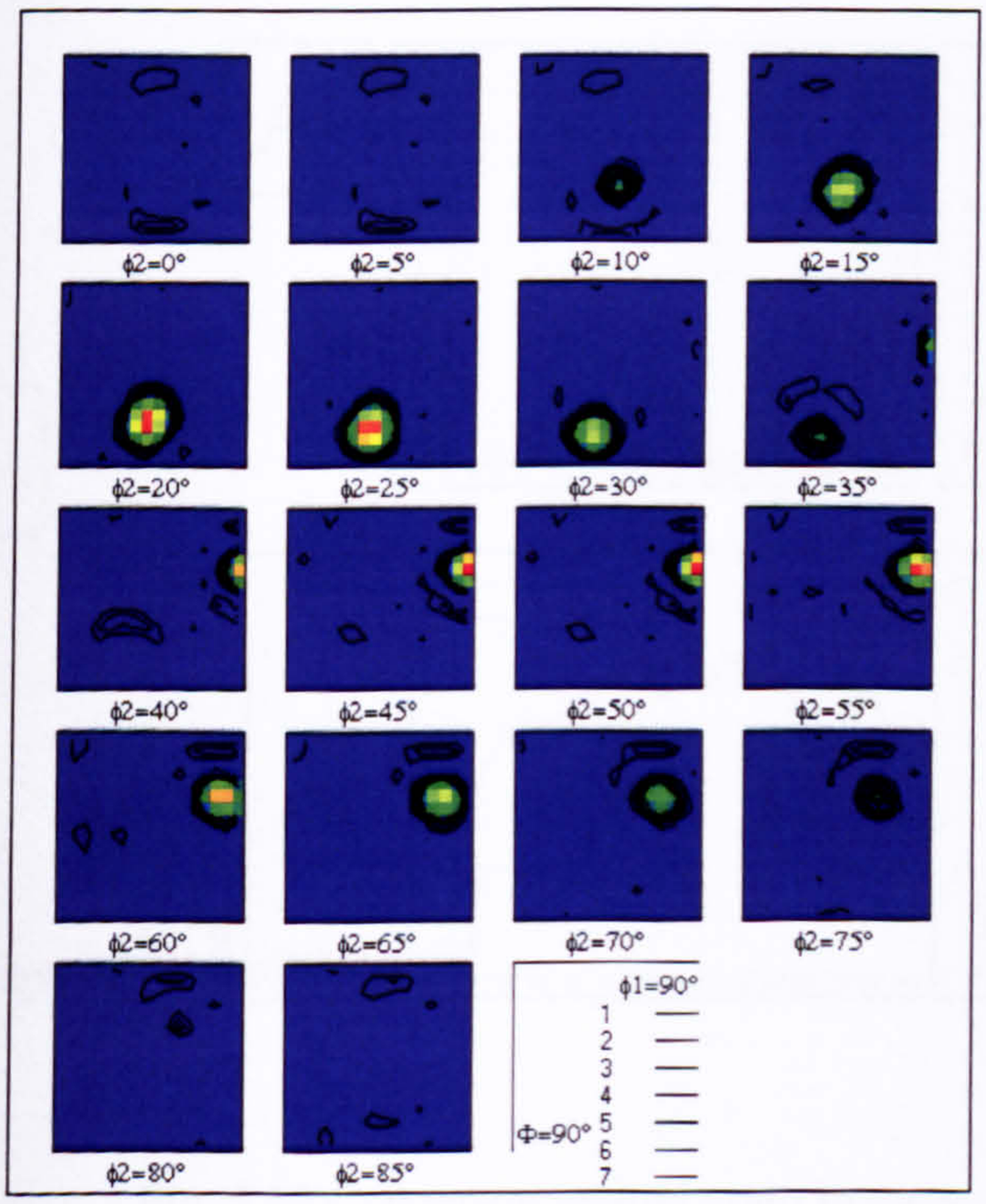

c

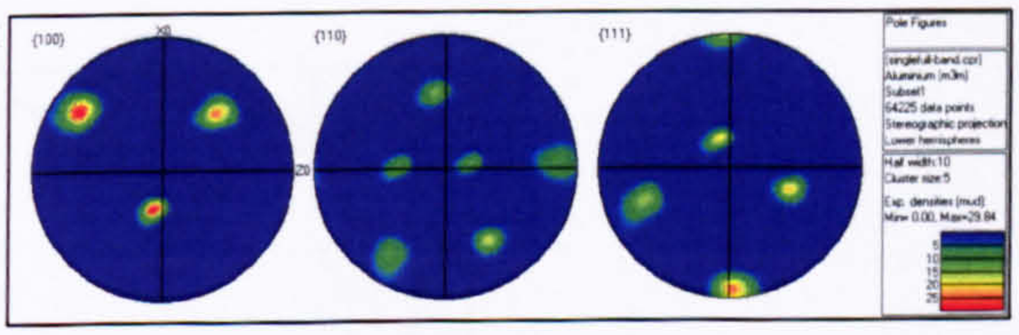

d

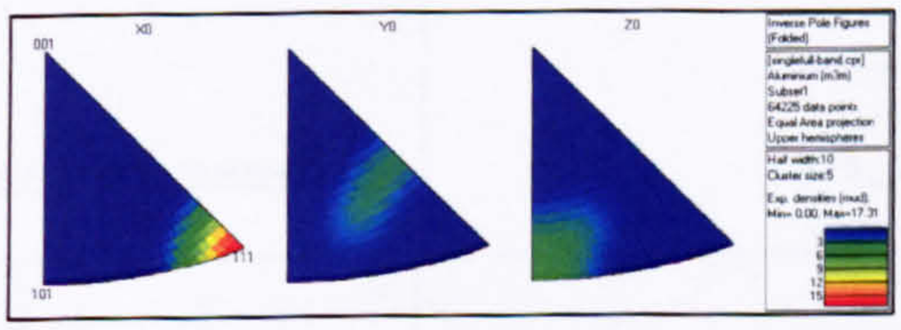

e

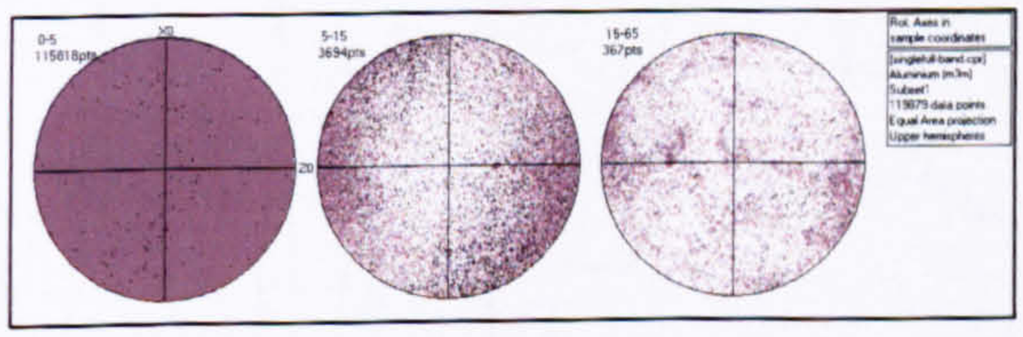

f

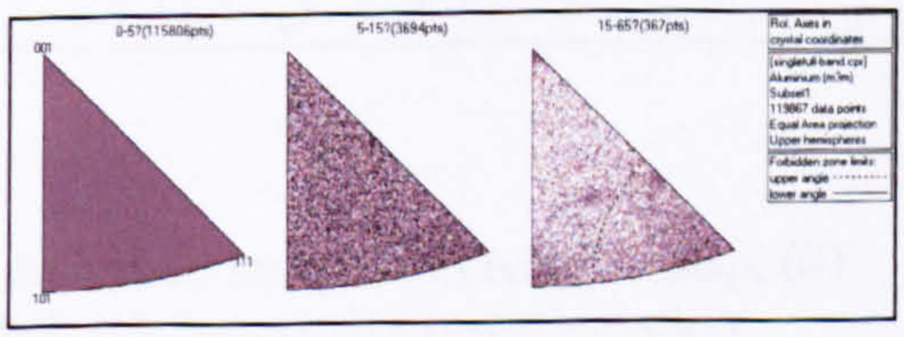

Fig. 5.11 Copper-orientated grain in the single deformed sample: (a) texture and boundary map, (b) ODF, (c) pole figures, (d) inverse pole figures, the distribution of misorientation axis vectors in (e) sample and (f) crystal lattice coordinates.

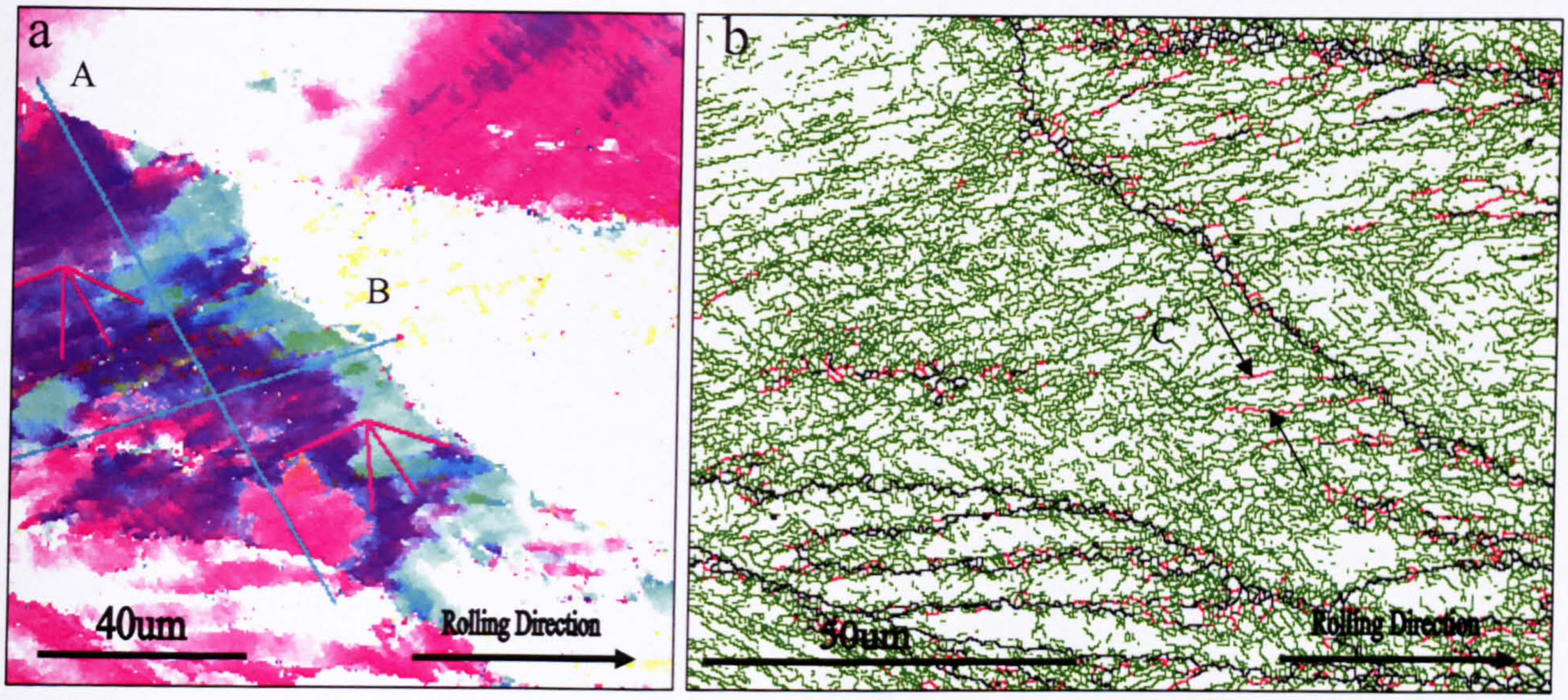

1.5-10°: green, 10-15°: red, >15°: black Step size=0.25μm

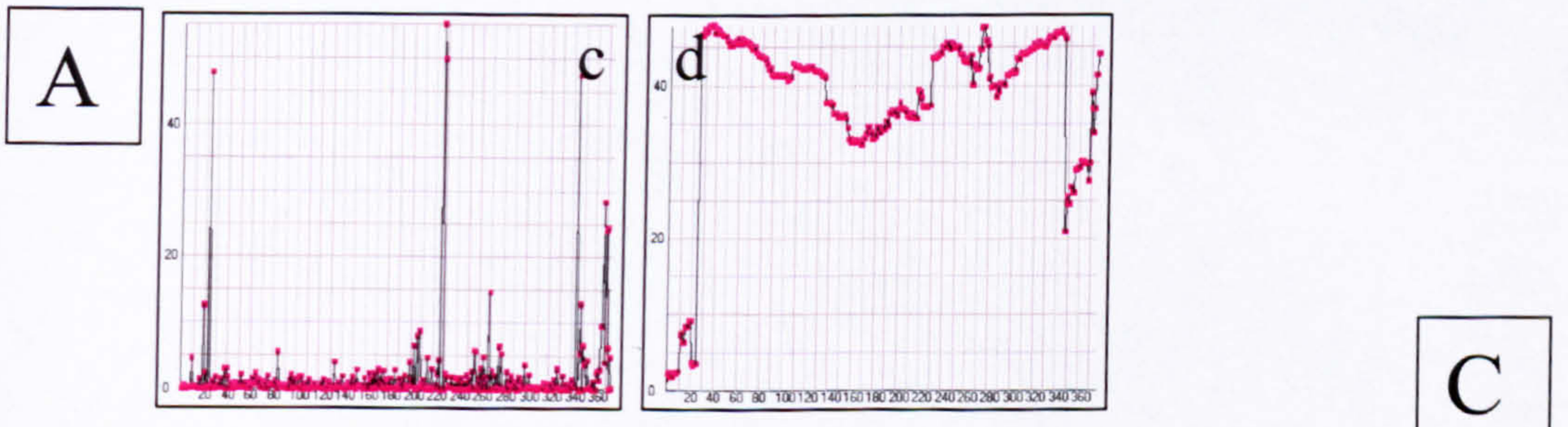

Fig. 5.12 Copper-orientated grain in the single deformed sample: (a) relative map, (b) orientation map, (c) (e) (g) relative and (d) (f) (h) cumulative misorientation distributions of line scans performed along A and B in (a), C in (b).

a

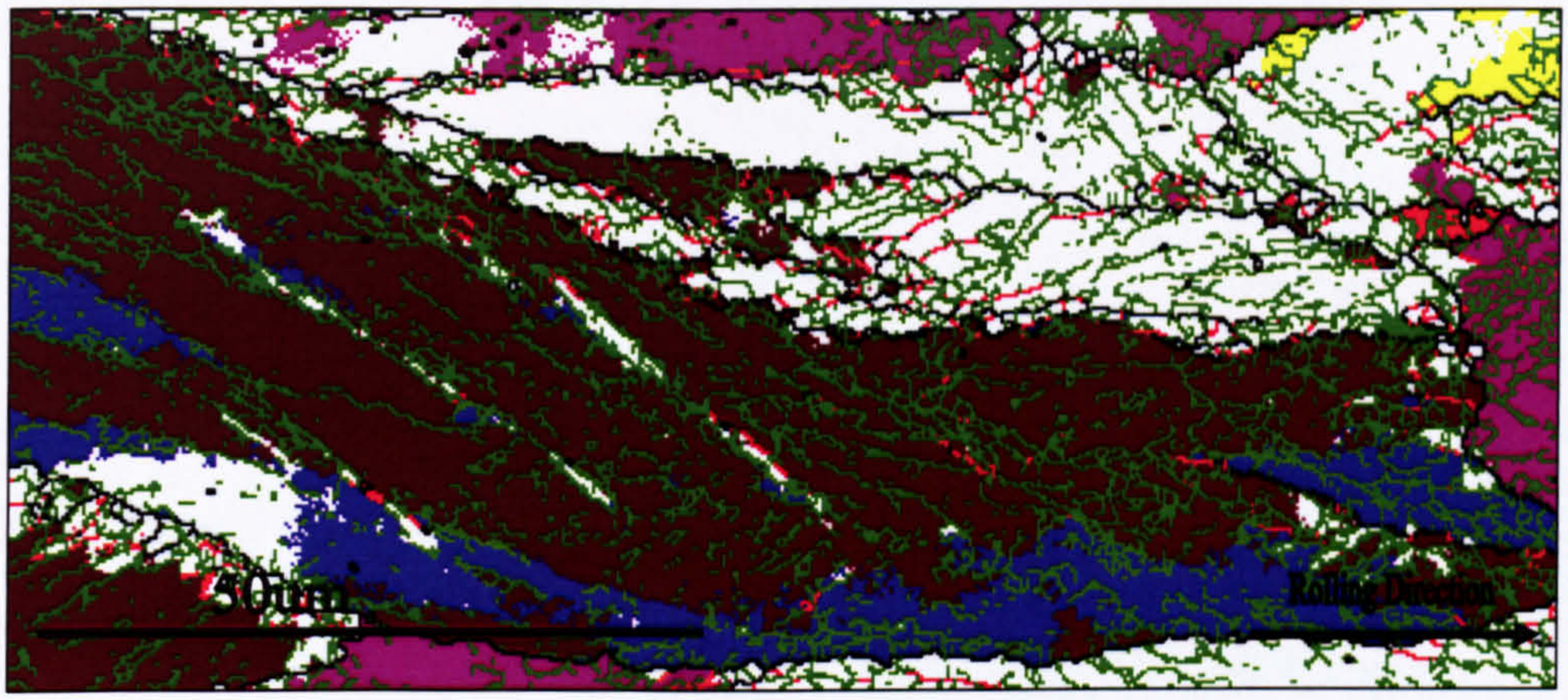

5-10°: green, 10-15°: red, >15°: black. Step size=0.25μm

b

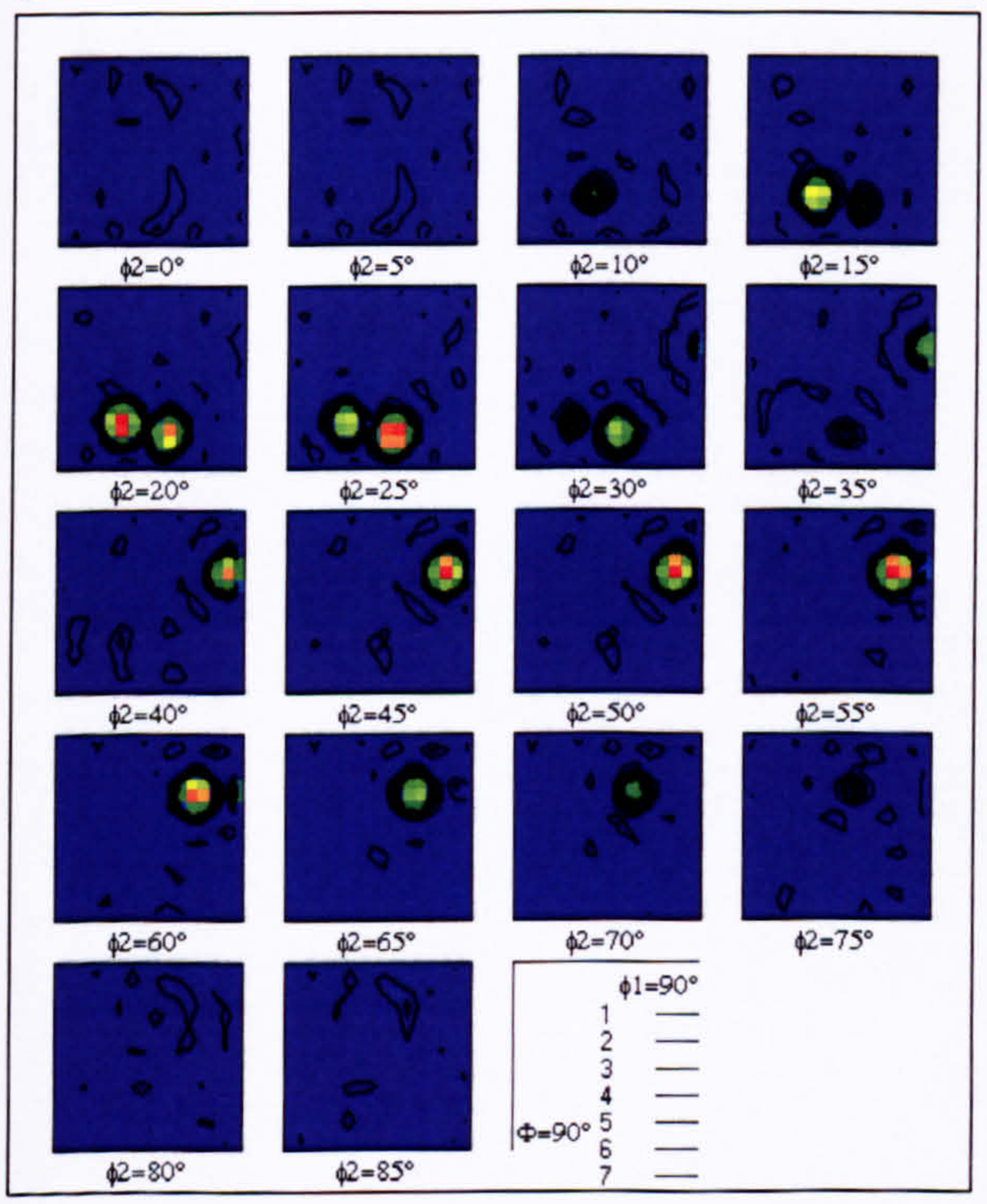

c

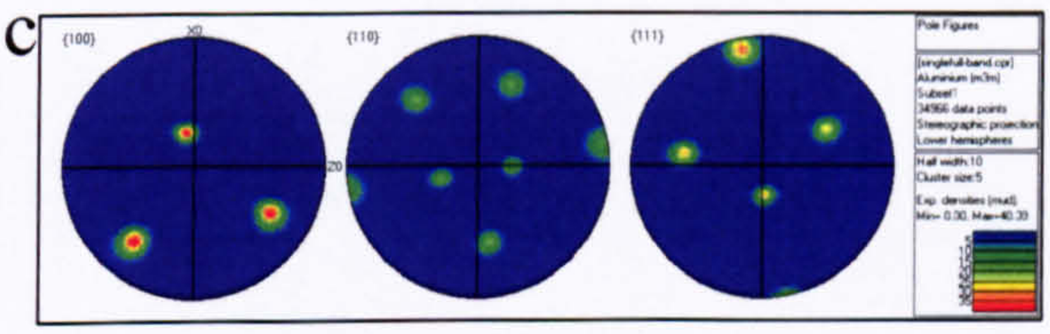

d

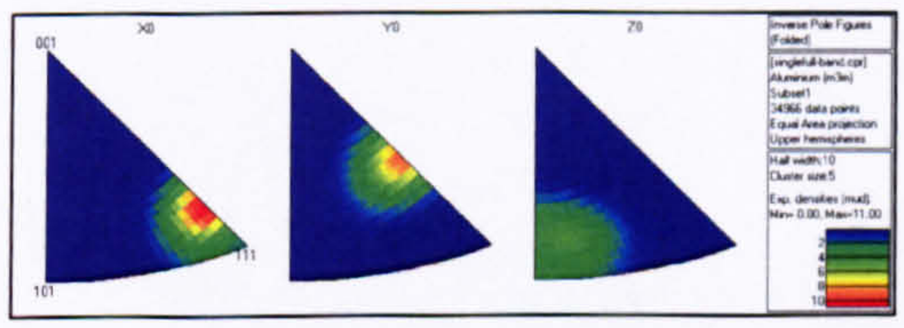

e

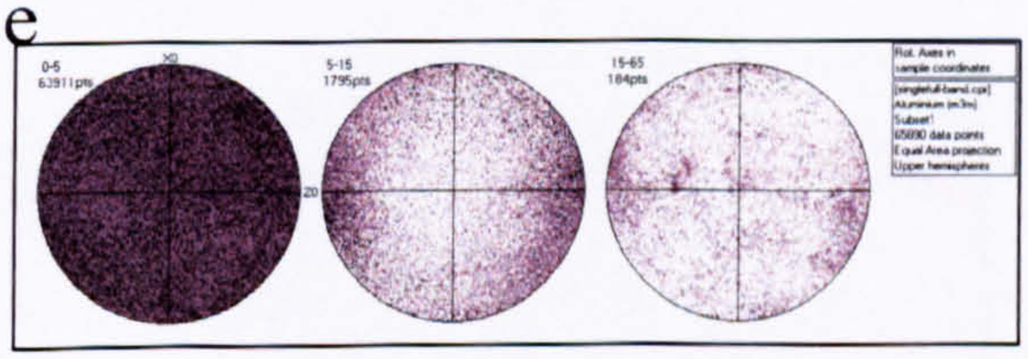

f

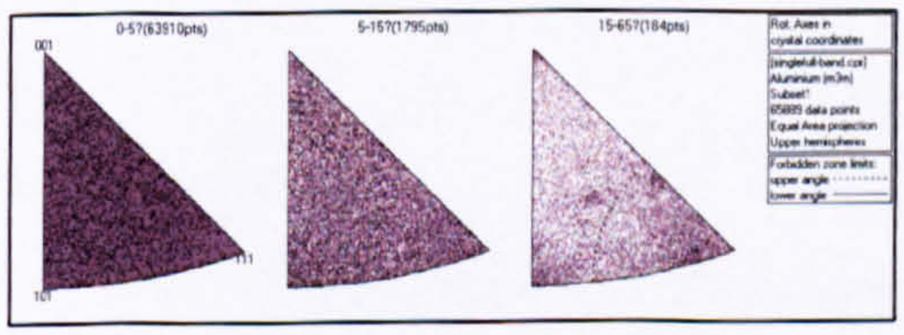

Fig. 5.13 S-orientated grain in the single deformed sample: (a) texture and boundary map, (b) ODF, (c) pole figures, (d) inverse pole figures, the distribution of misorientation axis vectors in (e) sample and (f) crystal lattice coordinates.

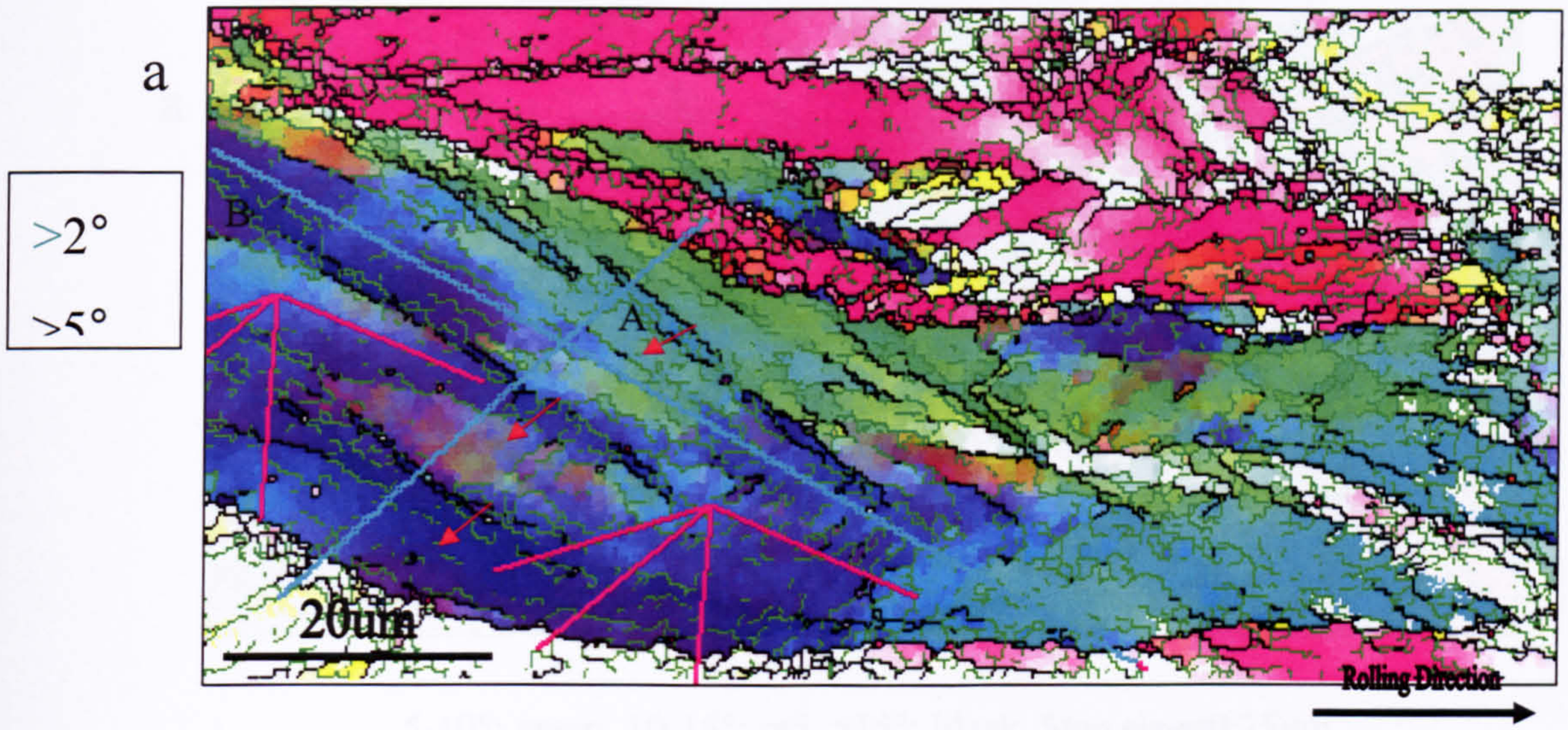

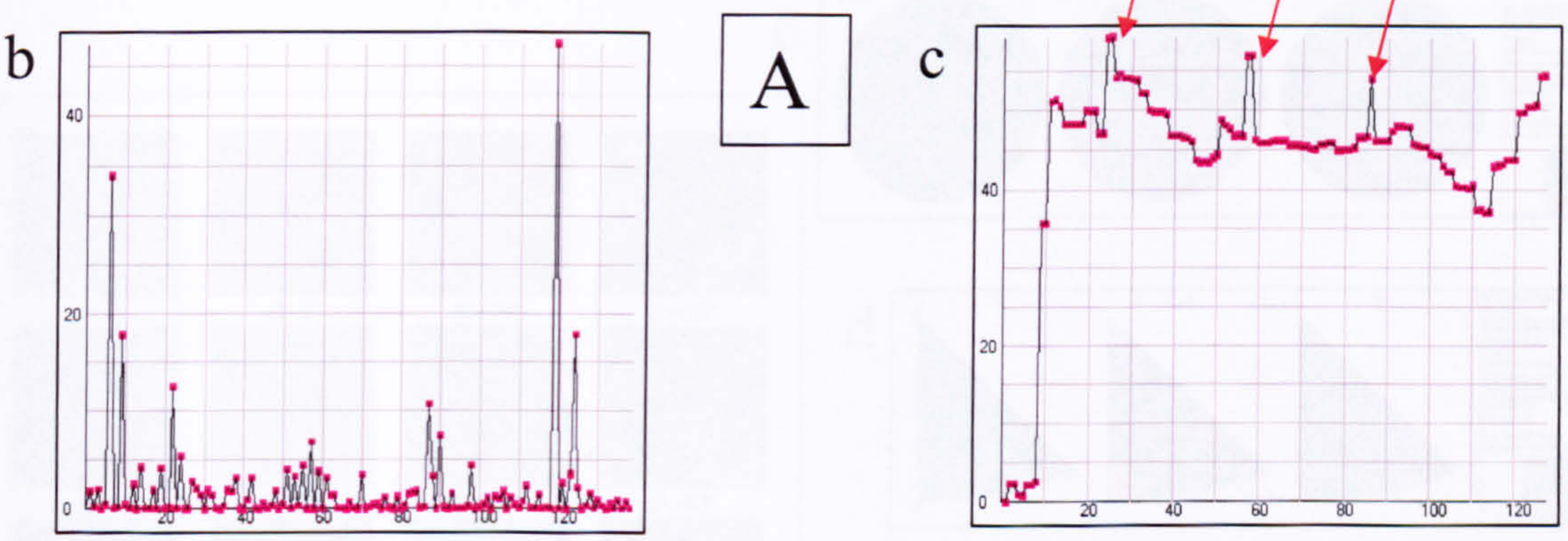

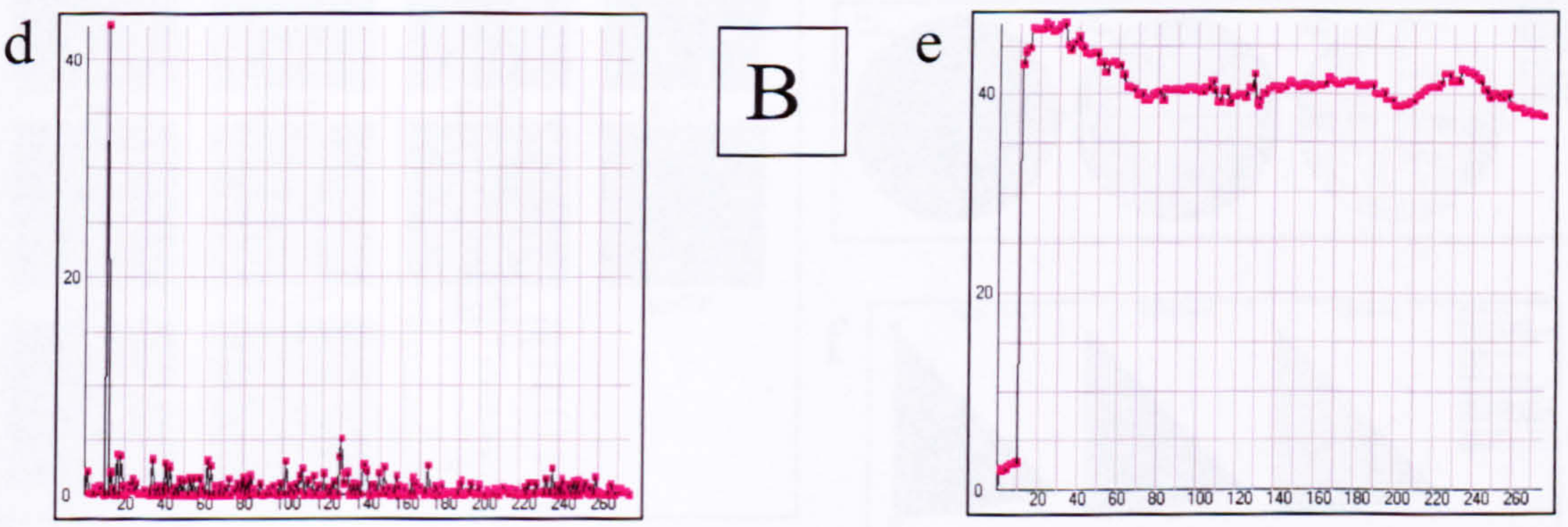

Fig. 5.14 S-orientated grain in the single deformed sample: (a) relative map, (b) (d) relative and (c) (e) cumulative misorientation distributions of line scans performed along A and B in (a).

a

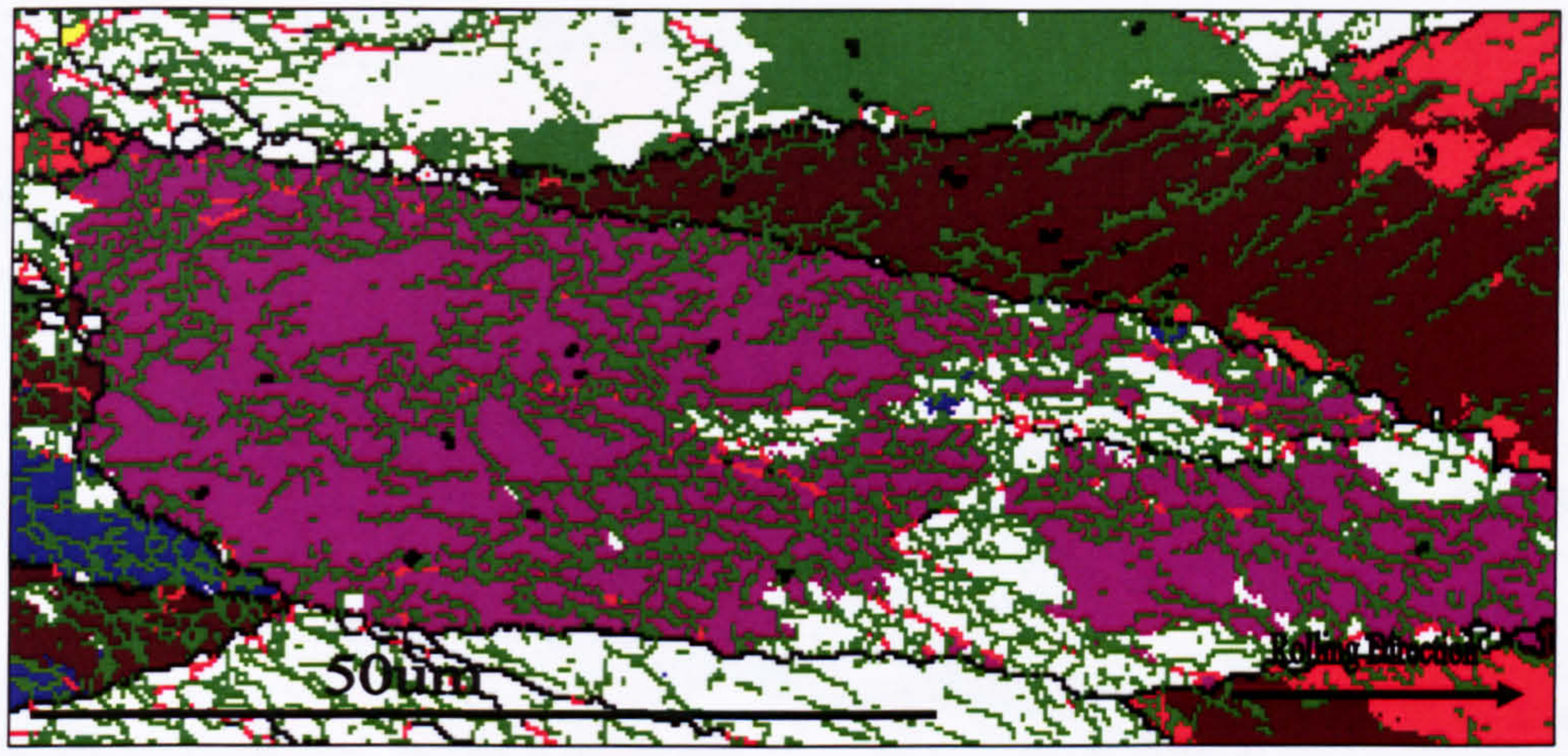

5-10°: green, 10-15°: red, >15°: black. Step size=0.25μm

b

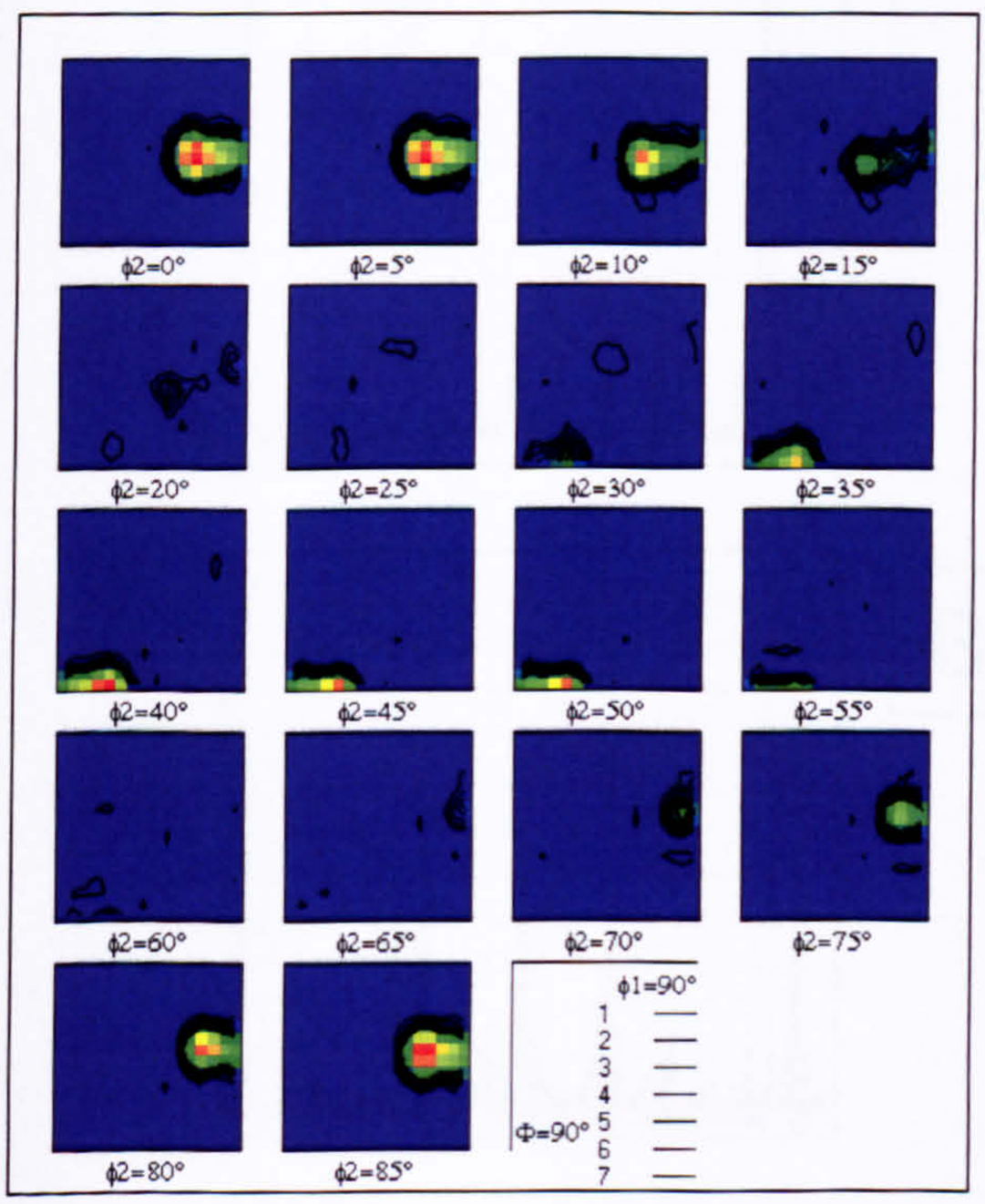

c

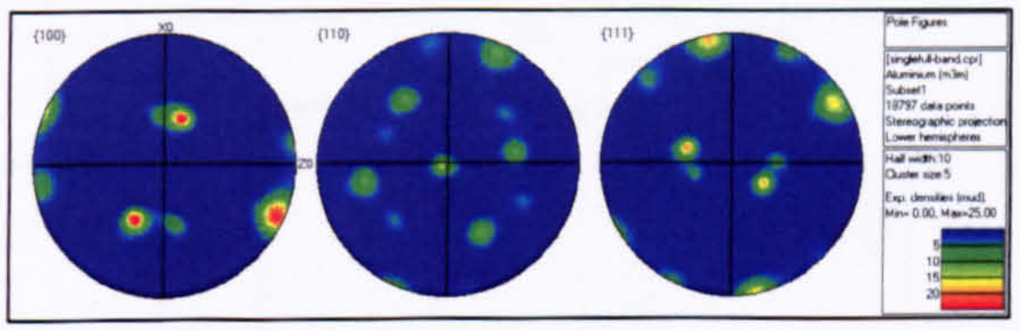

d

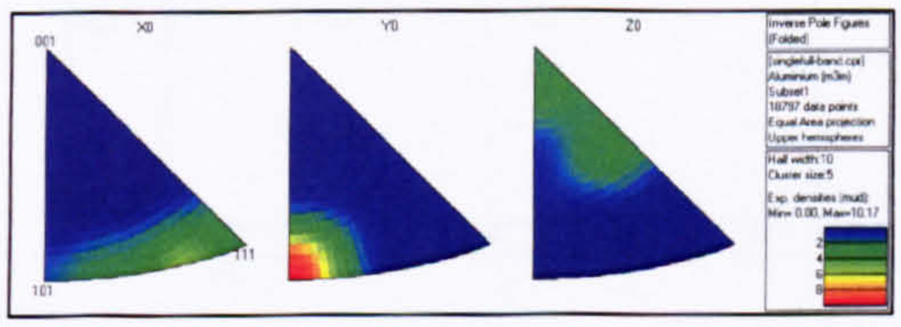

e

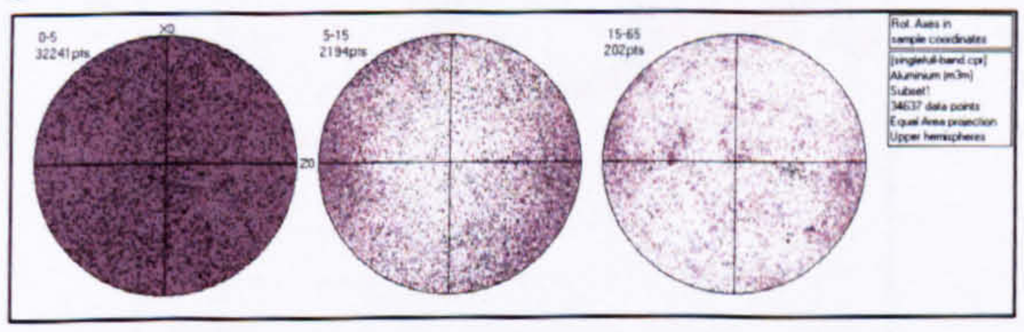

f

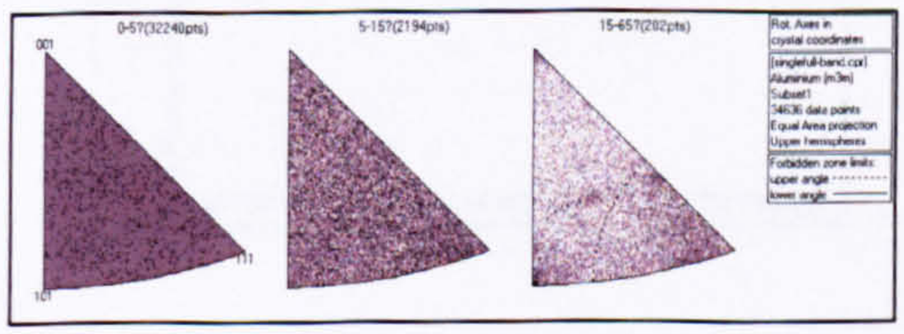

Fig. 5.15 P-orientated grain in the single deformed sample: (a) texture and boundary map, (b) ODF, (c) pole figures, (d) inverse pole figures, the distribution of misorientation axis vectors in (e) sample and (f) crystal lattice coordinates.

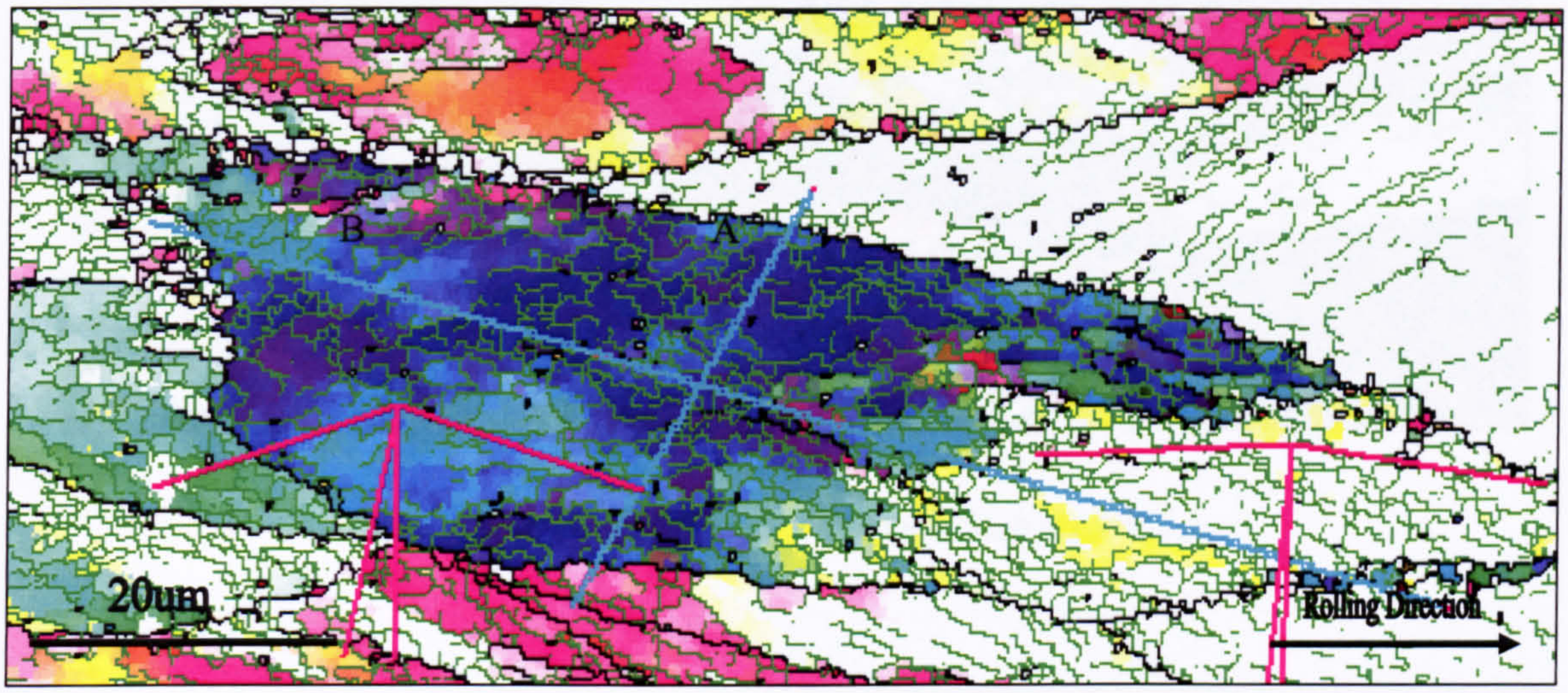

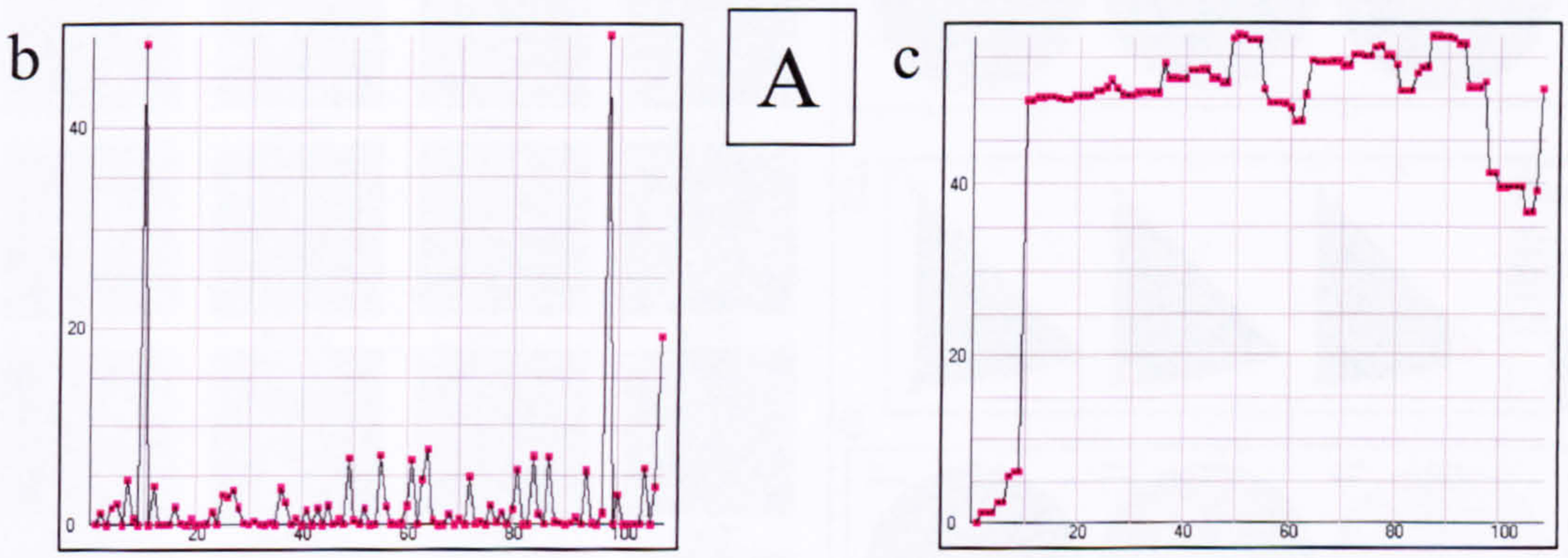

Fig. 5.16 P-orientated grain in the single deformed sample: (a) relative map, (b) (d) relative and (c) (e) cumulative misorientation distributions of line scans performed along A and B in (a).

a

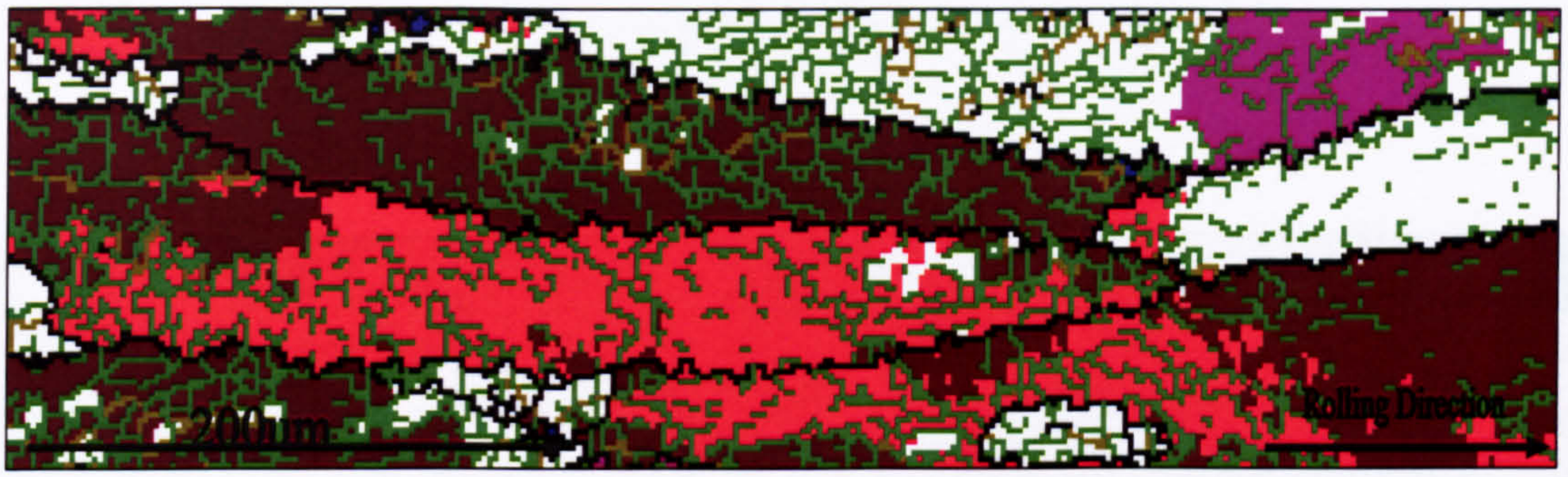

3-10°: green, 10-15°: red, >15°: black Step size=0.5μm

b

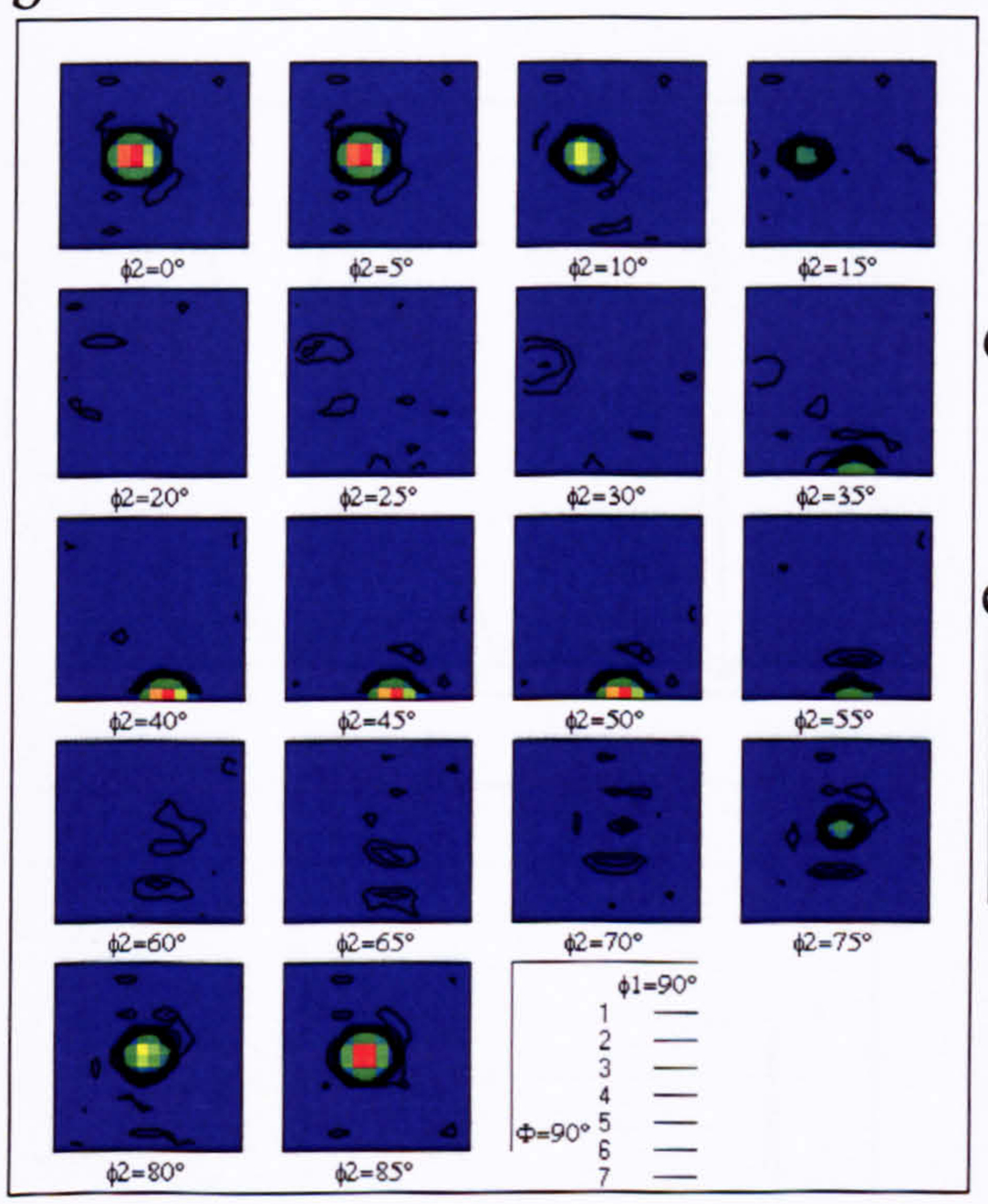

c

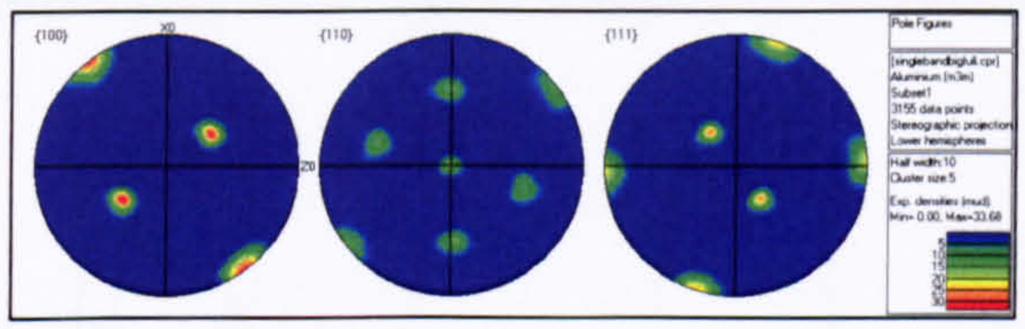

d

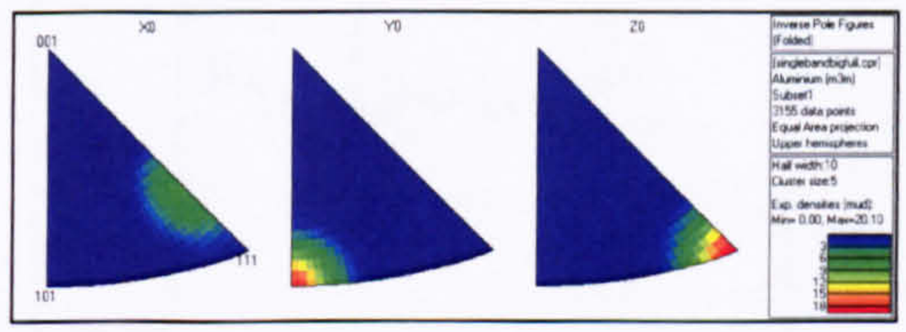

e

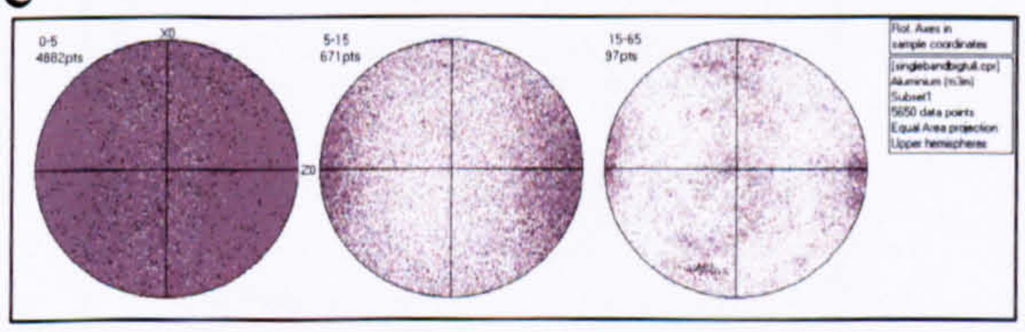

f

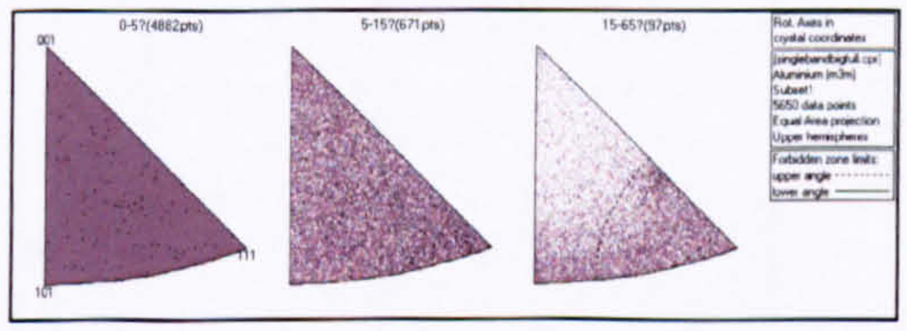

Fig. 5.17 Brass-orientated grain in the single deformed sample: (a) texture and boundary map, (b) ODF, (c) pole figures, (d) inverse pole figures, the distribution of misorientation axis vectors in (e) sample and (f) crystal lattice coordinates.

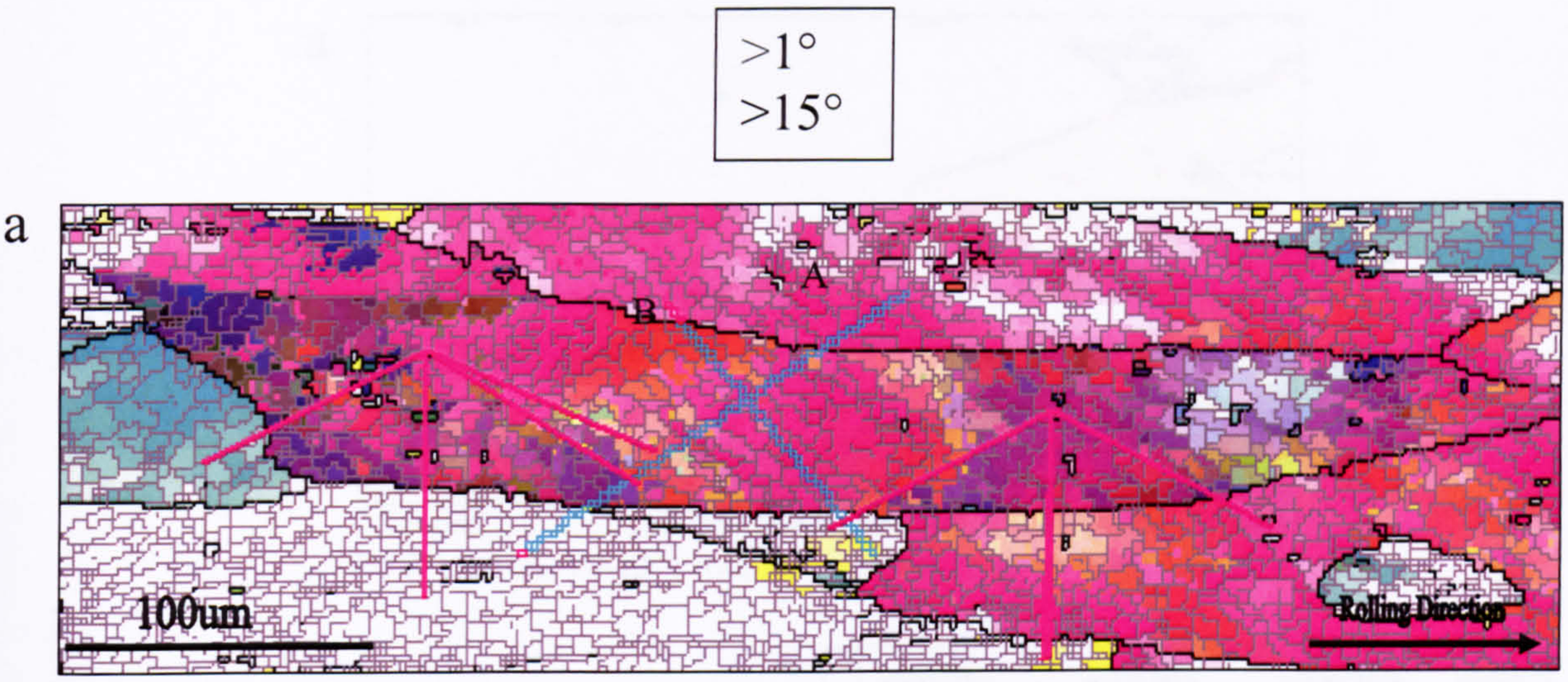

Fig. 5.18 Brass-orientated grain in the single deformed sample: (a) relative map, (b) (d) relative and (c) (e) cumulative misorientation distributions of line scans performed along A and B in (a).

a

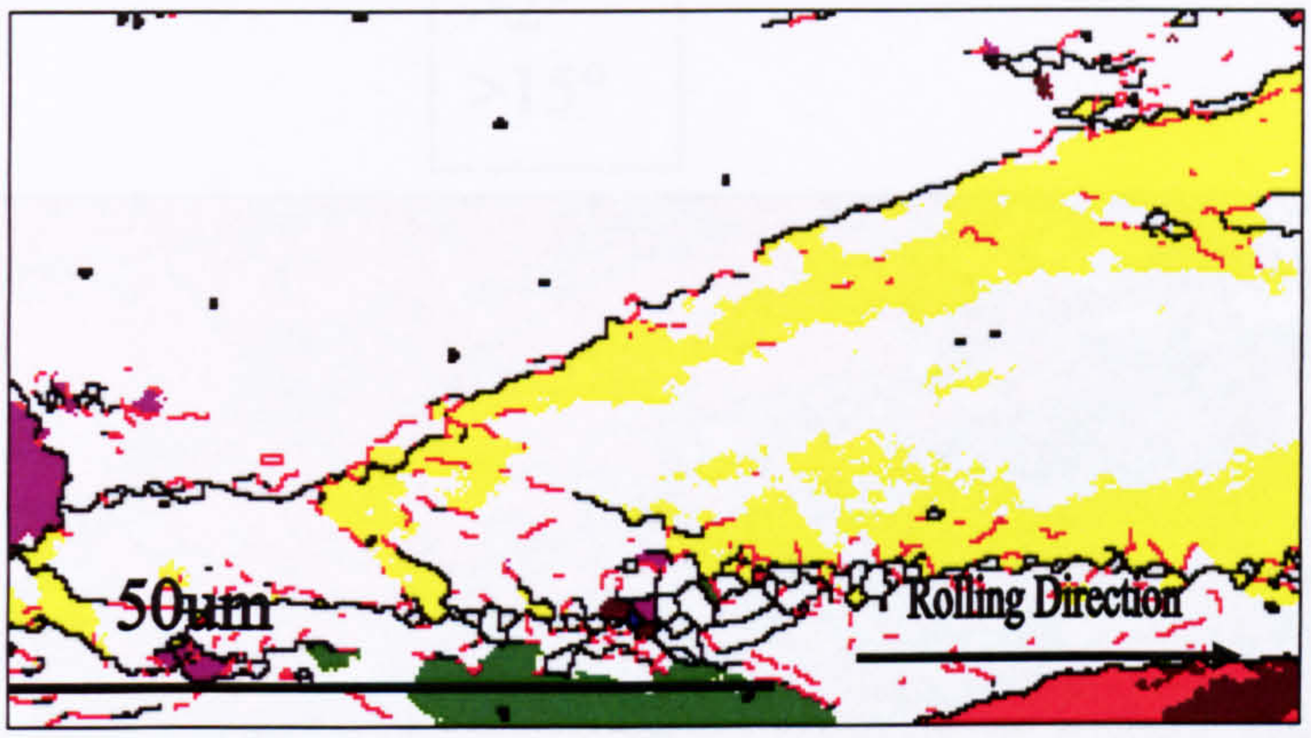

5-10°: green, 10-15°: red, >15°: black. Step size=0.25μm

b

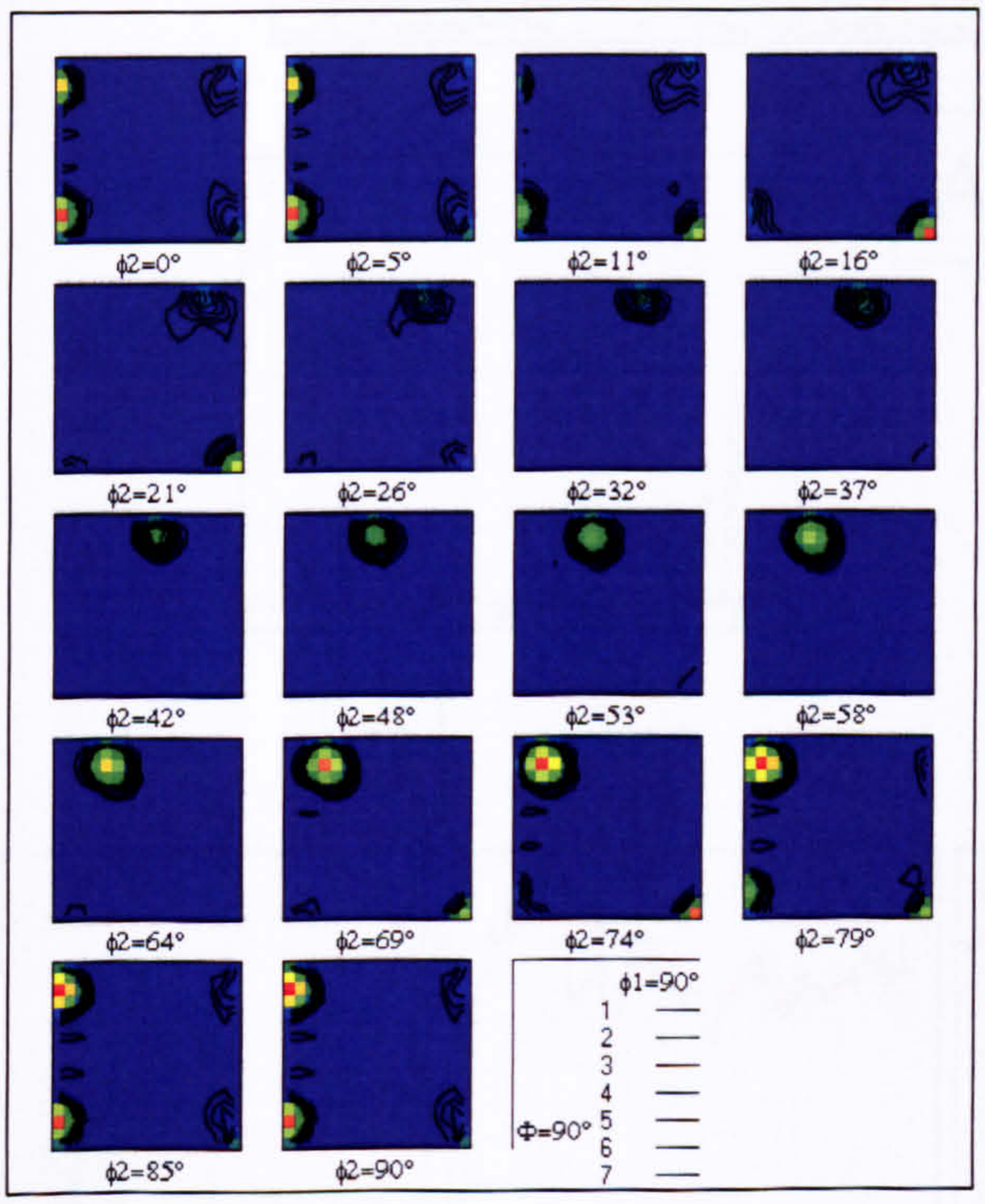

c

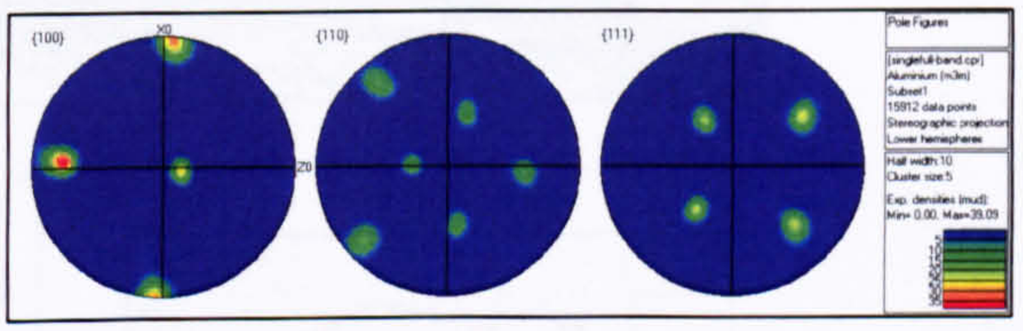

d

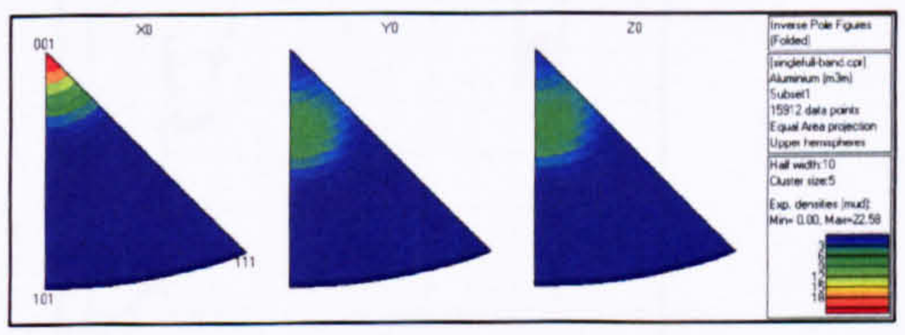

e

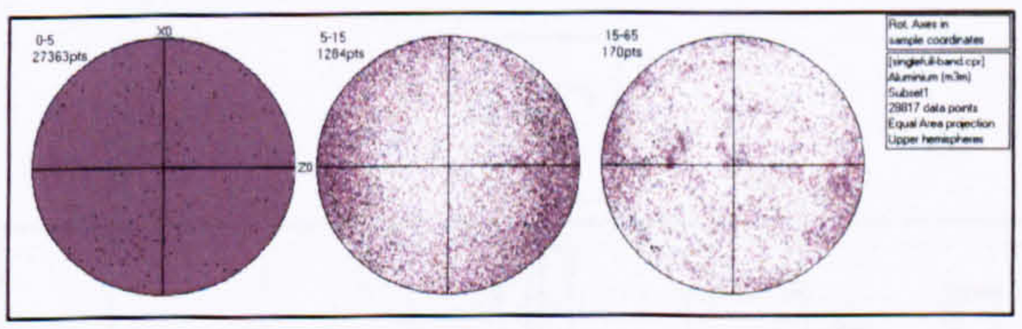

f

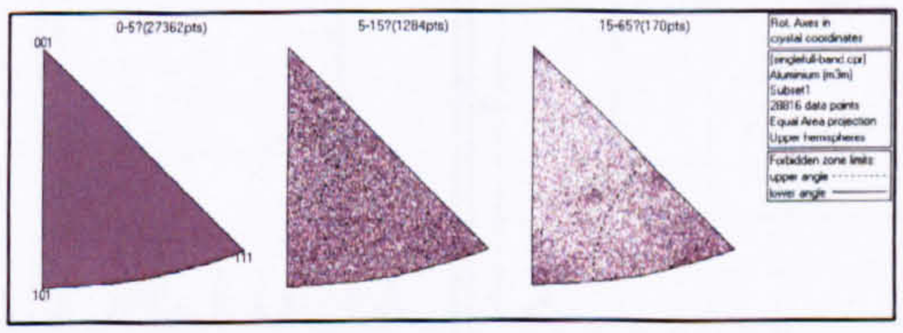

Fig. 5.19 Cube-orientated grain in the single deformed sample: (a) texture and boundary map, (b) ODF, (c) pole figures, (d) inverse pole figures, the distribution of misorientation axis vectors in (e) sample and (f) crystal lattice coordinates.

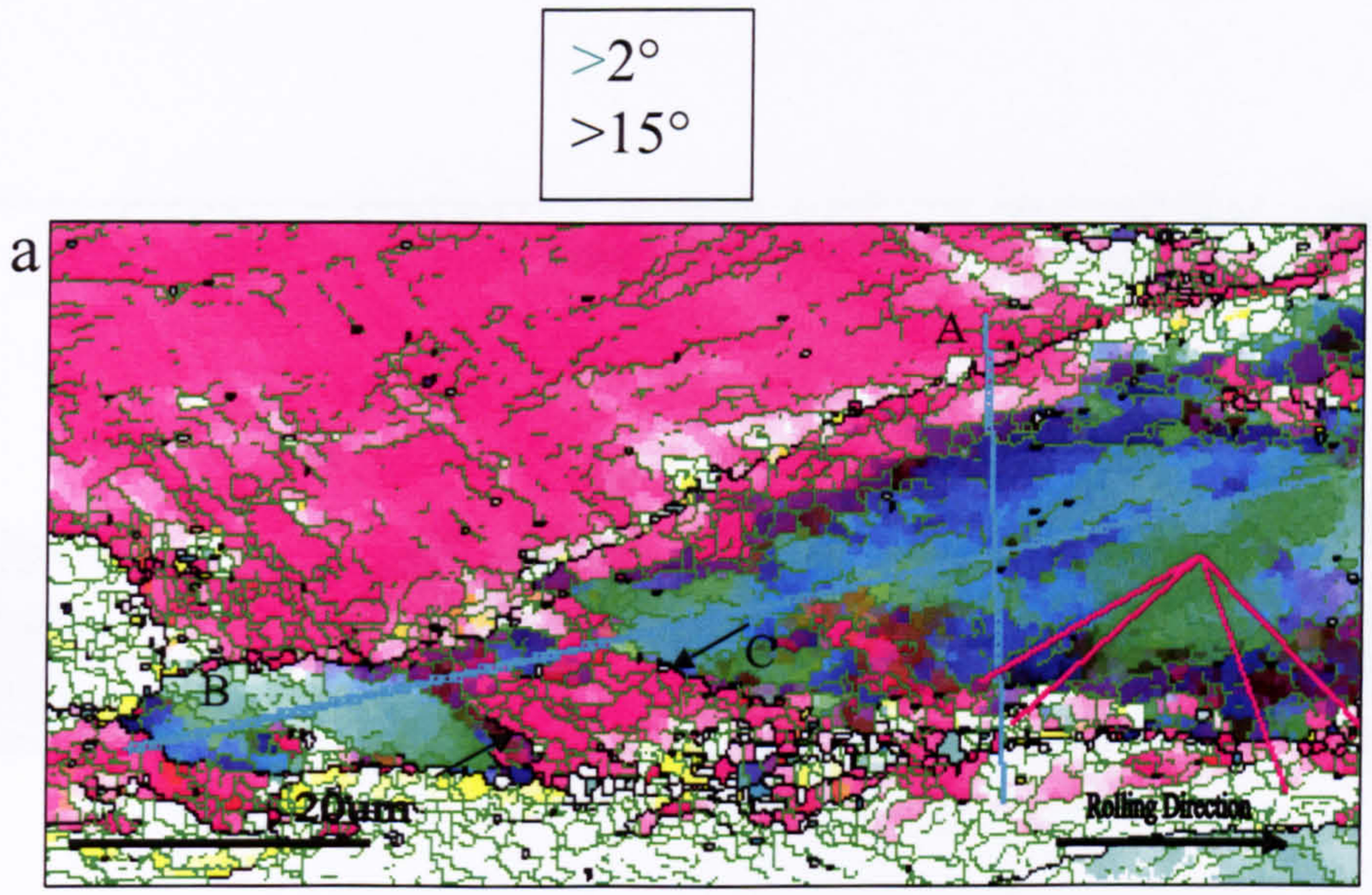

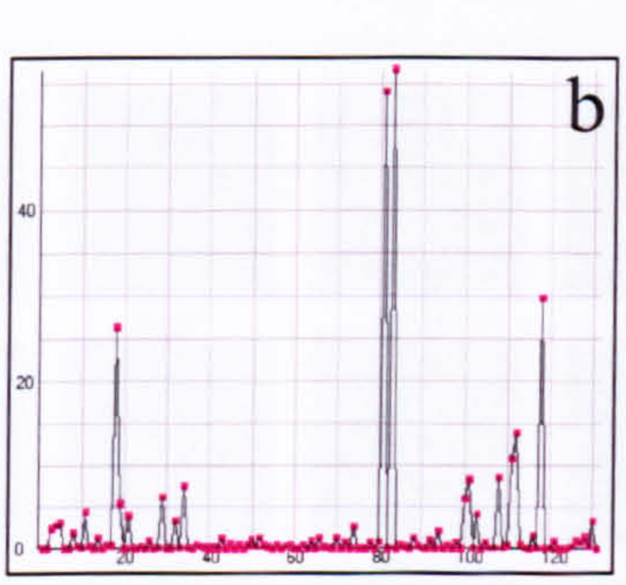

A

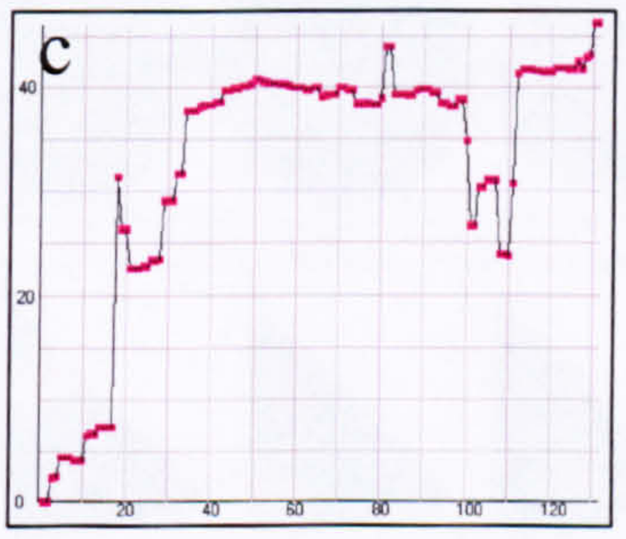

B

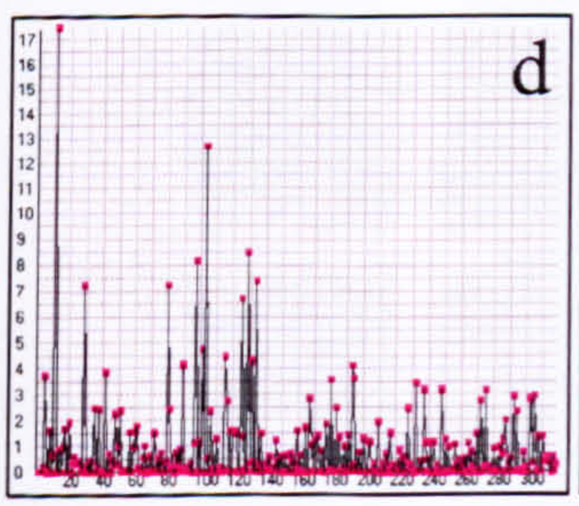

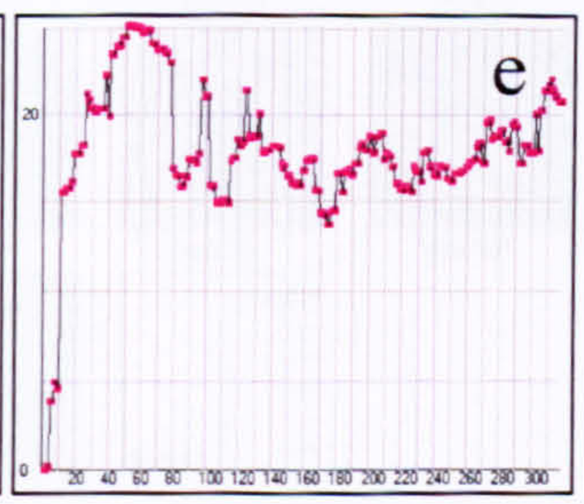

C

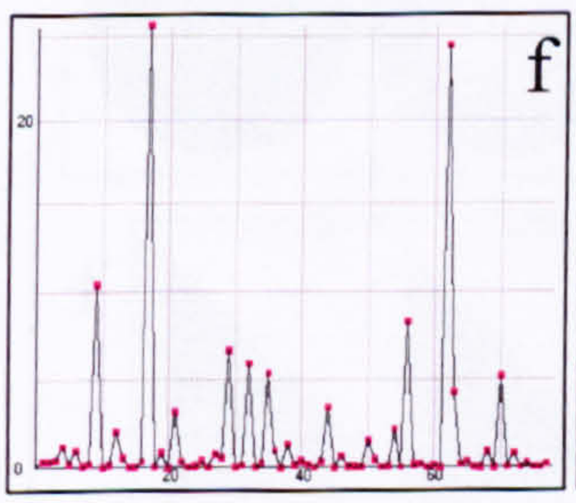

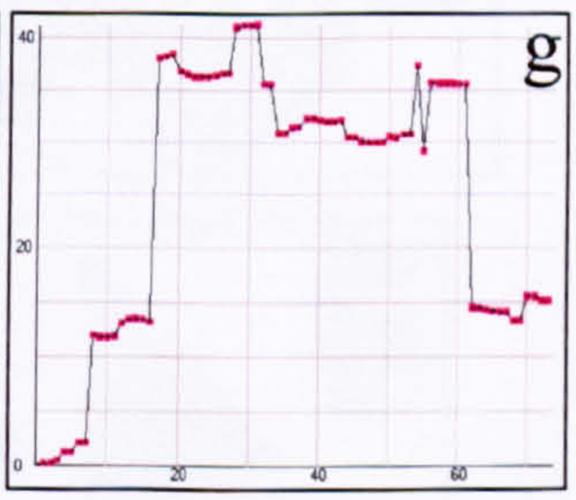

Fig. 5.20 Cube-orientated grain in the single deformed sample: (a) relative map, (b) (d) (f) relative and (c) (e) (g) cumulative misorientation distributions of line scans performed along A and B in (a).

a

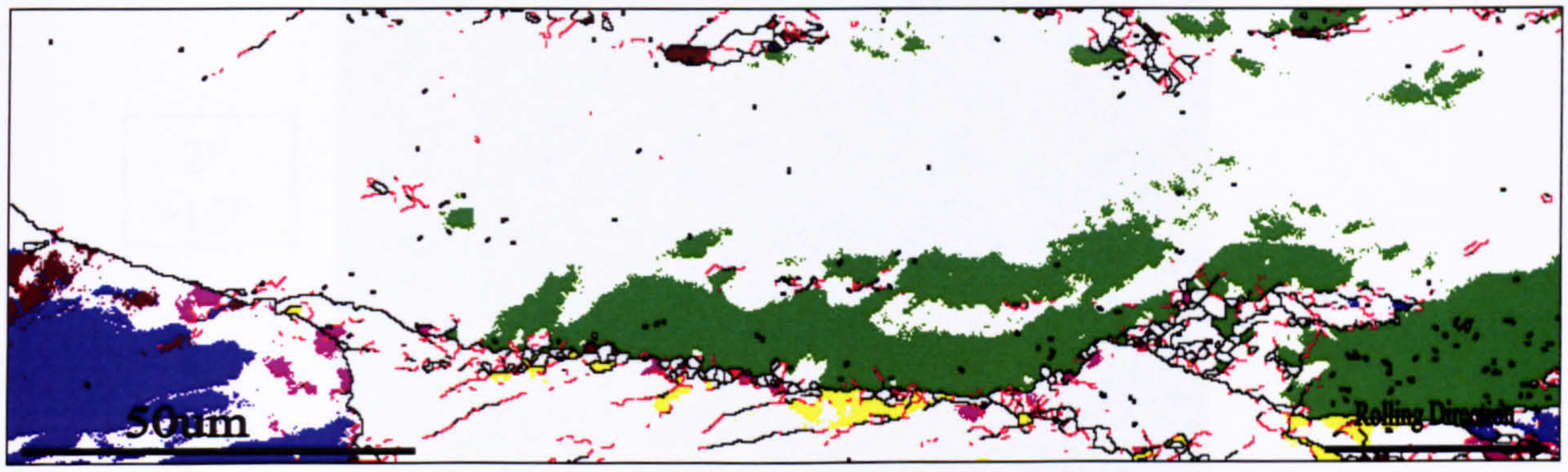

5-10°: green, 10-15°: red, >15°: black. Step size=0.25μm

b

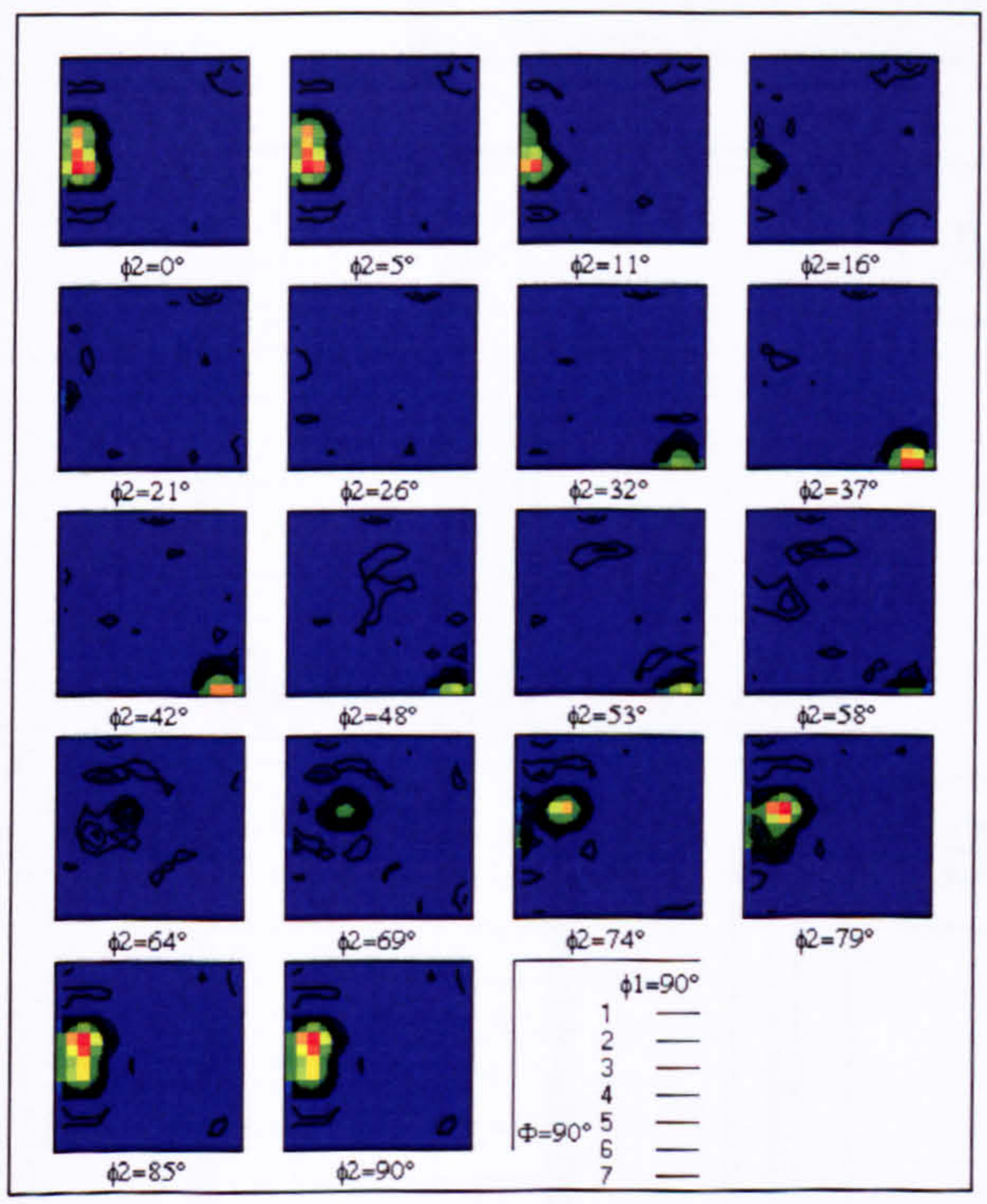

c

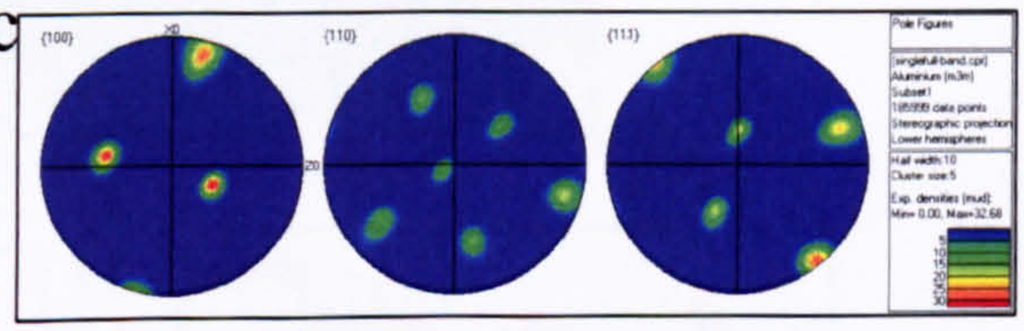

d

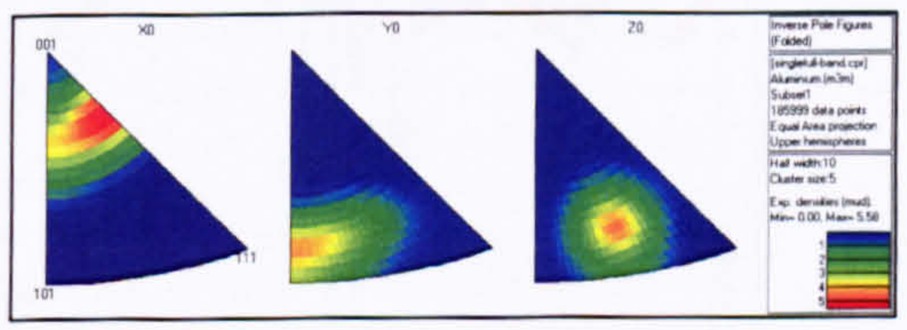

e

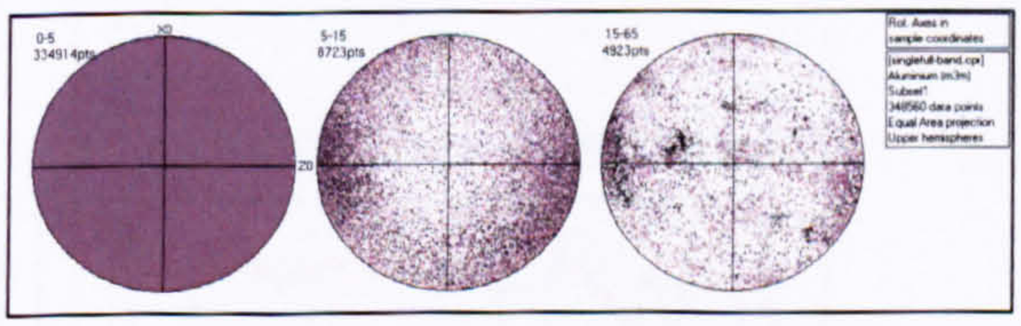

f

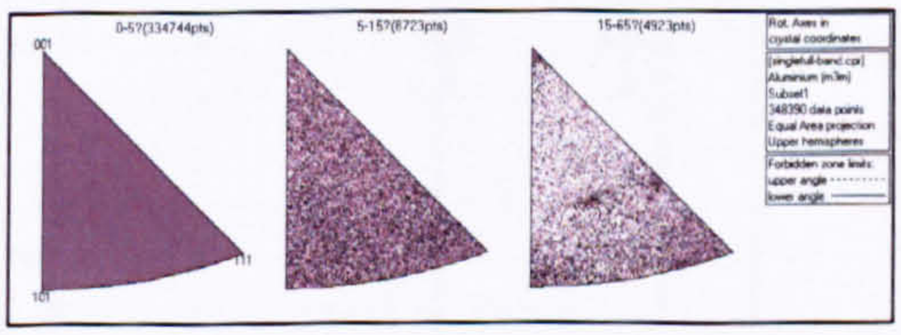

Fig. 5.21 Goss-orientated grain in the single deformed sample: (a) texture and boundary map, (b) ODF, (c) pole figures, (d) inverse pole figures, the distribution of misorientation axis vectors in (e) sample and (f) crystal lattice coordinates.

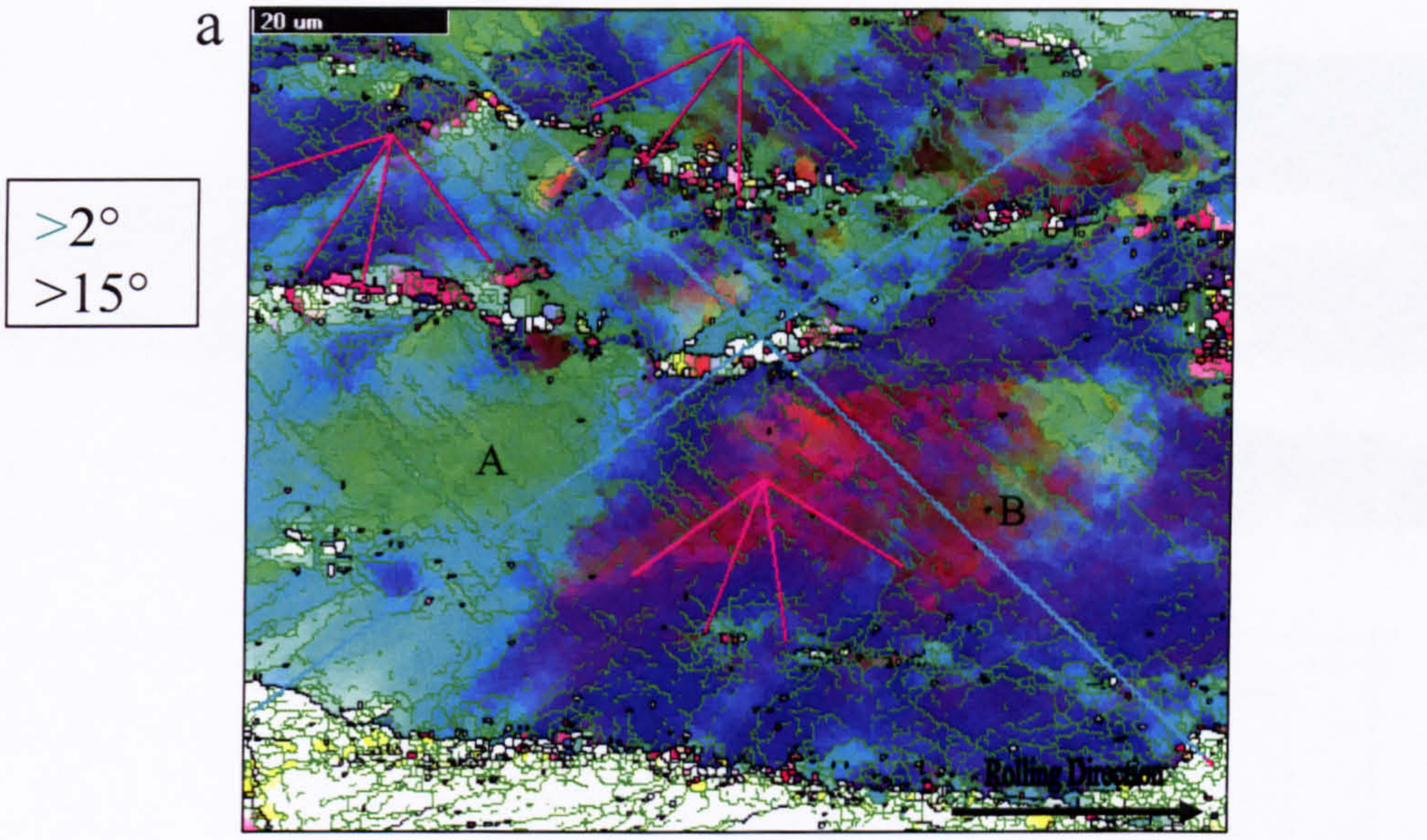

Fig. 5.22 Goss-orientated grain in the single deformed sample: (a) relative map, (b) (d) relative and (c) (e) cumulative misorientation distributions of line scans performed along A and B in (a).

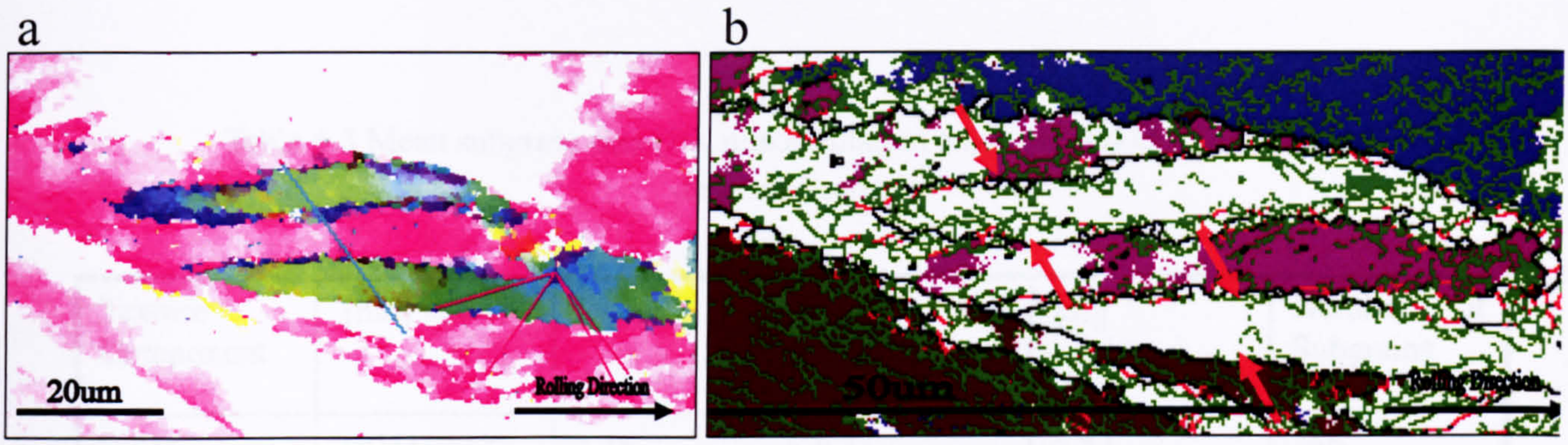

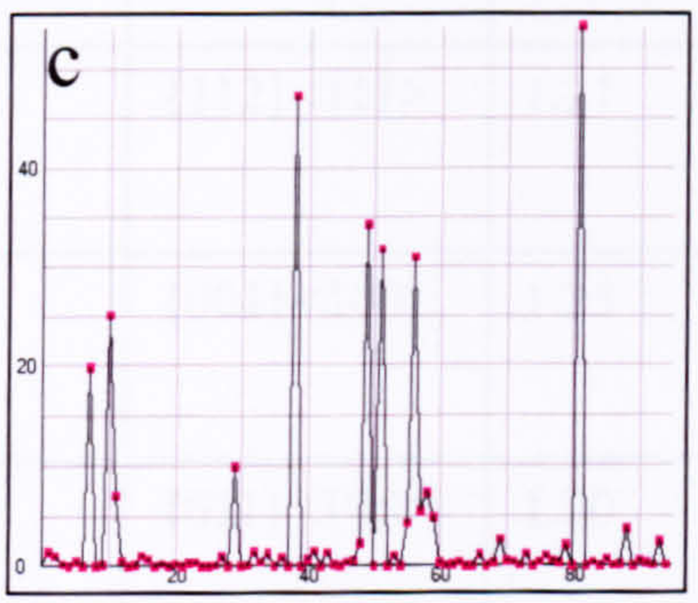

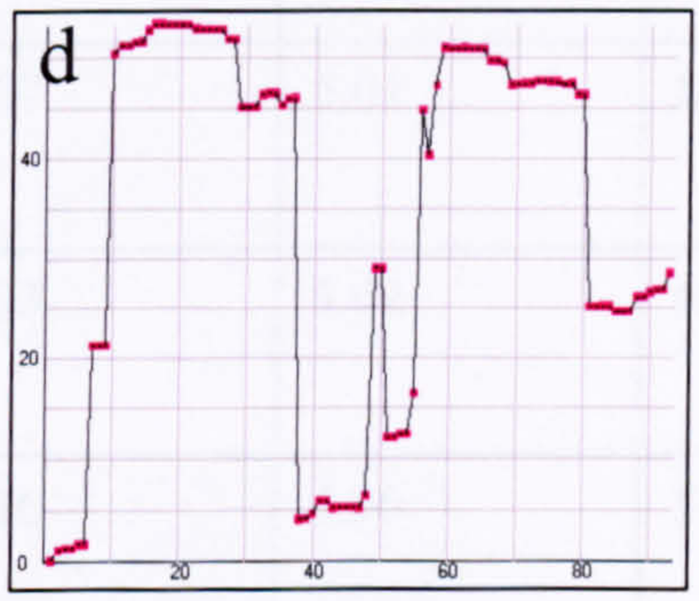

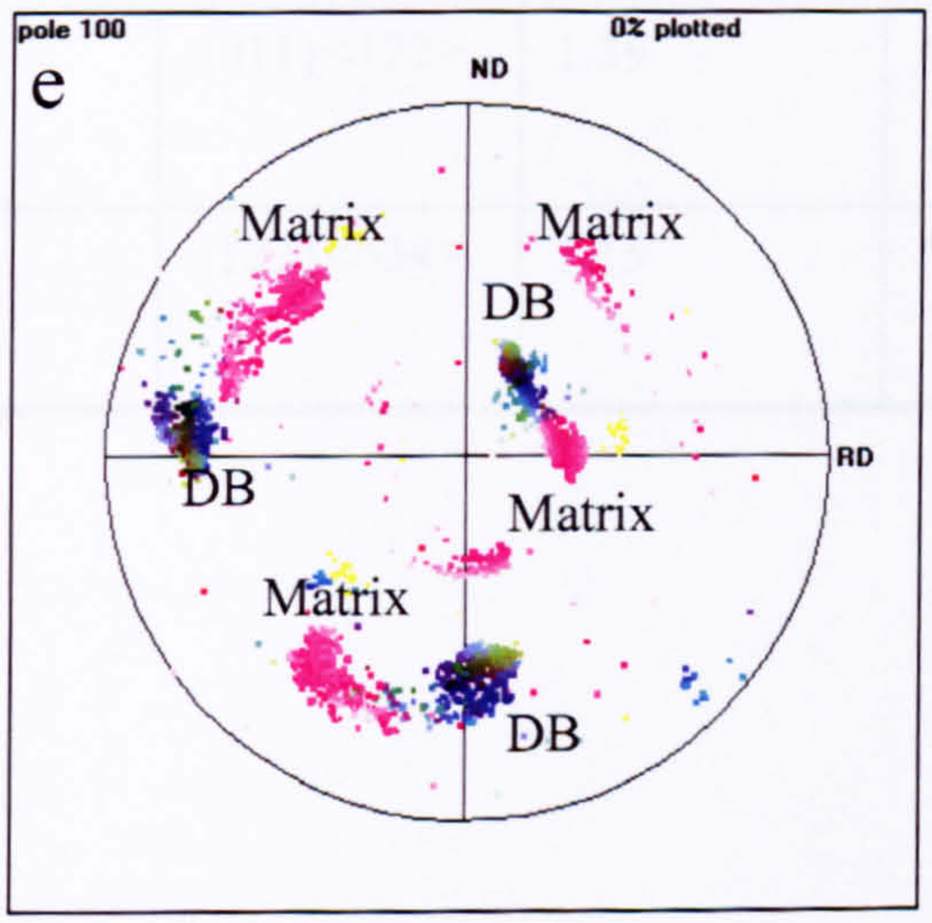

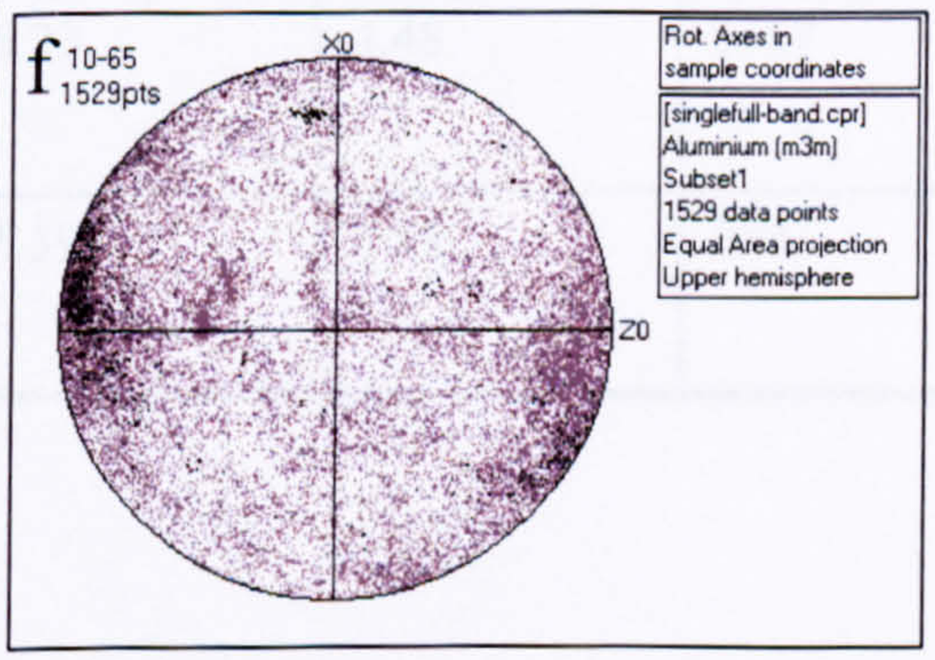

Fig. 5.23 Deformation banding in the single deformed sample: (a) relative map, (b) orientation map.(c) relative and (d) cumulative misorientation distributions of line scans performed along A and B in (a), e) pole figure, f) sample coordinates.

Table 5.3 Mean subgrain size (D), misorientation angle (è) and Θ/d in the single deformed sample

Texture Component	{hkl}<uvw>	D(μm)	Θ(°)	Θ/d	Number of Subgrains
Brass	{011}<112>	1.16	6.81	5.87	286
Copper	{112}<111>	1.21	6.07	5.01	824
Cube	{001}<100>	1.25	7.03	5.62	627
Goss	{011}<100>	1.20	5.96	4.96	513
P	{011}<122>	1.39	6.23	4.48	1117
S	{123}<634>	1.15	6.39	5.55	874

a

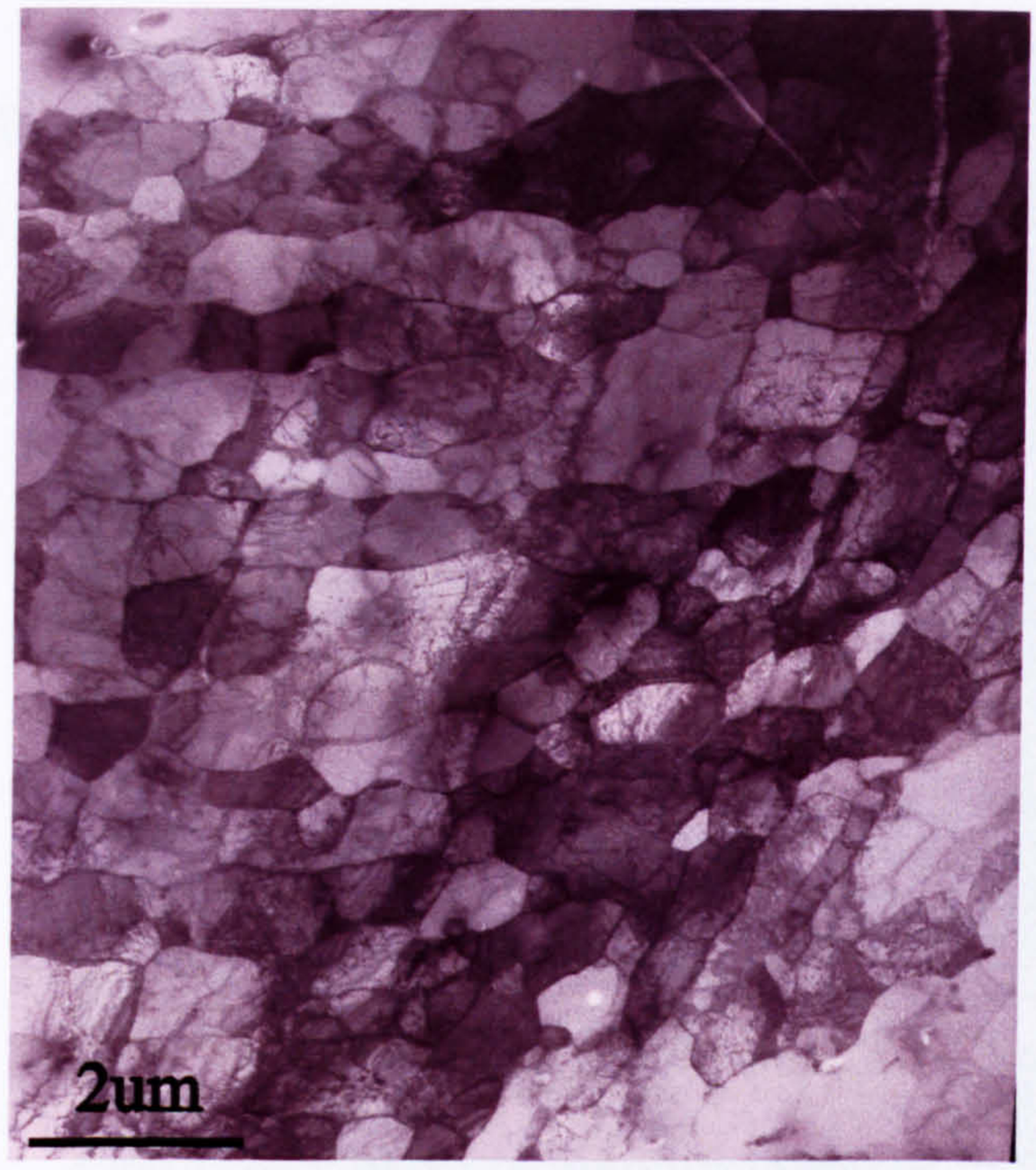

b

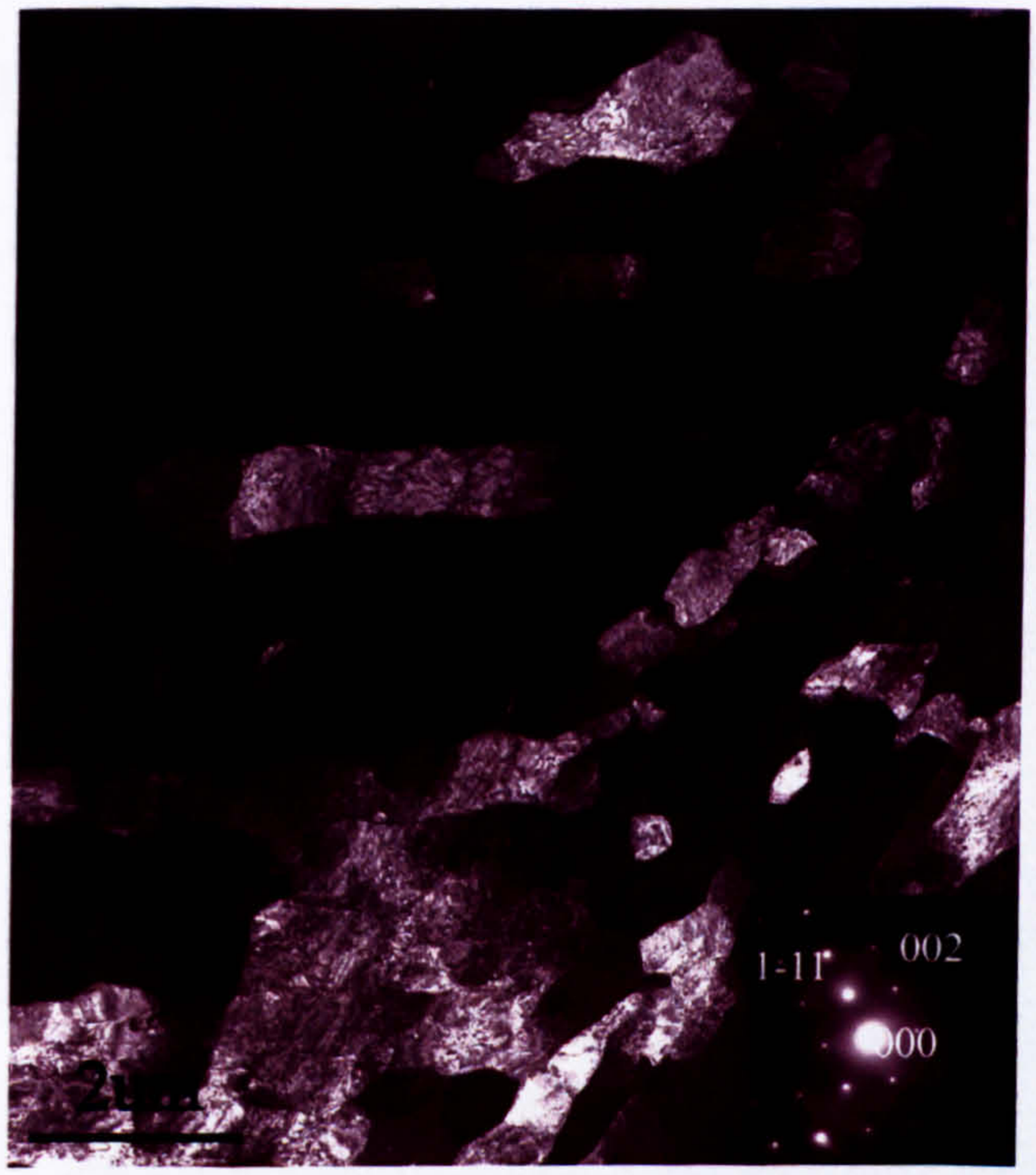

Fig. 5.24 TEM images after the single deformation, shows cell-block structure.

a

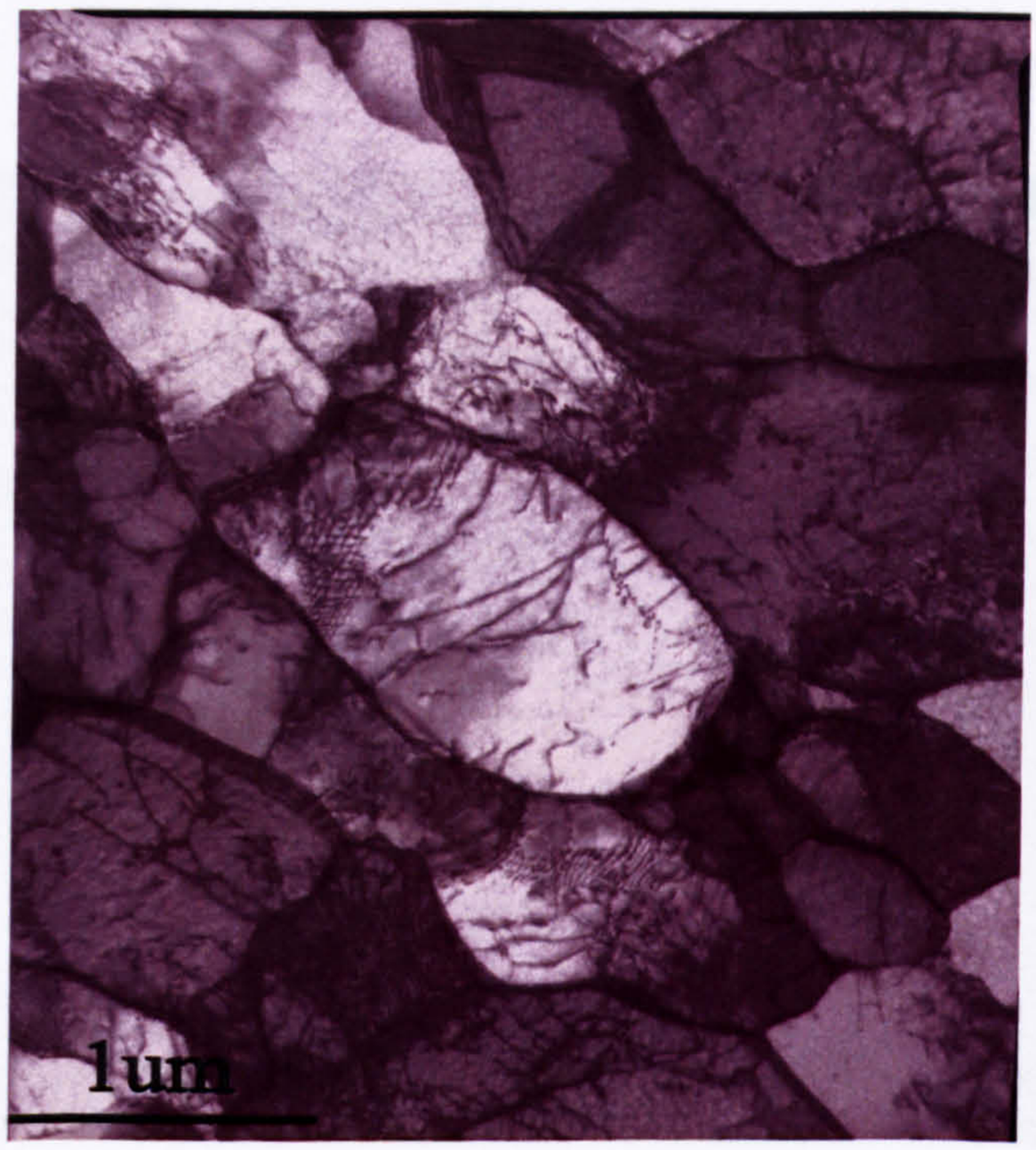

b

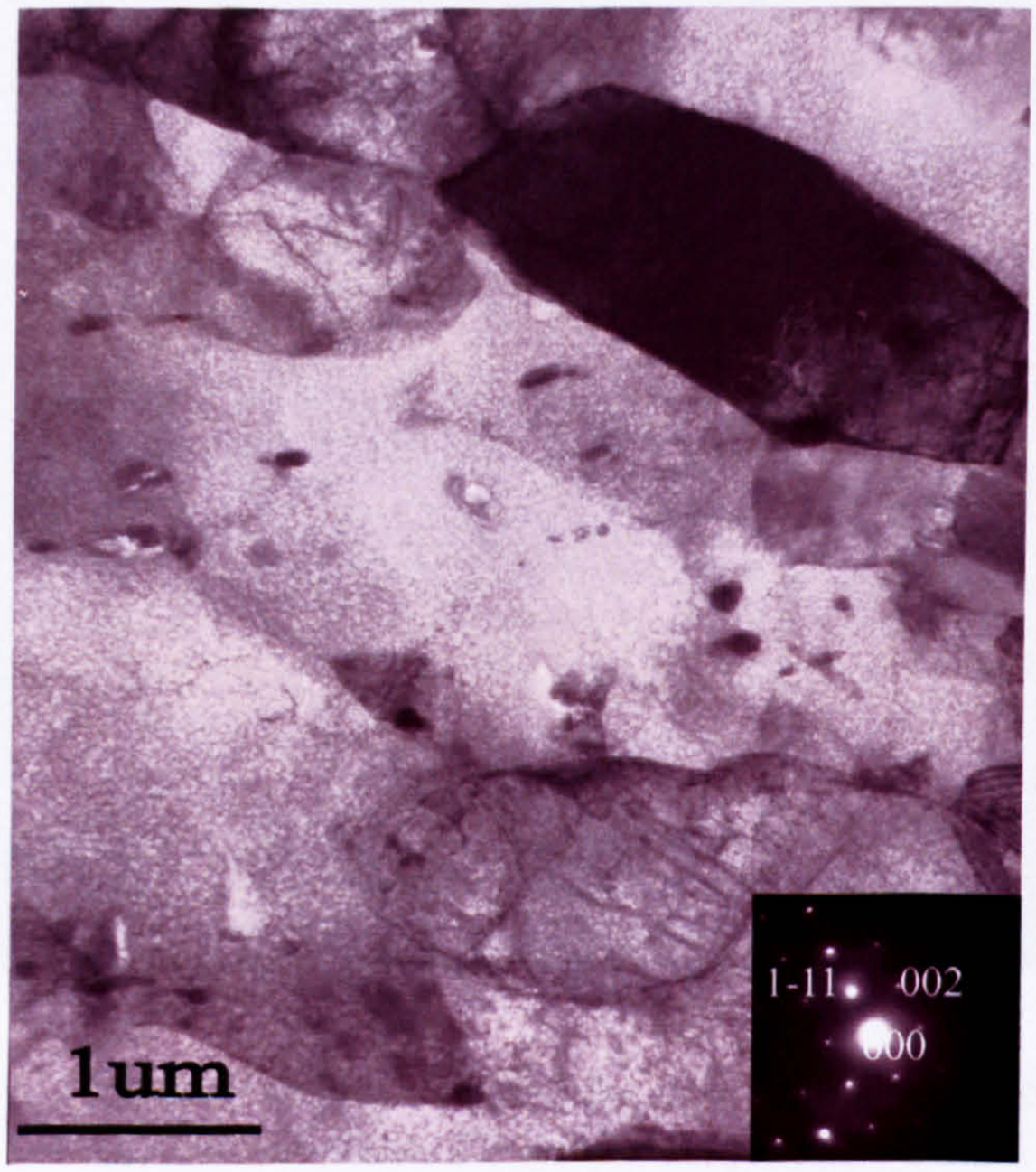

Fig. 5.25 TEM images after the single deformation show (a) dislocations structure and (b) particles within cell-block structure.

a

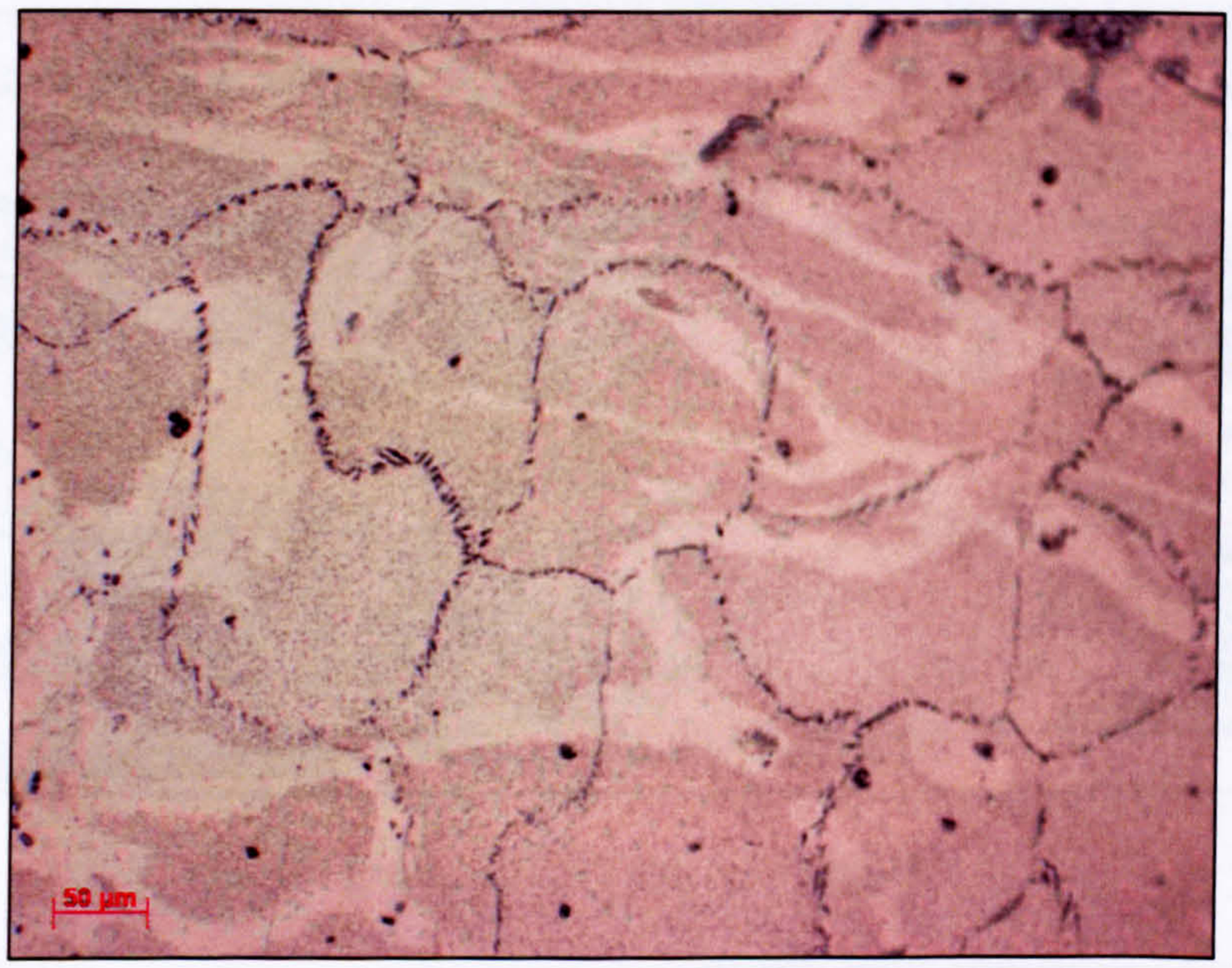

b

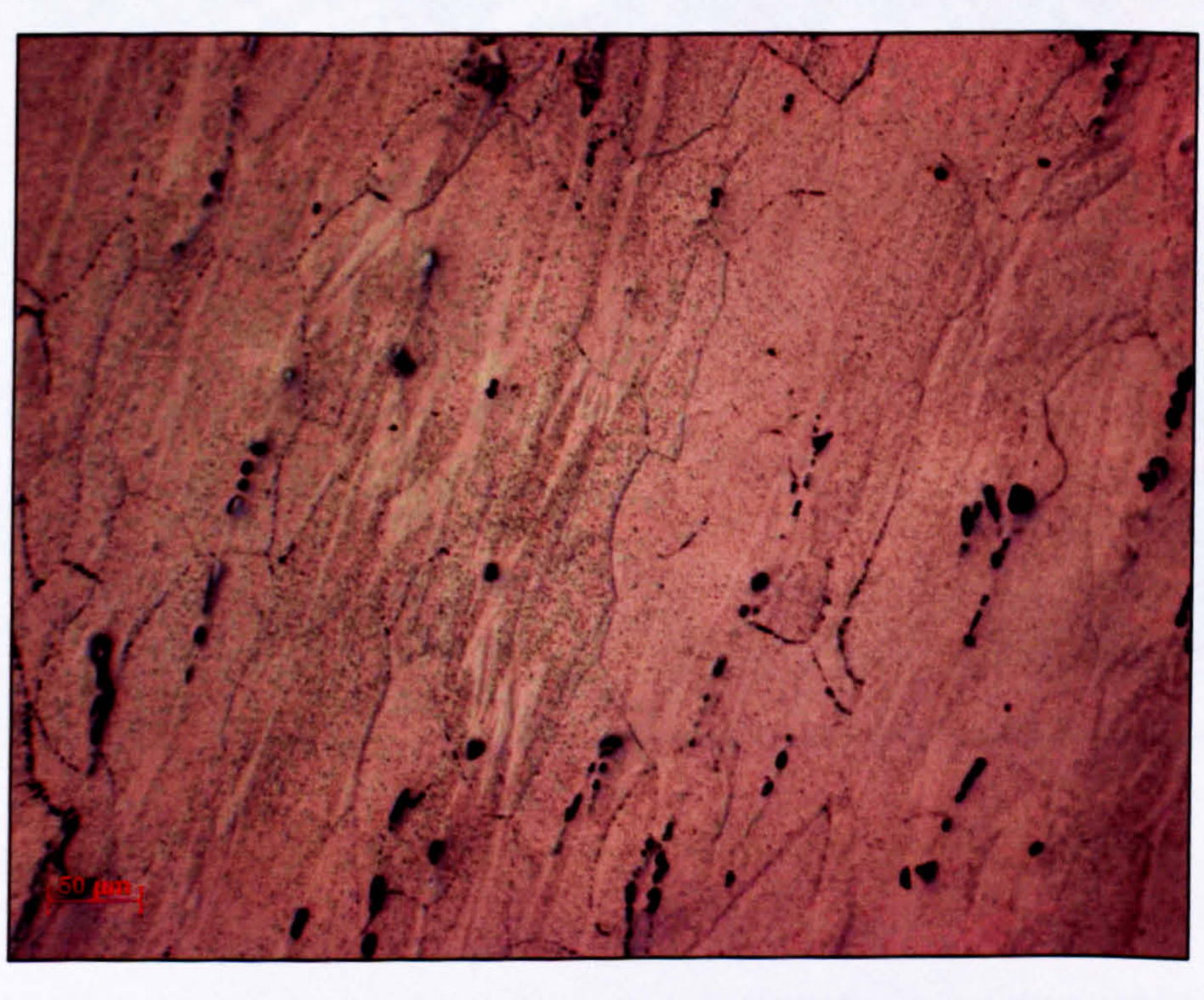

Fig. 5.26 Optical micrographs of deformed structure after the instantaneous deformation: (a) normal plane, (b) transverse plane.

a

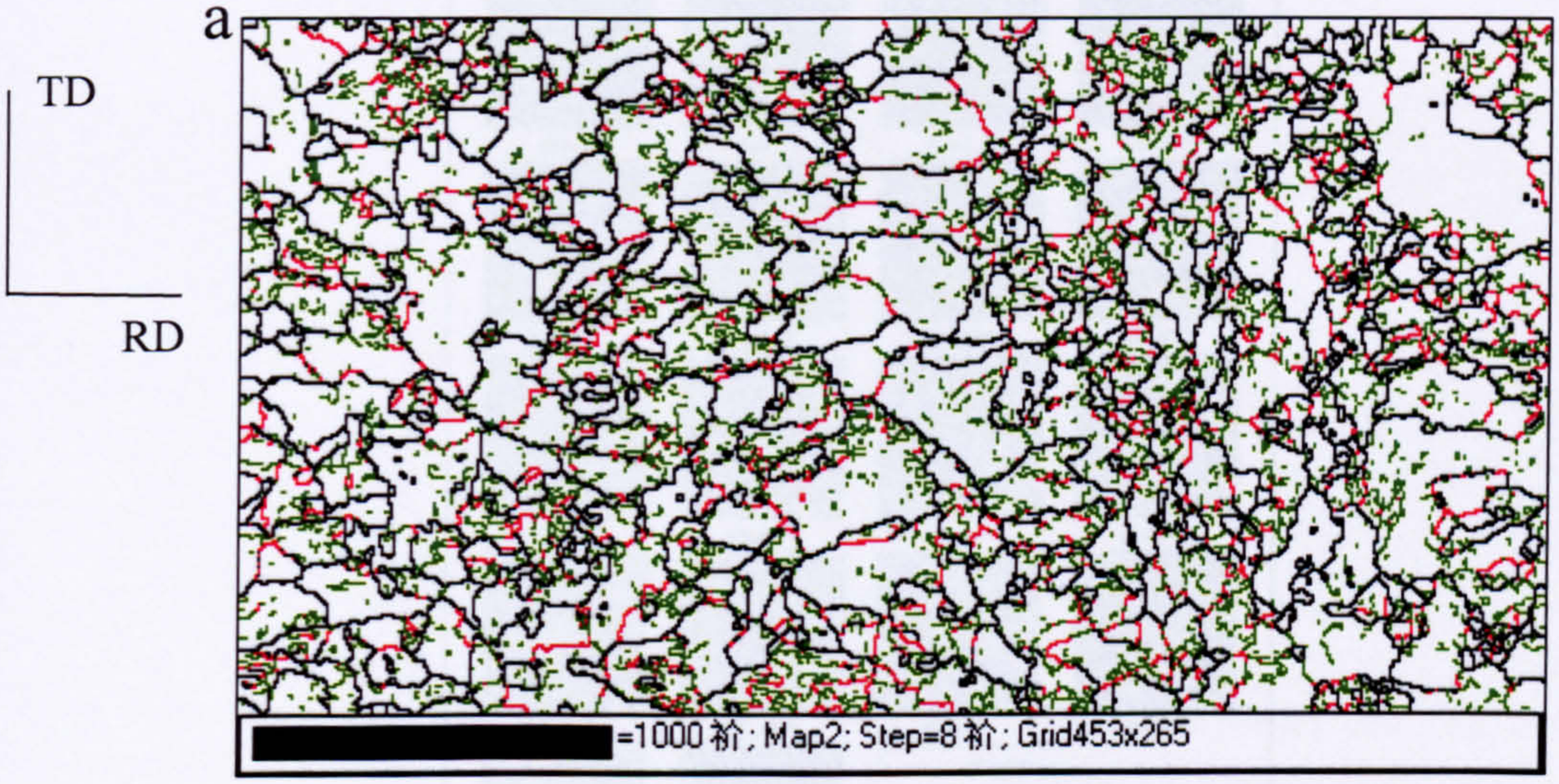

5-10°: green, 10-15°: red, >15°: black

b

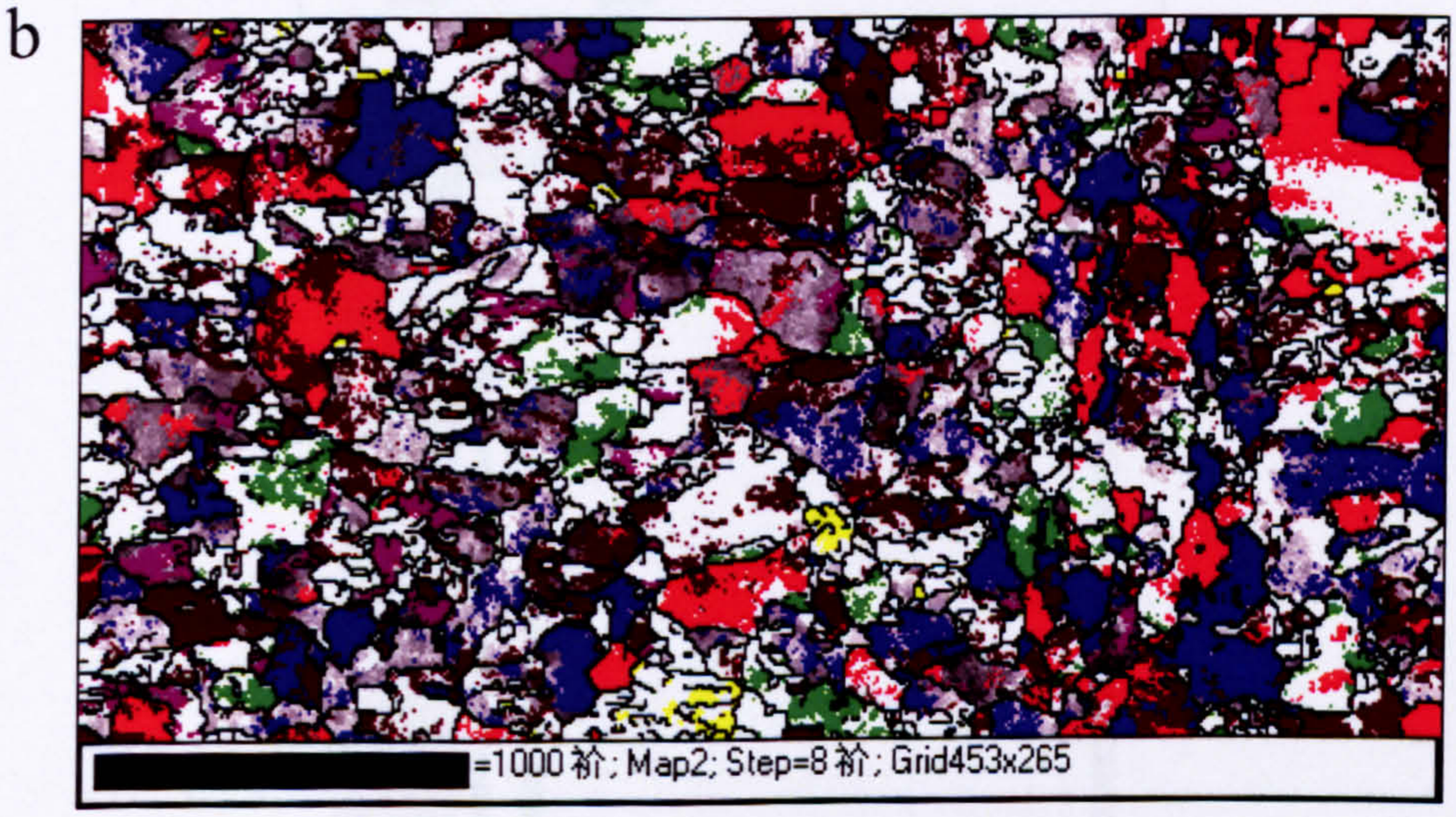

cube-yellow, p-purple, brass-red, copper-blue, goss-green, s-maroon

Fig. 5.27 (a) Orientation map and (b) texture components to the microstructure for the instantaneous deformed sample.

a

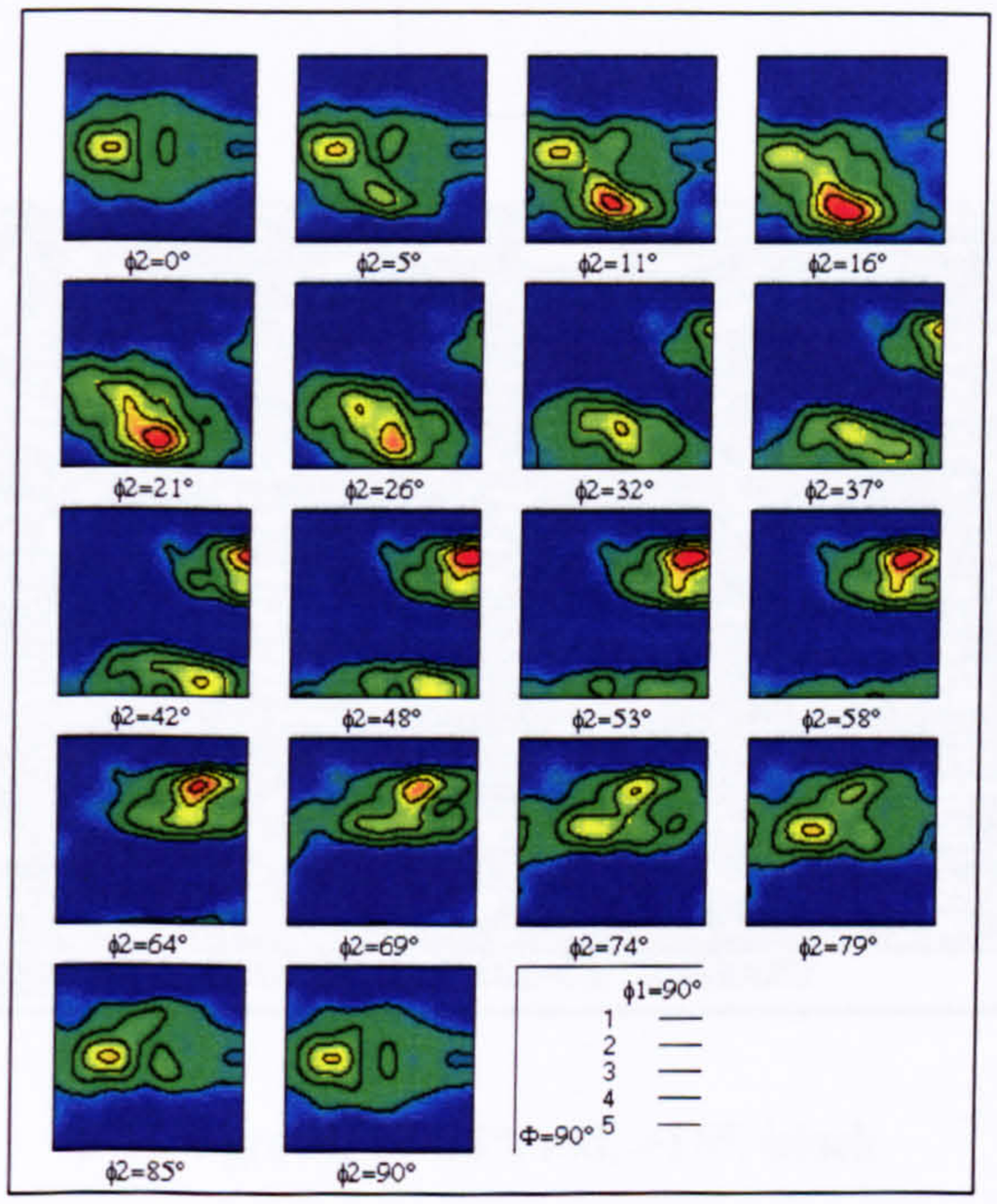

b

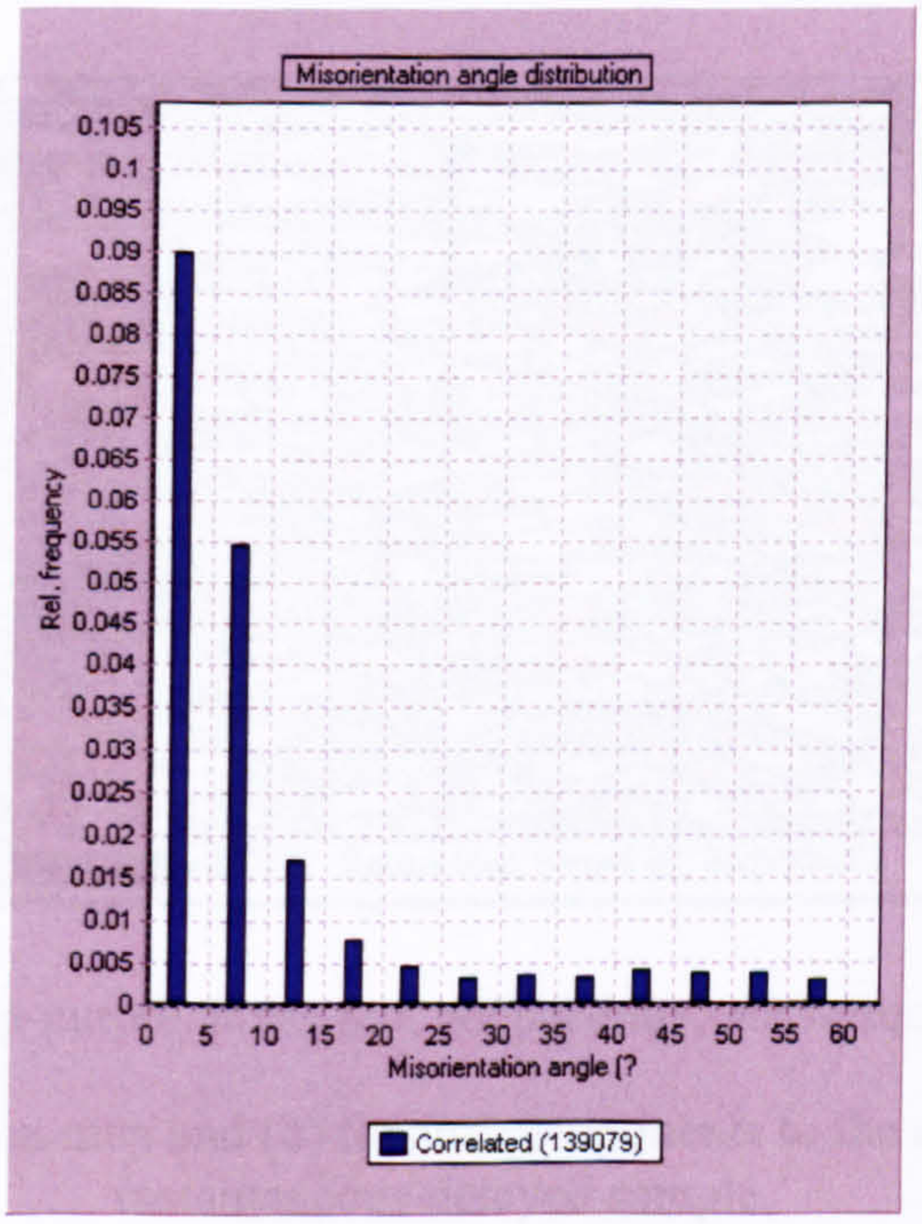

Fig. 5.28 EBSD results of the instantaneous deformed sample: a) orientation distribution functions (ODF) maps, b) misorientation angle distribution.

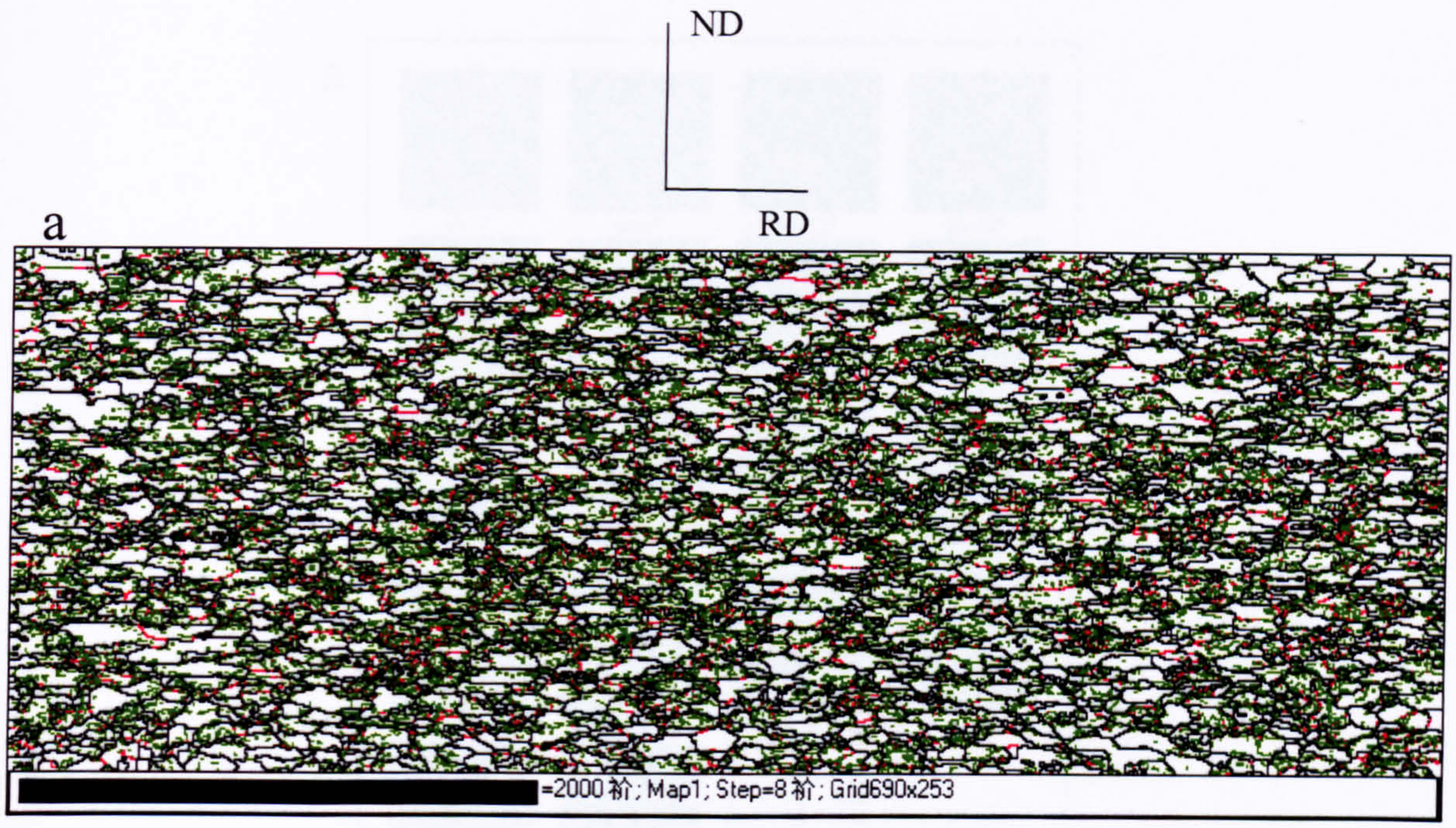

5-10°: green, 10-15°: red, >15°: black

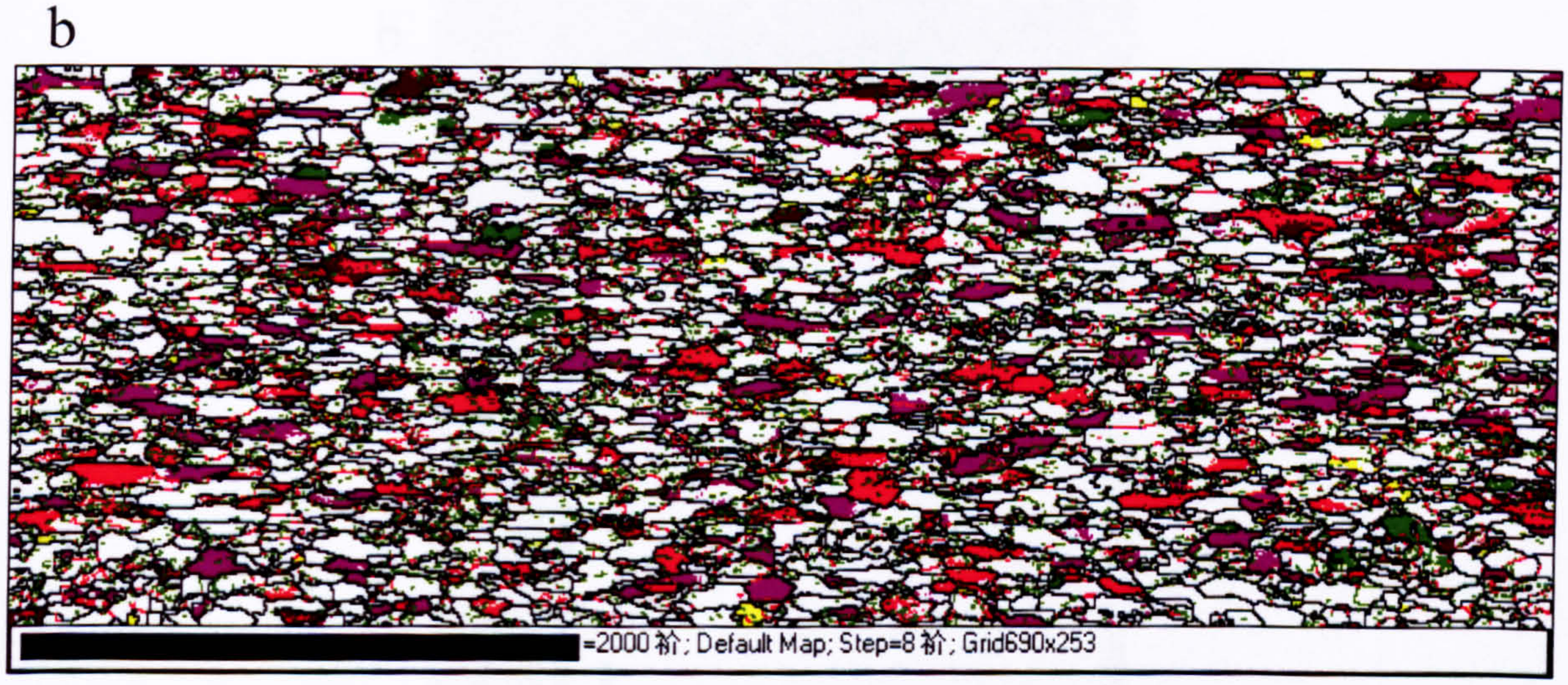

cube-yellow, p-purple, brass-red, copper-blue, goss-green, s-maroon

Fig. 5.29 (a) Orientation map and (b) texture components to the microstructure for the instantaneous delayed sample.

a

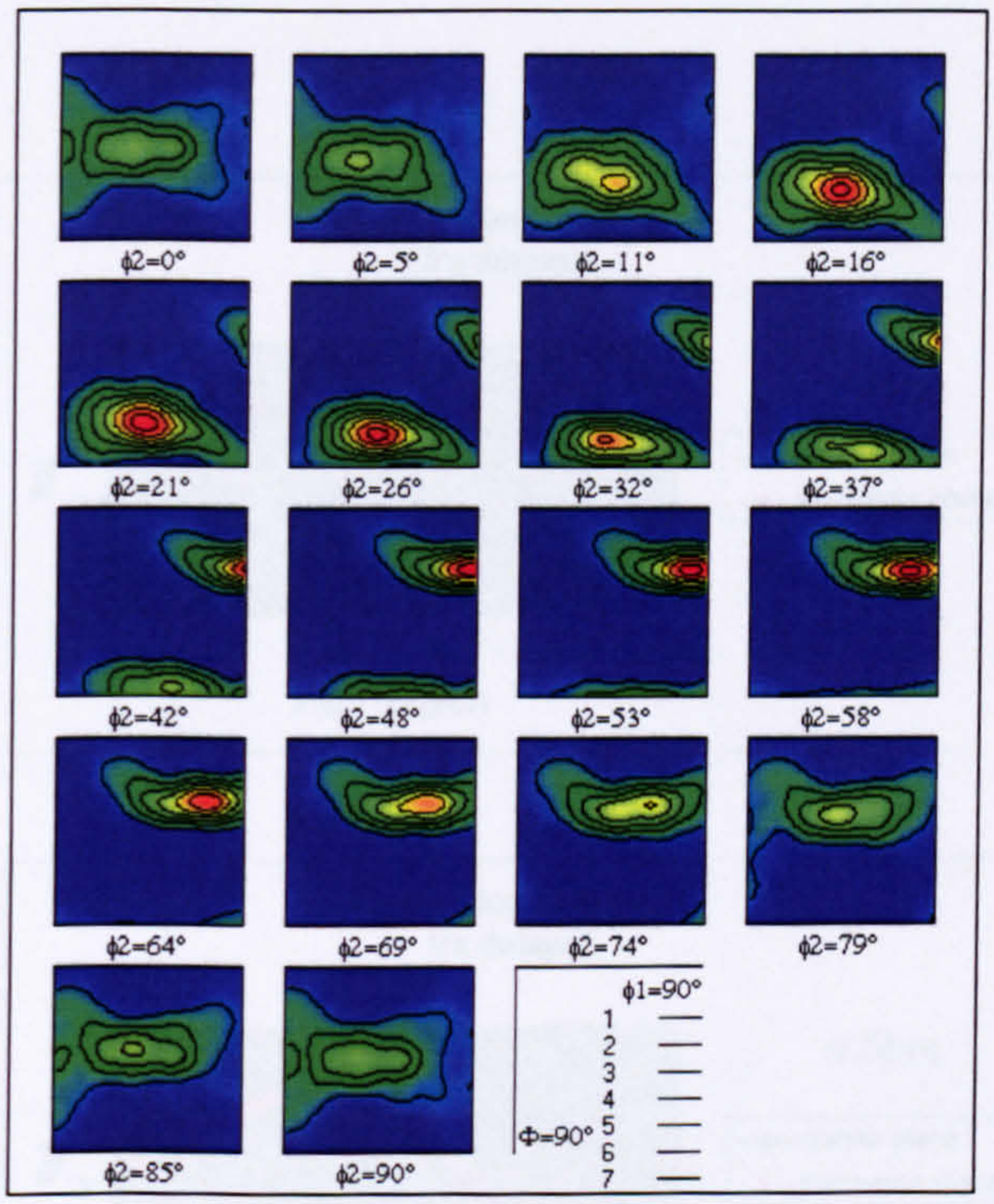

b

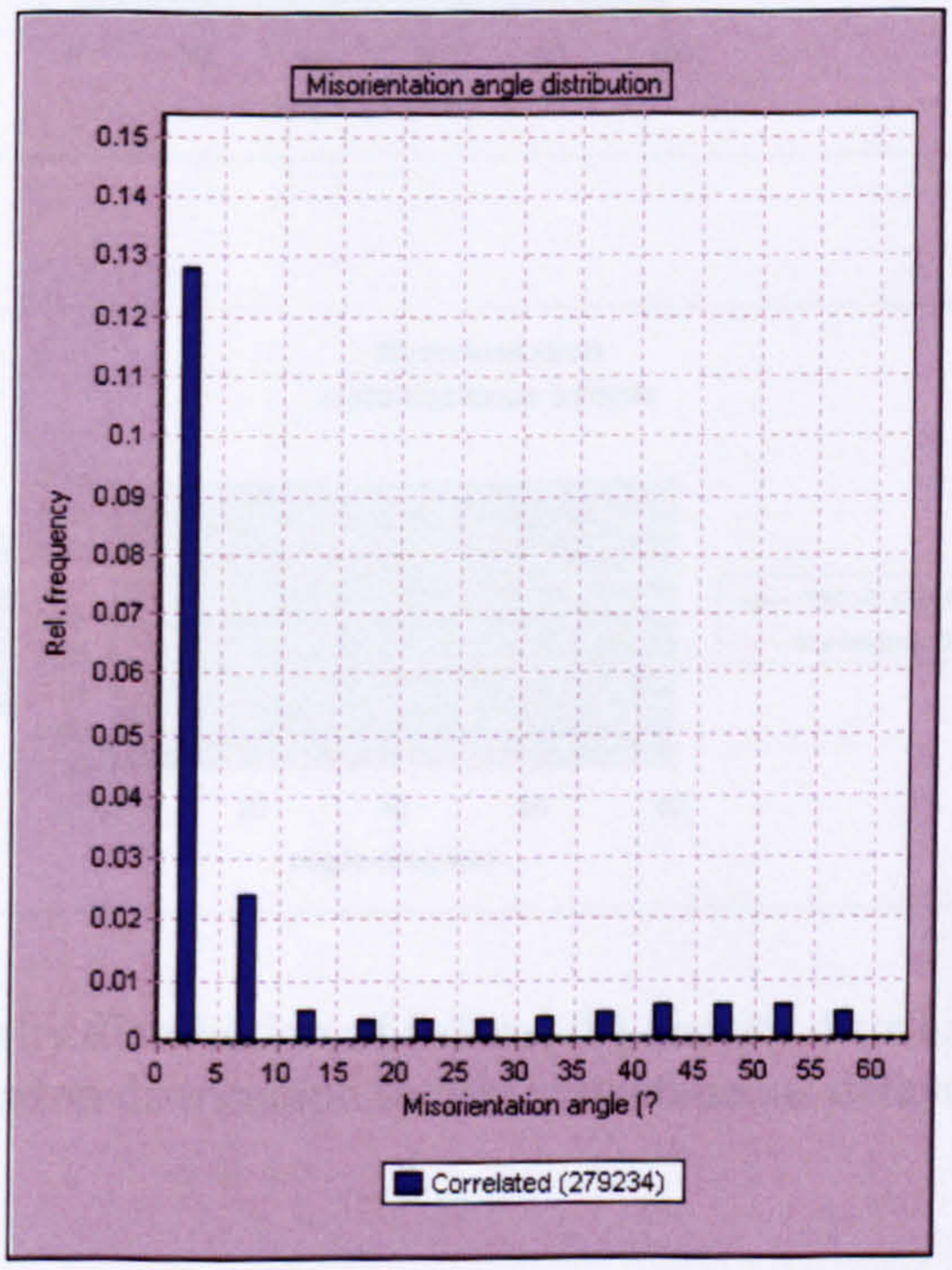

Fig. 5.30 EBSD results of the instantaneous delayed sample: a) orientation distribution functions (ODF) maps, b) misorientation angle distribution.

a

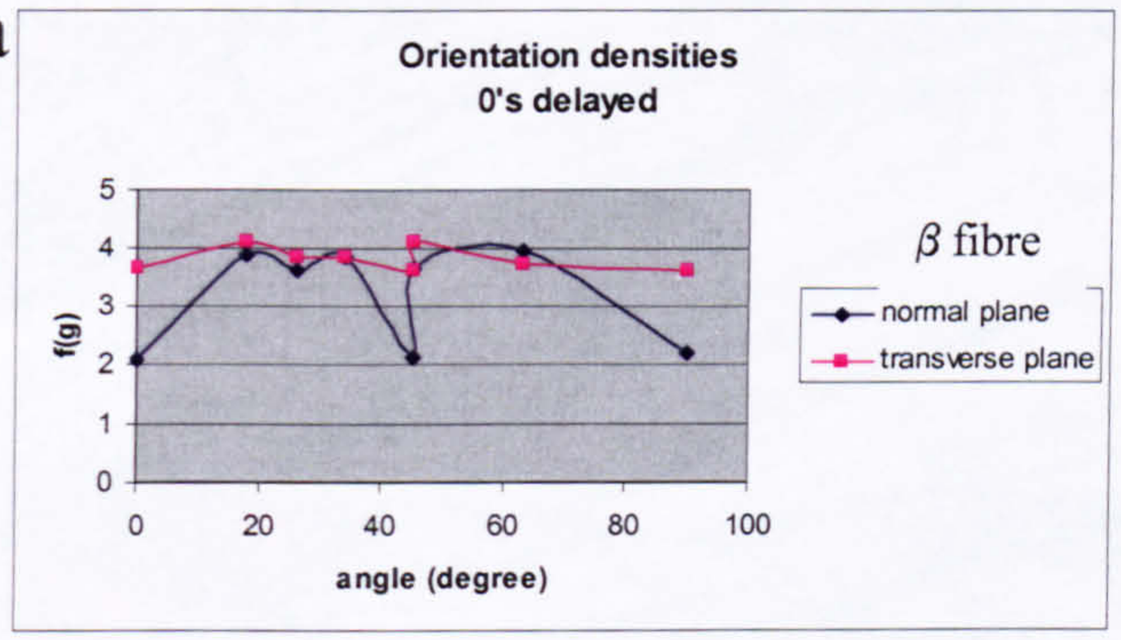

b

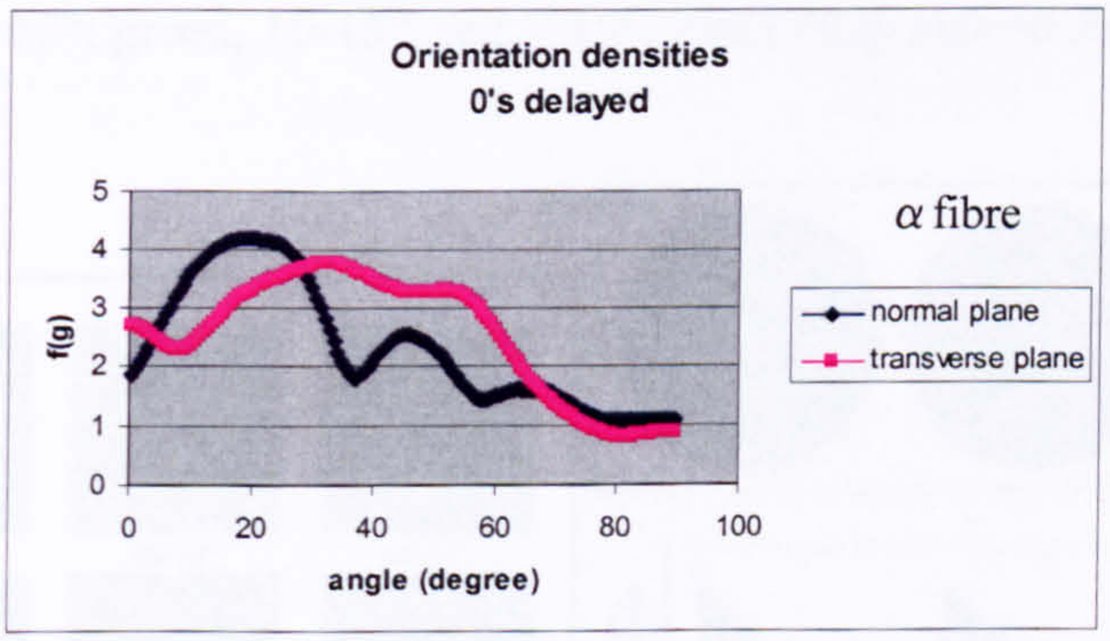

C

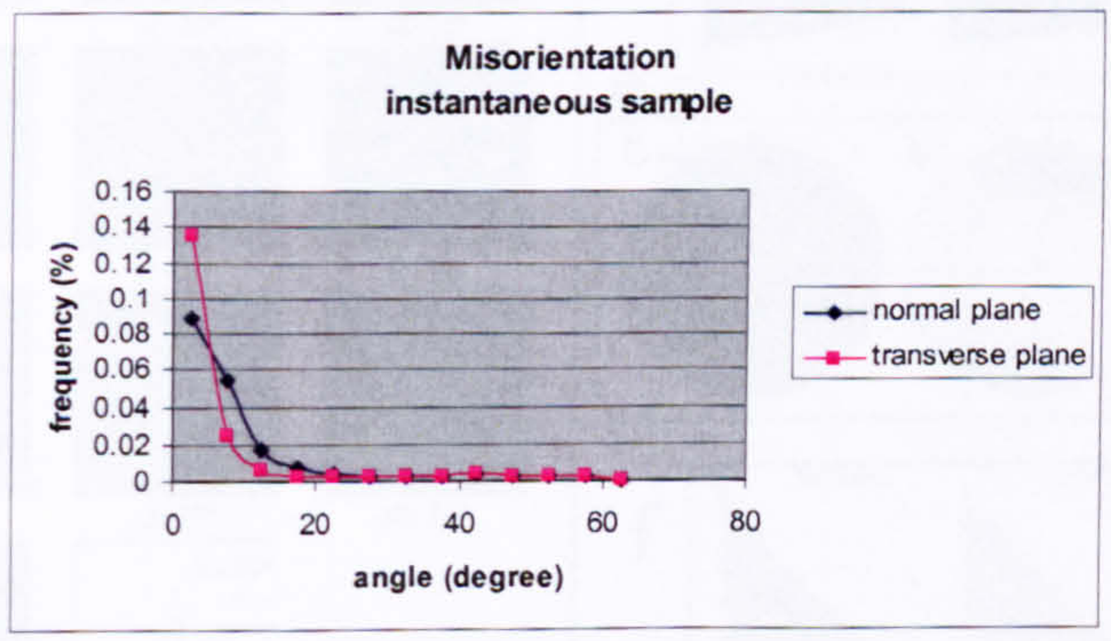

Fig. 5.31 (a) Density distribution of β fibre, (b) density distribution of α fibre, (c) misorientaiton distribution for the instantaneous delayed sample.

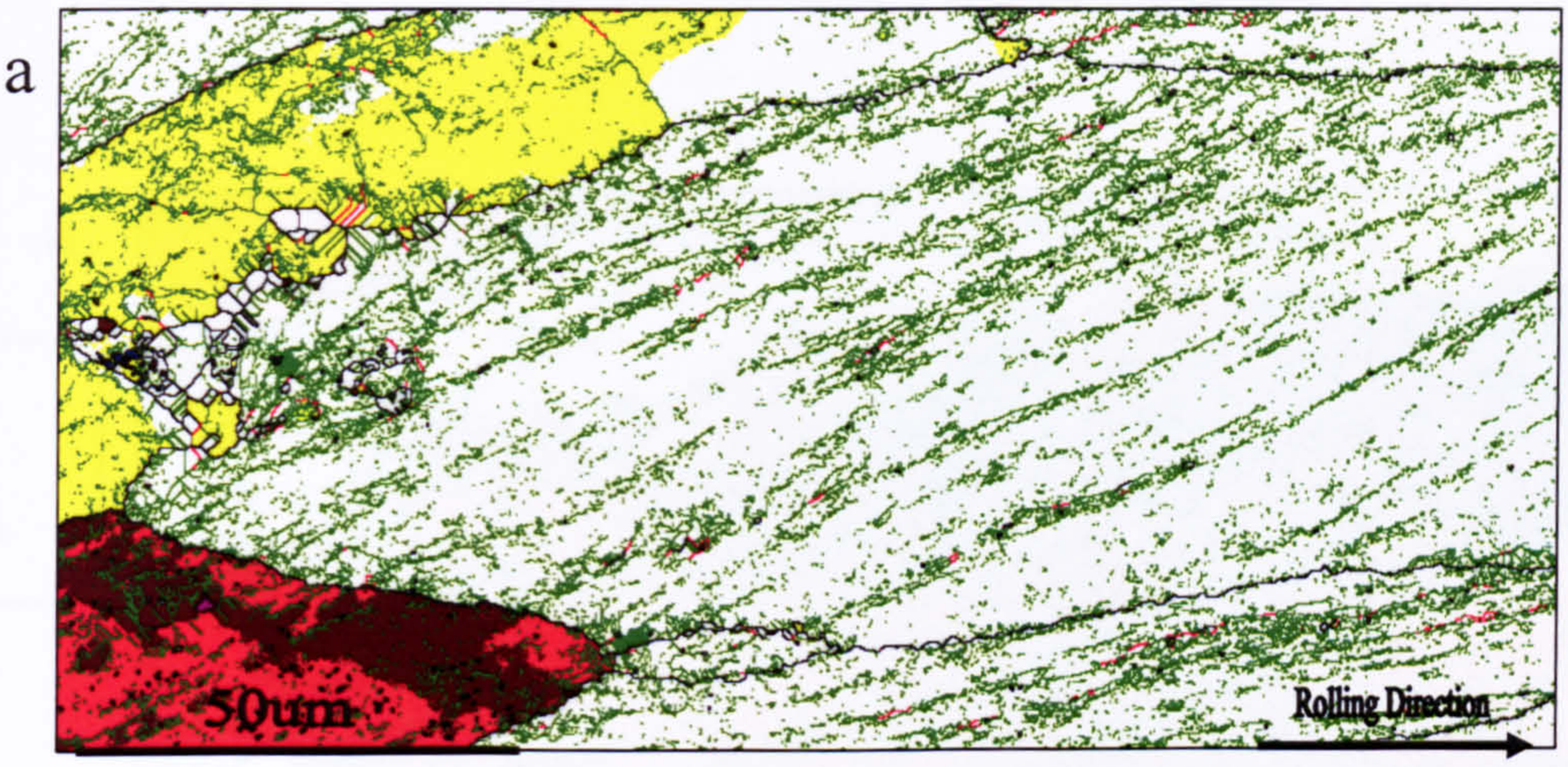

5-10°: green, 10-15°: red, >15°: black Step size=0.2μm

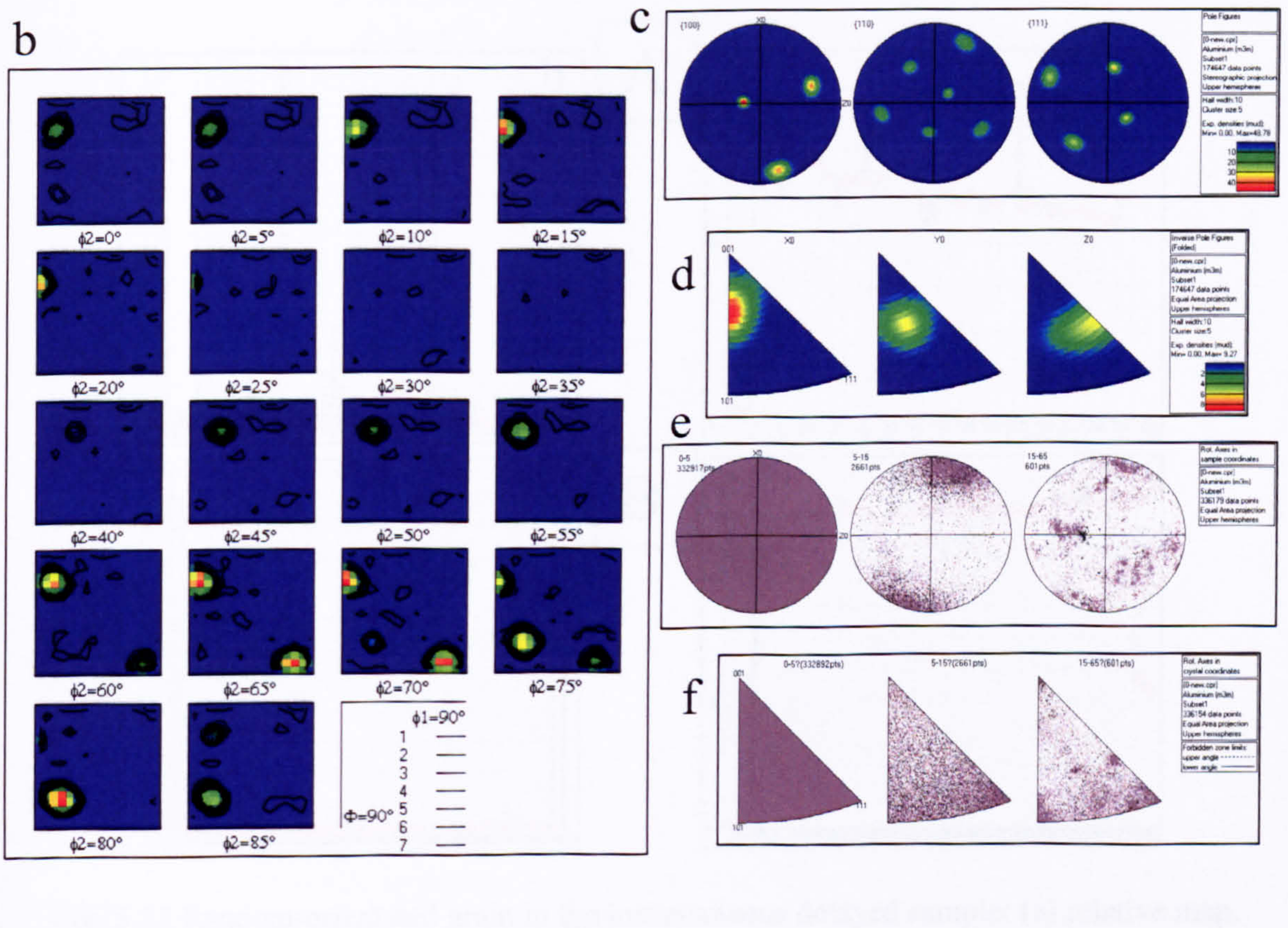

Fig. 5.32 Random-orientated grain in the instantaneous delayed sample: (a) texture and boundary map, (b) ODF, (c) pole figures, (d) inverse pole figures, the distribution of misorientation axis vectors in (e) sample and (f) crystal lattice coordinates.

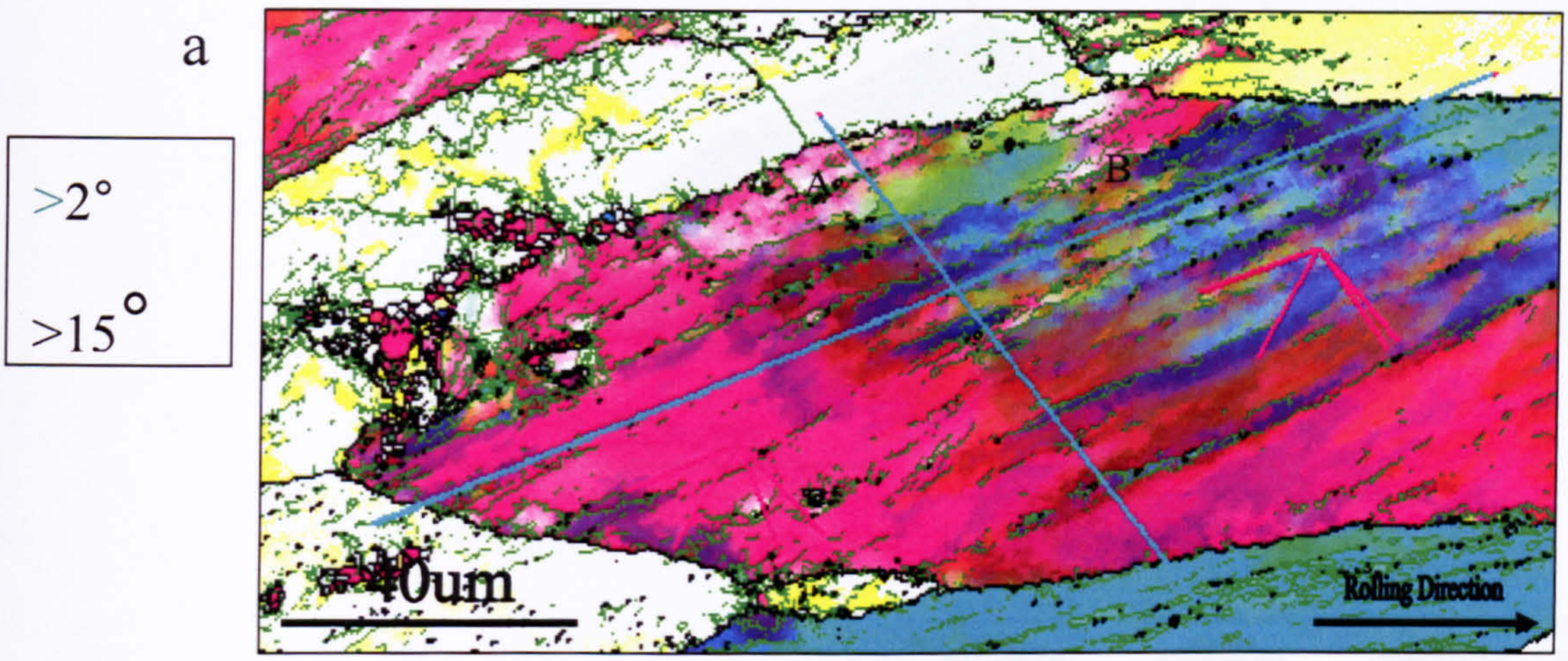

Fig. 5.33 Random-orientated grain in the instantaneous delayed sample: (a) relative map, (b) (d) relative and (c) (e) cumulative misorientation distributions of line scans performed along A and B in (a).

5-10°: green, 10-15°: red, >15°: black Step size=0.2μm

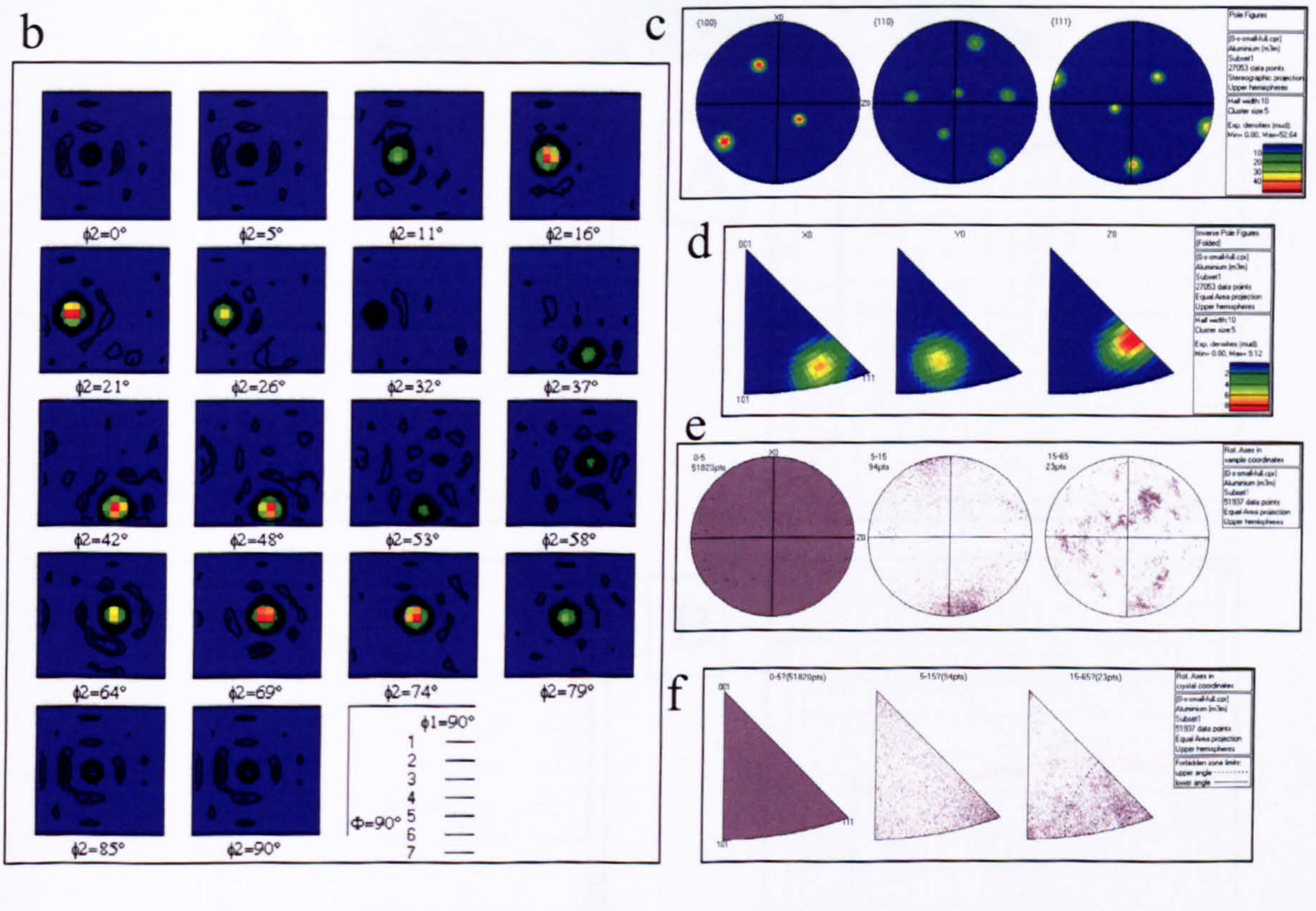

Fig. 5.34 S-orientated grain in the instantaneous delayed sample: (a) texture and boundary map, (b) ODF, (c) pole figures, (d) inverse pole figures, the distribution of misorientation axis vectors in (e) sample and (f) crystal lattice coordinates.

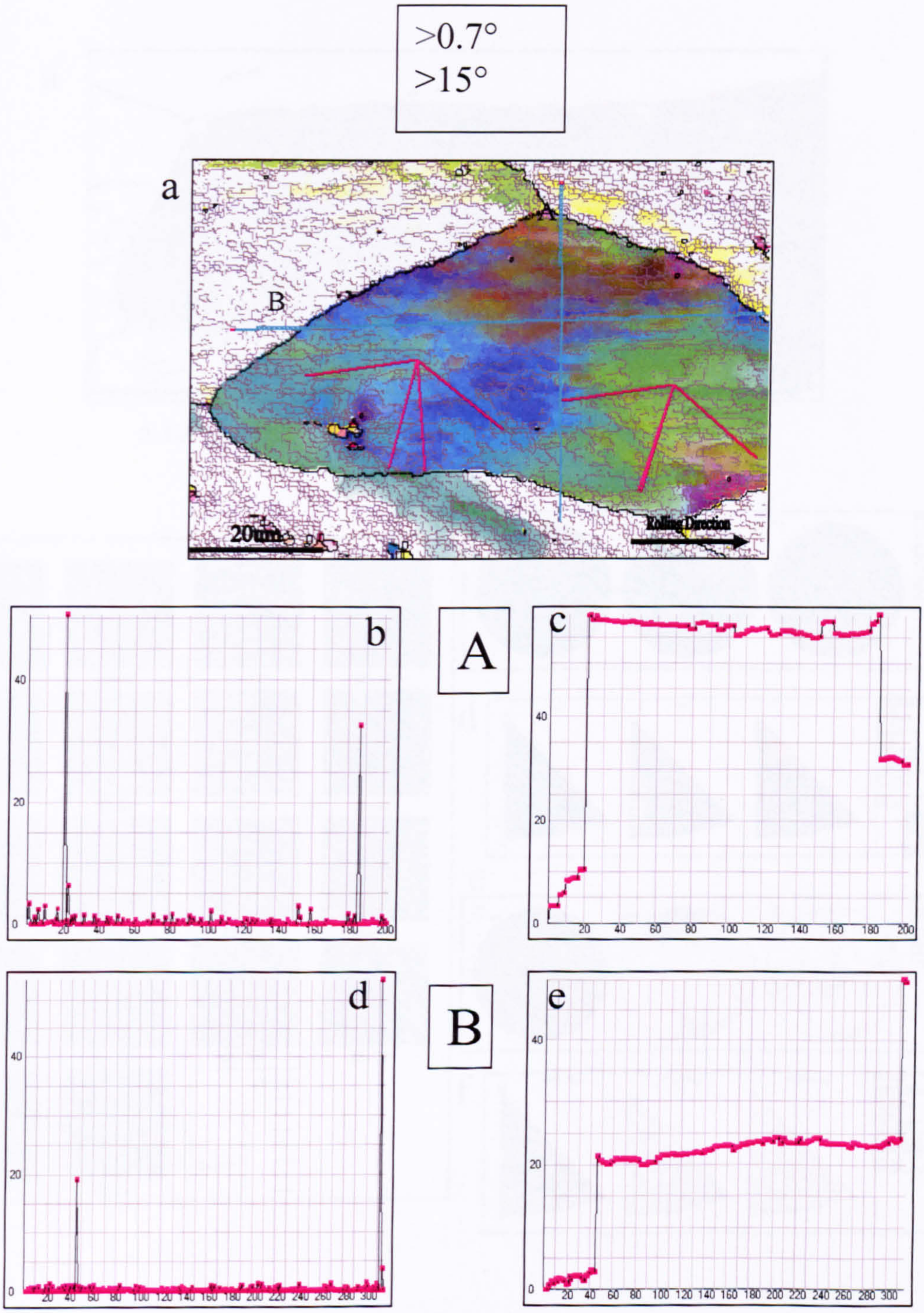

Fig. 5.35 S-orientated grain in the instantaneous delayed sample: (a) relative map, (b) (d) relative and (c) (e) cumulative misorientation distributions of line scans performed along A and B in (a).

a

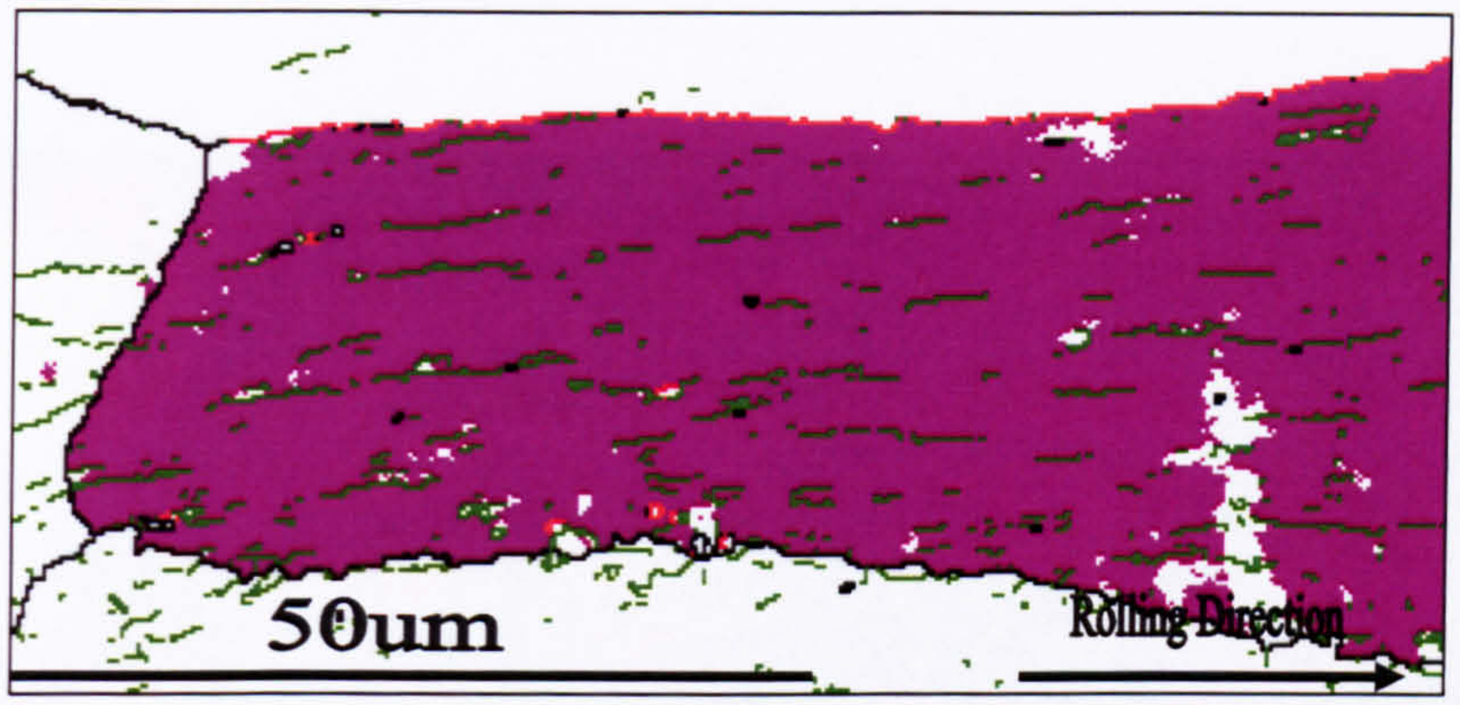

5-10°: green, 10-15°: red, >15°: black Step size=0.2μm

b

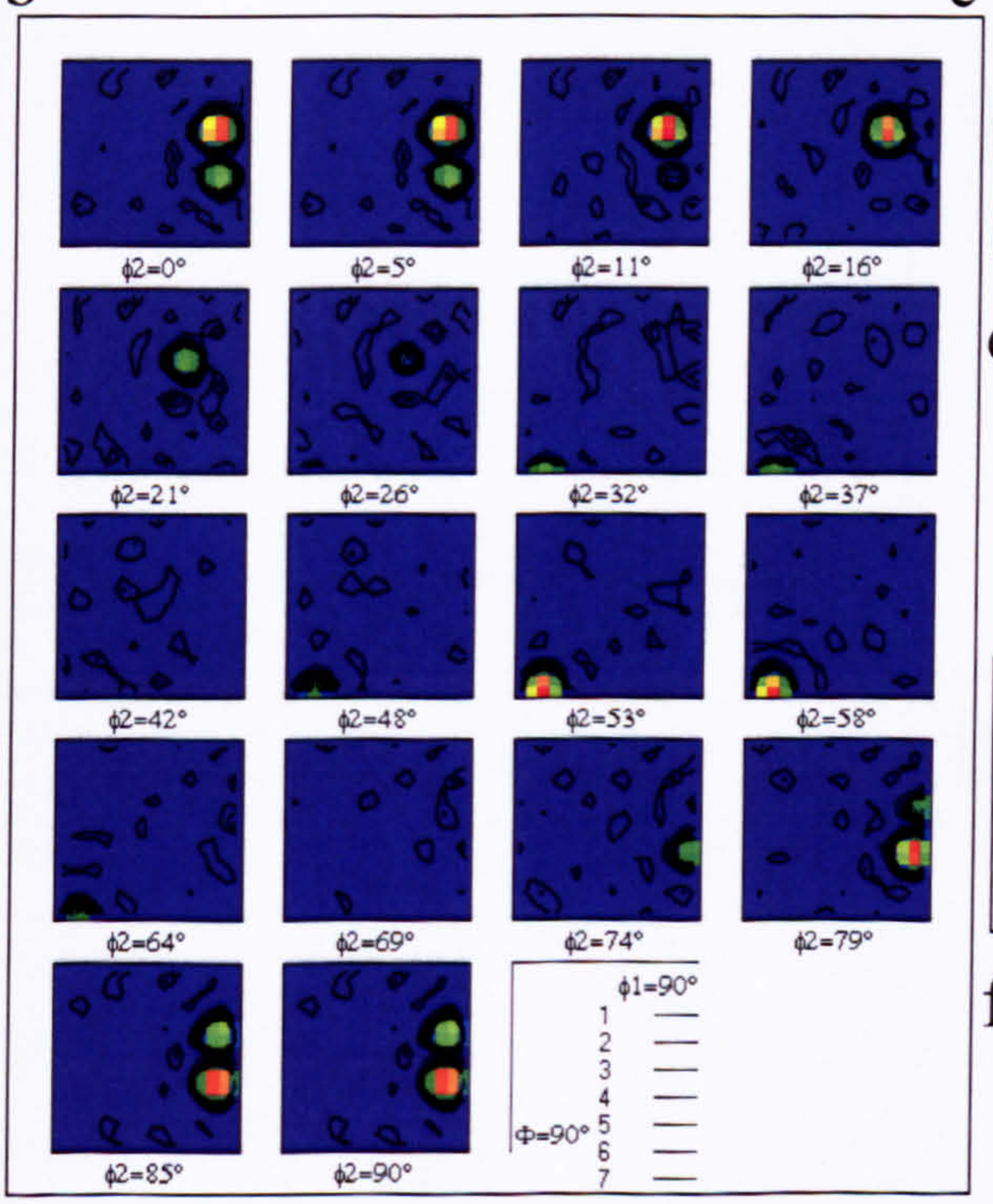

c

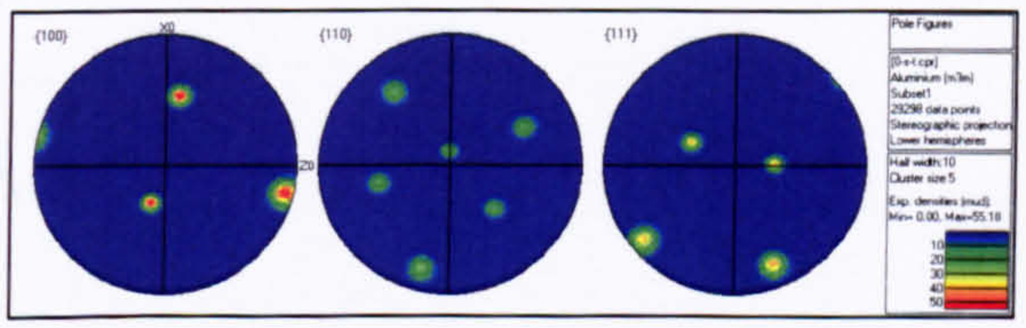

d

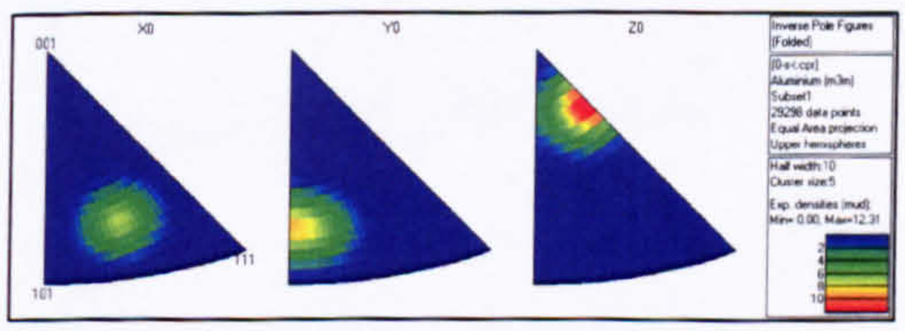

e

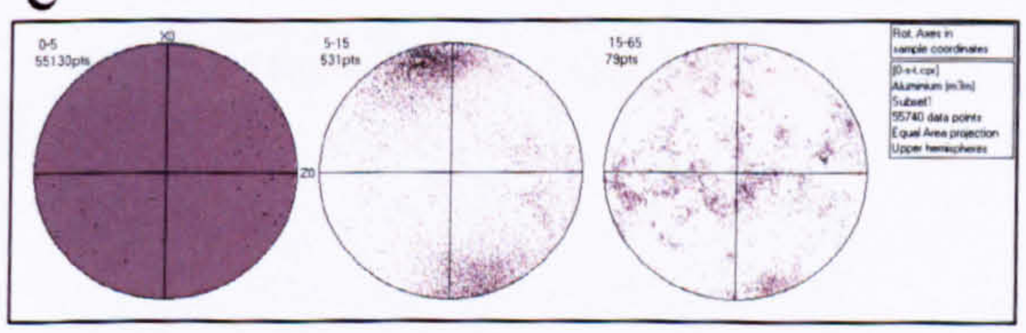

f

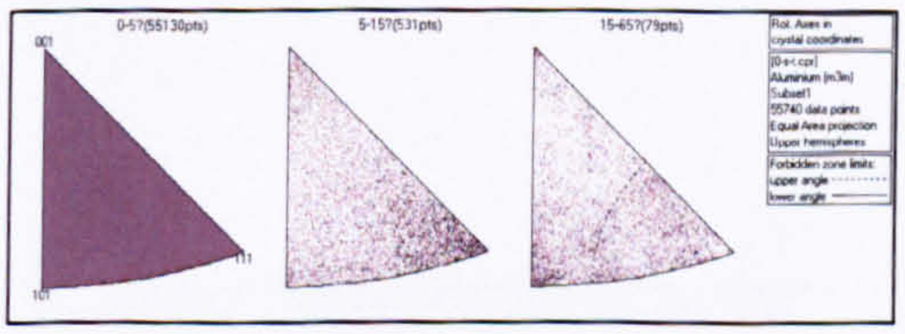

Fig. 5.36 P-orientated grain in the instantaneous delayed sample: (a) texture and boundary map, (b) ODF, (c) pole figures, (d) inverse pole figures, the distribution of misorientation axis vectors in (e) sample and (f) crystal lattice coordinates.

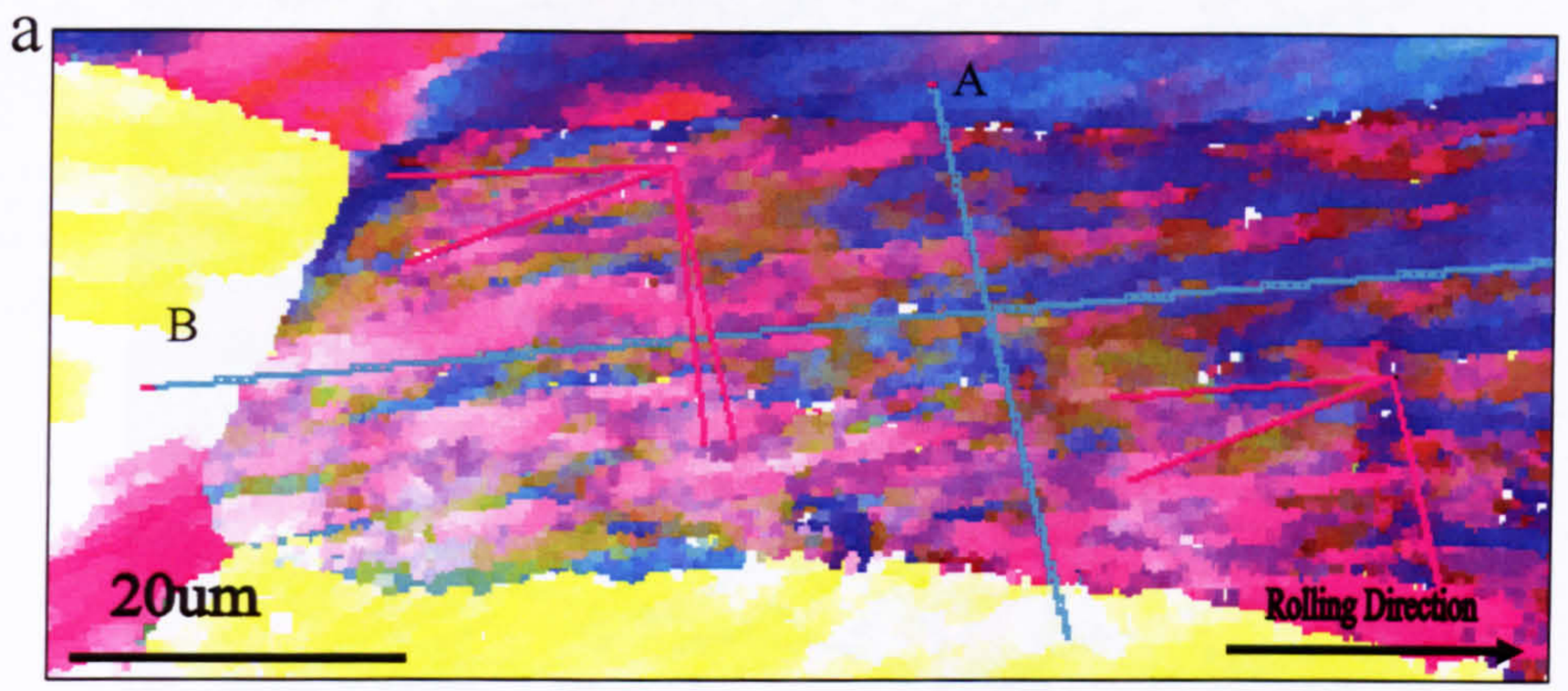

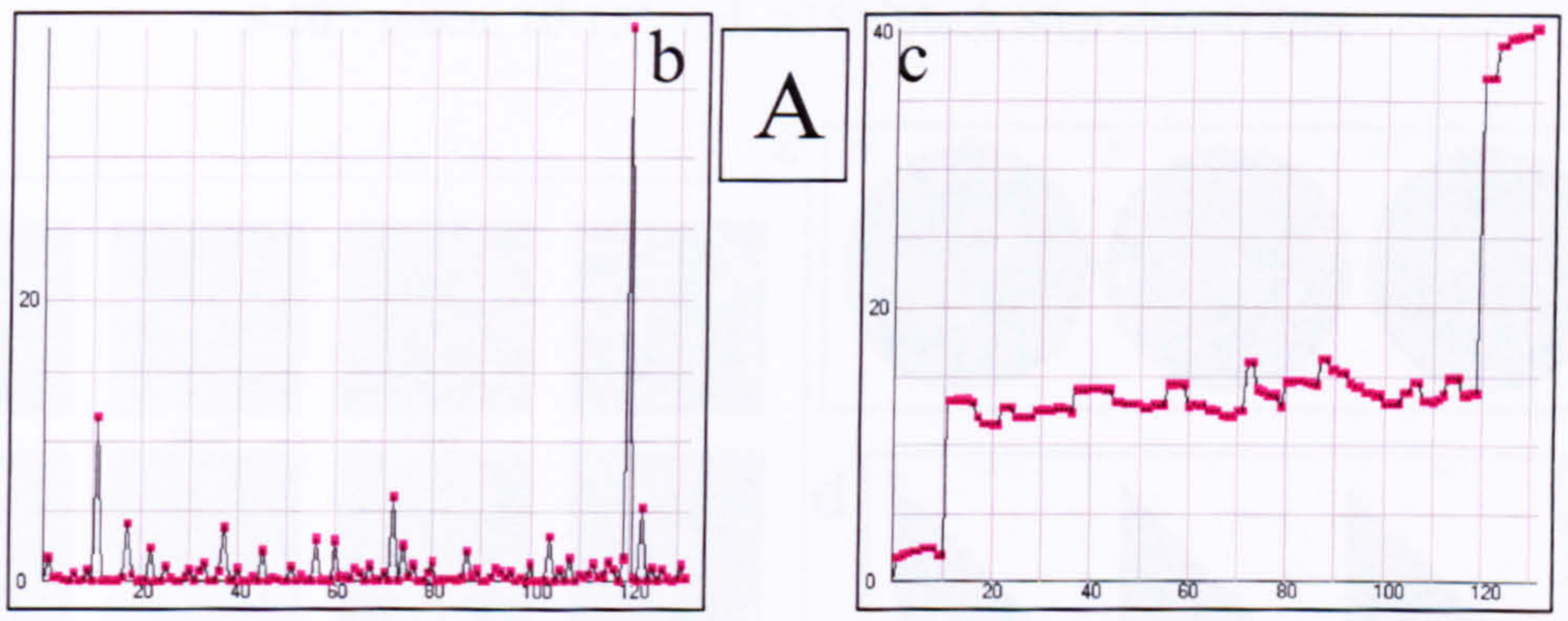

Fig. 5.37 P-orientated grain in the instantaneous delayed sample: (a) relative map, (b) (d) relative and (c) (e) cumulative misorientation distributions of line scans performed along A and B in (a).

a

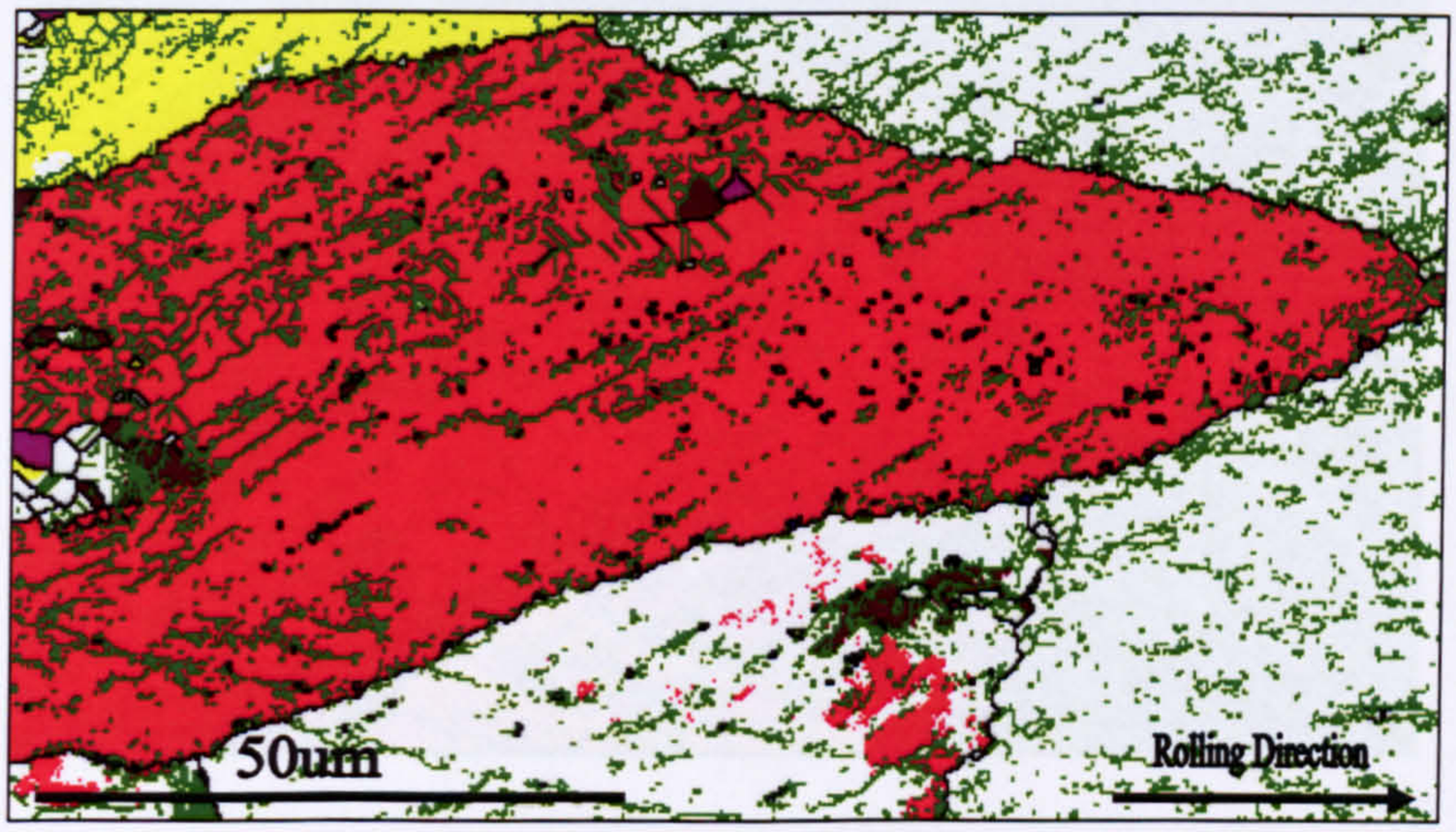

5-10°: green, 10-15°: red, >15°: black Step size=0.2μm

b

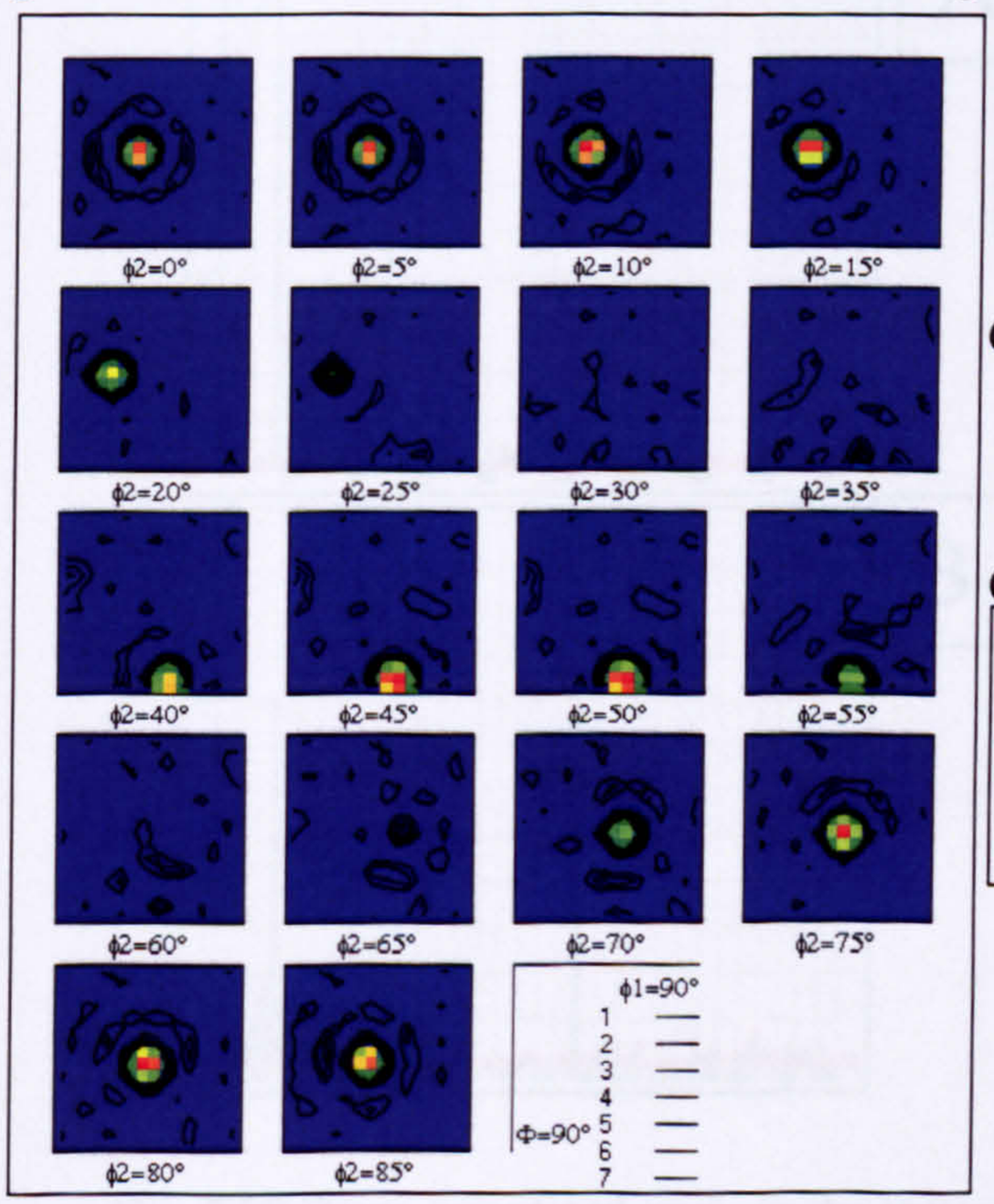

c

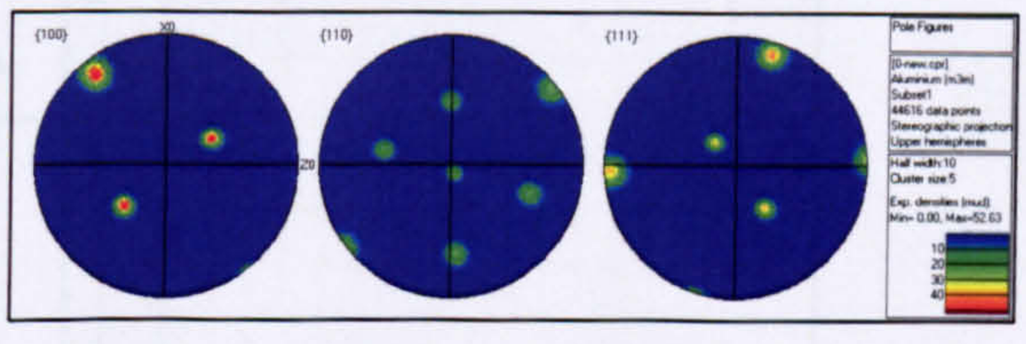

d

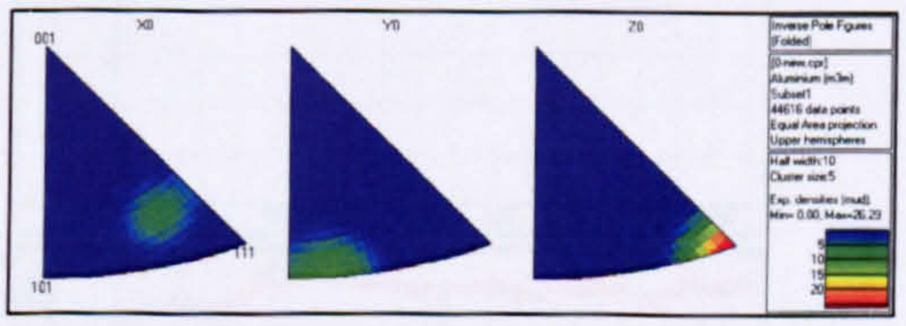

e

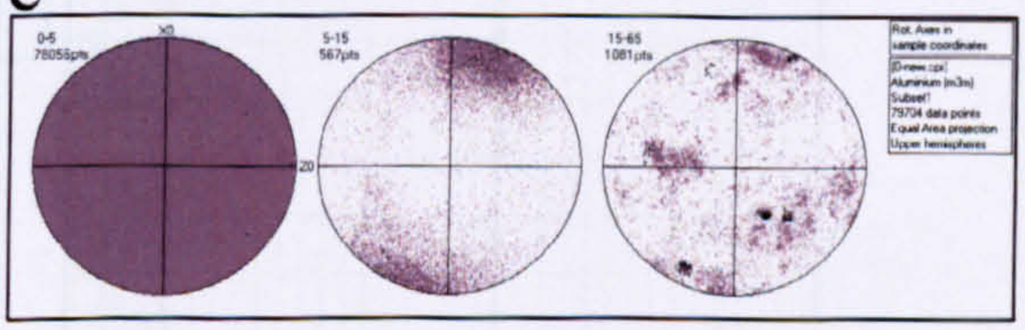

f

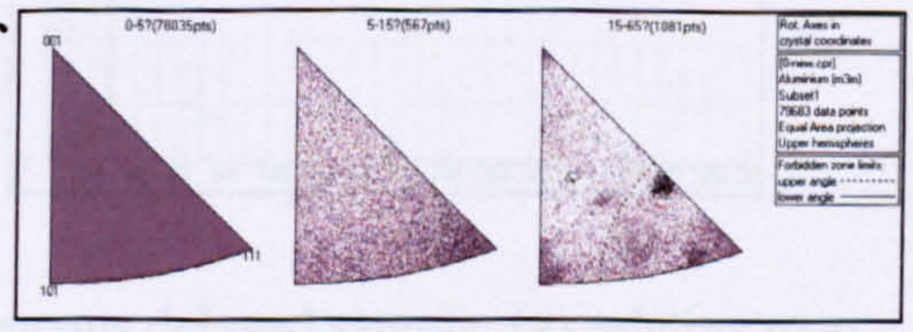

Fig. 5.38 Brass-orientated grain in the instantaneous delayed sample: (a) texture and boundary map, (b) ODF, (c) pole figures, (d) inverse pole figures, the distribution of misorientation axis vectors in (e) sample and (f) crystal lattice coordinates.

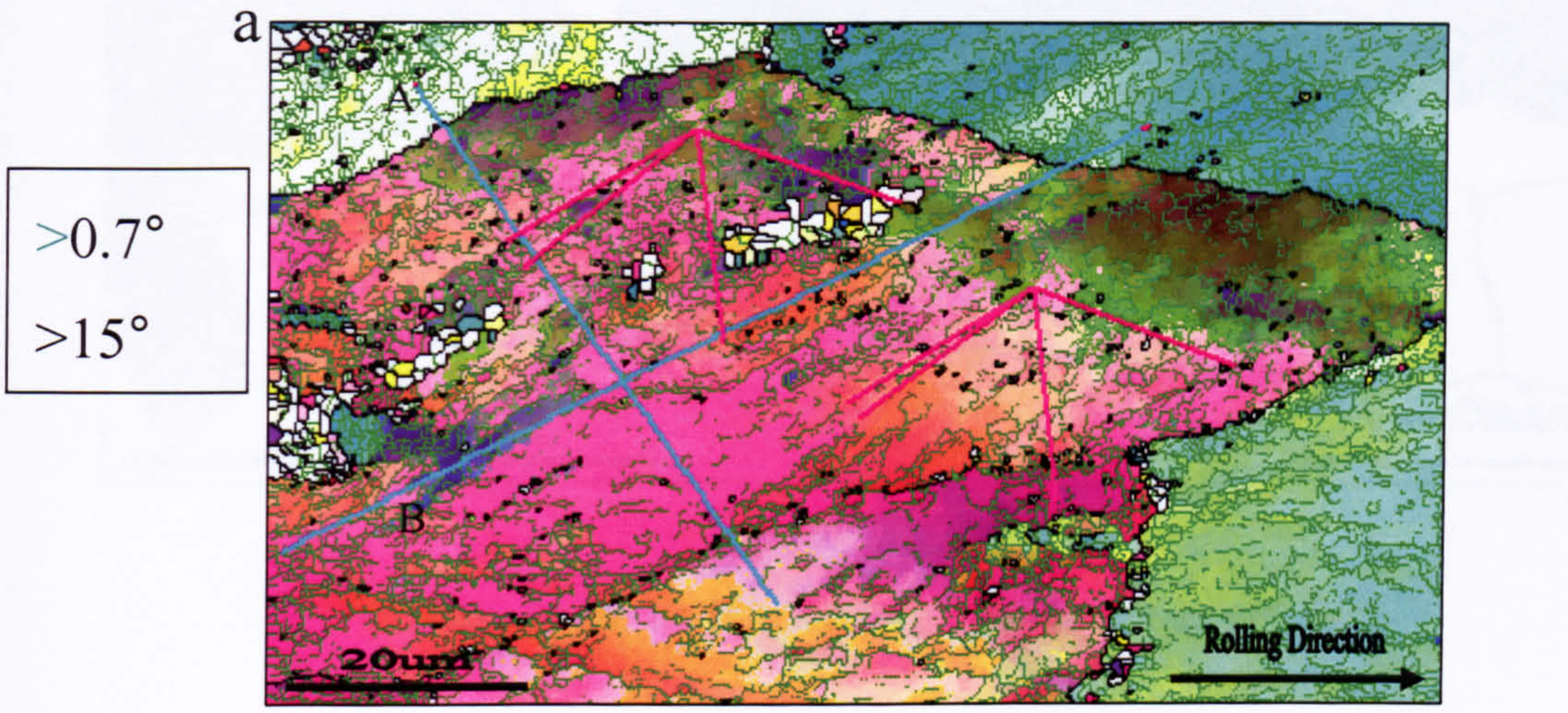

Fig. 5.39 Brass-orientated grain in the instantaneous delayed sample: (a) relative map, (b) (d) relative and (c) (e) cumulative misorientation distributions of line scans performed along A and B in (a).

a

5-10°: green, 10-15°: red, >15°: black Step size=0.2μm

b

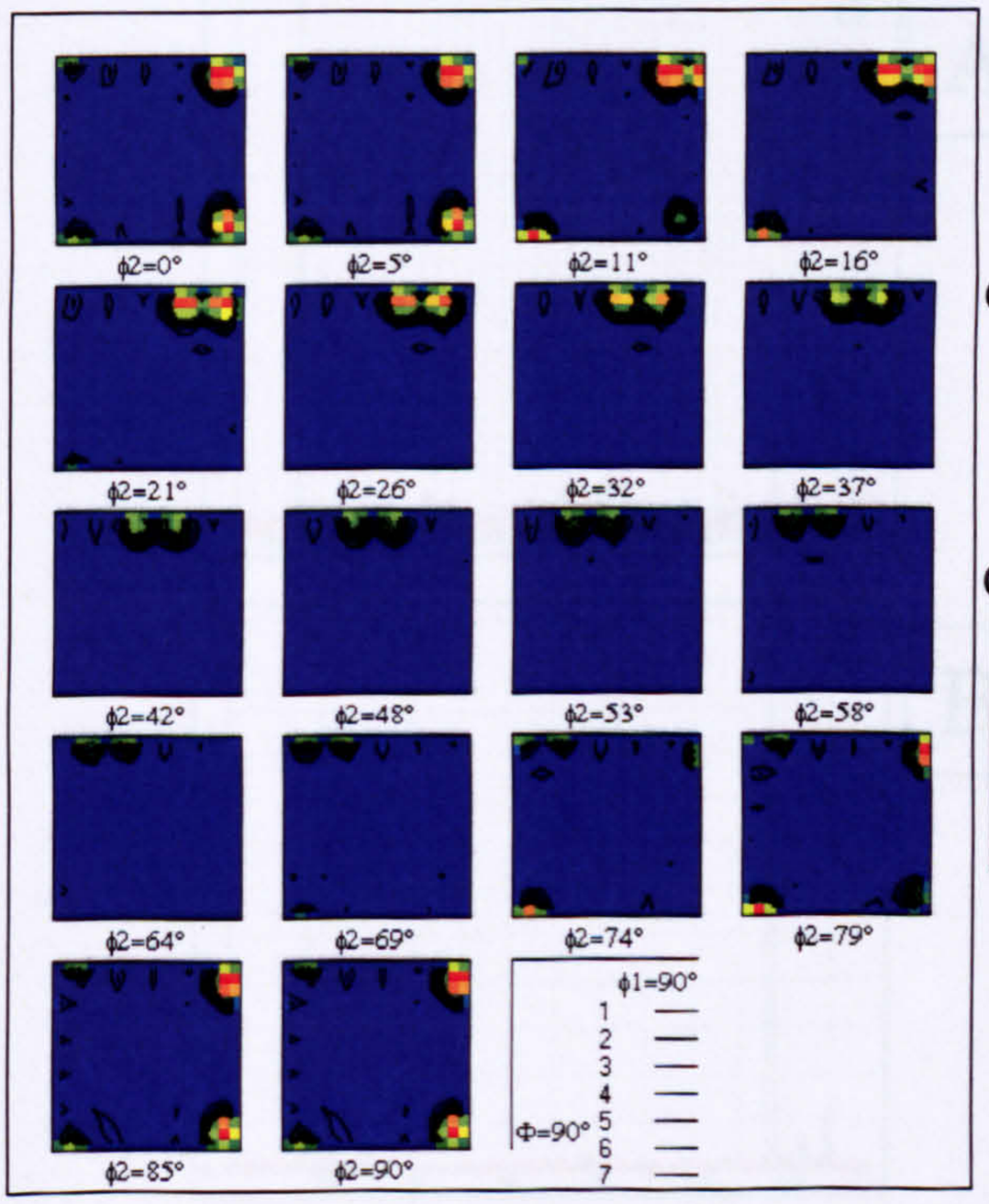

c

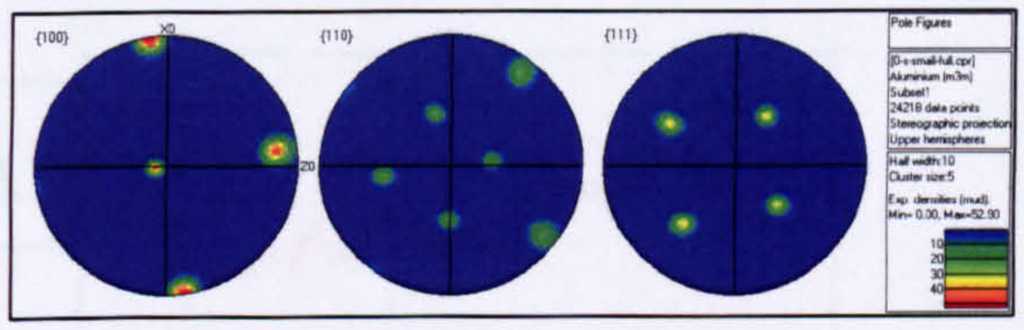

d

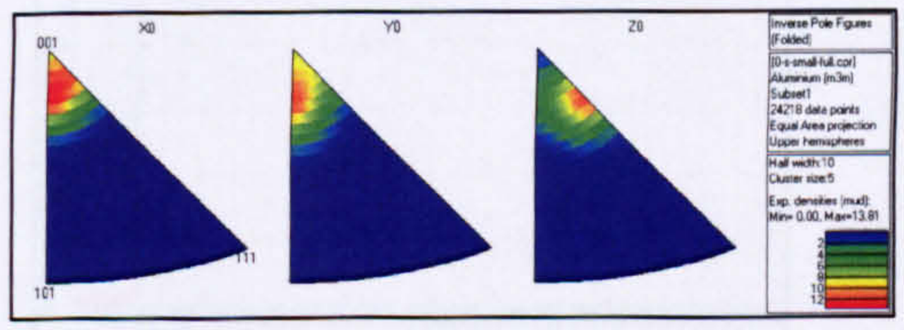

e

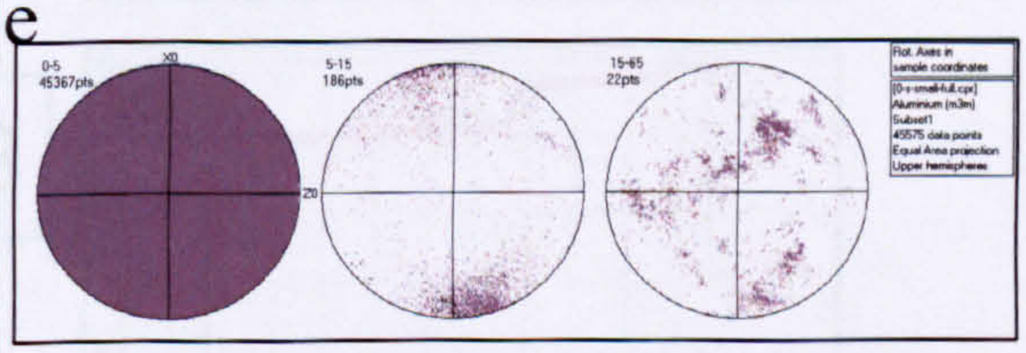

f

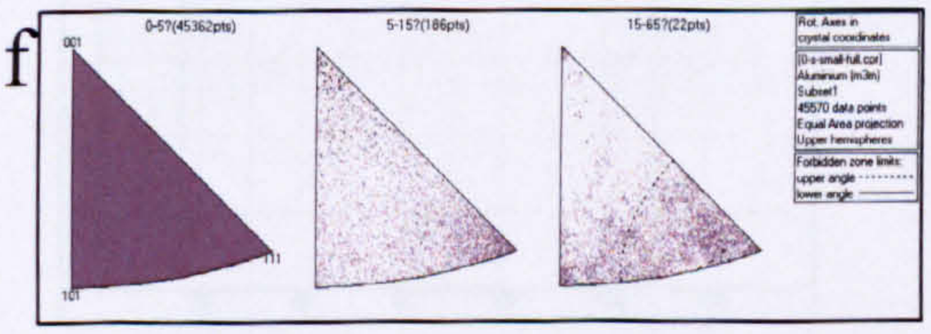

Fig. 5.40 Cube-orientated grain in the instantaneous delayed sample: (a) texture and boundary map, (b) ODF, (c) pole figures, (d) inverse pole figures, the distribution of misorientation axis vectors in (e) sample and (f) crystal lattice coordinates.

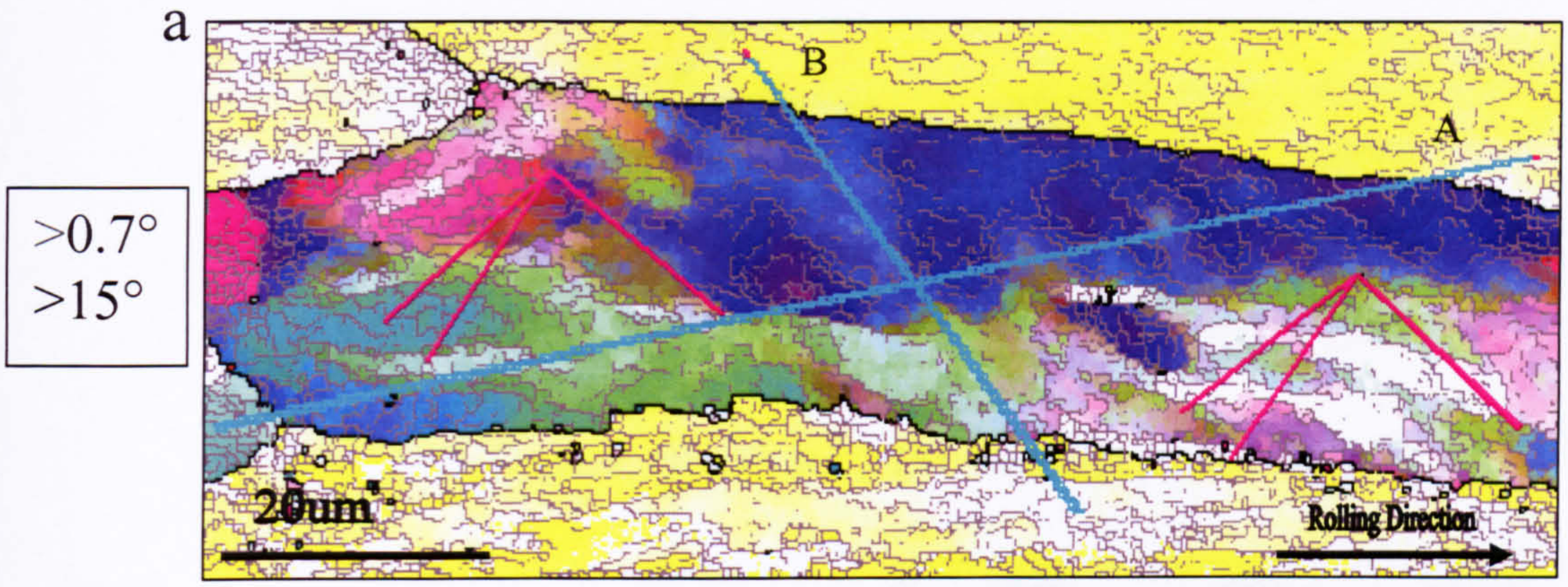

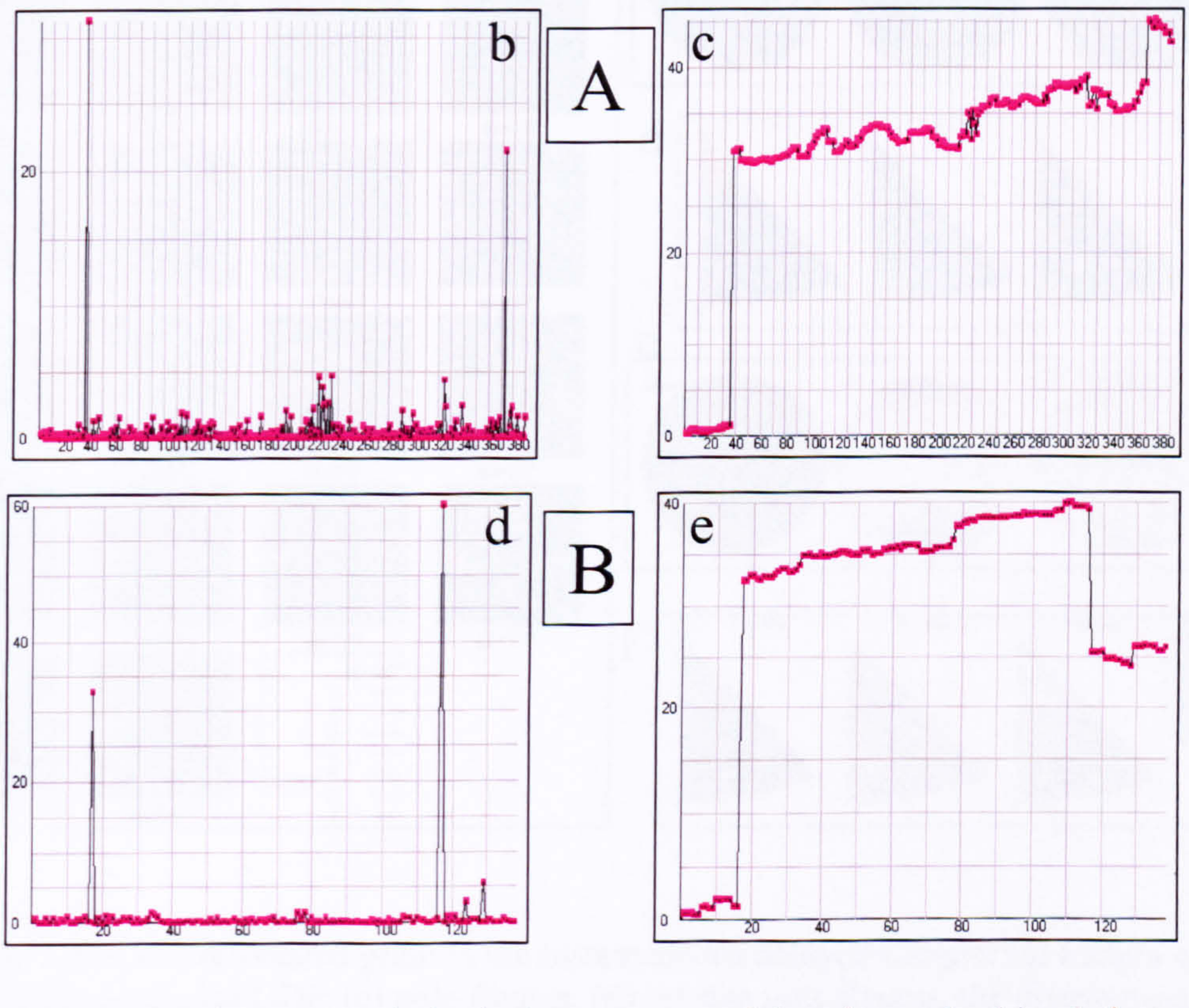

Fig. 5.41 Cube-orientated grain in the instantaneous delayed sample: (a) relative map, (b) (d) relative and (c) (e) cumulative misorientation distributions of line scans performed along A and B in (a).

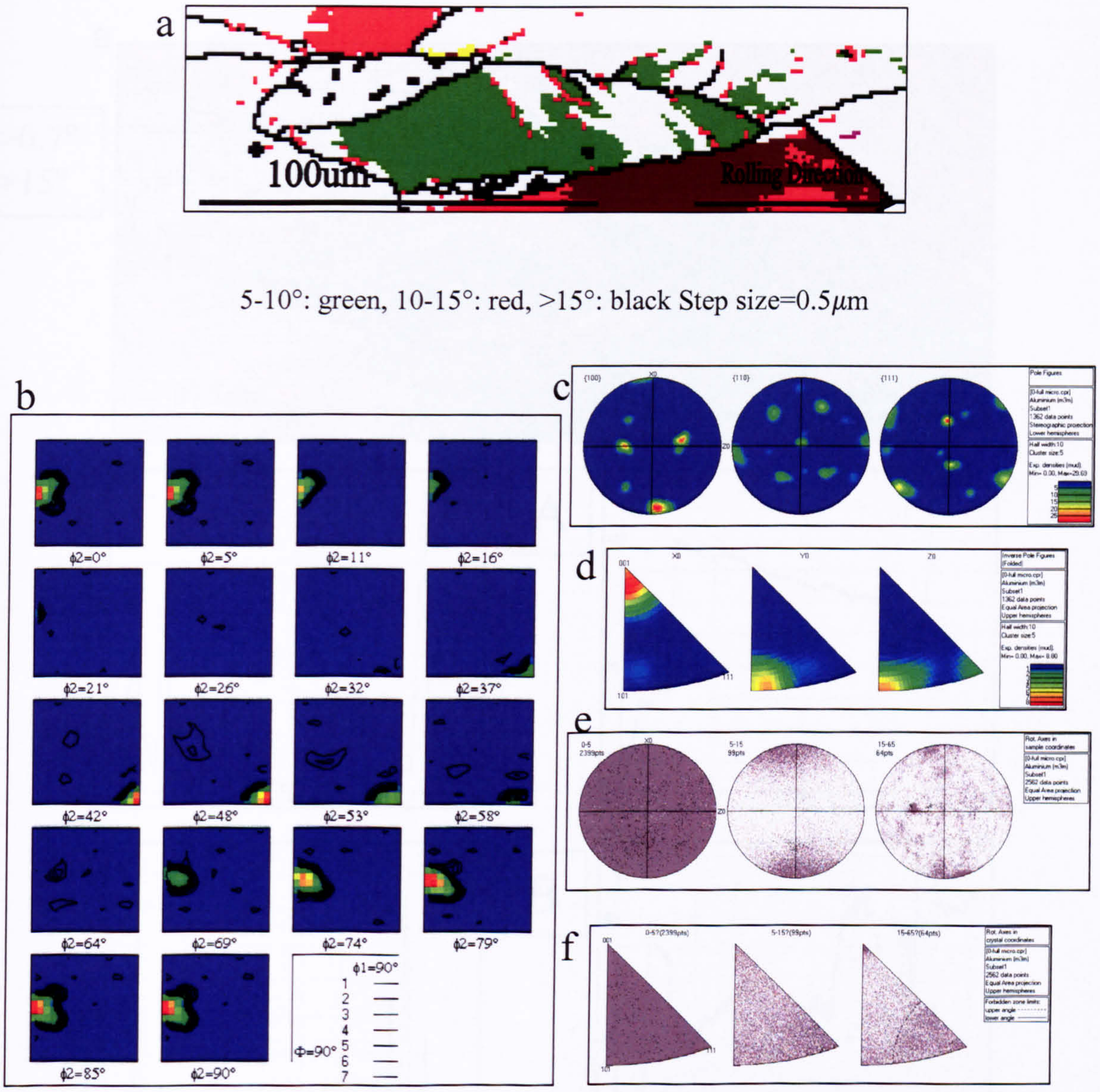

Fig. 5.42 Goss-orientated grain in the instantaneous delayed sample: (a) texture and boundary map, (b) ODF, (c) pole figures, (d) inverse pole figures, the distribution of misorientation axis vectors in (e) sample and (f) crystal lattice coordinates.

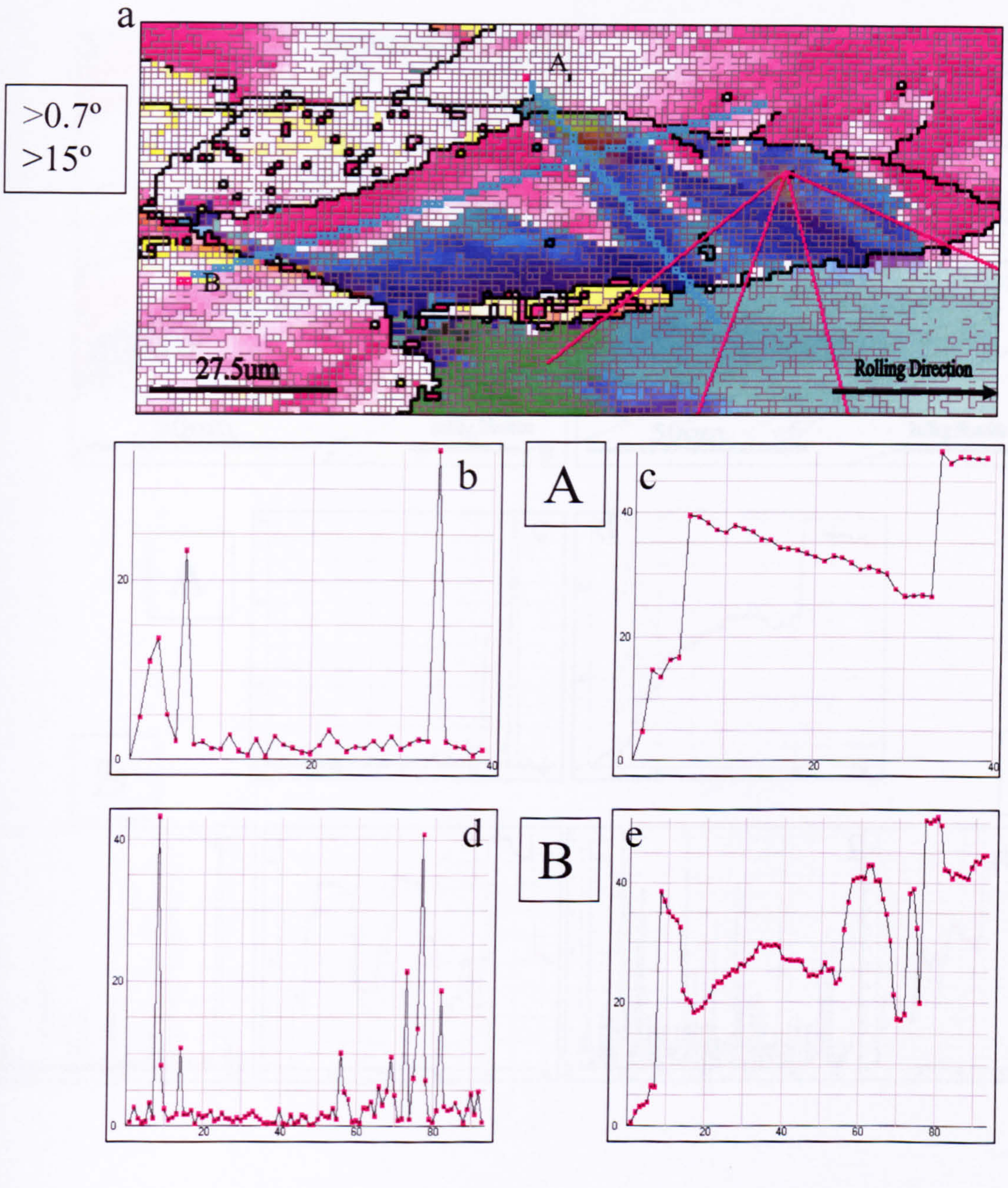

Fig. 5.43 Goss-orientated grain in the instantaneous delayed sample: (a) relative map, (b) (d) relative and (c) (e) cumulative misorientation distributions of line scans performed along A and B in (a).

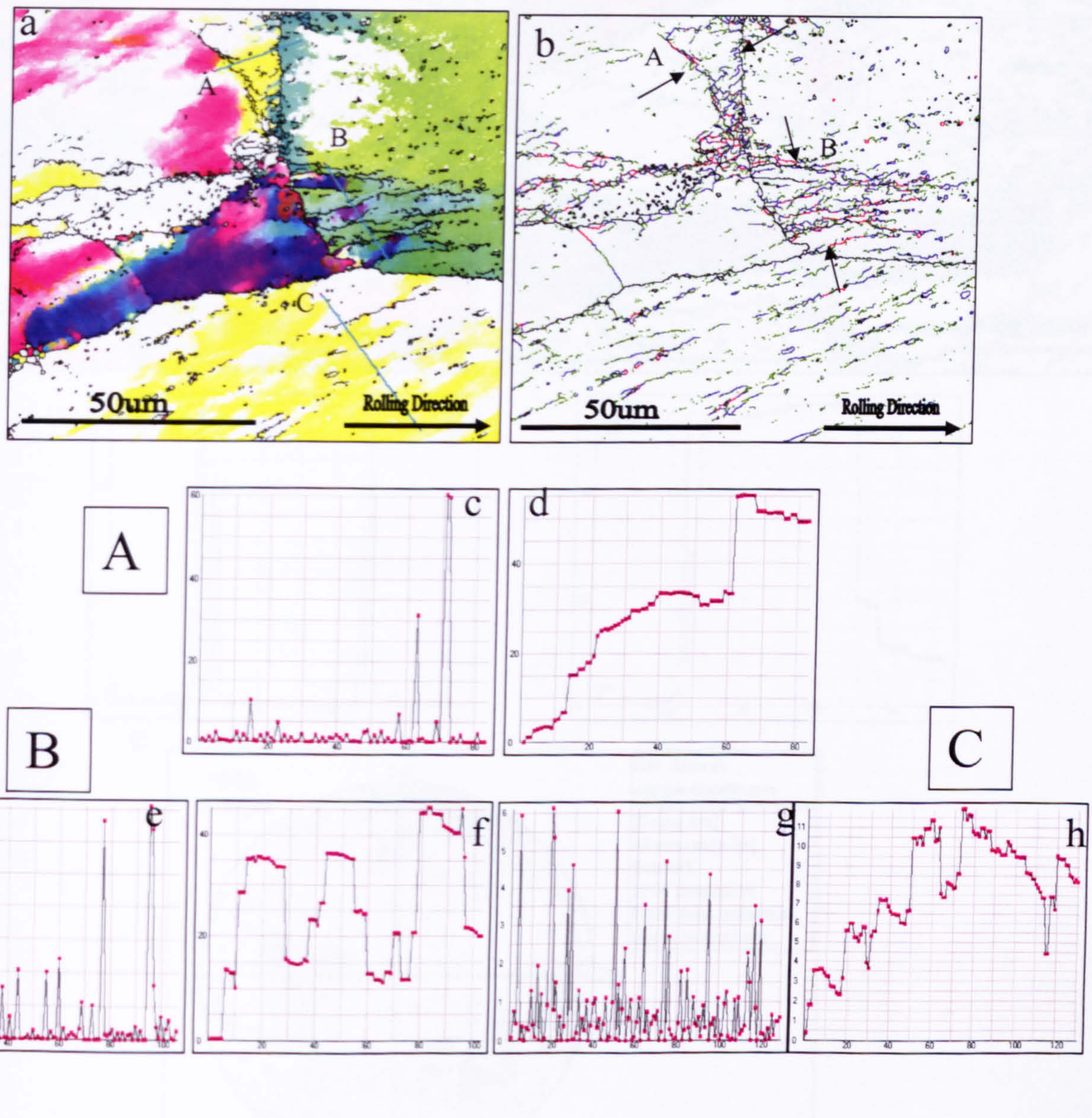

Fig. 5.44 Deformation banding in the instantaneous delayed sample: (a) relative map, (b) orientation map, (c) (e) (g) relative and (d) (f) (h) cumulative misorientation distributions of line scans performed along A B and C in (a).

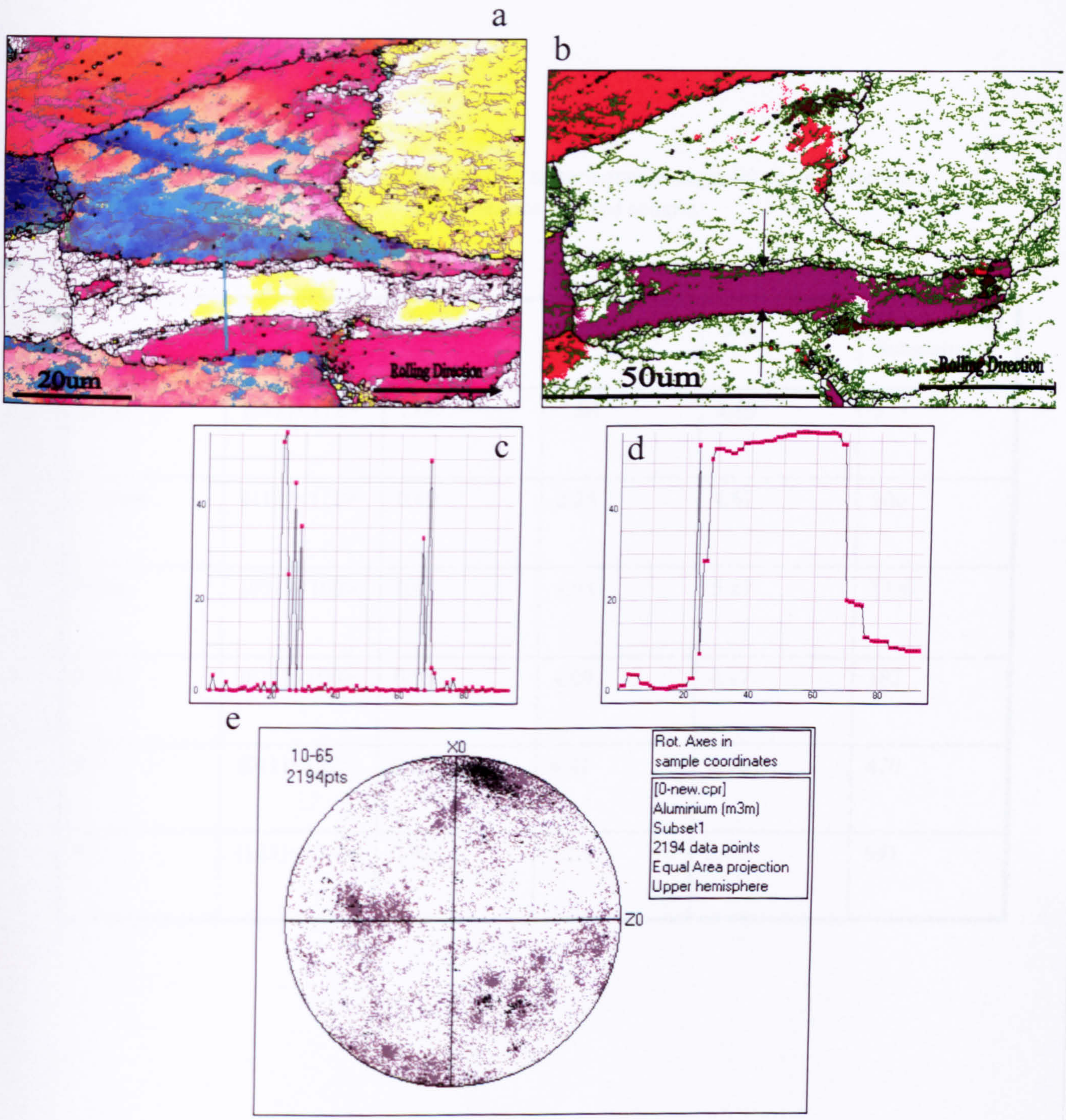

Fig. 5.45 Deformation banding in the instantaneous delayed sample: (a) relative map, (b) orientation map, (c) relative and (d) cumulative misorientation distributions of line scans performed along A and B in (a), e) cample coordinate.

Table 5.4 Mean subgrain size (D), misorientation angle (è) and Θ/d for the instantaneous delayed sample

	{hkl}<uvw>	D(μm)	Θ(°)	Θ/d	Number of Subgrains
Brass	{011}<112>	1.00	4.80	4.80	575
Copper	{112}<111>	0.49	2.26	4.61	200
Cube	{001}<100>	0.95	5.03	5.29	1306
Goss	{011}<100>	0.98	4.09	4.17	182
P	{011}<122>	0.90	4.41	4.90	470
S	{123}<634>	0.90	5.10	5.66	691

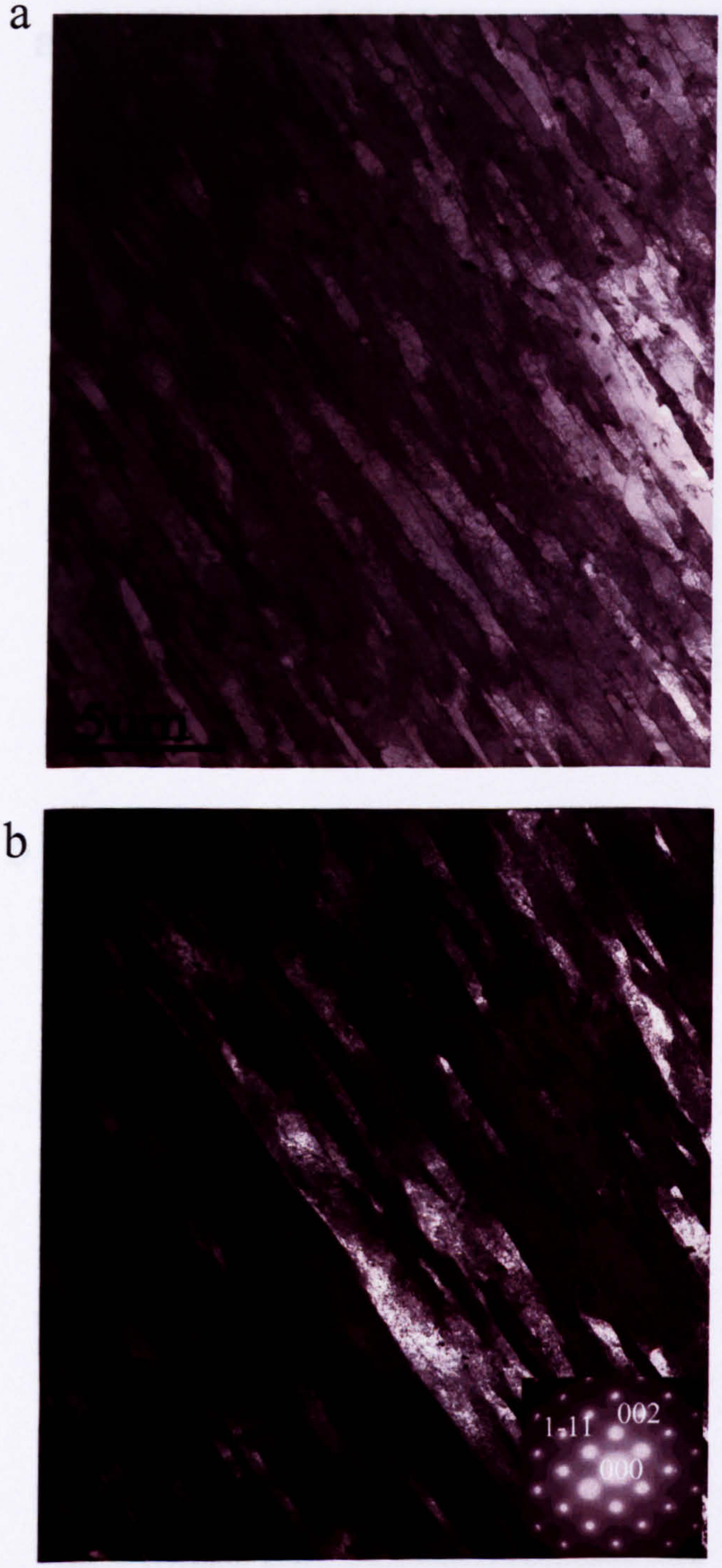

Fig. 5.46 TEM images after the instantaneous deformation, shows microband structure.

a

b

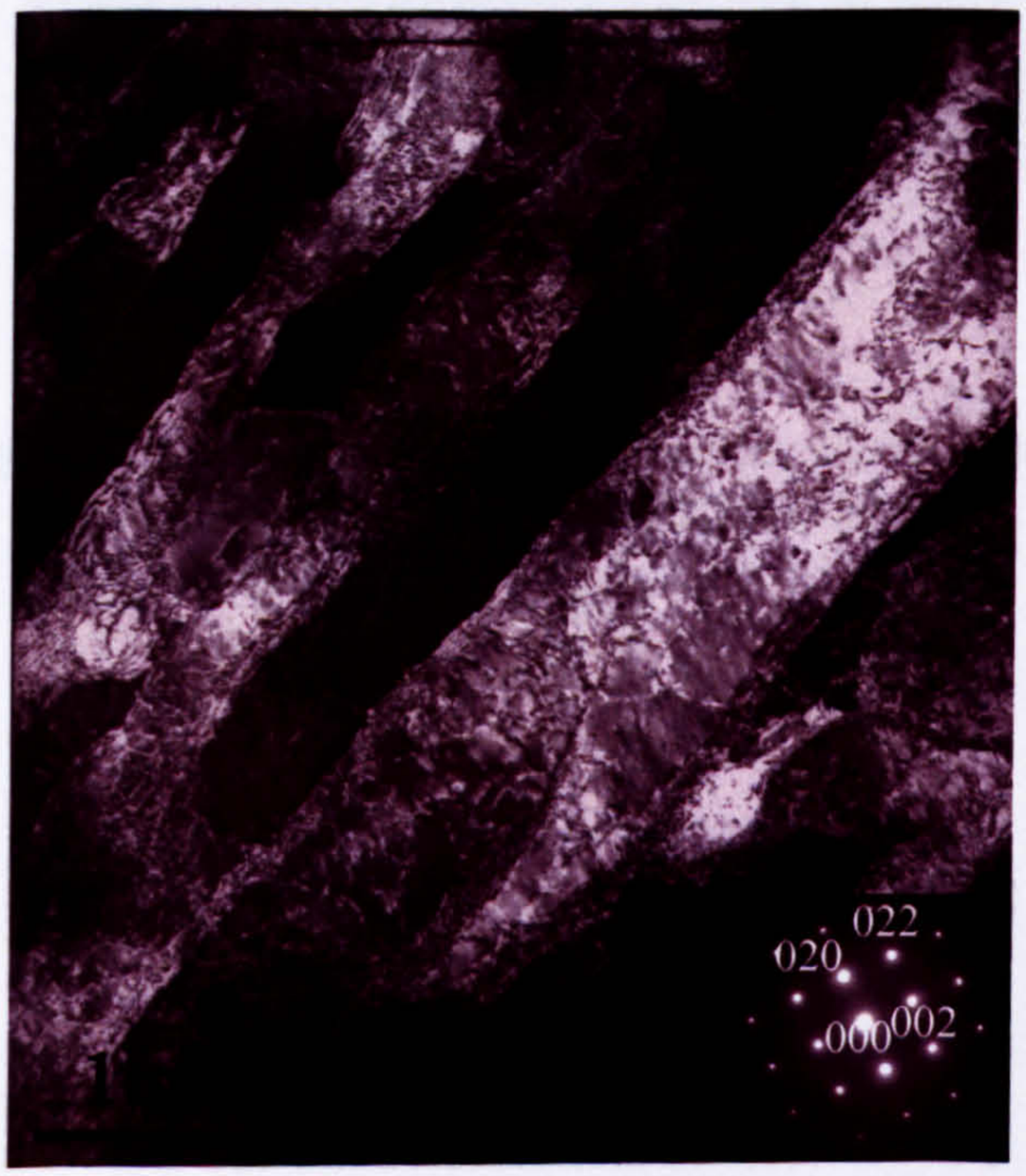

Fig. 5.47 TEM images after the instantaneous deformation, shows dislocations structure in Microband.

Fig. 5.48 TEM image after the instantaneous deformation, shows grain boundary offsets at DDW/MB-grain boundary intersections.

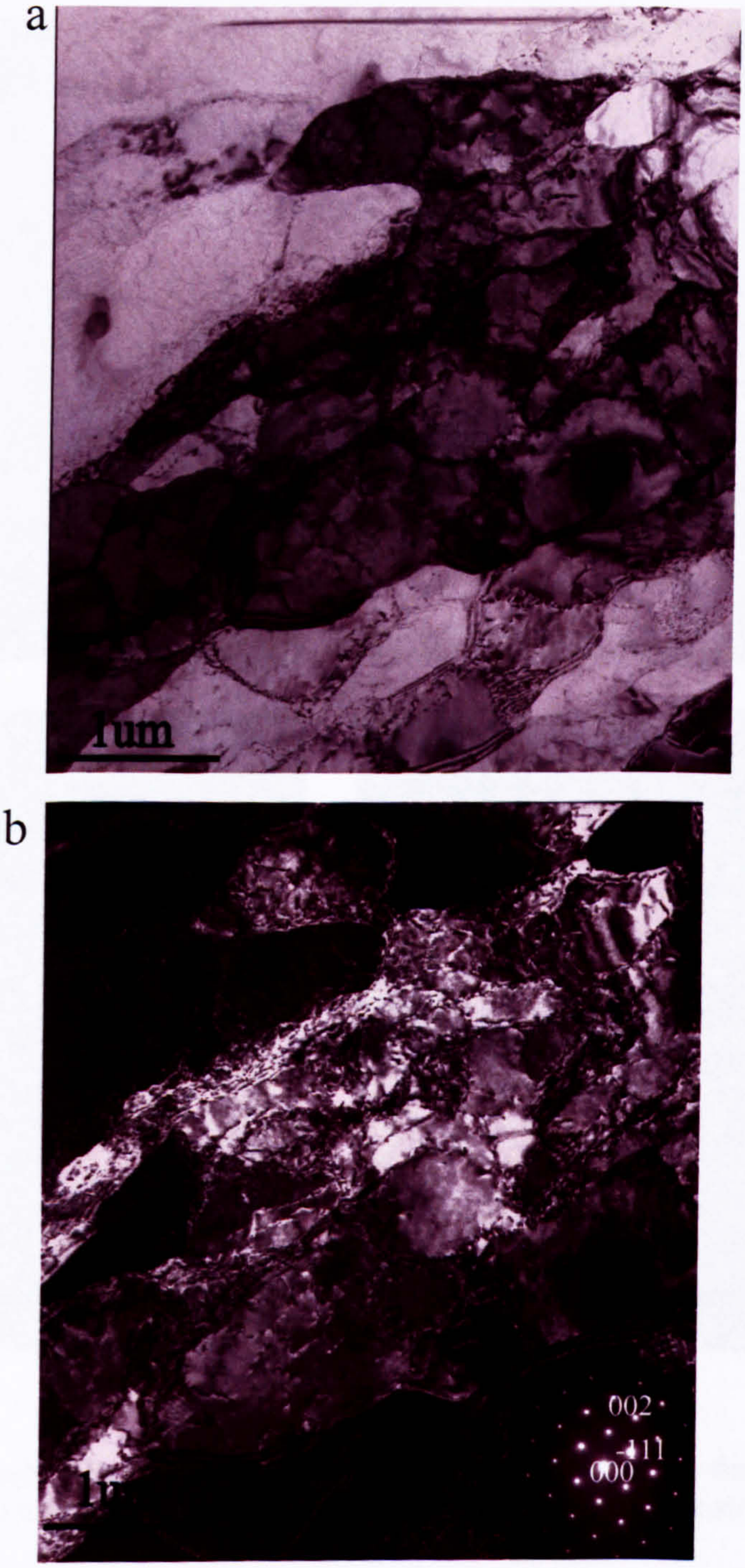

Fig. 5.49 TEM images after the instantaneous deformation, shows the cell-structure with dense tangled dislocations between DDWs: (a) bright field image, (b) dark field image.

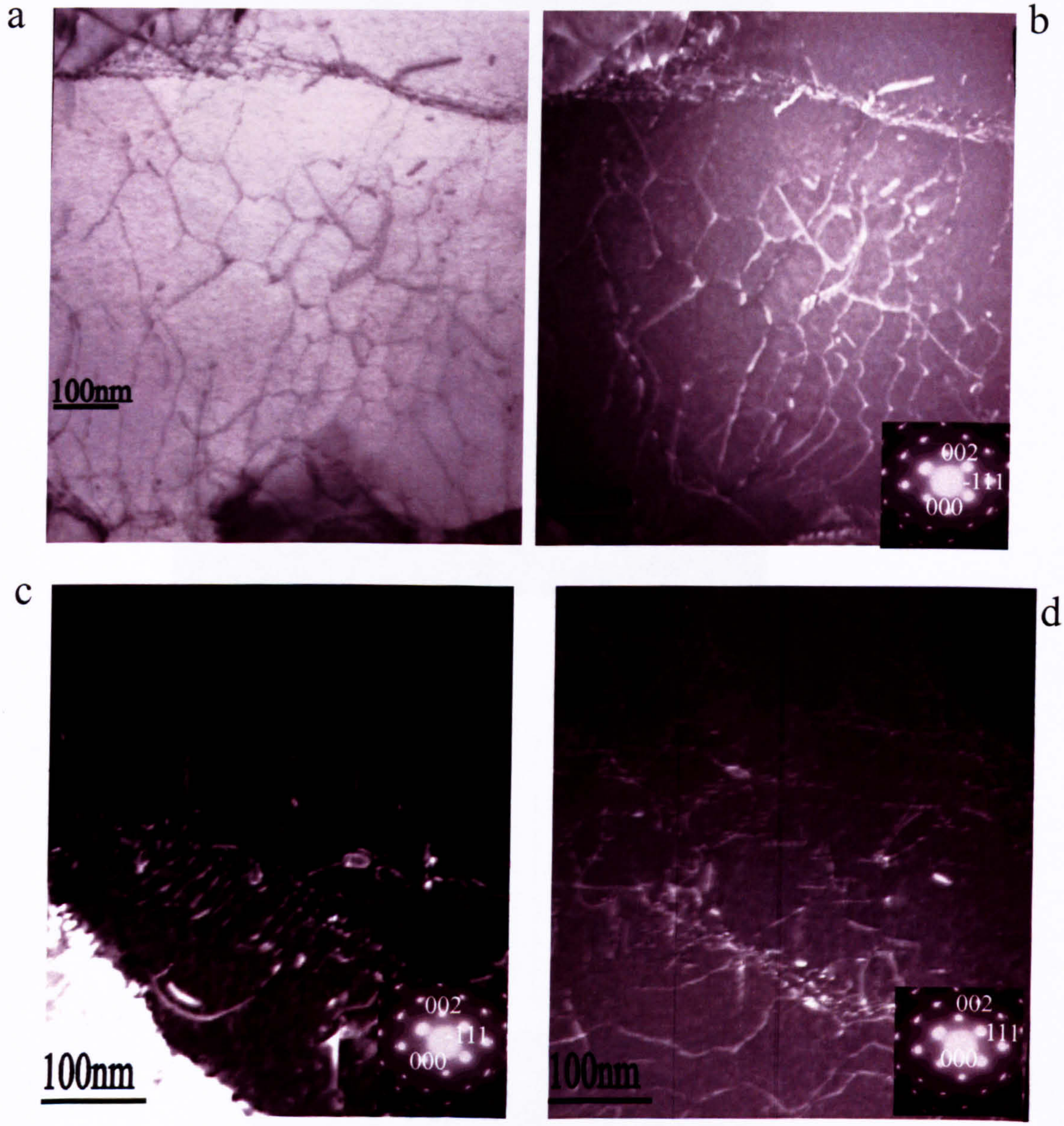

Fig. 5.50 TEM images after the instantaneous deformation, shows the dislocations structure: (a) (b) network structure, (c) dislocation forest, (d) tangle structure.

a

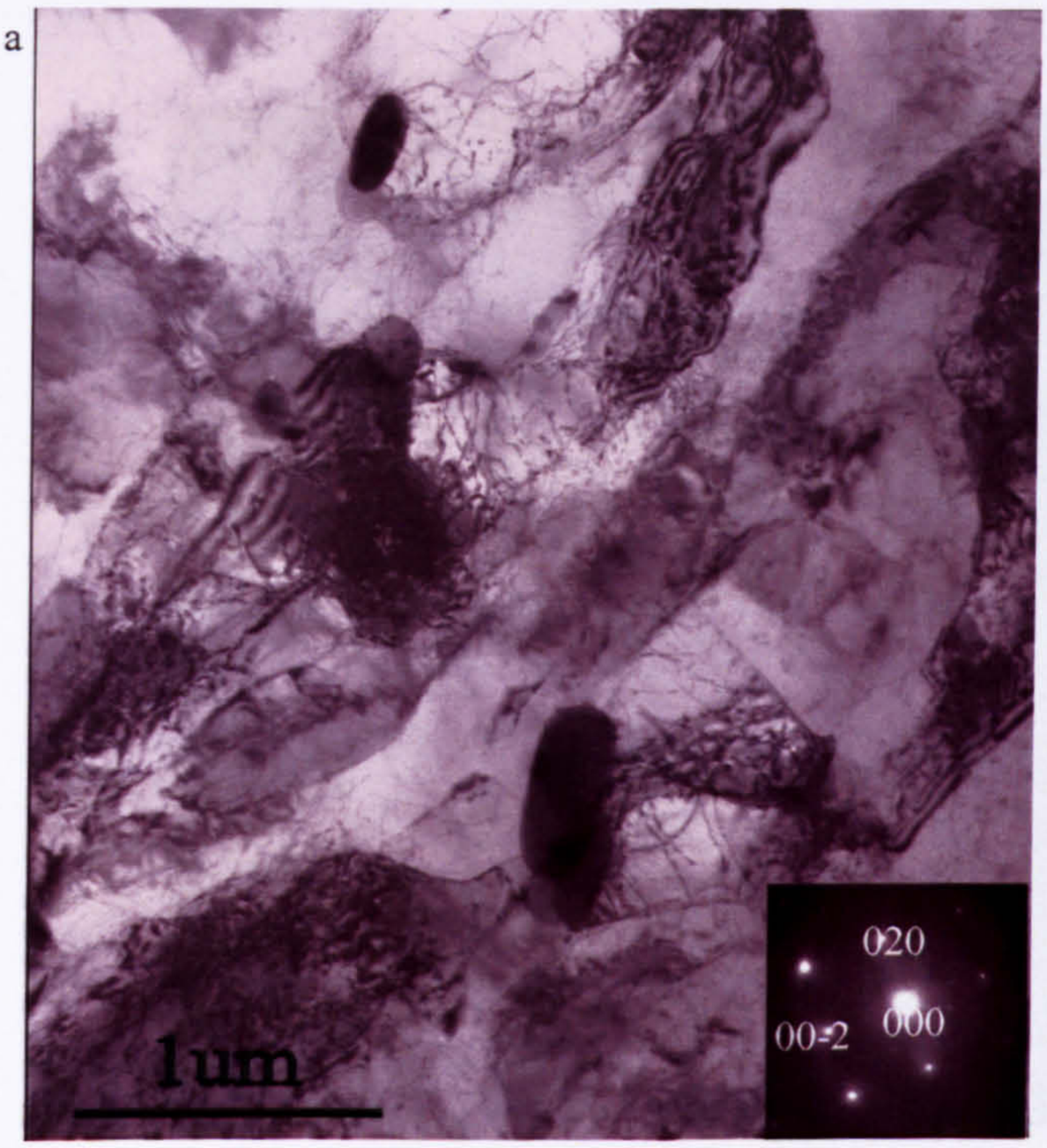

b

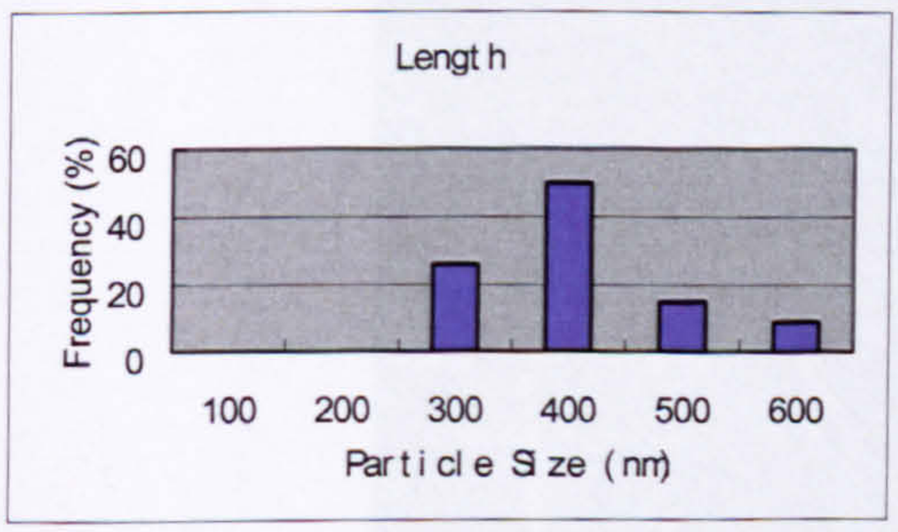

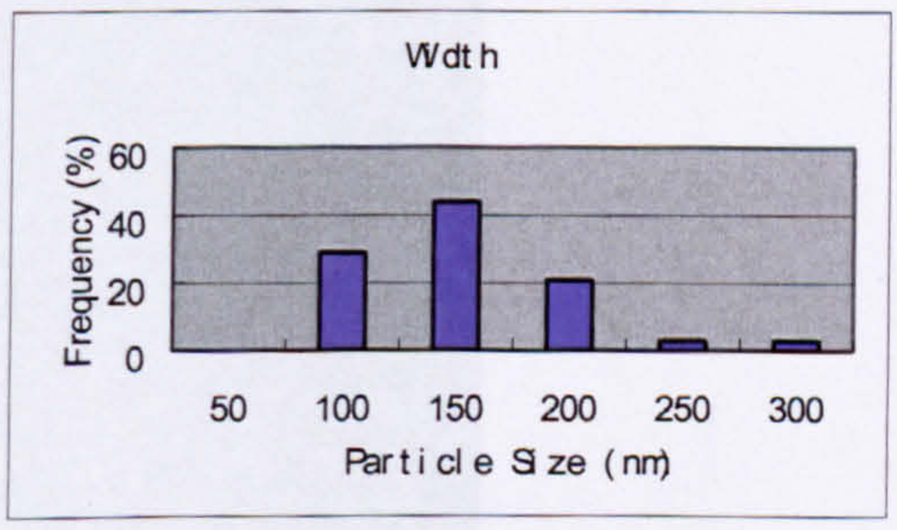

c

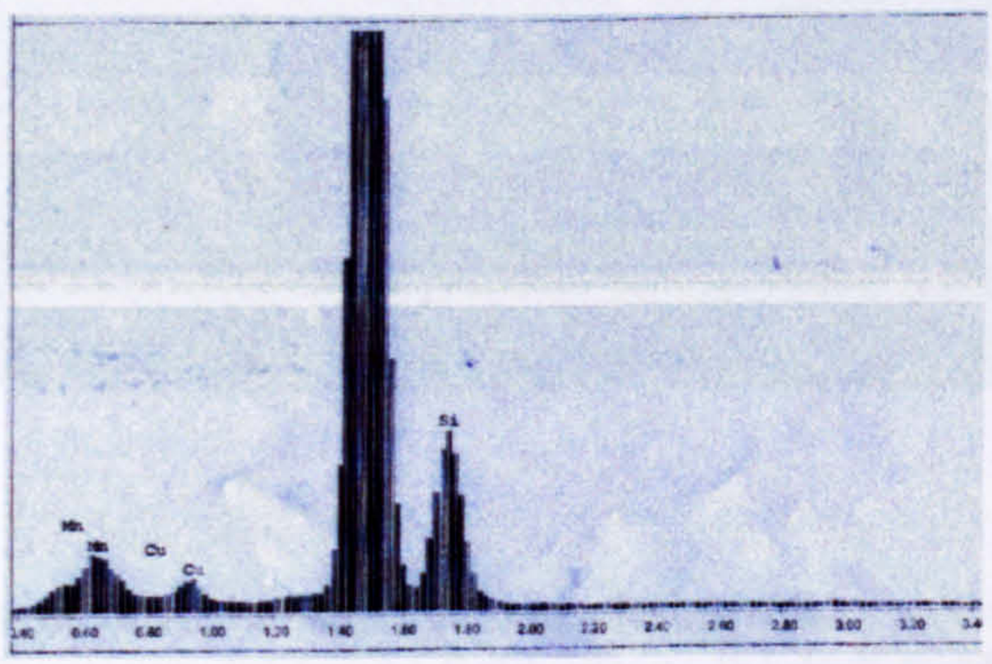

Fig. 5.51 Particle size analysis in the instantaneous delayed sample: (a) TEM image, (b) particle size distribution, (c) EDS spectrum.

a

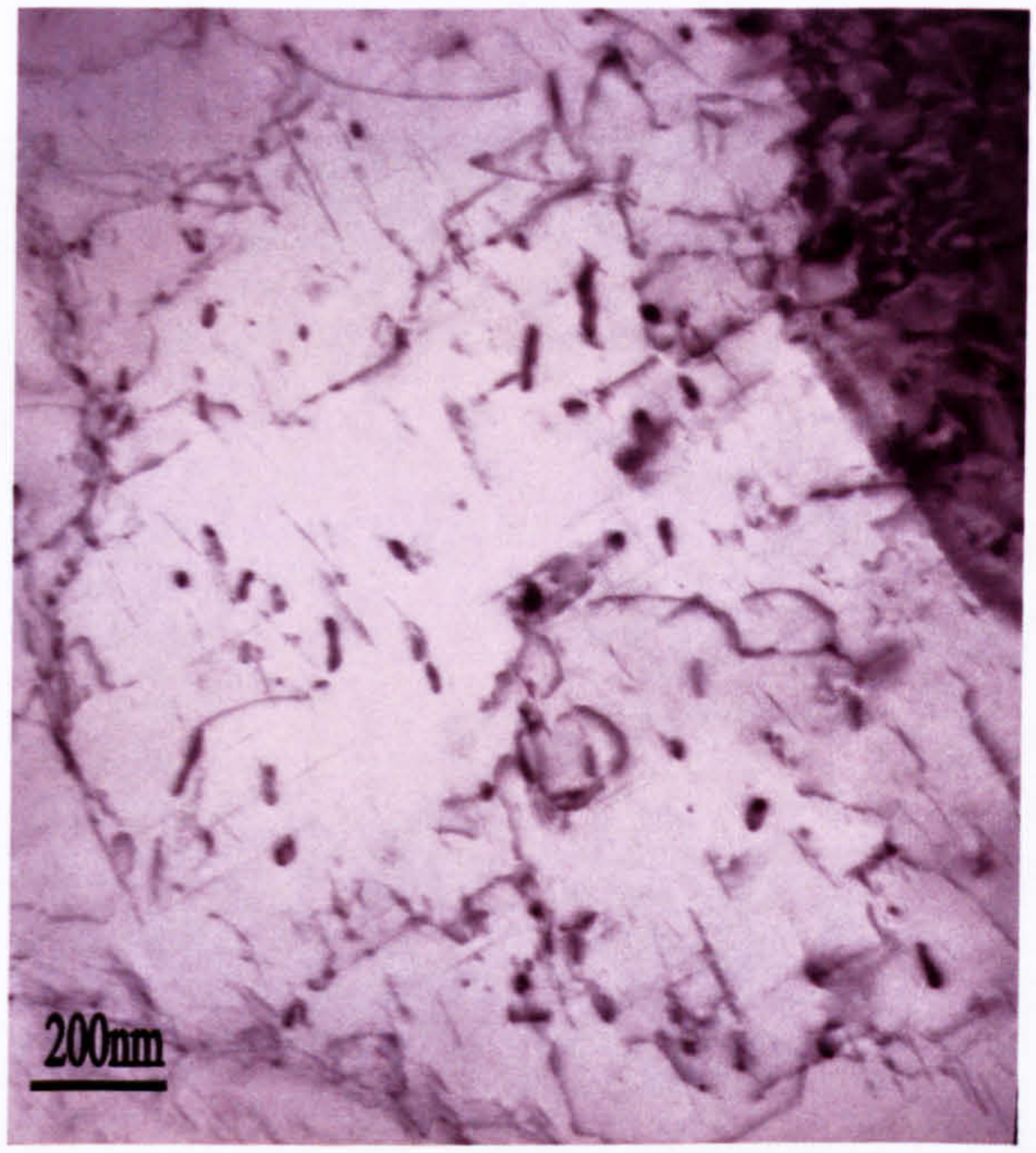

b

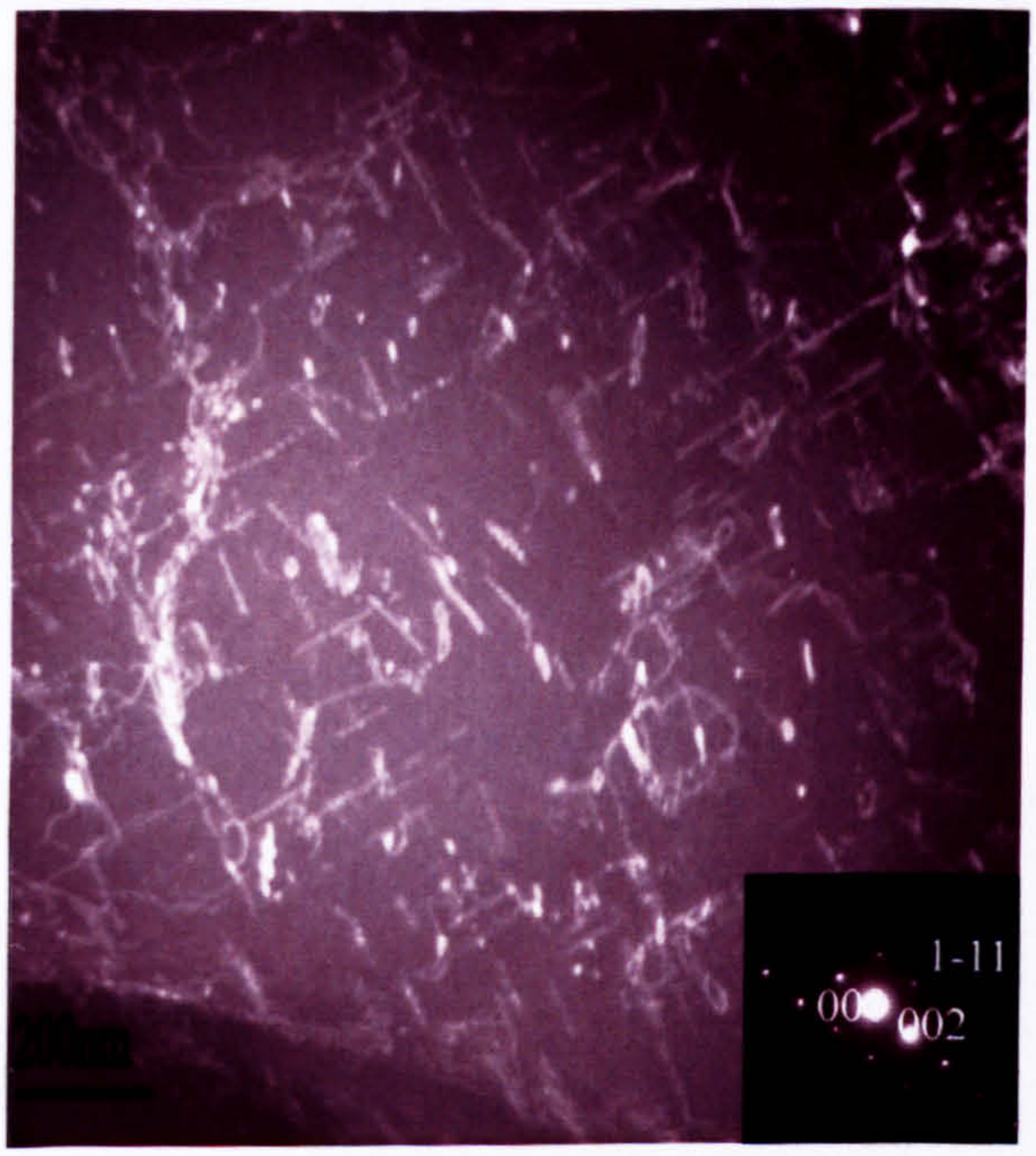

Fig. 5.52 TEM images after the instantaneous deformation, shows some small phases formed on dislocations: (a) bright field image, (b) dark field image. (g=001)

a

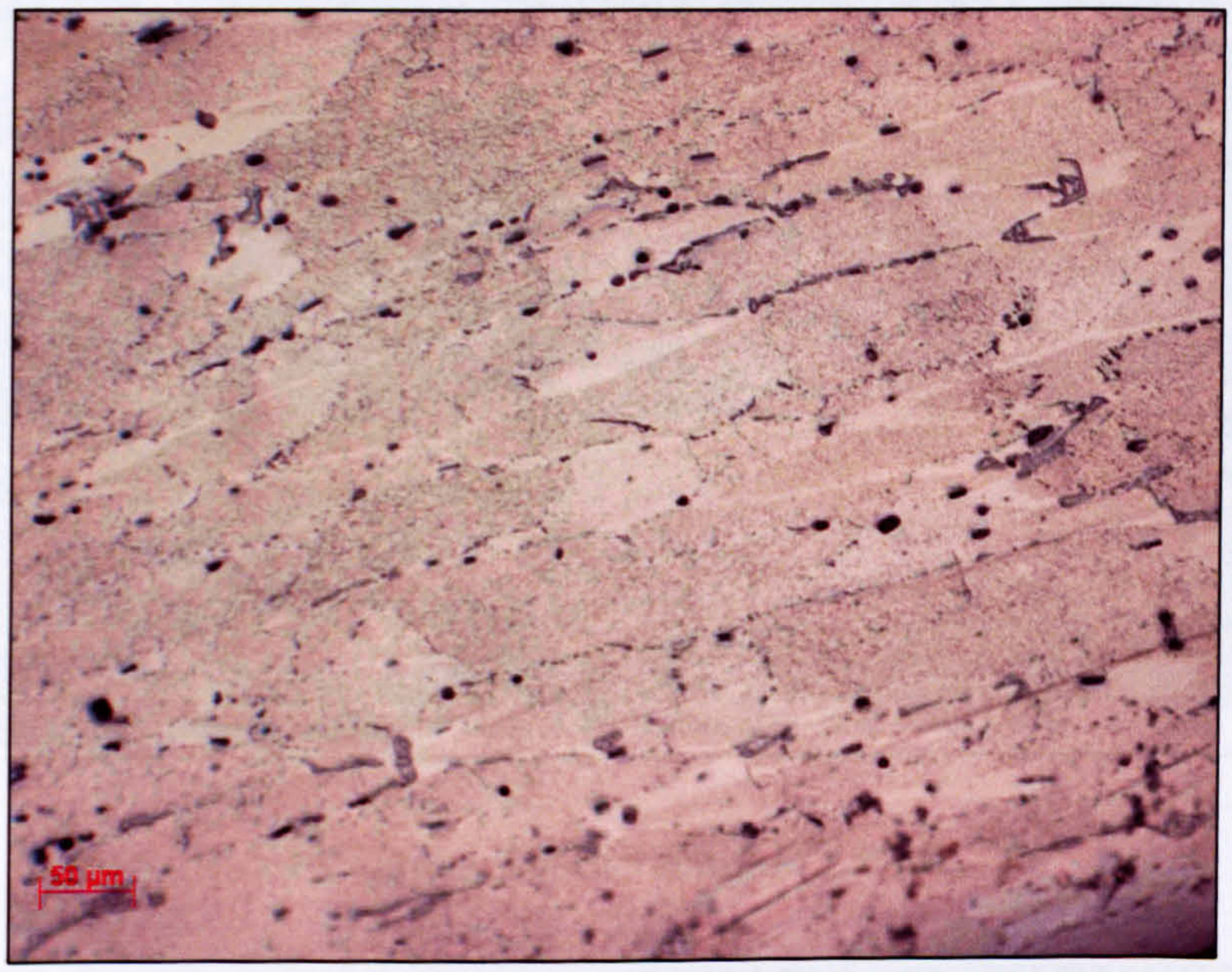

b

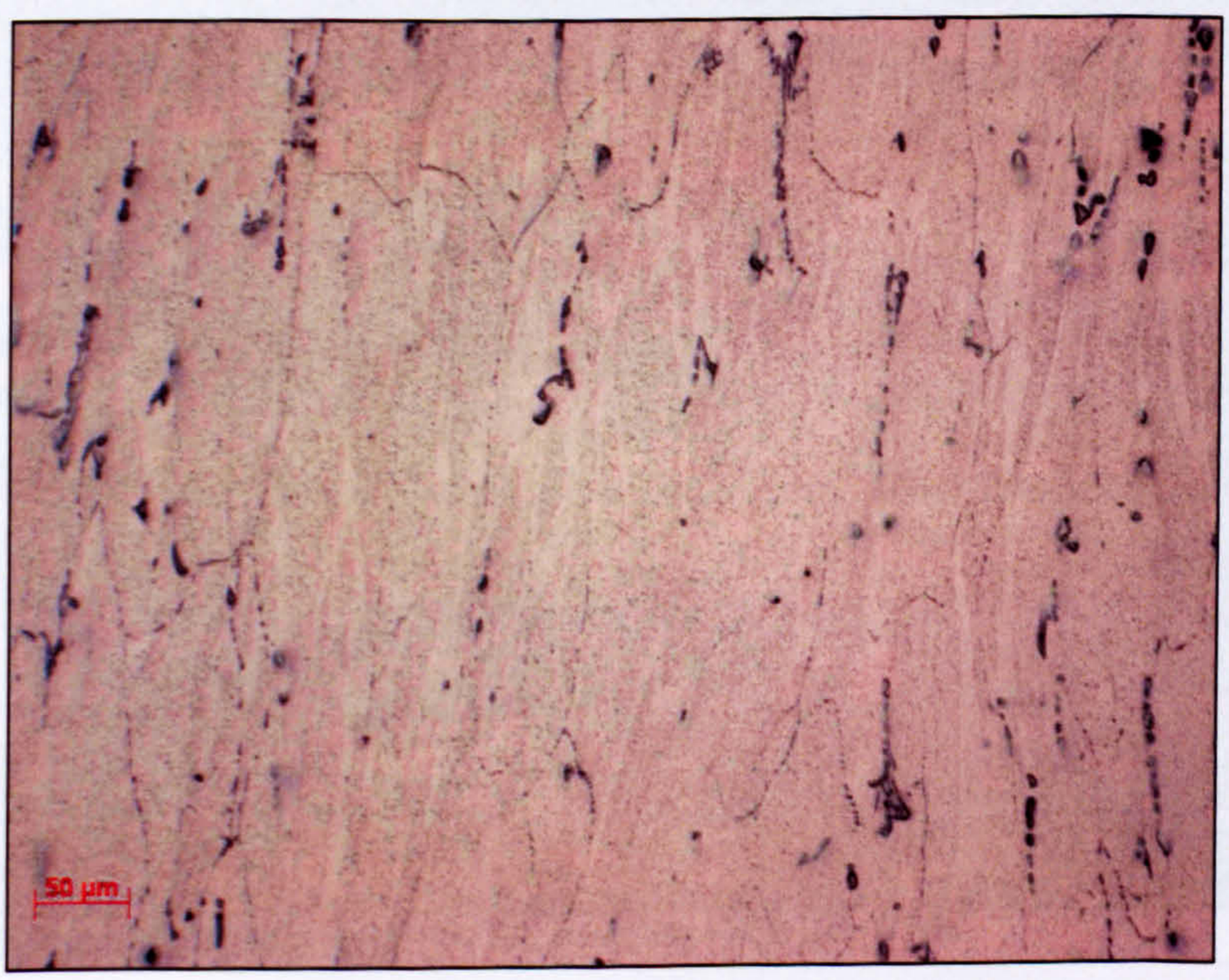

Fig. 5.53 Optical micrographs of deformed structure after the 6 seconds delayed deformation: (a) normal plane, (b) transverse plane.

a

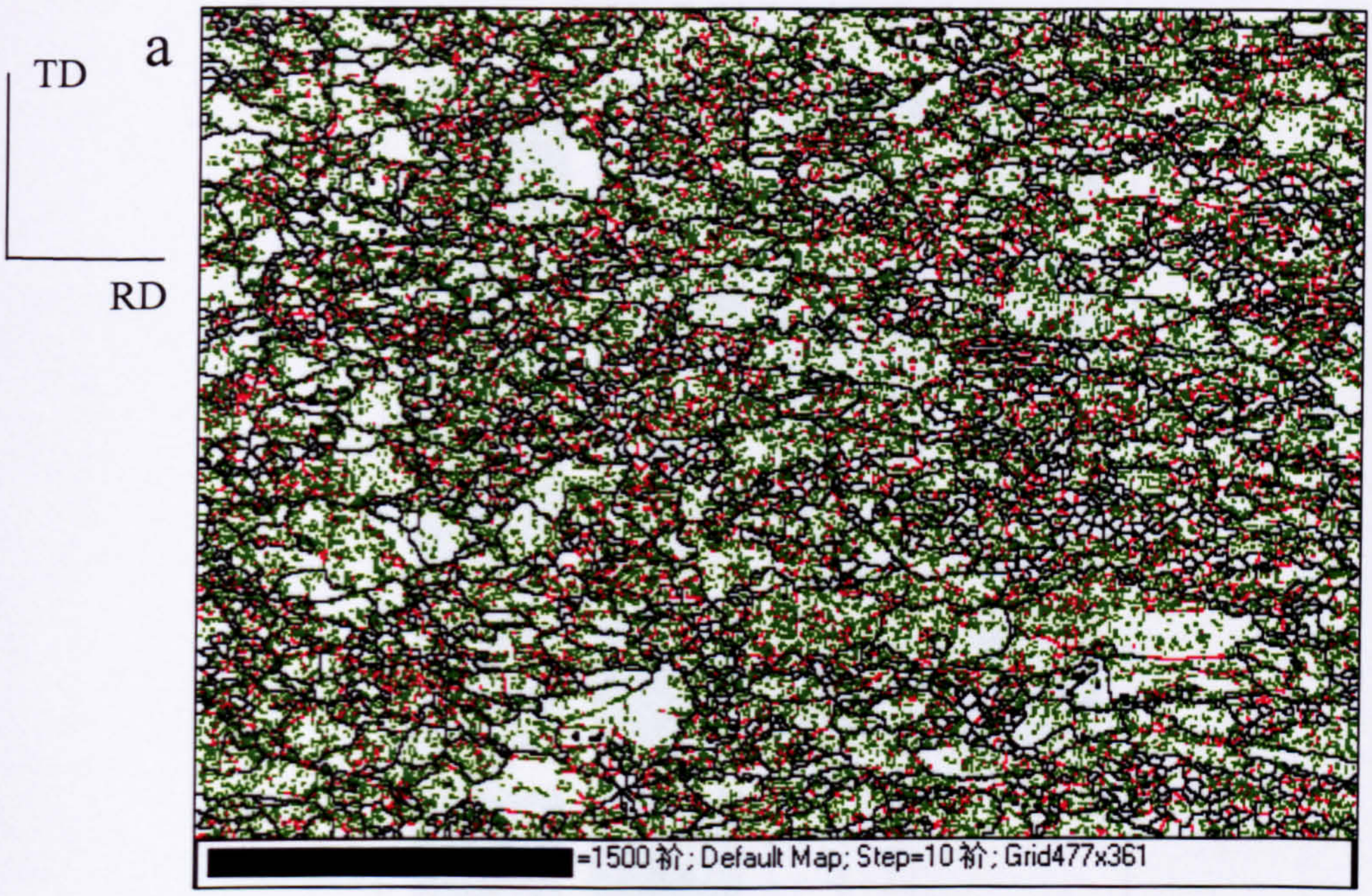

5-10°: green, 10-15°: red, >15°: black

b

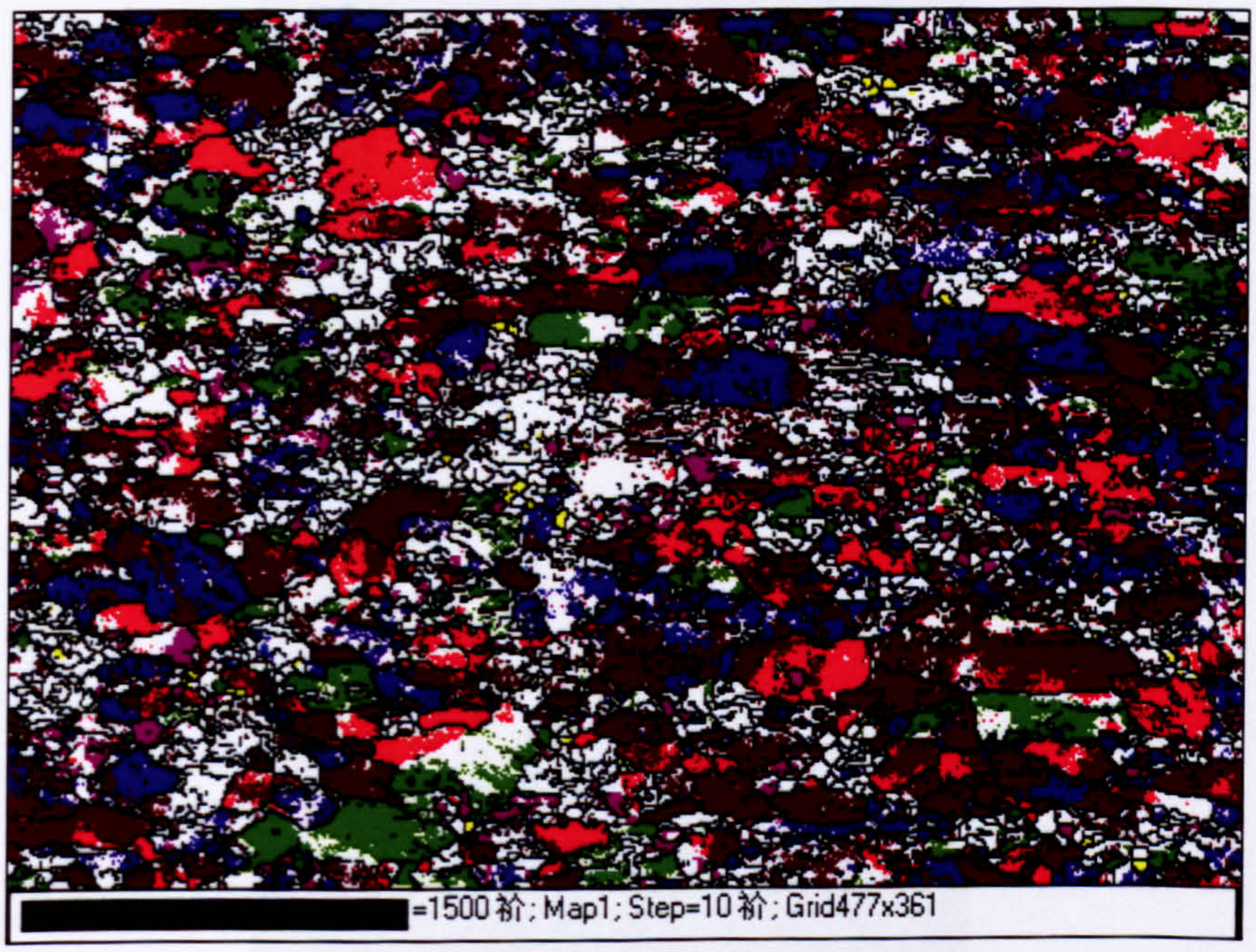

cube-yellow, p-purple, brass-red, copper-blue, goss-green, s-maroon

Fig. 5.54 EBSD results after the 6 seconds delayed deformation: (a) orientation map, (b) texture map.

a

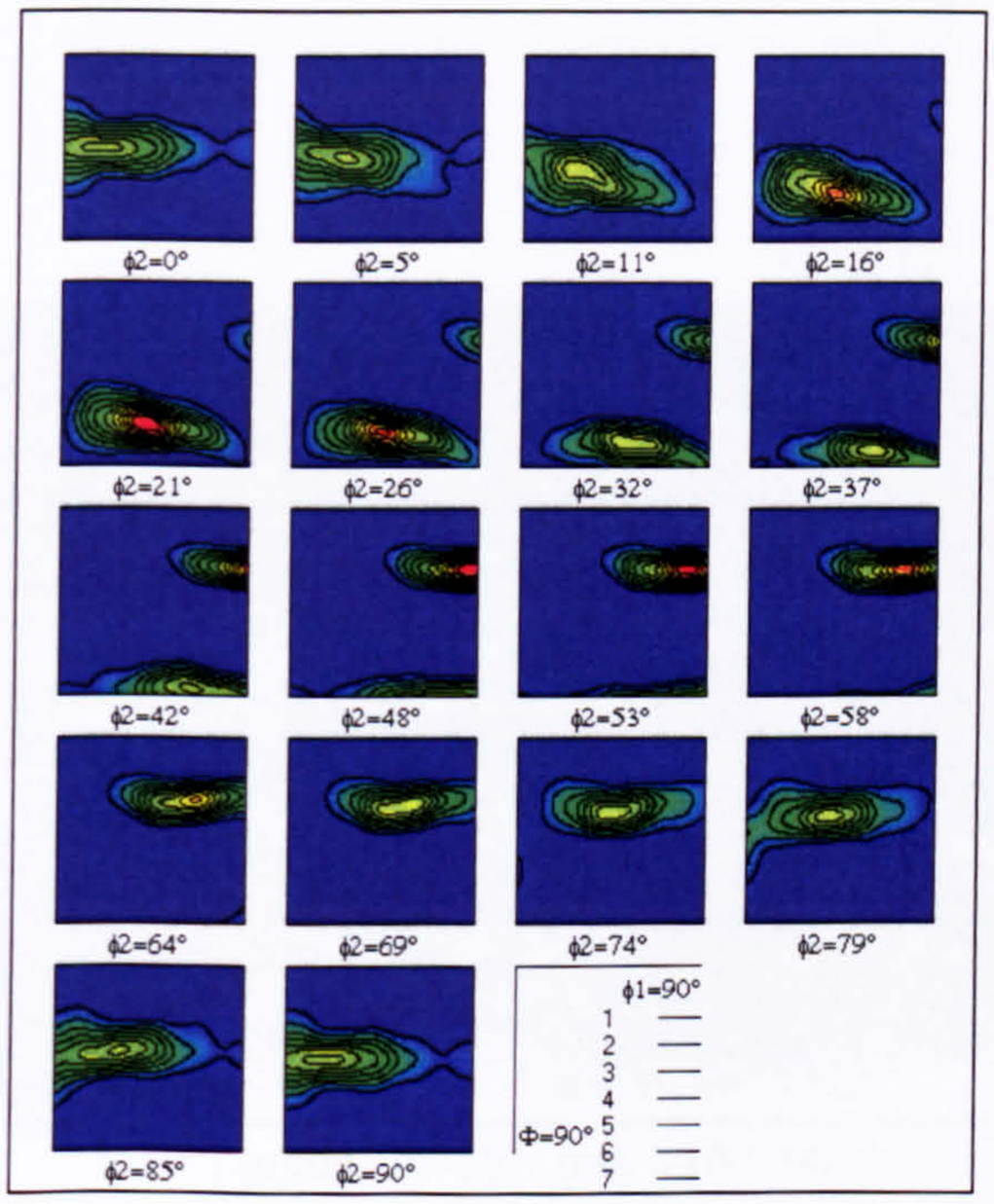

b

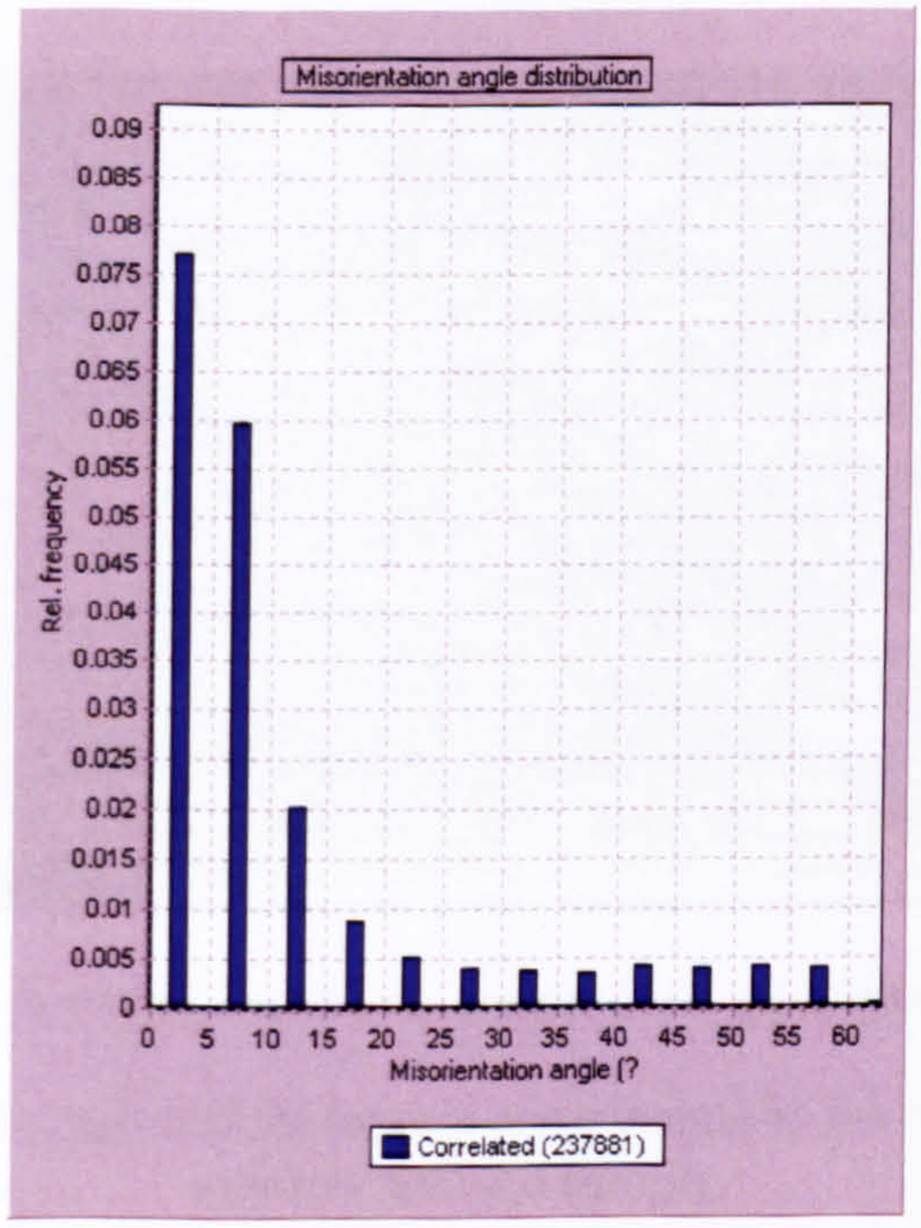

Fig. 5.55 EBSD results of the 6 seconds delayed deformed sample: (a) orientation distribution functions (ODF) maps, (b) misorientation angle distribution.

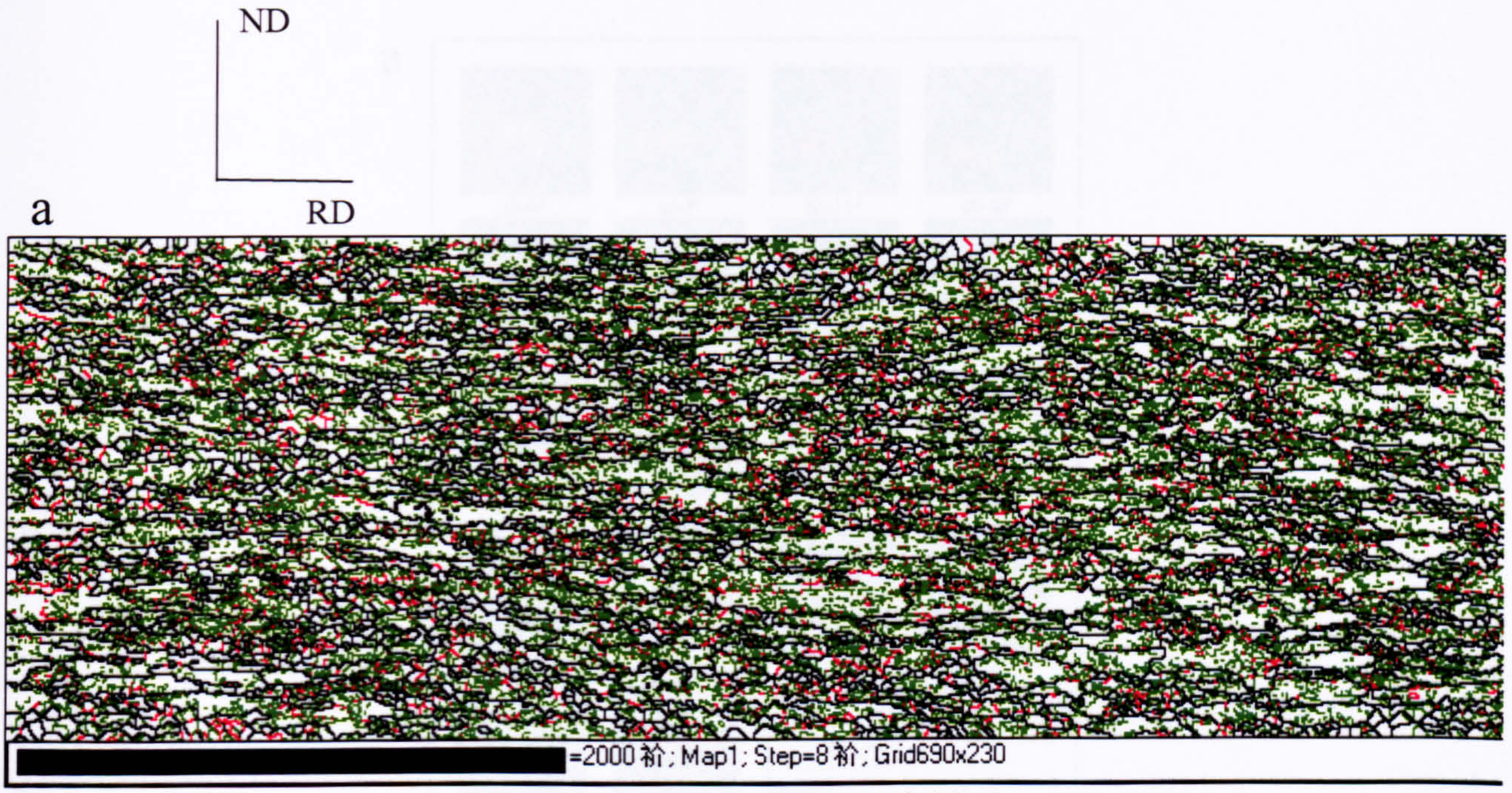

5-10°: green, 10-15°: red, >15°: black

b

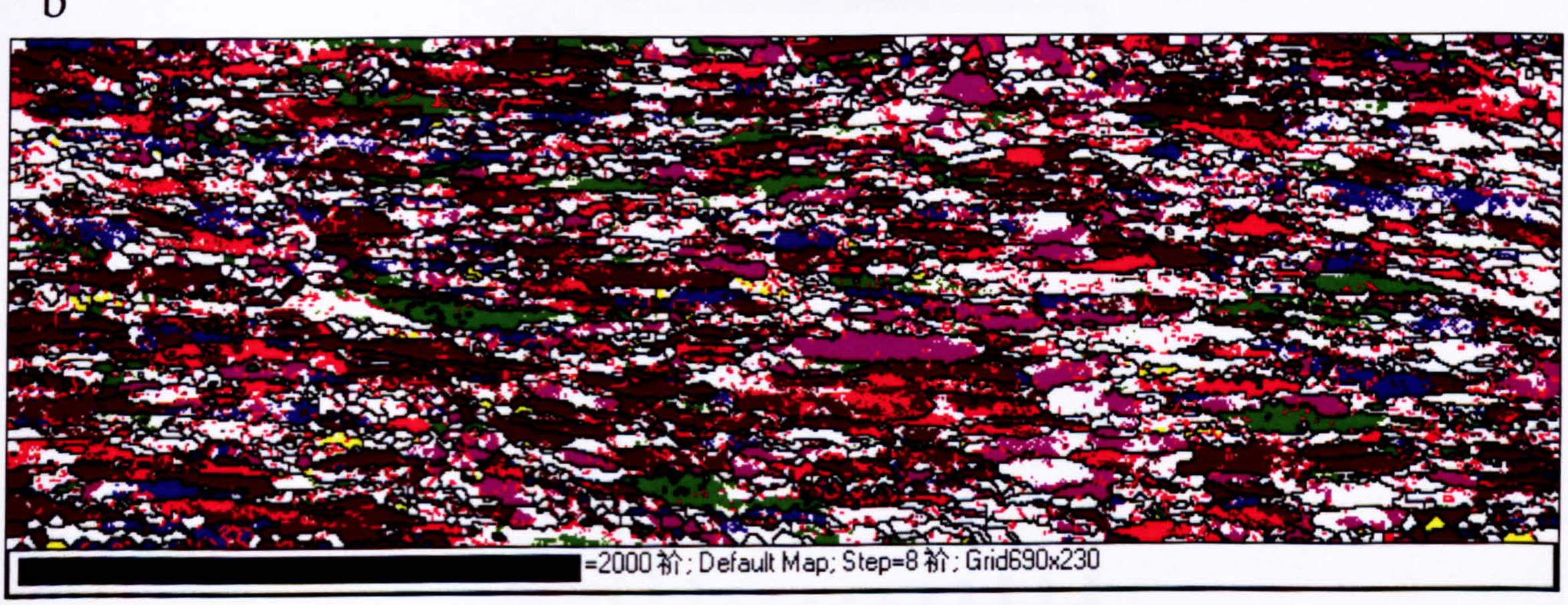

cube-yellow, p-purple, brass-red, copper-blue, goss-green, s-maroon

Fig. 5.56 (a) Orientation map and (b) texture components to the microstructure for the 6 seconds delayed sample.

a

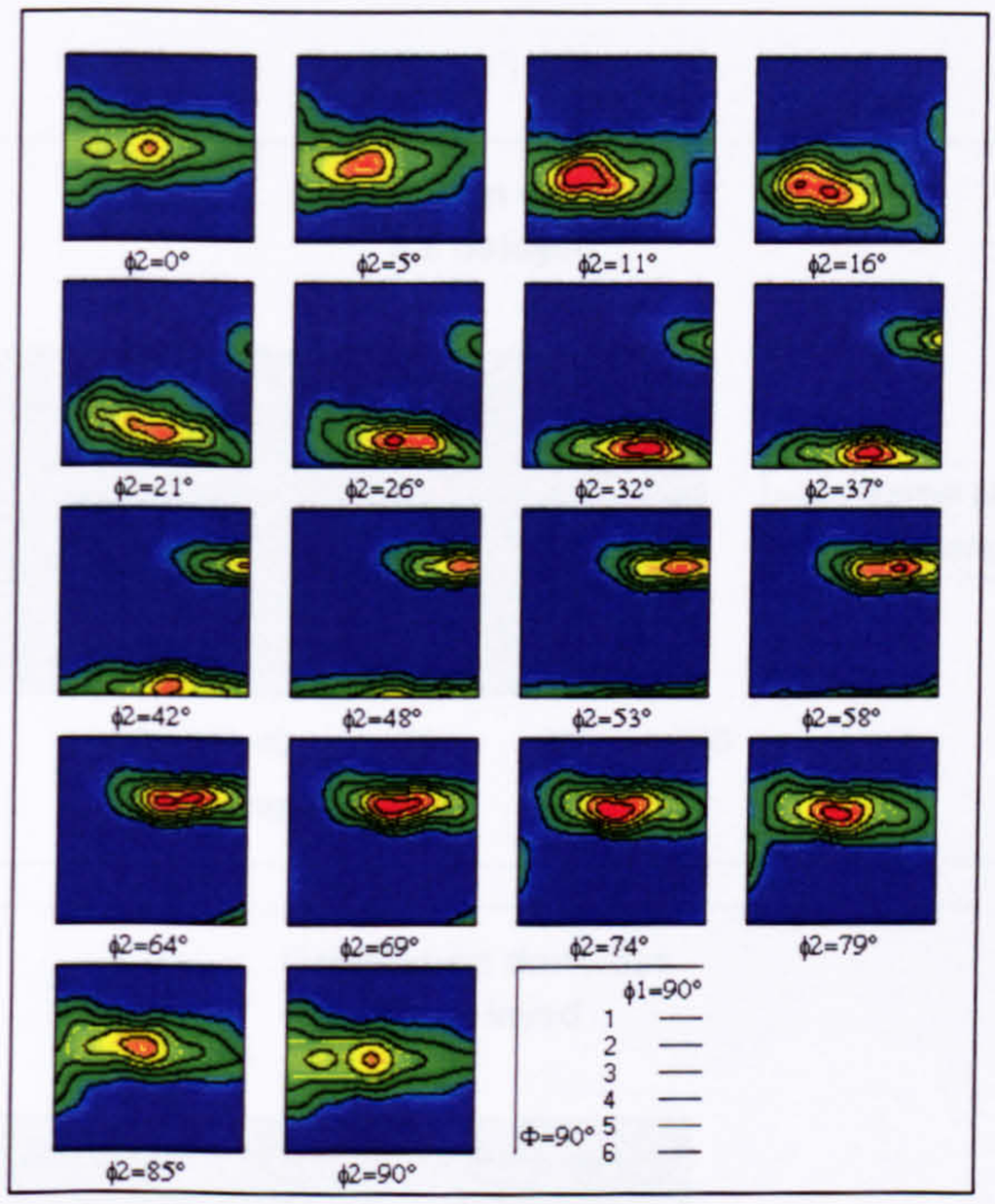

b

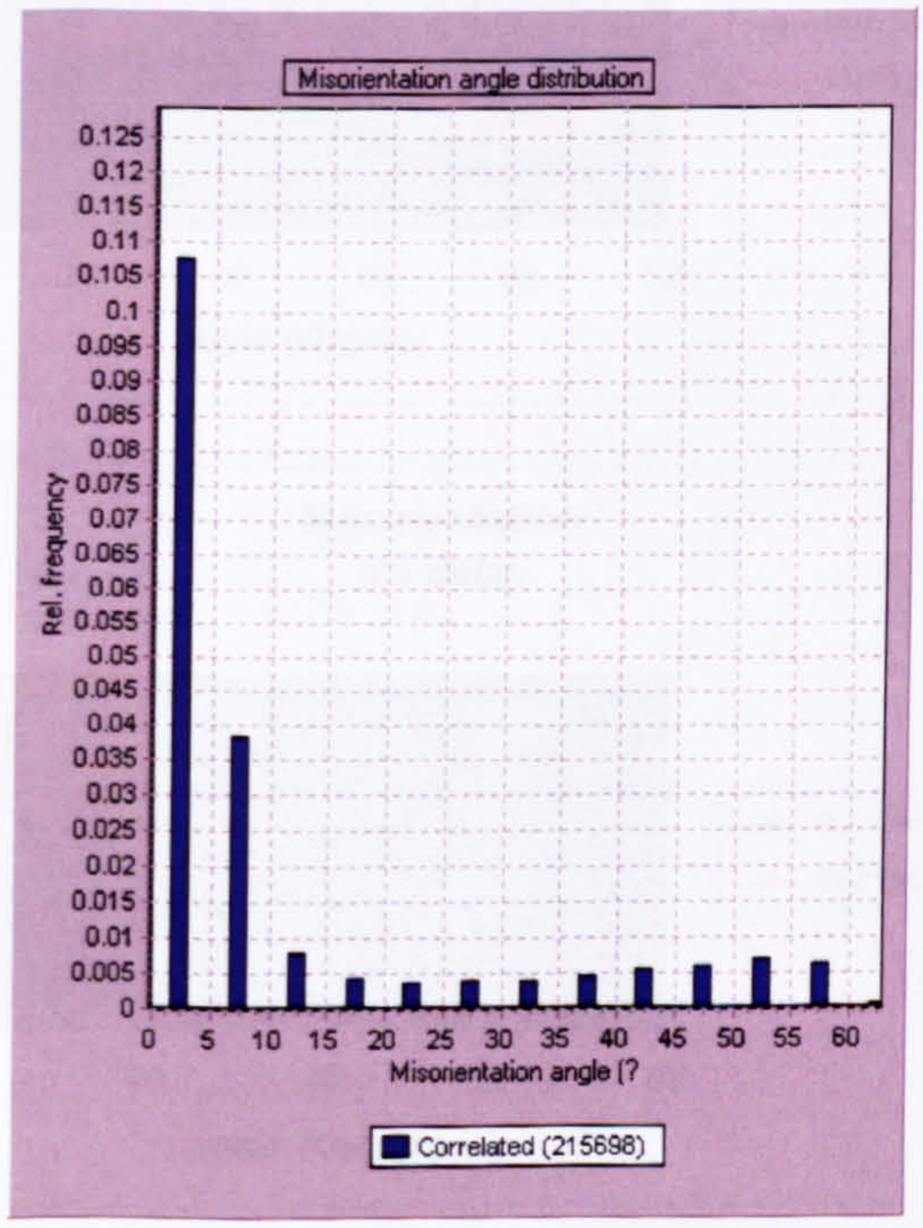

Fig. 5.57 EBSD results of the 6 seconds delayed deformed sample: (a) orientation distribution functions (ODF) maps, (b) misorientation angle distribution.

a

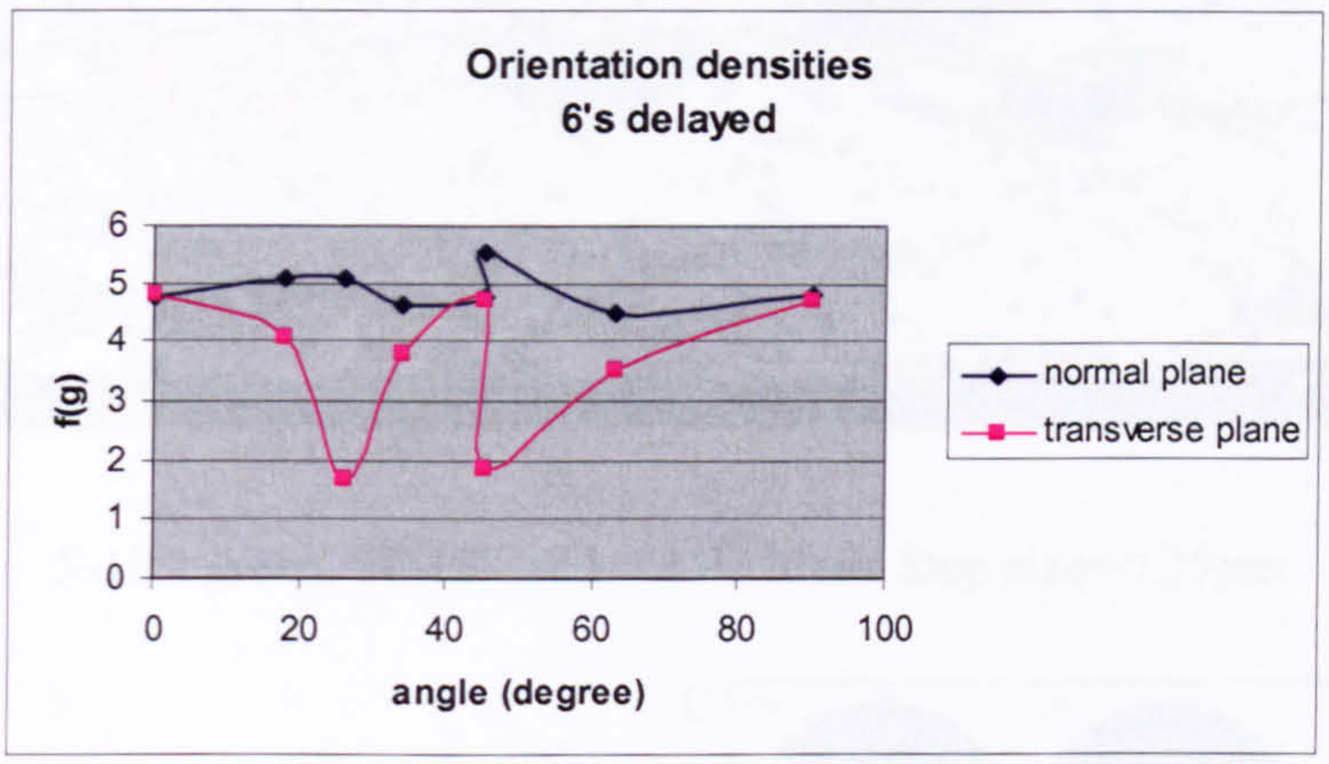

b

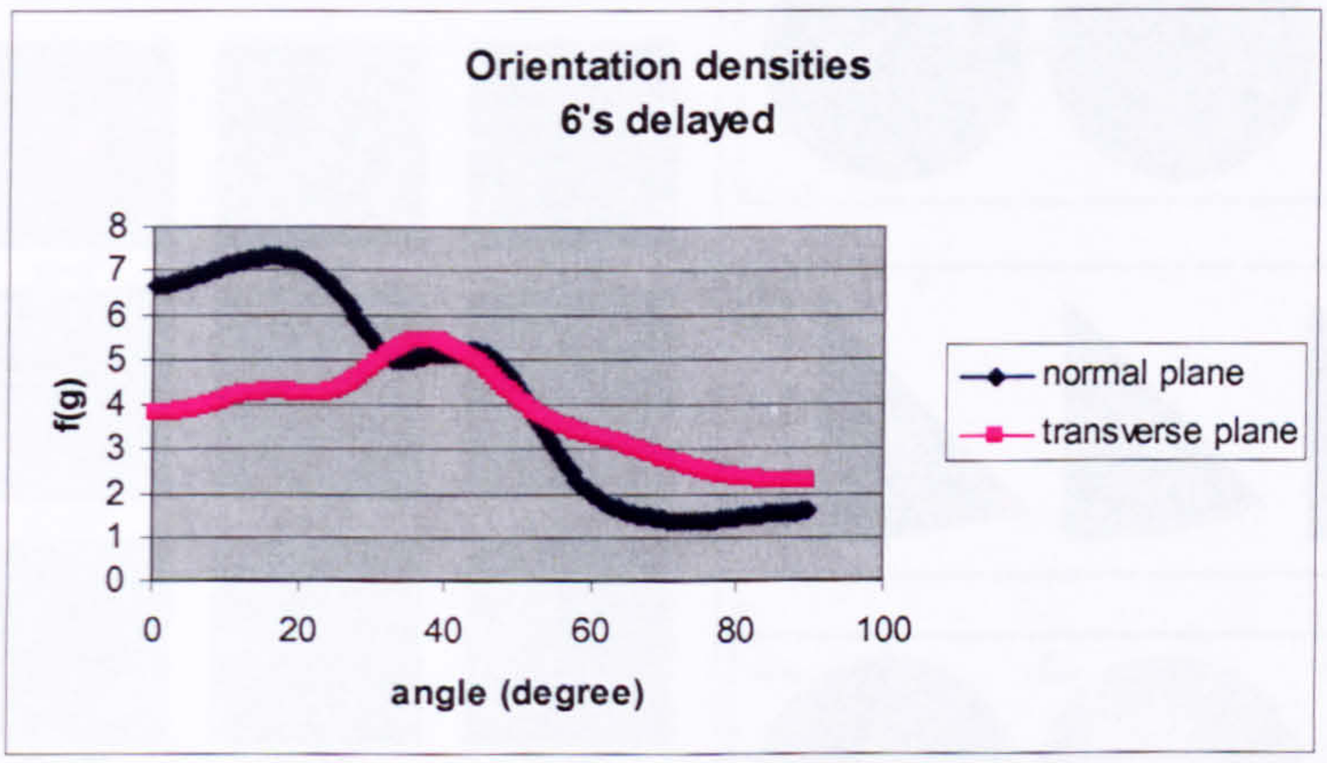

c

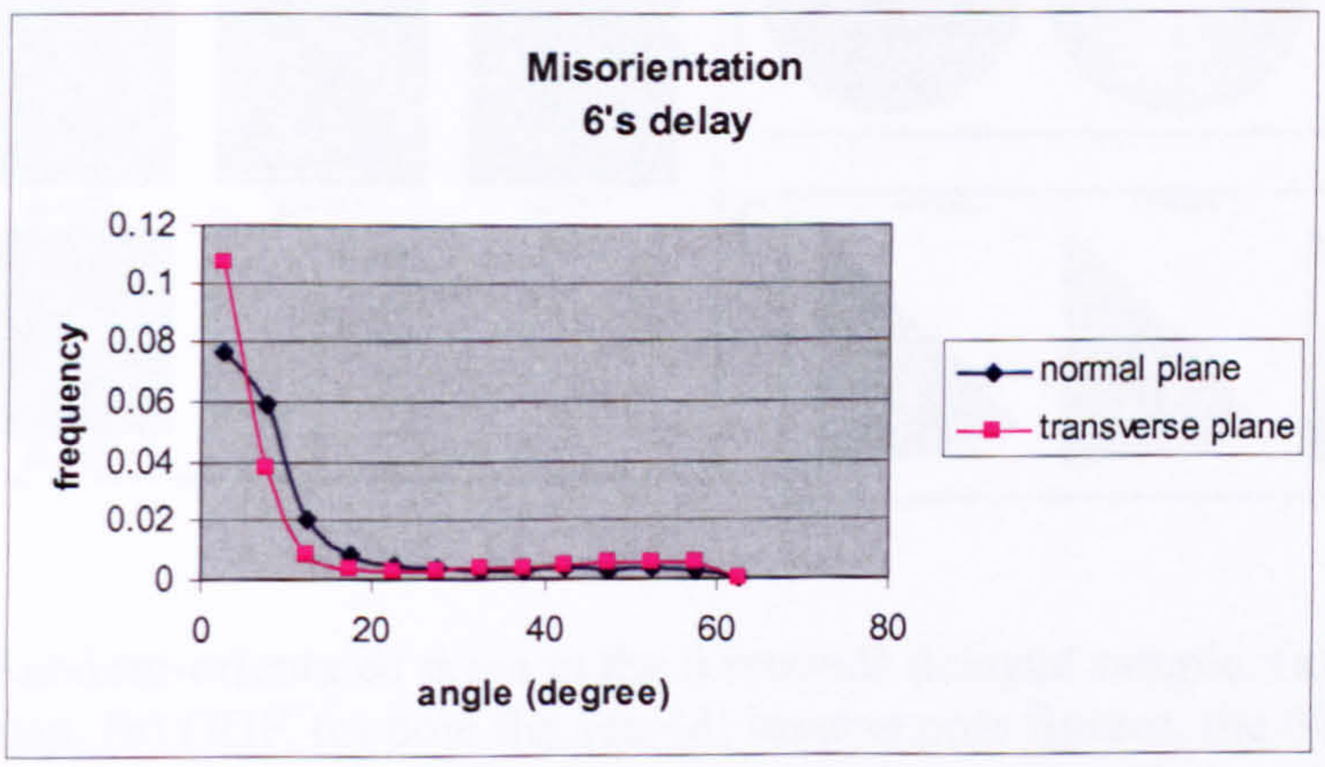

Fig. 5.58 (a) Density distribution of β fibre, (b) density distribution of α fibre, (c) misorientaiton distribution for the 6 seconds delayed deformed sample.

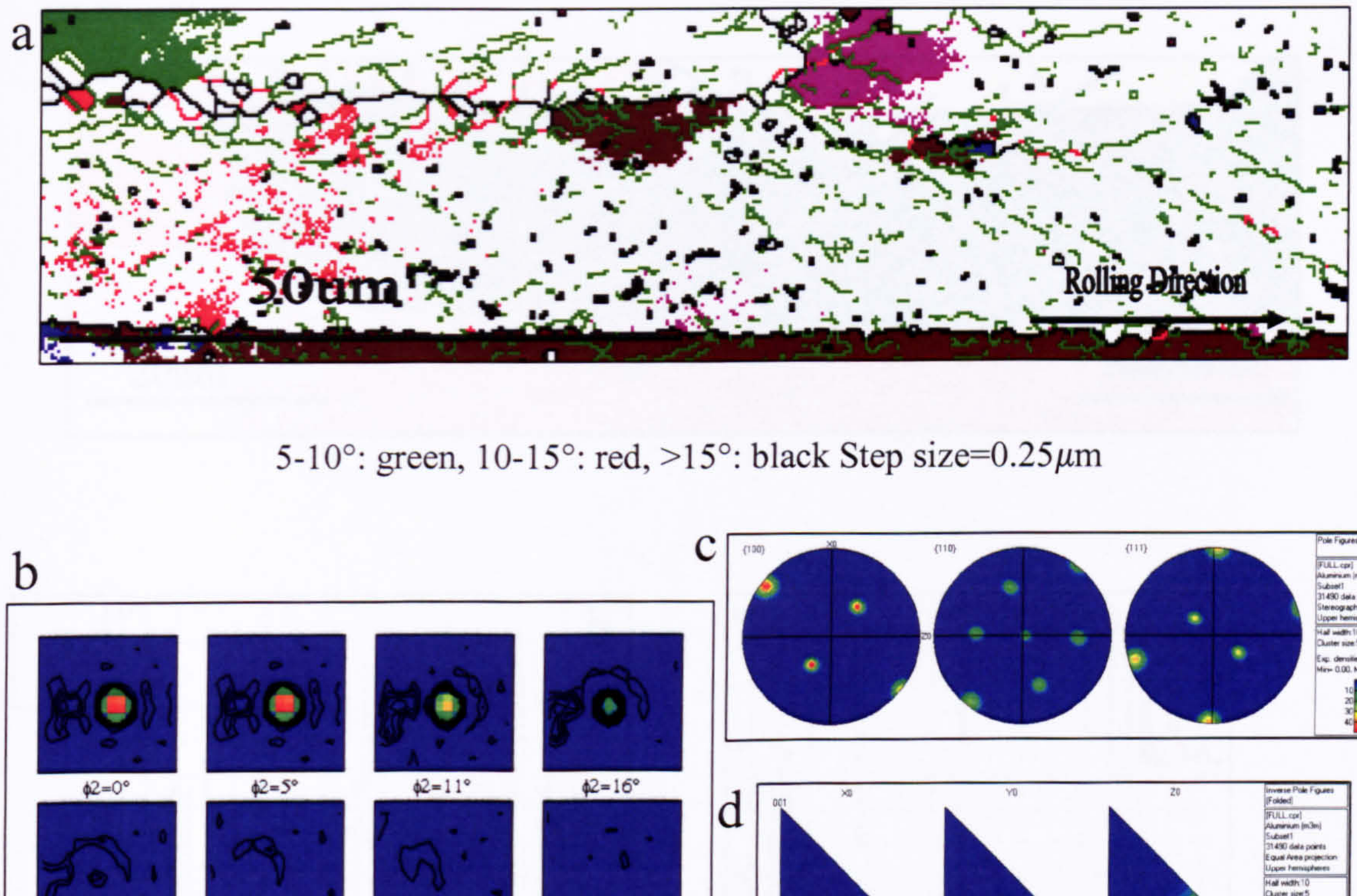

Fig. 5.59 Random-orientated grain in the 6 seconds delayed sample: (a) texture and boundary map, (b) ODF, (c) pole figures, (d) inverse pole figures, the distribution of misorientation axis vectors in (e) sample and (f) crystal lattice coordinates.

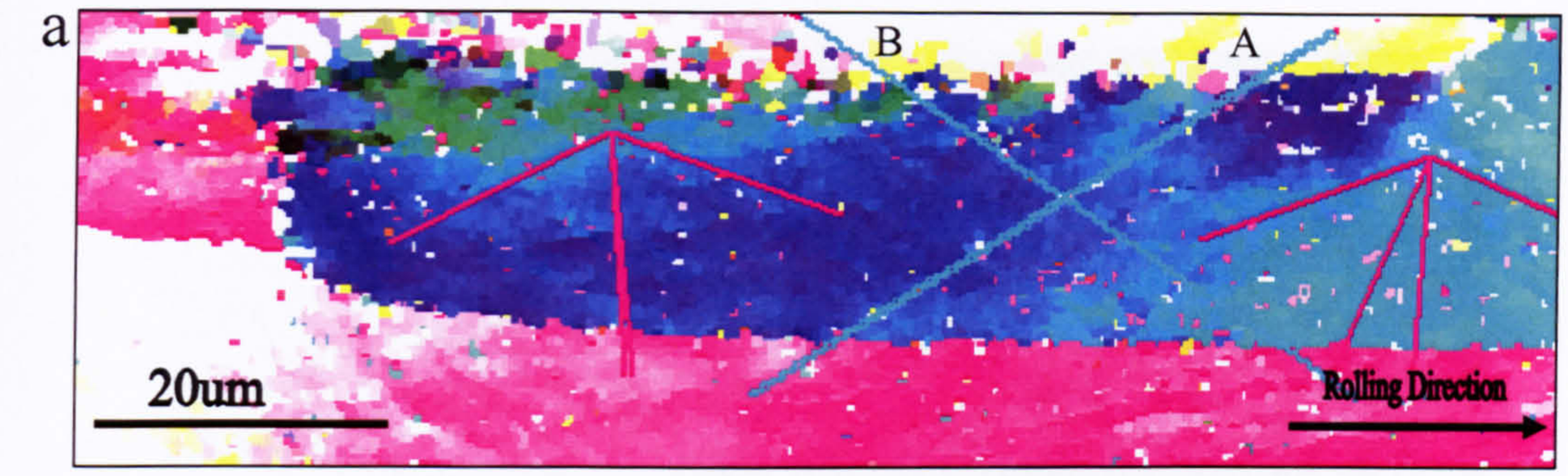

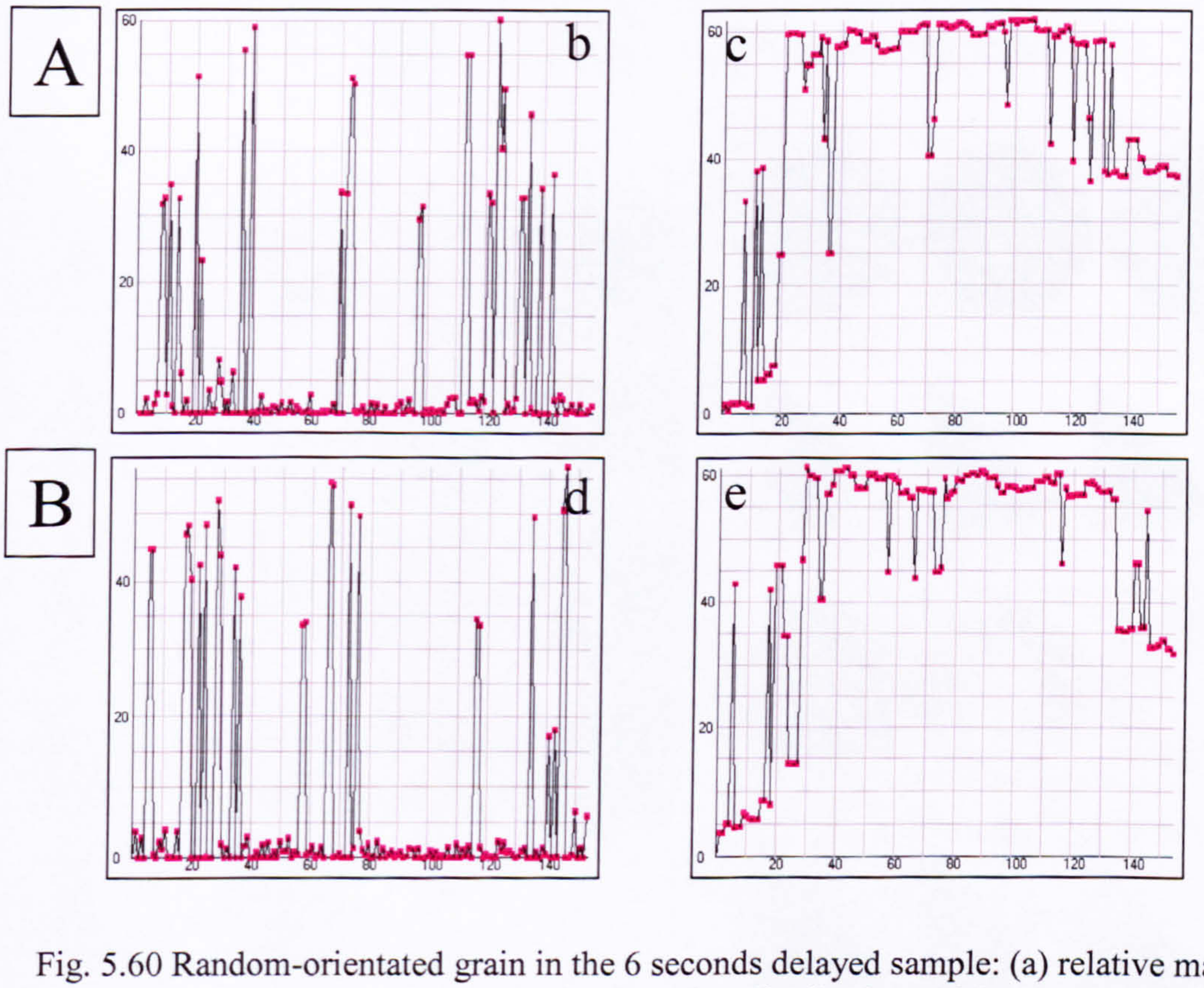

Fig. 5.60 Random-orientated grain in the 6 seconds delayed sample: (a) relative map, (b) (d) relative and (c) (e) cumulative misorientation distributions of line scans performed along A and B in (a).

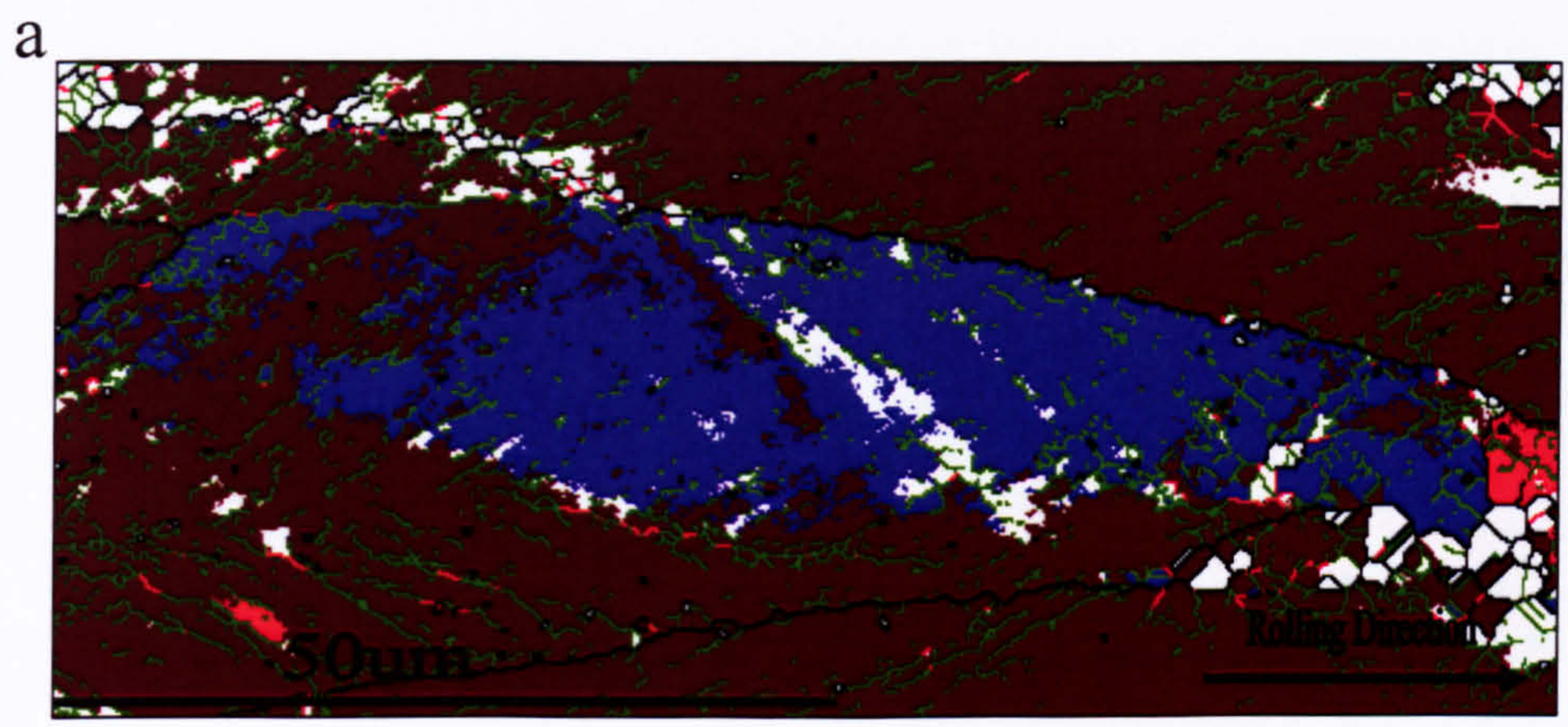

5-10°: green, 10-15°: red, >15°: black Step size=0.25μm

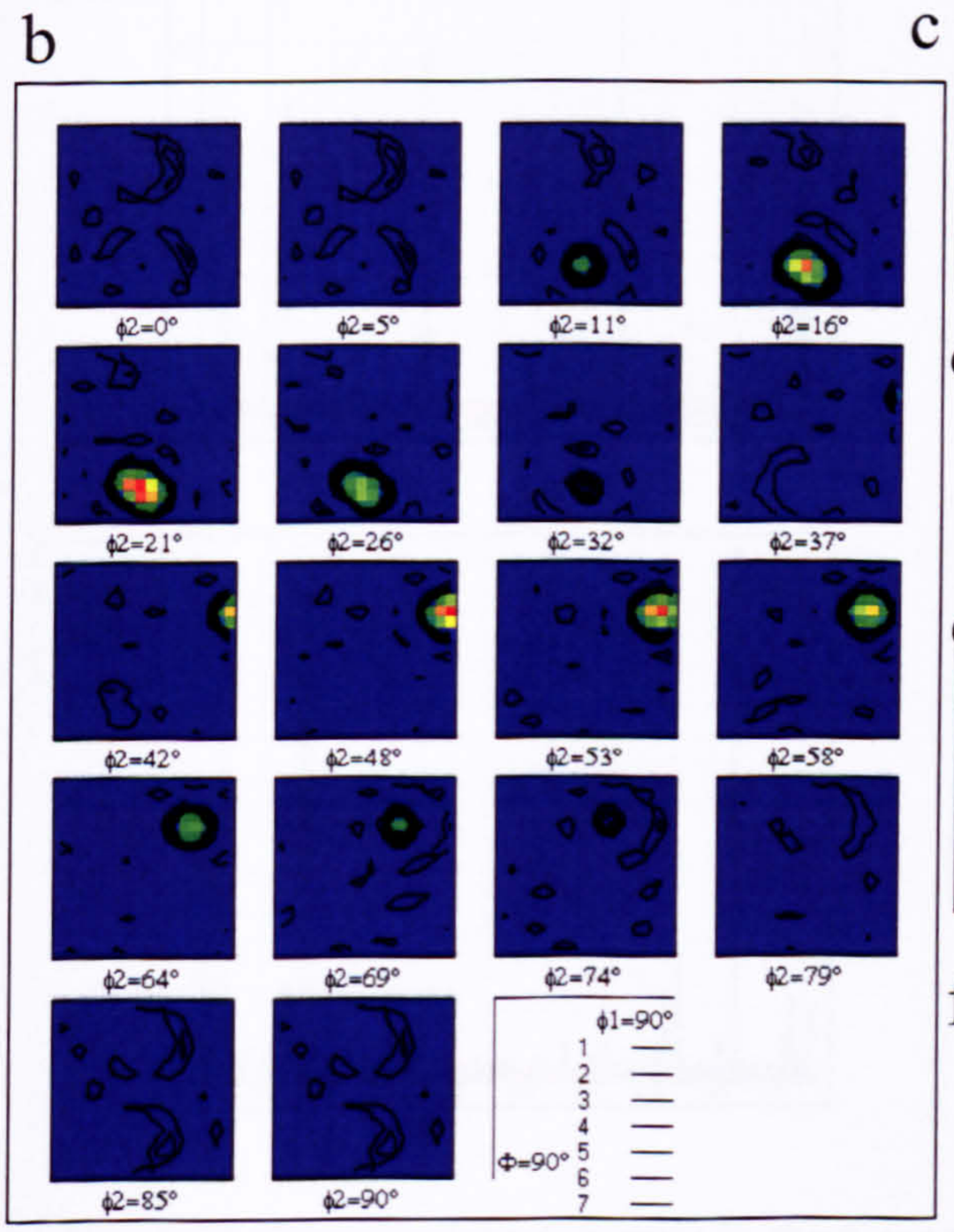

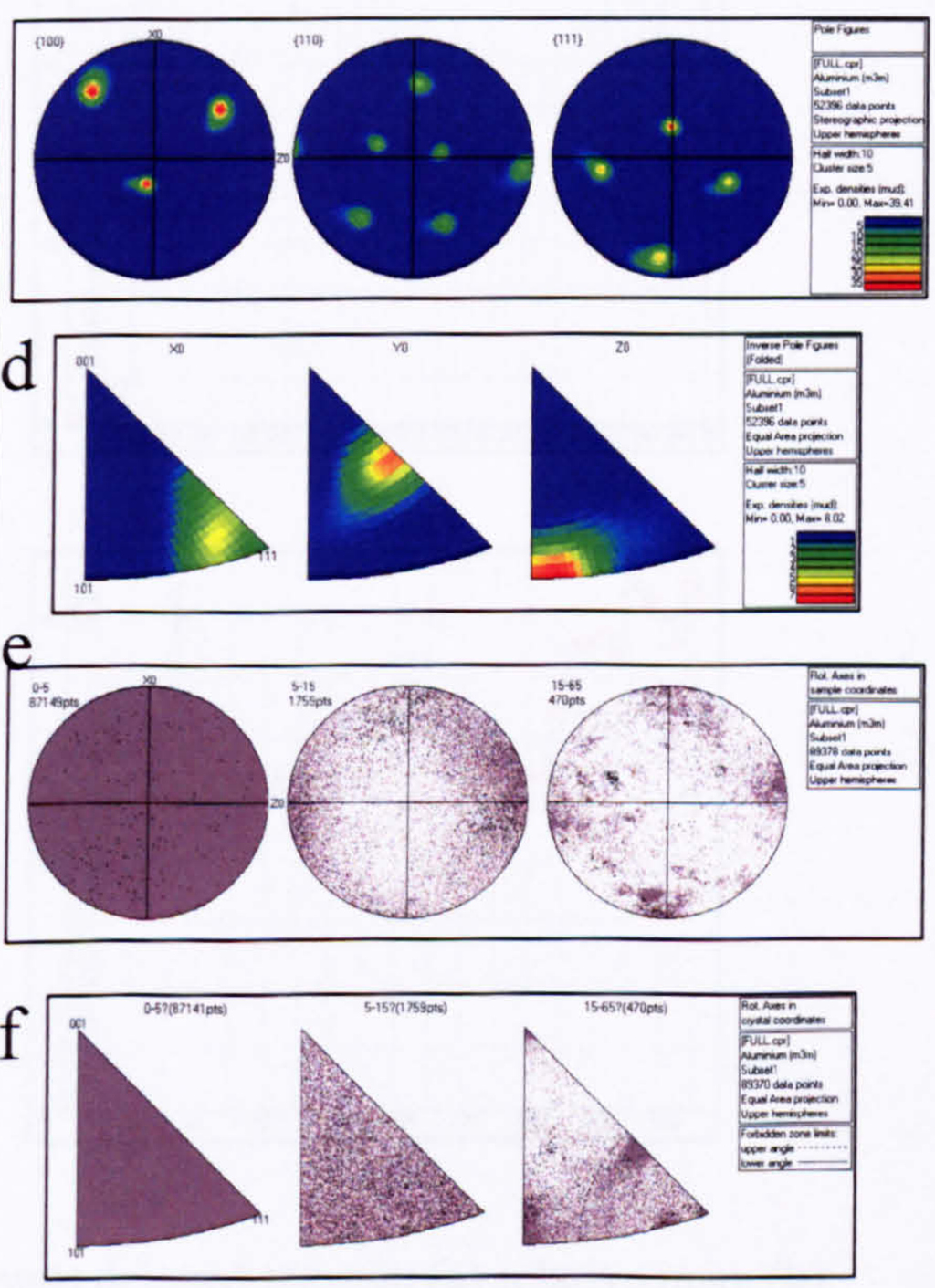

Fig. 5.61 Copper-orientated grain in the 6 seconds delayed sample: (a) texture and boundary map, (b) ODF, (c) pole figures, (d) inverse pole figures, the distribution of misorientation axis vectors in (e) sample and (f) crystal lattice coordinates.

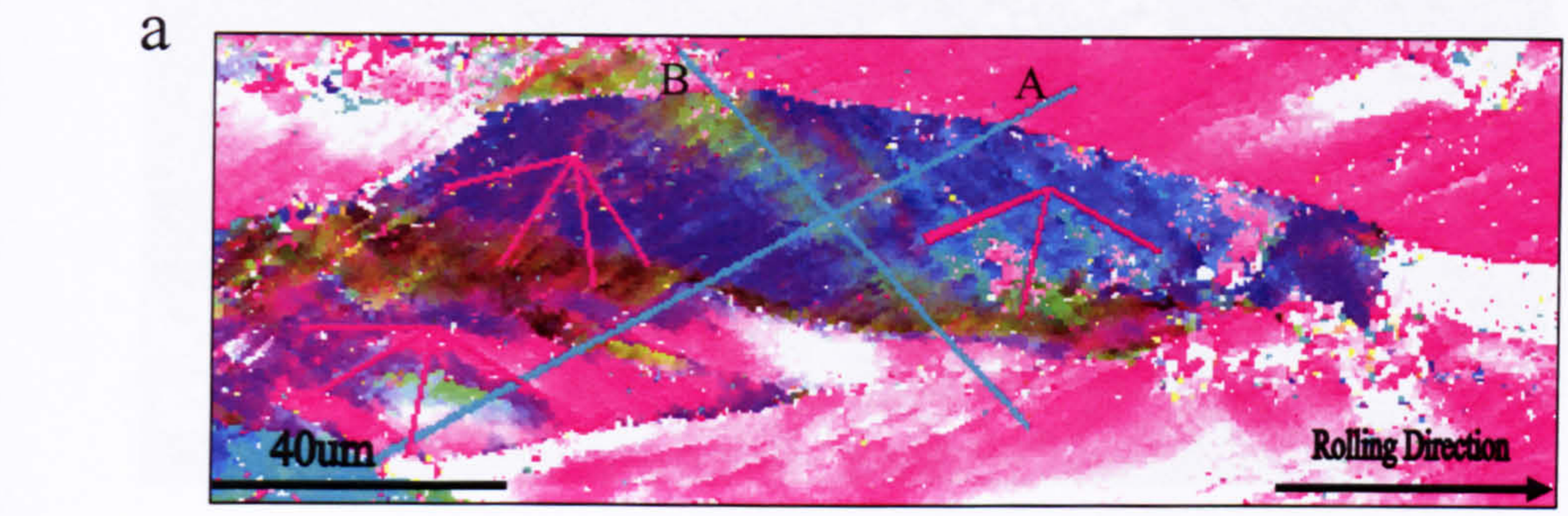

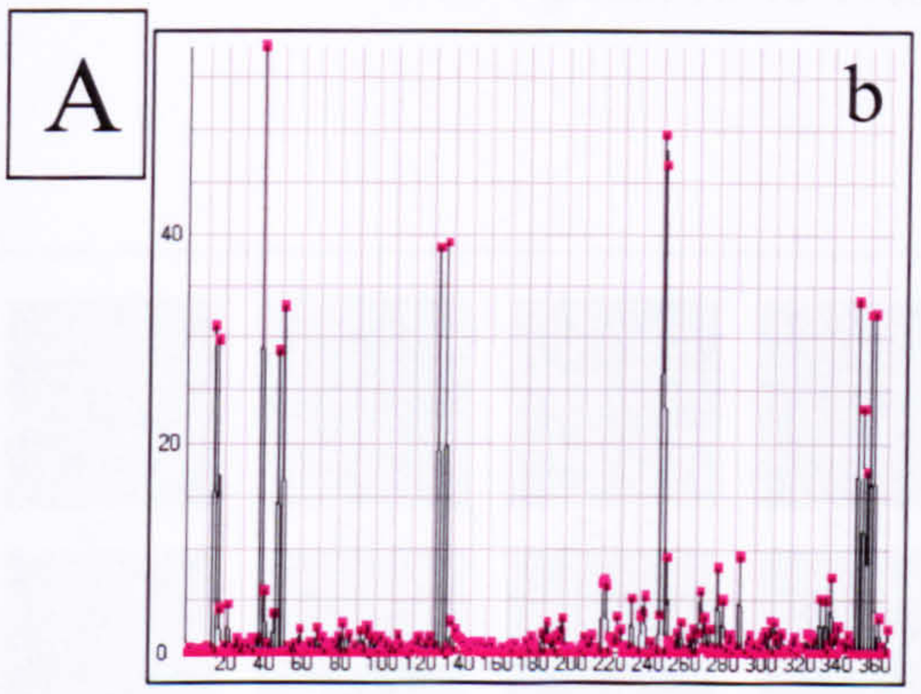

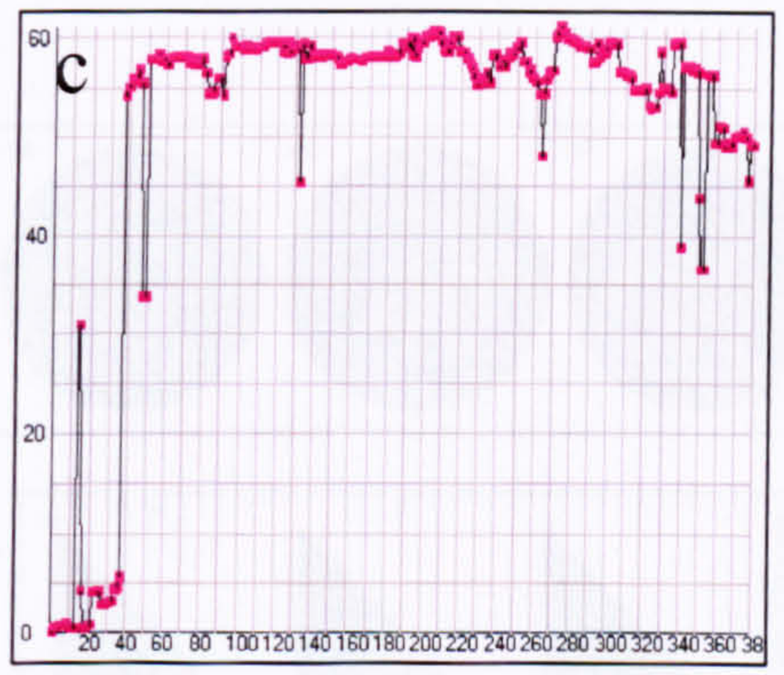

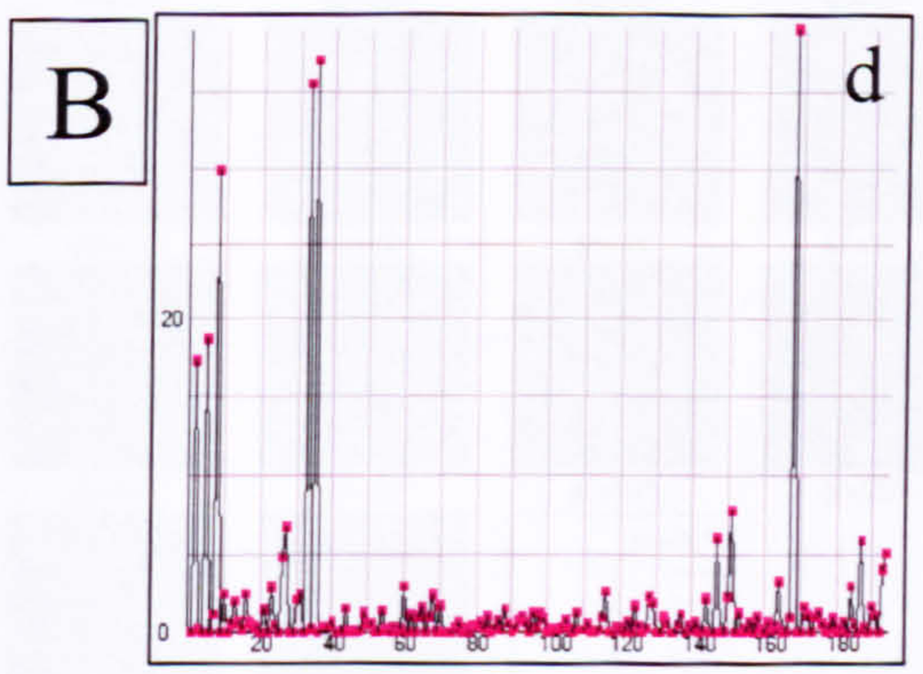

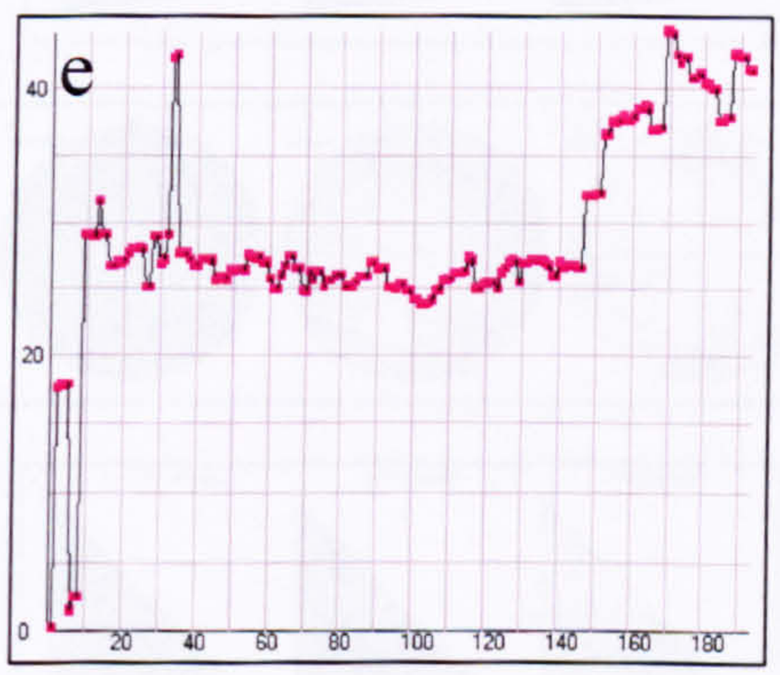

Fig. 5.62 Copper-orientated grain in the 6 seconds delayed sample: (a) relative map, (b) (d) relative and (c) (e) cumulative misorientation distributions of line scans performed along A and B in (a).

a

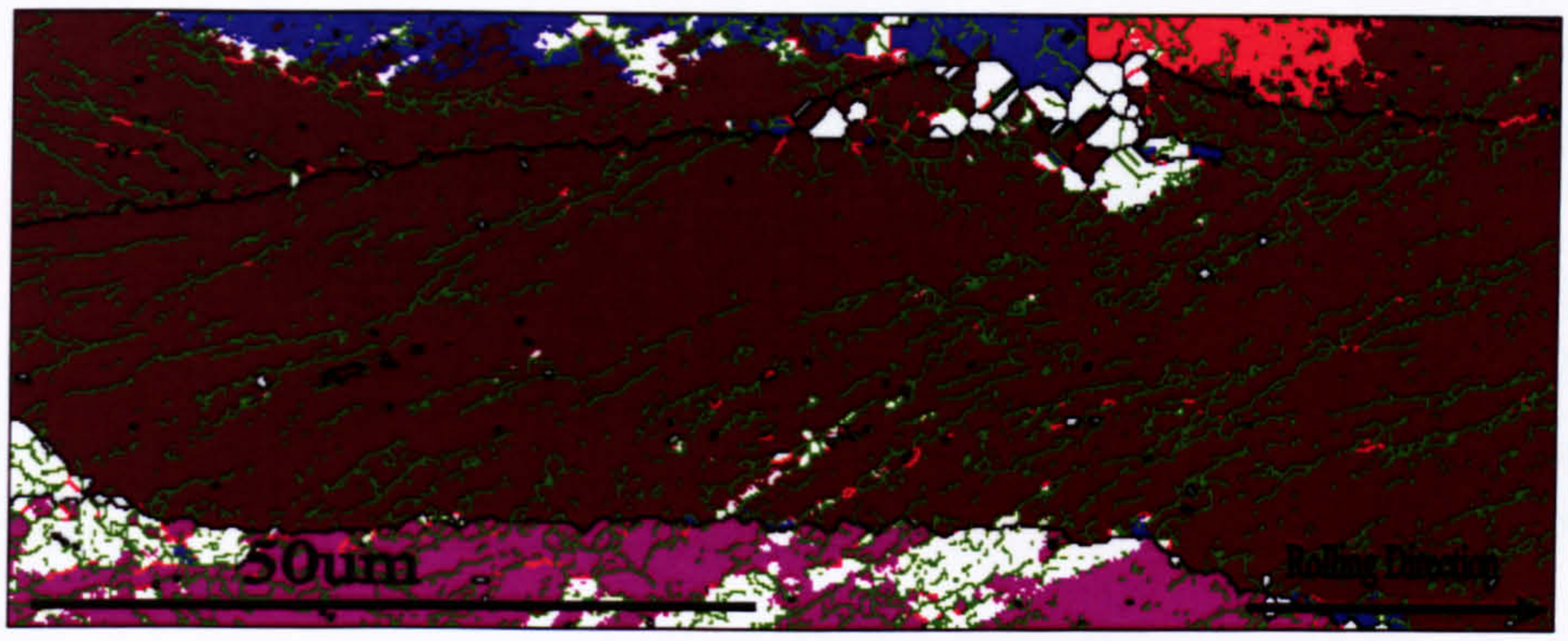

3-10°: green, 10-15°: red, >15°: black Step size=0.25μm

b

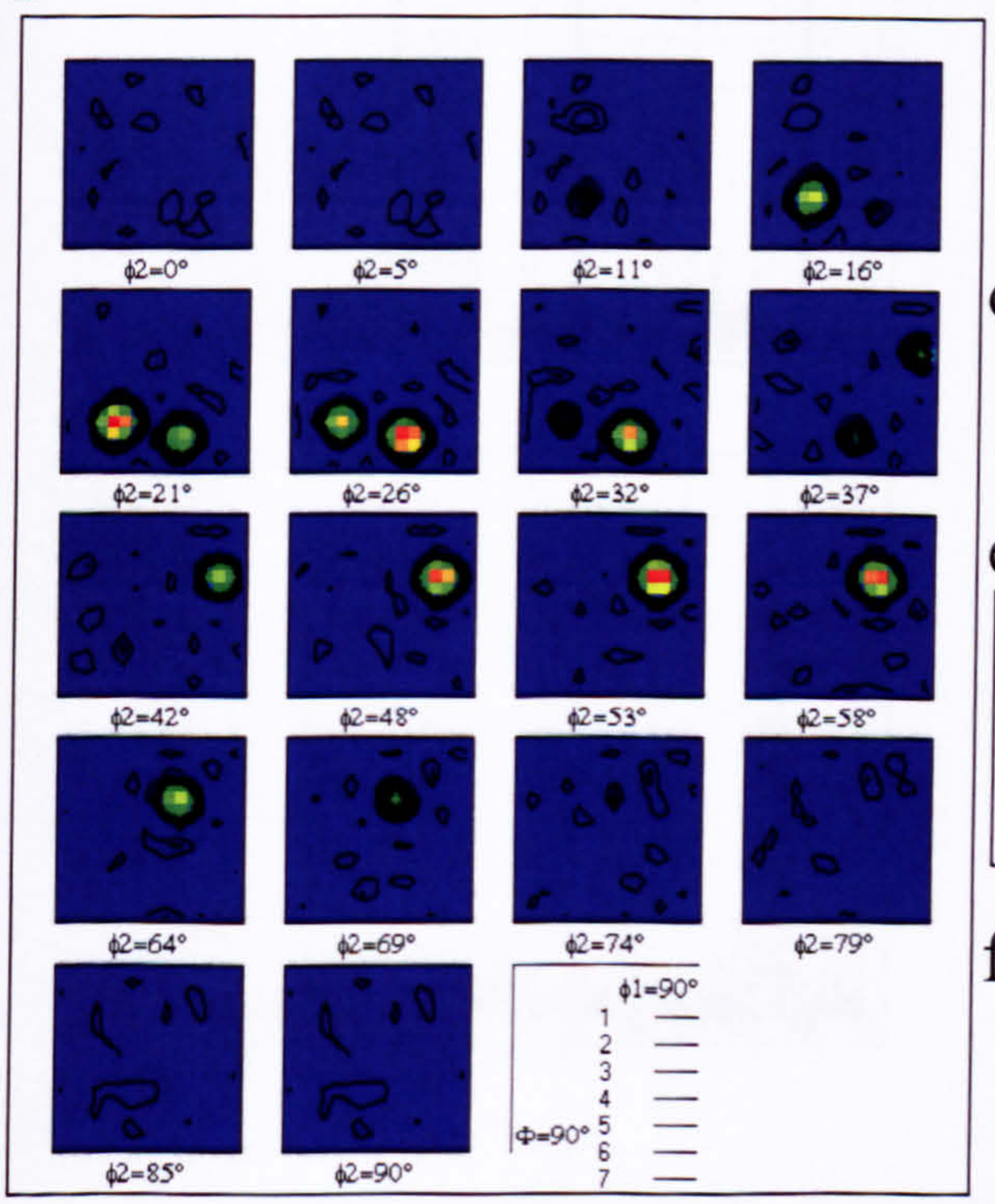

c

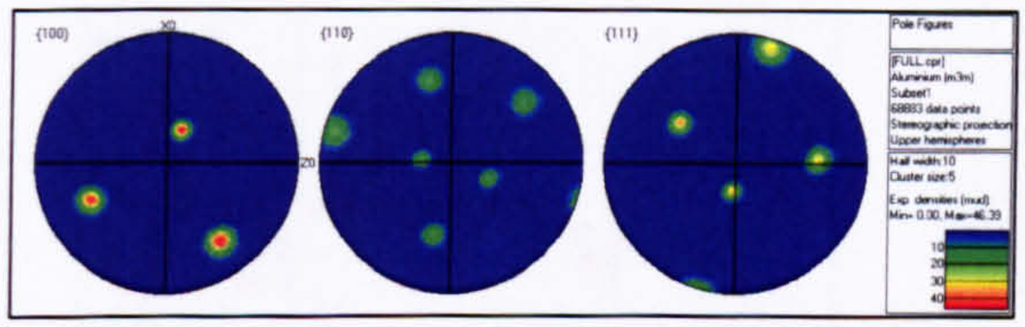

d

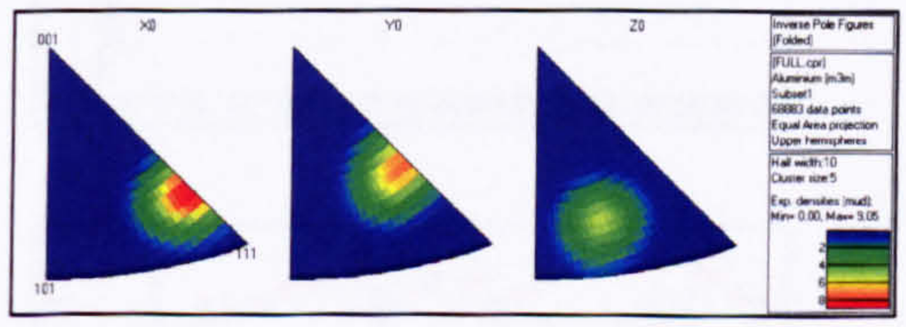

e

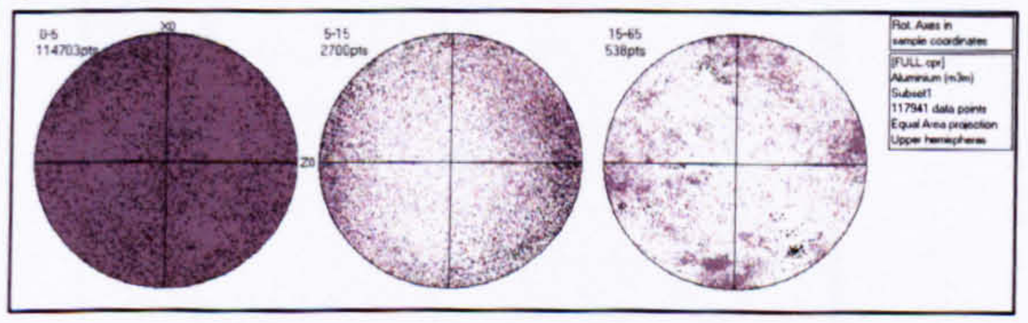

f

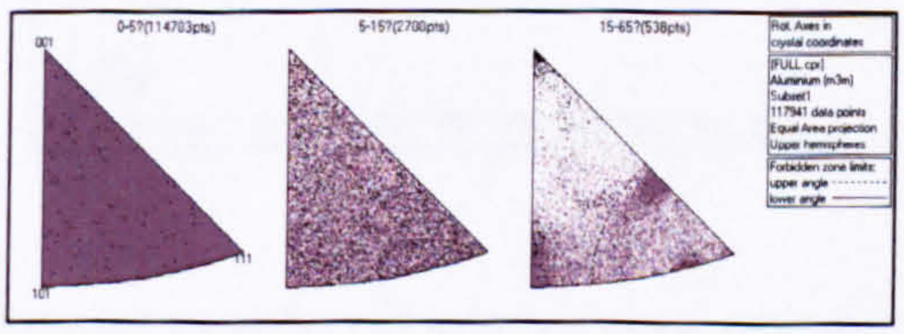

Fig. 5.63 S-orientated grain in the 6 seconds delayed sample: (a) texture and boundary map, (b) ODF, (c) pole figures, (d) inverse pole figures, the distribution of misorientation axis vectors in (e) sample and (f) crystal lattice coordinates.

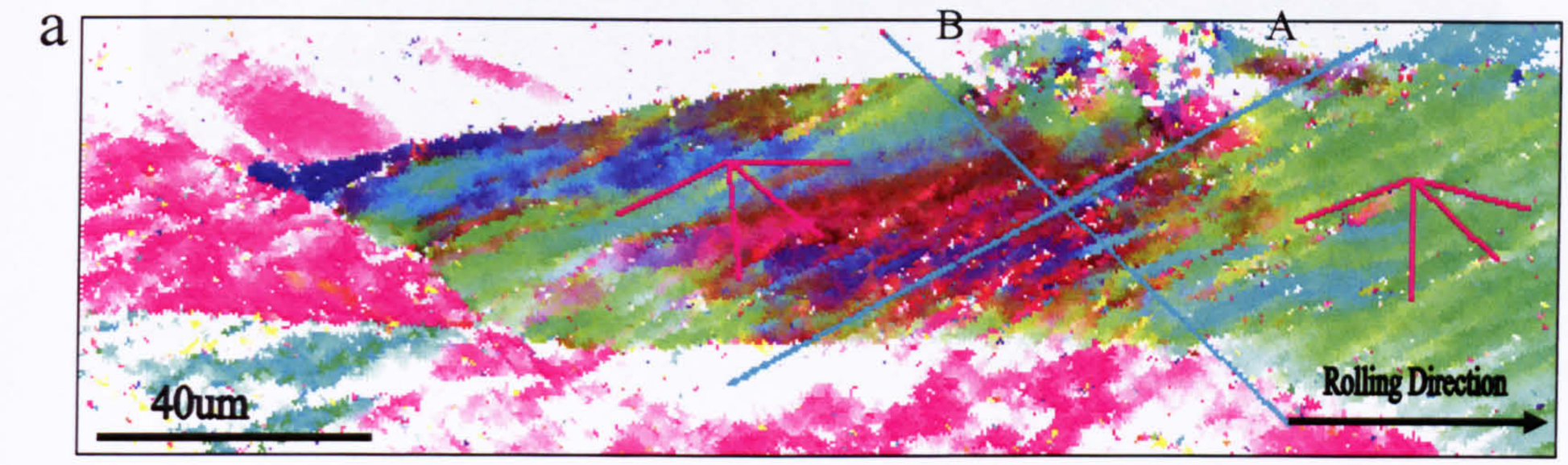

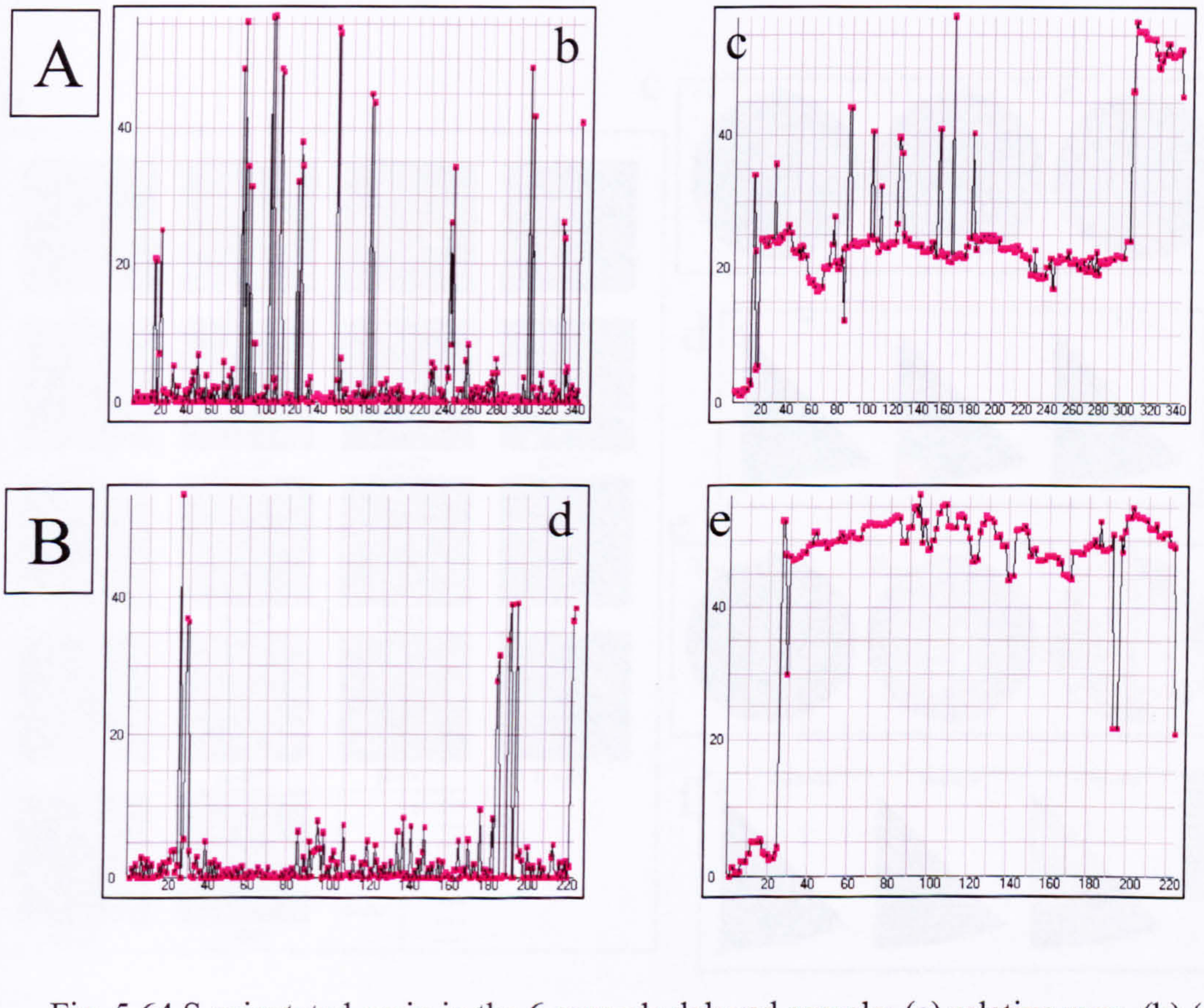

Fig. 5.64 S-orientated grain in the 6 seconds delayed sample: (a) relative map, (b) (d) relative and (c) (e) cumulative misorientation distributions of line scans performed along A and B in (a).

a

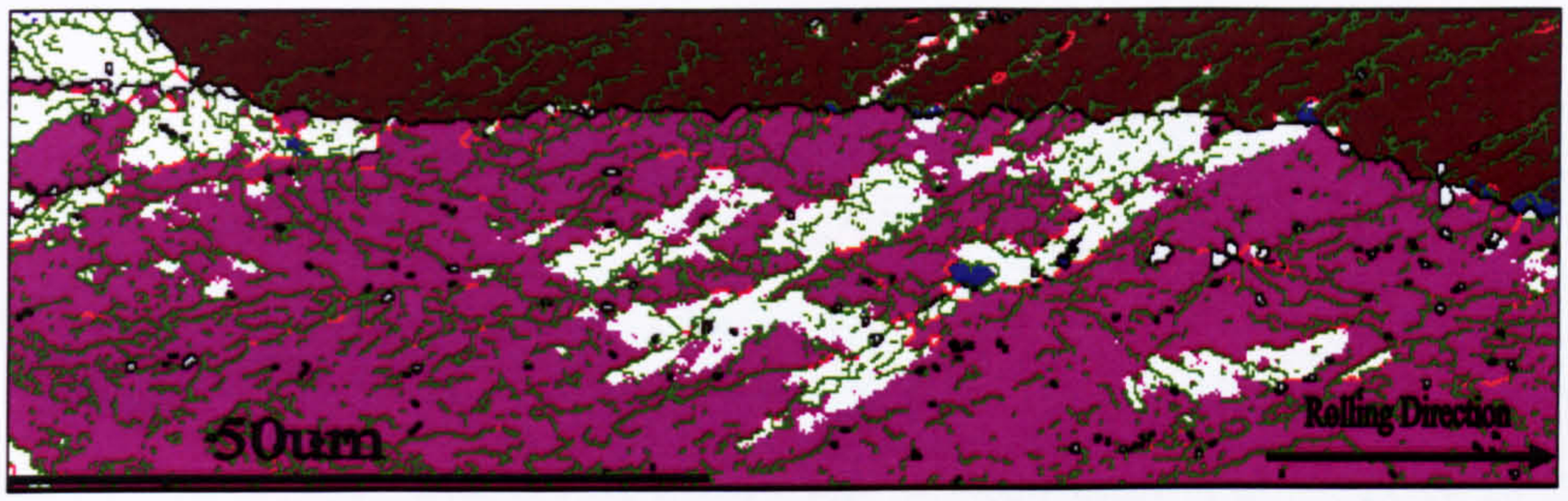

5-10°: green, 10-15°: red, >15°: black Step size=0.25μm

b

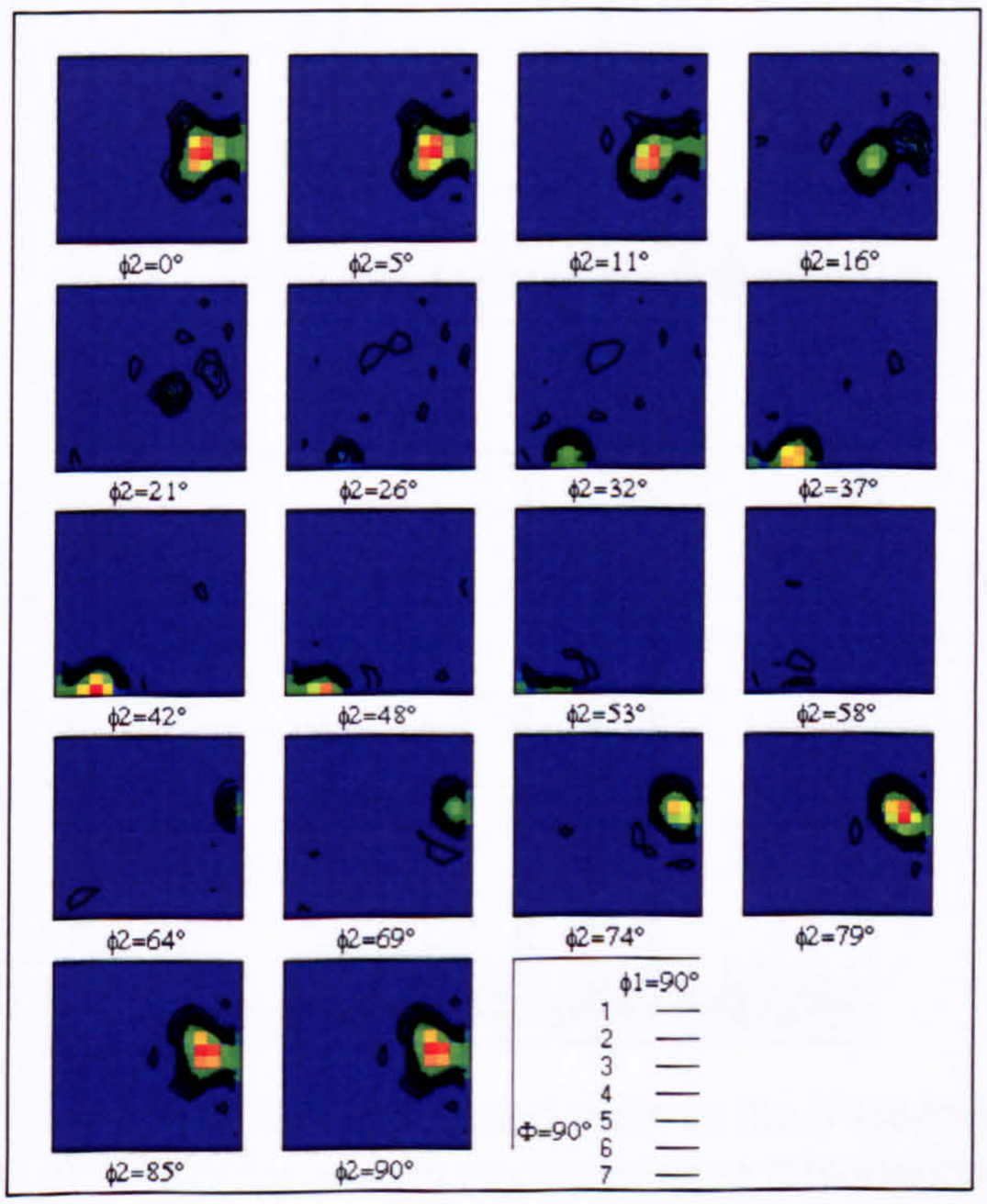

c

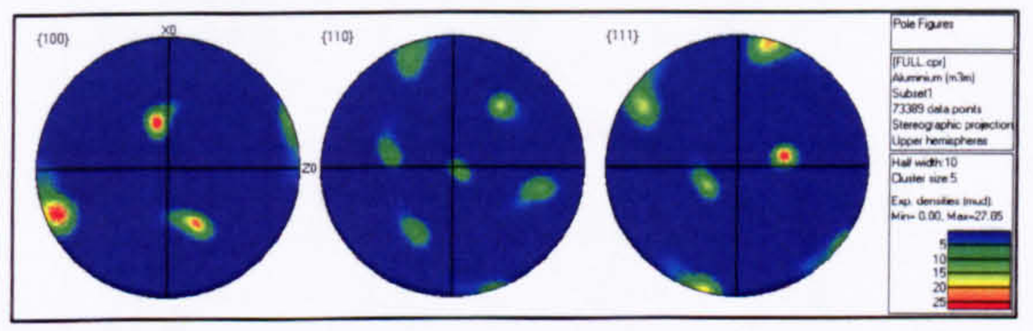

d

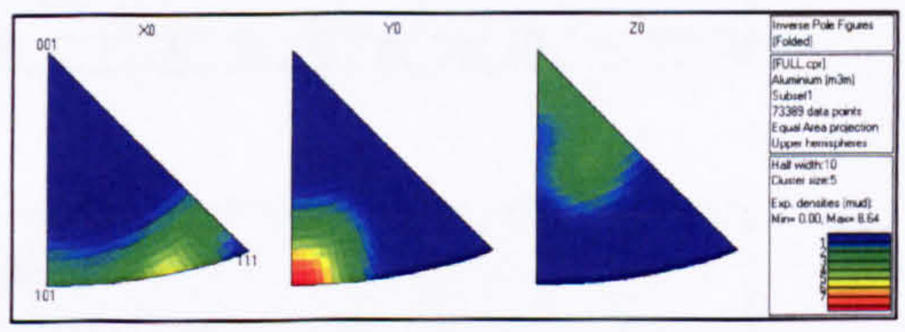

e

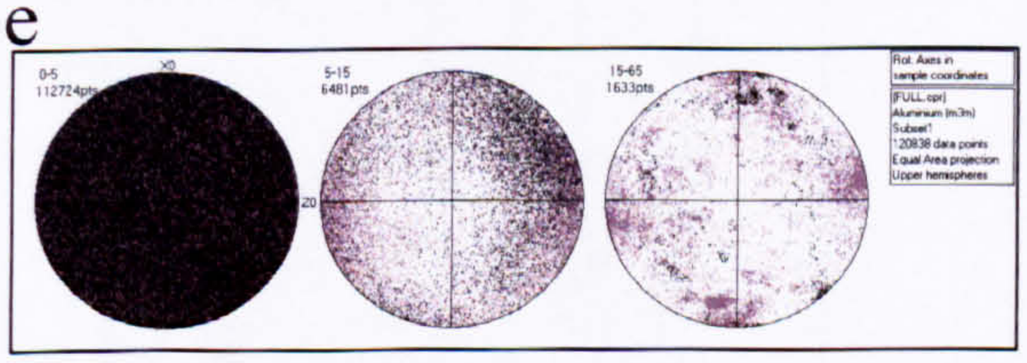

f

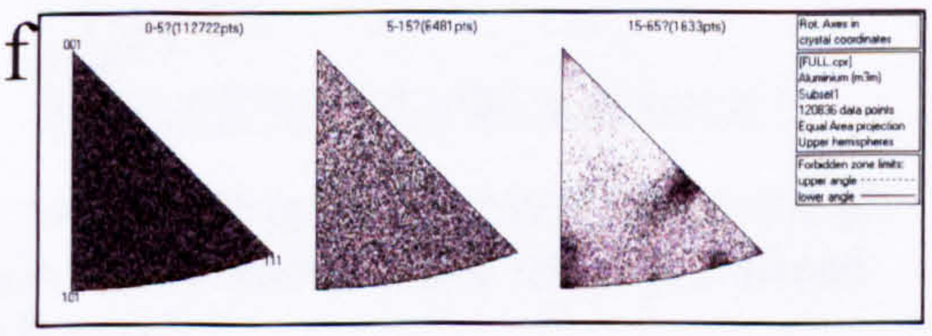

Fig. 5.65 P-orientated grain in the 6 seconds delayed sample: (a) texture and boundary map, (b) ODF, (c) pole figures, (d) inverse pole figures, the distribution of misorientation axis vectors in (e) sample and (f) crystal lattice coordinates.

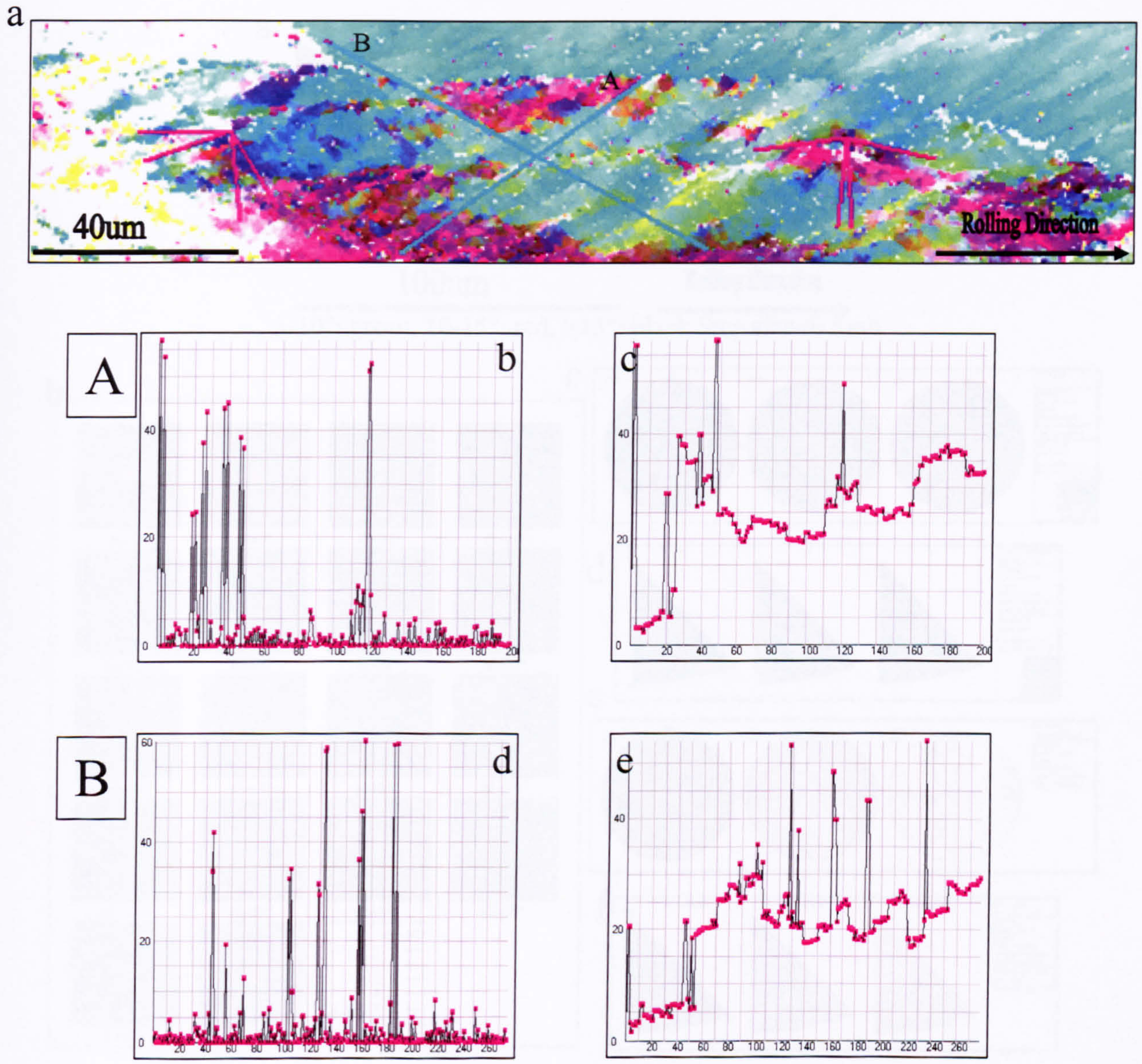

Fig. 5.66 P-orientated grain in the 6 seconds delayed sample: (a) relative map, (b) (d) relative and (c) (e) cumulative misorientation distributions of line scans performed along A and B in (a).

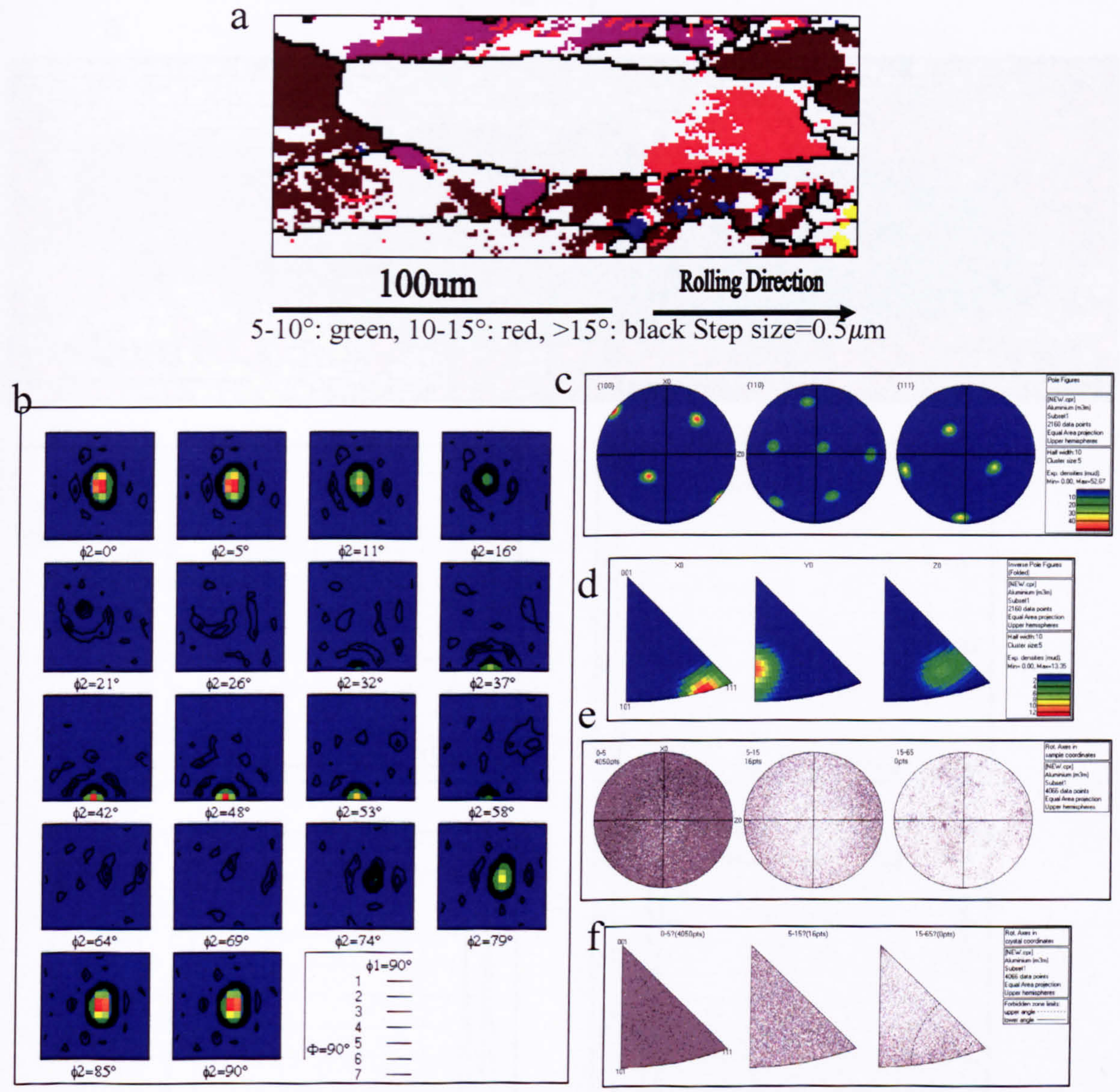

Fig. 5.67 Brass-orientated grain in the 6 seconds delayed sample: (a) texture and boundary map, (b) ODF, (c) pole figures, (d) inverse pole figures, the distribution of misorientation axis vectors in (e) sample and (f) crystal lattice coordinates.

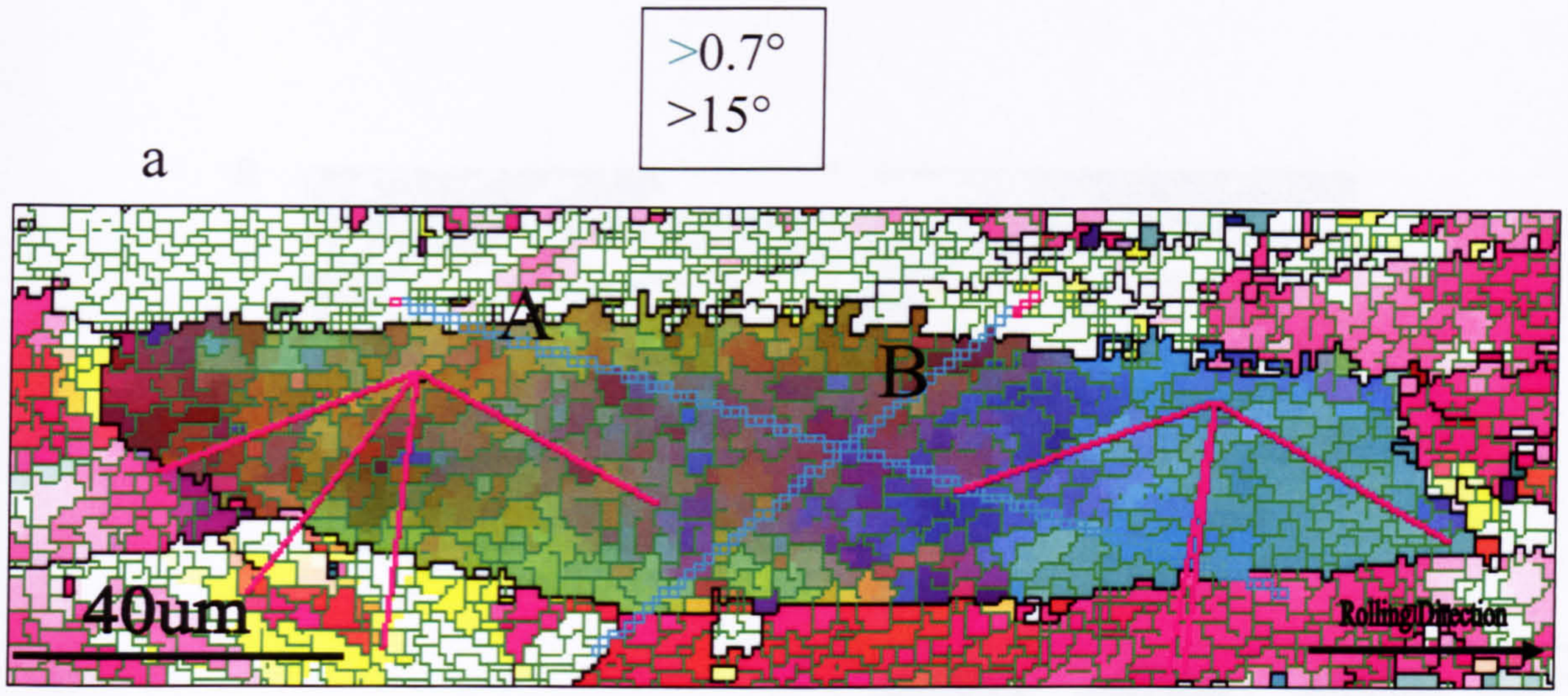

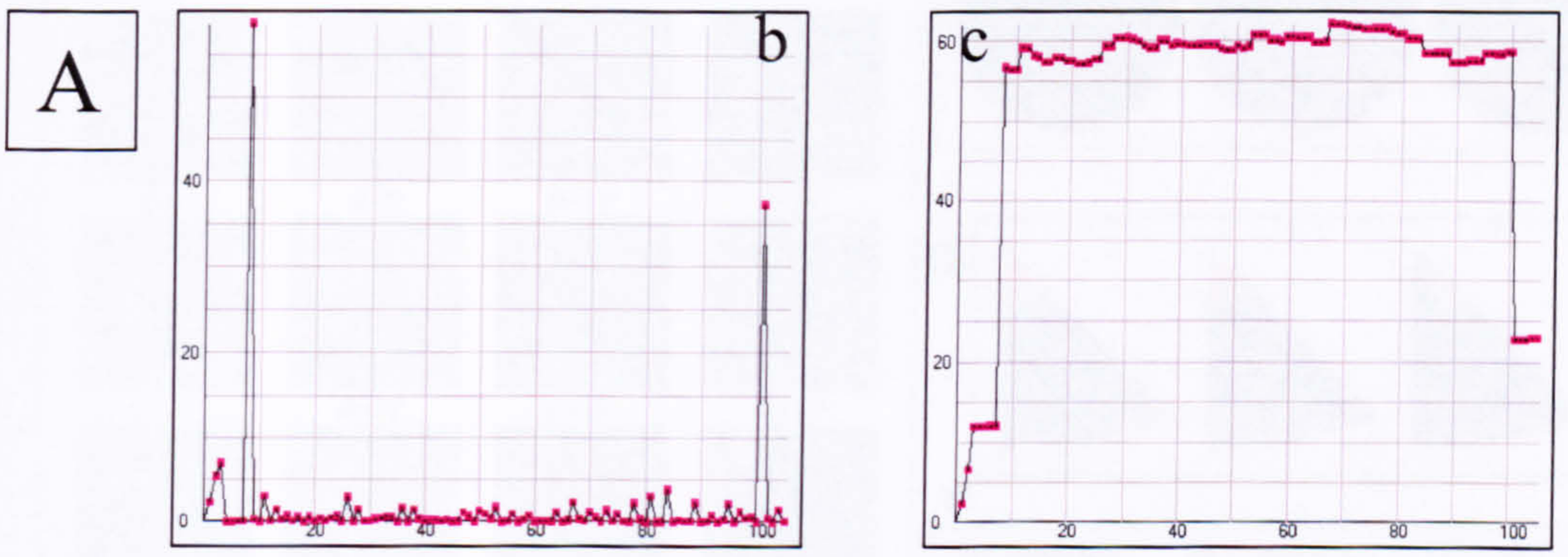

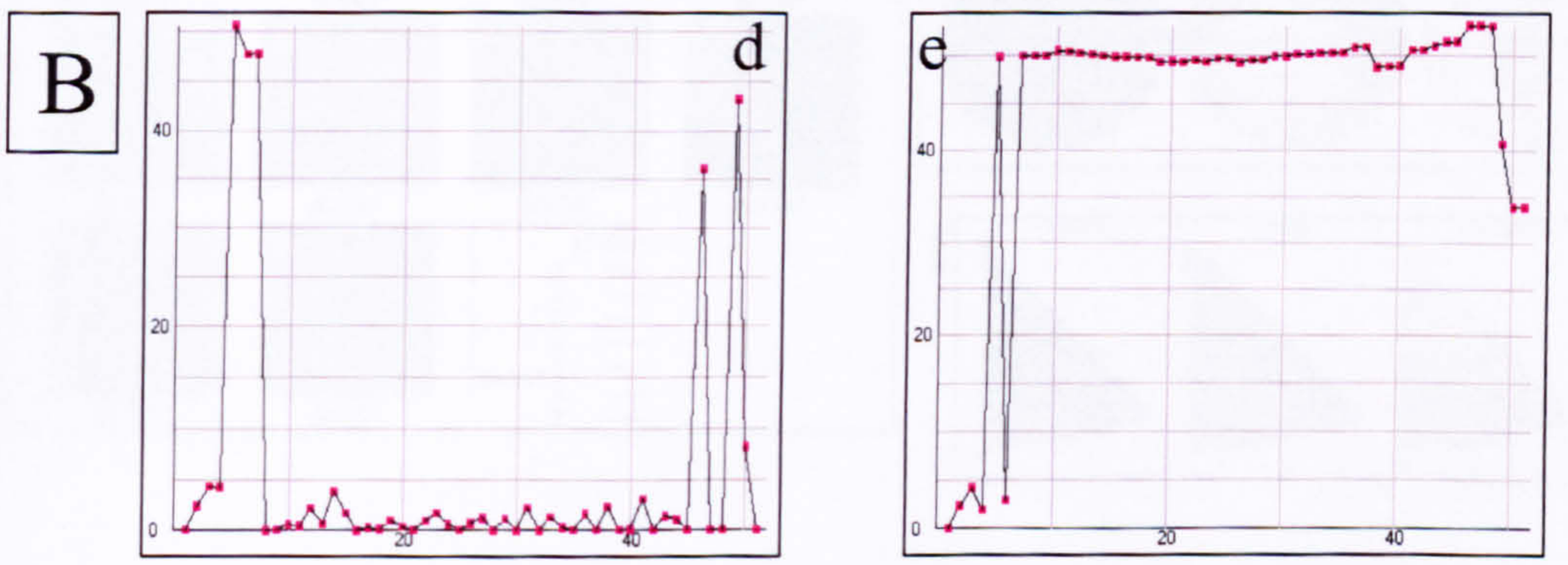

Fig. 5.68 Brass-orientated grain in the 6 seconds delayed sample: (a) relative map, (b) (d) relative and (c) (e) cumulative misorientation distributions of line scans performed along A and B in (a).

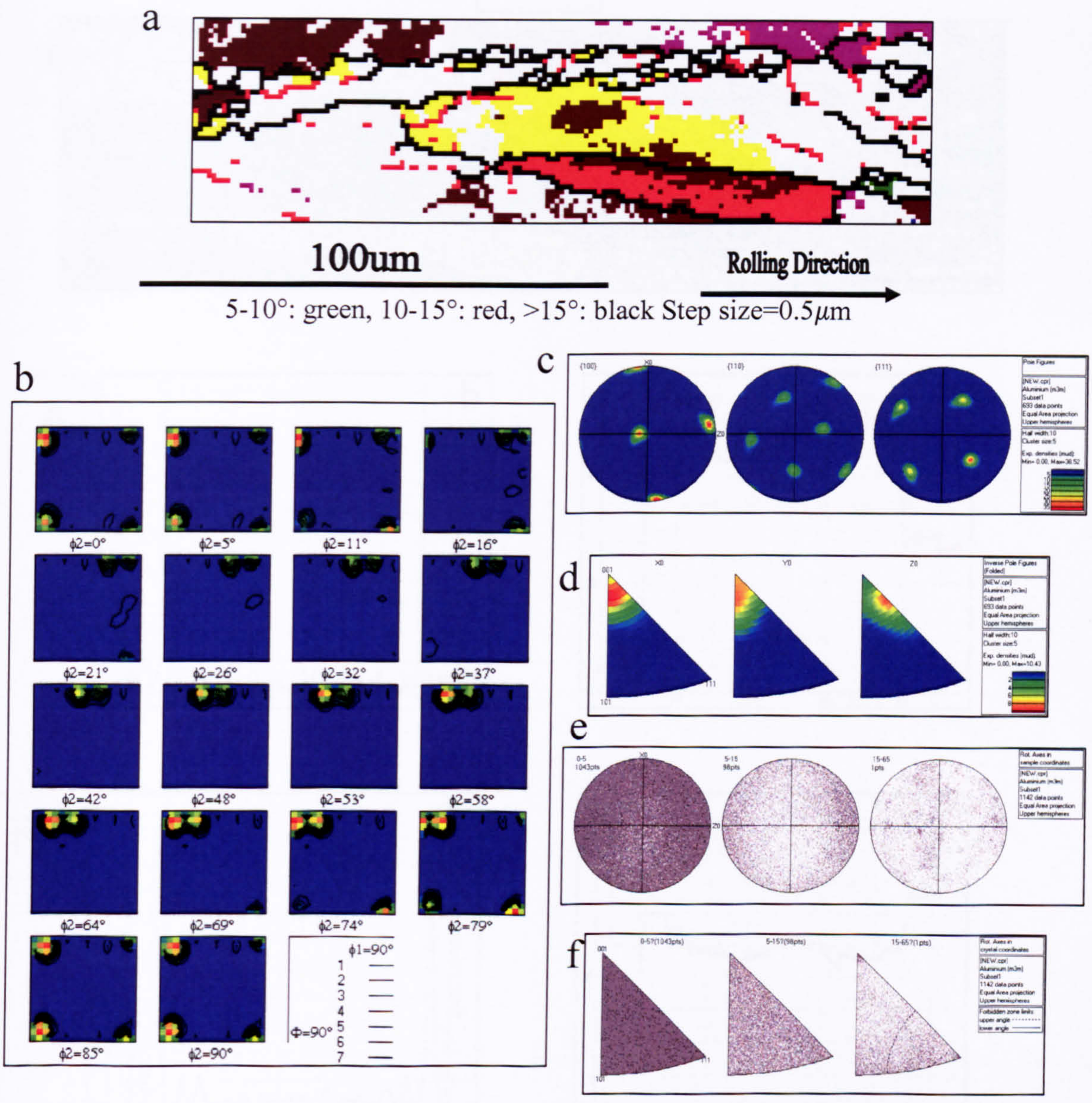

Fig. 5.69 Cube-orientated grain in the 6 seconds delayed sample: (a) texture and boundary map, (b) ODF, (c) pole figures, (d) inverse pole figures, the distribution of misorientation axis vectors in (e) sample and (f) crystal lattice coordinates.

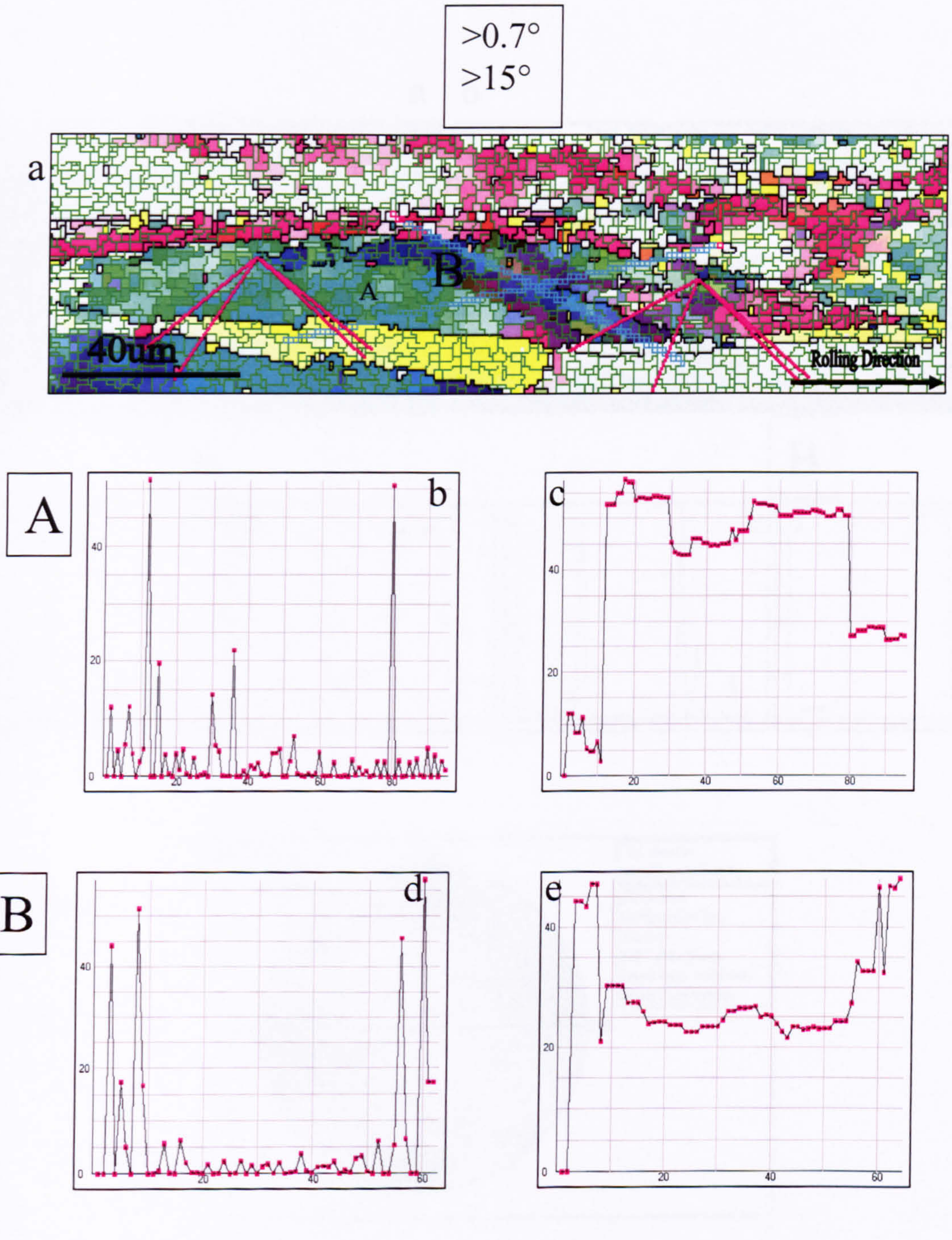

Fig. 5.70 Cube-orientated grain in the 6 seconds delayed sample: (a) relative map, (b) (d) relative and (c) (e) (h) (j) cumulative misorientation distributions of line scans performed along A and B in (a).

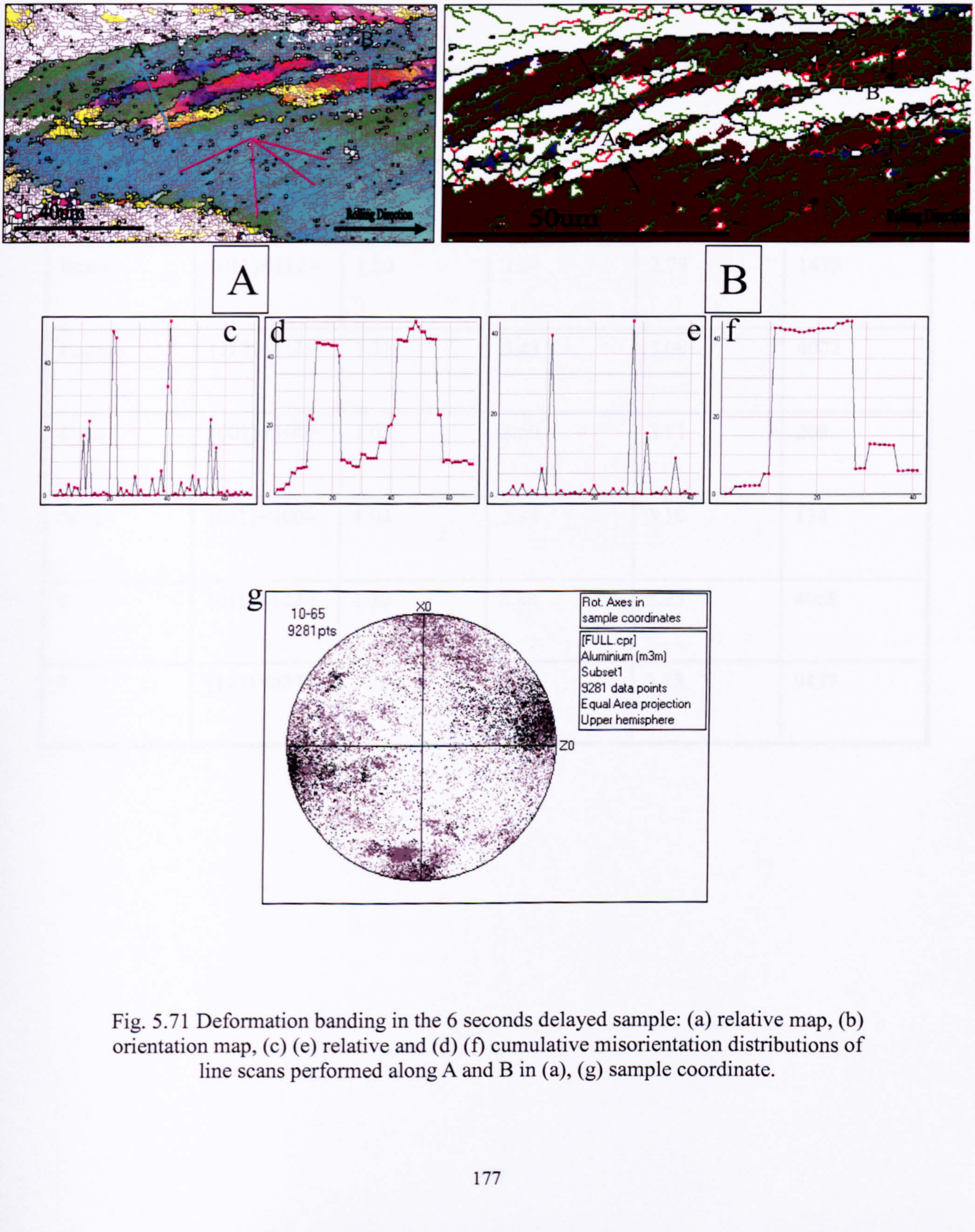

Fig. 5.71 Deformation banding in the 6 seconds delayed sample: (a) relative map, (b) orientation map, (c) (e) relative and (d) (f) cumulative misorientation distributions of line scans performed along A and B in (a), (g) sample coordinate.

Table 5.5 Mean subgrain size (D), misorientation angle (è) and Θ/d for the 6 seconds delayed sample

Texture Component	{hkl}<uvw>	D(μm)	Θ(°)	Θ/d	Number of Subgrains
Brass	{011}<112>	1.20	3.34	2.78	1478
Copper	{112}<111>	1.11	3.43	3.09	4072
Cube	{001}<100>	1.05	3.69	3.51	208
Goss	{011}<100>	1.04	3.32	3.19	134
P	{011}<122>	1.20	3.88	3.23	4068
S	{123}<634>	1.22	3.89	3.18	9437

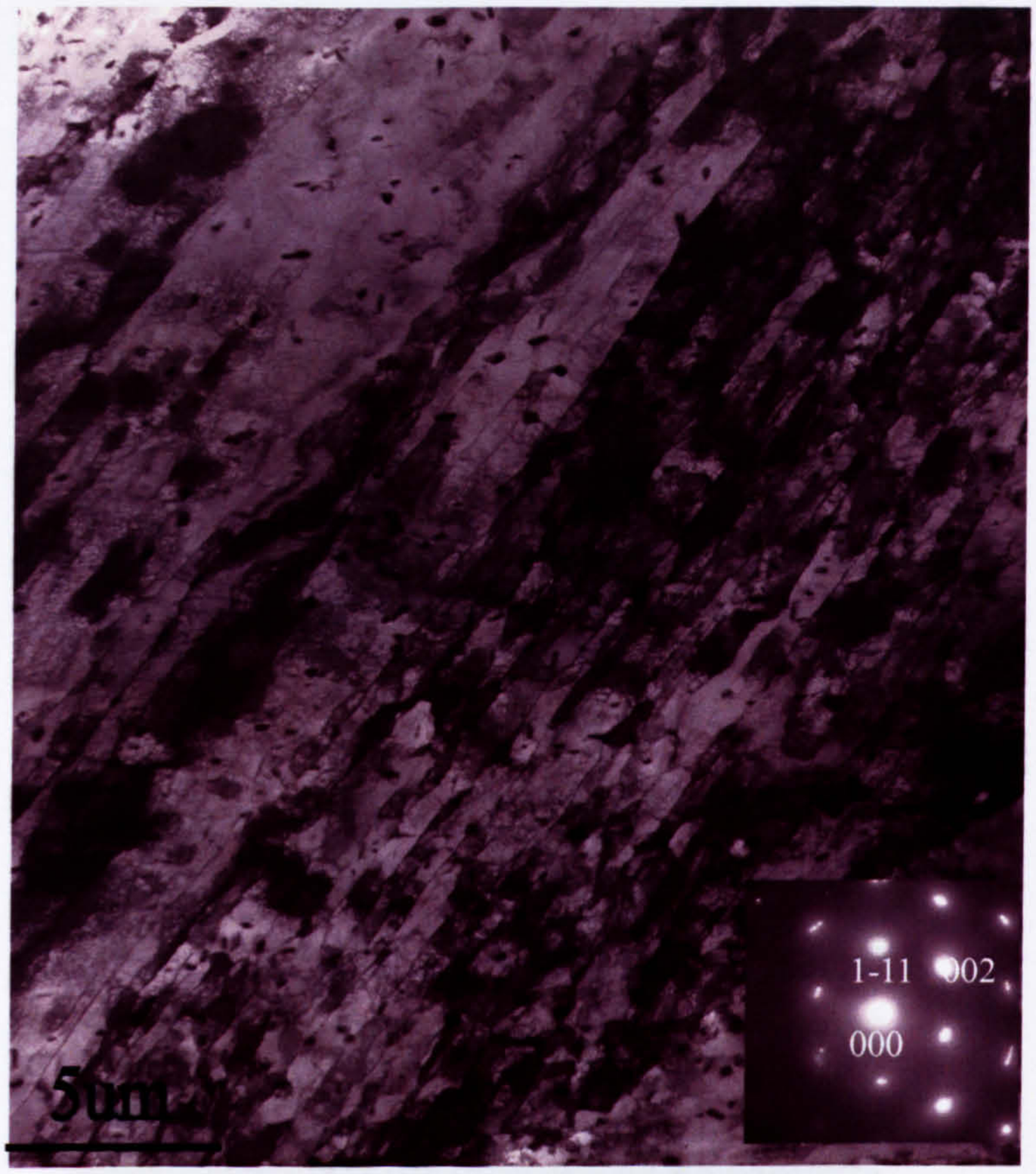

Fig. 5.72 TEM images after the 6 seconds delayed deformation, shows microband structure.

a

b

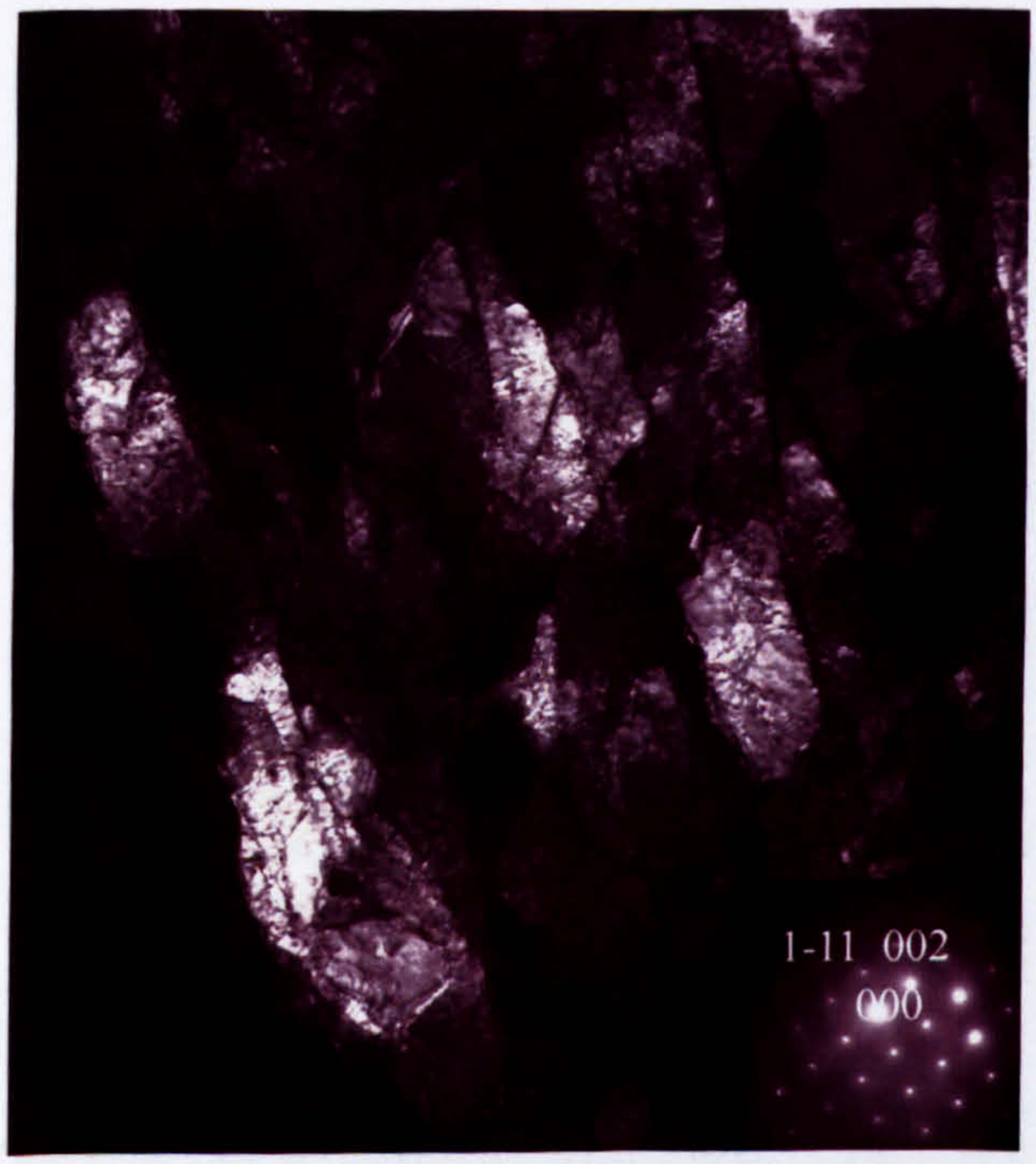

Fig. 5.73 TEM images after the 6 seconds delayed deformation, shows microband structure.

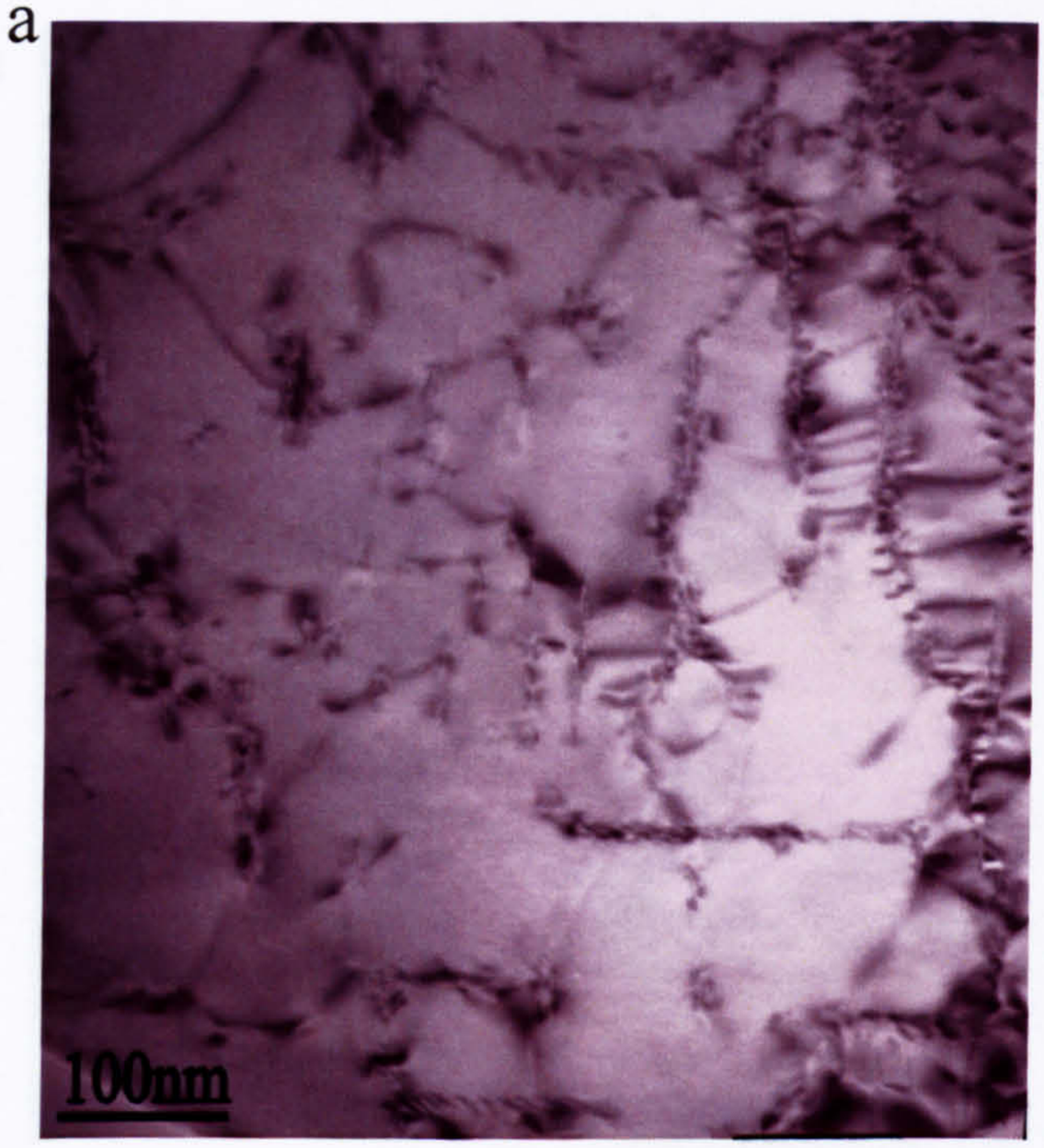

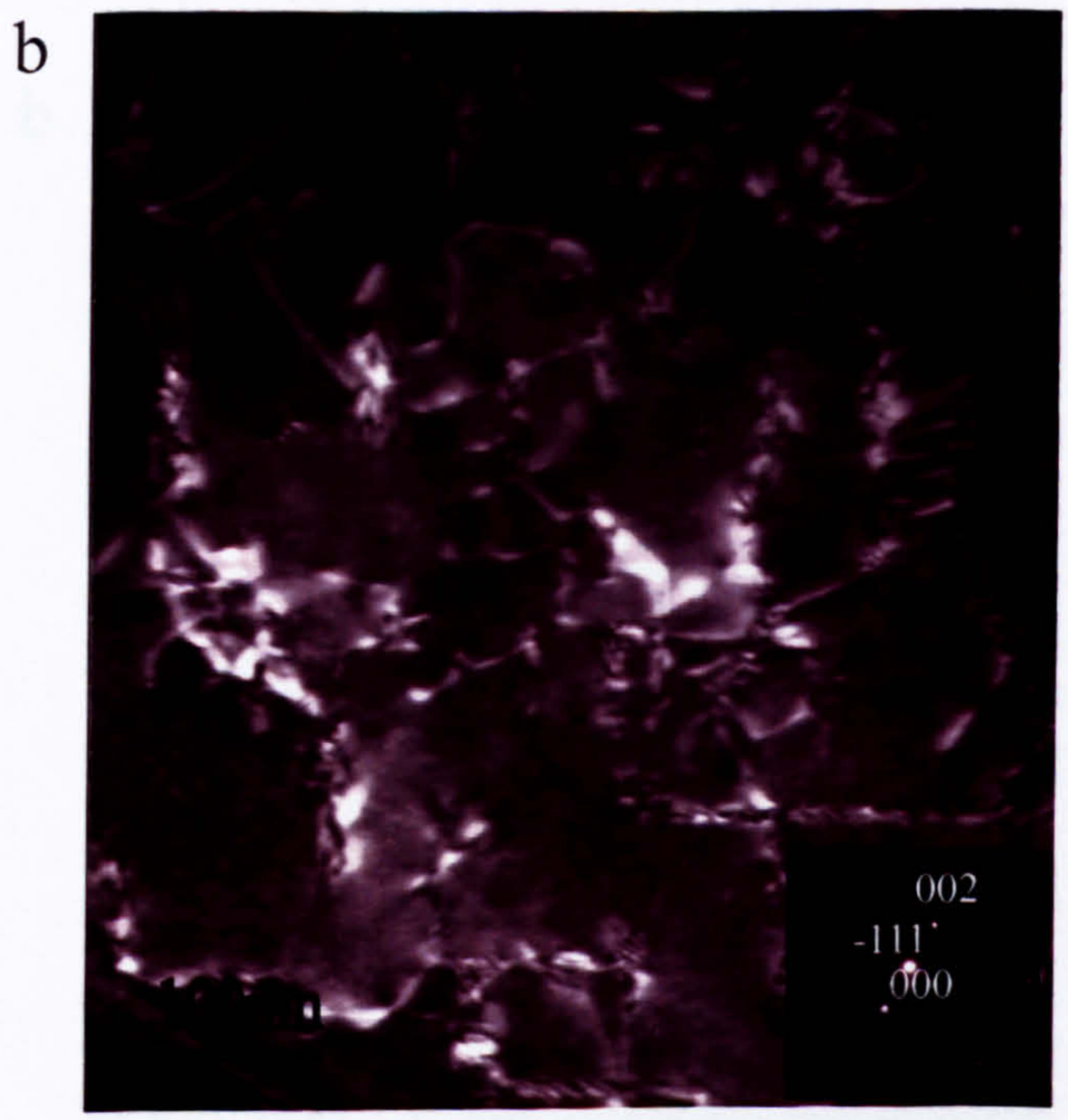

Fig. 5.74 TEM images after the 6 seconds delayed deformation, shows the tangle dislocation structure within microbands.

a

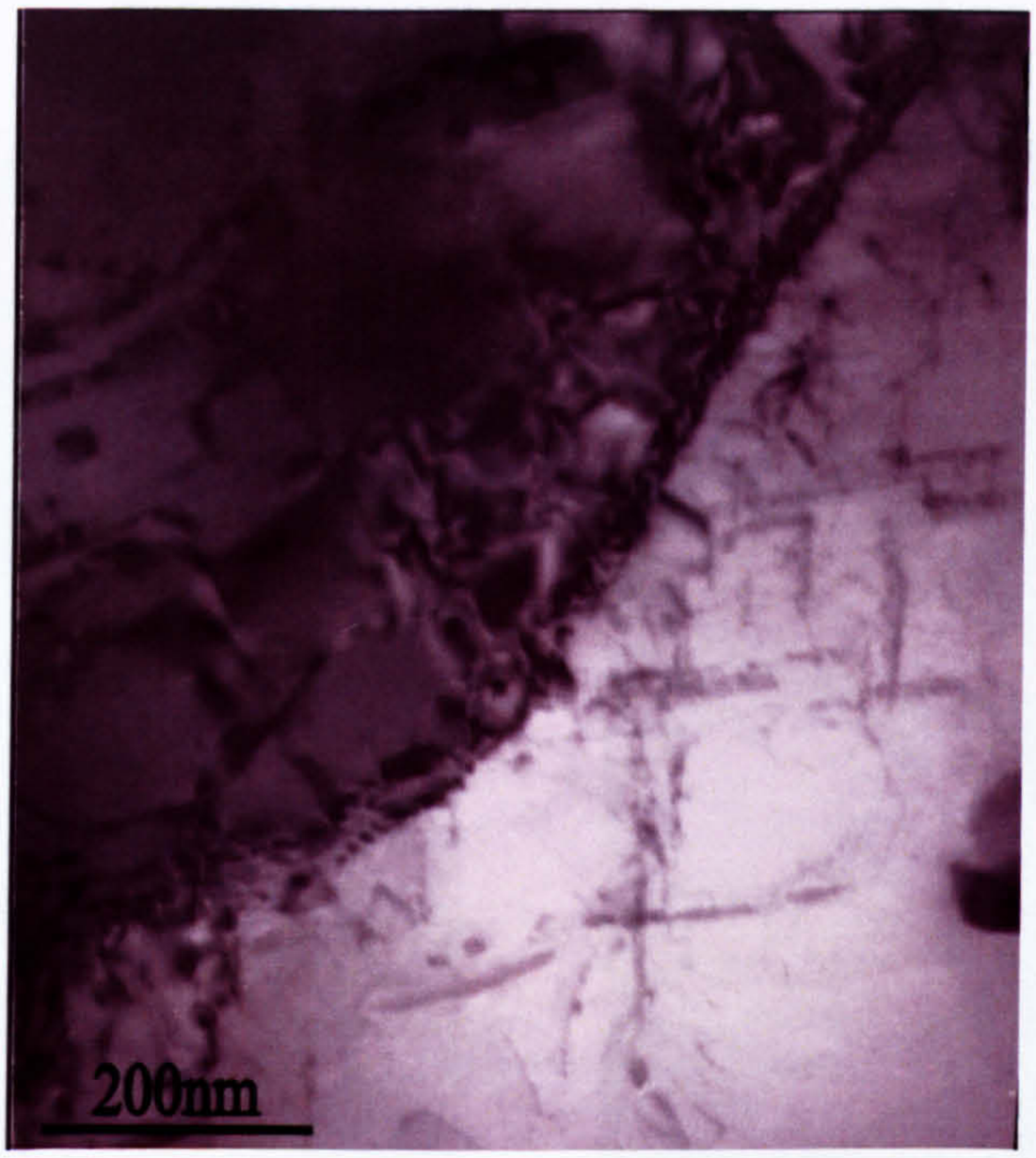

b

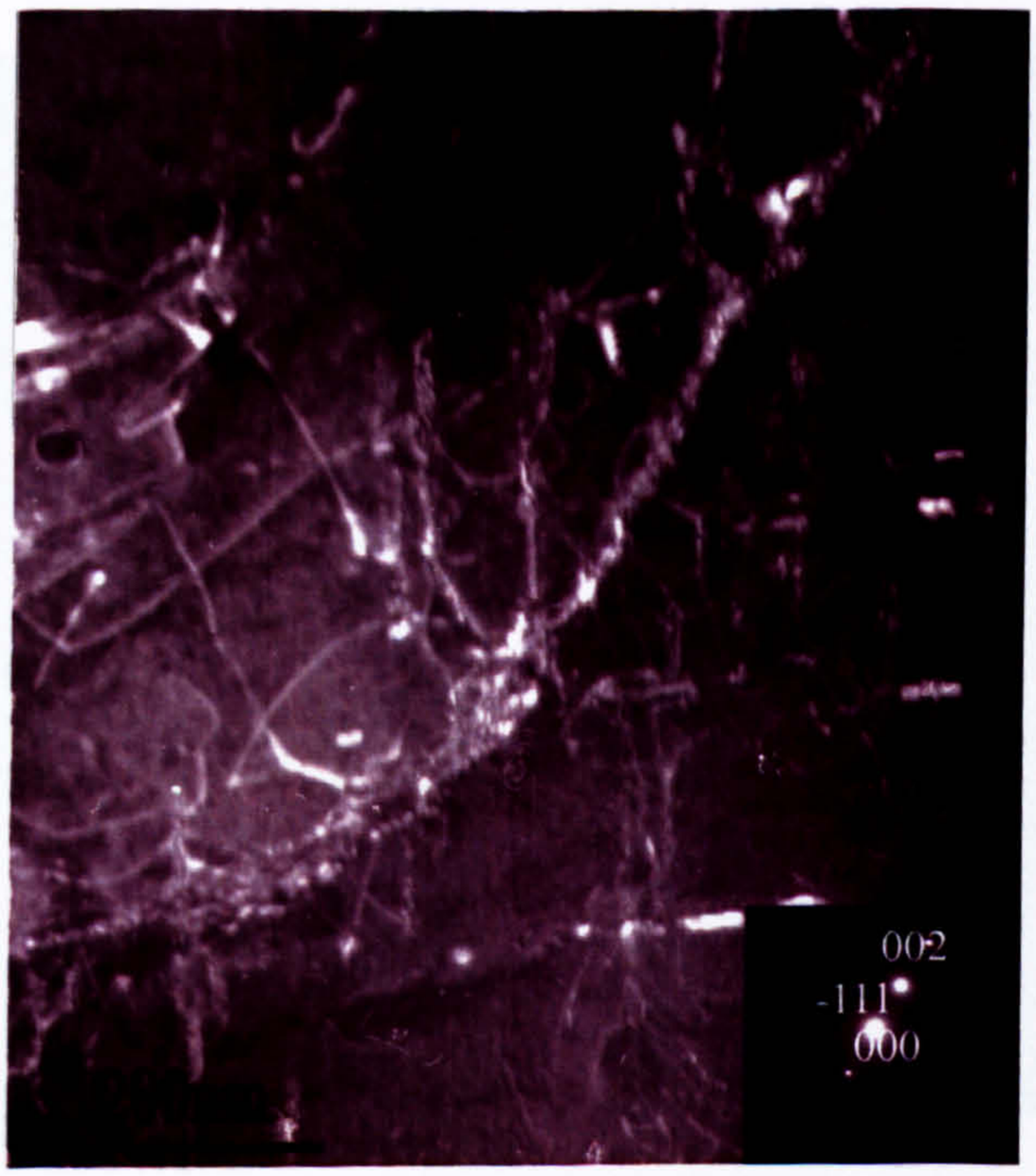

Fig. 5.75 TEM images after the 6 seconds delayed deformation, shows the precipitates formed in microband wall.

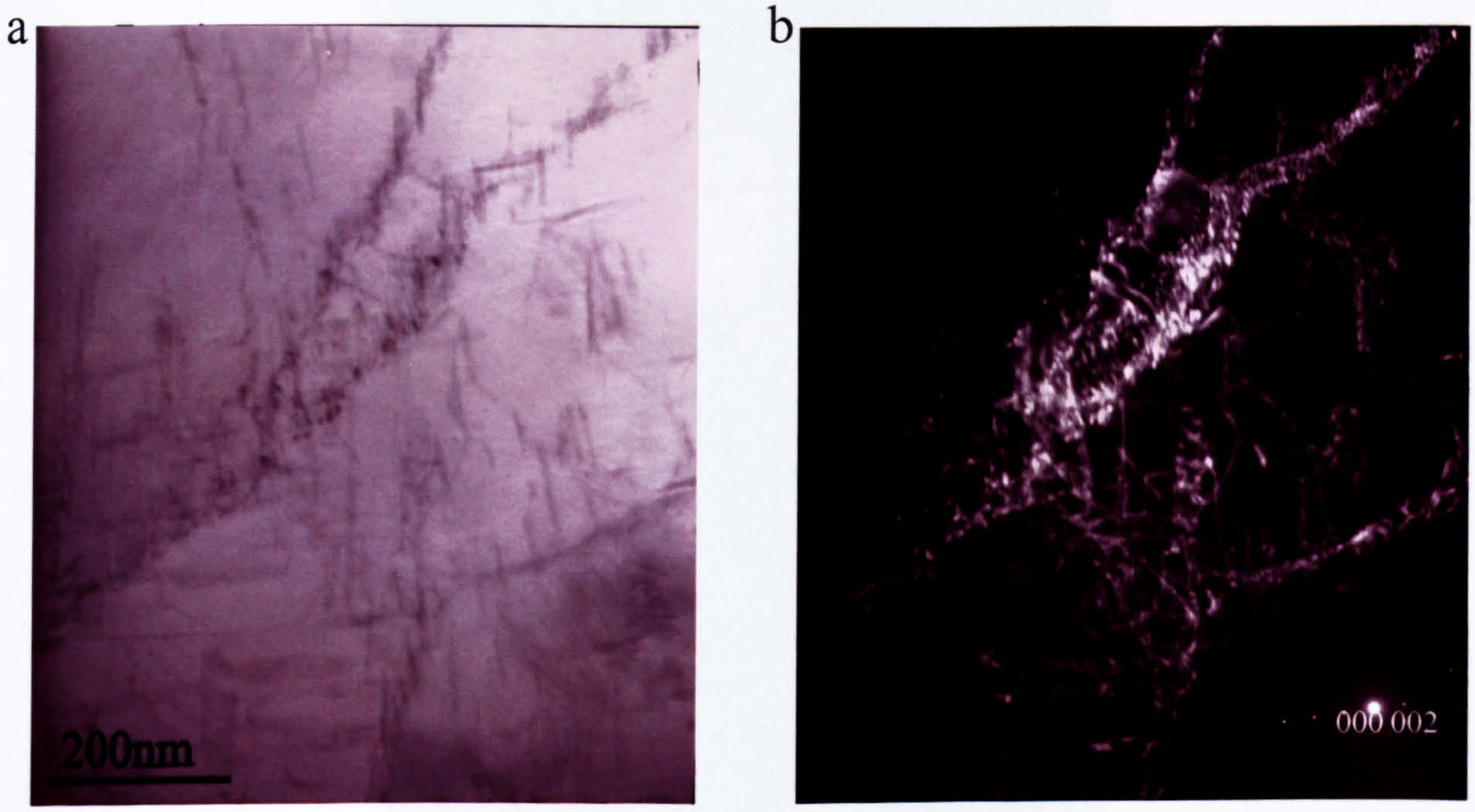

Fig. 5.76 TEM images after the 6 seconds delayed deformation, shows precipitates.

a

b

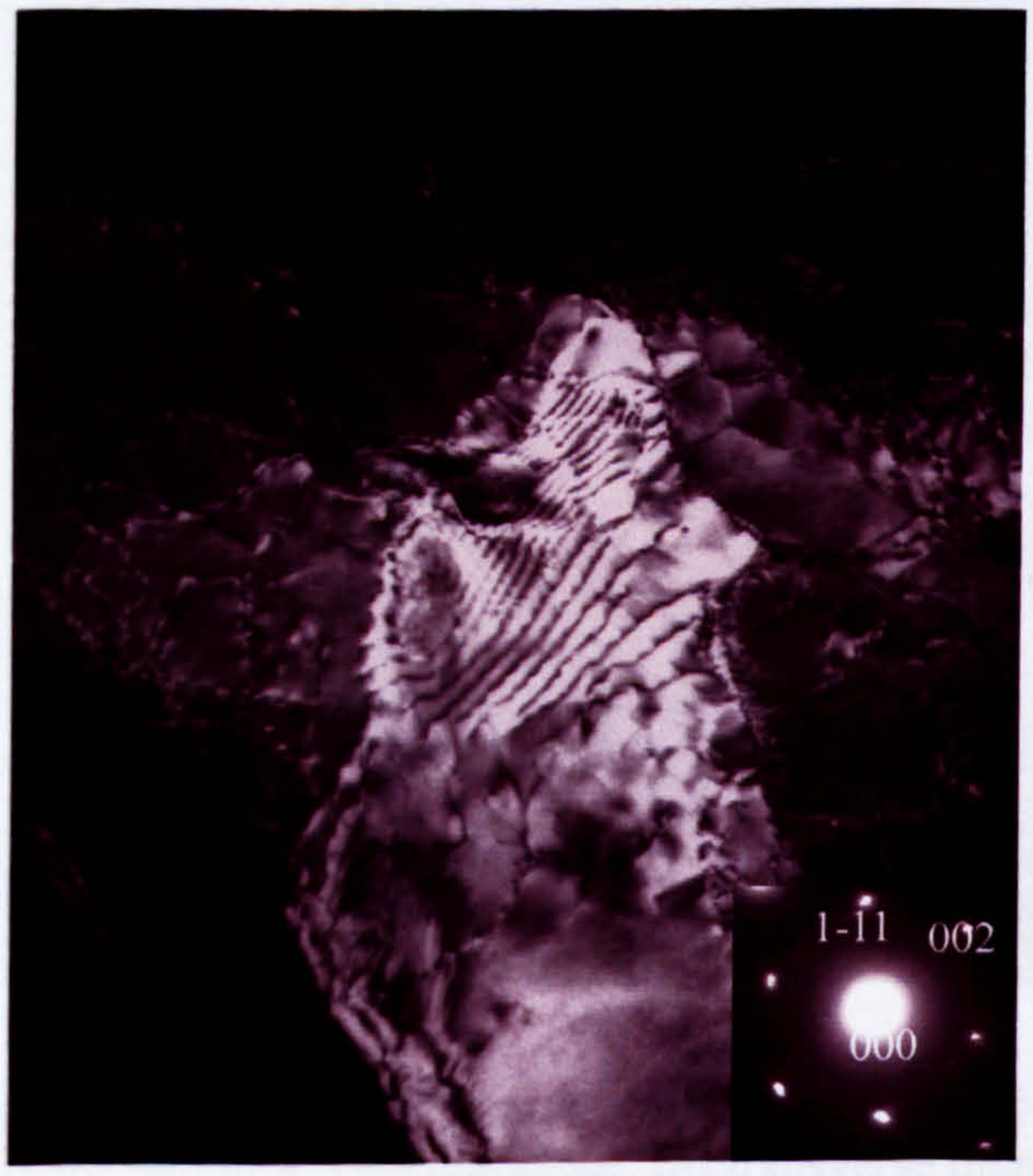

Fig. 5.77 TEM images after the 6 seconds delayed deformation, shows dislocation structure.

a

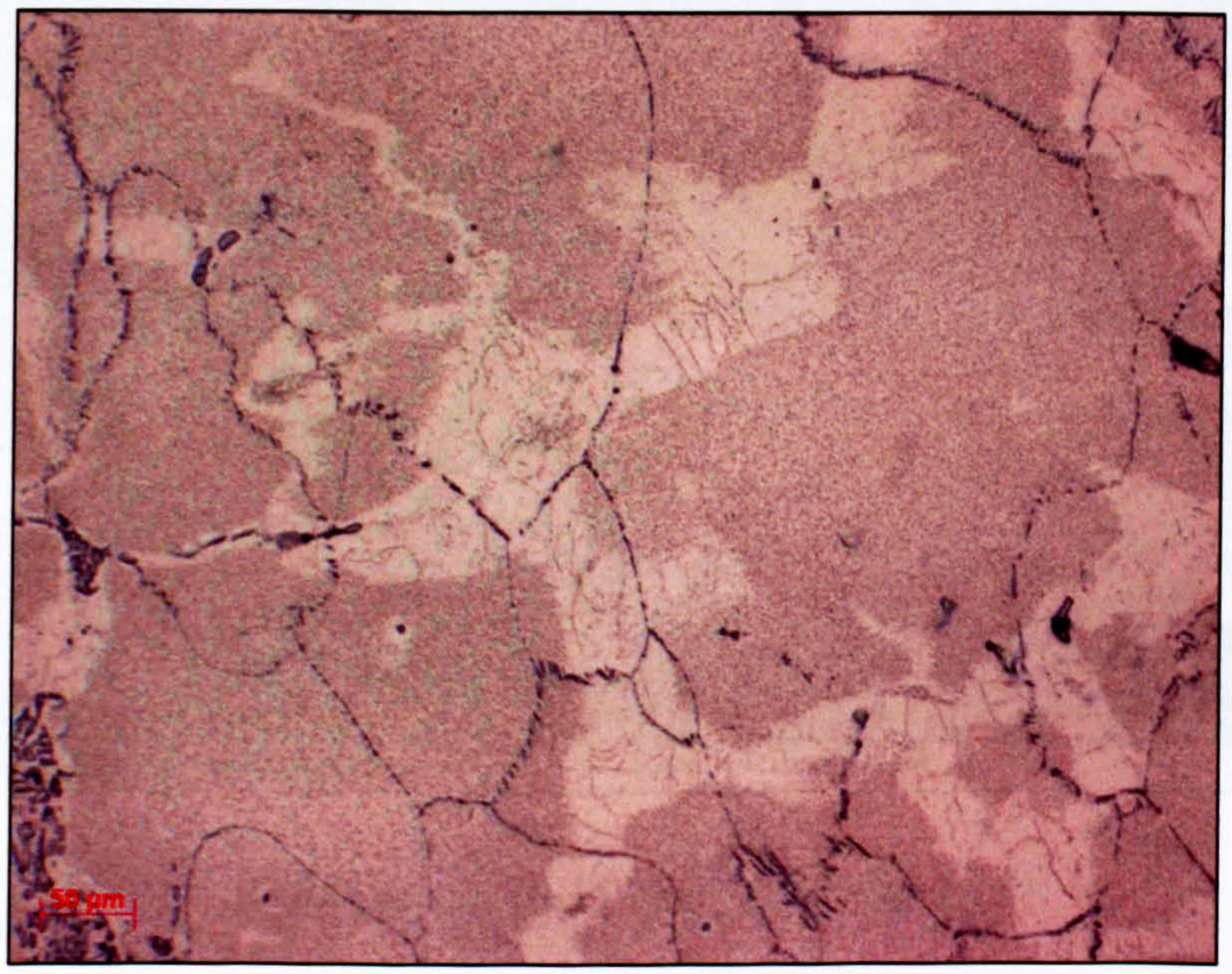

b

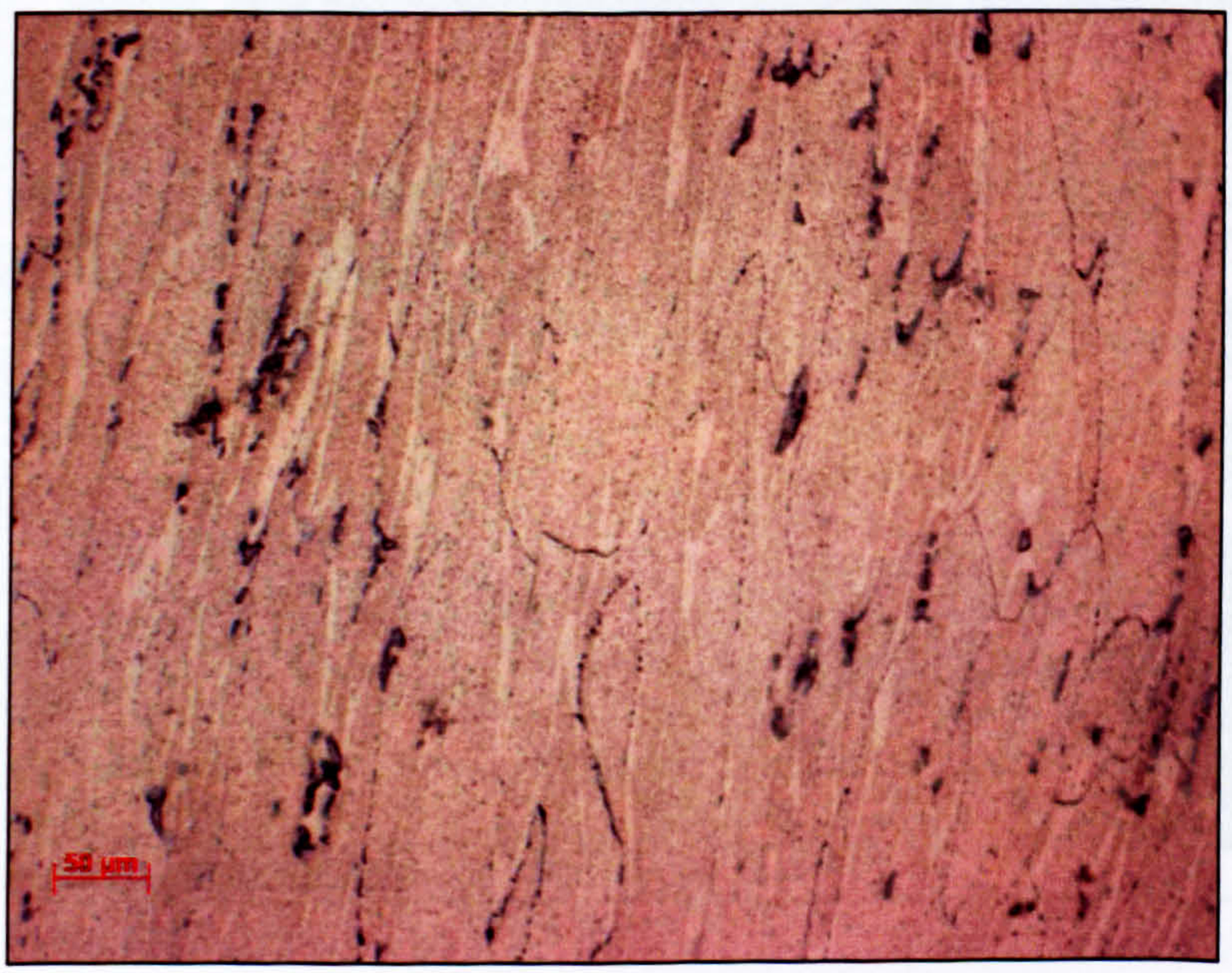

Fig. 5.78 Optical micrographs of deformed structure after the 60 seconds delayed deformation: (a) normal plane, (b) transverse plane.

a

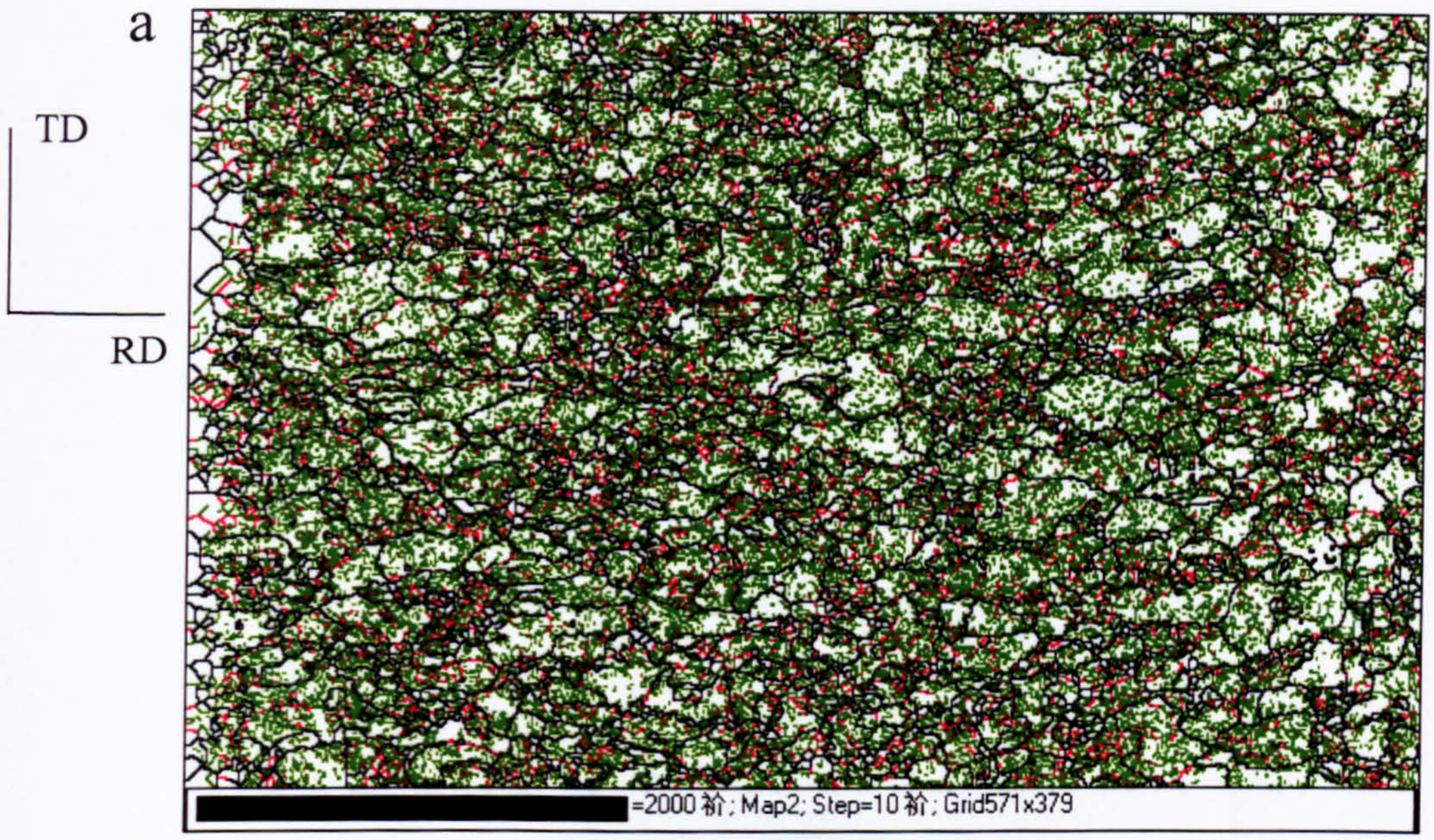

5-10°: green, 10-15°: red, >15°: black

b

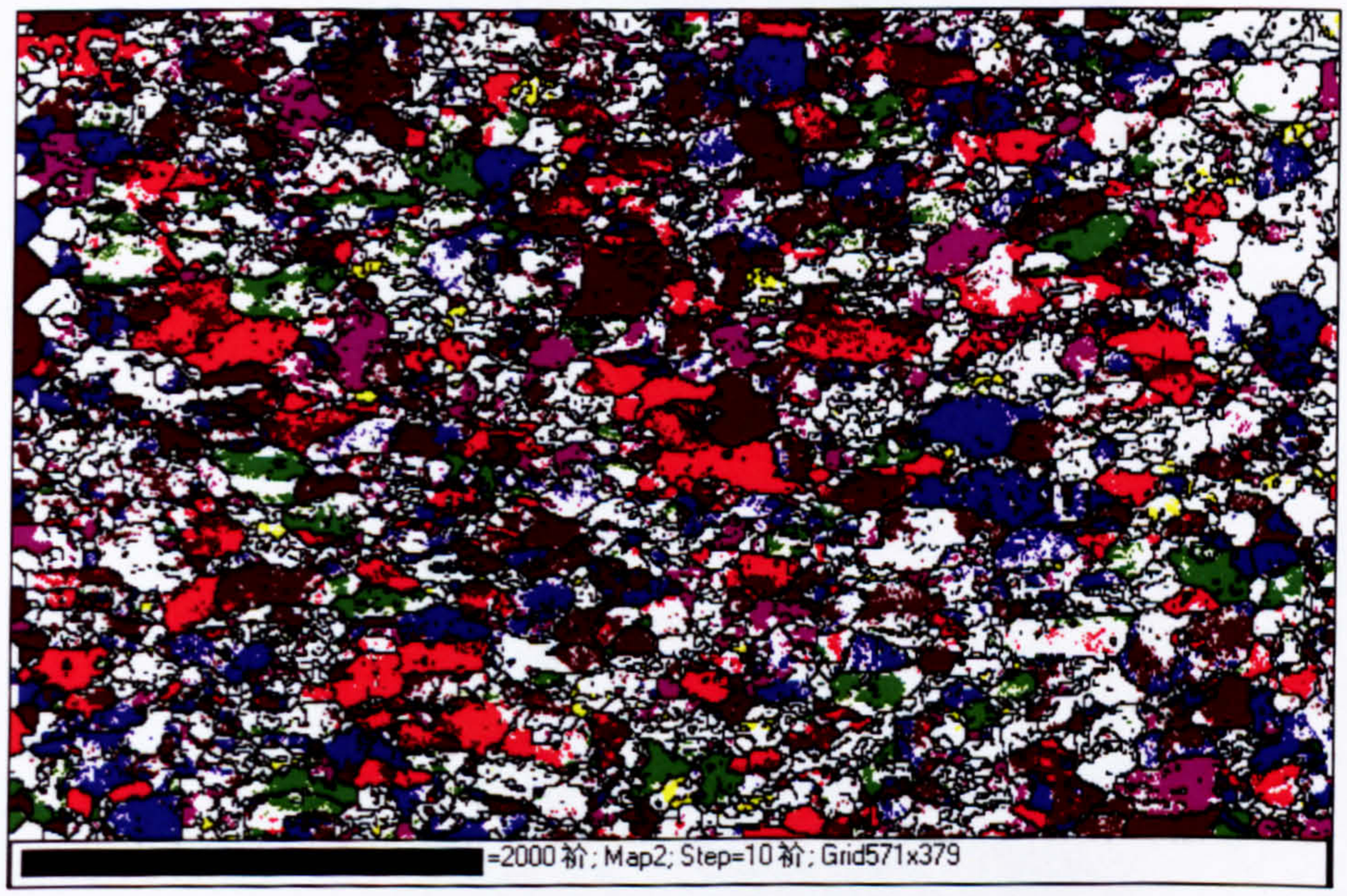

cube-yellow, p-purple, brass-red, copper-blue, goss-green, s-maroon

Fig. 5.79 (a) Orientation map and (b) texture components to the microstructure for the 60 seconds delayed sample.

a

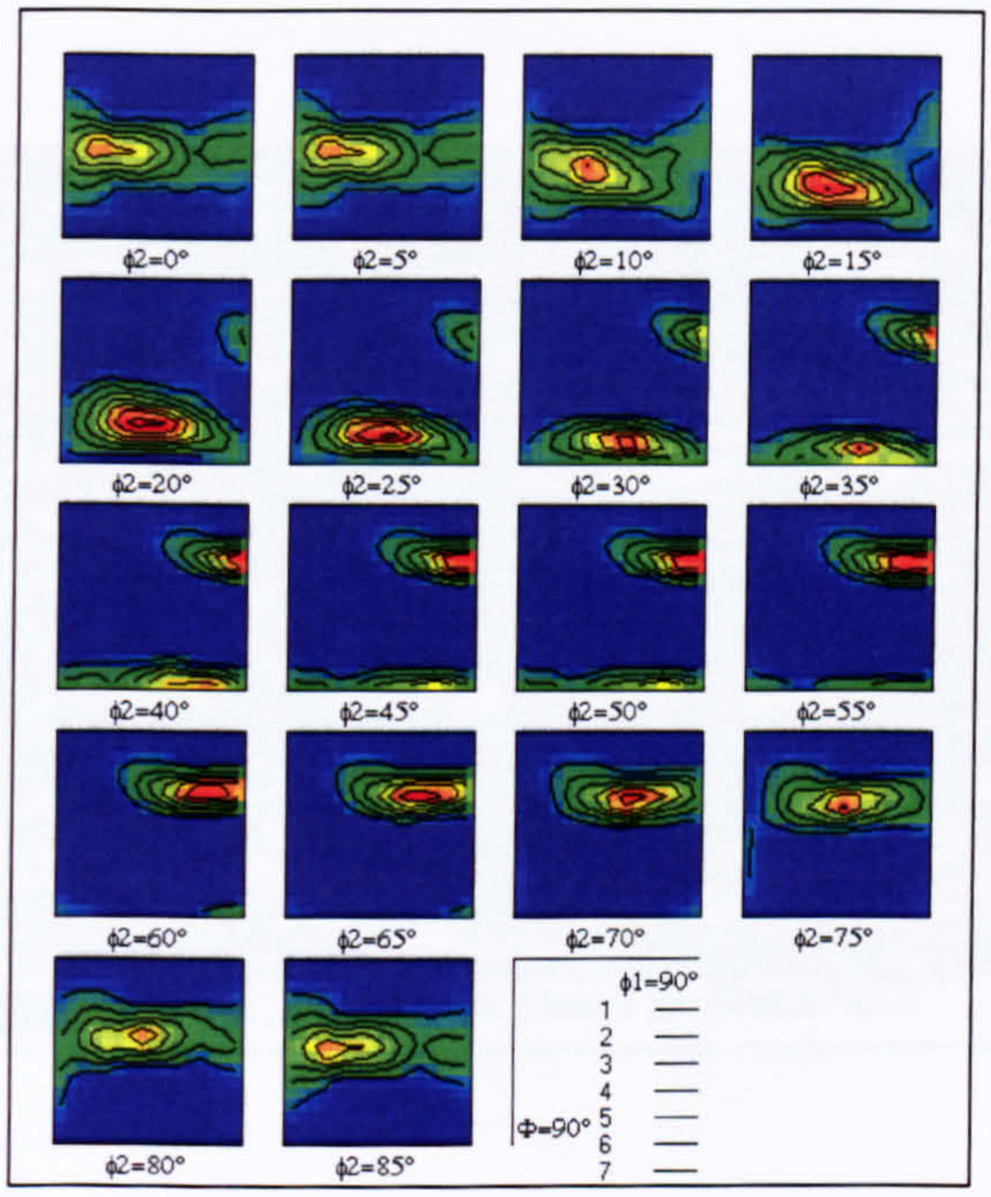

b

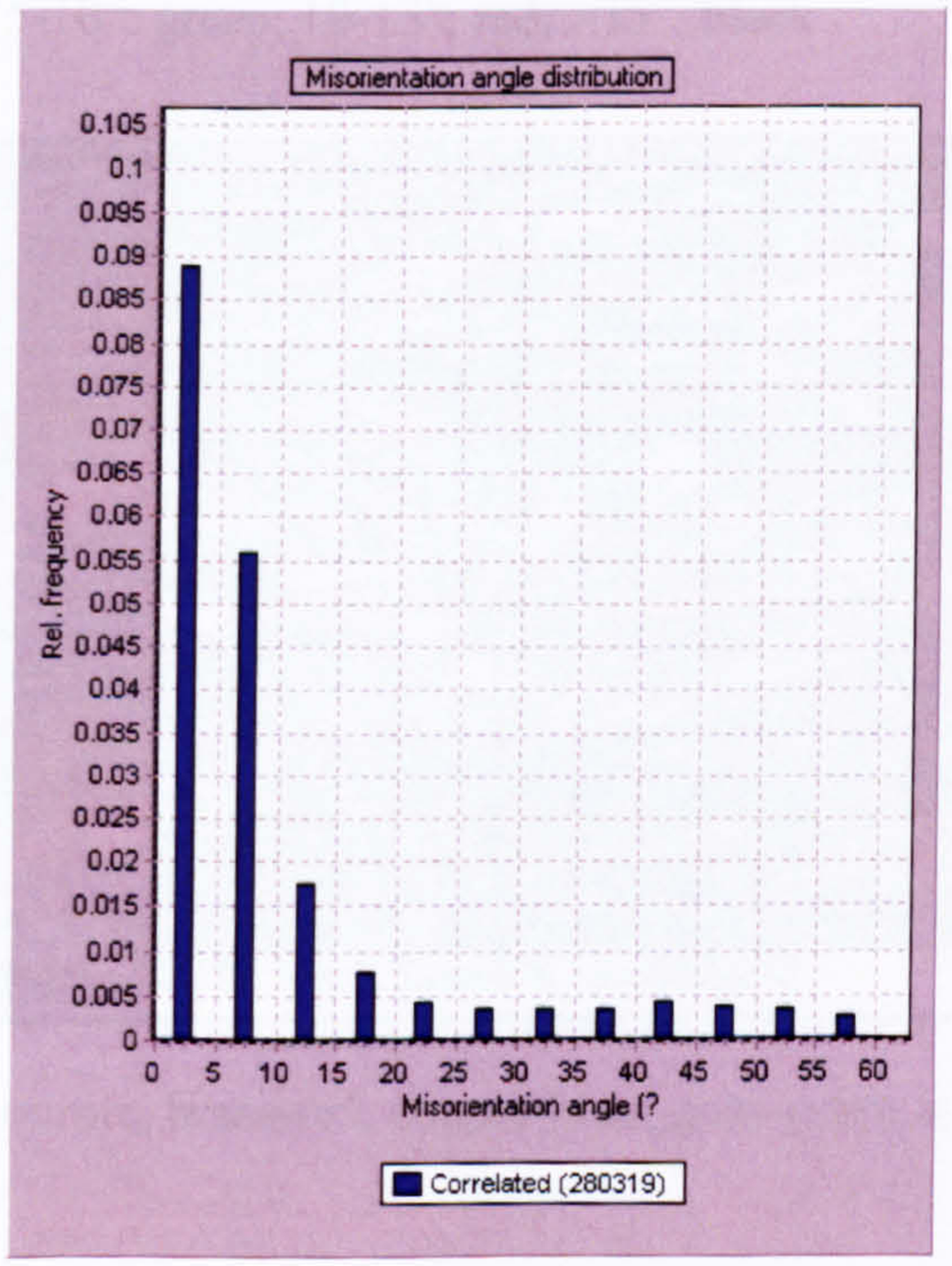

Fig. 5.80 EBSD results of the 60 seocnds delayed sample: (a) orientation distribution functions (ODF) maps, (b) misorientation angle distribution.

a

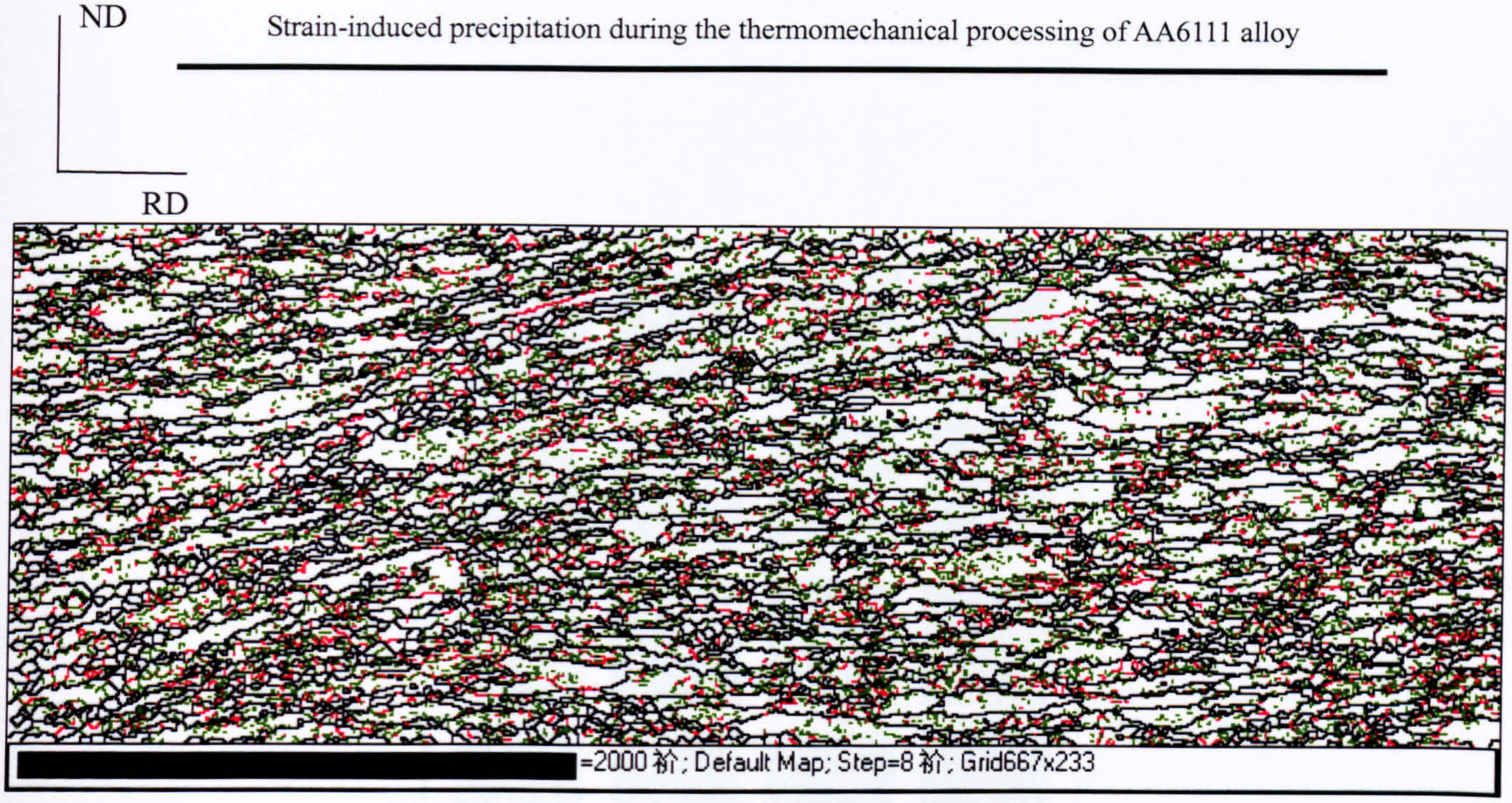

5-10°: green, 10-15°: red, >15°: black

b

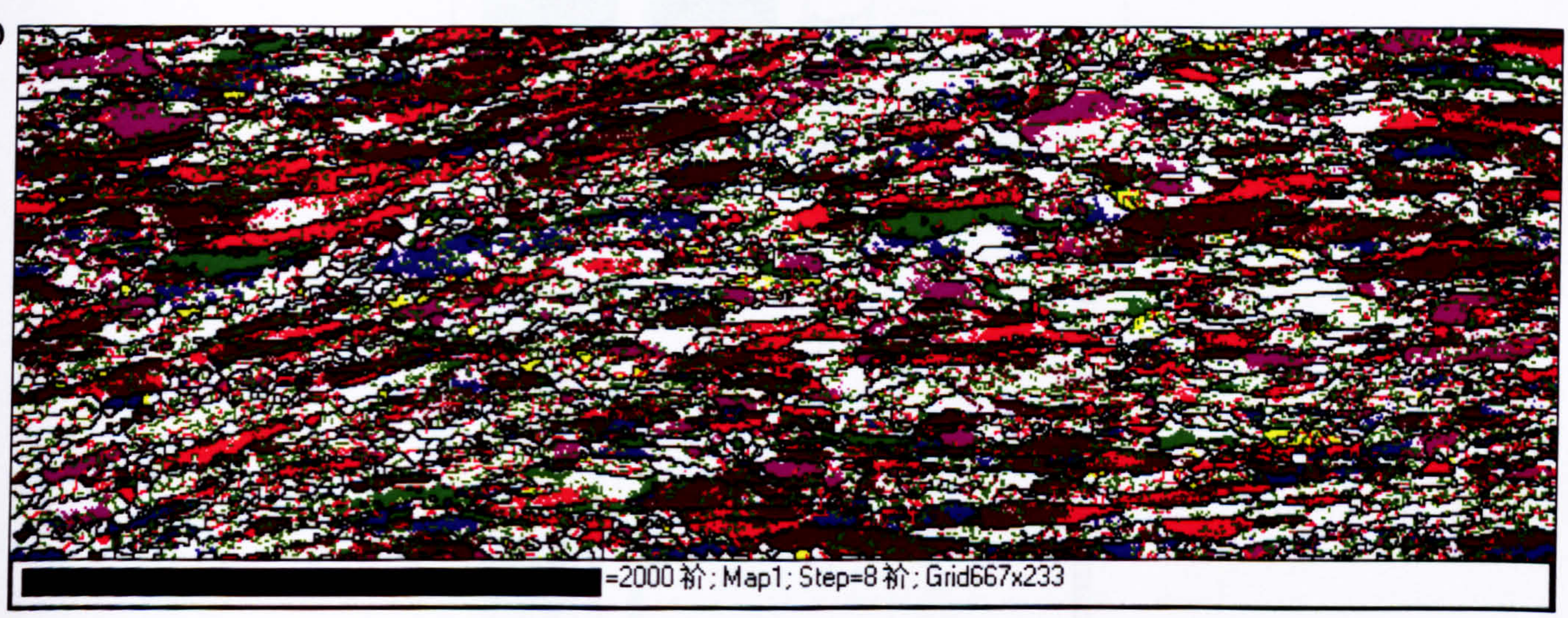

cube-yellow, p-purple, brass-red, copper-blue, goss-green, s-maroon

Fig. 5.81 (a) Orientation map and (b) texture components to the microstructure for the 60 seconds delayed sample.

a

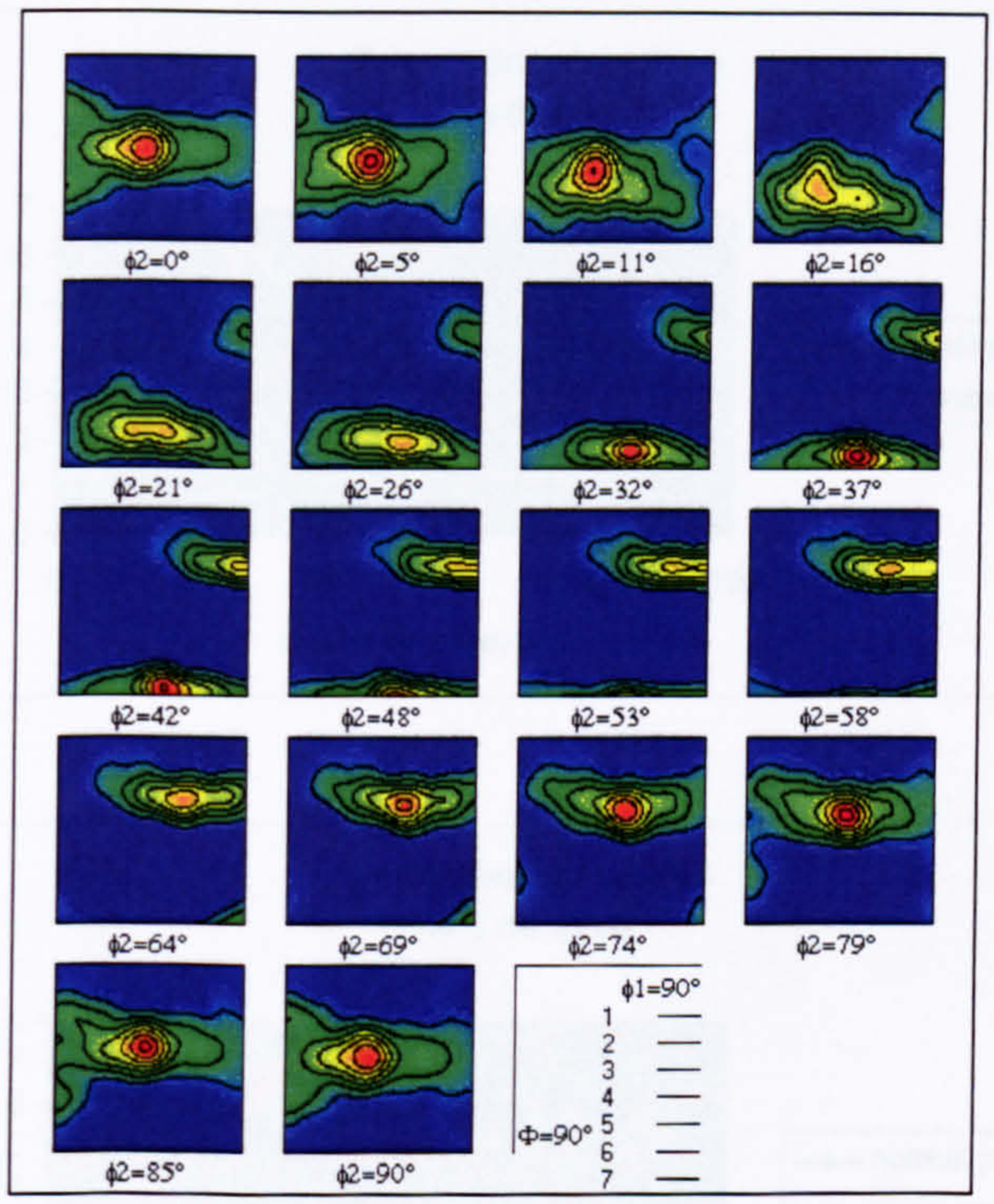

b

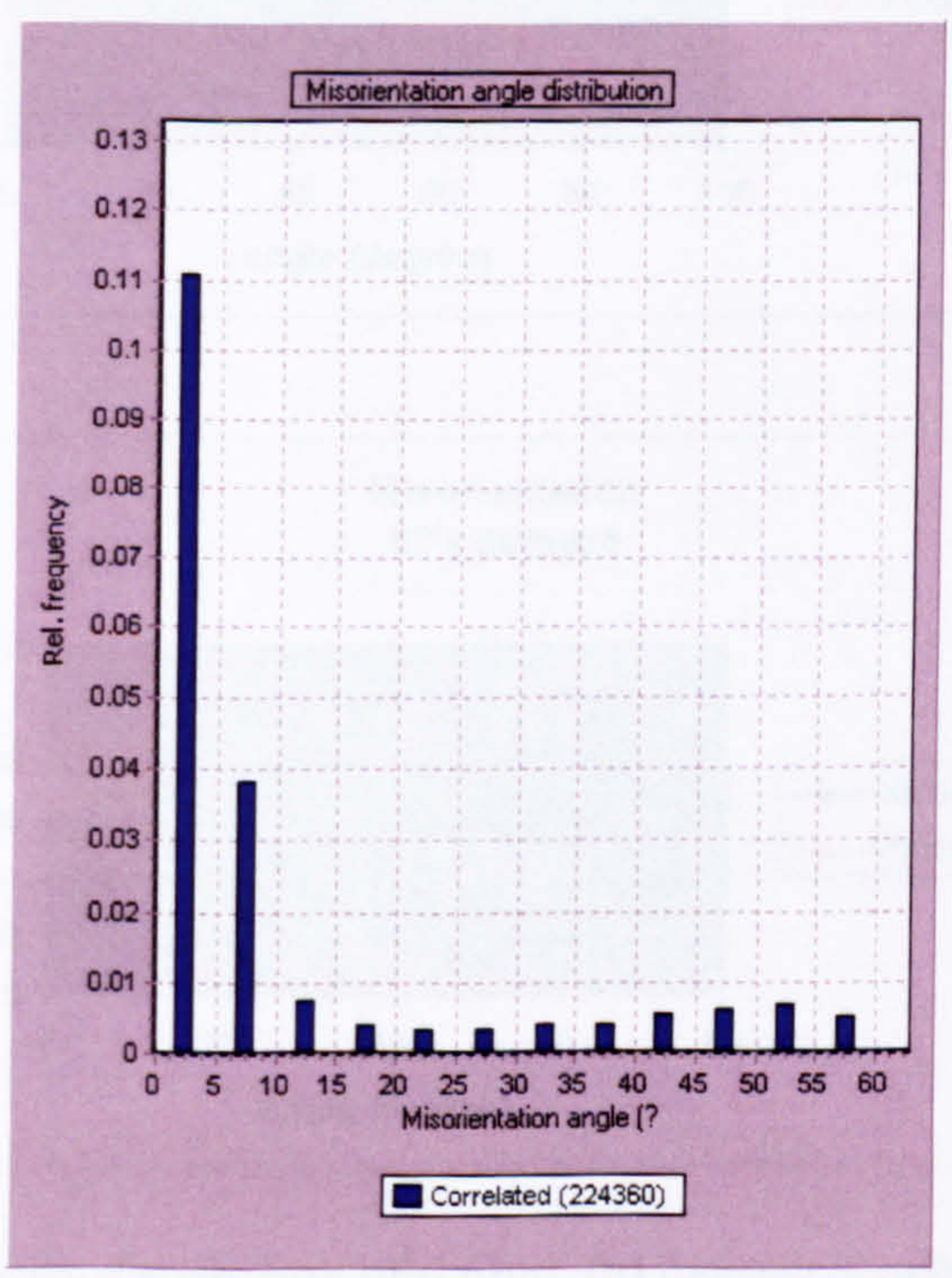

Fig. 5.82 EBSD results of the 60 seconds delayed sample: (a) orientation distribution functions (ODF) maps, (b) misorientation angle distribution.

a

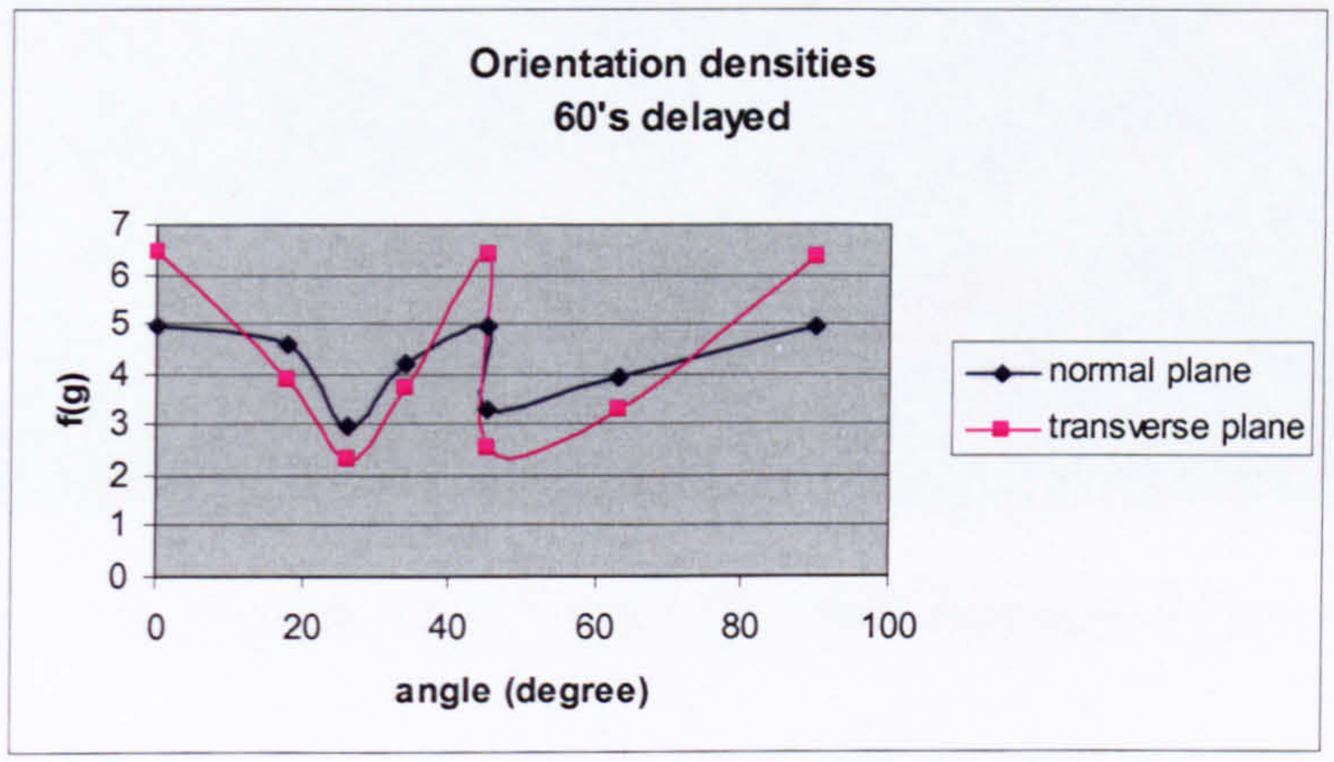

b

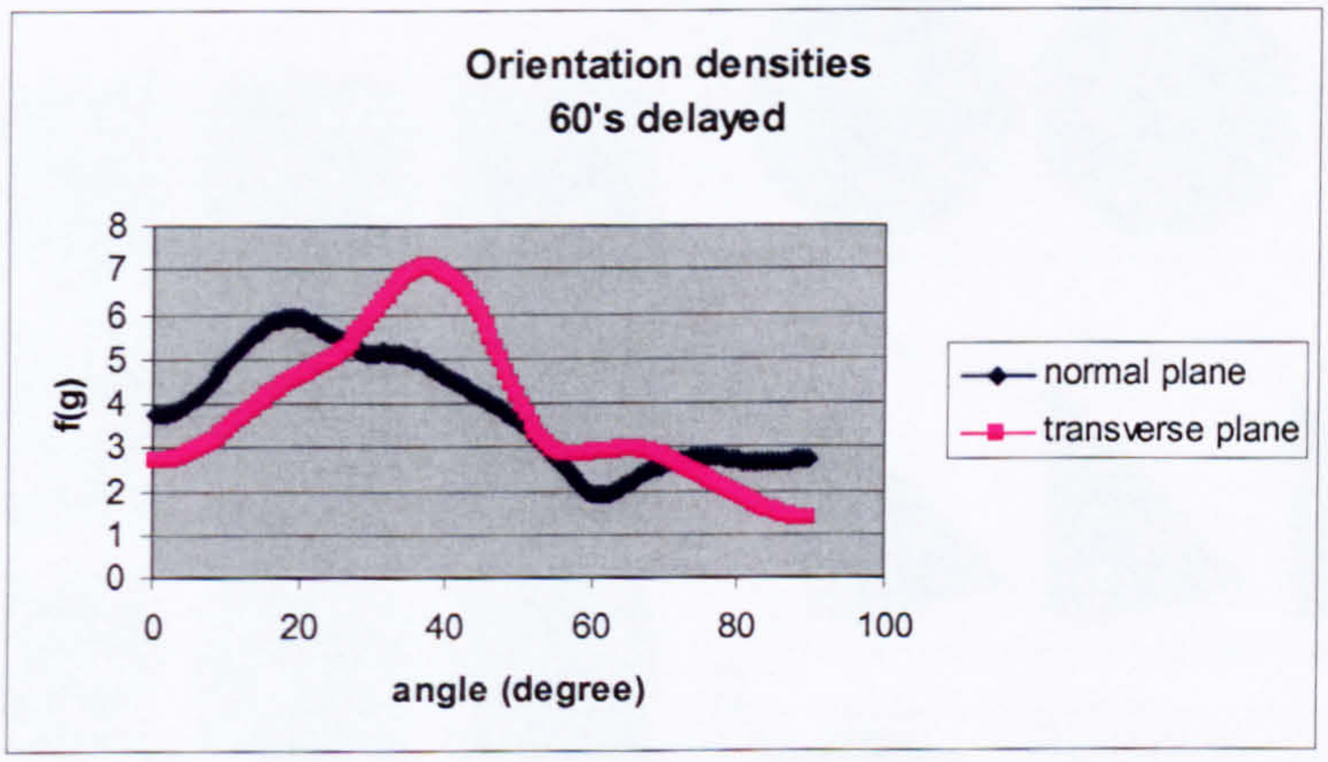

C

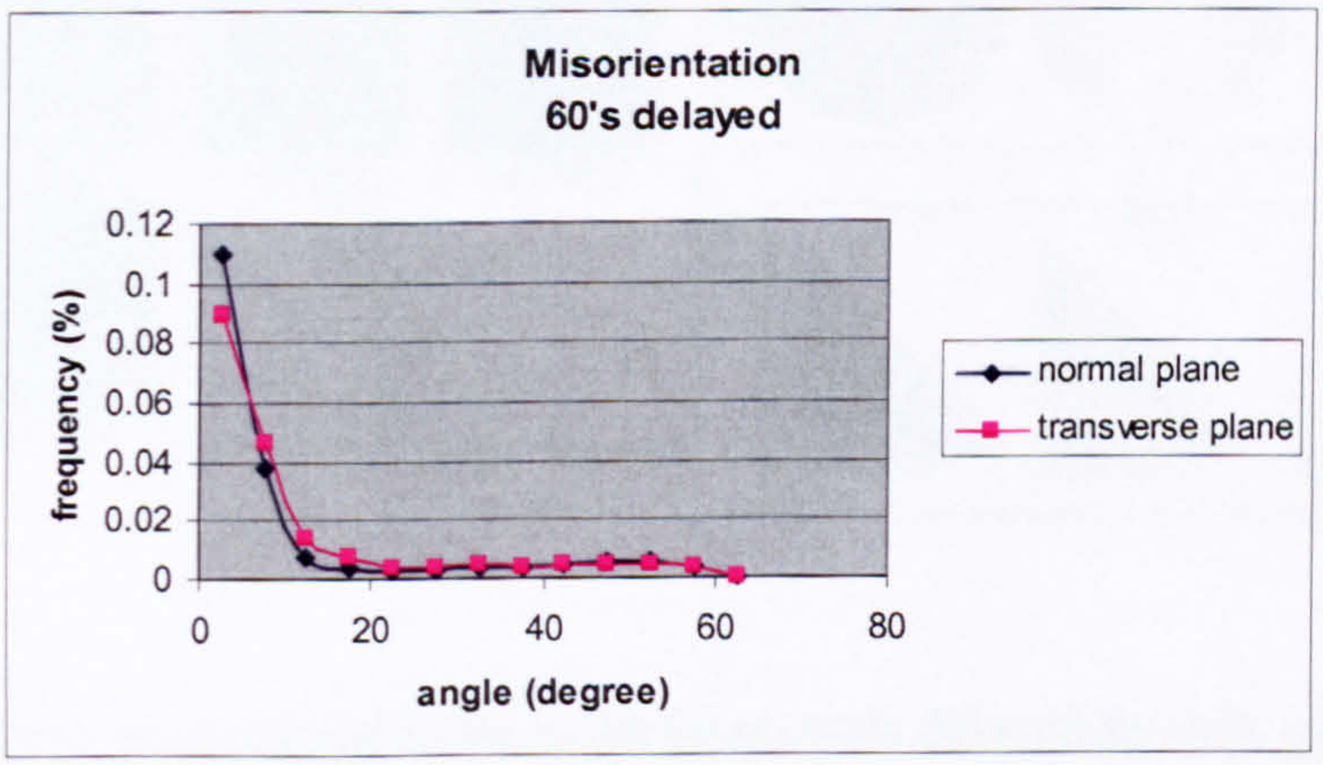

Fig. 5.83 (a) Density distribution of β fibre, (b) density distribution of α fibre, (c) misorientaiton distribution for the 60 seconds delayed sample.

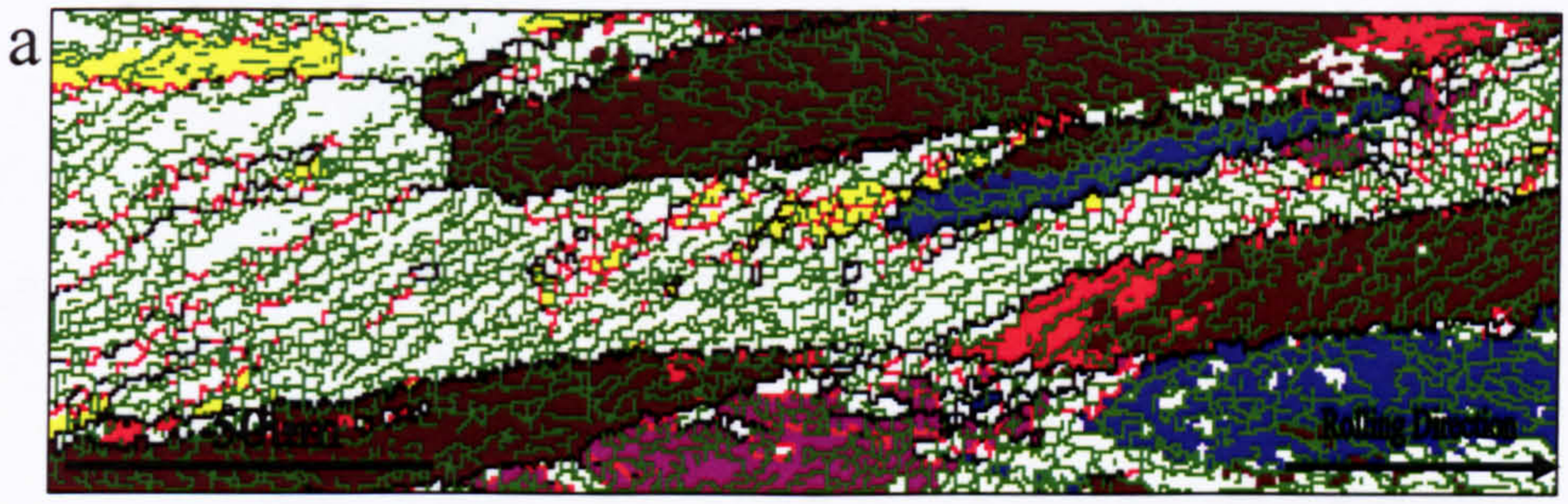

2-10°: green, 10-15°: red, >15°: black Step size=0.5μm

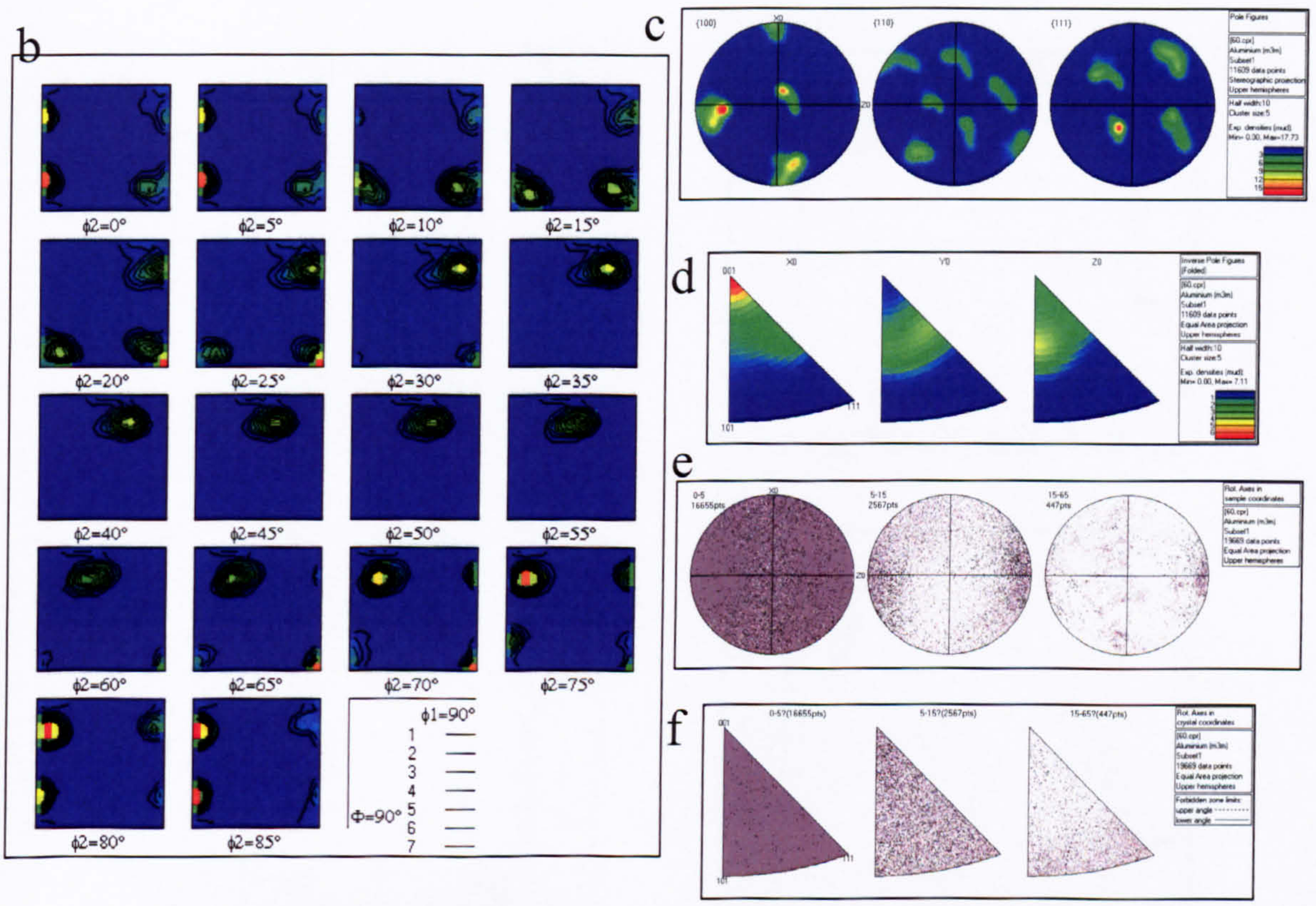

Fig. 5.84 Random-orientated grain in the 60 seconds delayed sample: (a) texture and boundary map, (b) ODF, (c) pole figures, (d) inverse pole figures, the distribution of misorientation axis vectors in (e) sample and (f) crystal lattice coordinates.

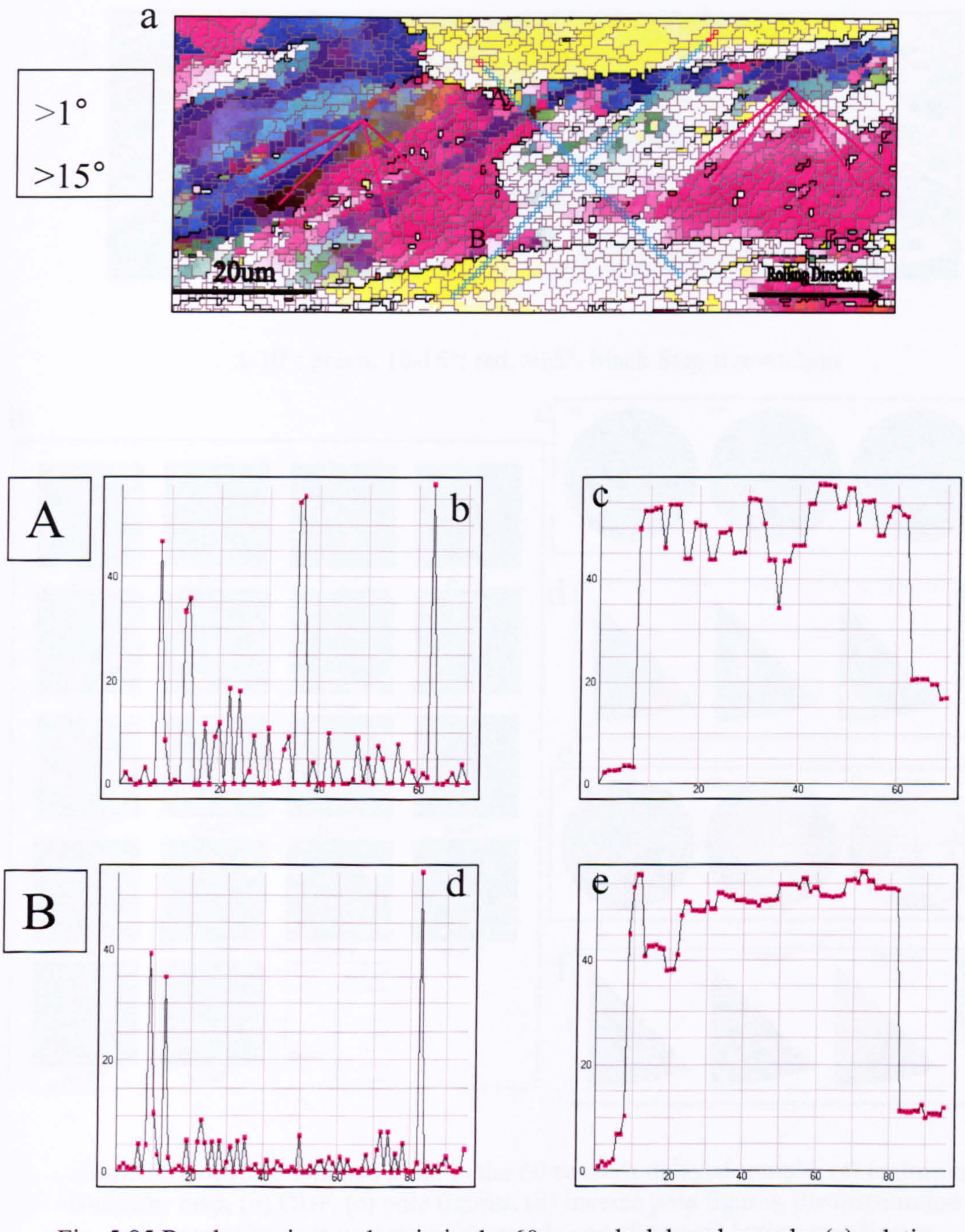

Fig. 5.85 Random-orientated grain in the 60 seconds delayed sample: (a) relative map, (b (d) relative and (c) (e) cumulative misorientation distributions of line scans performed along A and B in (a).

a

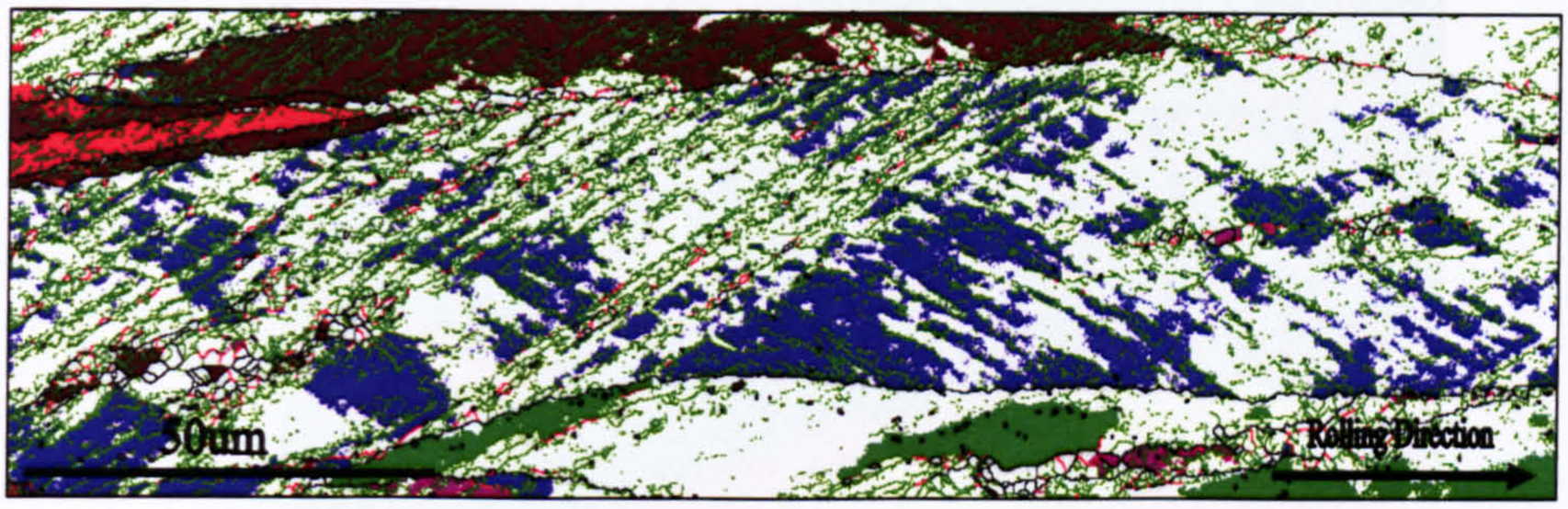

5-10°: green, 10-15°: red, >15°: black Step size=0.2μm

b

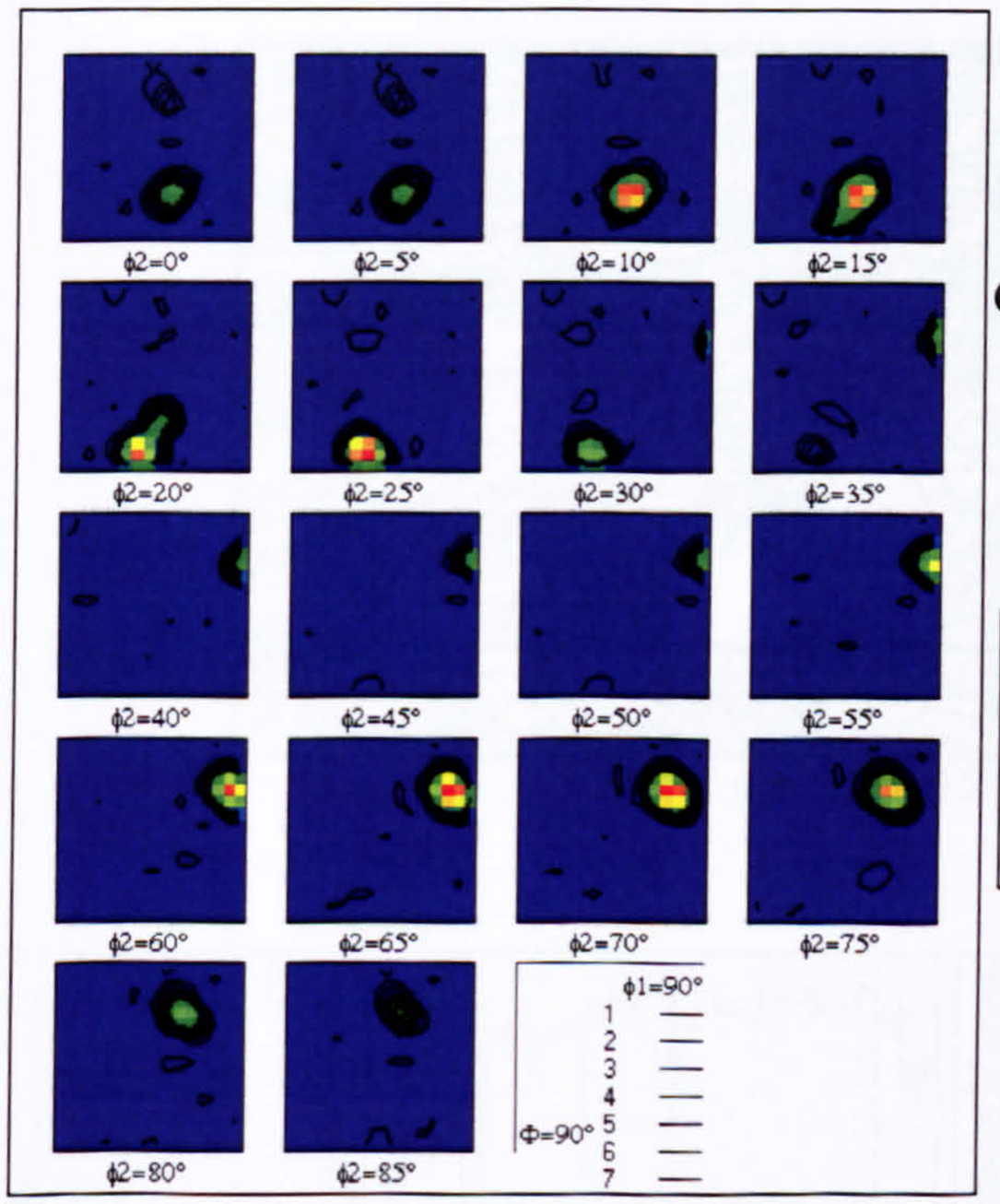

c

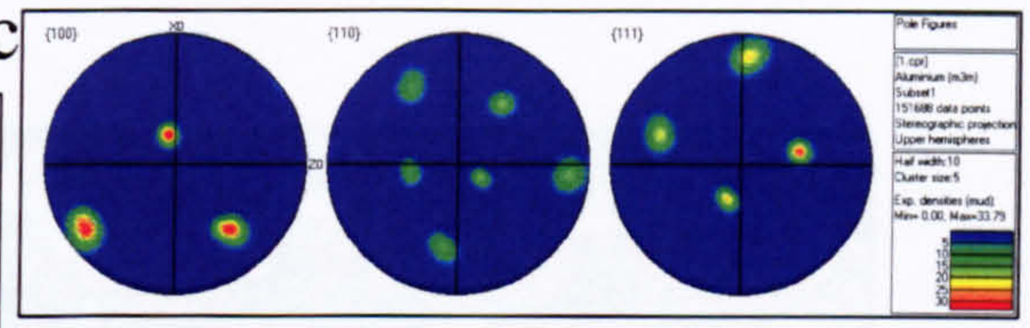

d

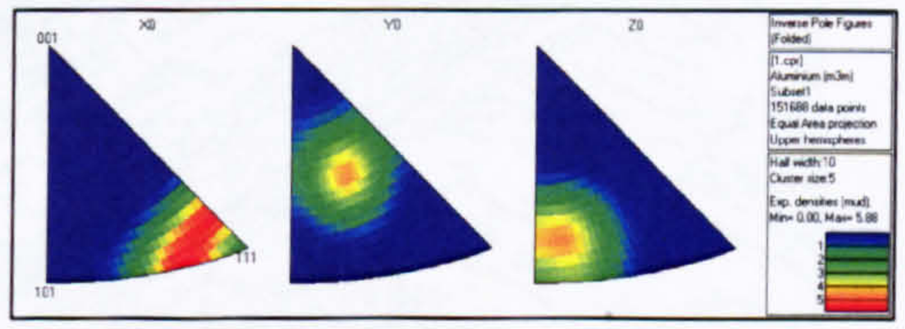

e

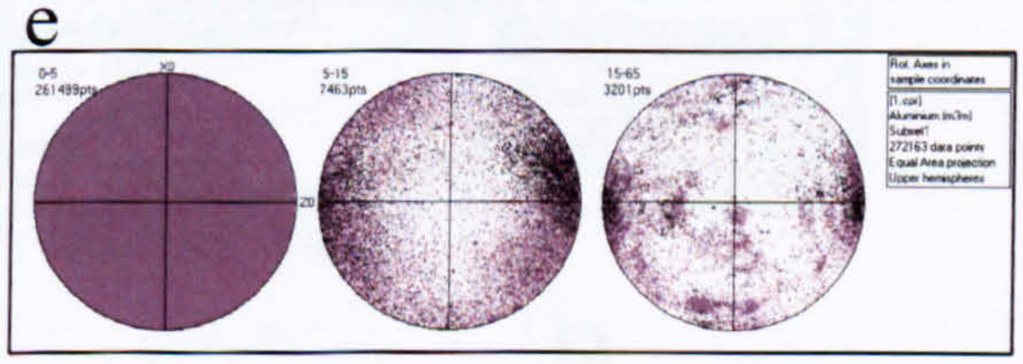

f

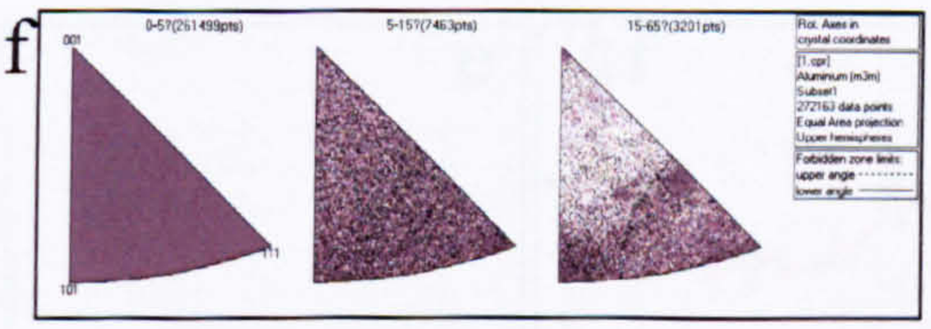

Fig. 5.86 Copper-orientated grain in the 60 seconds delayed sample: (a) texture and boundary map, (b) ODF, (c) pole figures, (d) inverse pole figures, the distribution of misorientation axis vectors in (e) sample and (f) crystal lattice coordinates.

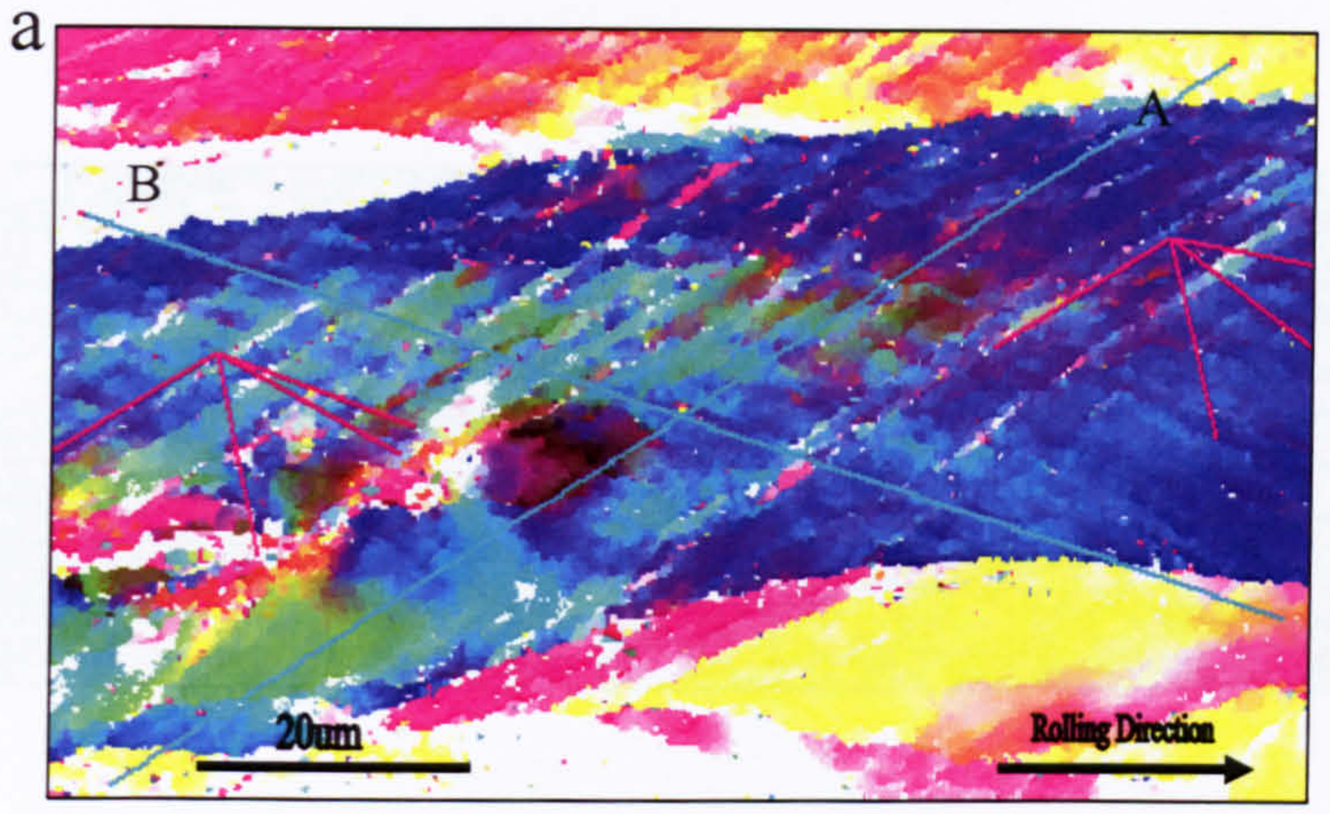

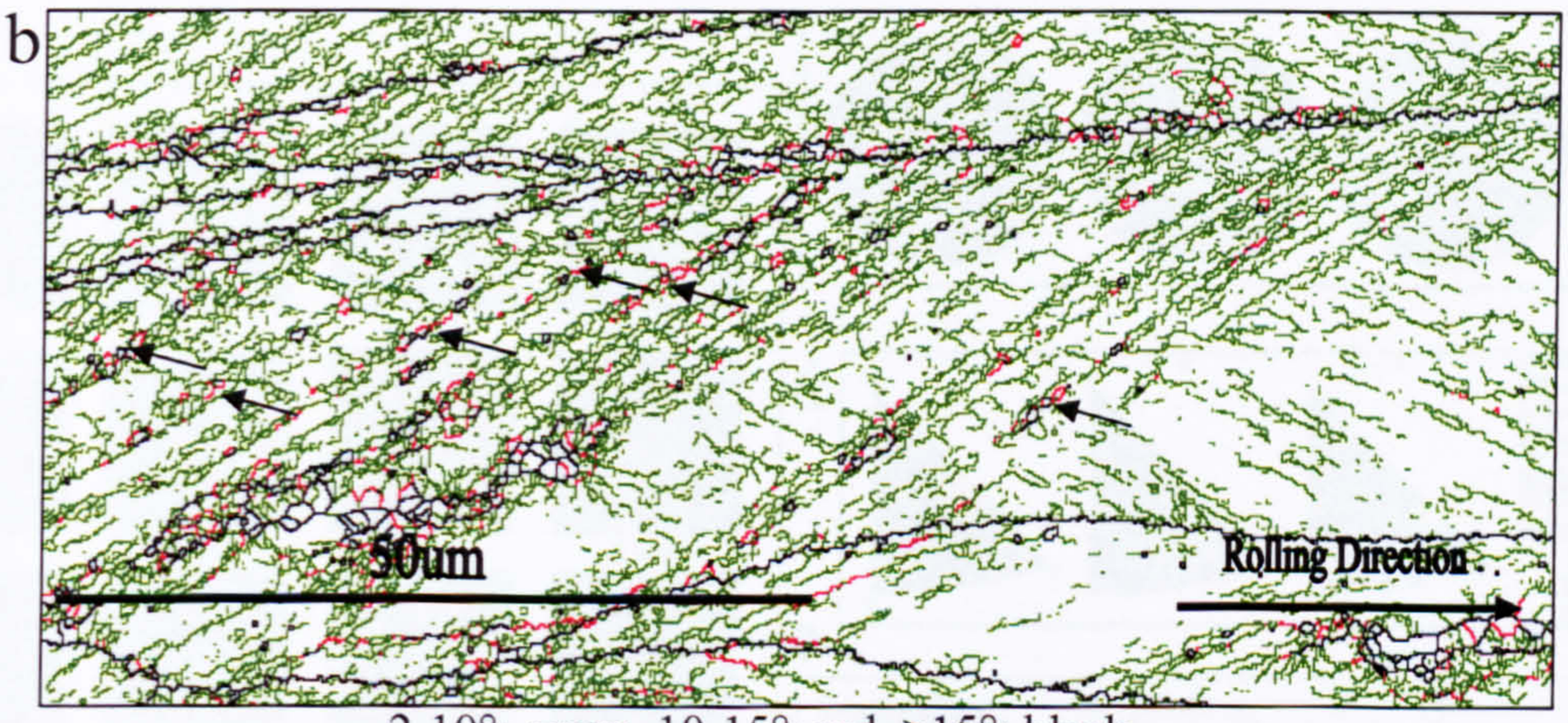

2-10°: green, 10-15°: red, >15°: black

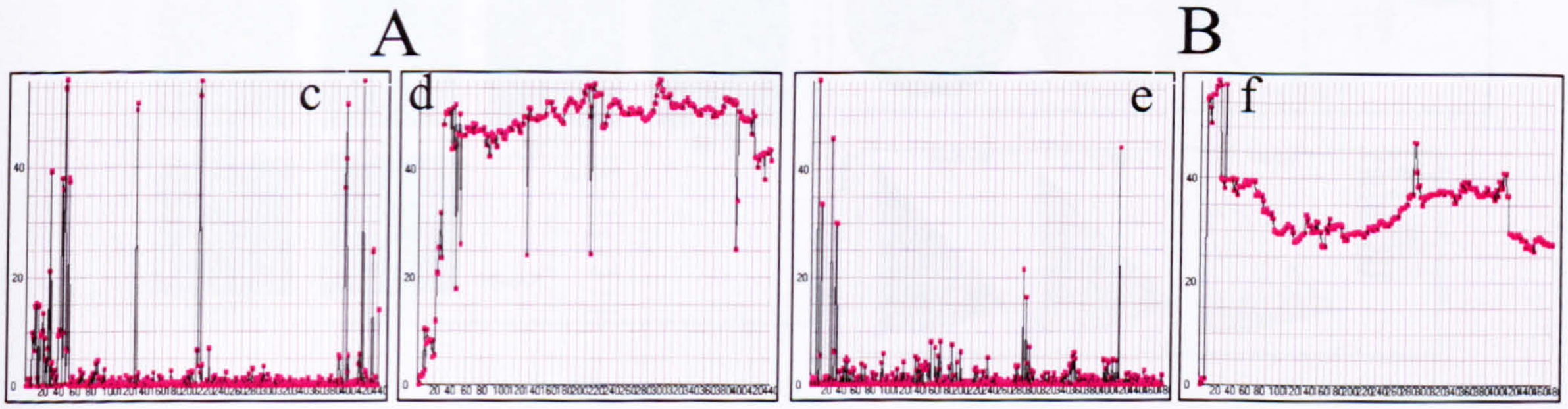

Fig. 5.87 Copper-orientated grain in the 60 seconds delayed sample: (a) relative map, (b) orientation map. (c) (e) relative and (d) (f) cumulative misorientation distributions of line scans performed along A and B in (a).

a

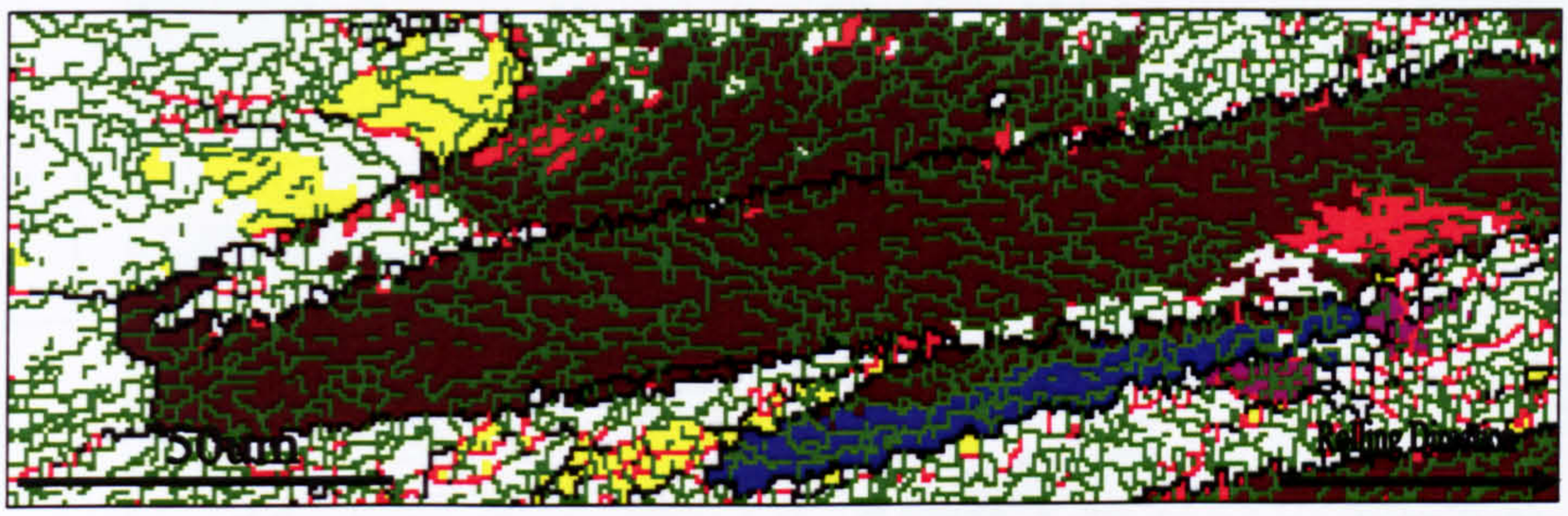

2-10°: green, 10-15°: red, >15°: black Step size=0.5μm

b

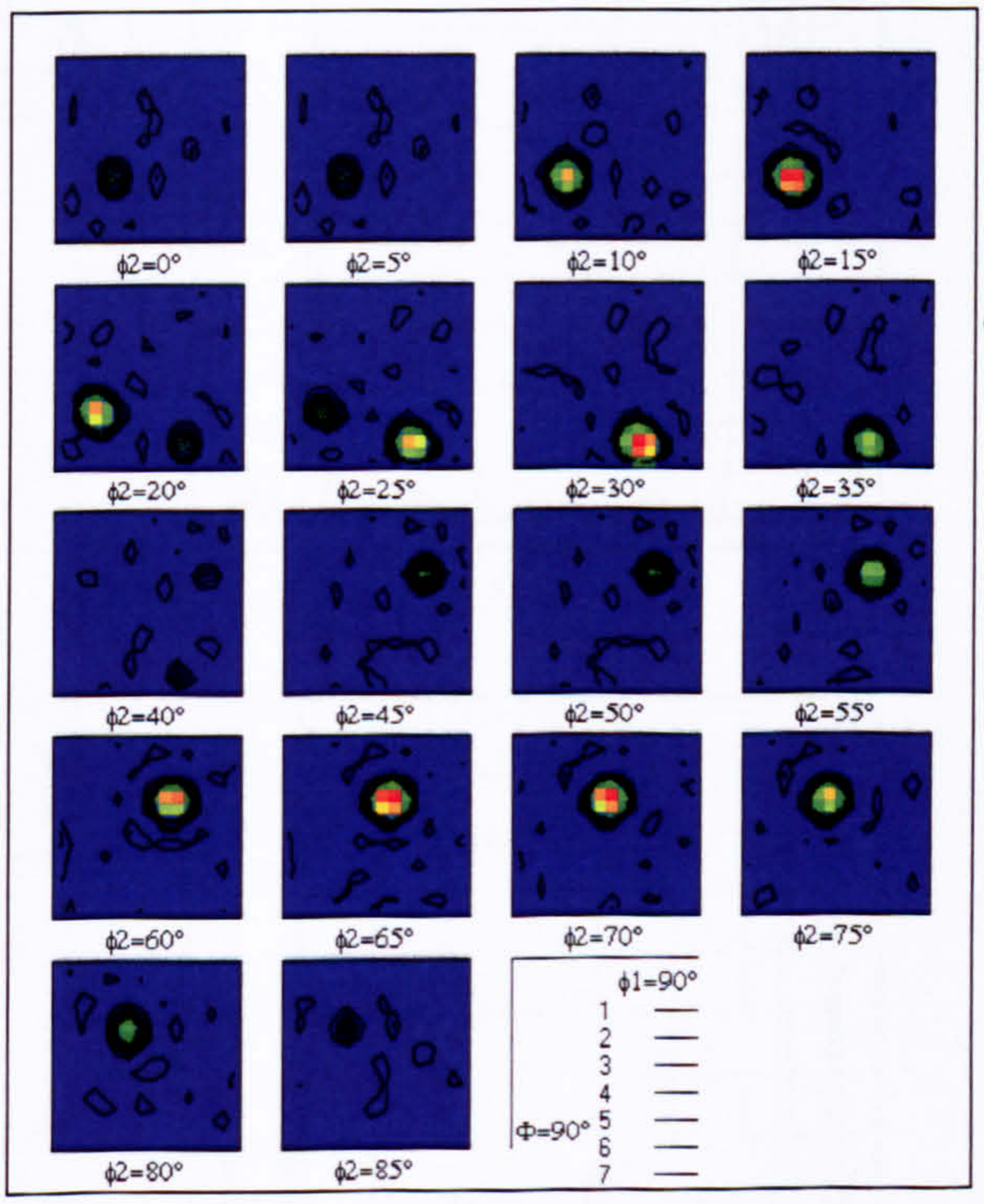

c

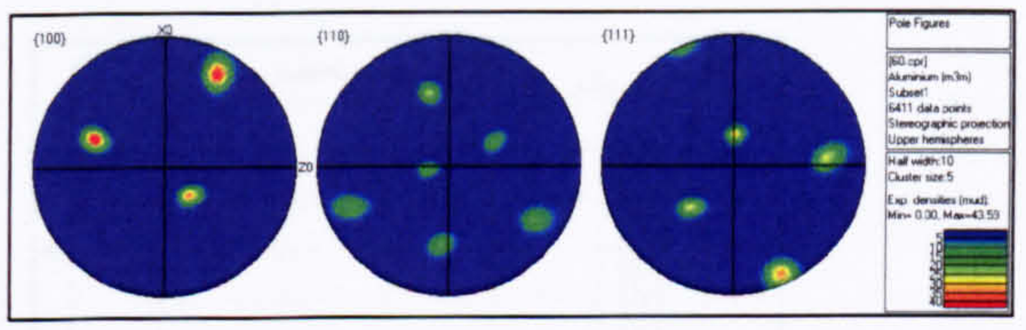

d

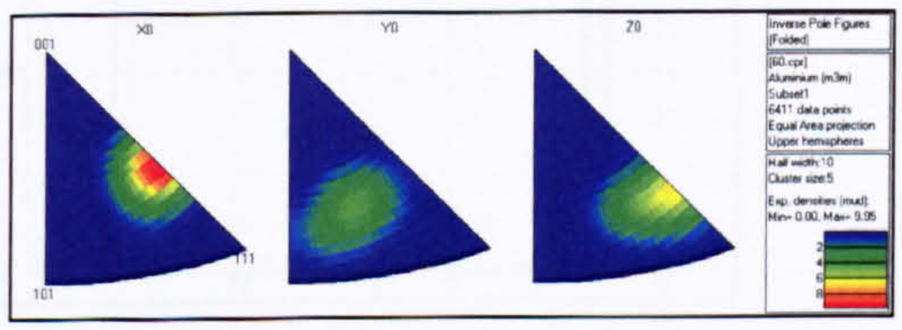

e

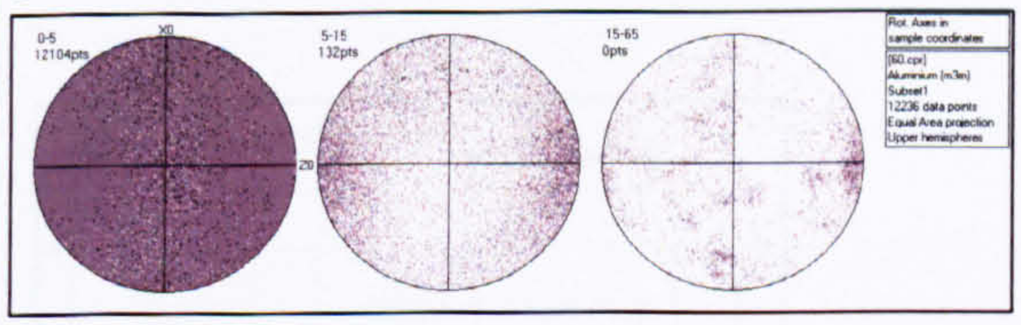

f

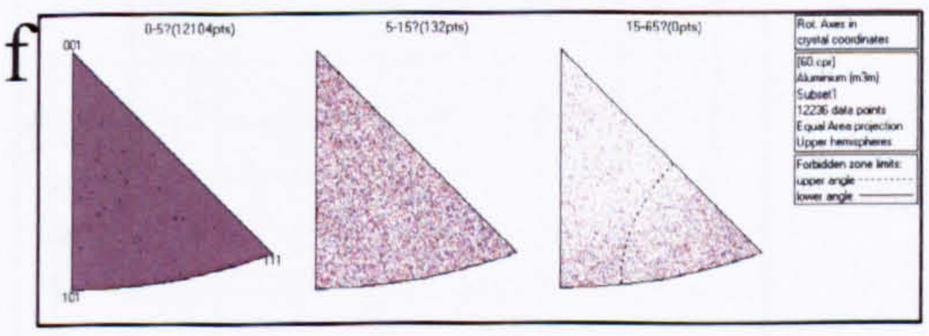

Fig. 5.88 S-orientated grain in the 60 seconds delayed sample: (a) texture and boundary map, (b) ODF, (c) pole figures, (d) inverse pole figures, the distribution of misorientation axis vectors in (e) sample and (f) crystal lattice coordinates.

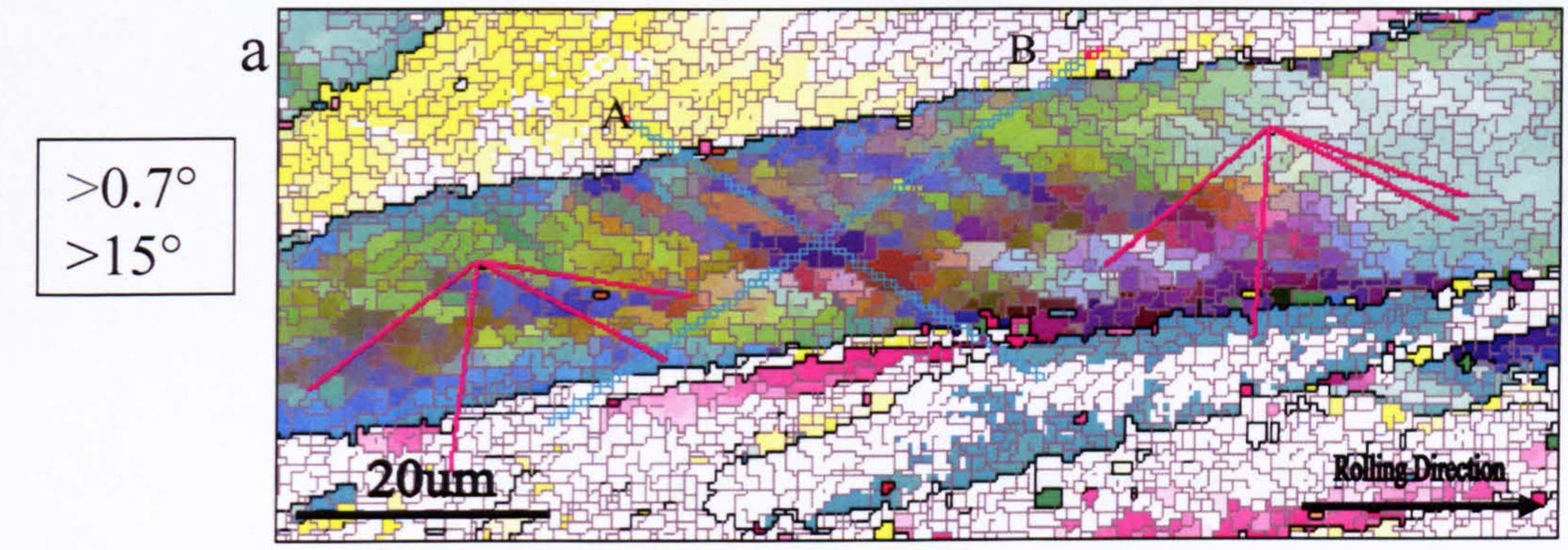

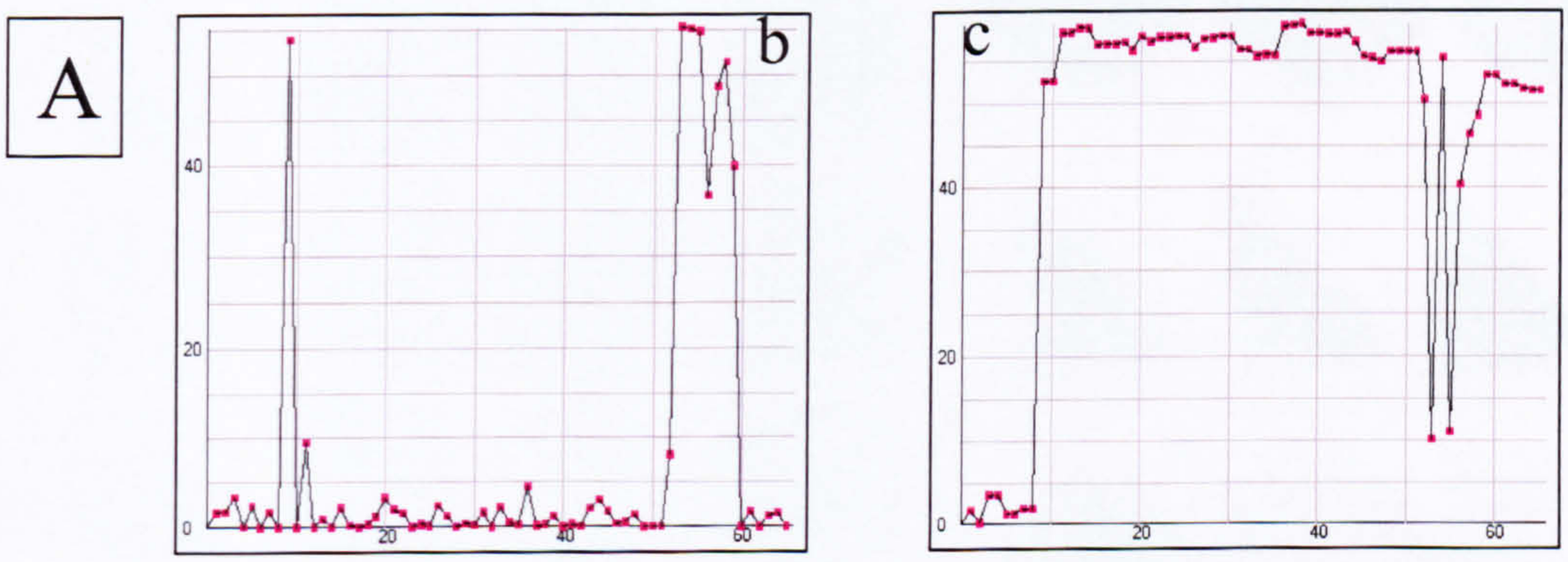

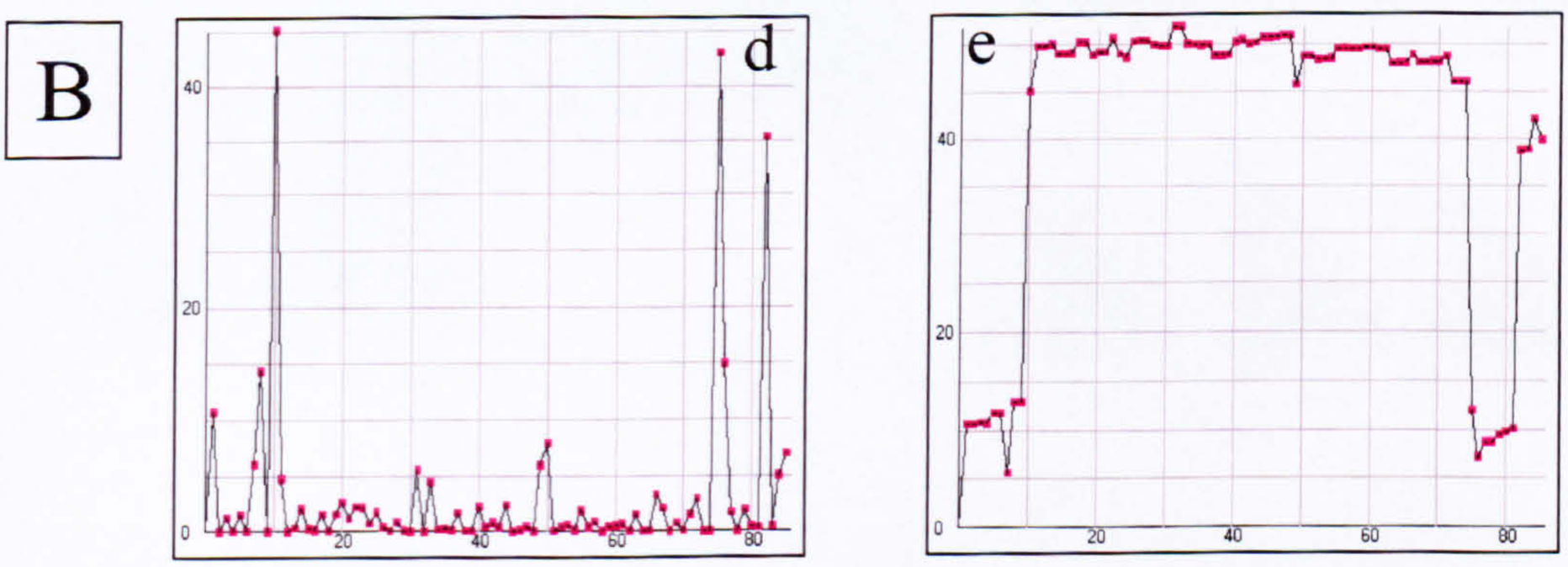

Fig. 5.89 S-orientated grain in the 60 seconds delayed sample: (a) relative map, (b) (d) relative and (c) (e) cumulative misorientation distributions of line scans performed along A and B in (a).

a

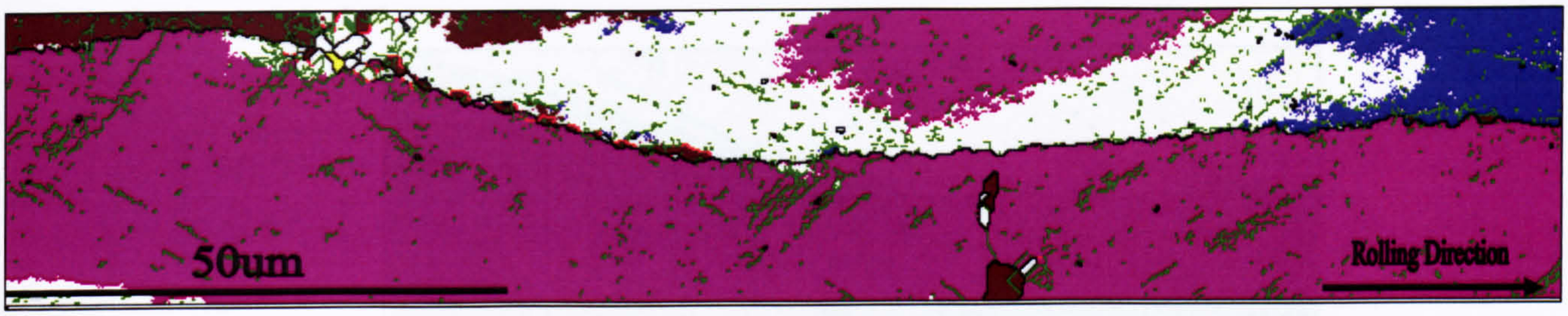

5-10°: green, 10-15°: red, >15°: black Step size=0.2μm

b

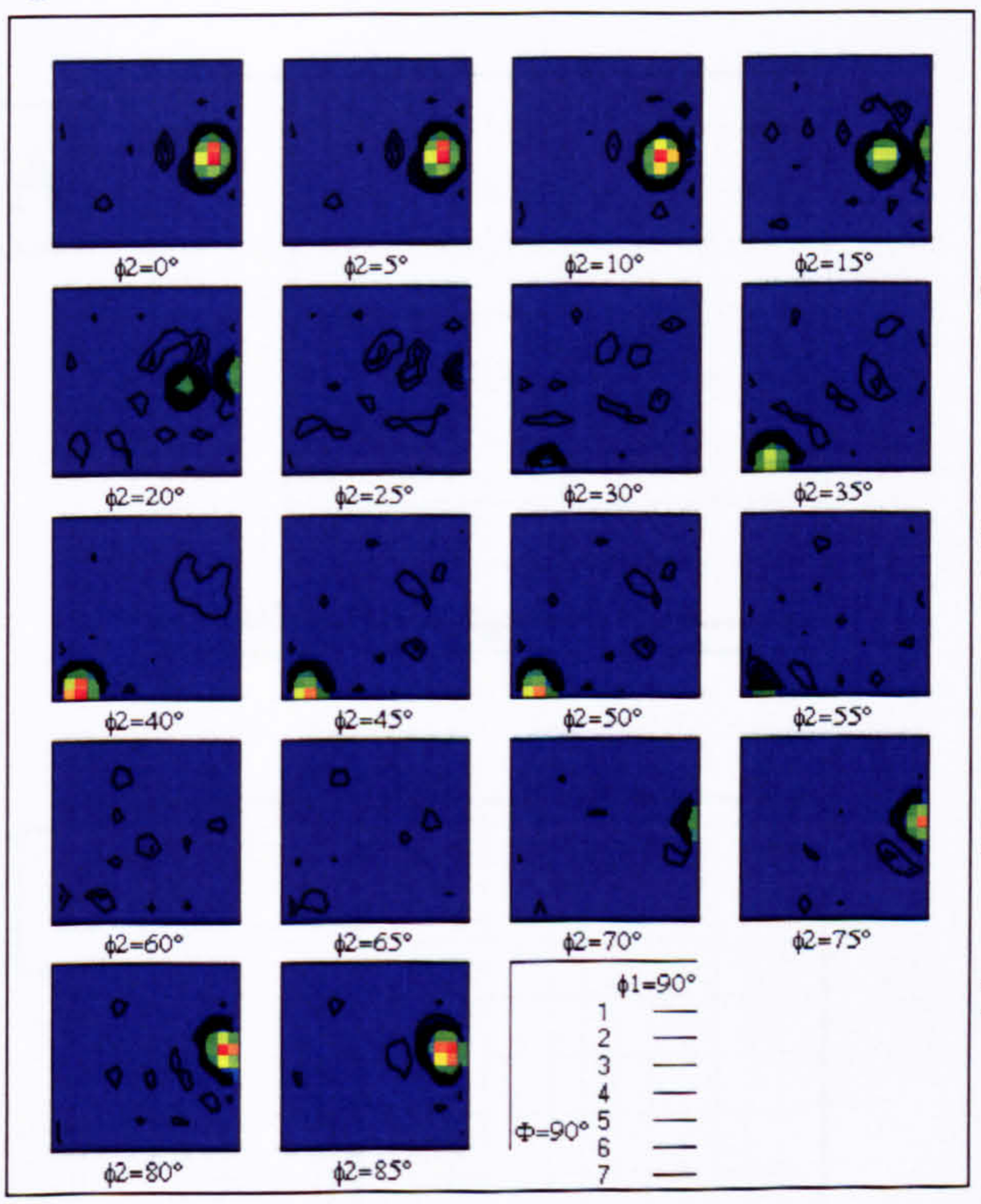

c

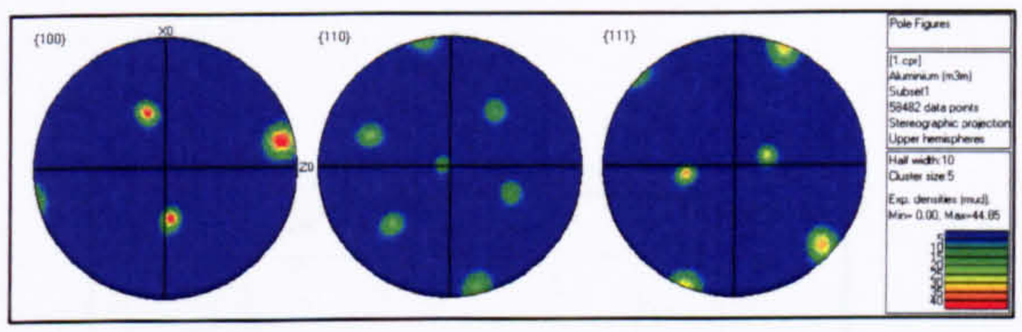

d

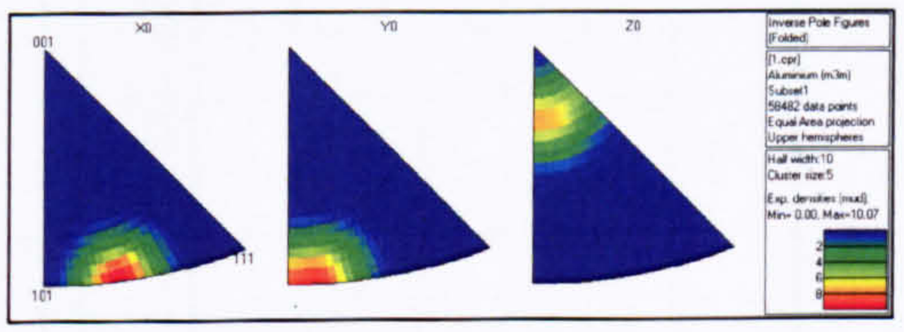

e

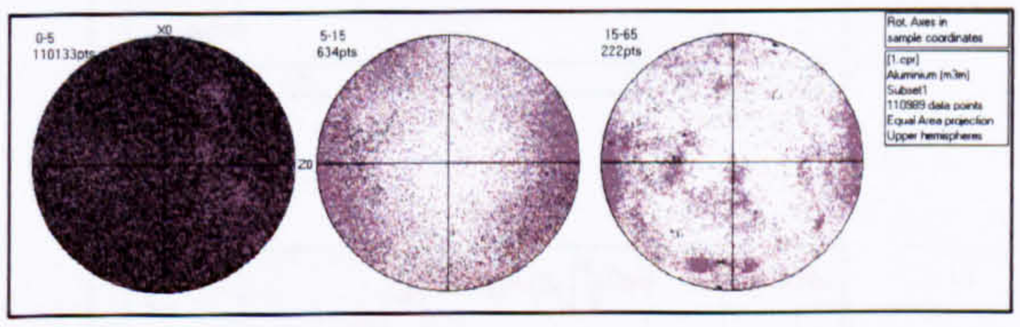

f

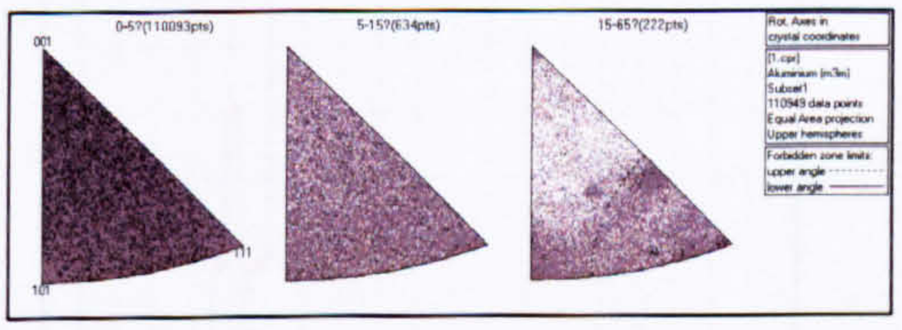

Fig. 5.90 P-orientated grain in the 60 seconds delayed sample: (a) texture and boundary map, (b) ODF, (c) pole figures, (d) inverse pole figures, the distribution of misorientation axis vectors in (e) sample and (f) crystal lattice coordinates.

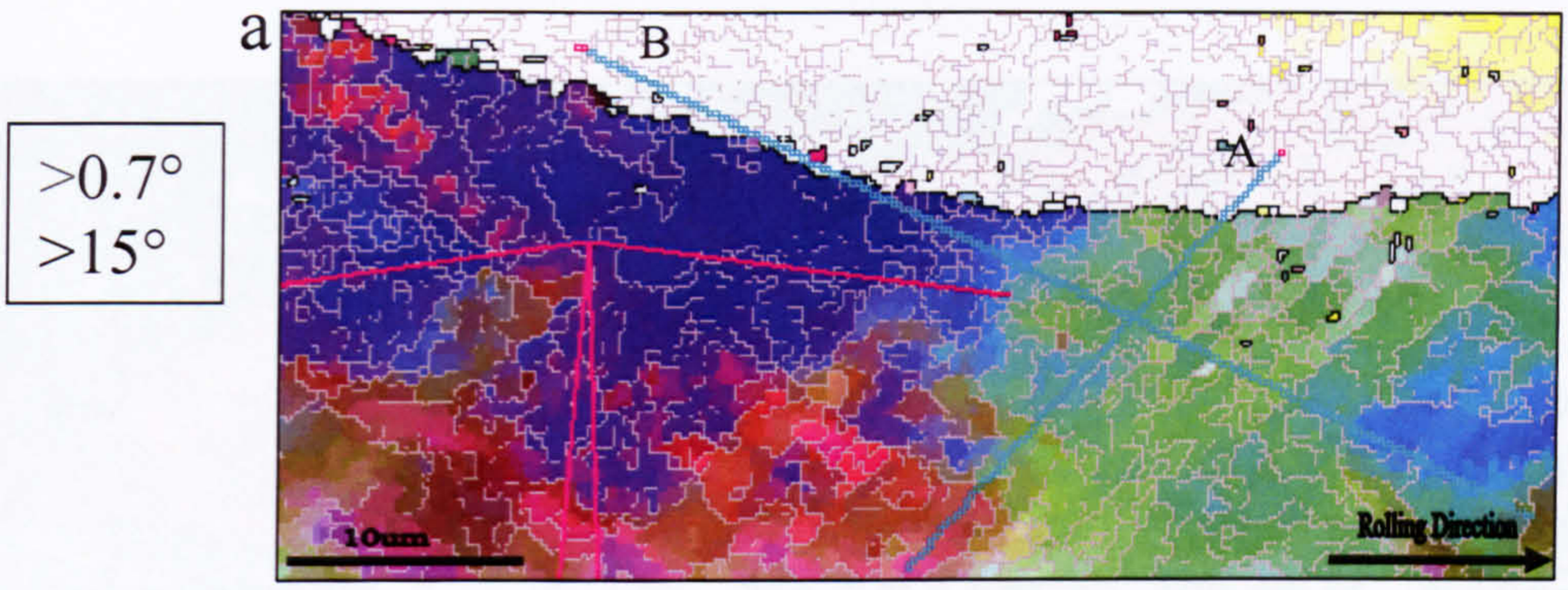

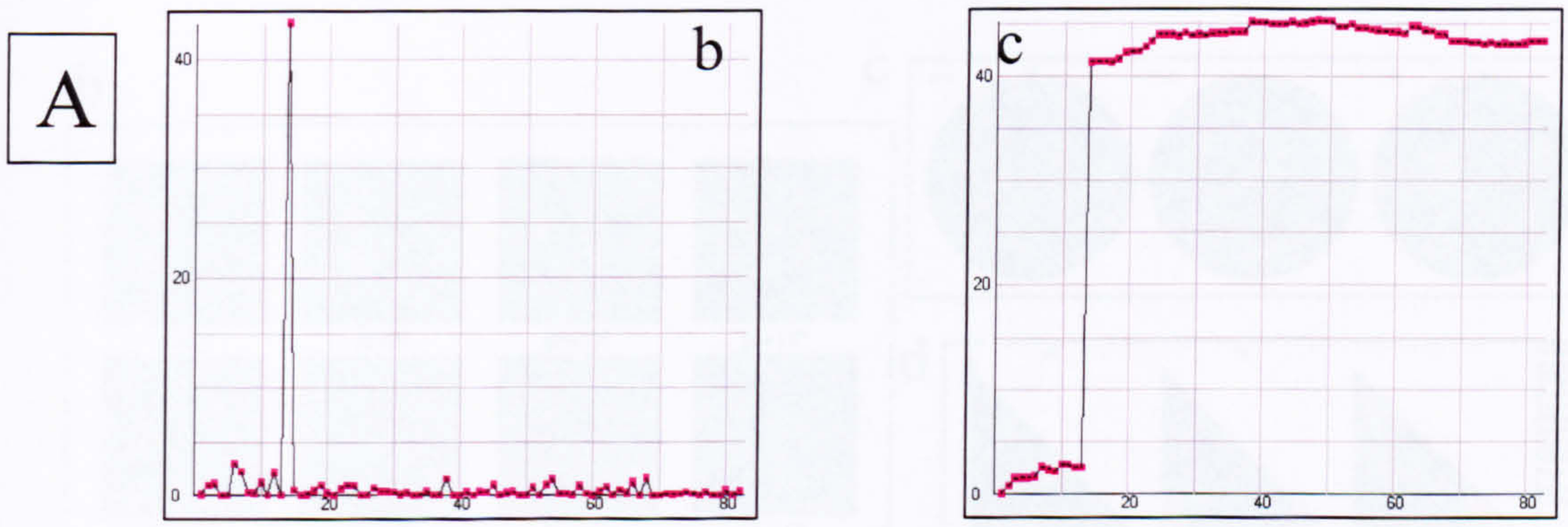

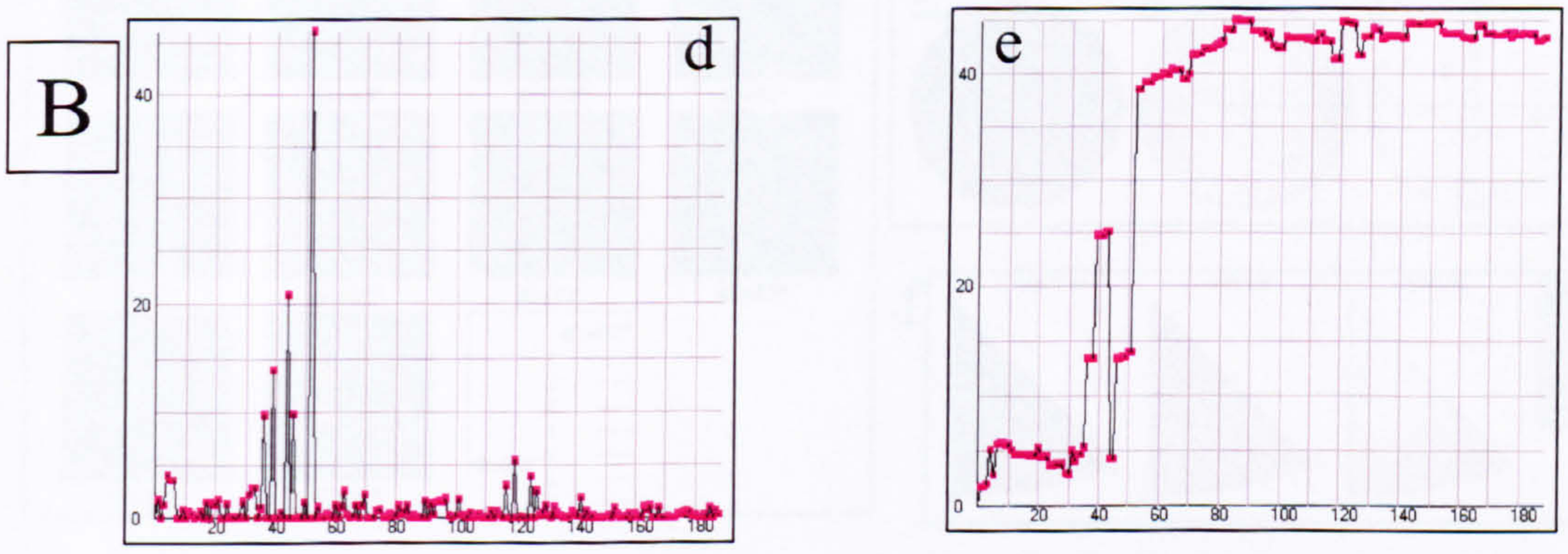

Fig. 5.91 P-orientated grain in the 60 seconds delayed sample: (a) relative map, (b) (d) relative and (c) (e) cumulative misorientation distributions of line scans performed along A and B in (a).

a

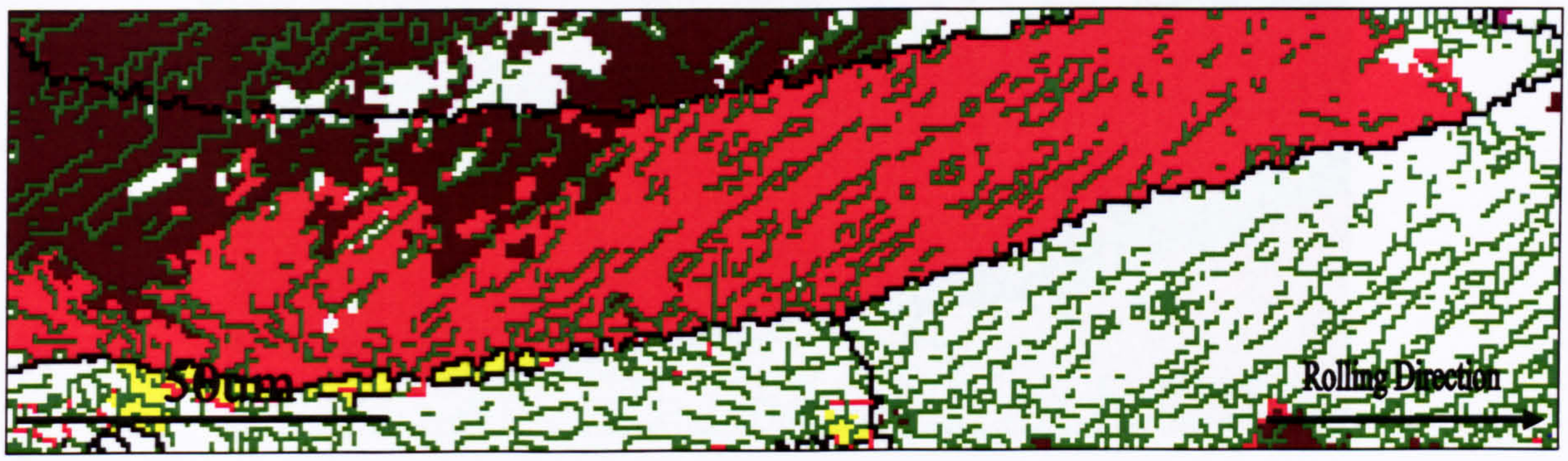

2-10°: green, 10-15°: red, >15°: black Step size=0.5μm

b

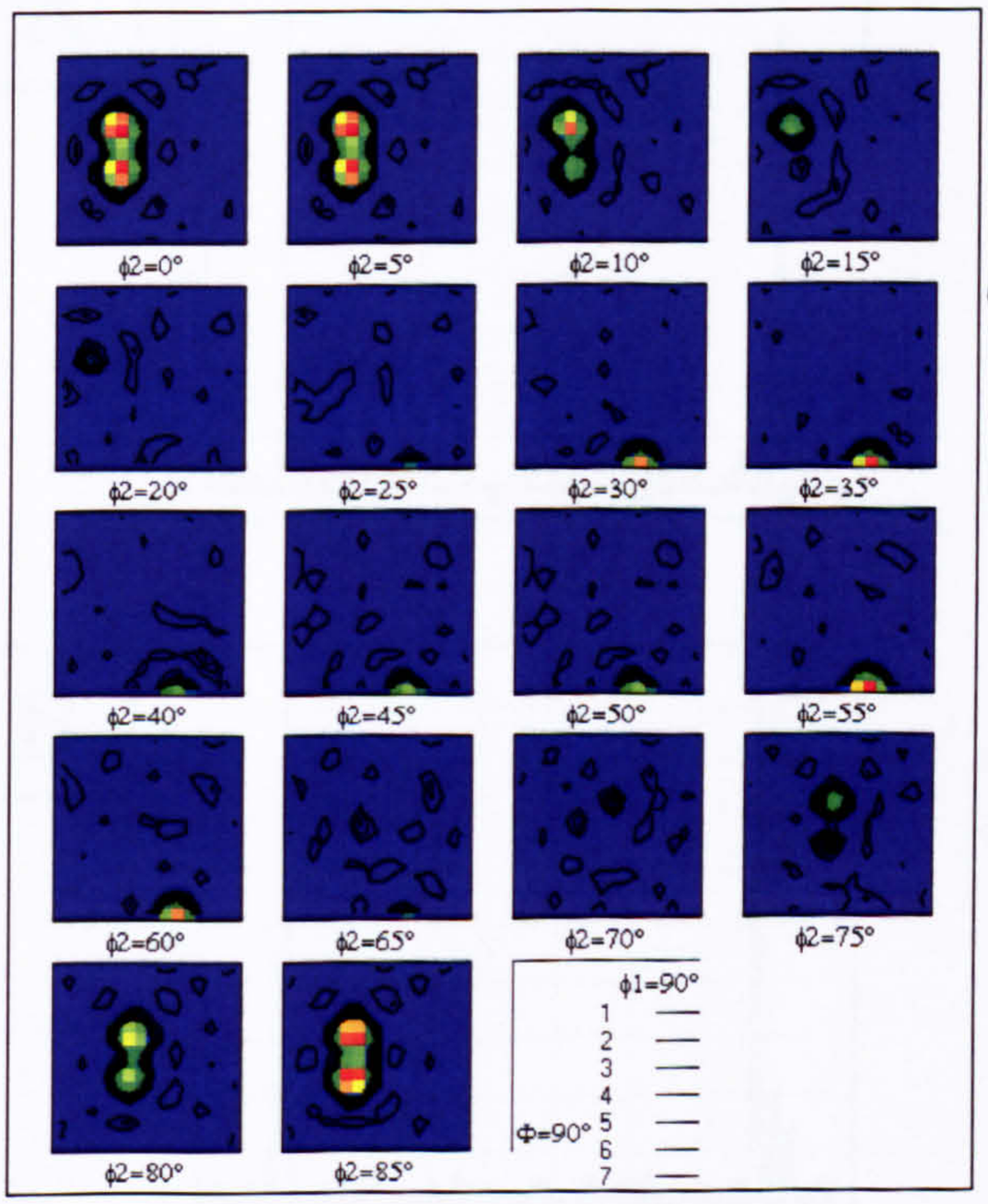

c

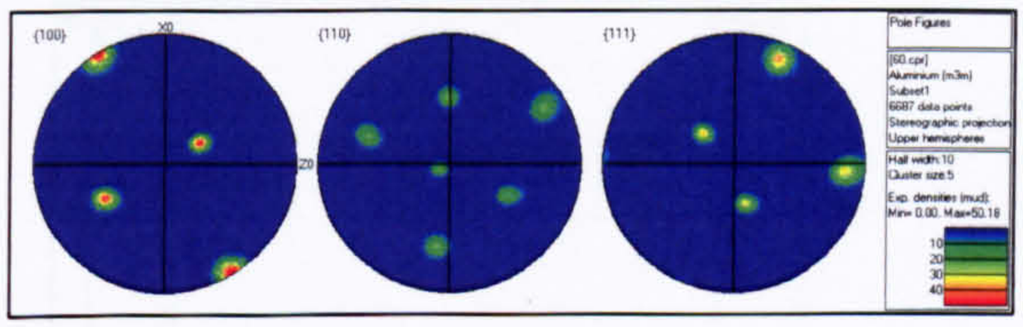

d

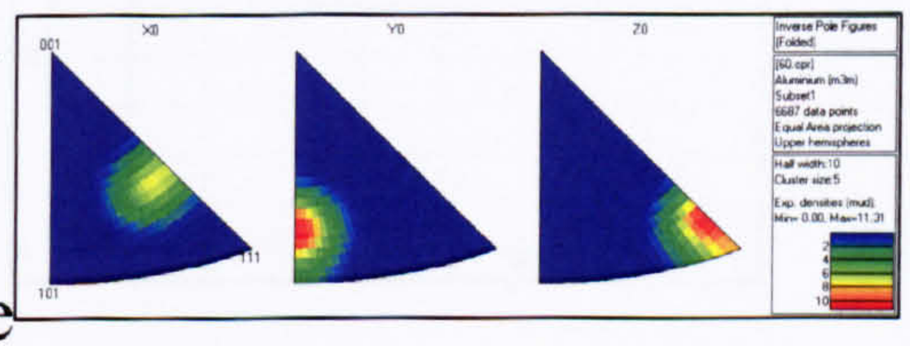

e

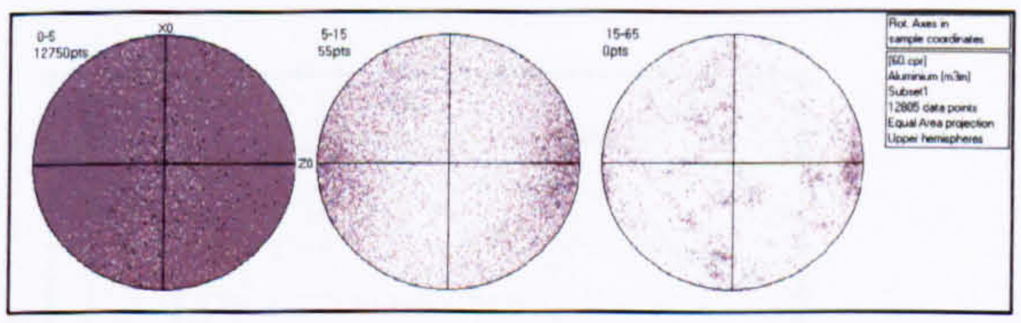

f

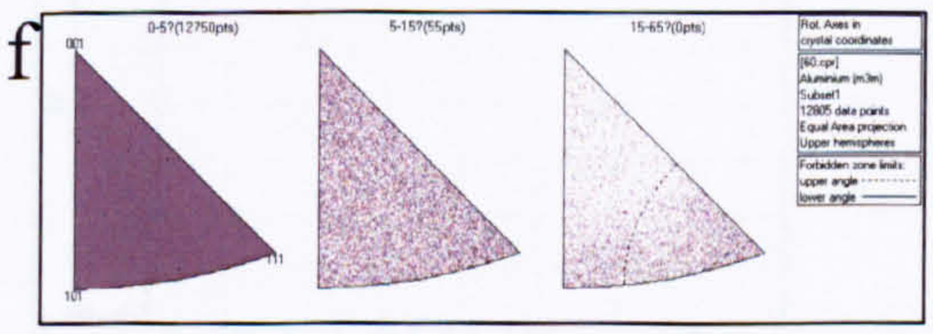

Fig. 5.92 Brass-orientated grain in the 60 seconds delayed sample: (a) texture and boundary map, (b) ODF, (c) pole figures, (d) inverse pole figures, the distribution of misorientation axis vectors in (e) sample and (f) crystal lattice coordinates.

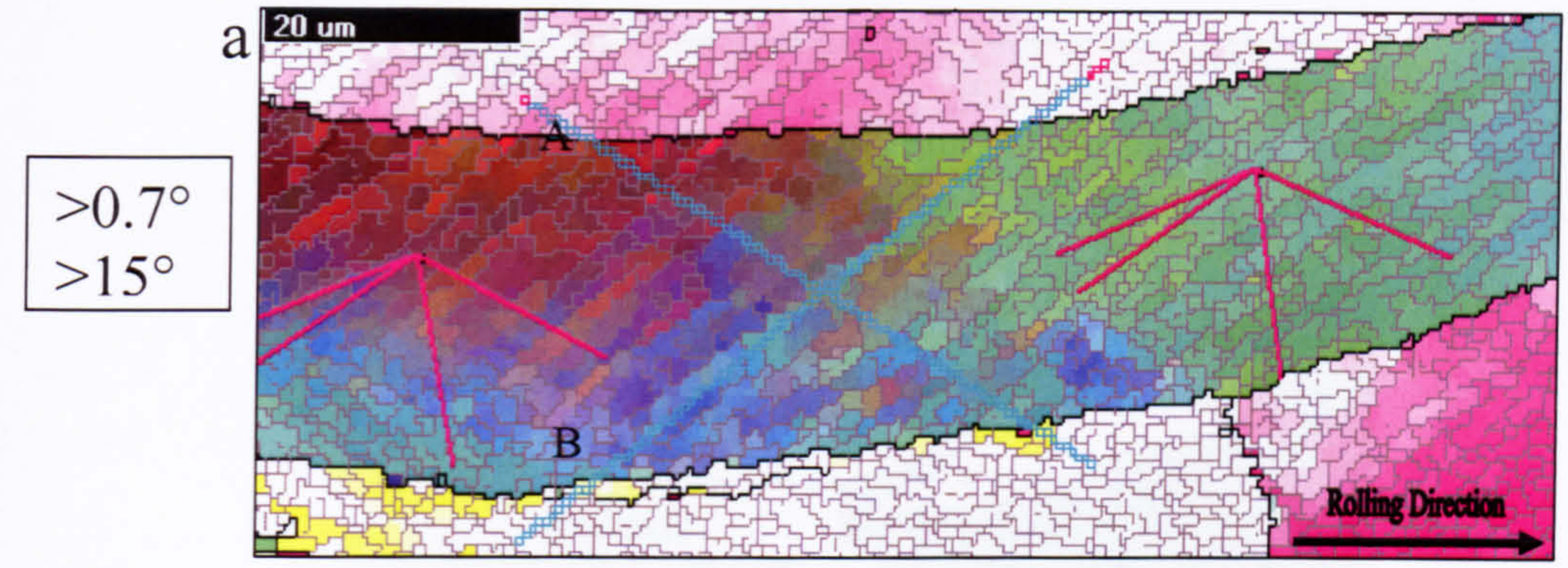

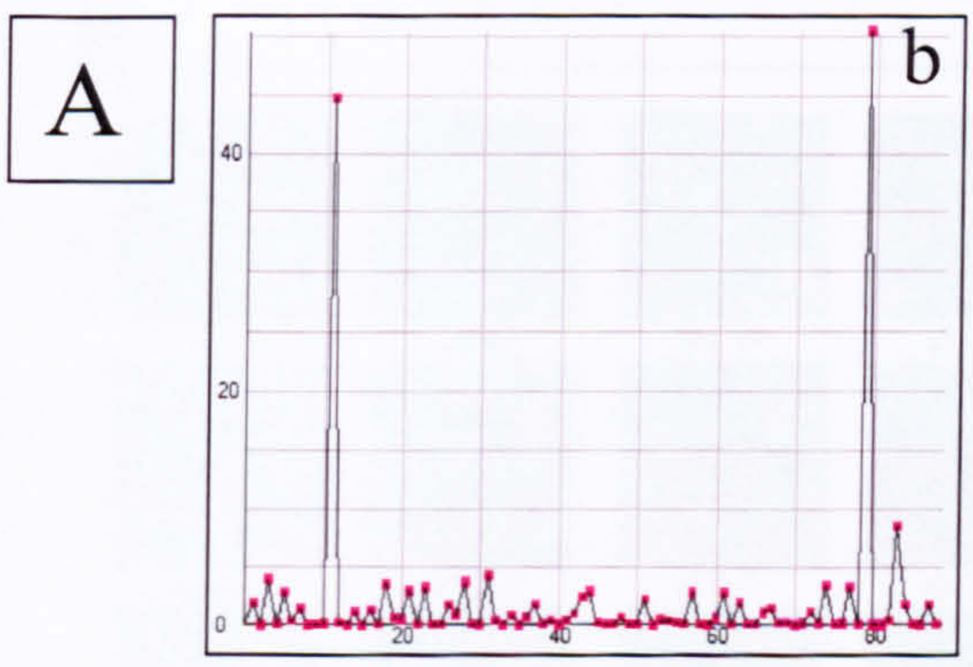

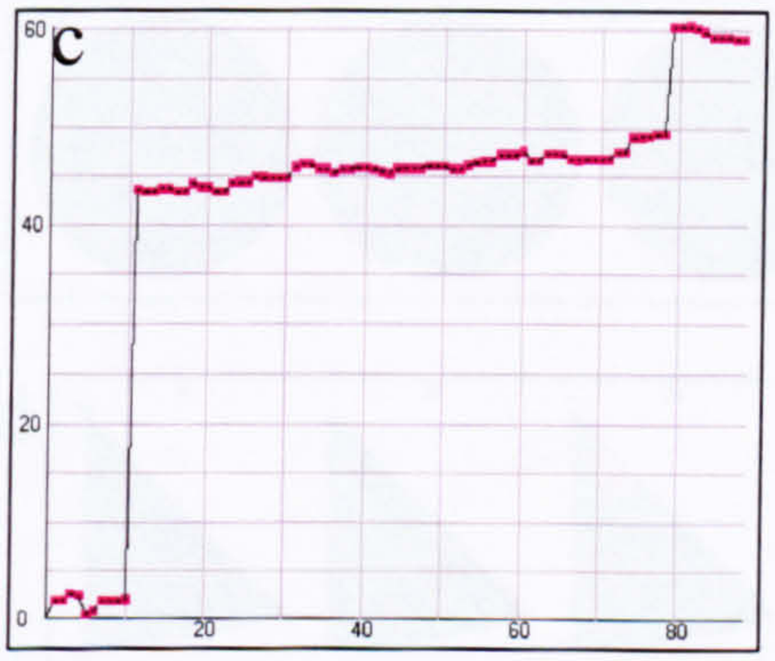

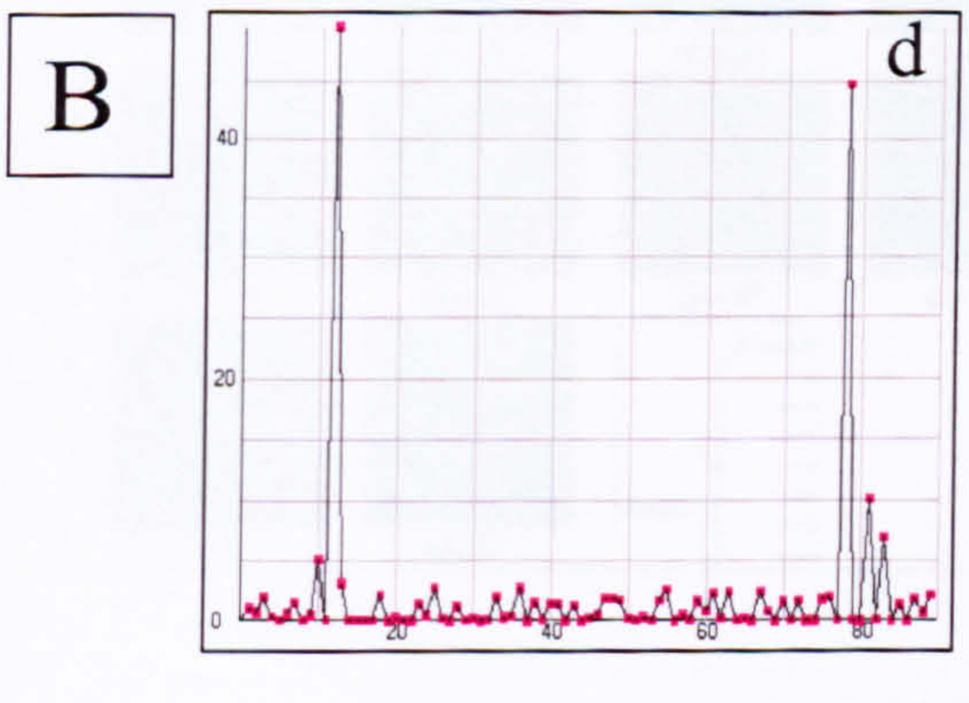

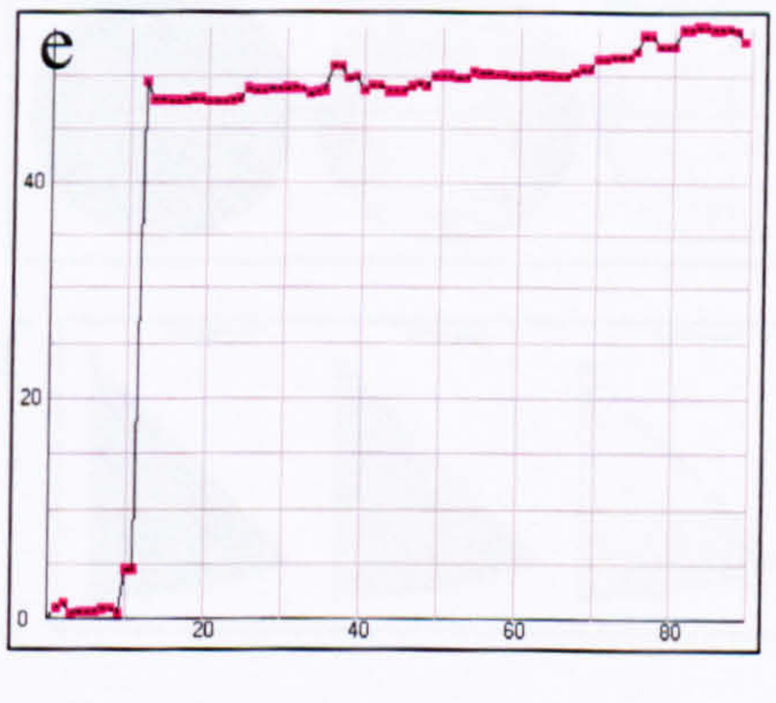

Fig. 5.93 Brass-orientated grain in the 60 seconds delayed sample: (a) relative map, (b) (d) relative and (c) (e) cumulative misorientation distributions of line scans performed along A and B in (a).

a

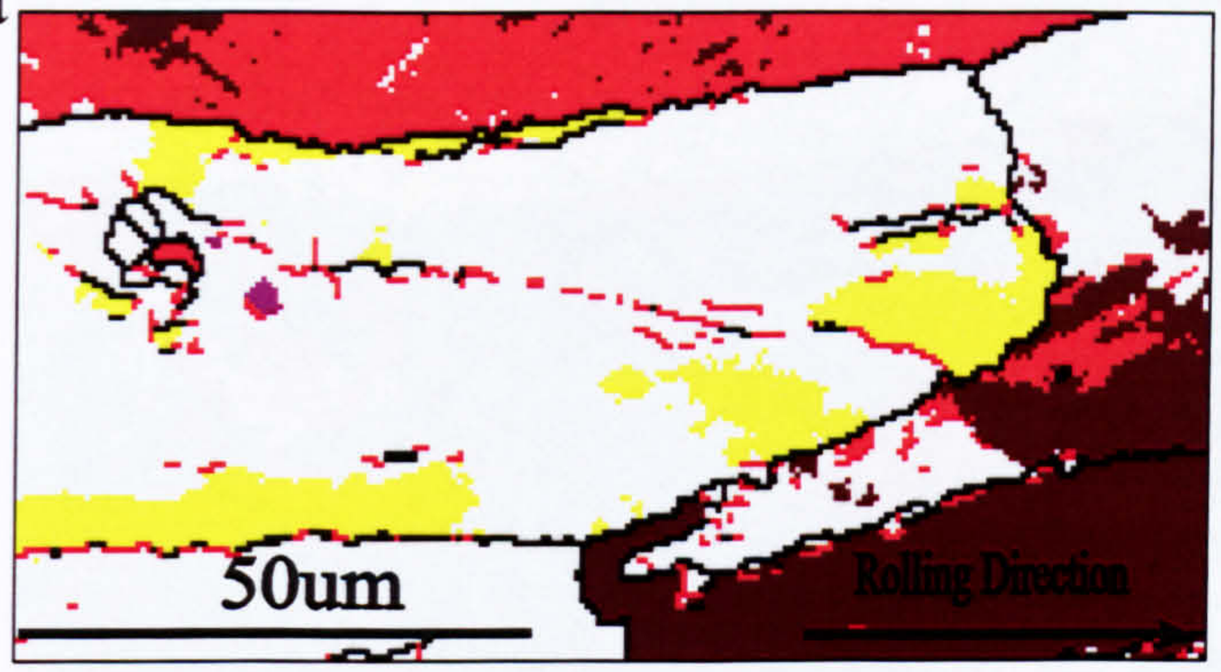

2-10°: green, 10-15°: red, >15°: black Step size=0.5μm

b

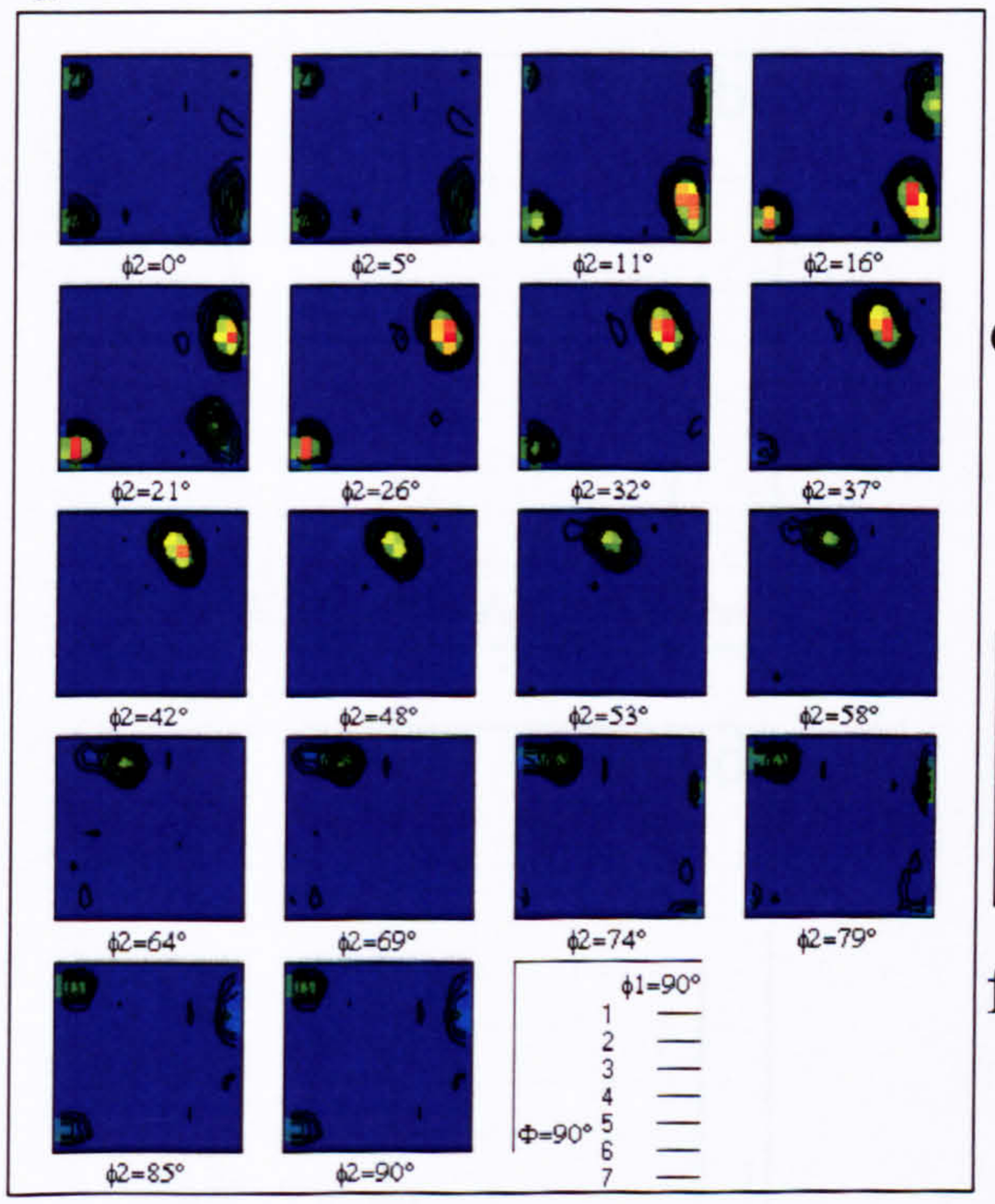

c

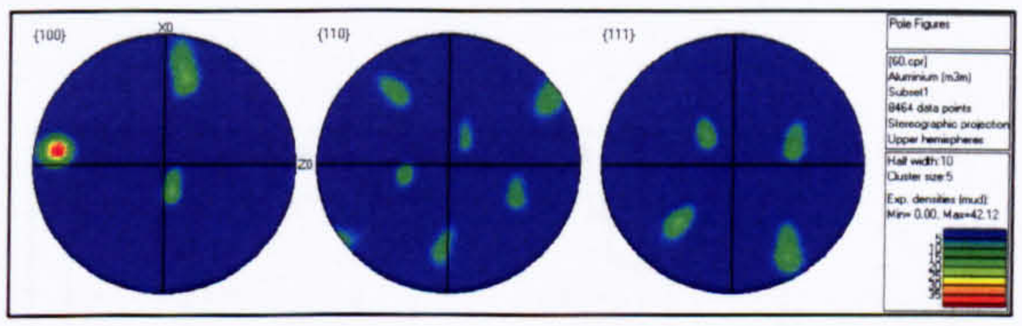

d

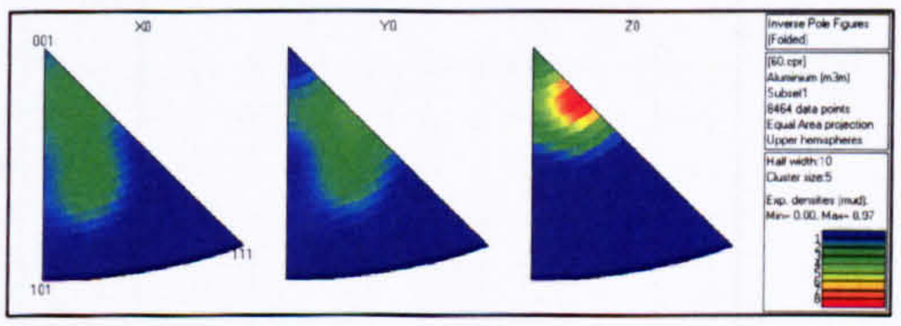

e

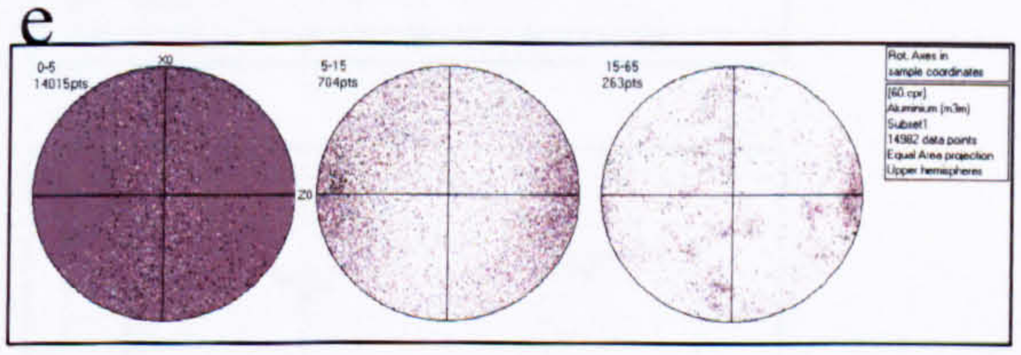

f

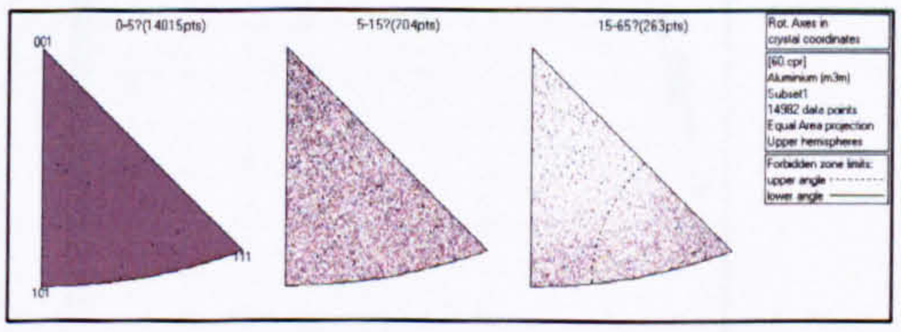

Fig. 5.94 Cube-orientated grain in the 60 seconds delayed sample: (a) texture and boundary map, (b) ODF, (c) pole figures, (d) inverse pole figures, the distribution of misorientation axis vectors in (e) sample and (f) crystal lattice coordinates.

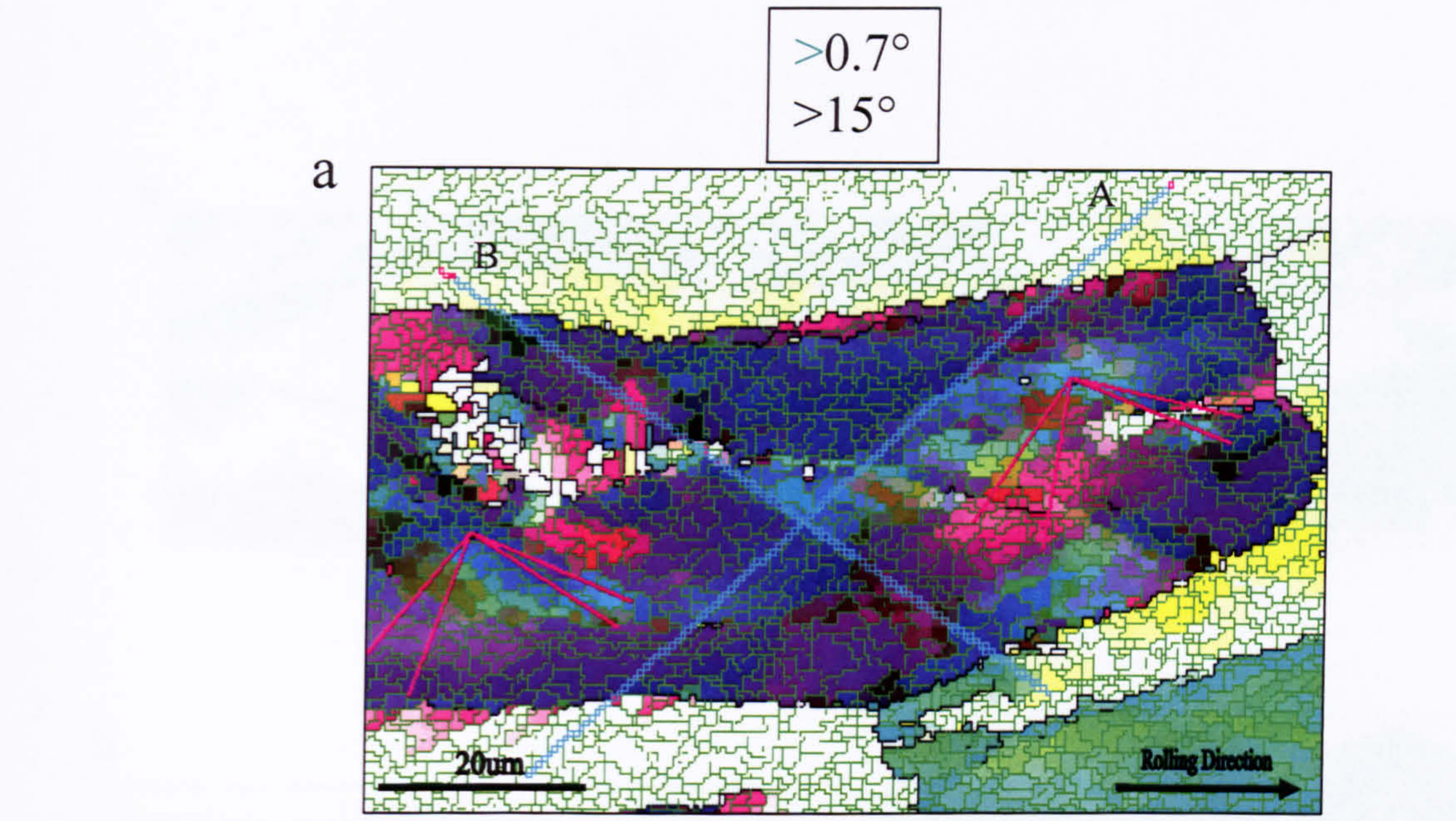

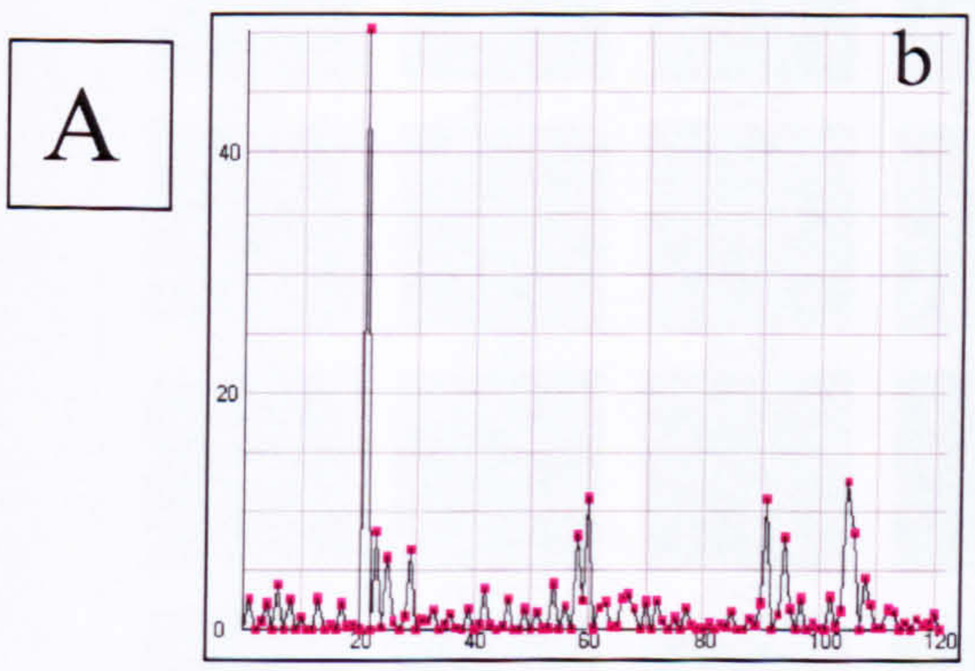

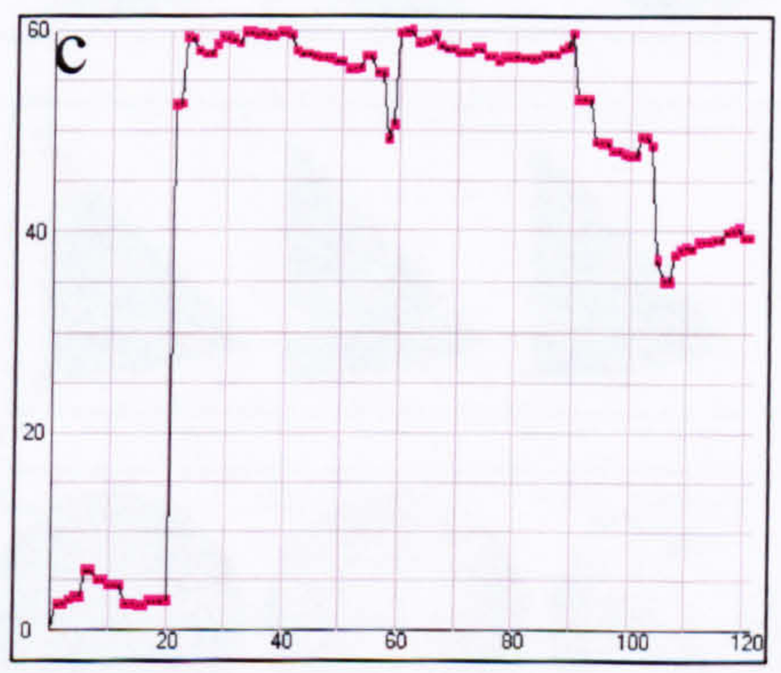

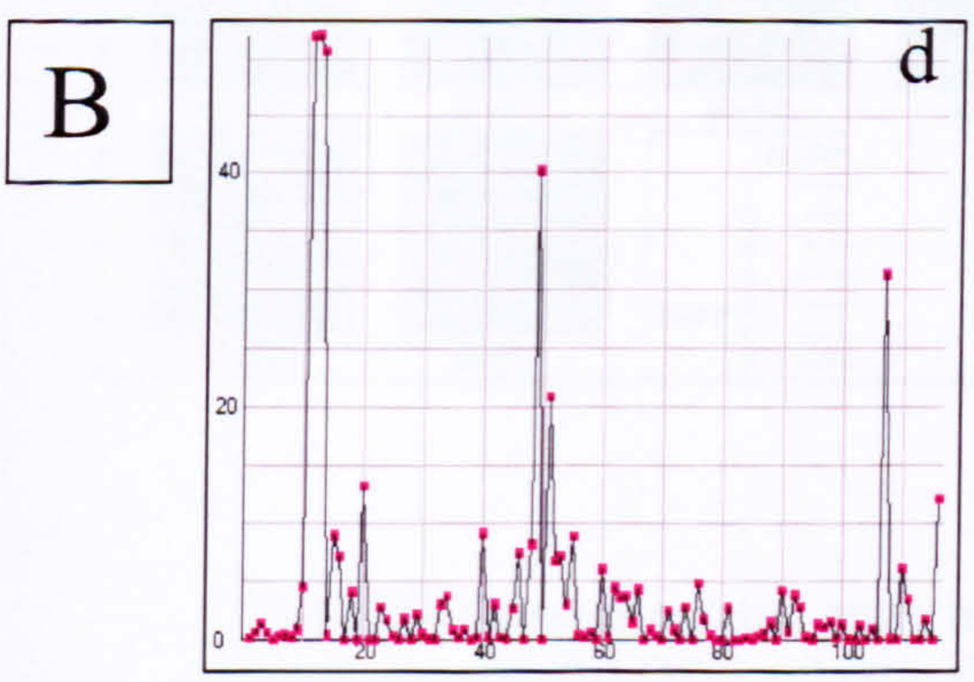

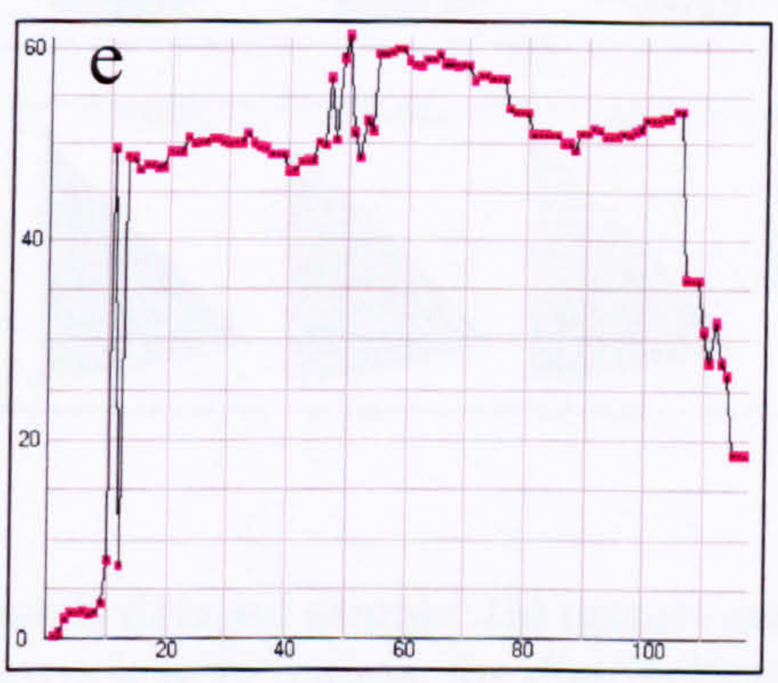

Fig. 5.95 Cube-orientated grain in the 60 seconds delayed sample: (a) relative map, (b) (d) relative and (c) (e) cumulative misorientation distributions of line scans performed along A and B in (a).

a

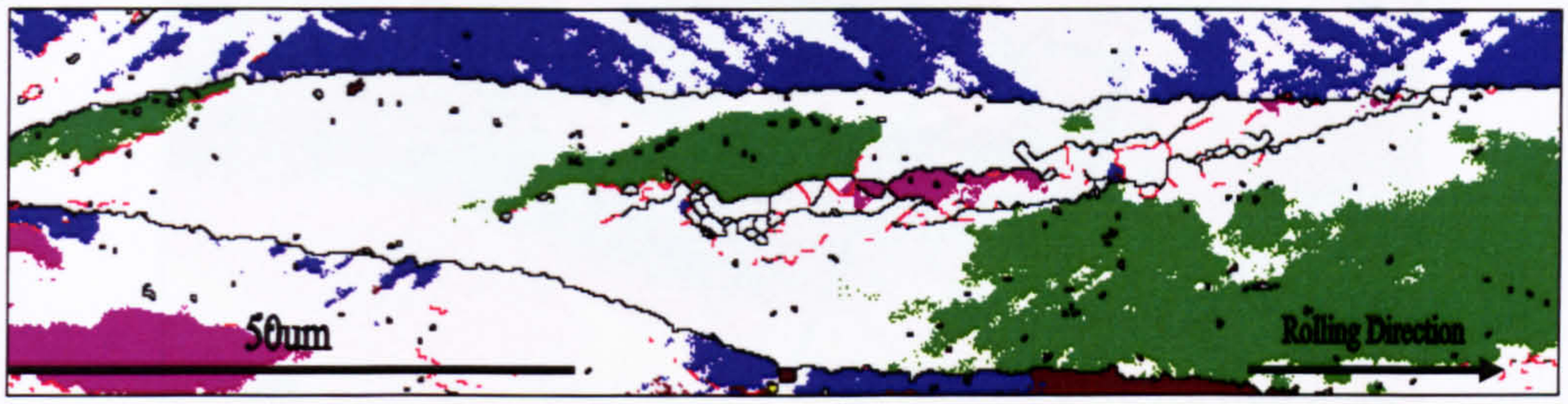

2-10°: green, 10-15°: red, >15°: black Step size=0.2μm

b

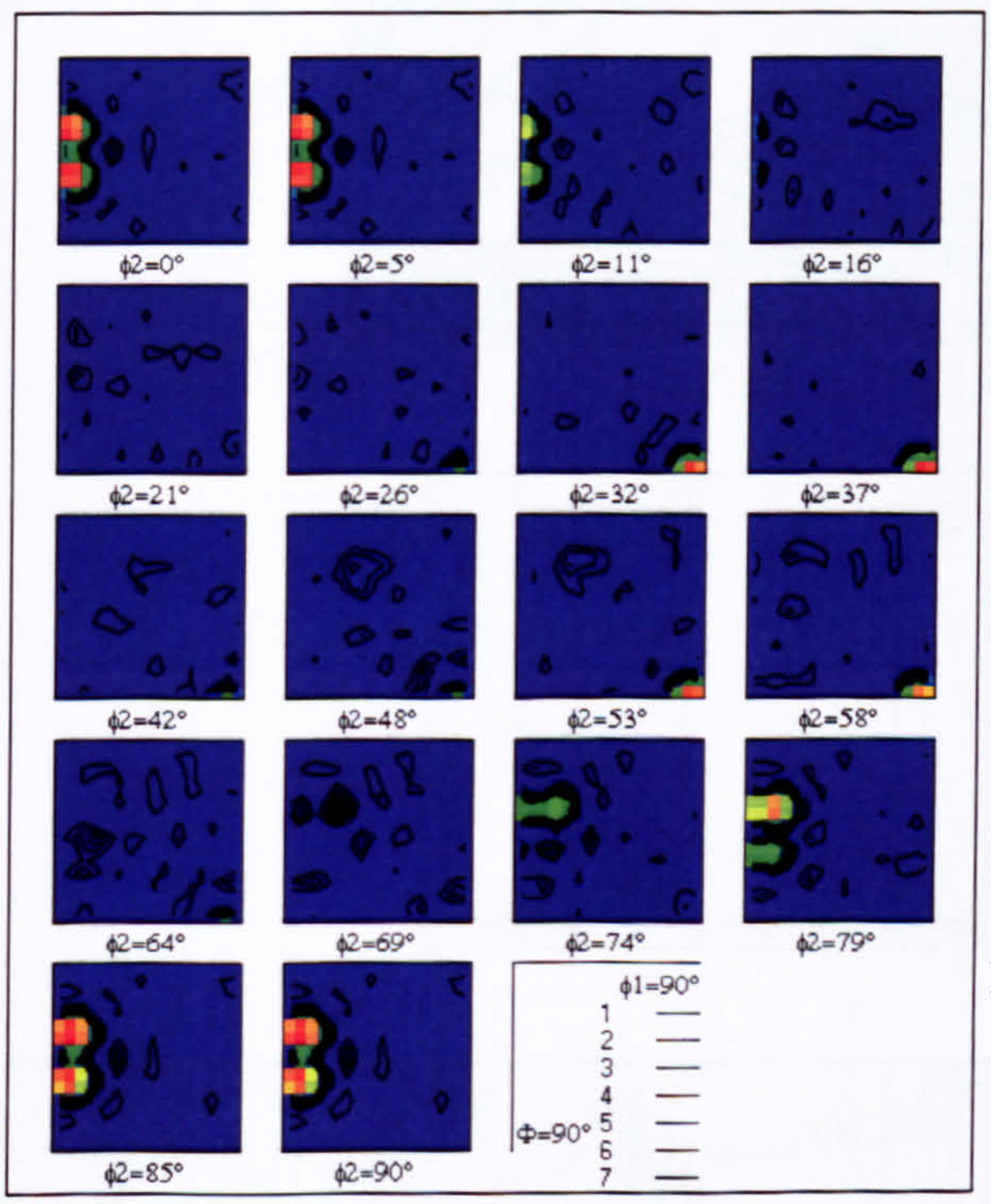

c

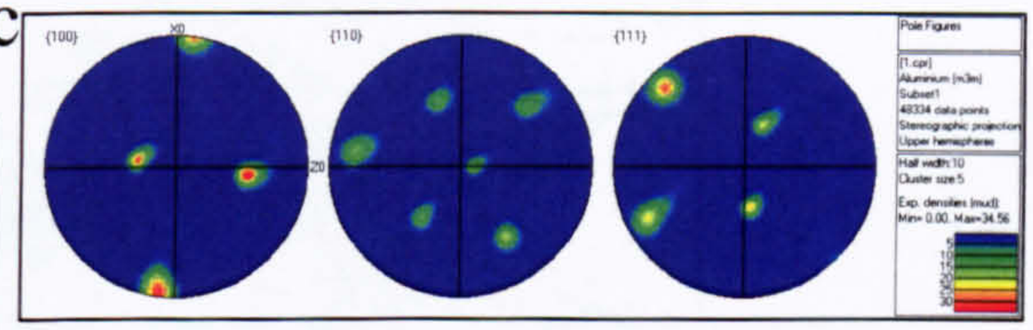

d

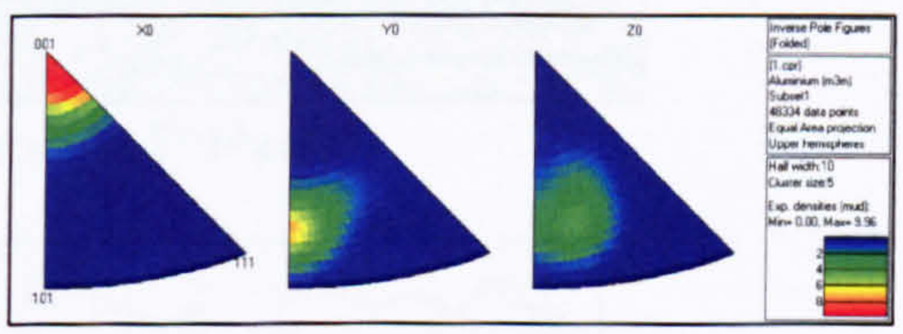

e

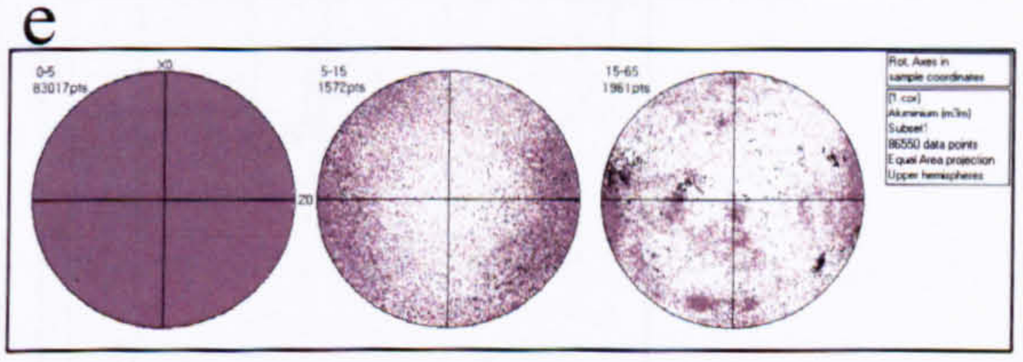

f

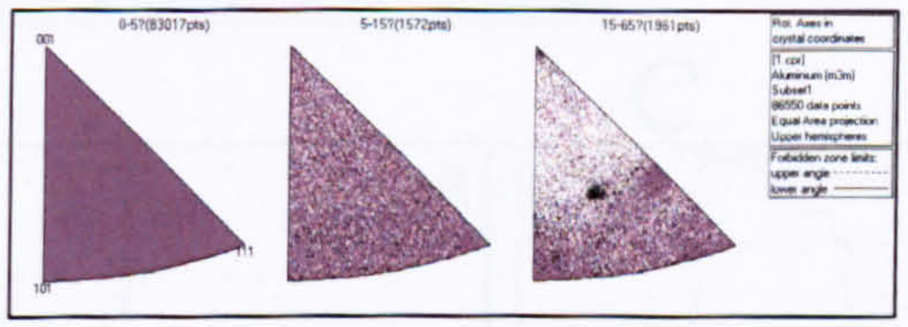

Fig. 5.96 Goss-orientated grain in the 60 seconds delayed sample: (a) texture and boundary map, (b) ODF, (c) pole figures, (d) inverse pole figures, the distribution of misorientation axis vectors in (e) sample and (f) crystal lattice coordinates.

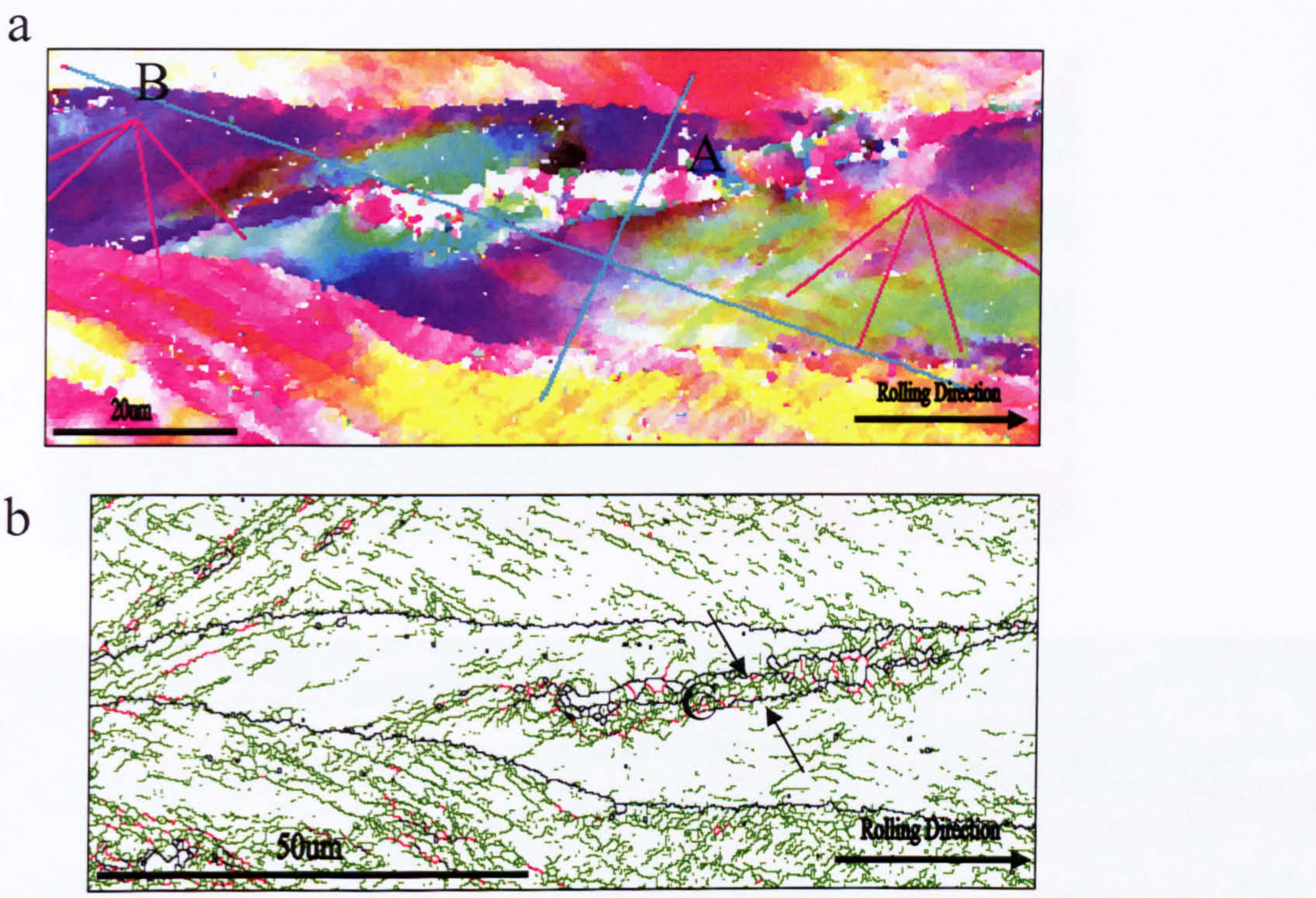

Fig. 5.97 Goss-orientated grain in the 60 seconds delayed sample: (a) relative map, (b) orientation map, (c) (e) (g) relative and (d) (f) (h) cumulative misorientation distributions of line scans performed along A and B in (a), C in (b).

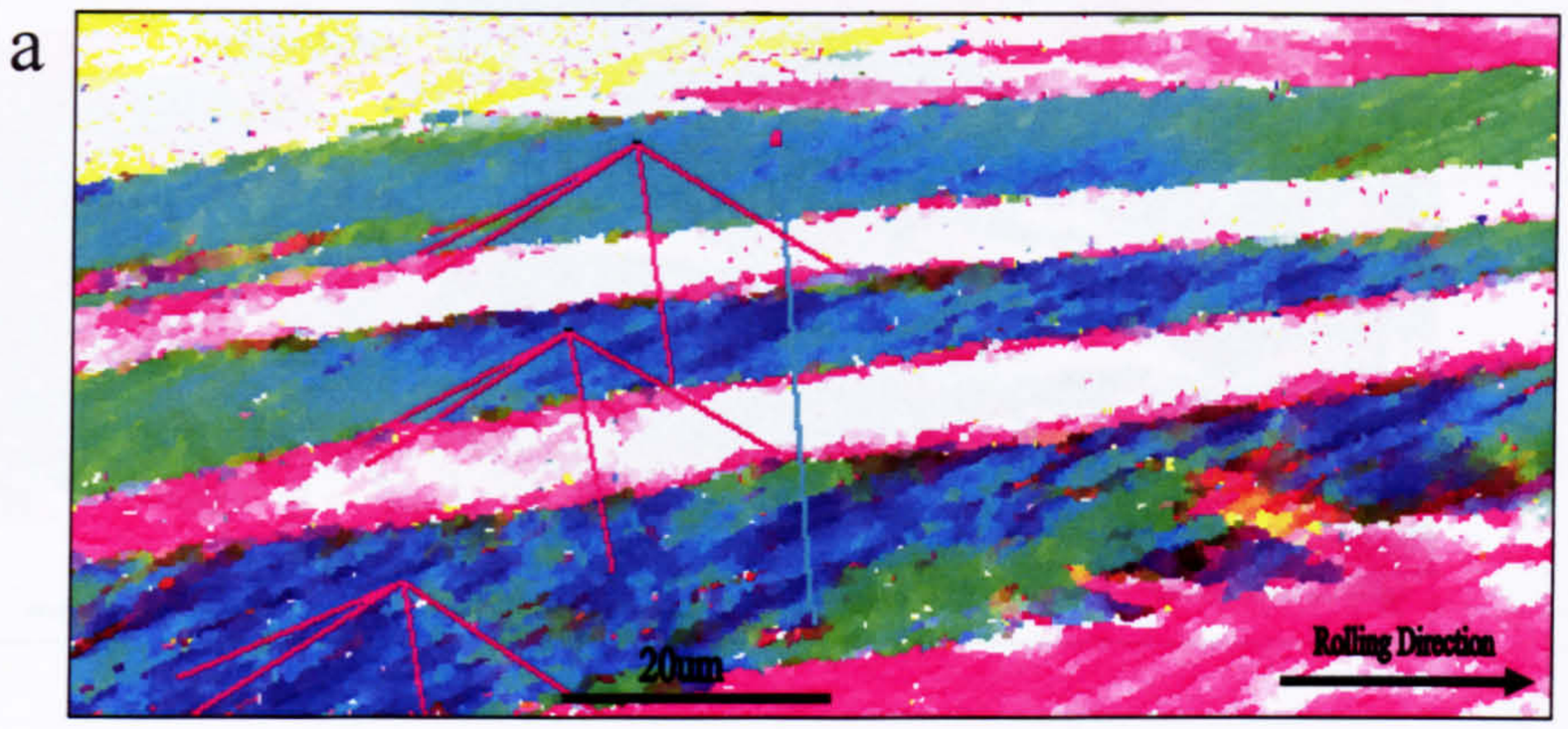

5-10°: green, 10-15°: red, >15°: black

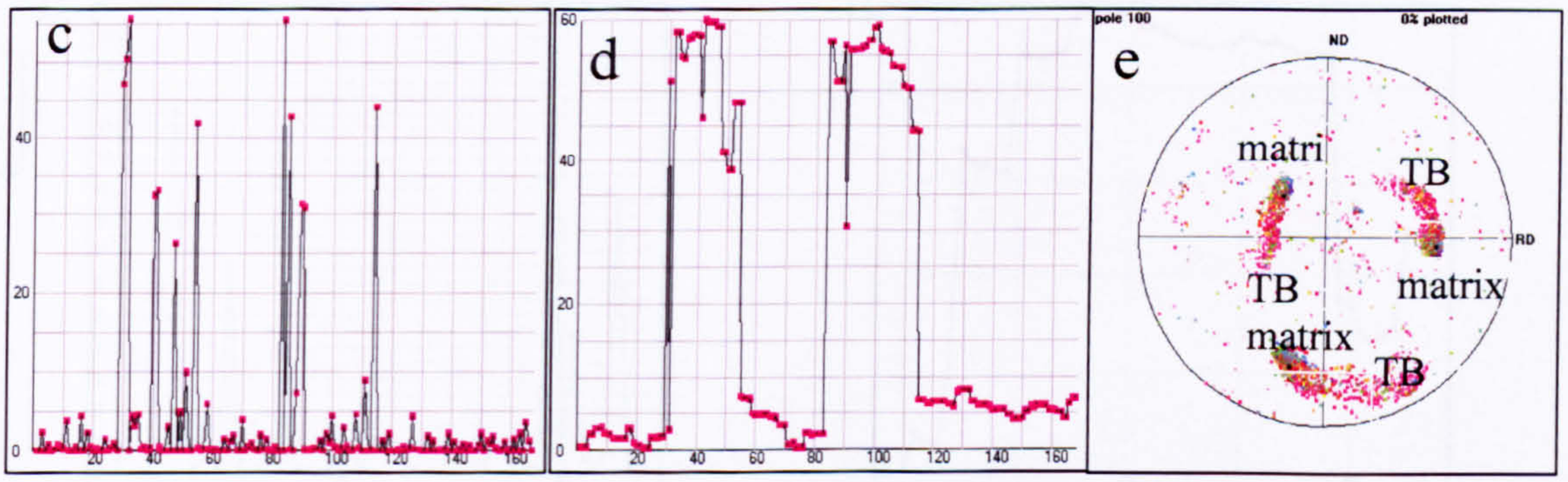

Fig. 5.98 Deformation banding in the 60 seconds delayed sample: (a) relative map, (b) texture and boundary map, (c) relative and (d) cumulative misorientation distributions of line scans performed along A and B in (a), (e) sample coordinate.

a

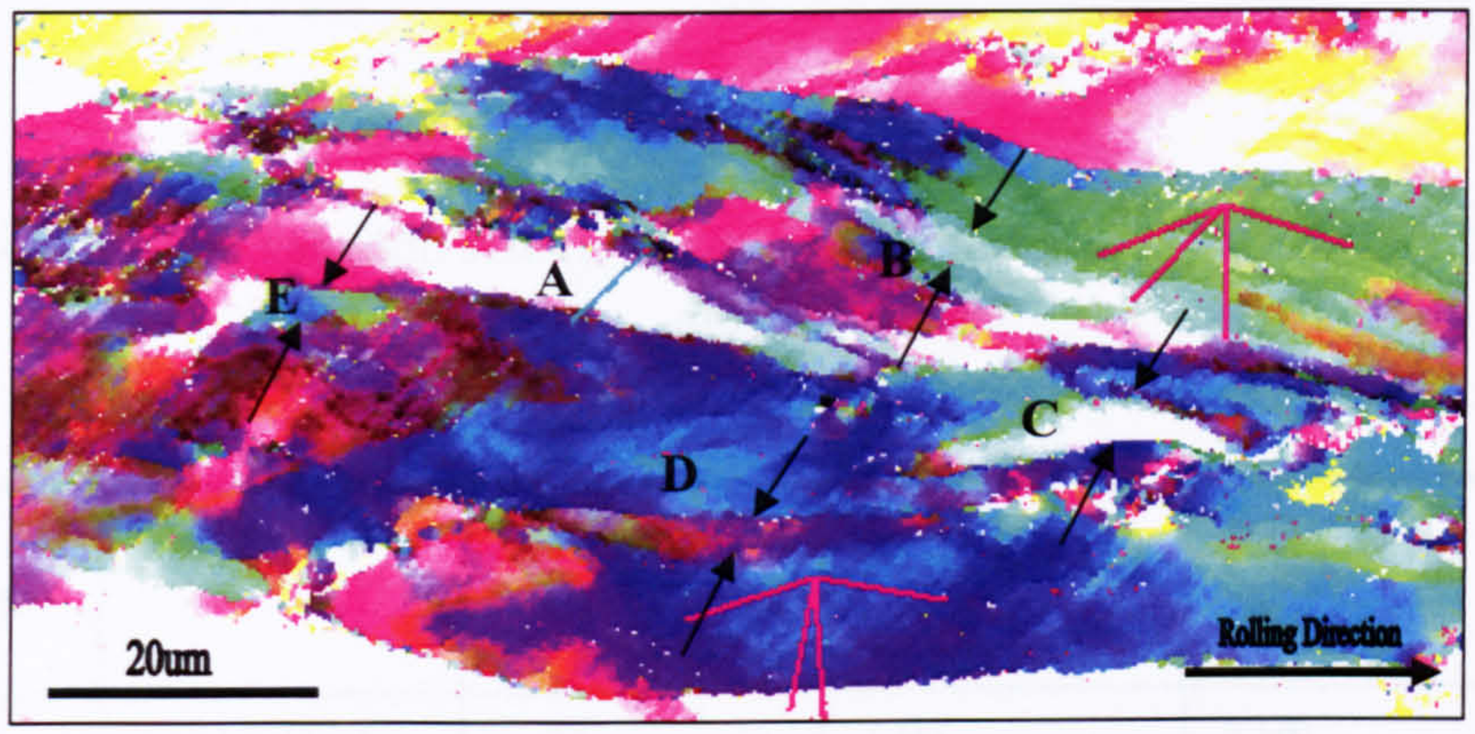

b

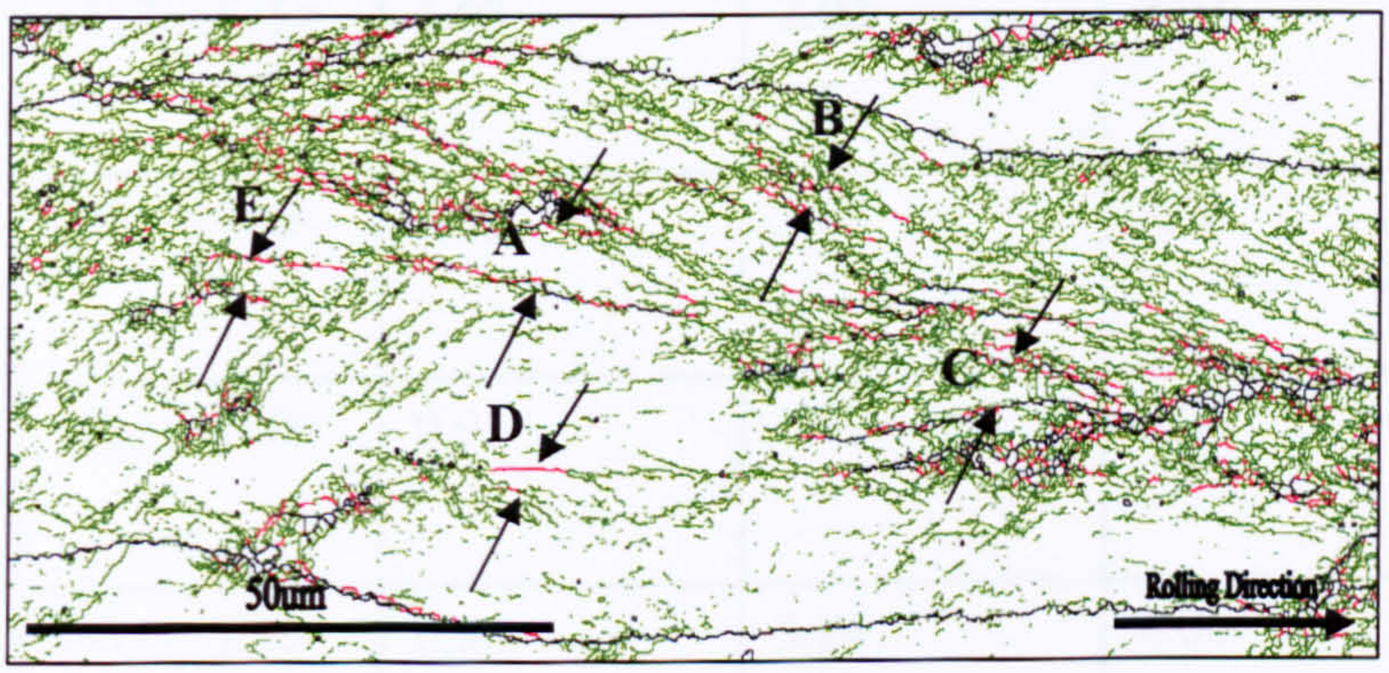

5-10°: green, 10-15°: red, >15°: black

c

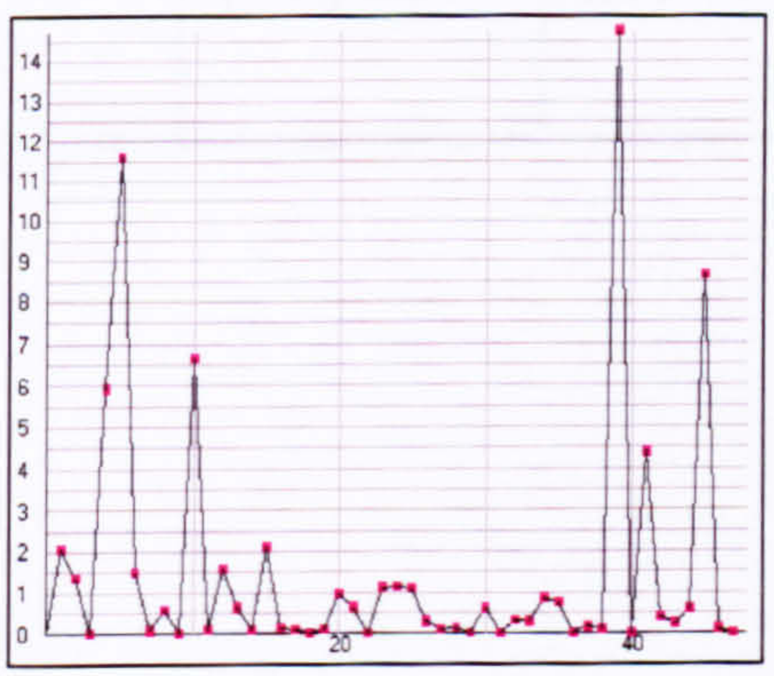

d

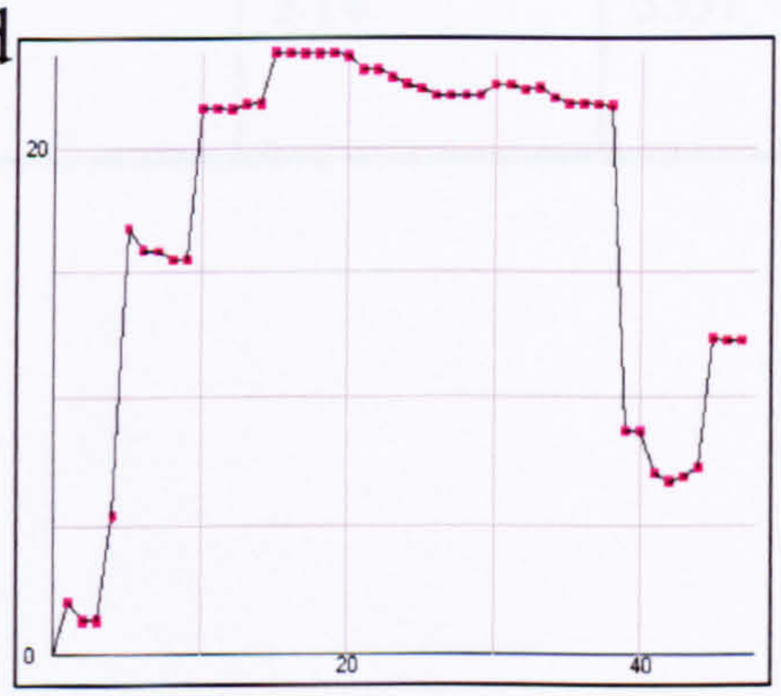

Fig. 5.99 Deformation banding in the 60 seconds delayed sample: (a) relative map, (b) orientation map. (c) relative and (d) cumulative misorientation distributions of line scans performed along A and B in (a).

Table 5.6 Mean subgrain size (D), misorientation angle (è) and Θ/d for the 60 seconds delayed sample

Texture Component	{hkl}<uvw>	D(μm)	Θ(°)	Θ/d	Number of Subgrains
Brass	{011}<112>	1.02	3.05	2.99	3458
Copper	{112}<111>	1.03	3.02	2.93	4238
Cube	{001}<100>	1.03	3.88	3.76	773
Goss	{011}<100>	0.91	1.82	2.00	22
P	{011}<122>	0.96	3.84	4.00	2062
S	{123}<634>	1.04	3.27	3.14	5551

a

b

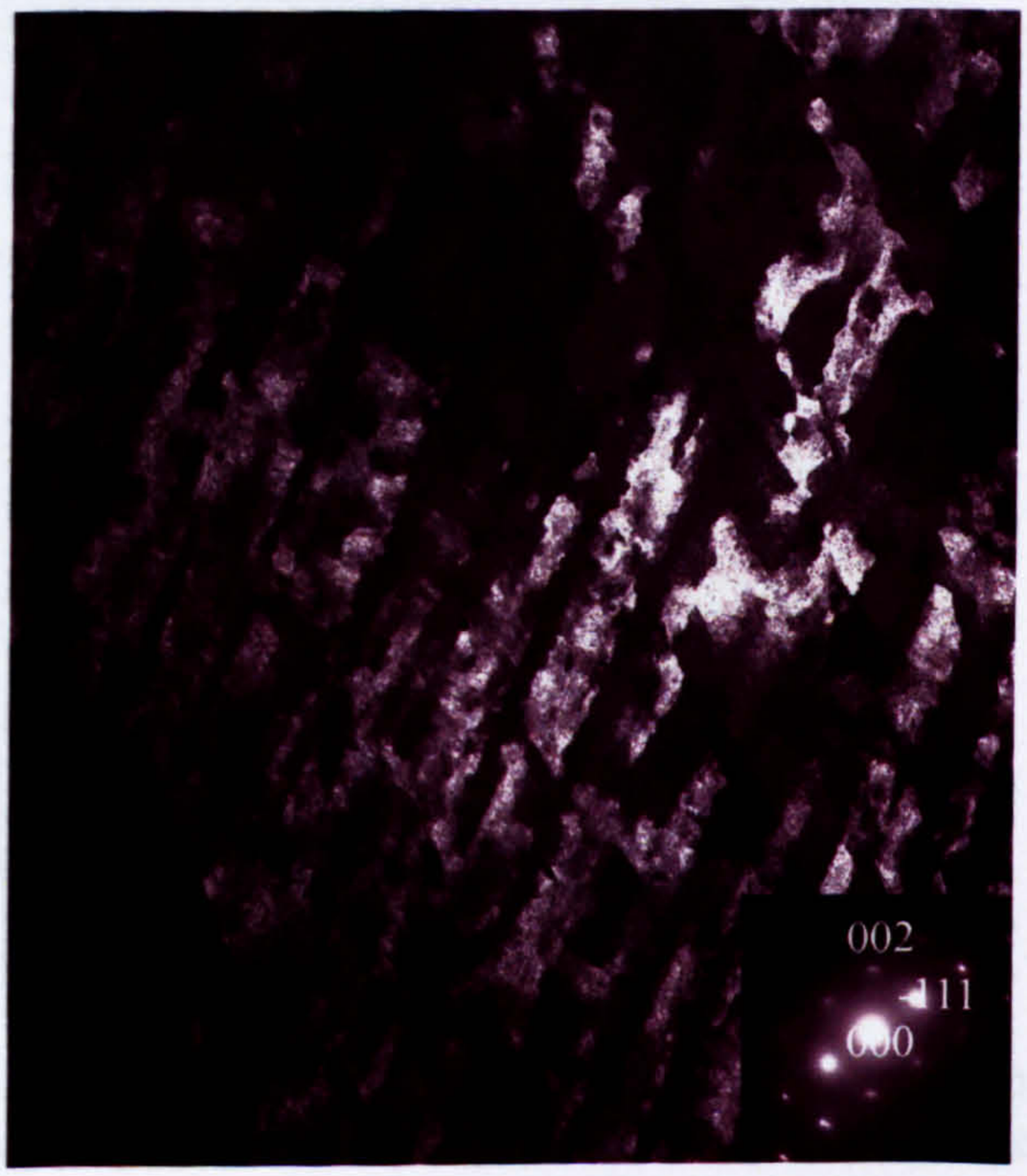

Fig. 5.100 TEM images after the 60 seconds delayed deformation, shows microband structure.

a

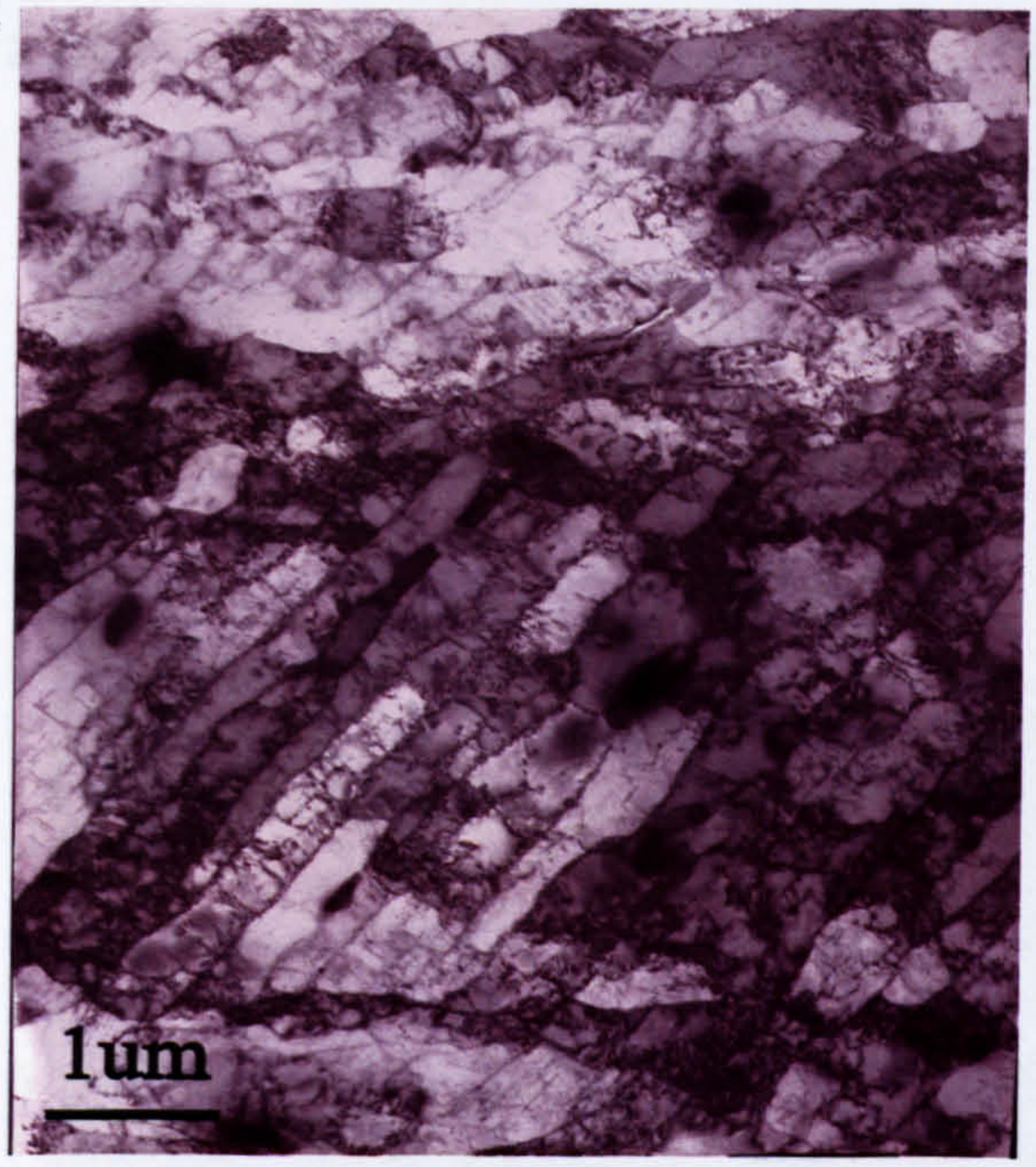

b

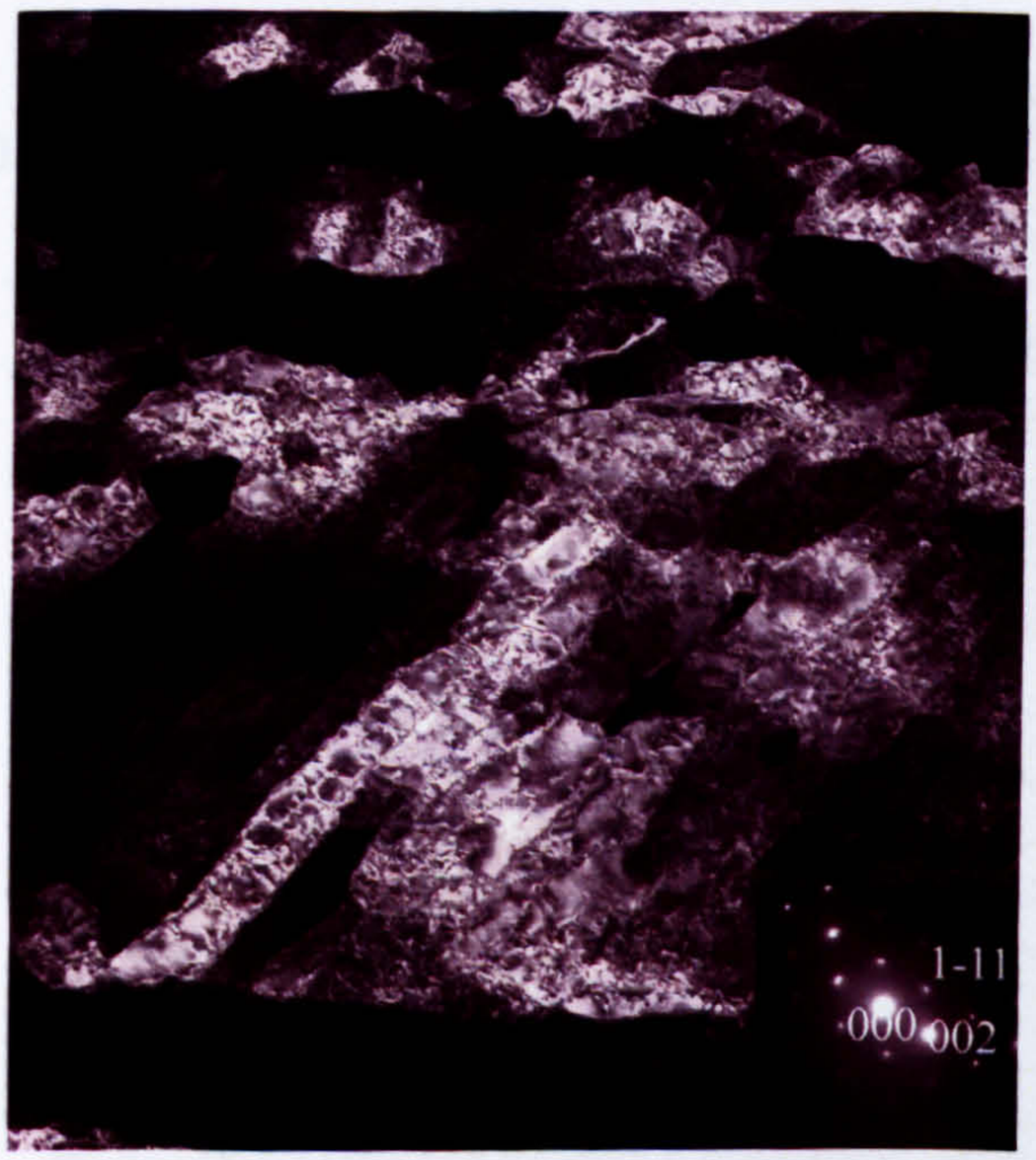

Fig. 5.101 TEM images after the 60 seconds delayed deformation, shows a well-developed microbands structure bounded by the GNBs: (a) bright field image, (b) dark field image.

a

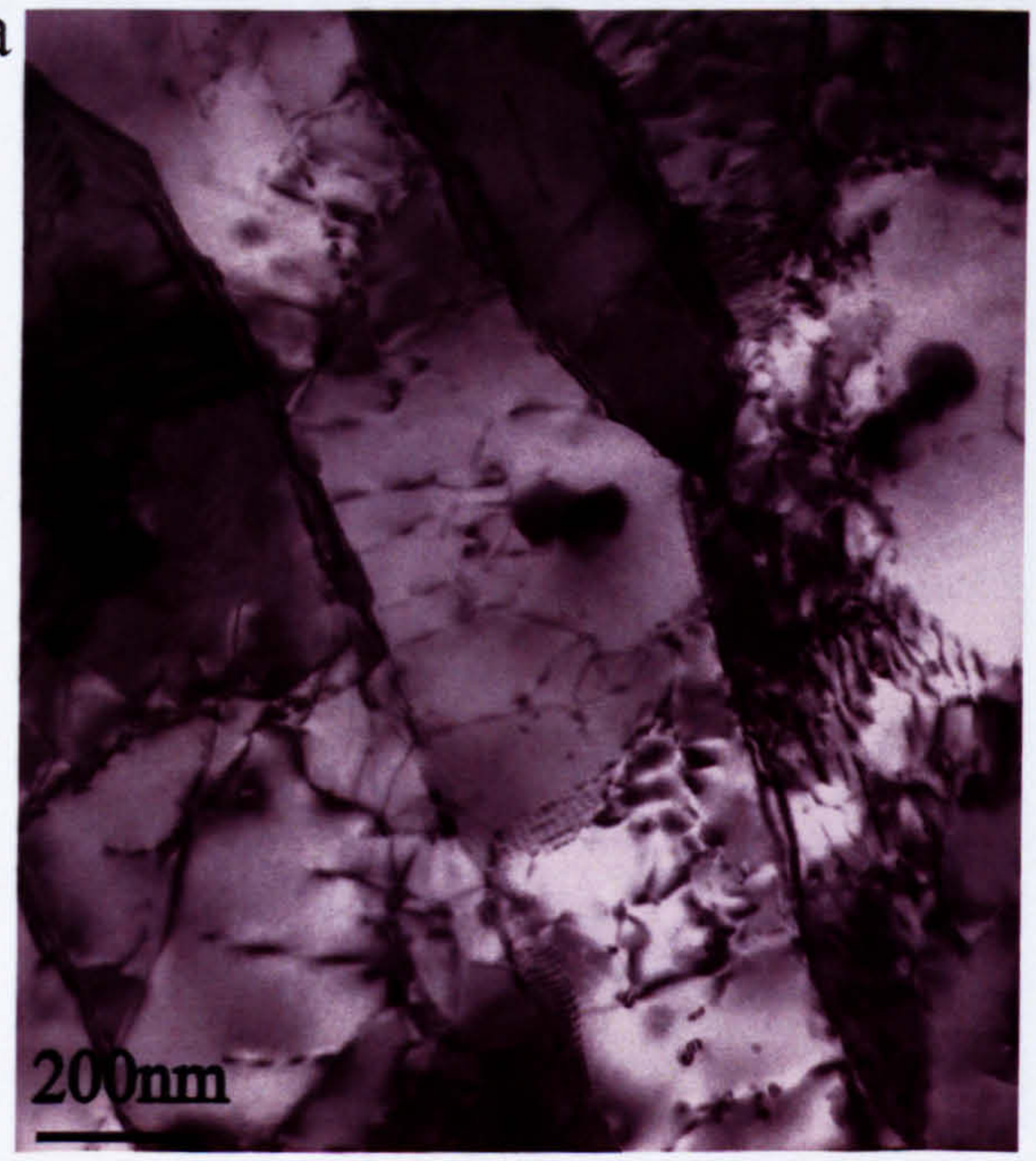

b

Fig. 5.102 TEM images after the 60 seocnds delayed deformation, shows the dense tangled dislocations within the microbands: (a) bright field image, (b) dark field image.

a

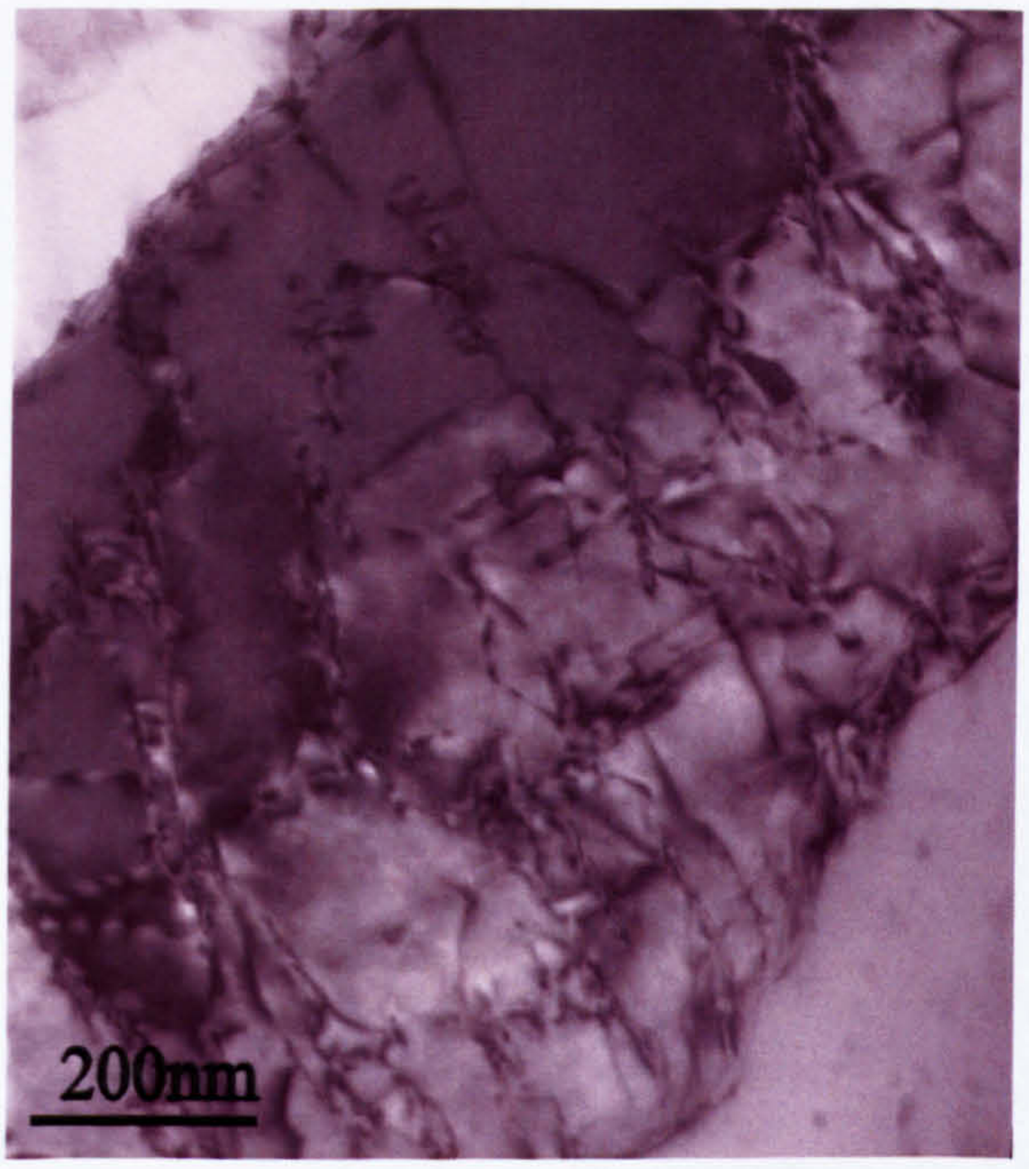

b

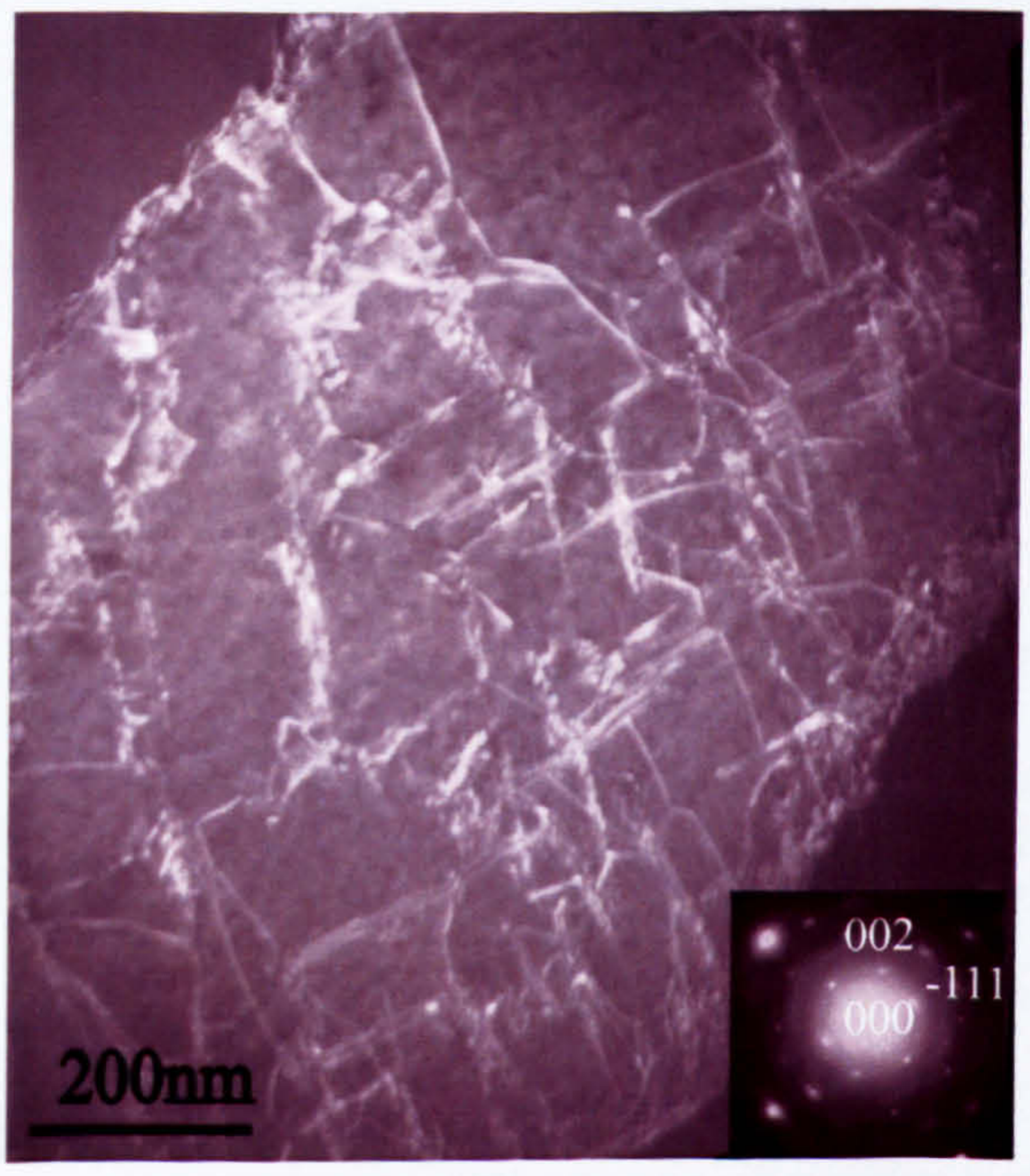

Fig. 5.103 TEM images after the 60 seconds delayed deformation shows the lath-shaped Q' phases and dense dislocations within microbands: (a) bright field image, (b) dark field image.

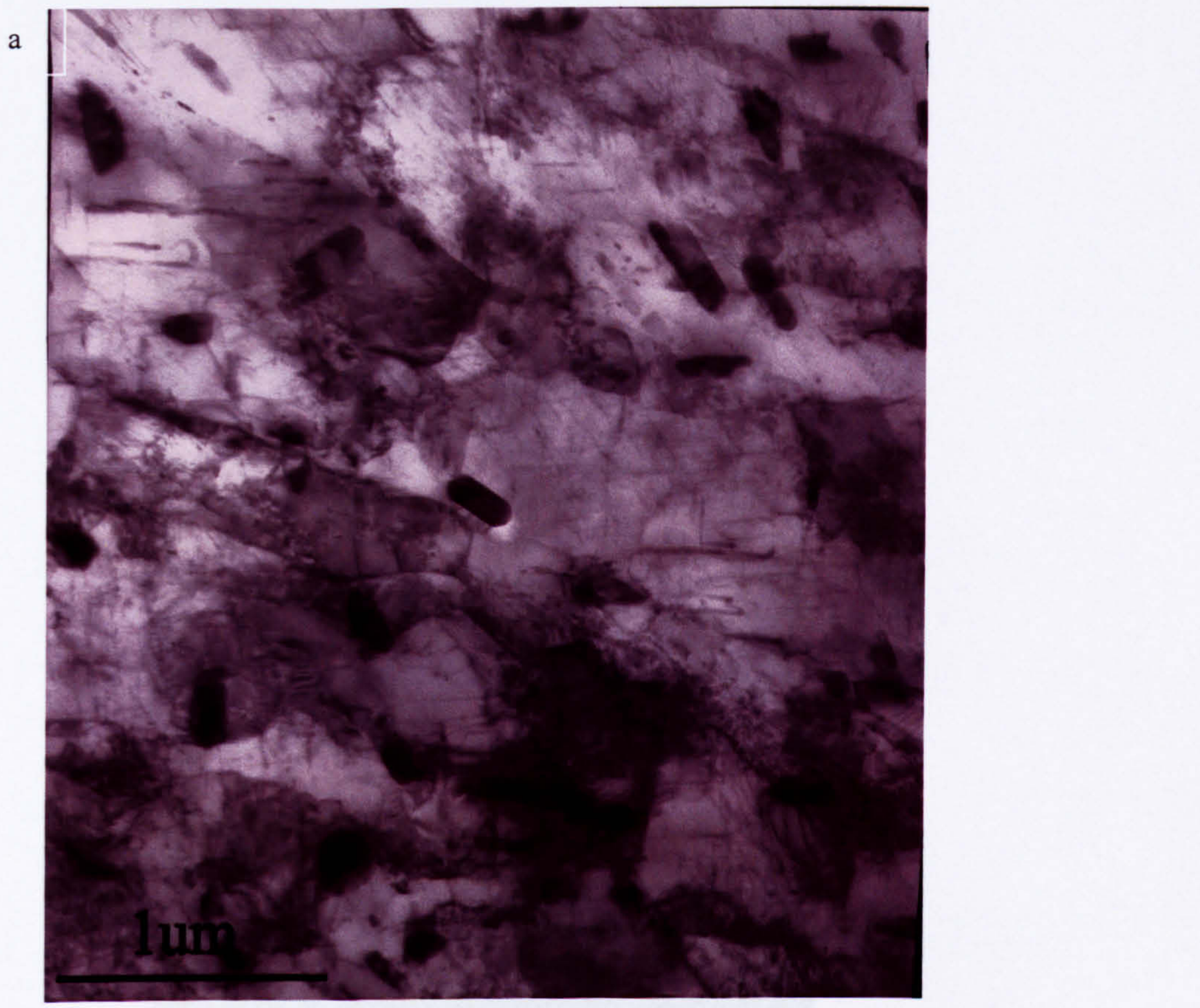

Fig. 5.104 Q phase size analysis after the 60 seconds delayed deformation: (a) TEM image, (b) diffraction pattern, (c) EDS spectrum, (d) size distribution.

a

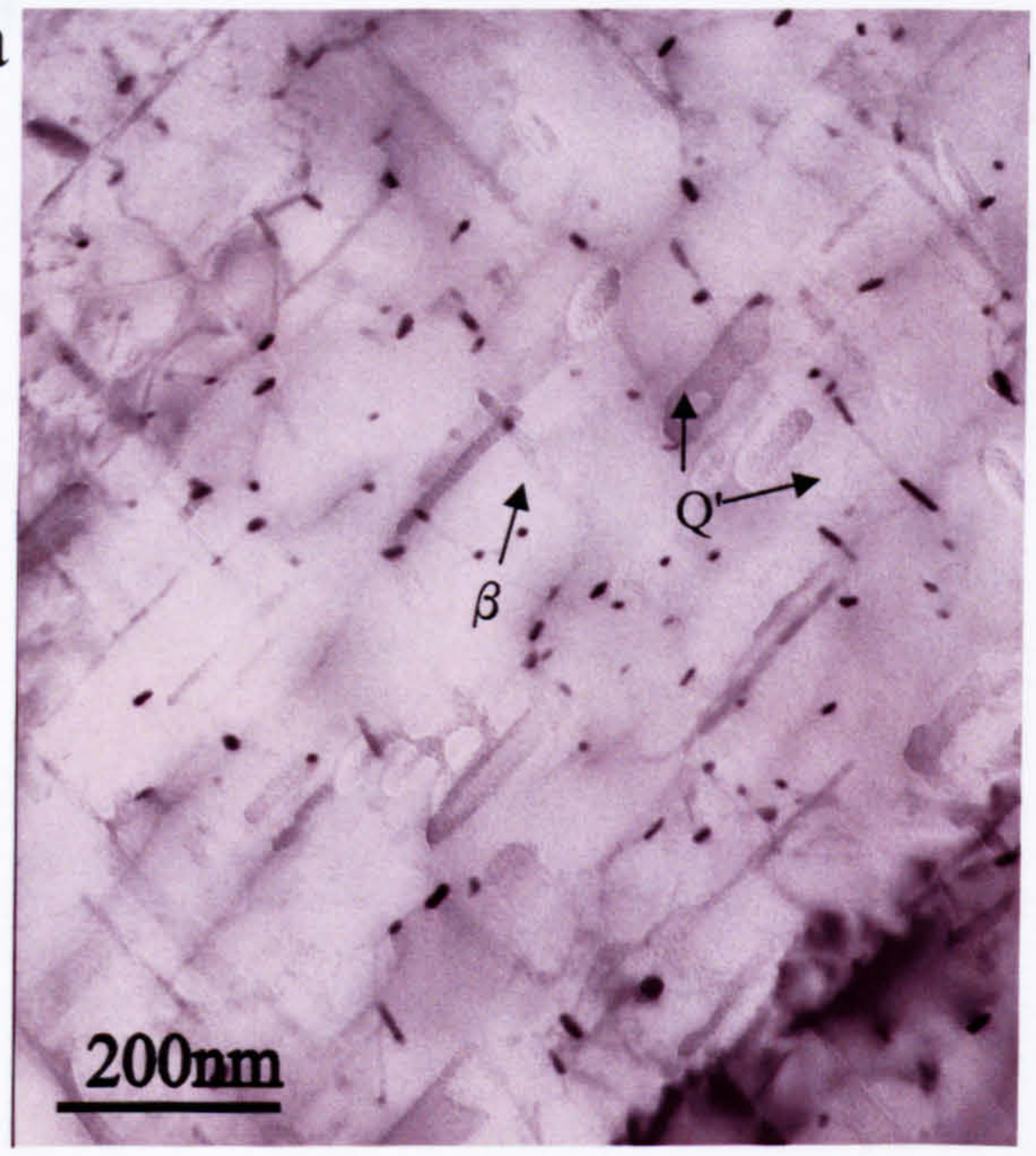

b

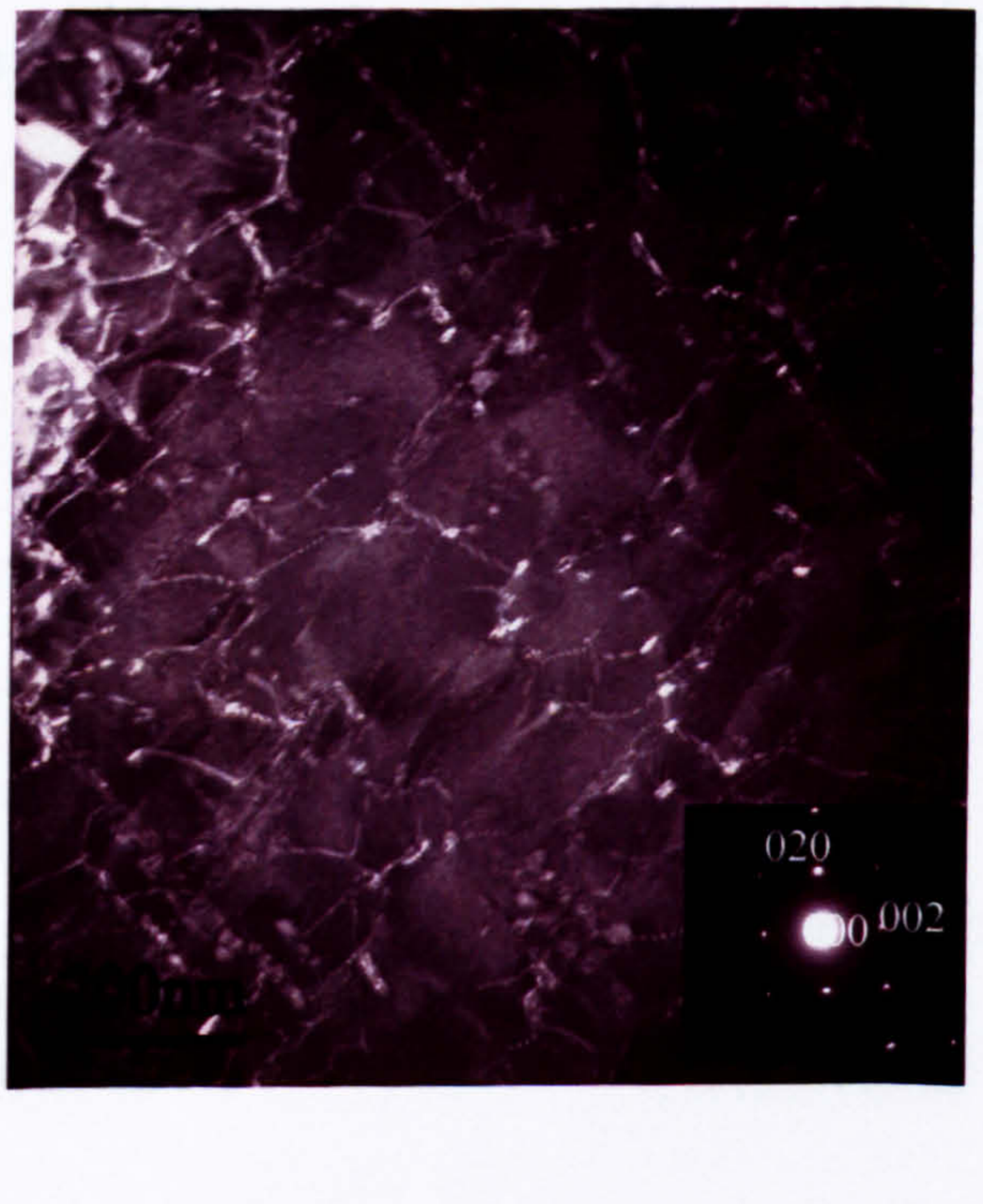

Fig. 5.105 TEM images after the 60 seconds delayed deformation, shows β´and Q´ phase formed on dislocations: (a) bright field image, (b) dark field image.

a

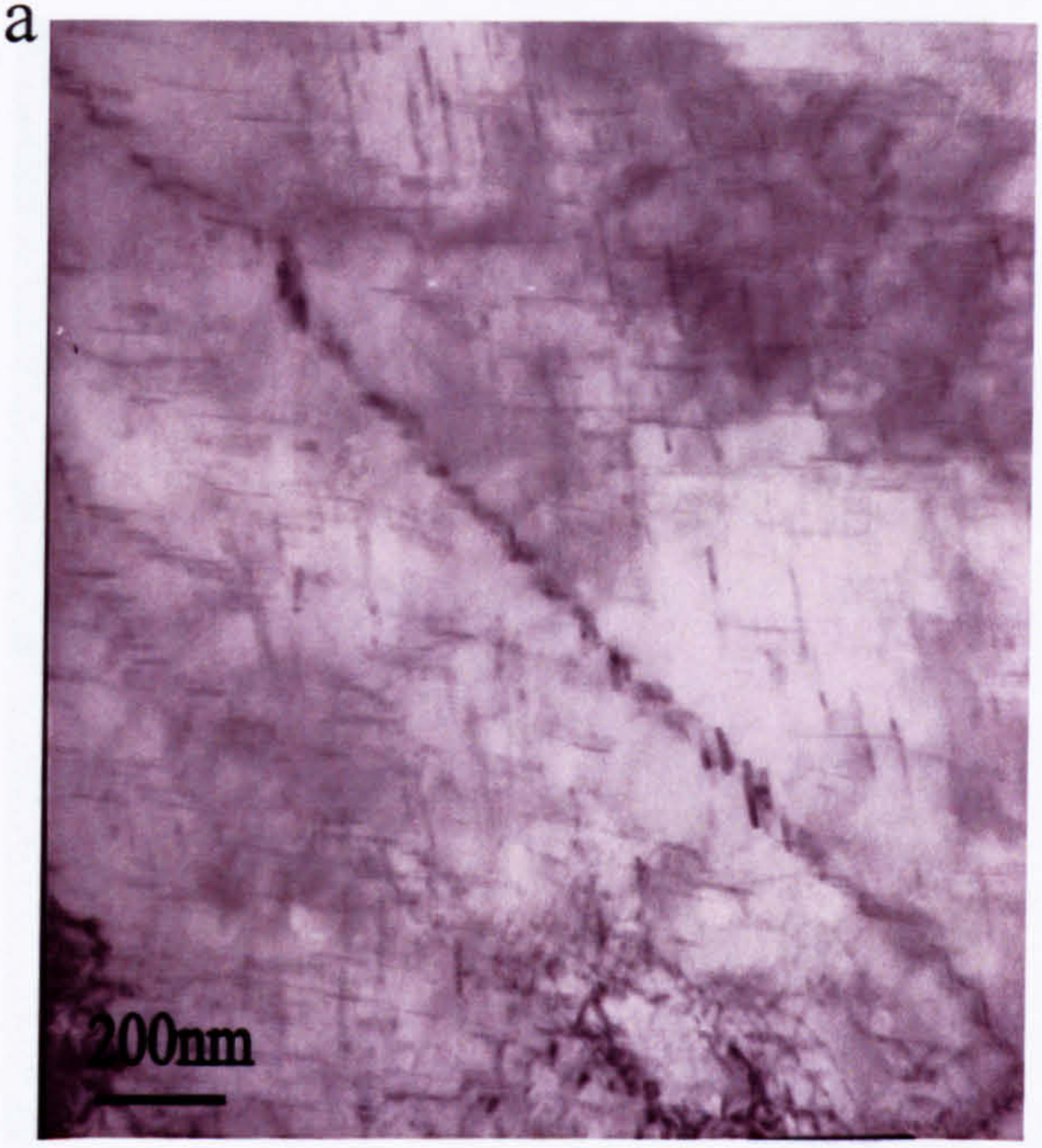

b

Fig. 5.106 TEM images after the 60 seconds delayed deformation, shows the small lath-shaped Q' phases formed on subgrain boundary: (a) bright field image, (b) dark field image.

a

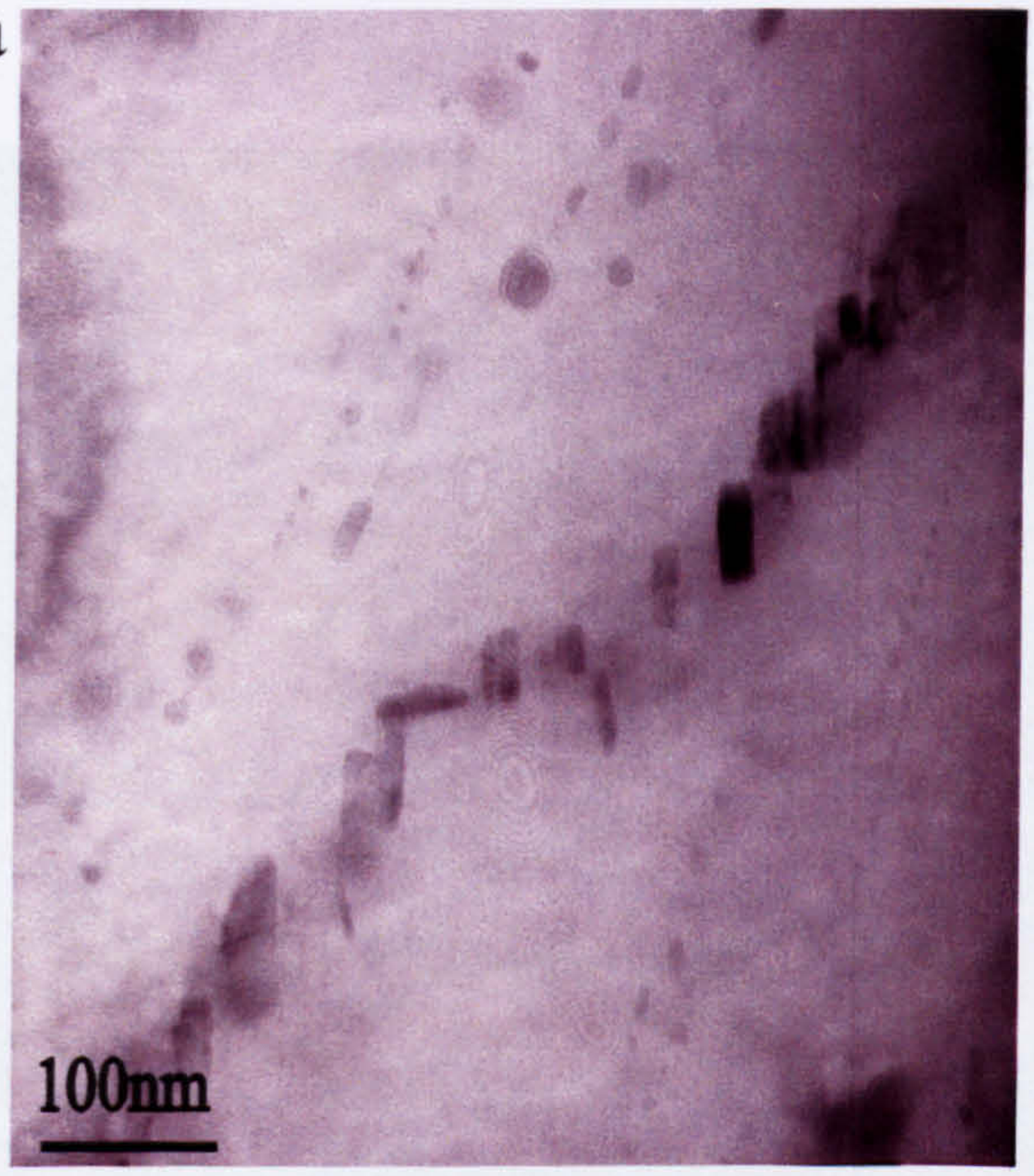

b

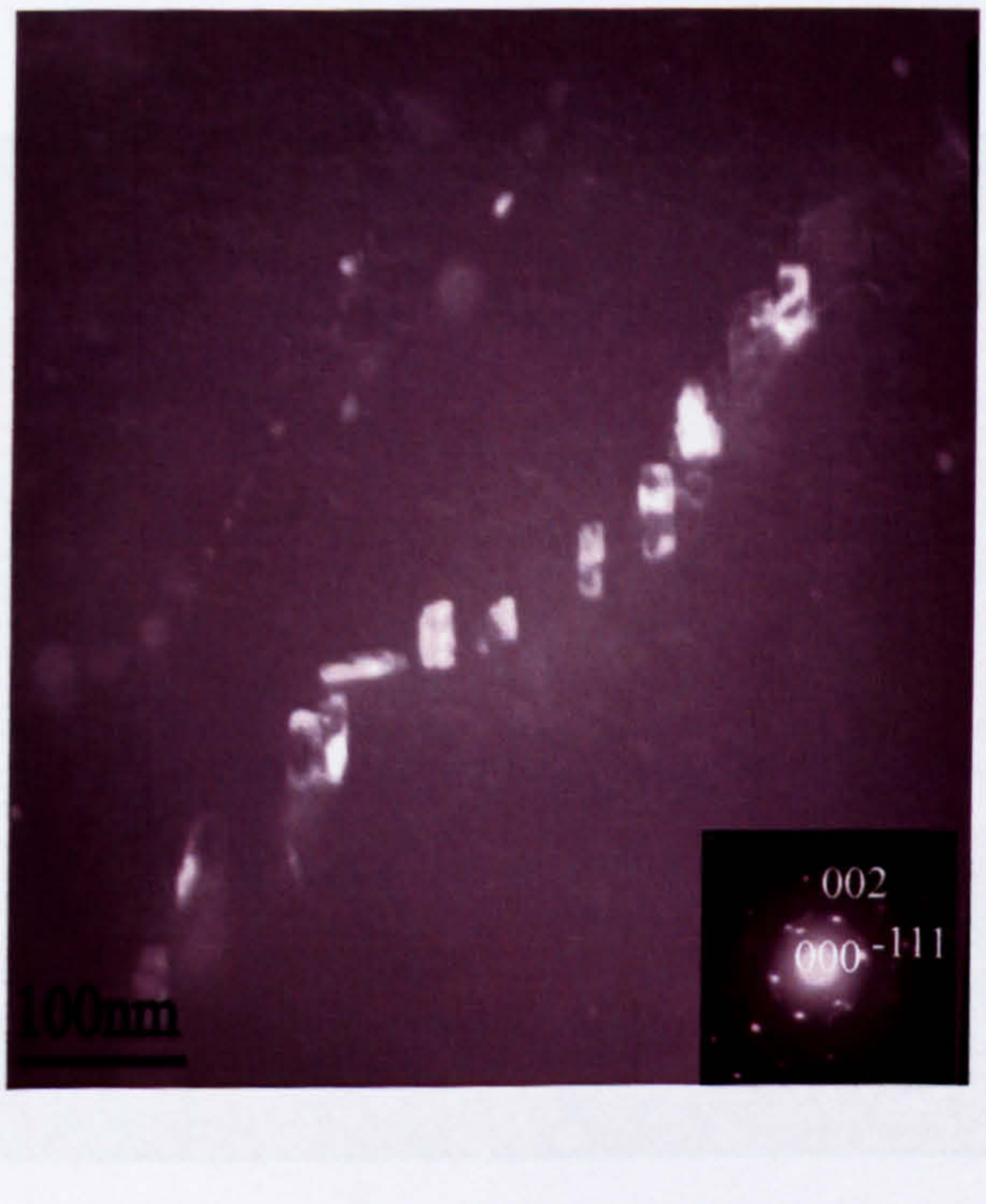

Fig. 5.107 TEM images after the 60 seconds delayed deformation, shows the small lath-shaped Q' phases formed on subgrain boundary: (a) bright field image, (b) dark field image.

a

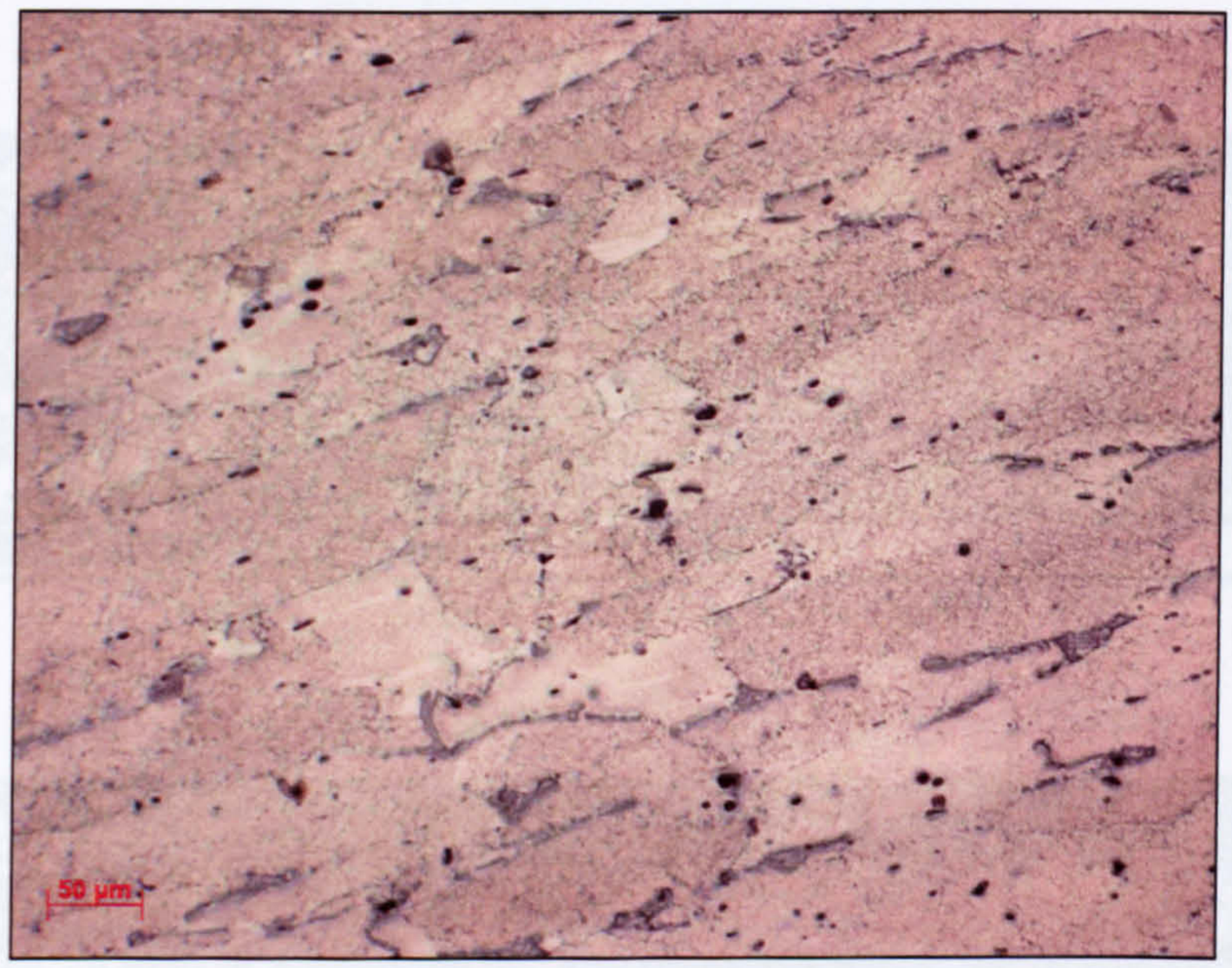

b

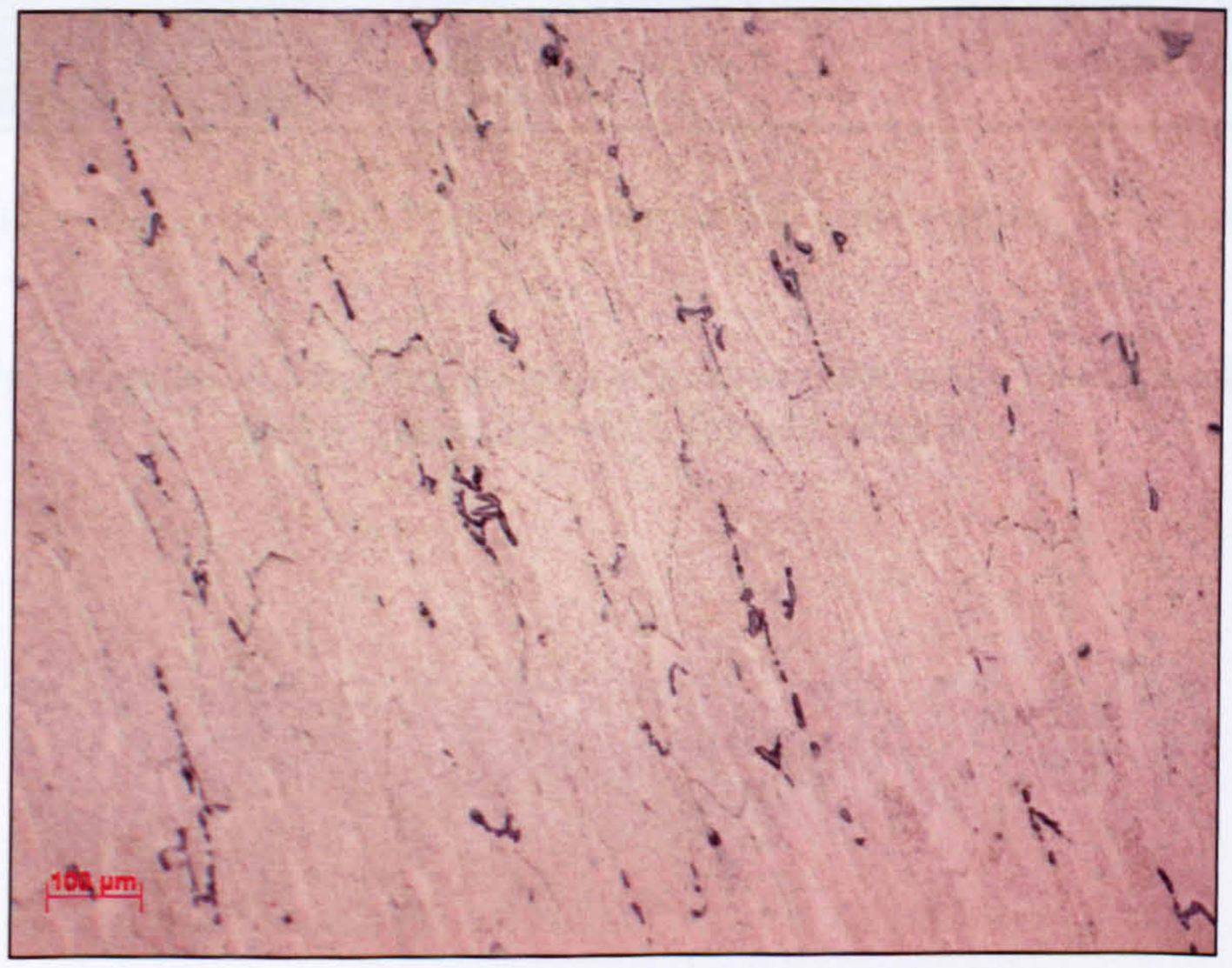

Fig. 5.108 Optical micrographs of deformed structure after the 600 seconds delayed deformation: (a) normal plane, (b) transverse plane.

a

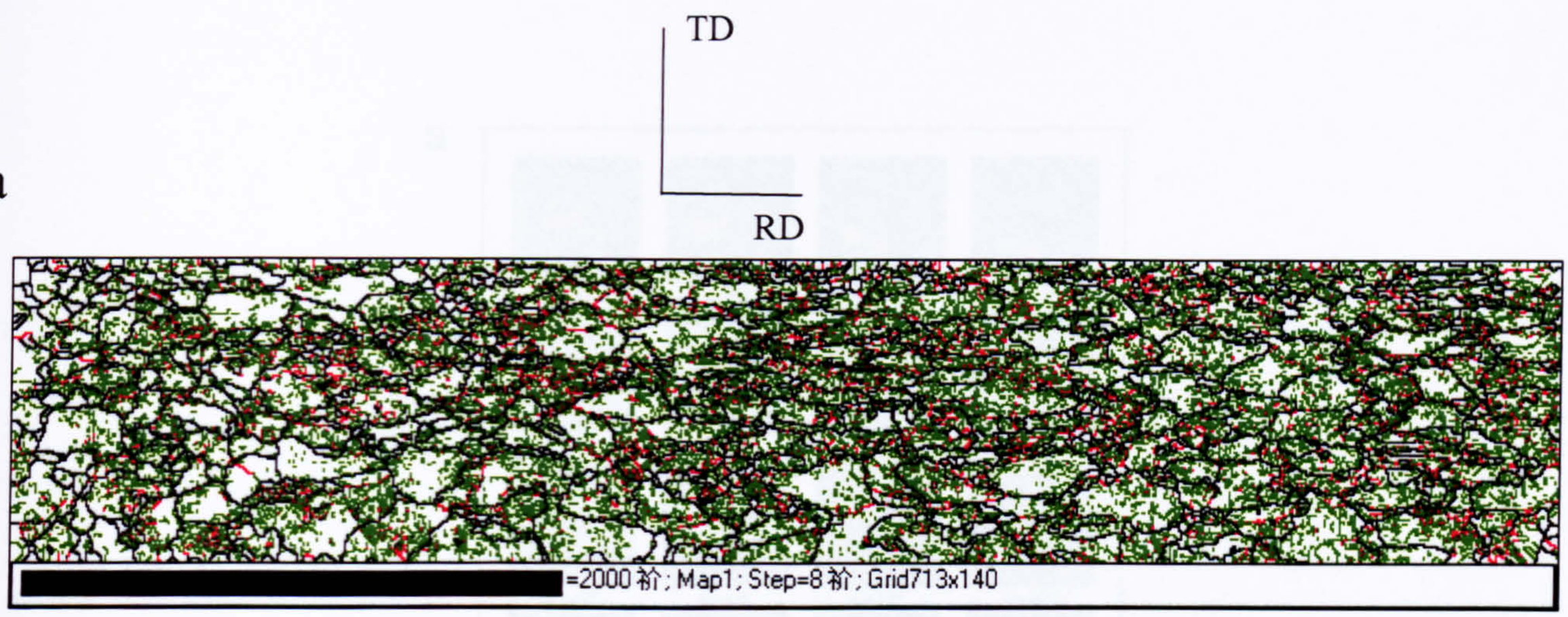

5-10°: green, 10-15°: red, >15°: black

b

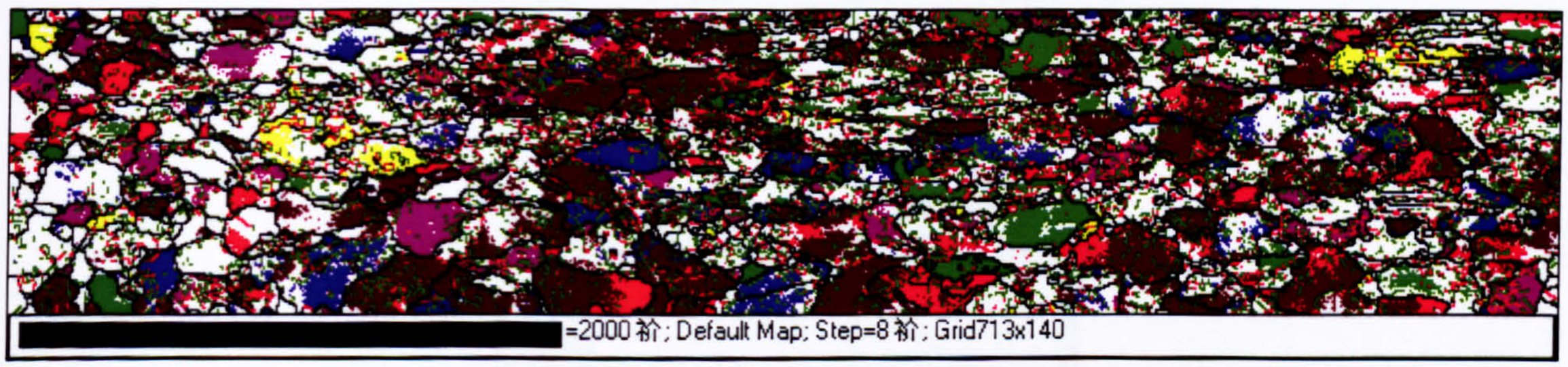

cube-yellow, p-purple, brass-red, copper-blue, goss-green, s-maroon

Fig. 5.109 (a) Orientation map and (b) texture components to the microstructure for the 600 seconds delayed deformed sample.

a

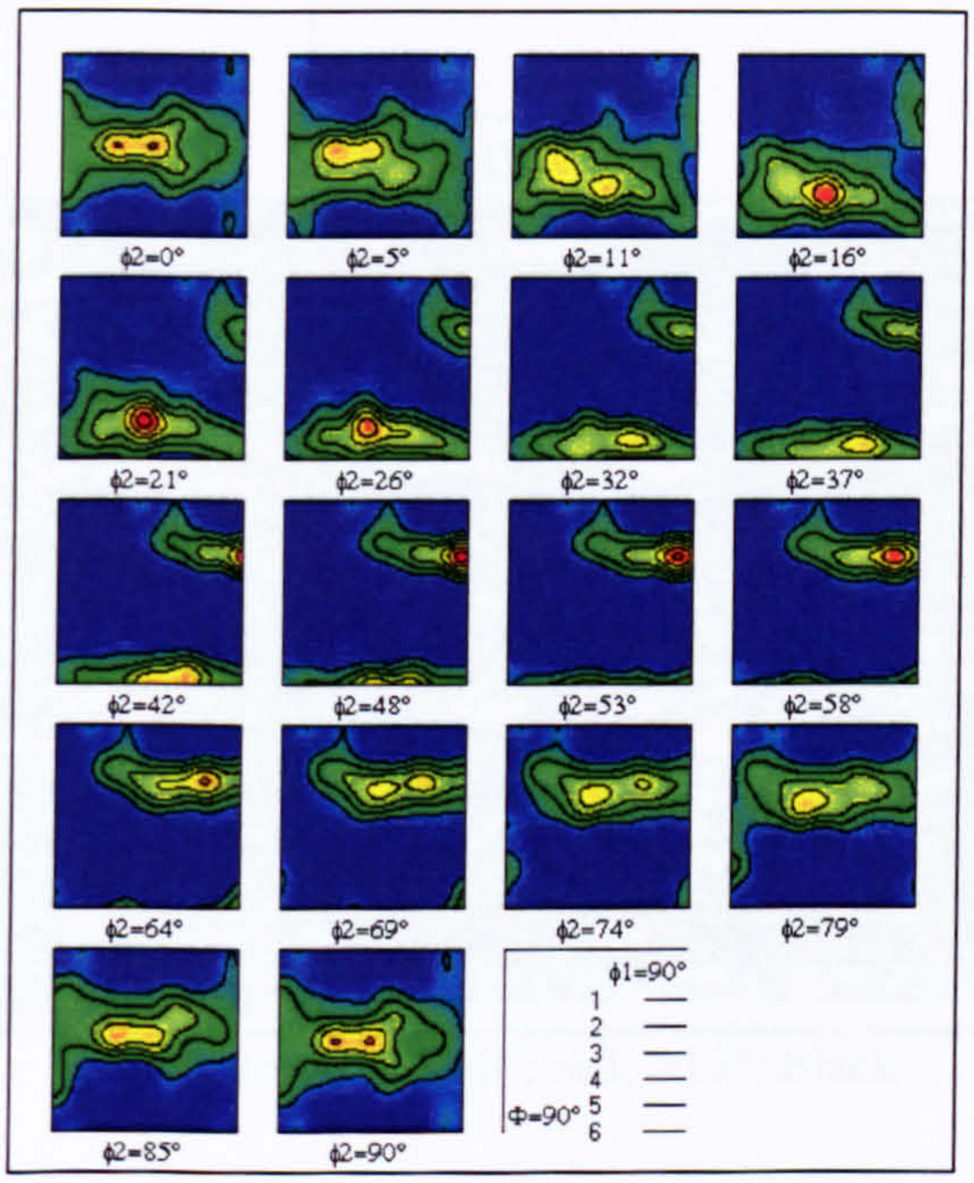

b

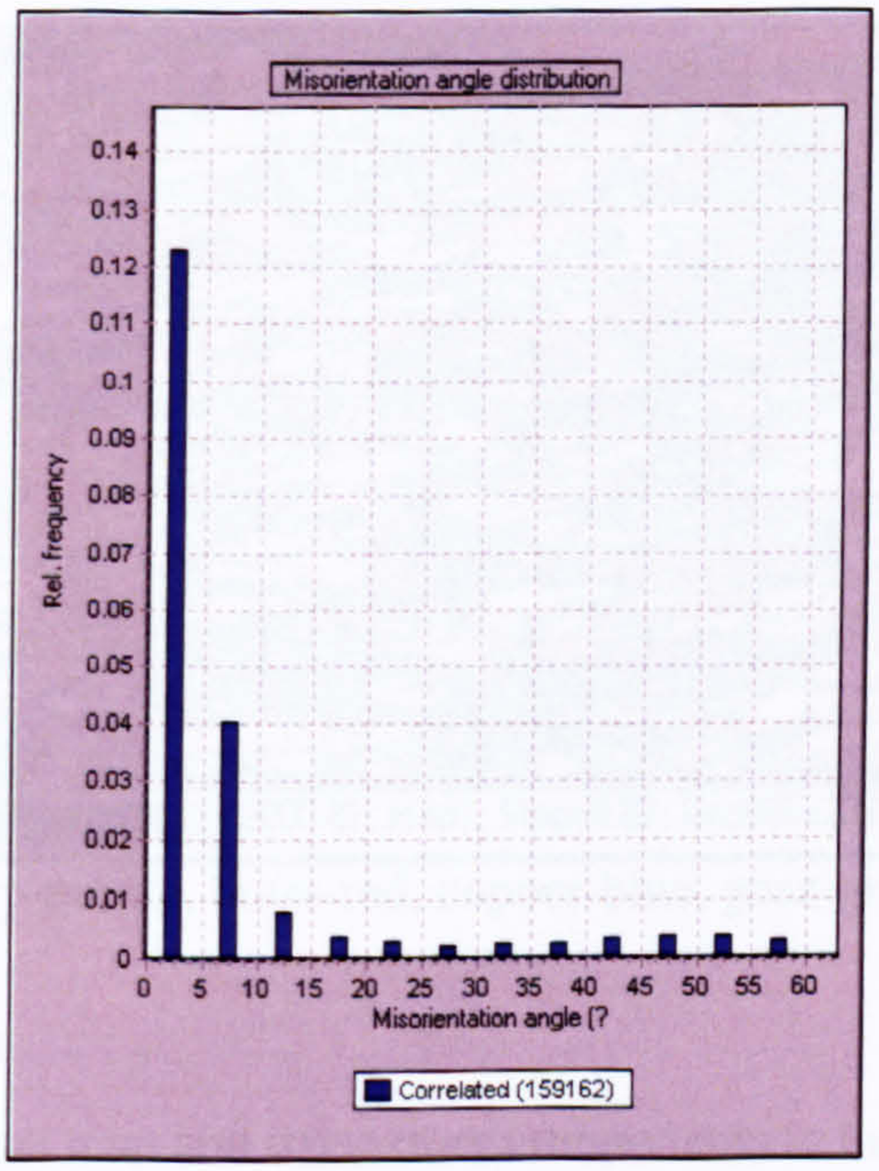

Fig. 5.110 EBSD results of the 600 seconds delayed sample: (a) orientation distribution functions (ODF) maps, (b) misorientation angle distribution.

a

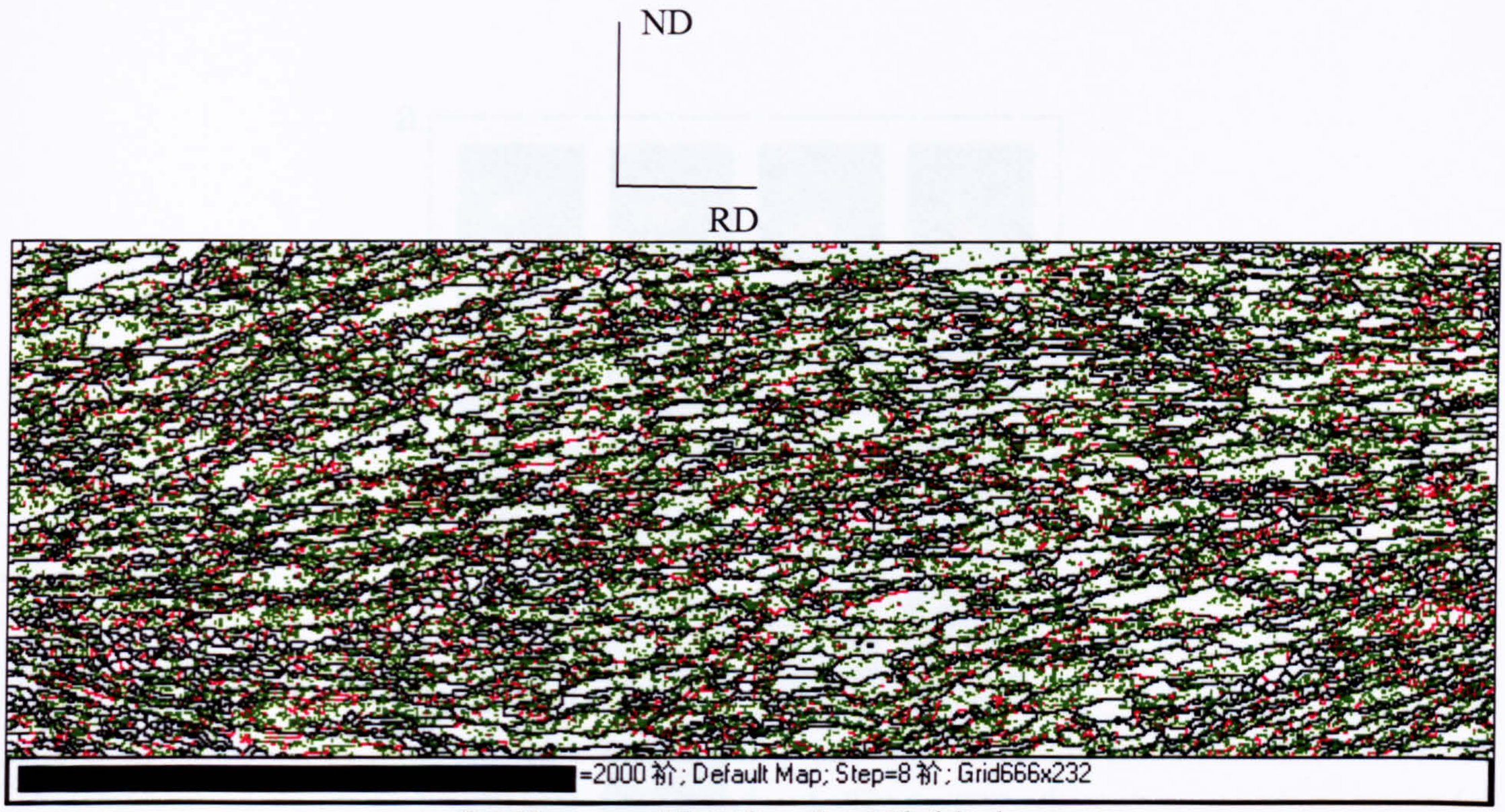

5-10°: green, 10-15°: red, >15°: black

b

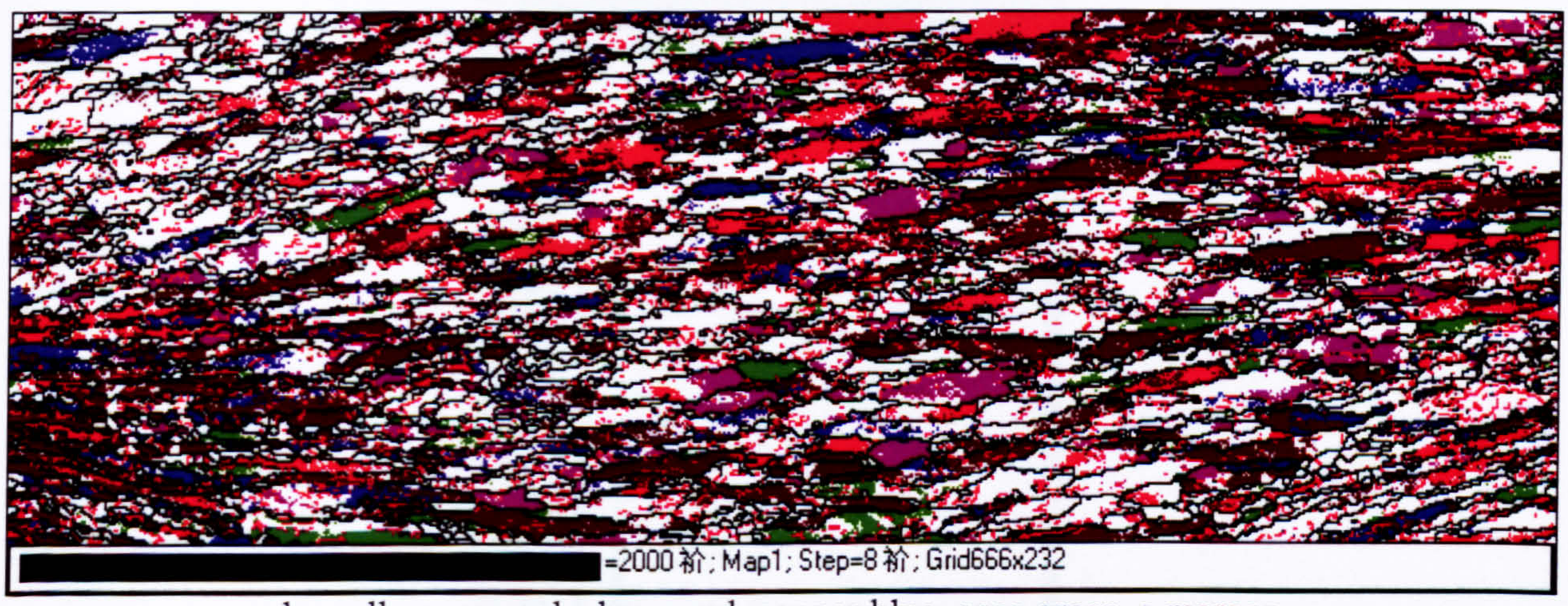

cube-yellow, p-purple, brass-red, copper-blue, goss-green, s-maroon

Fig. 5.111 (a) Orientation map and (b) texture components to the microstructure for the 600 seconds delayed deformed sample.

a

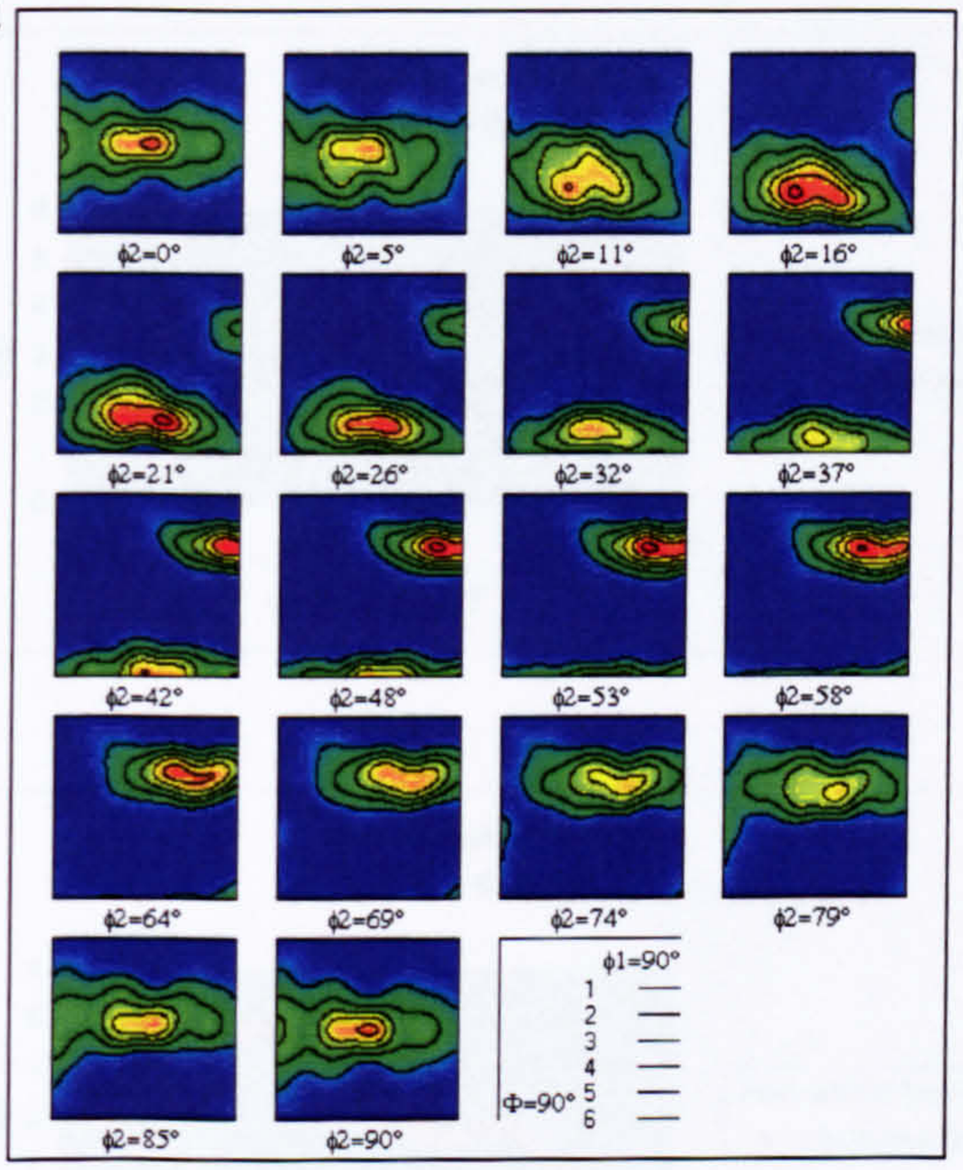

b

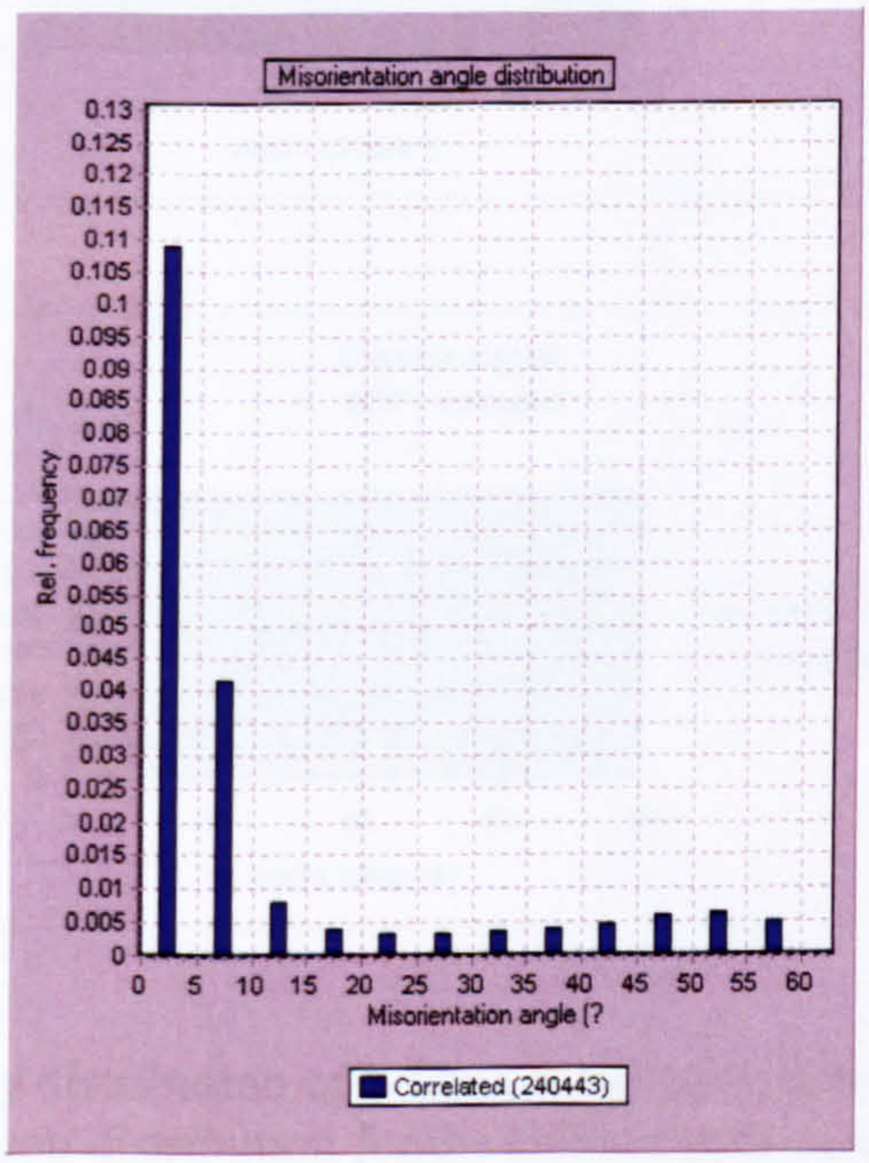

Fig. 5.112 EBSD results of the 600 seconds delayed sample: (a) orientation distribution functions (ODF) maps, (b) misorientation angle distribution.

a

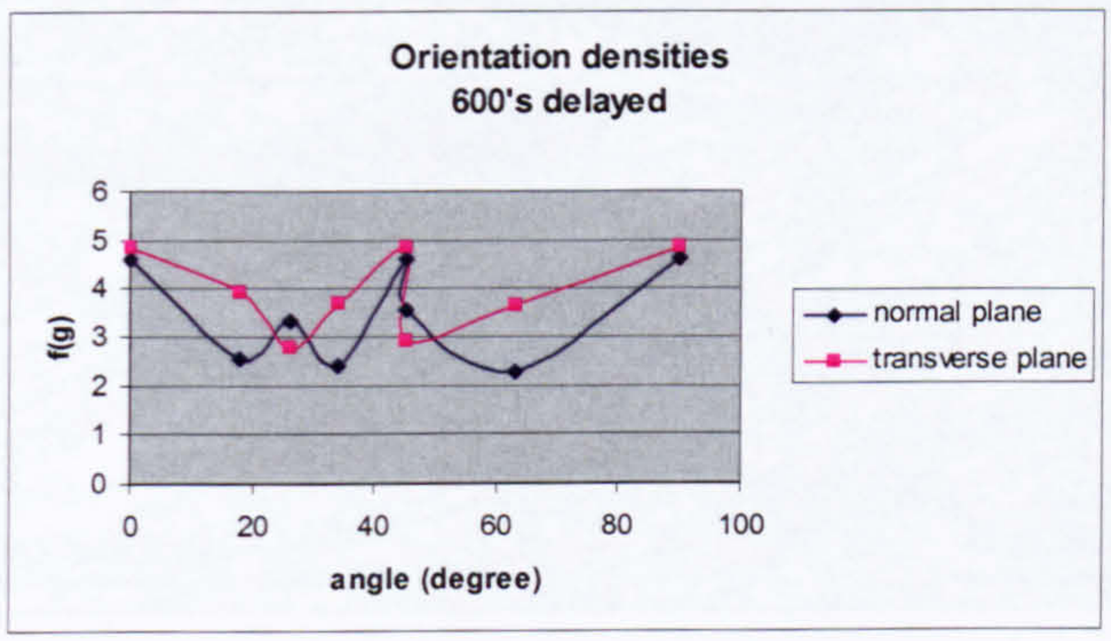

b

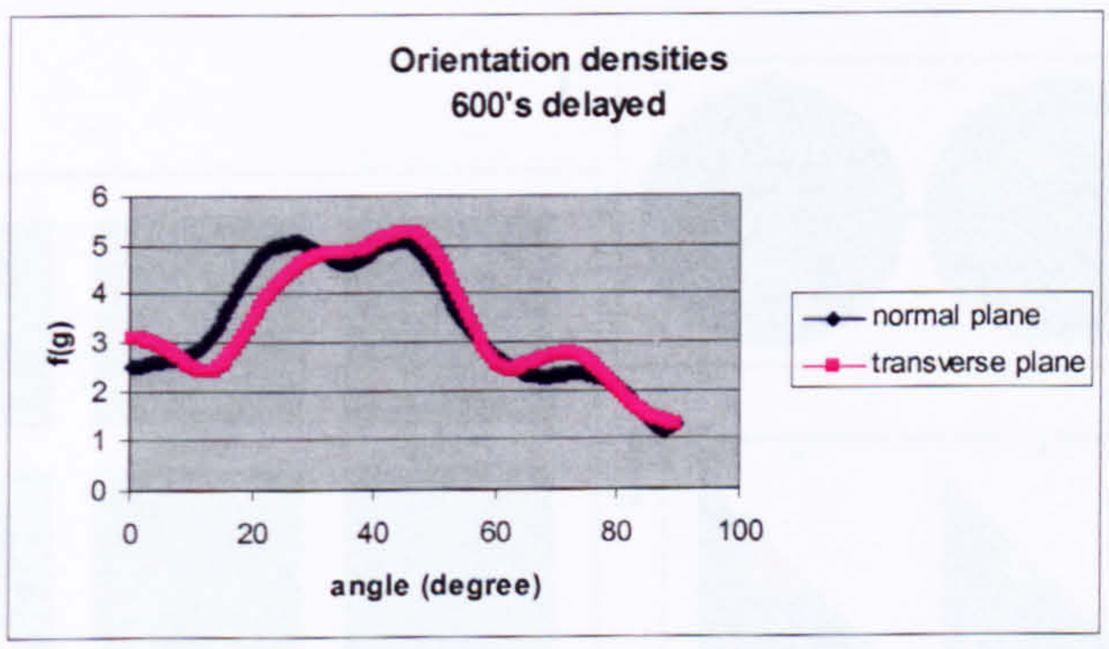

C

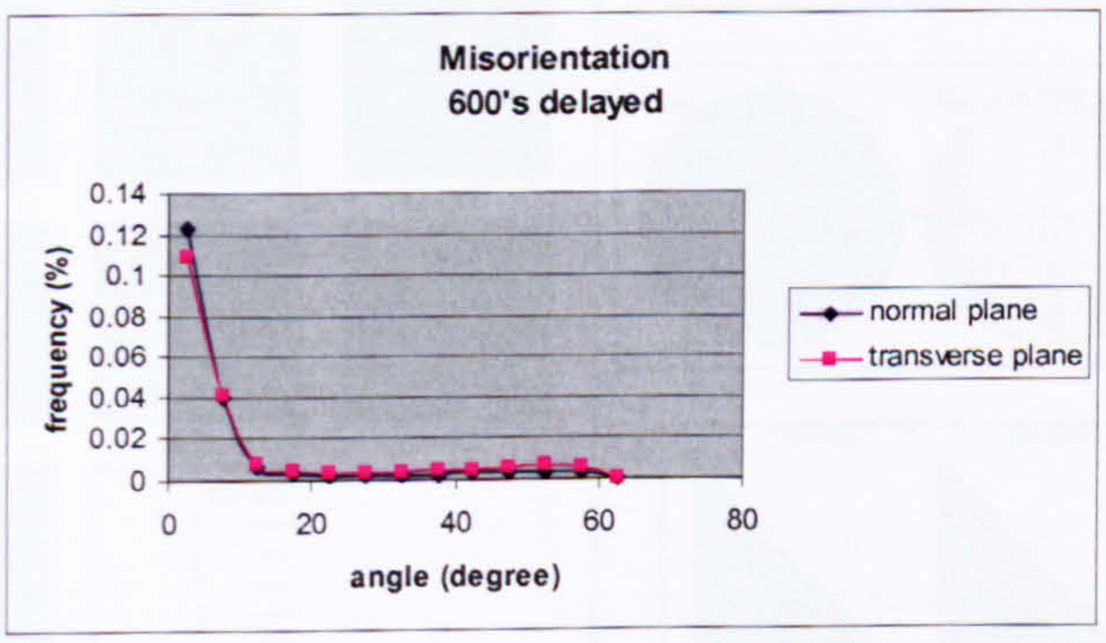

Fig. 5.113 a) Density distribution of β fibre, (b) density distribution of α fibre, (c) misorientaiton distribution for the 600 seconds delayed sample.

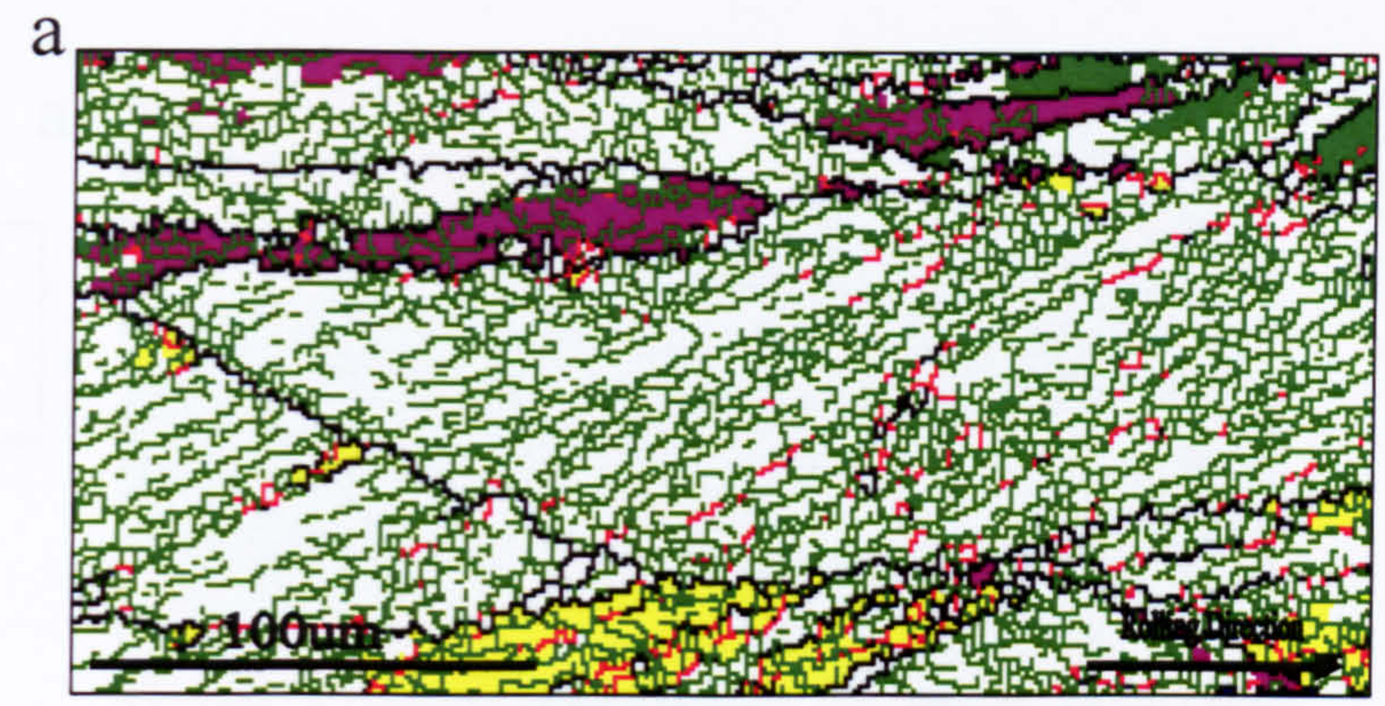

2-10°: green, 10-15°: red, >15°: black Step size=0.5μm

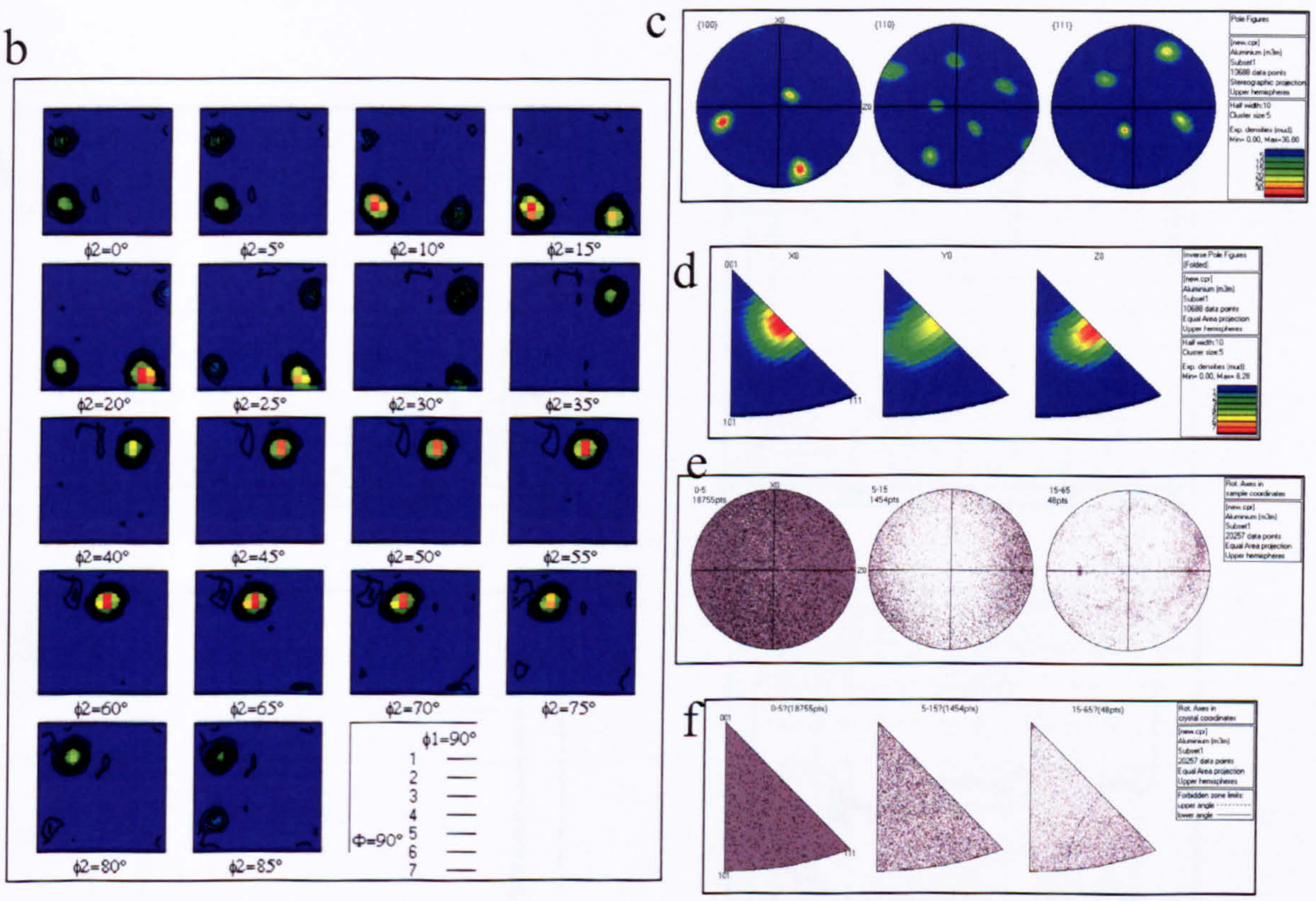

Fig. 5.114 Random-orientated grain in the 600 seconds delayed sample: (a) texture and boundary map, (b) ODF, (c) pole figures, (d) inverse pole figures, the distribution of misorientation axis vectors in (e) sample and (f) crystal lattice coordinates.

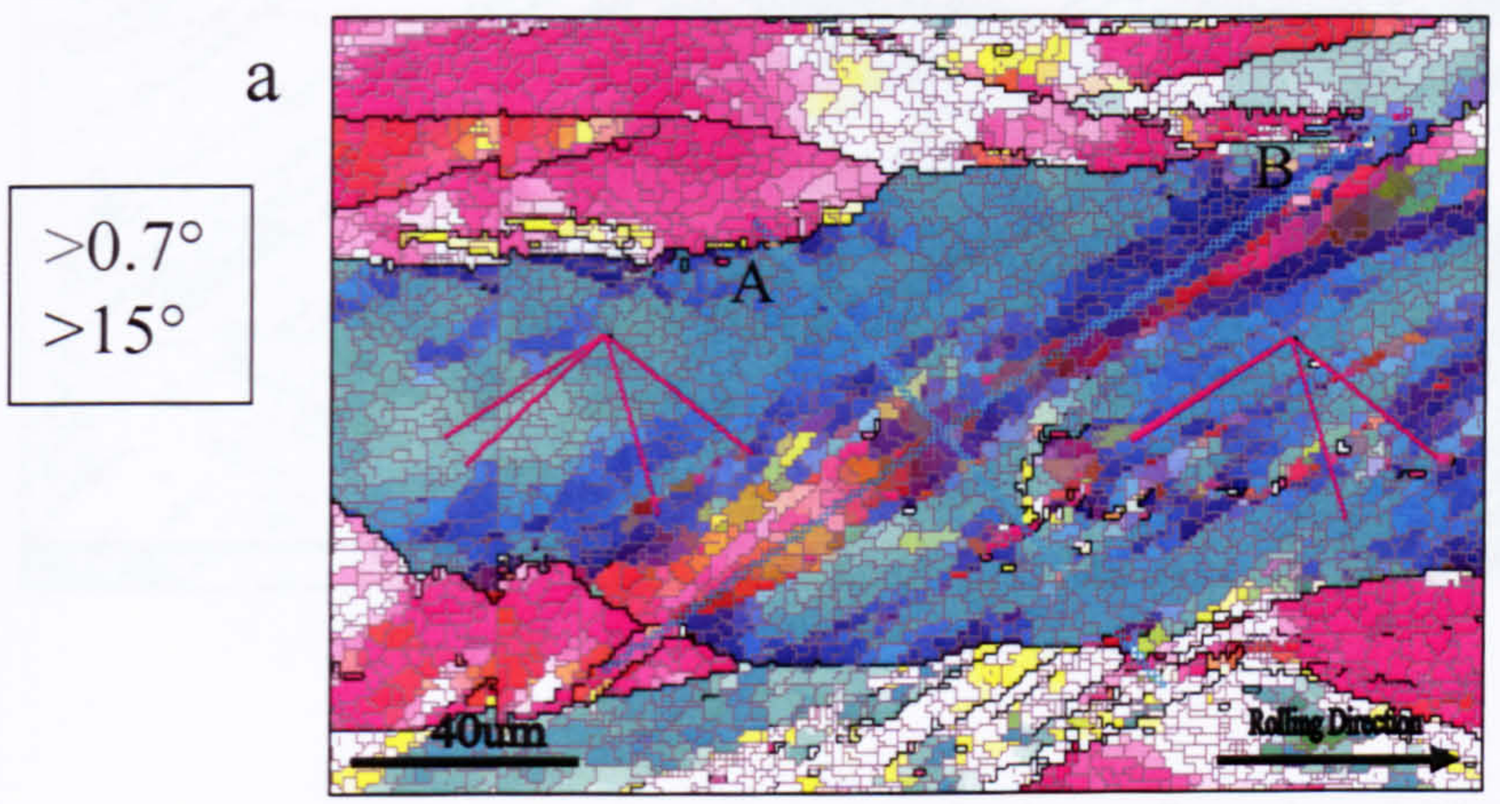

Fig. 5.115 Random-orientated grain in the 600 seconds delayed sample: (a) relative map, (b) (d) relative and (c) (e) cumulative misorientation distributions of line scans performed along A and B in (a).

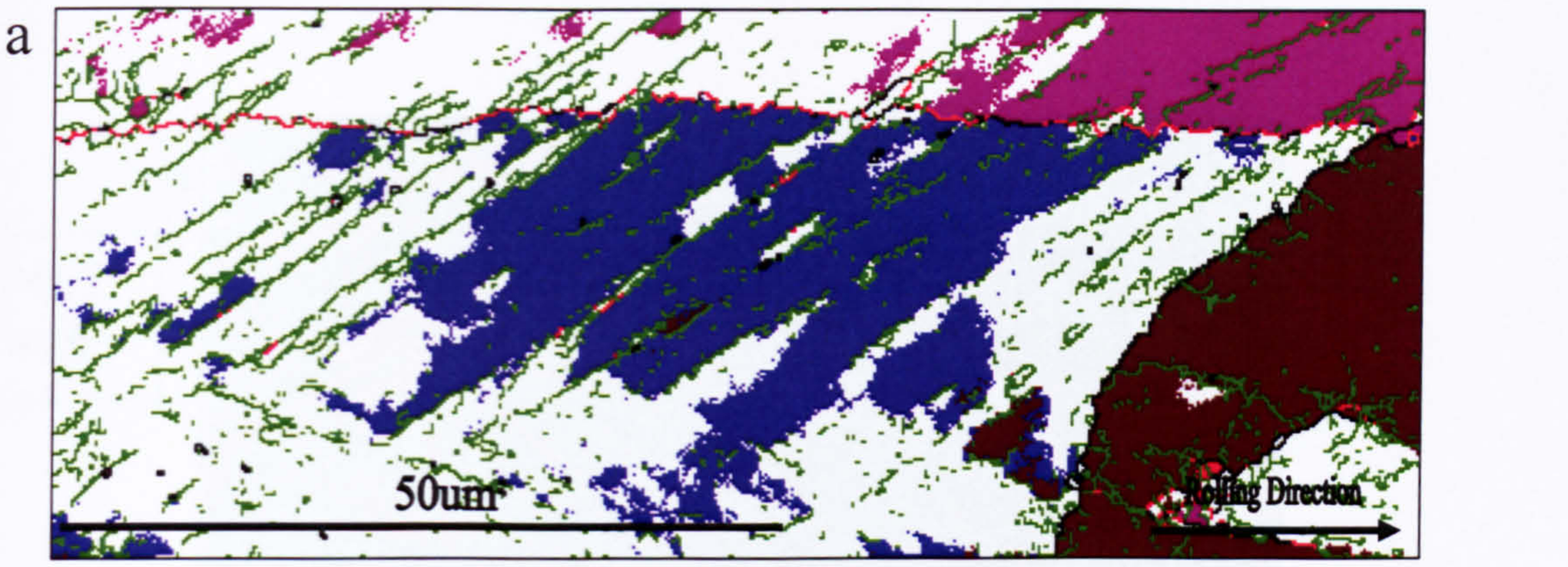

5-10°: green, 10-15°: red, >15°: black Step size=0.25μm

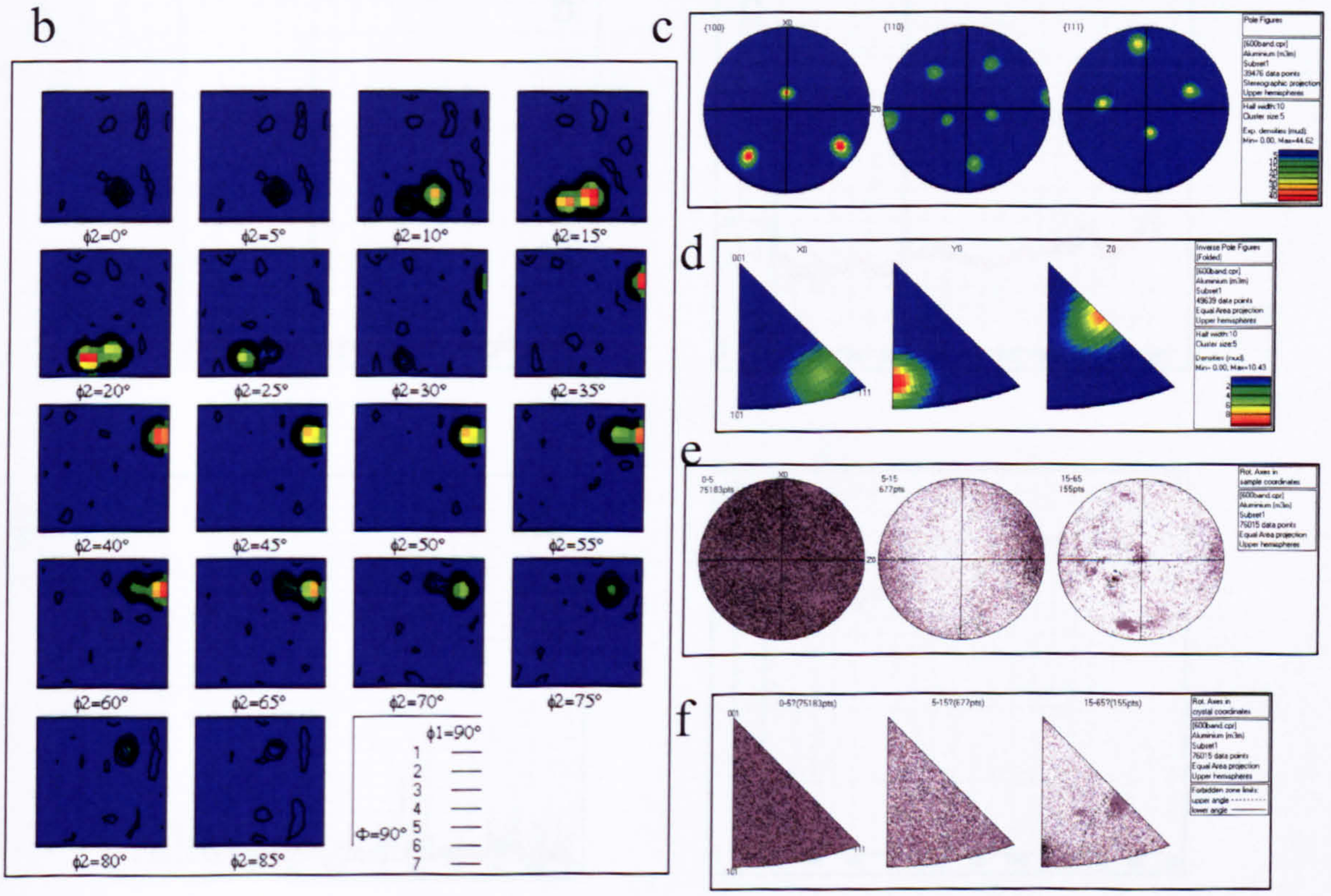

Fig. 5.116 Copper-orientated grain in the 600 seconds delayed sample: (a) texture and boundary map, (b) ODF, (c) pole figures, (d) inverse pole figures, the distribution of misorientation axis vectors in (e) sample and (f) crystal lattice coordinates.

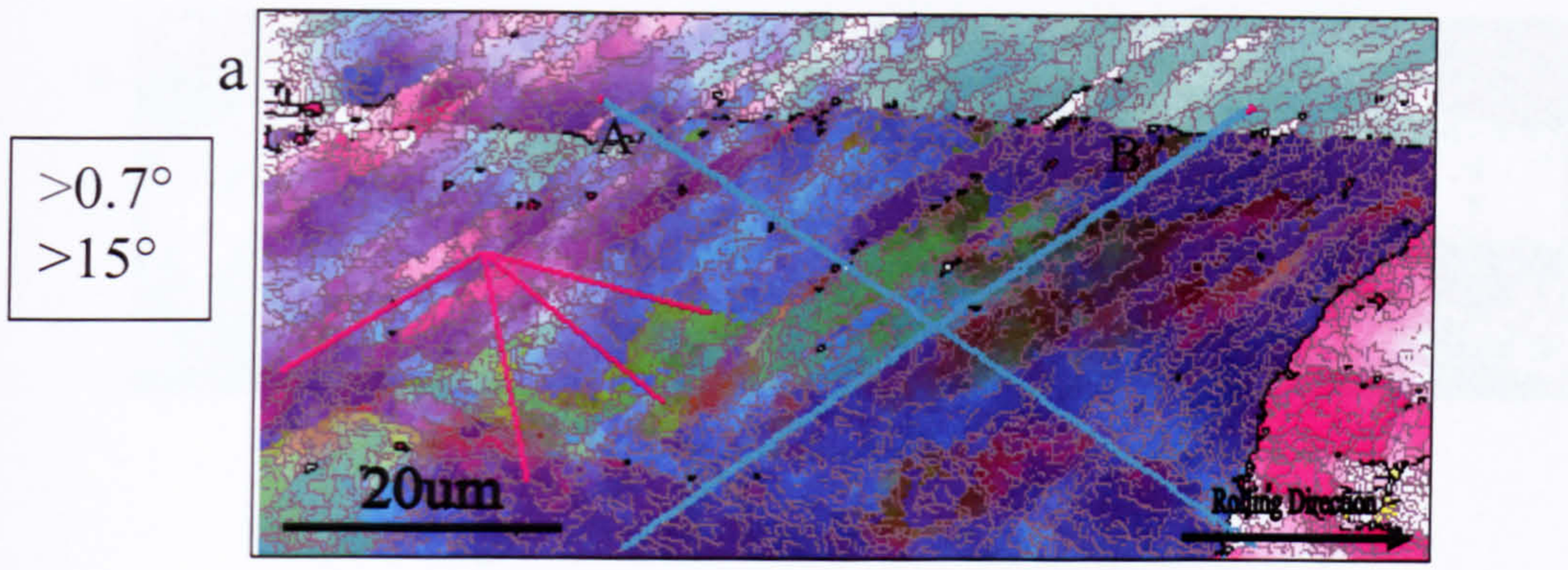

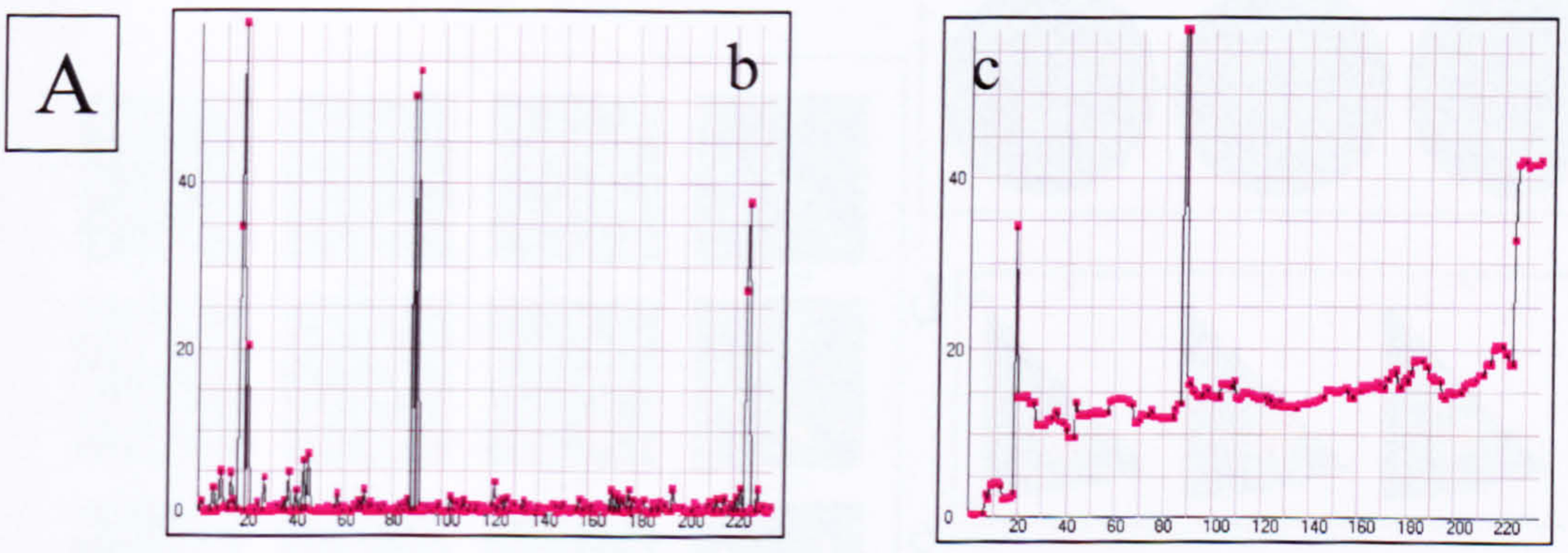

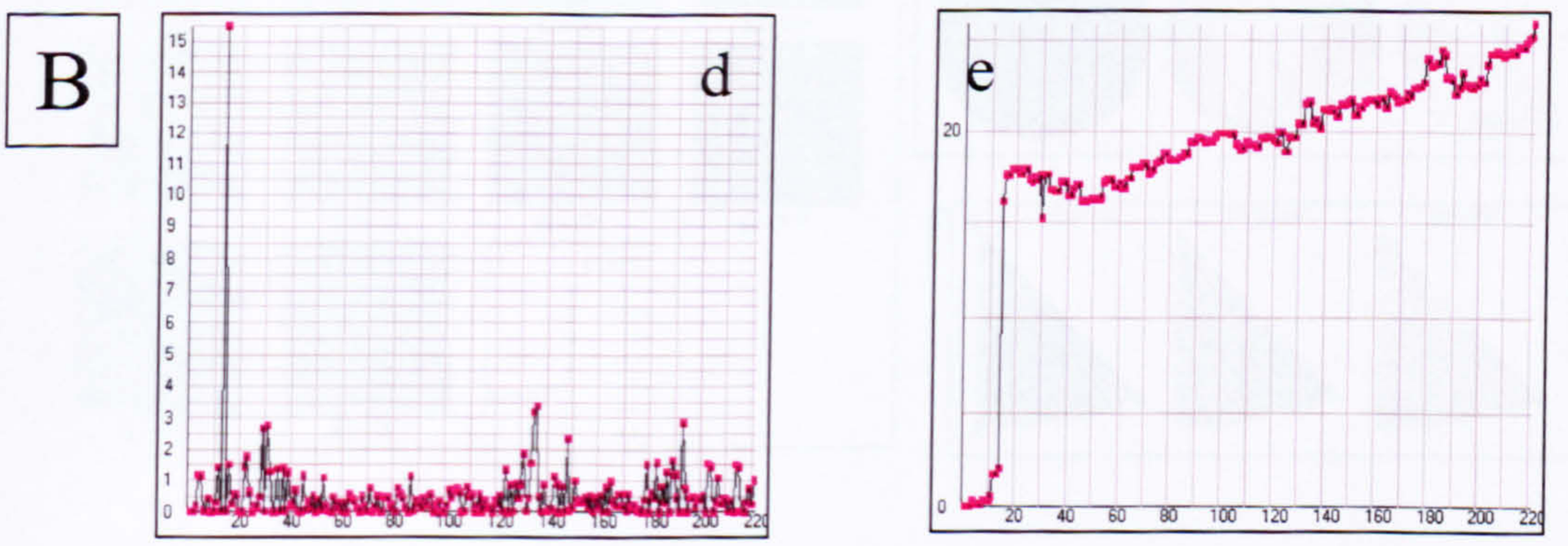

Fig. 5.117 Copper-orientated grain in the 600 seconds delayed sample: (a) relative map, (b) (d) relative and (c) (e) cumulative misorientation distributions of line scans performed along A and B in (a).

5-10°: green, 10-15°: red, >15°: black Step size=0.25μm

Fig. 5.118 S-orientated grain in the 600 seconds delayed sample: (a) texture and boundary map, (b) ODF, (c) pole figures, (d) inverse pole figures, the distribution of misorientation axis vectors in (e) sample and (f) crystal lattice coordinates.

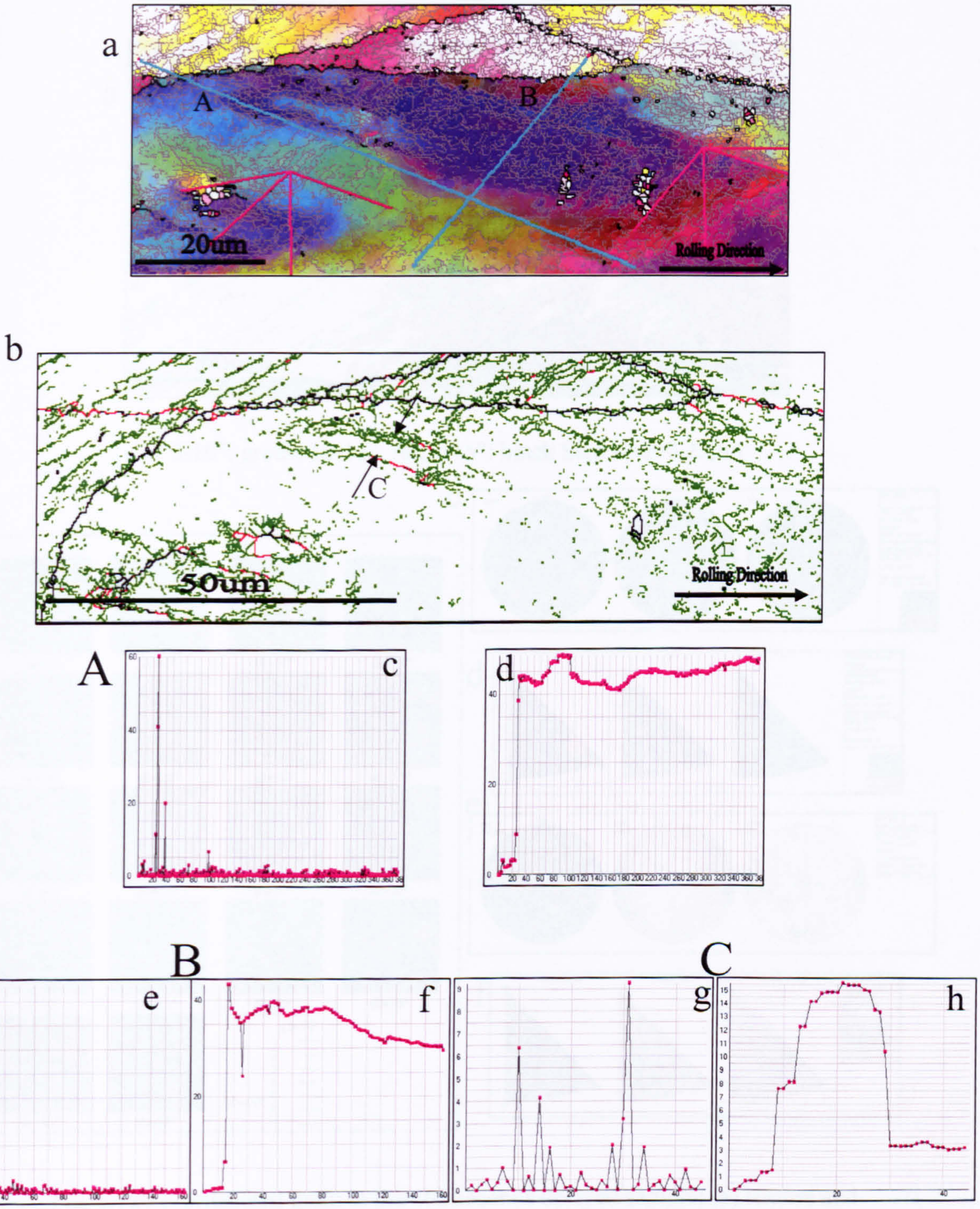

Fig. 5.119 S-orientated grain in the 600 seconds delayed sample: (a) relative map, (b) orientation map, (c) (e) (g) relative and (d) (f) (h) cumulative misorientation distributions of line scans performed along A and B in (a), C in (b).

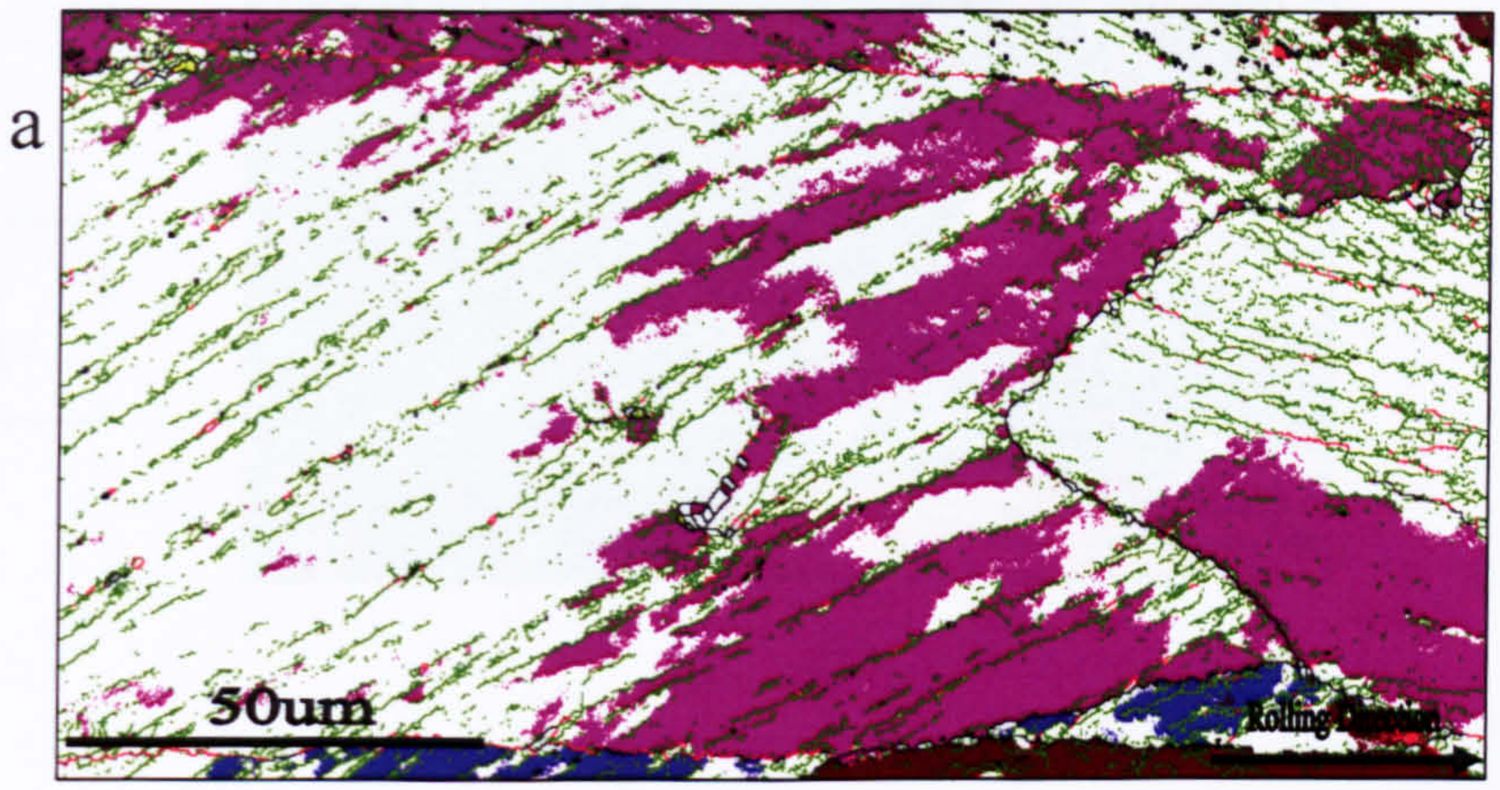

5-10°: green, 10-15°: red, >15°: black Step size=0.25μm

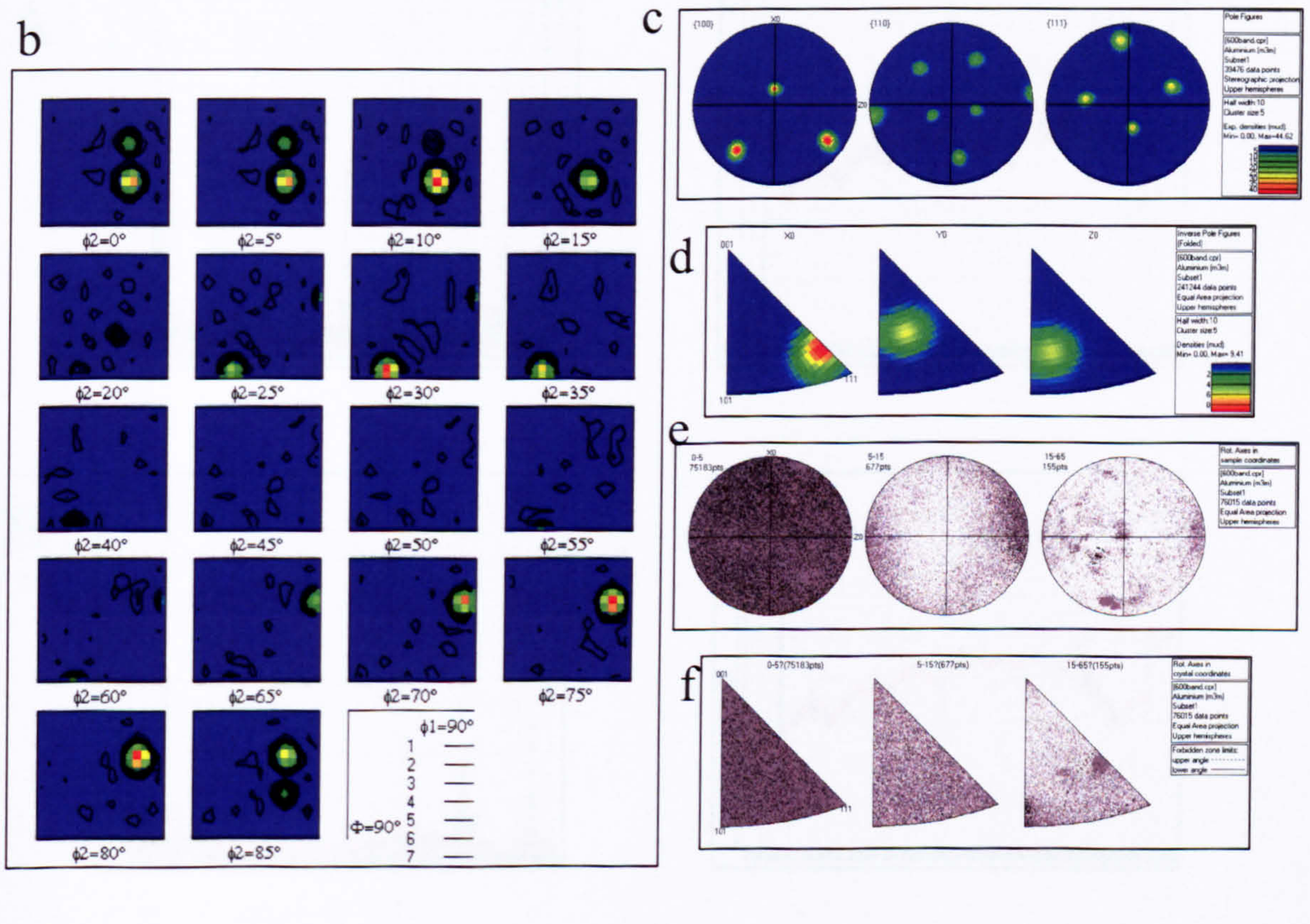

Fig. 5.120 P-orientated grain in the 600 seconds delayed sample: (a) texture and boundary map, (b) ODF, (c) pole figures, (d) inverse pole figures, the distribution of misorientation axis vectors in (e) sample and (f) crystal lattice coordinates.

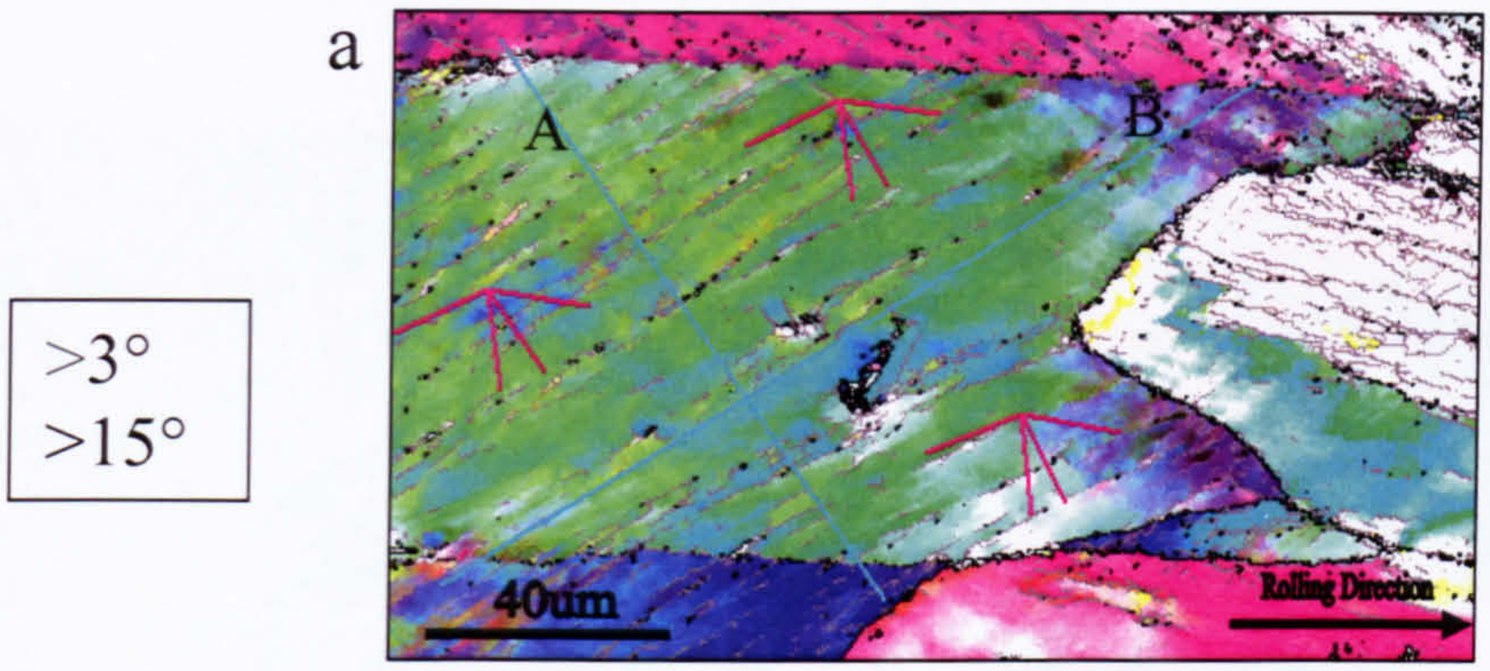

Fig. 5.121 P-orientated grain in the 600 seconds delayed sample: (a) relative map, (b) (d) relative and (c) (e) cumulative misorientation distributions of line scans performed along A and B in (a).

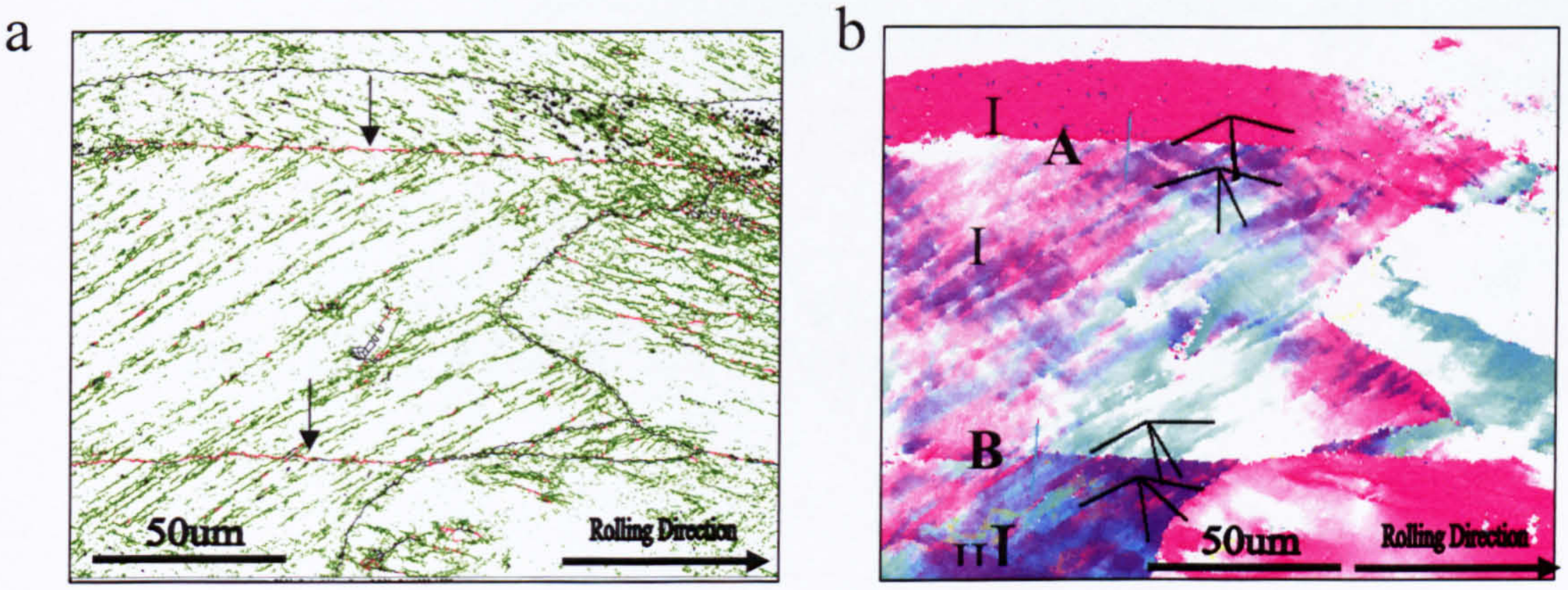

5-10°: green, 10-15°: red, >15°: black

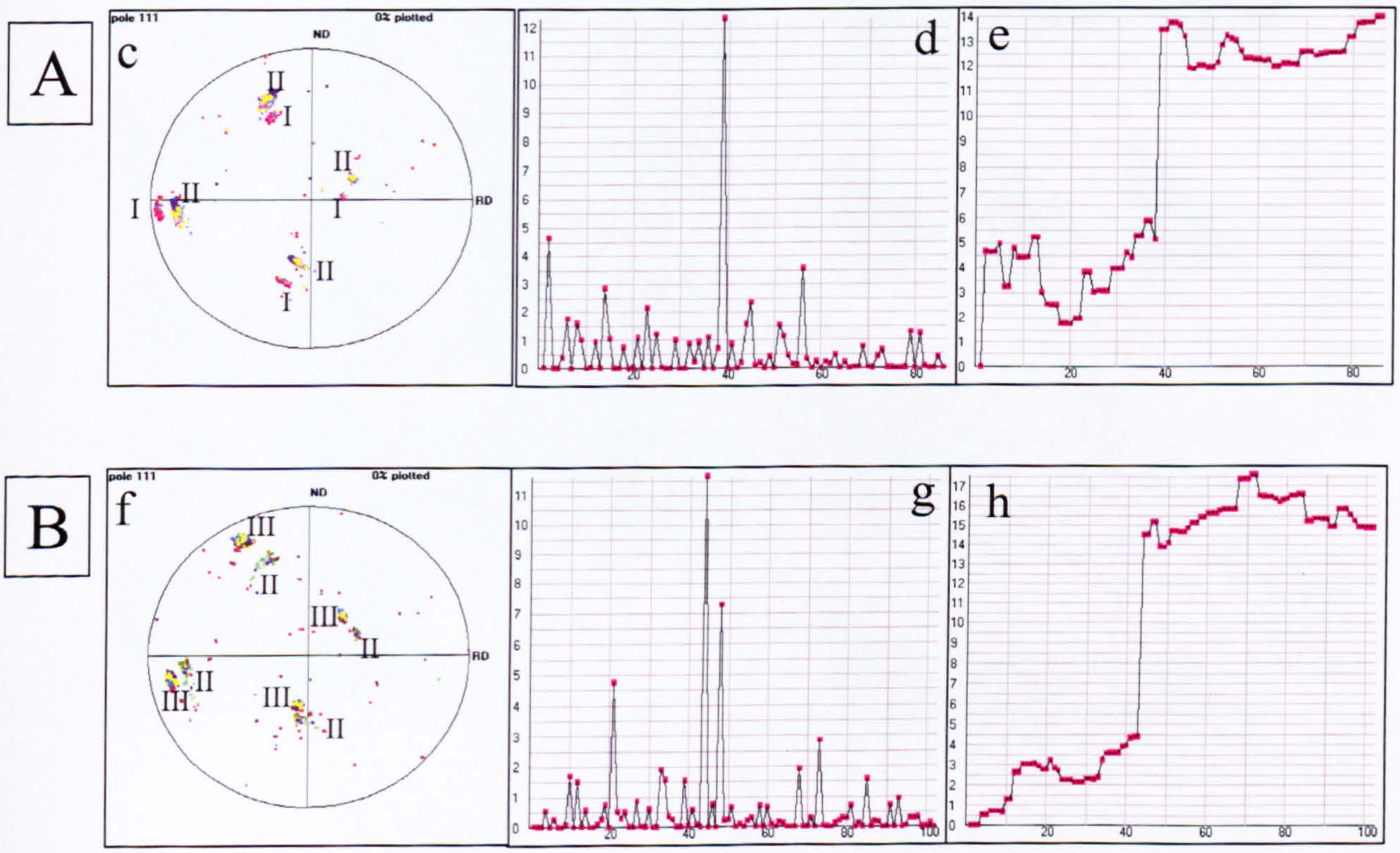

Fig. 5.122 P-orientated grain in the 600 seconds delayed sample: (a) relative map, (b) orientation map.(c) (f) 100 pole figures (d) (g) relative and (e) (h) cumulative misorientation distributions of line scans performed along A and B in (b).

Fig. 5.123 Brass-orientated grain in the 600 seconds delayed sample: (a) texture and boundary map, (b) ODF, (c) pole figures, (d) inverse pole figures, the distribution of misorientation axis vectors in (e) sample and (f) crystal lattice coordinates.

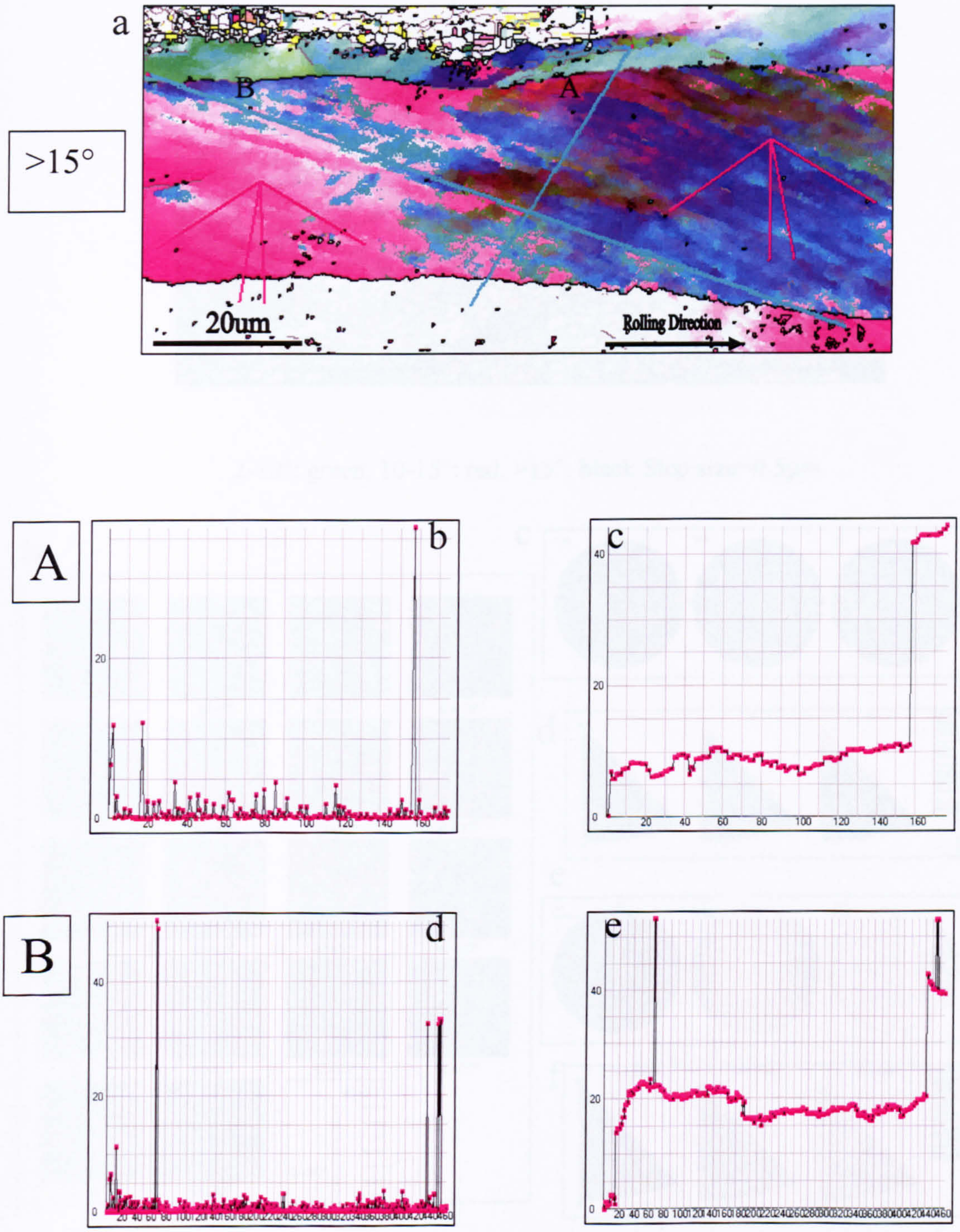

Fig. 5.124 Brass-orientated grain in the 600 seconds delayed sample: (a) relative map, (b) (d) relative and (c) (e) cumulative misorientation distributions of line scans performed along A and B in (a).

a

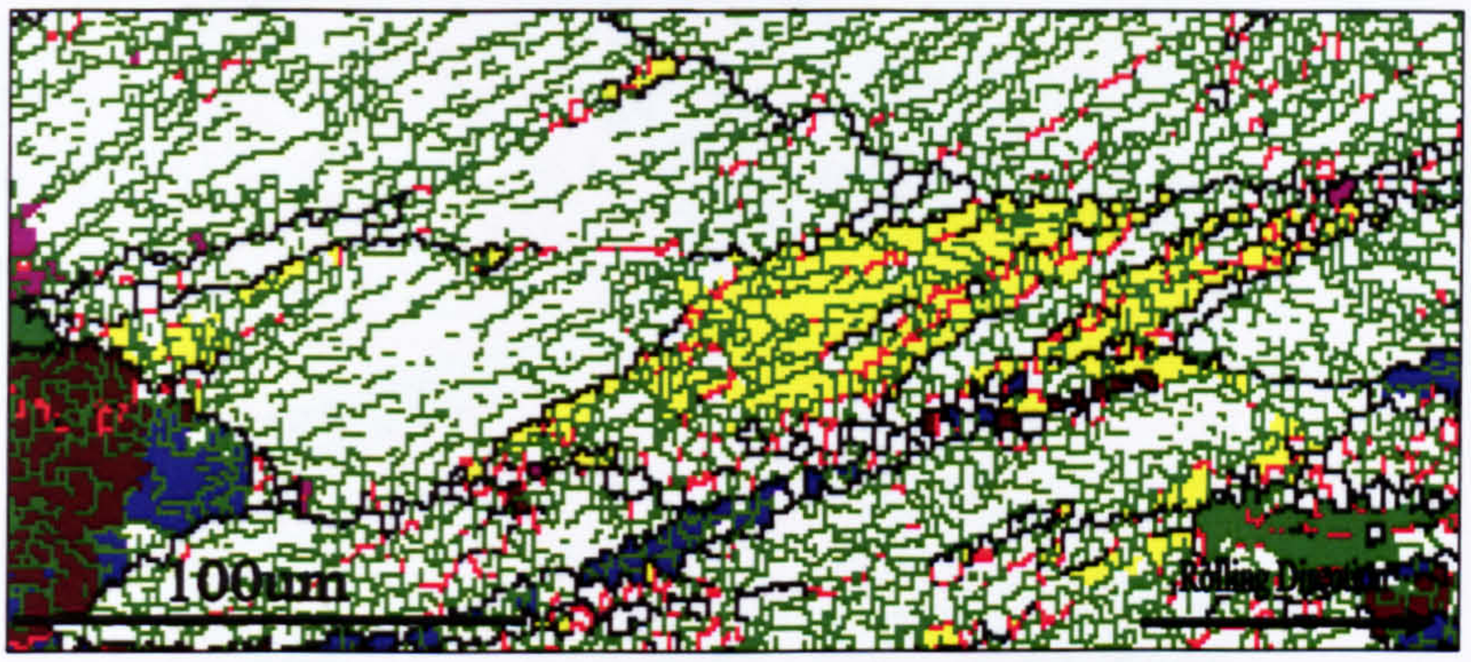

2-10°: green, 10-15°: red, >15°: black Step size=0.5μm

b

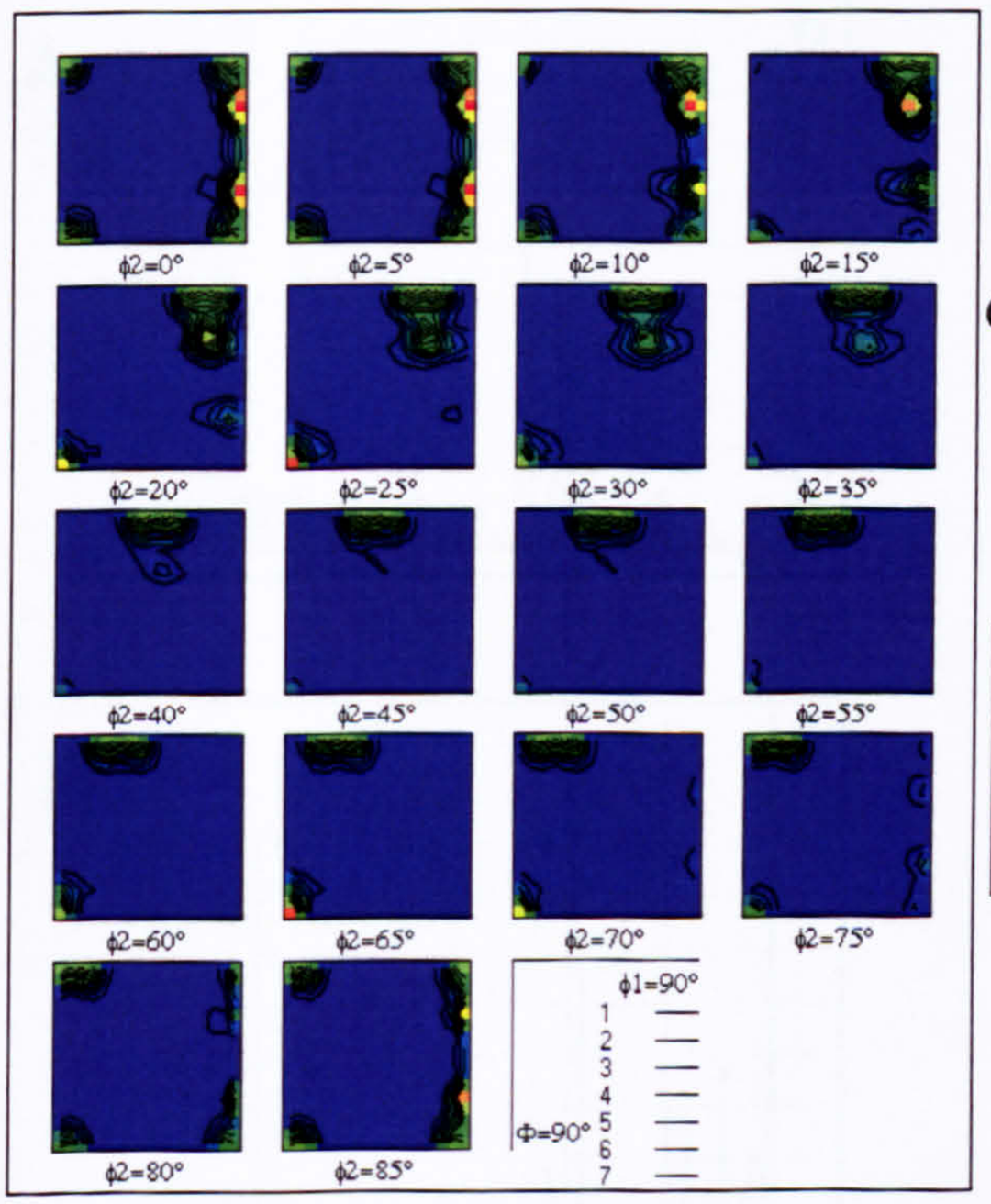

c

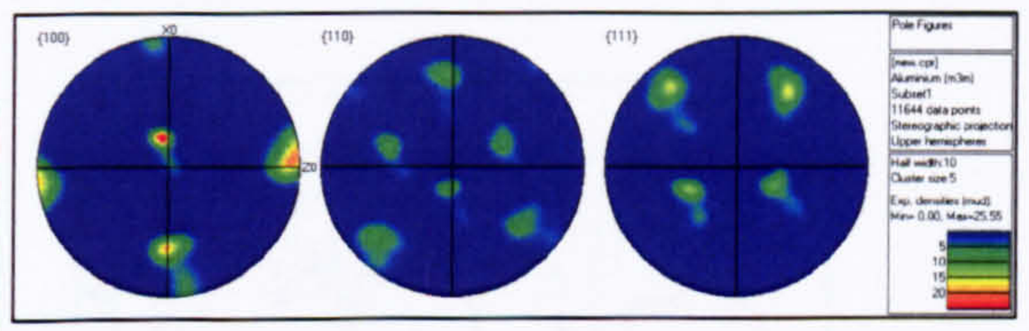

d

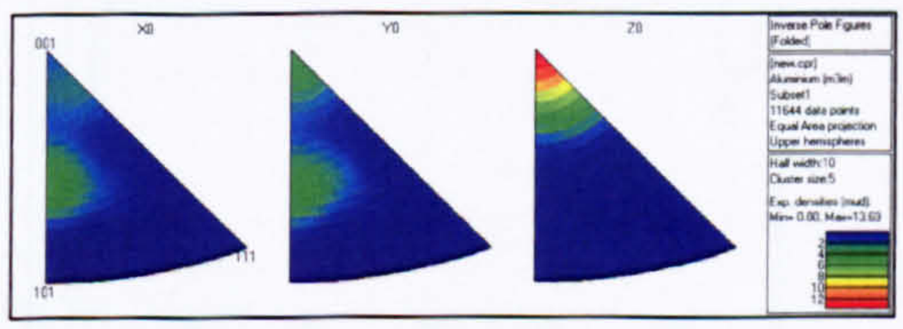

e

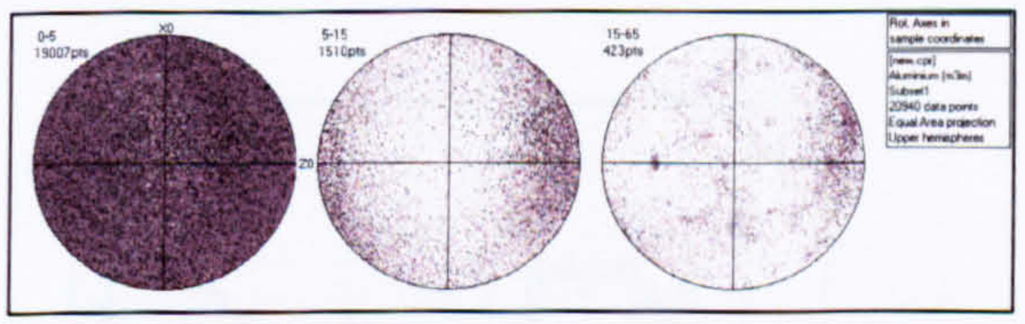

f

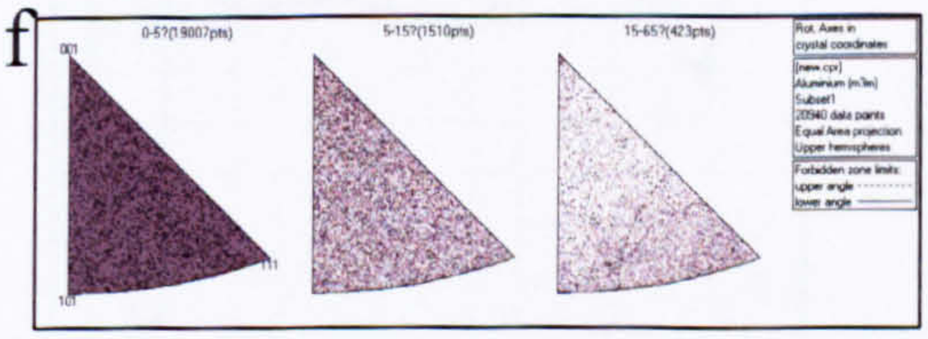

Fig. 5.125 Cube-orientated grain in the 600 seconds delayed sample: (a) texture and boundary map, (b) ODF, (c) pole figures, (d) inverse pole figures, the distribution of misorientation axis vectors in (e) sample and (f) crystal lattice coordinates.

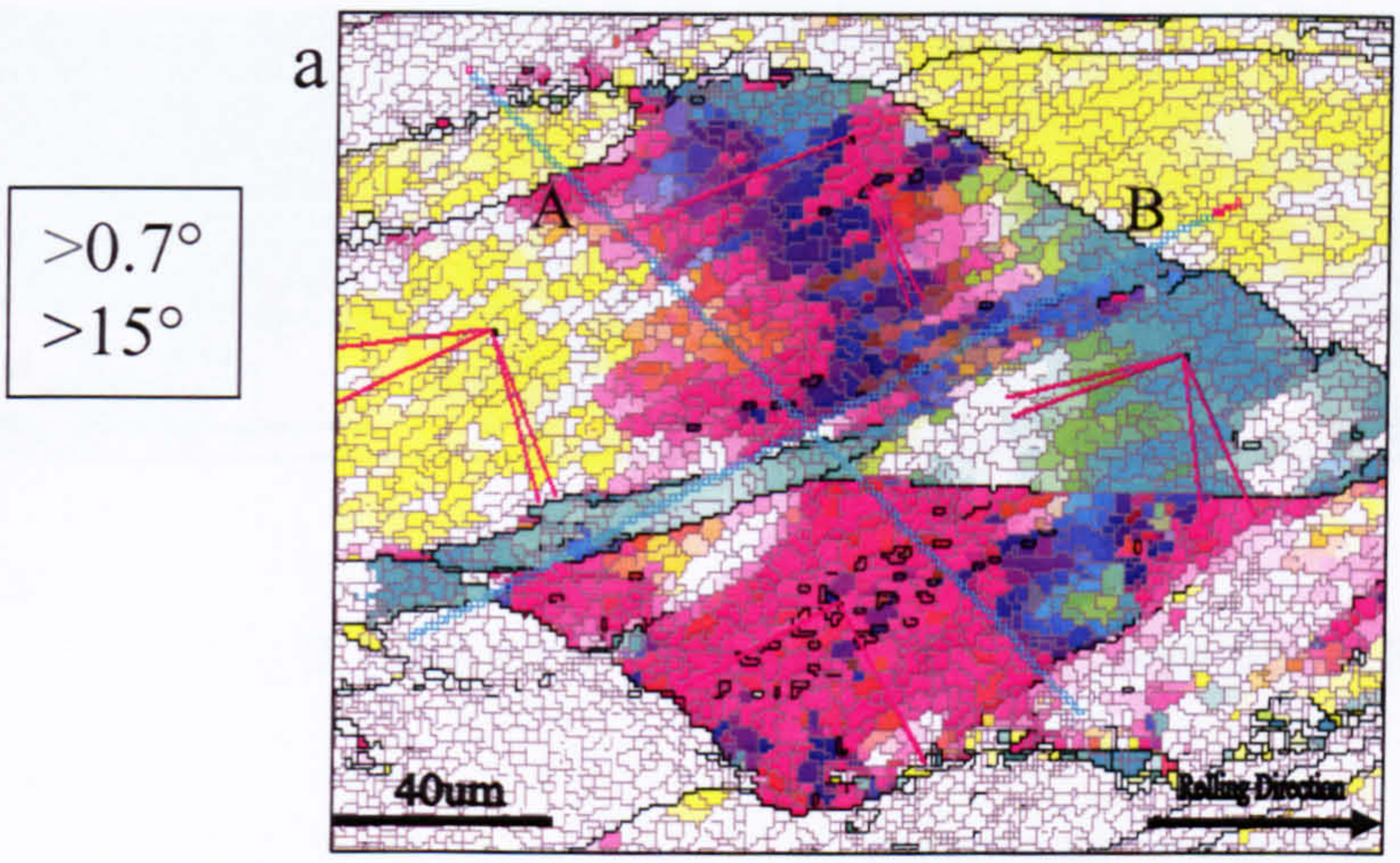

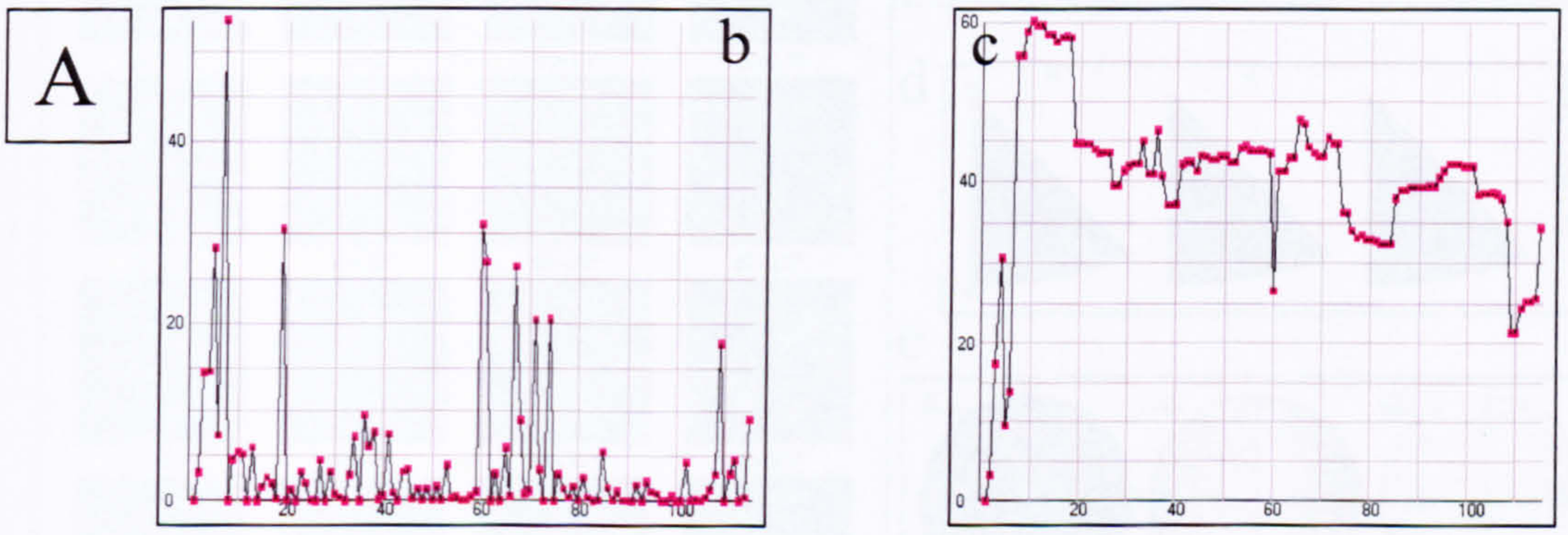

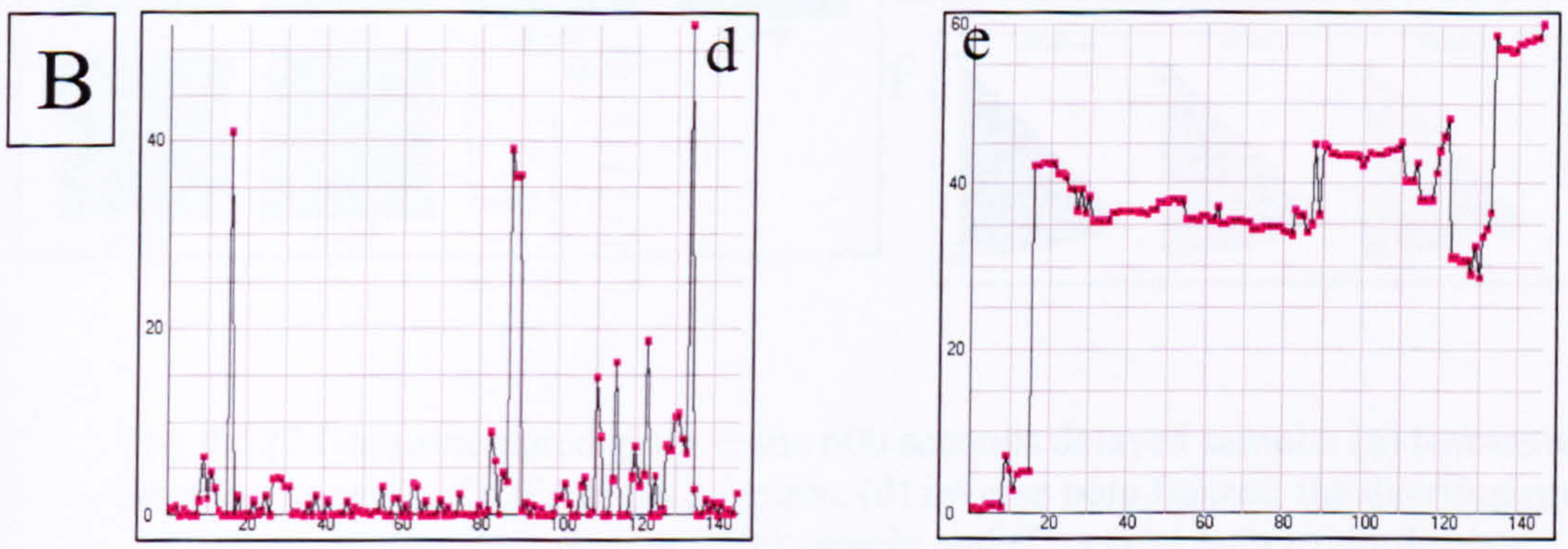

Fig. 5.126 Cube-orientated grain in the 600 seconds delayed sample: (a) relative map, (b) (d) relative and (c) (e) cumulative misorientation distributions of line scans performed along A and B in (a).

a

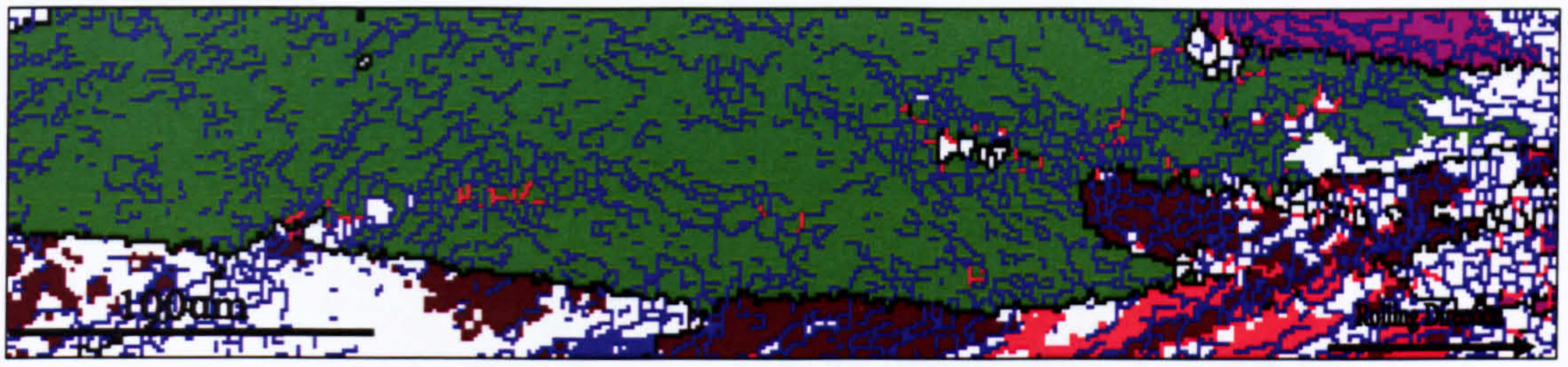

2-10°: blue, 10-15°: red, >15°: black Step size=0.5μm

b

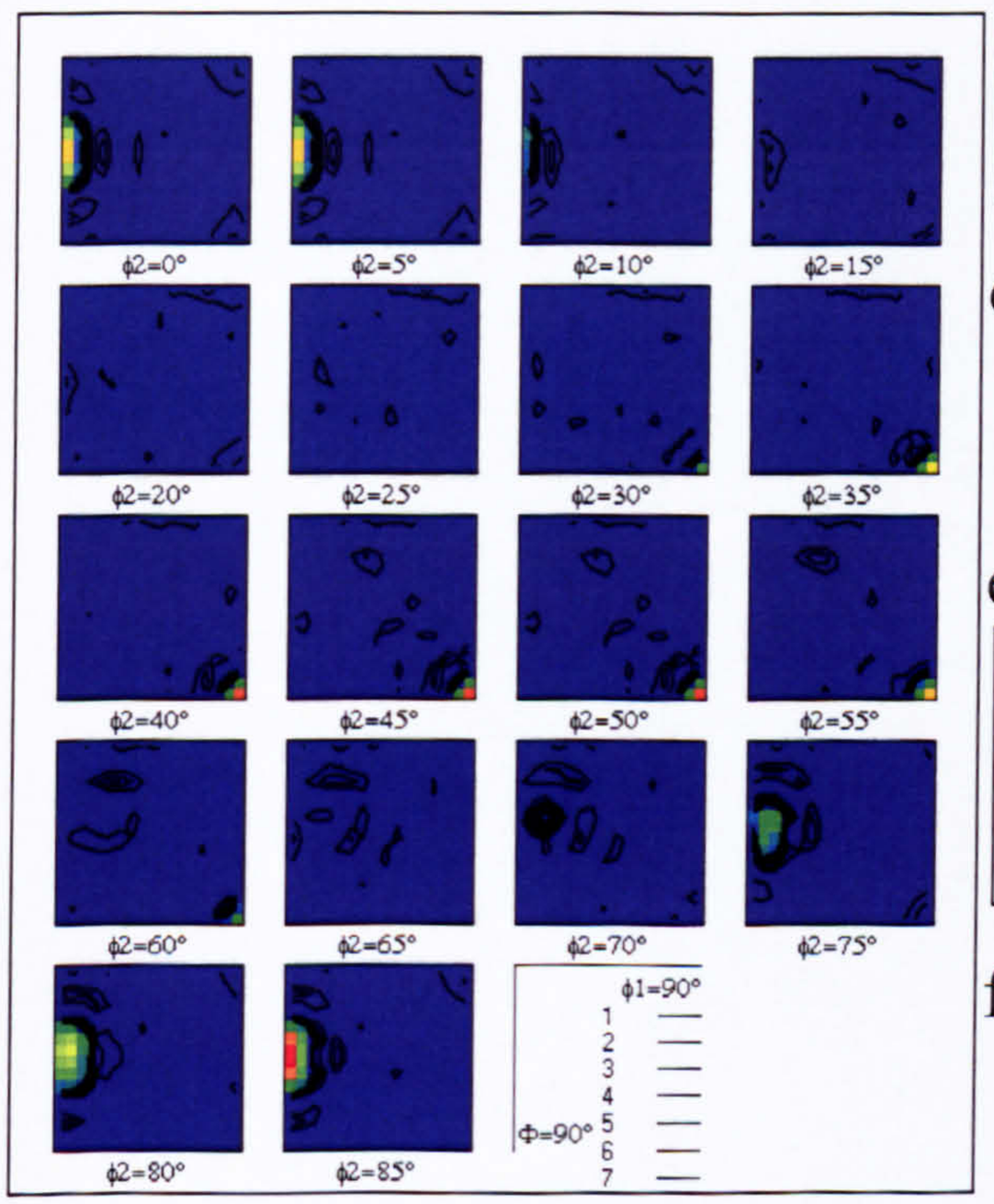

c

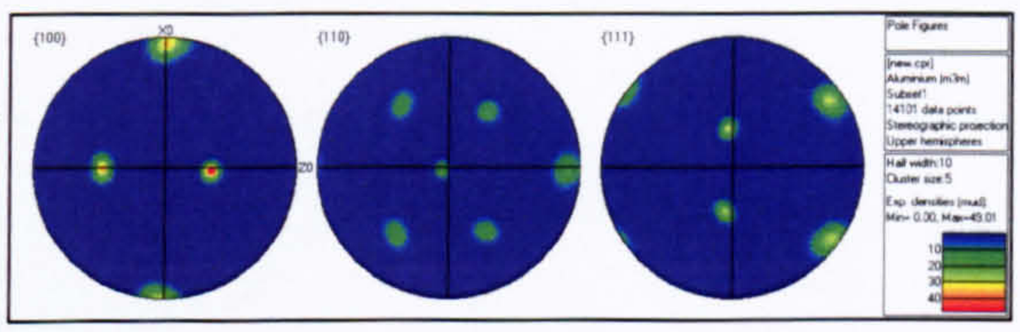

d

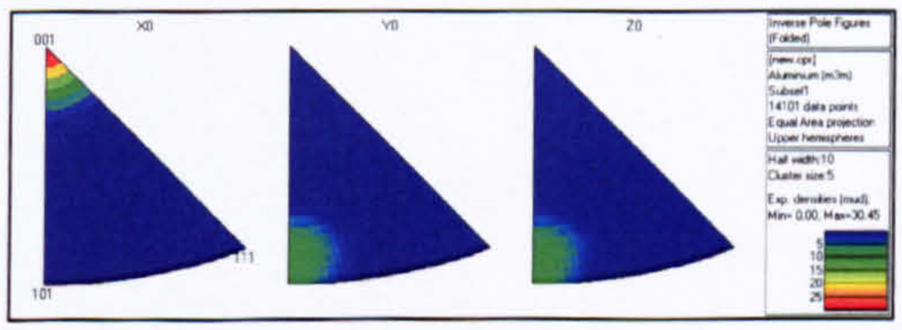

e

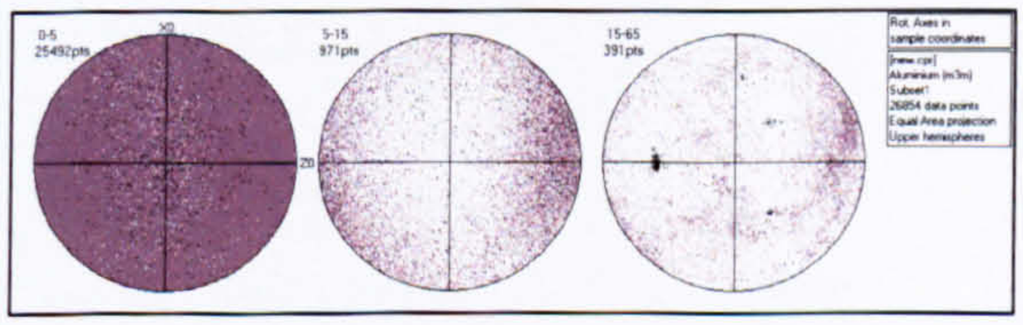

f

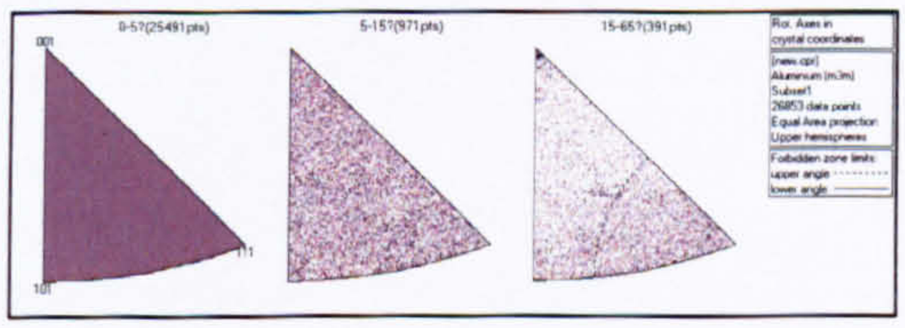

Fig. 5.127 Goss-orientated grain in the 600 seconds delayed sample: (a) texture and boundary map, (b) ODF, (c) pole figures, (d) inverse pole figures, the distribution of misorientation axis vectors in (e) sample and (f) crystal lattice coordinates.

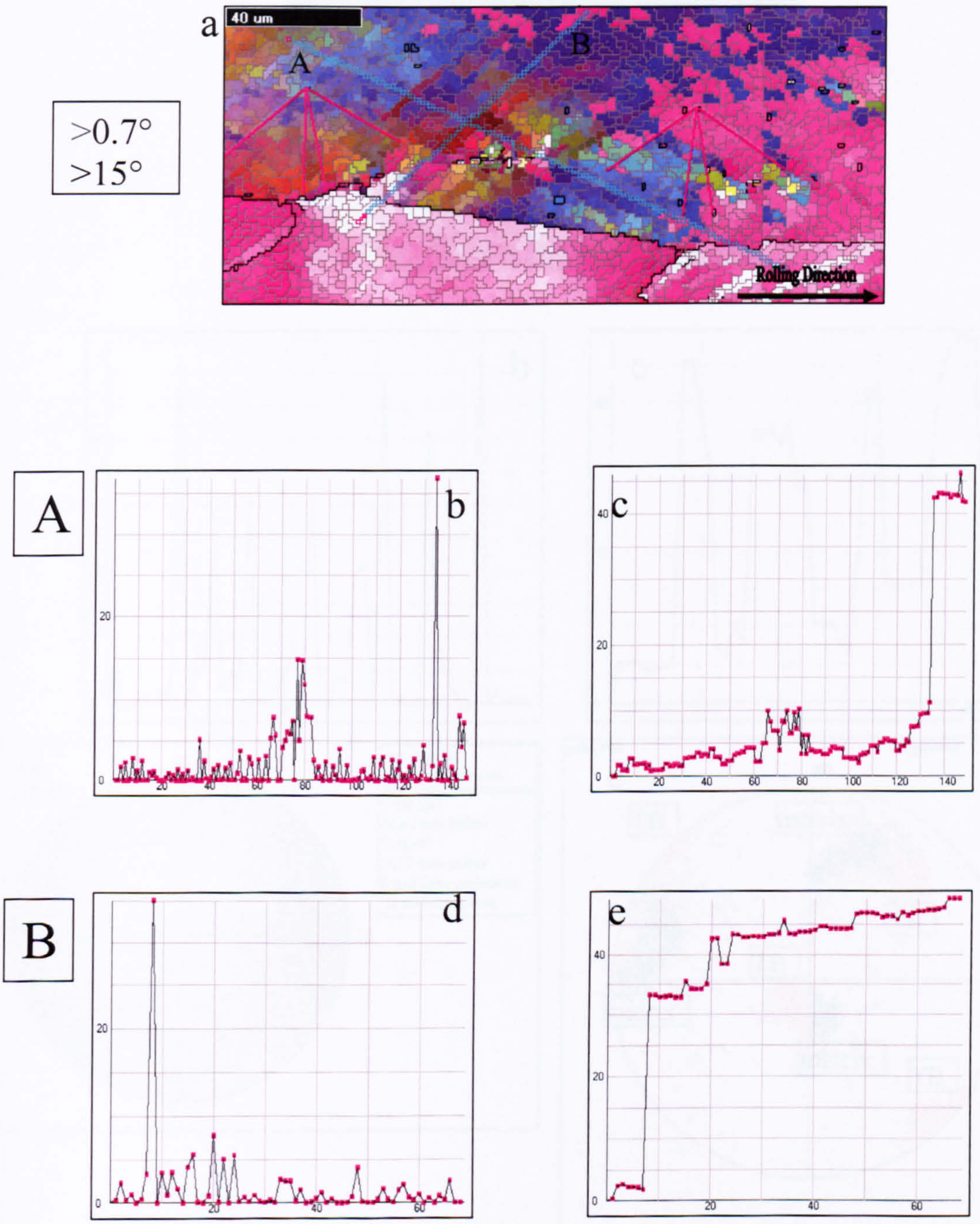

Fig. 5.128 Goss-orientated grain in the 600 seconds delayed sample: (a) relative map, (b) (d) relative and (c) (e) cumulative misorientation distributions of line scans performed along A and B in (a).

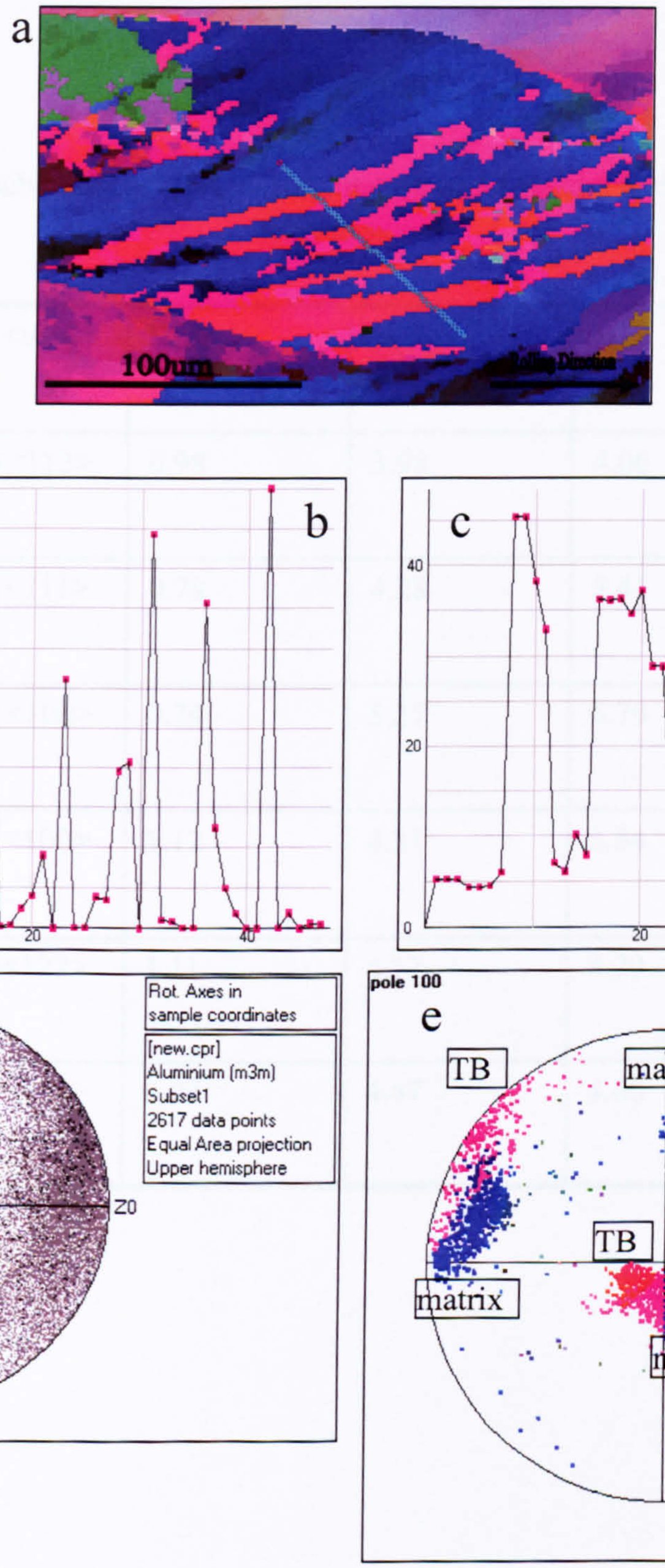

Fig. 5.129 Deformation banding in the 600 seconds delayed sample: (a) relative map, (b) relative and (c) cumulative misorientation distributions of line scans performed along the line in (a), (d) sample coordinate, (e) 100 pole figure.

Table 5.7 Mean subgrain size (D), misorientation angle (è) and Θ/d for the 600 seconds delayed sample

Texture Component	{hkl}<uvw>	D(μm)	Θ(°)	Θ/d	Number of Subgrains
Brass	{011}<112>	0.98	3.98	4.06	1087
Copper	{112}<111>	0.79	4.28	5.41	1737
Cube	{001}<100>	0.79	5.37	6.79	204
Goss	{011}<100>	1.12	4.31	3.84	441
P	{011}<122>	1.11	4.77	4.29	1586
S	{123}<634>	0.97	4.47	4.60	1802

a

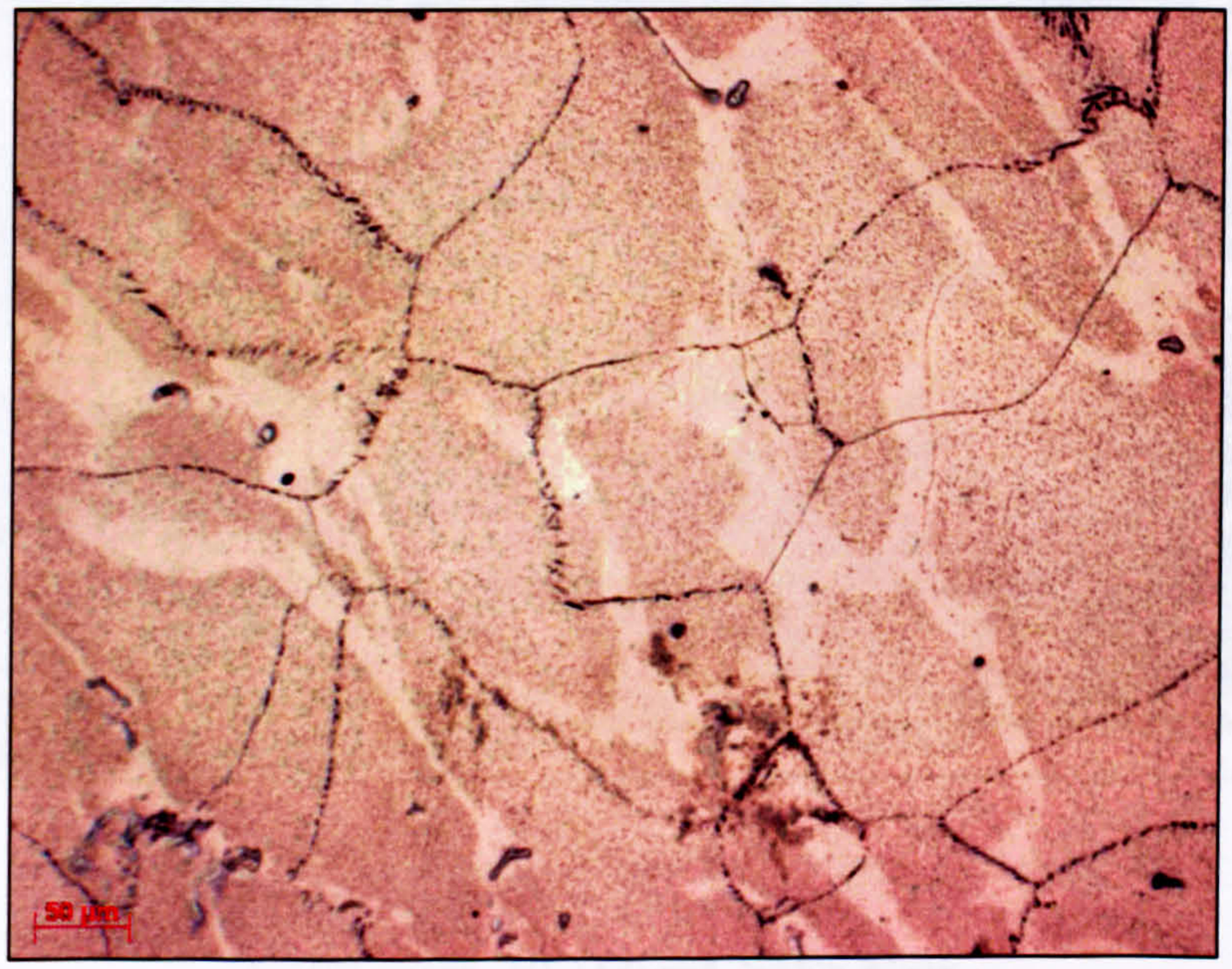

b

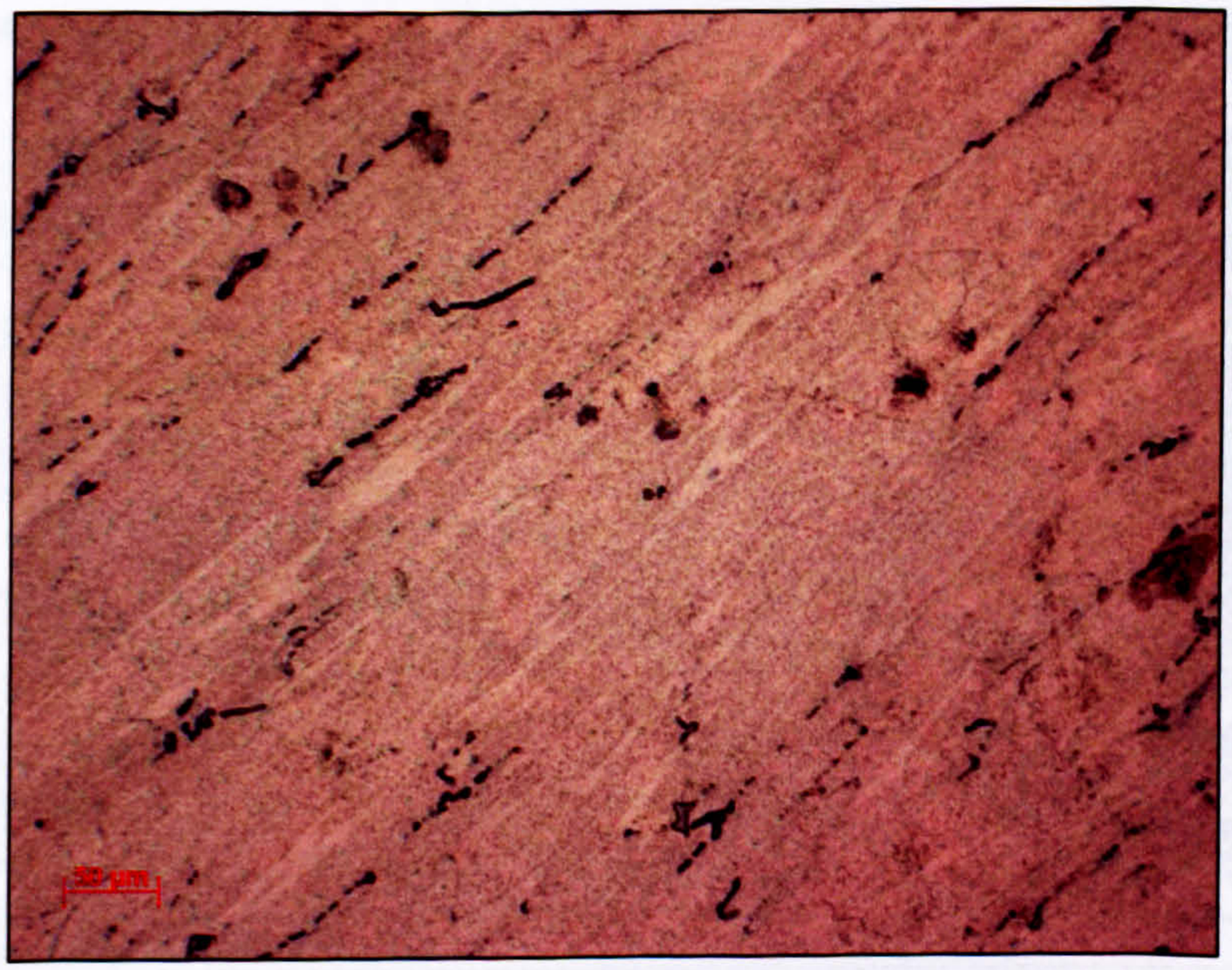

Fig. 5.130 Optical micrographs of deformed structure after the 6000 seconds delayed time deformation: (a) normal plane, (b) transverse plane.

a

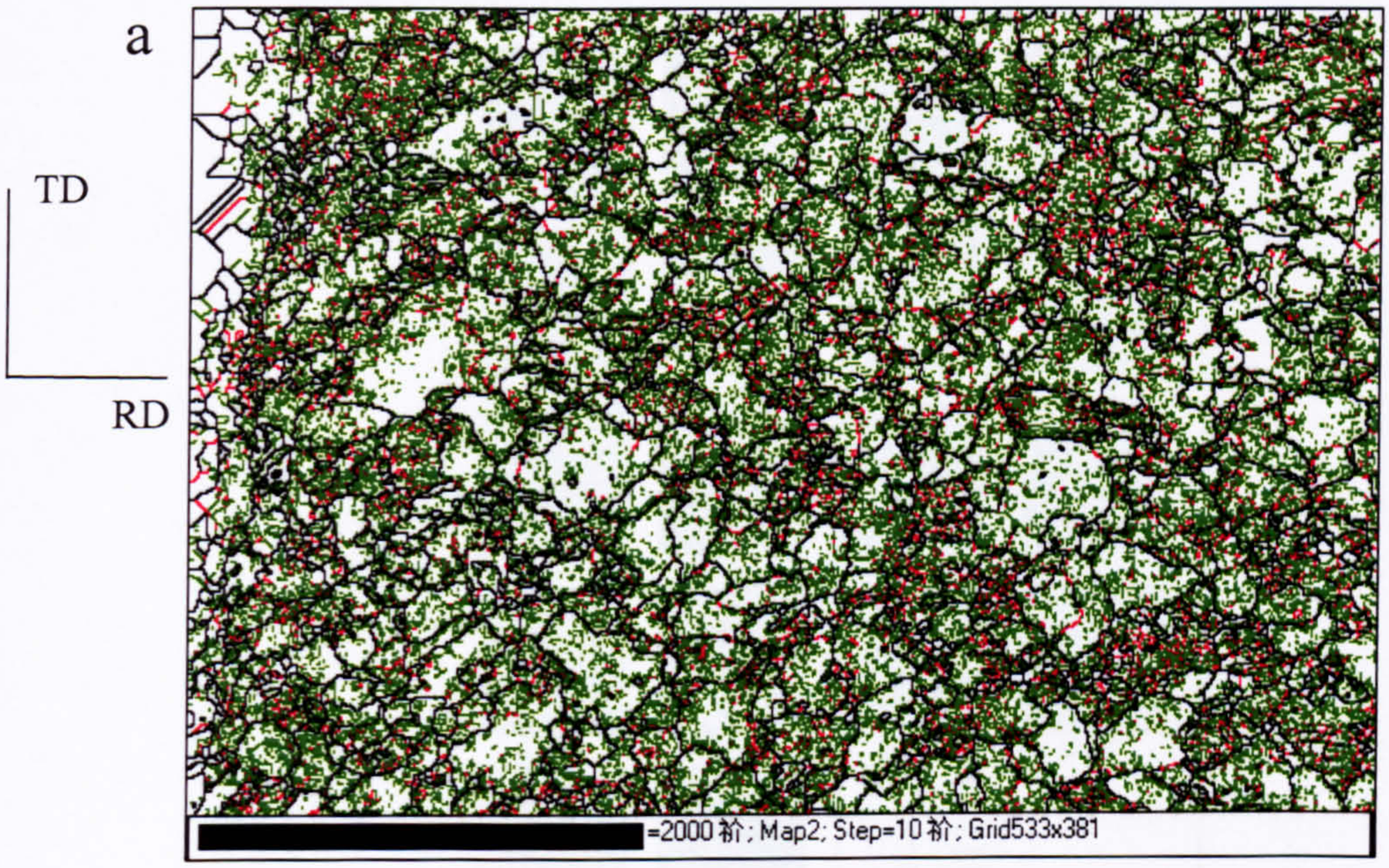

5-10°: green, 10-15°: red, >15°: black

b

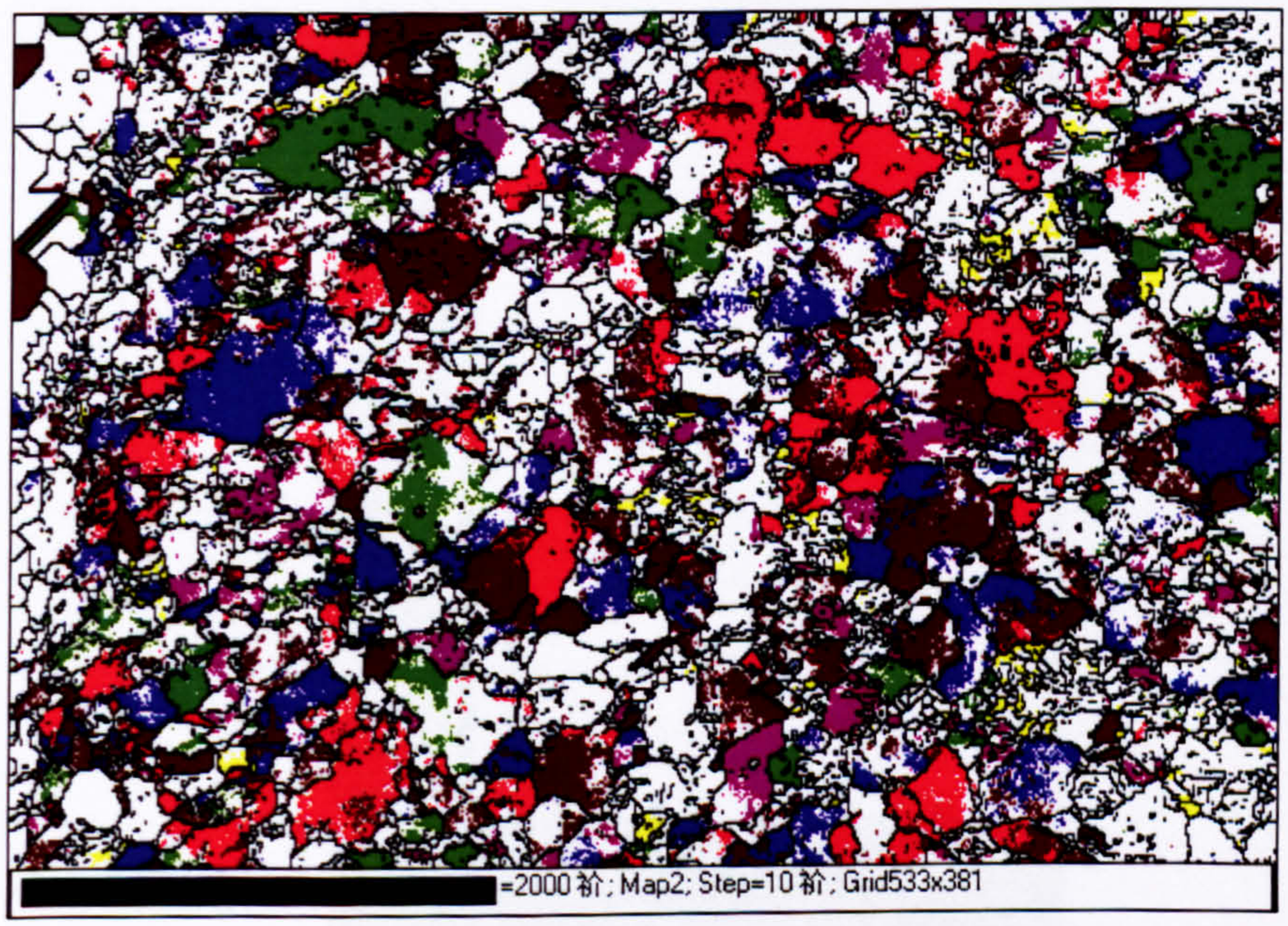

cube-yellow, p-purple, brass-red, copper-blue, goss-green, s-maroon

Fig. 5.131 (a) Orientation map and (b) texture components to the microstructure for the 6000 seconds delayed sample.

a

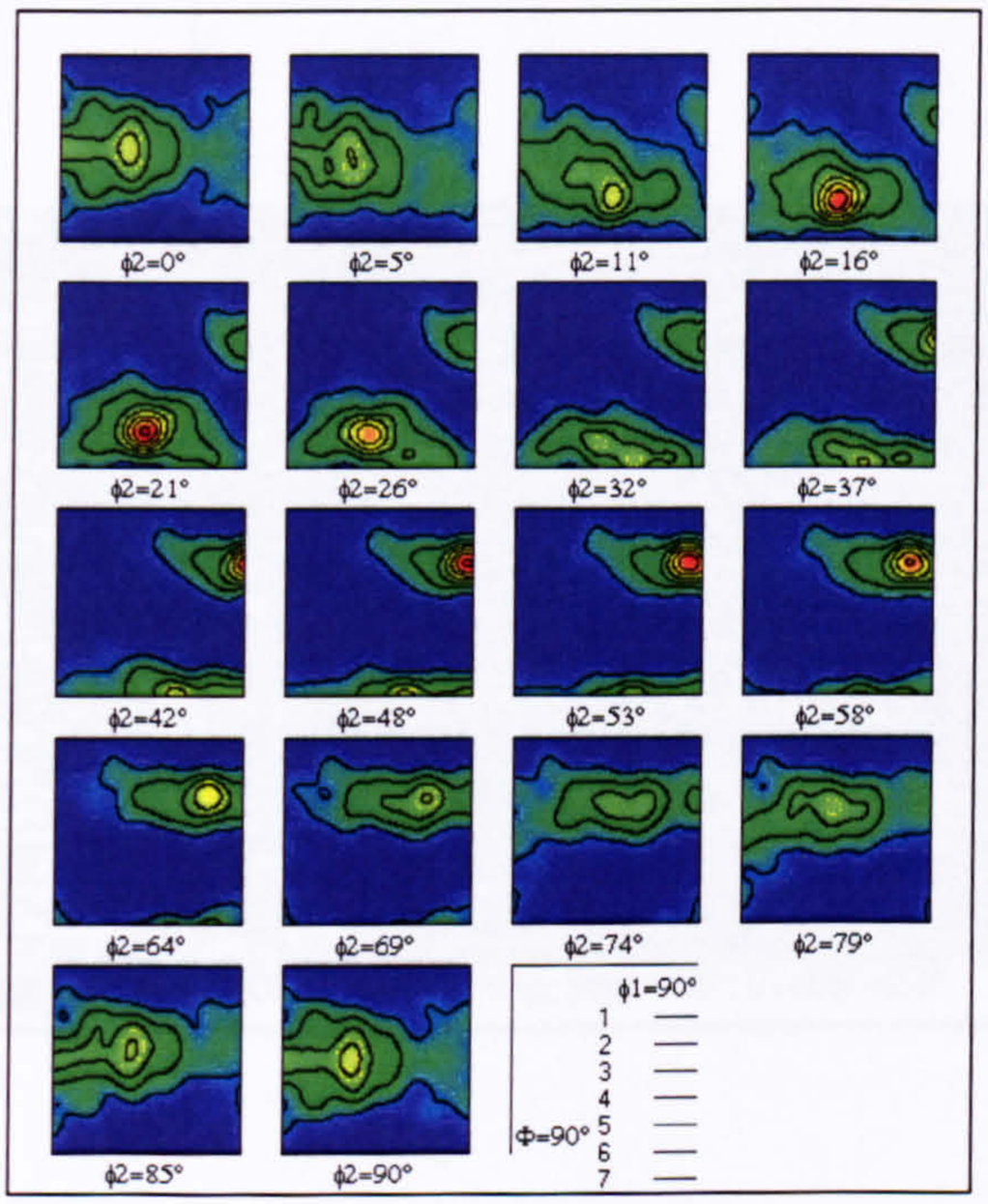

b

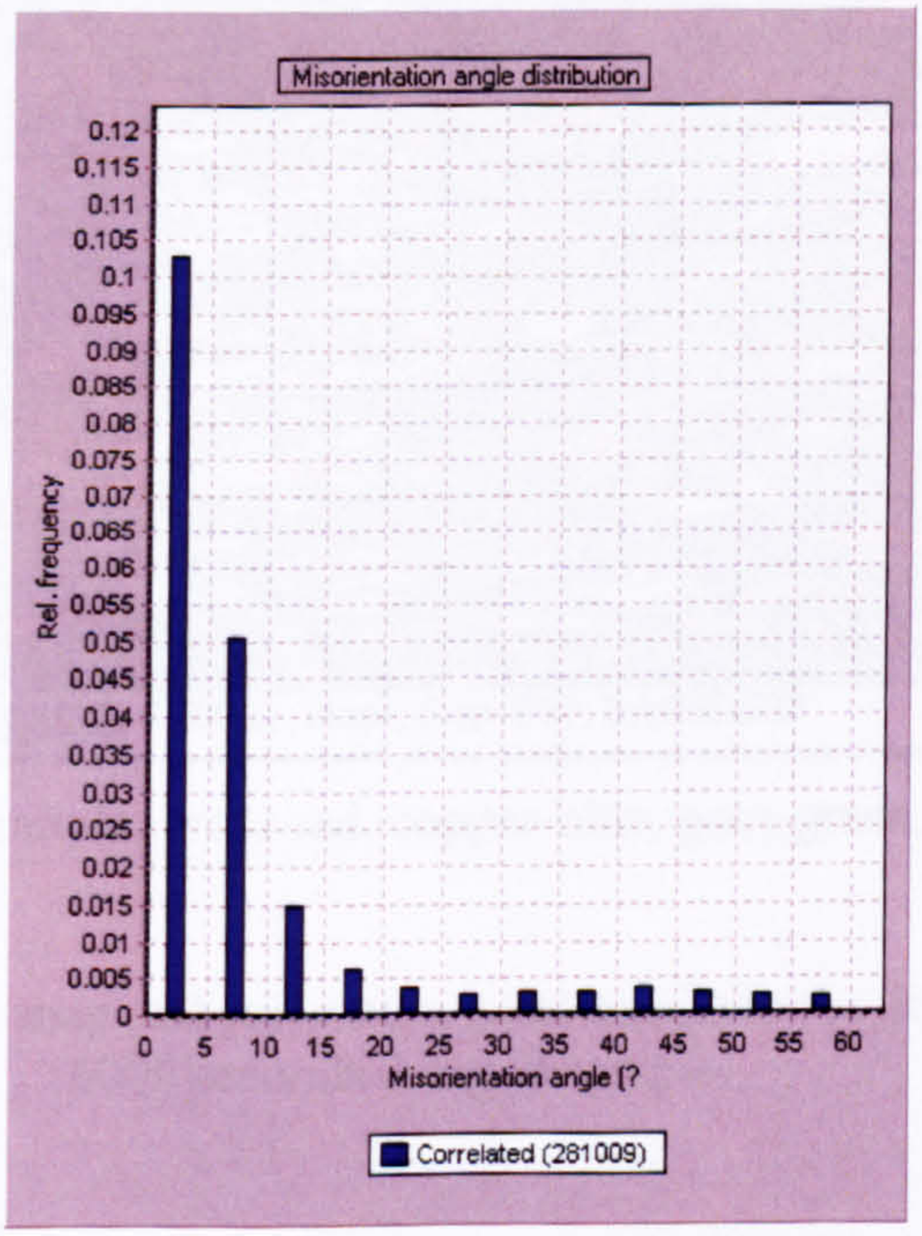

Fig. 5.132 EBSD results of the 6000 seconds delayed sample: (a) orientation distribution functions (ODF) maps, (b) misorientation angle distribution.

a

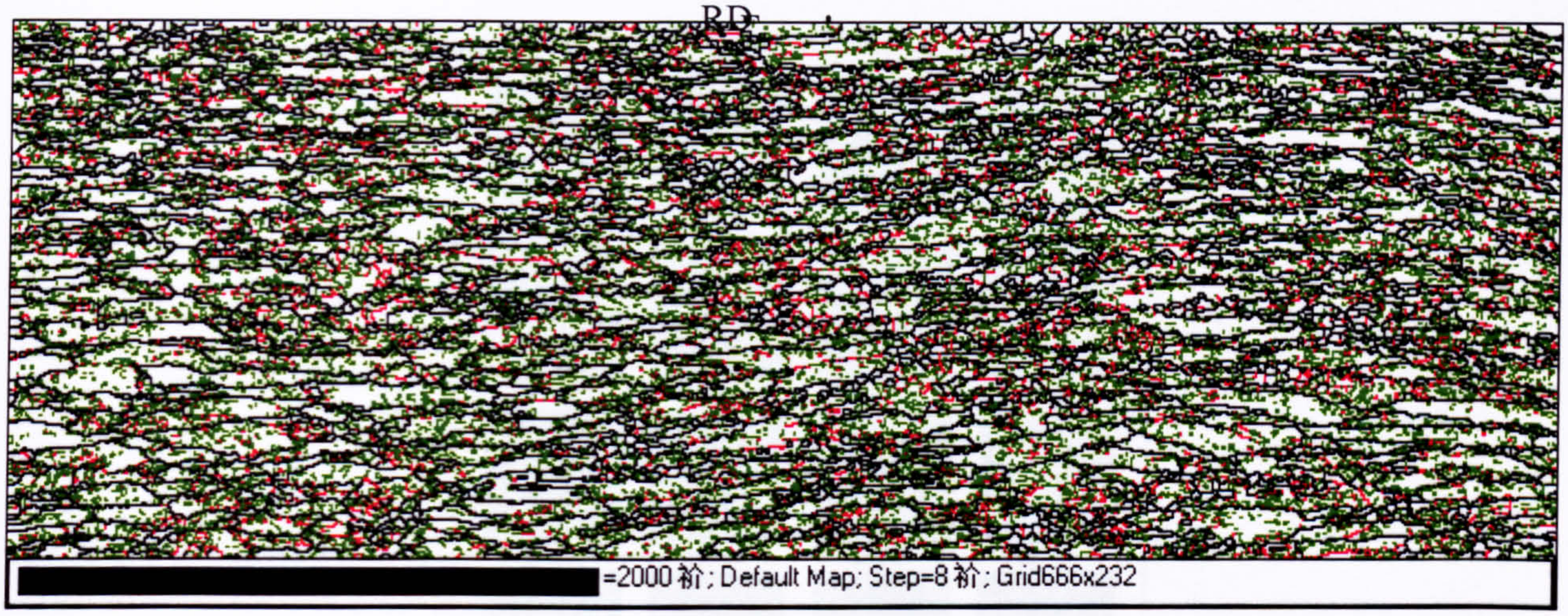

5-10°: green, 10-15°: red, >15°: black

b

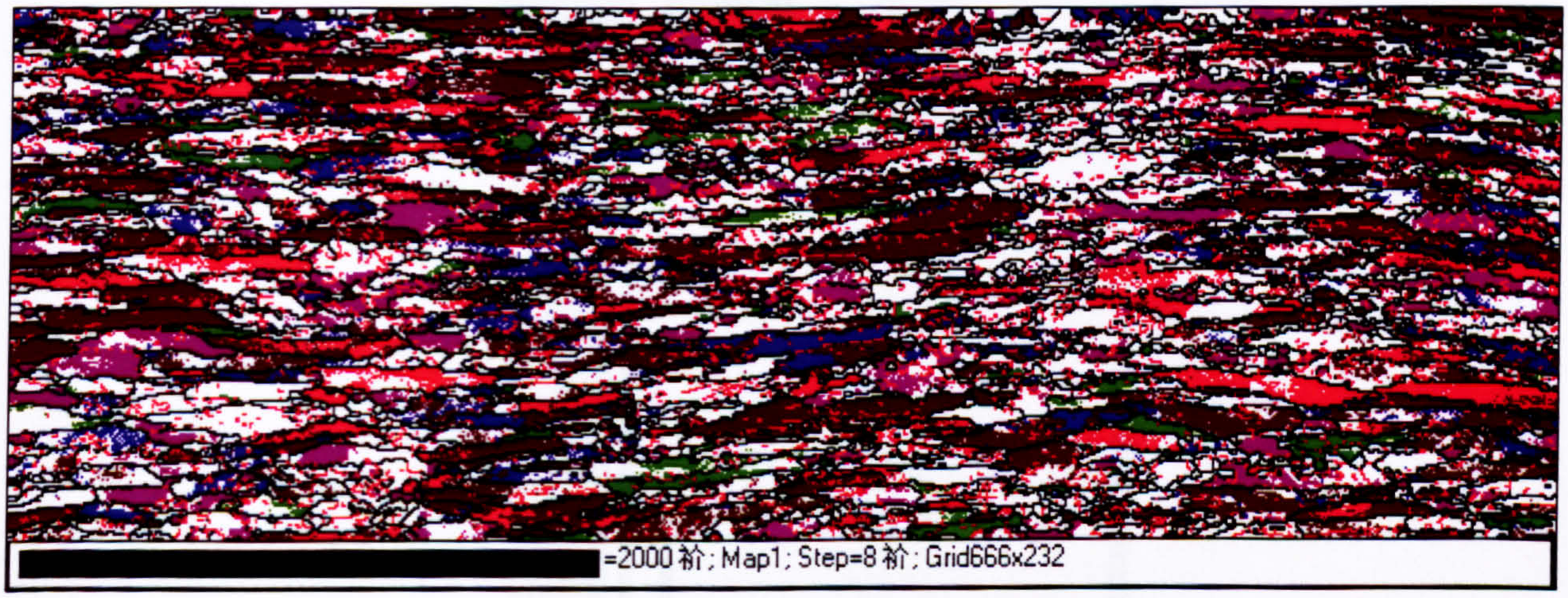

cube-yellow, p-purple, brass-red, copper-blue, goss-green, s-maroon

Fig. 5.133 (a) Orientation map and (b) texture components to the microstructure for the 6000 seconds delayed sample.

a

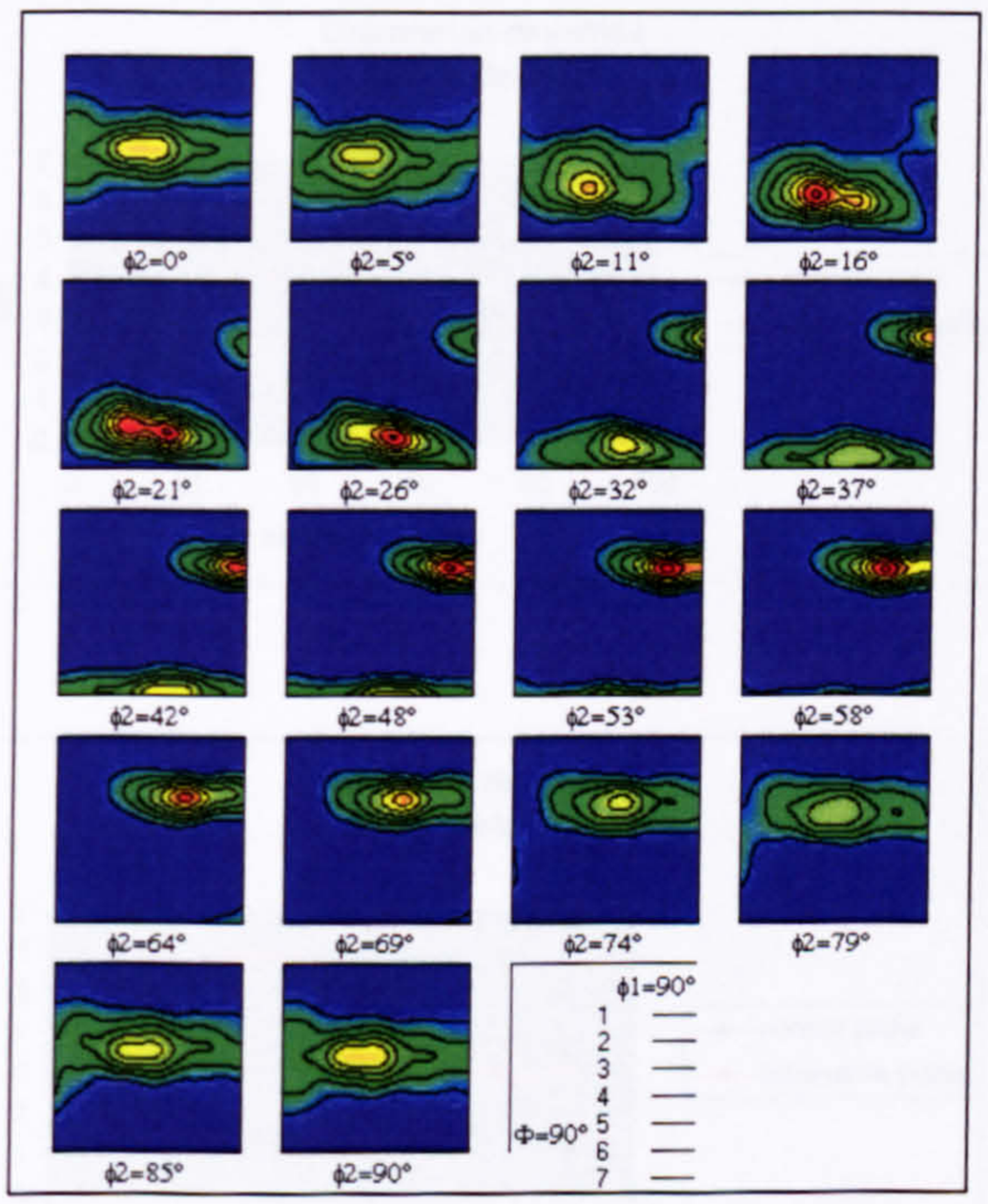

b

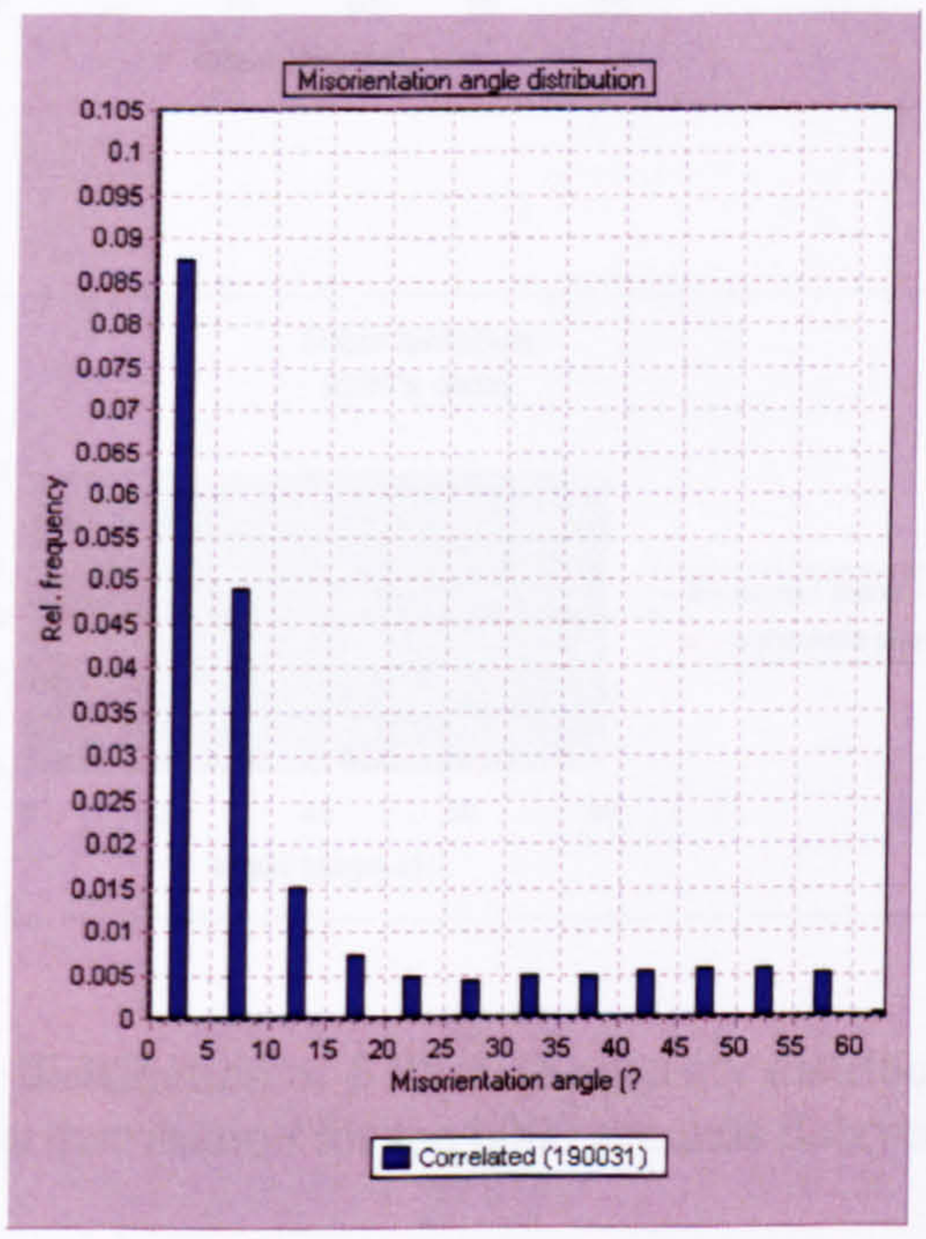

Fig. 5.134 EBSD results of the 6000 seconds delayed sample: (a) orientation distribution functions (ODF) maps, (b) misorientation angle distribution.

a

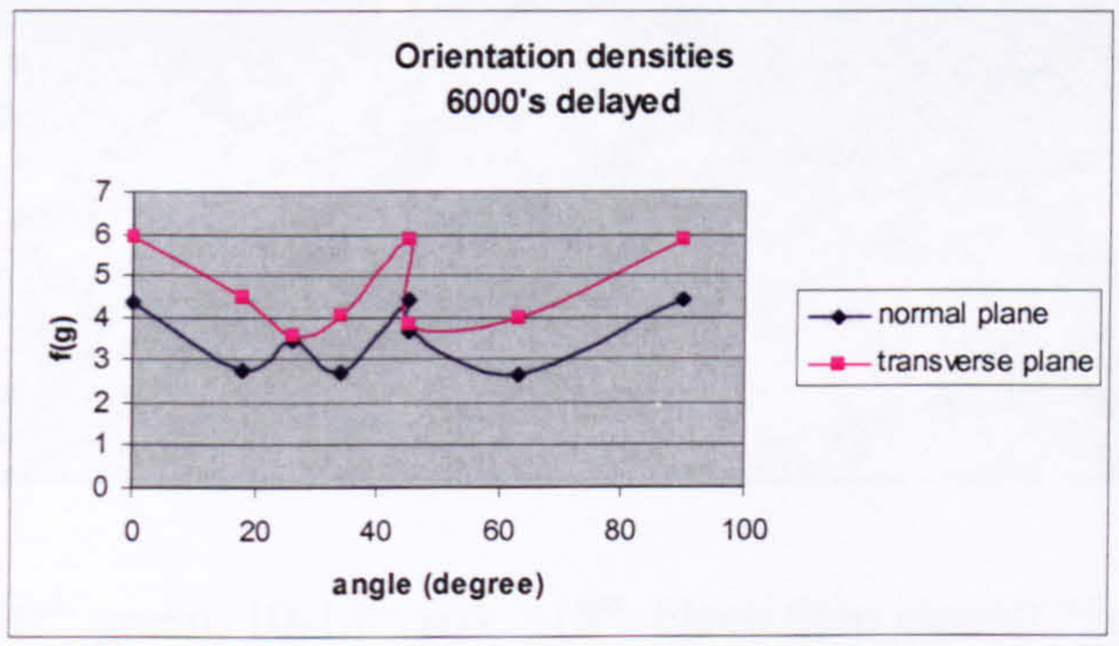

b

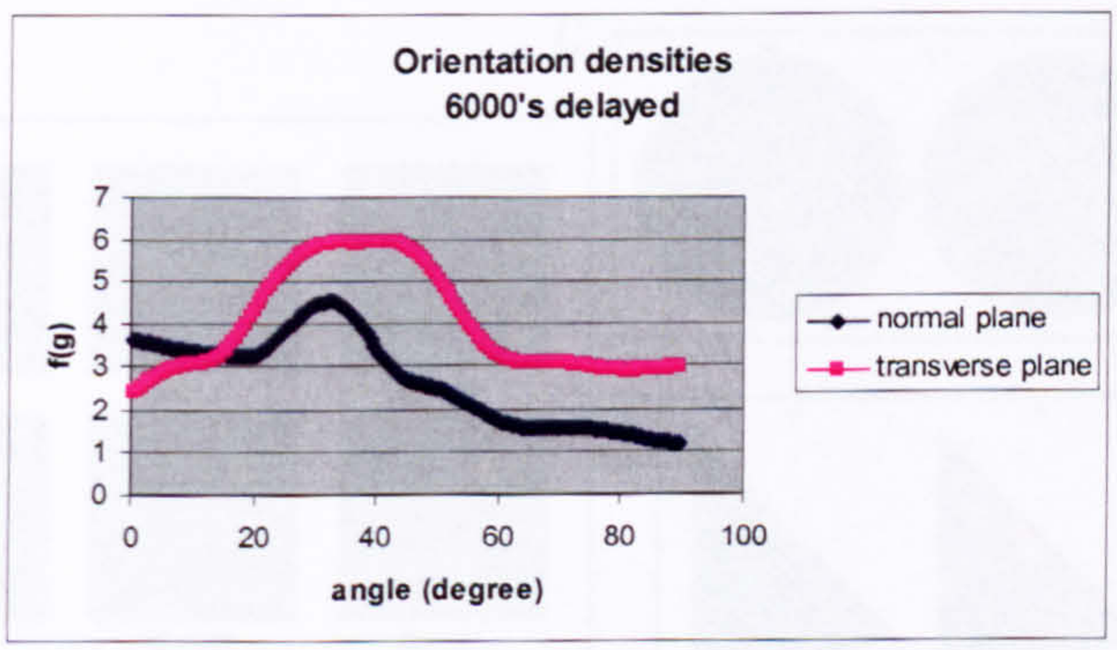

C

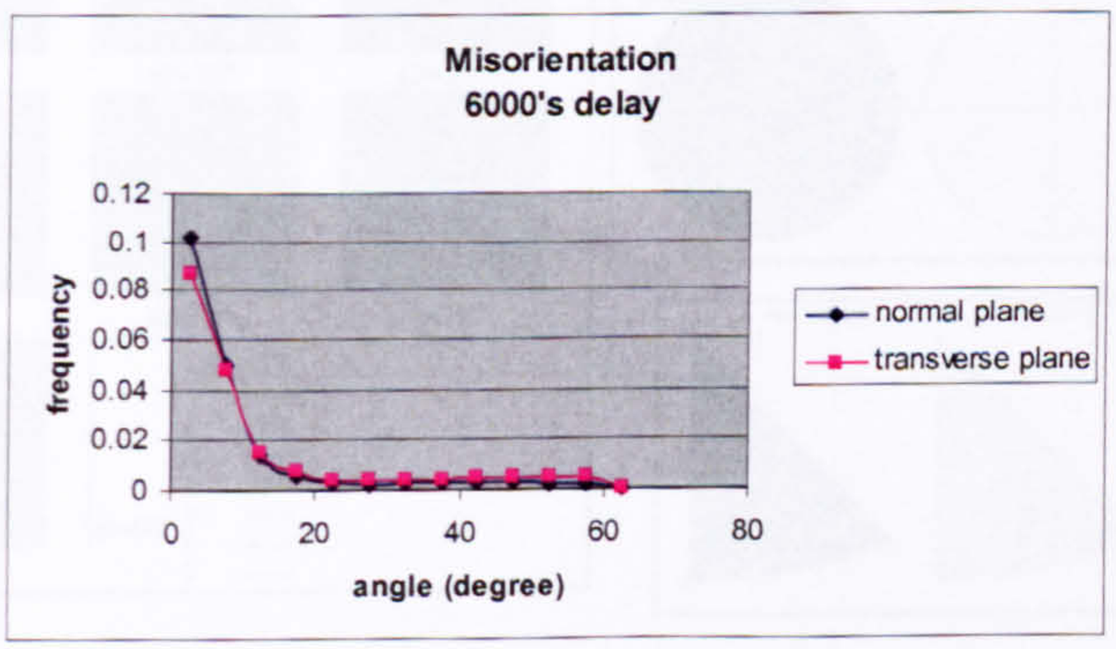

Fig. 5.135 (a) Density distribution of β fibre, (b) density distribution of α fibre, (c) misorientaiton distribution for the 6000 seconds delayed sample.

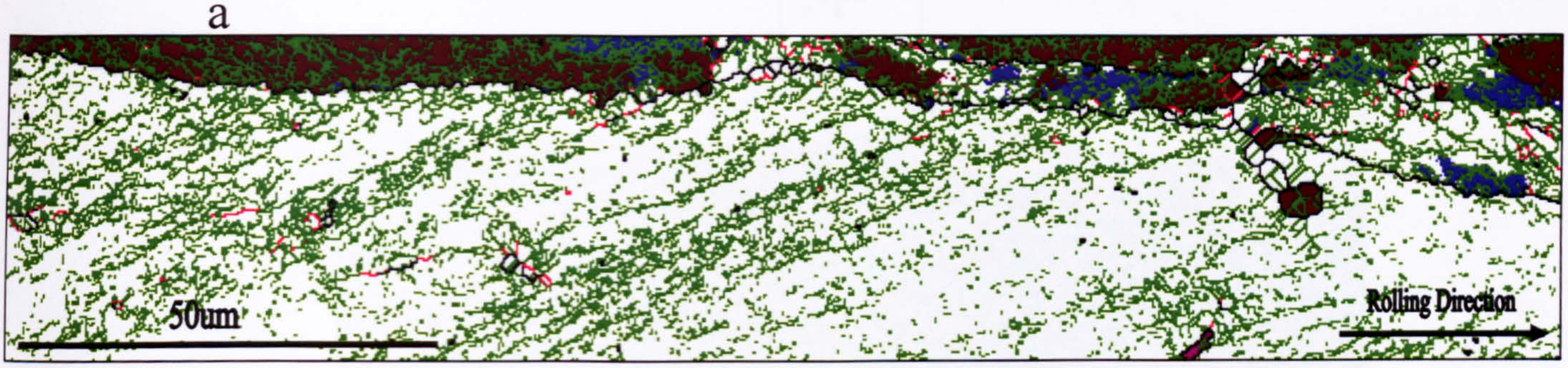

5-10°: green, 10-15°: red, >15°: black Step size=0.25μm

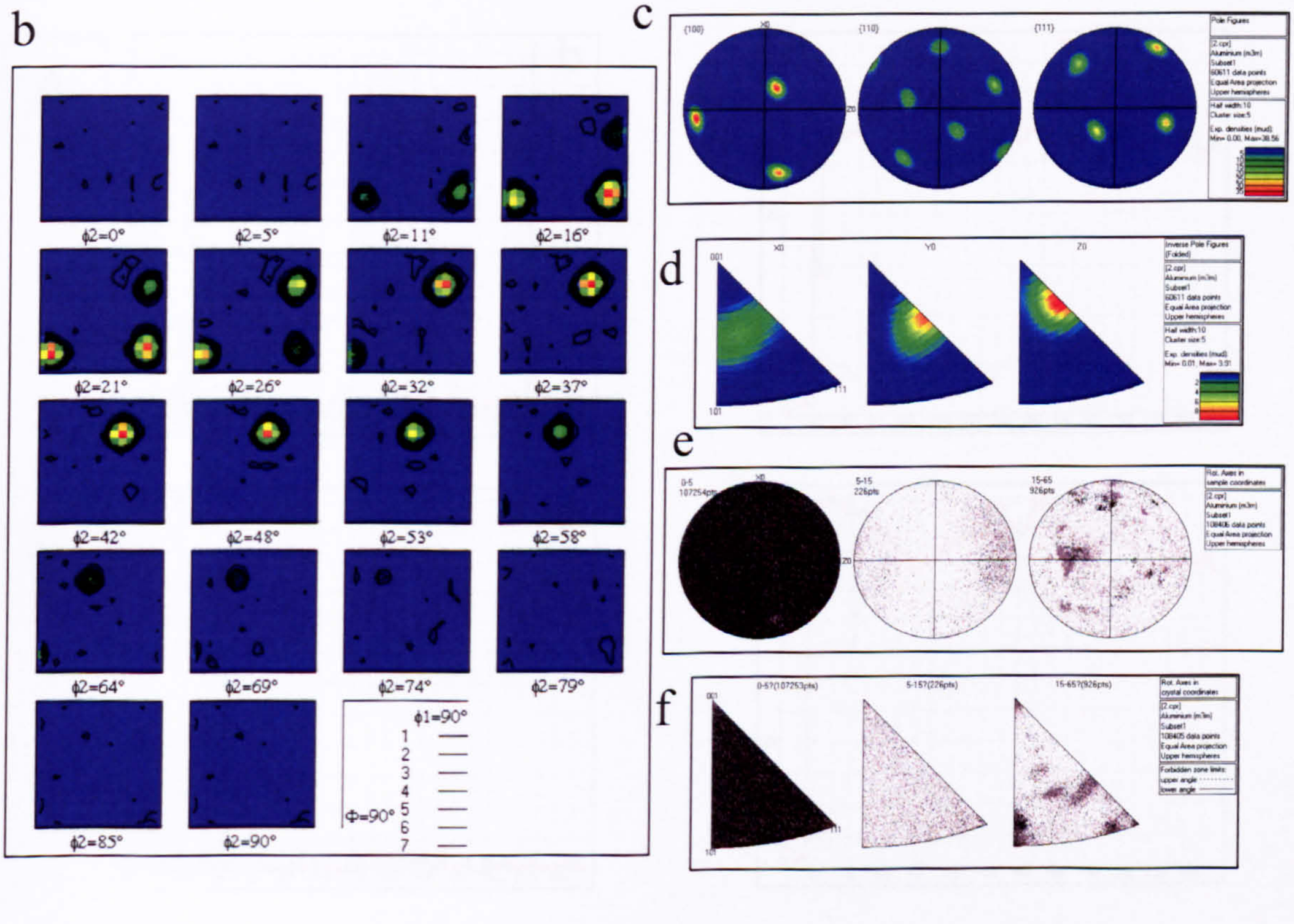

Fig. 5.136 Random-orientated grain in the 6000 seconds delayed sample: (a) texture and boundary map, (b) ODF, (c) pole figures, (d) inverse pole figures, the distribution of misorientation axis vectors in (e) sample and (f) crystal lattice coordinates.

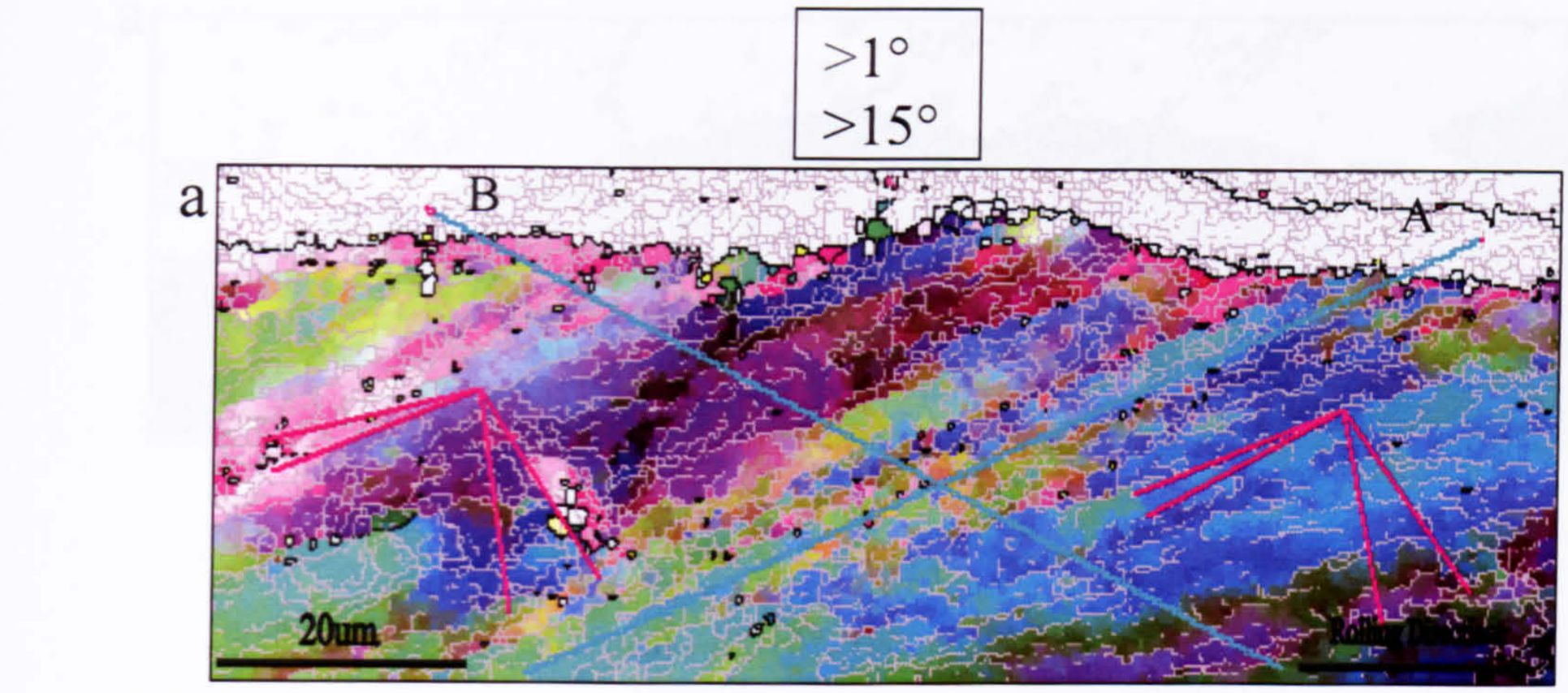

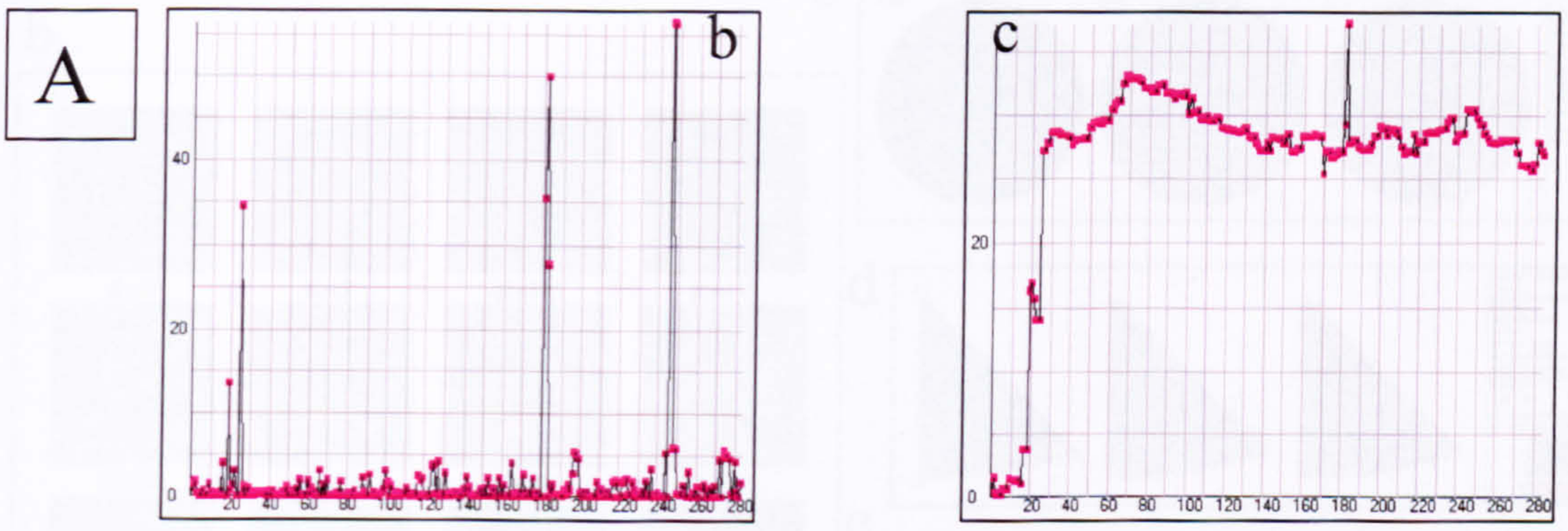

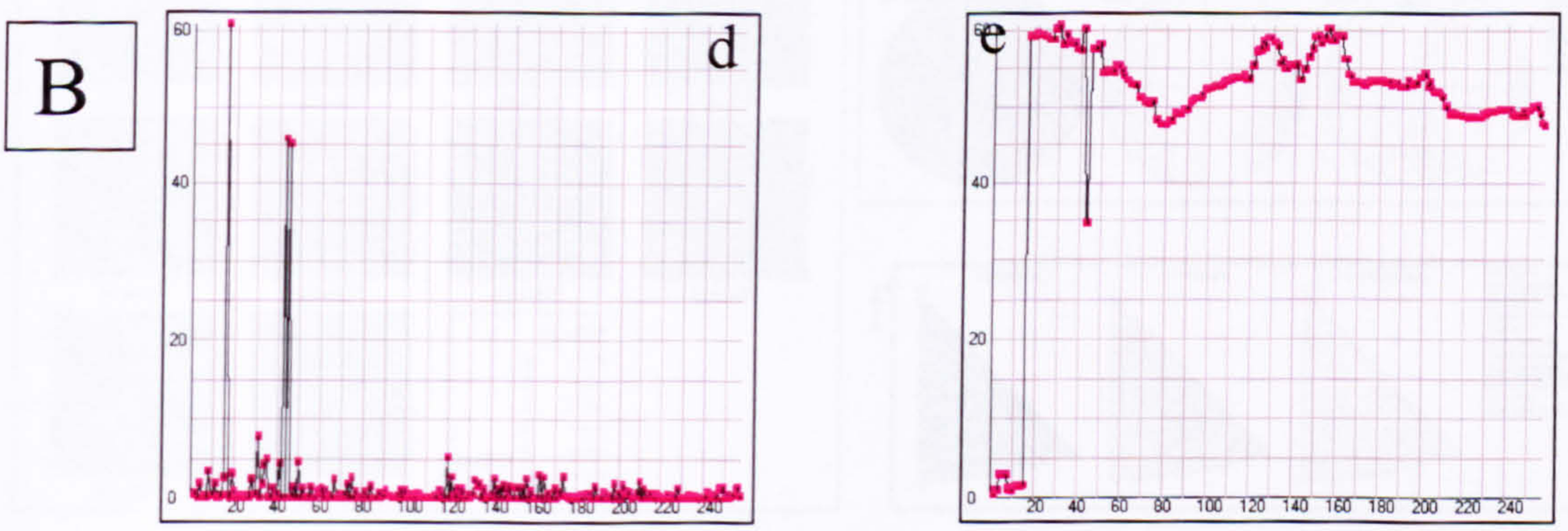

Fig. 5.137 Random-orientated grain in the 6000 seconds delayed sample: (a) relative map, (b) (d) relative and (c) (e) cumulative misorientation distributions of line scans performed along A and B in (a).

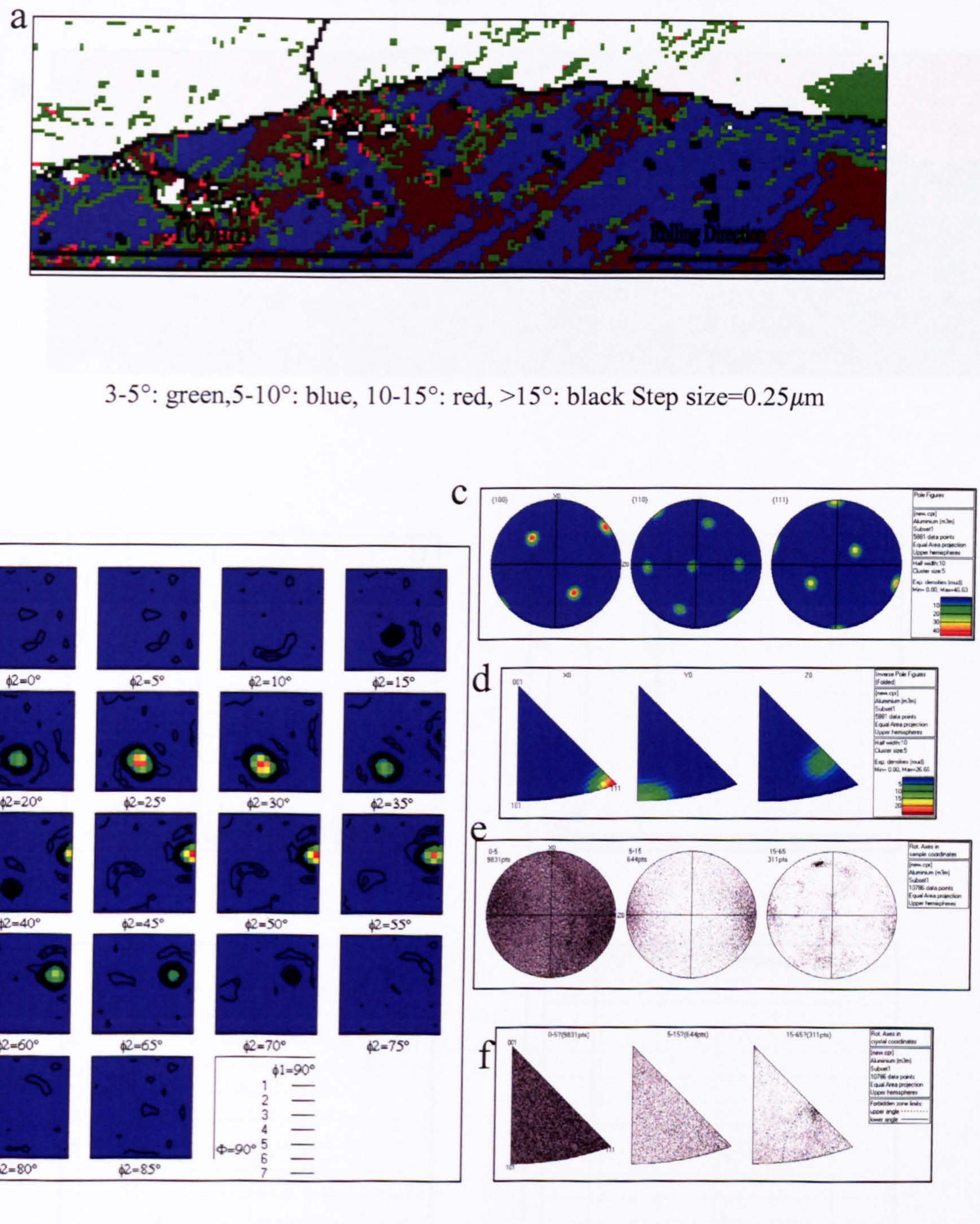

3-5°: green,5-10°: blue, 10-15°: red, >15°: black Step size=0.25μm

Fig. 5.138 Copper-orientated grain in the 6000 seconds delayed sample: (a) texture and boundary map, (b) ODF, (c) pole figures, (d) inverse pole figures, the distribution of misorientation axis vectors in (e) sample and (f) crystal lattice coordinates.

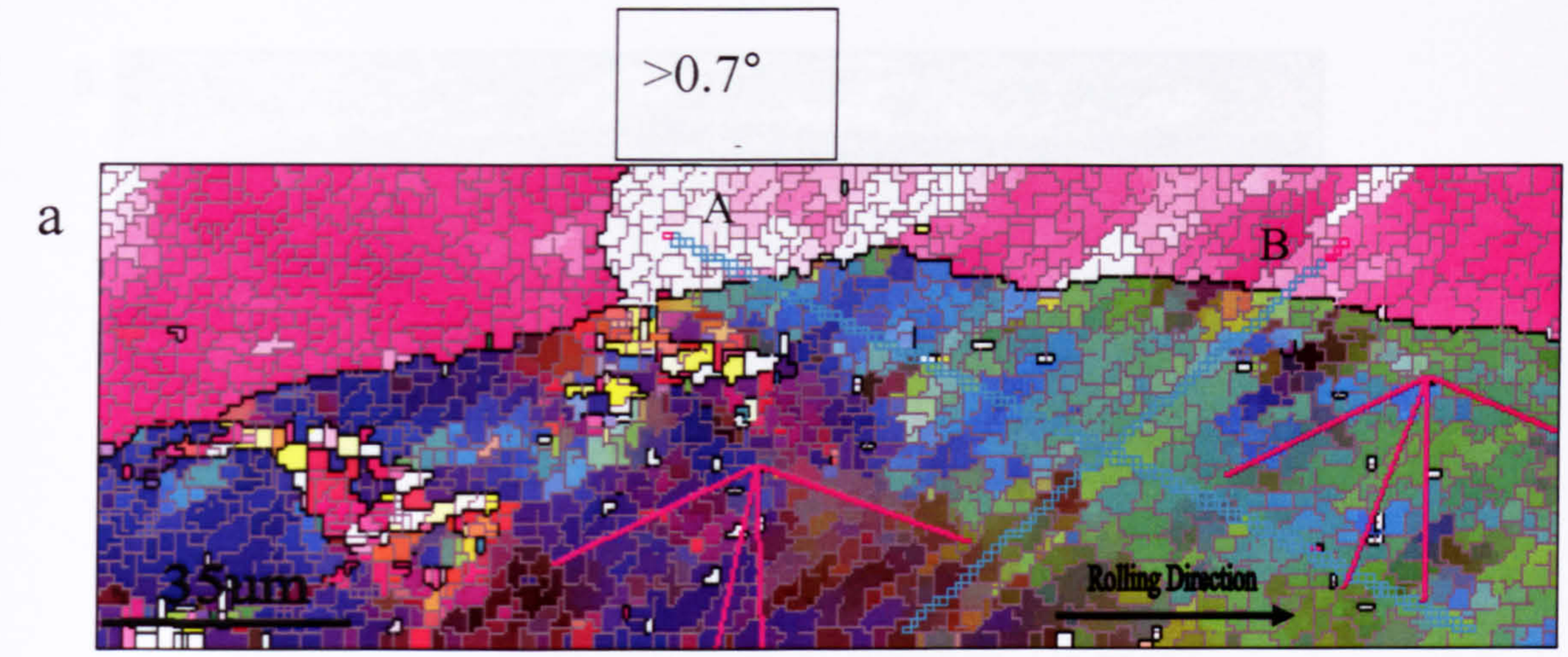

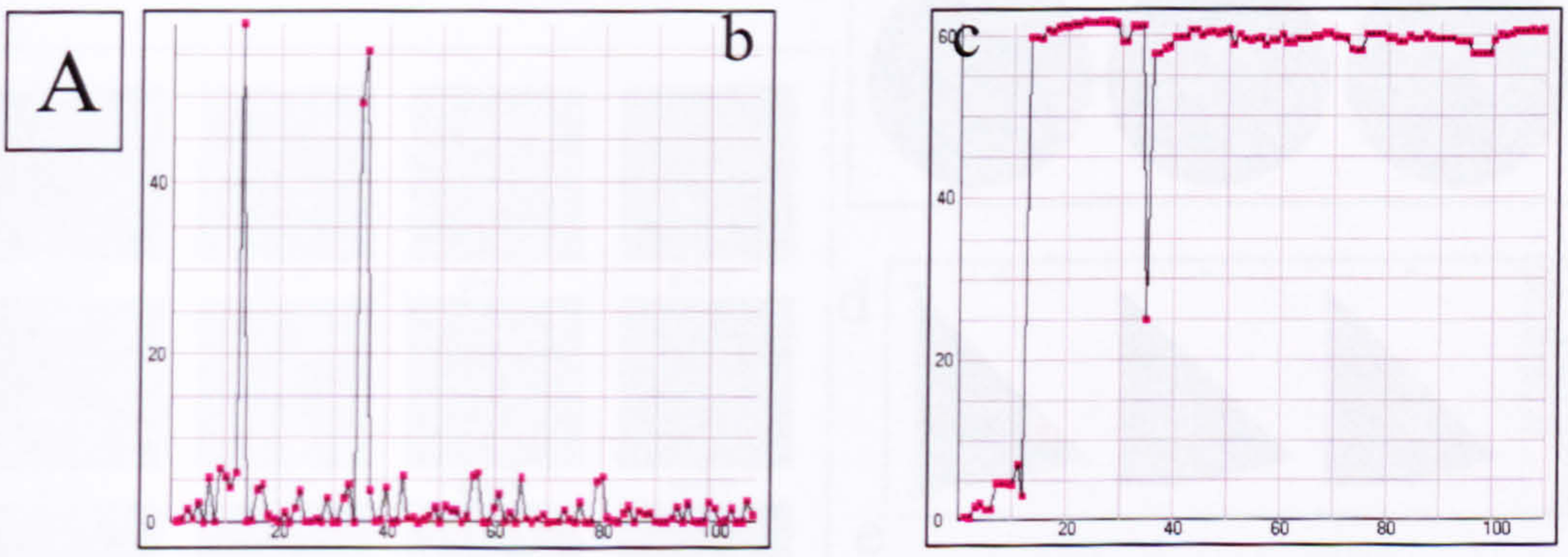

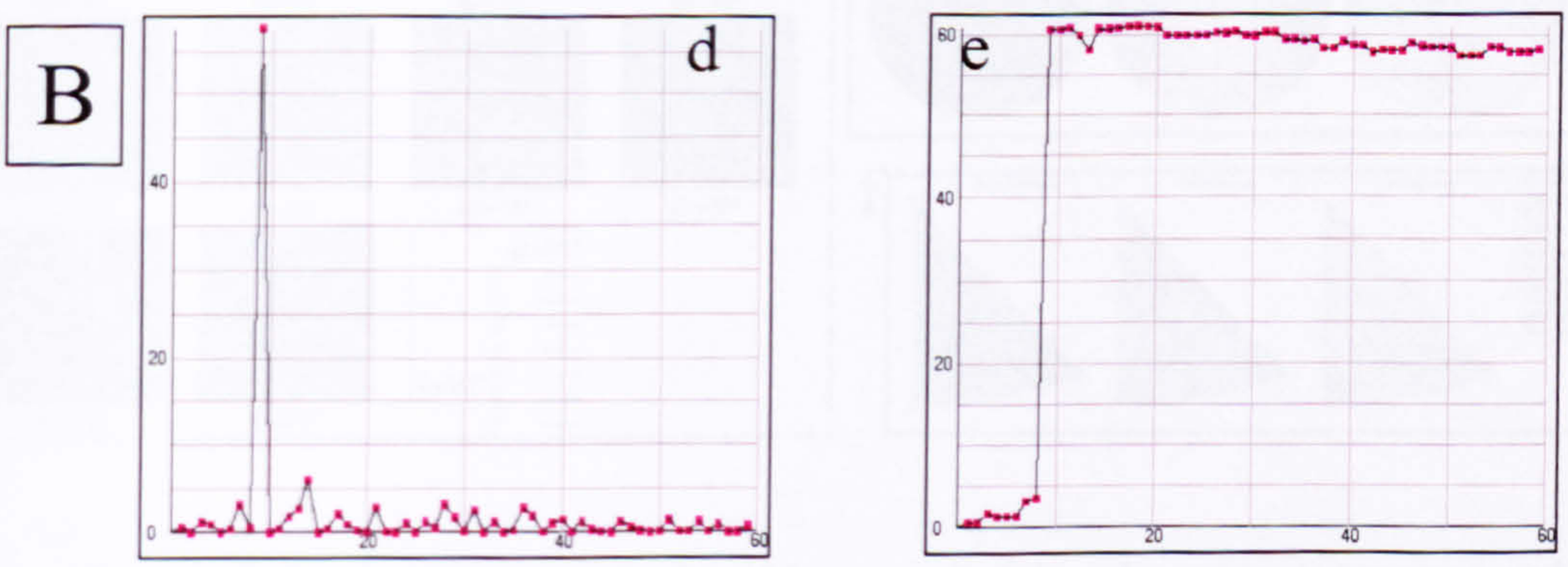

Fig. 5.139 Copper-orientated grain in the 6000 seconds delayed sample: (a) relative map, (b) (d) relative and (c) (e) cumulative misorientation distributions of line scans performed along A and B in (a).

a

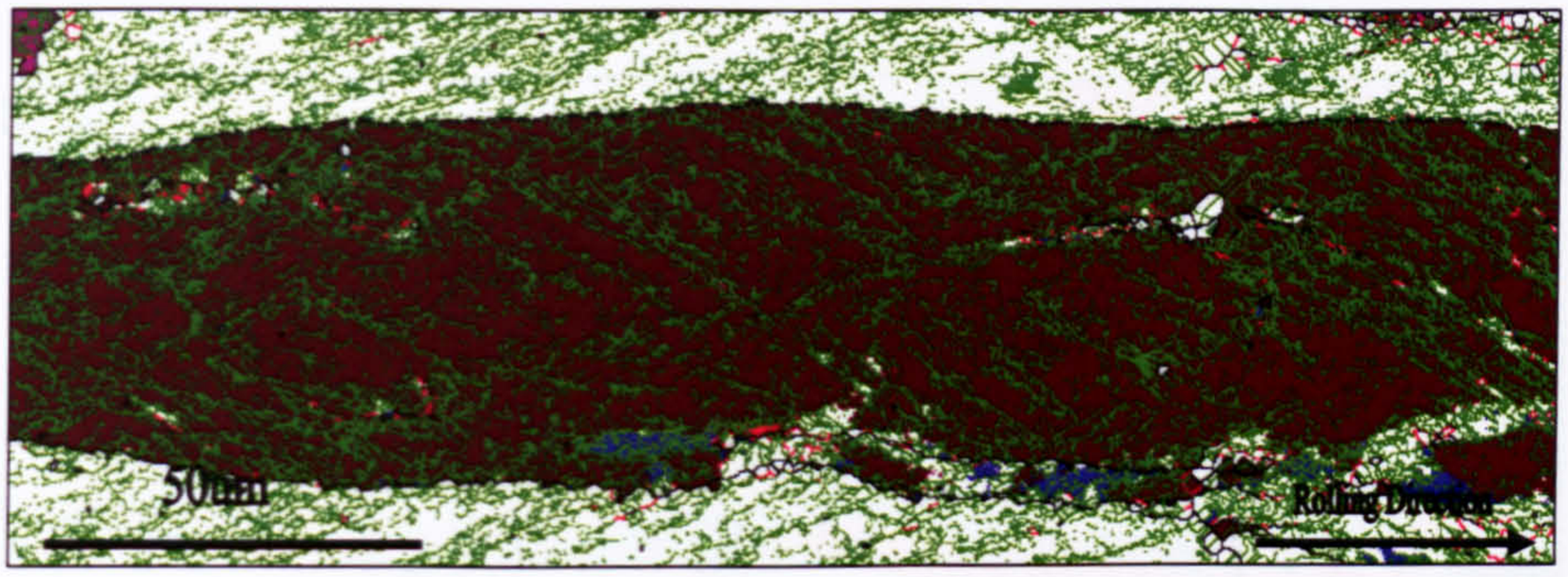

5-10°: green, 10-15°: red, >15°: black Step size=0.25μm

b

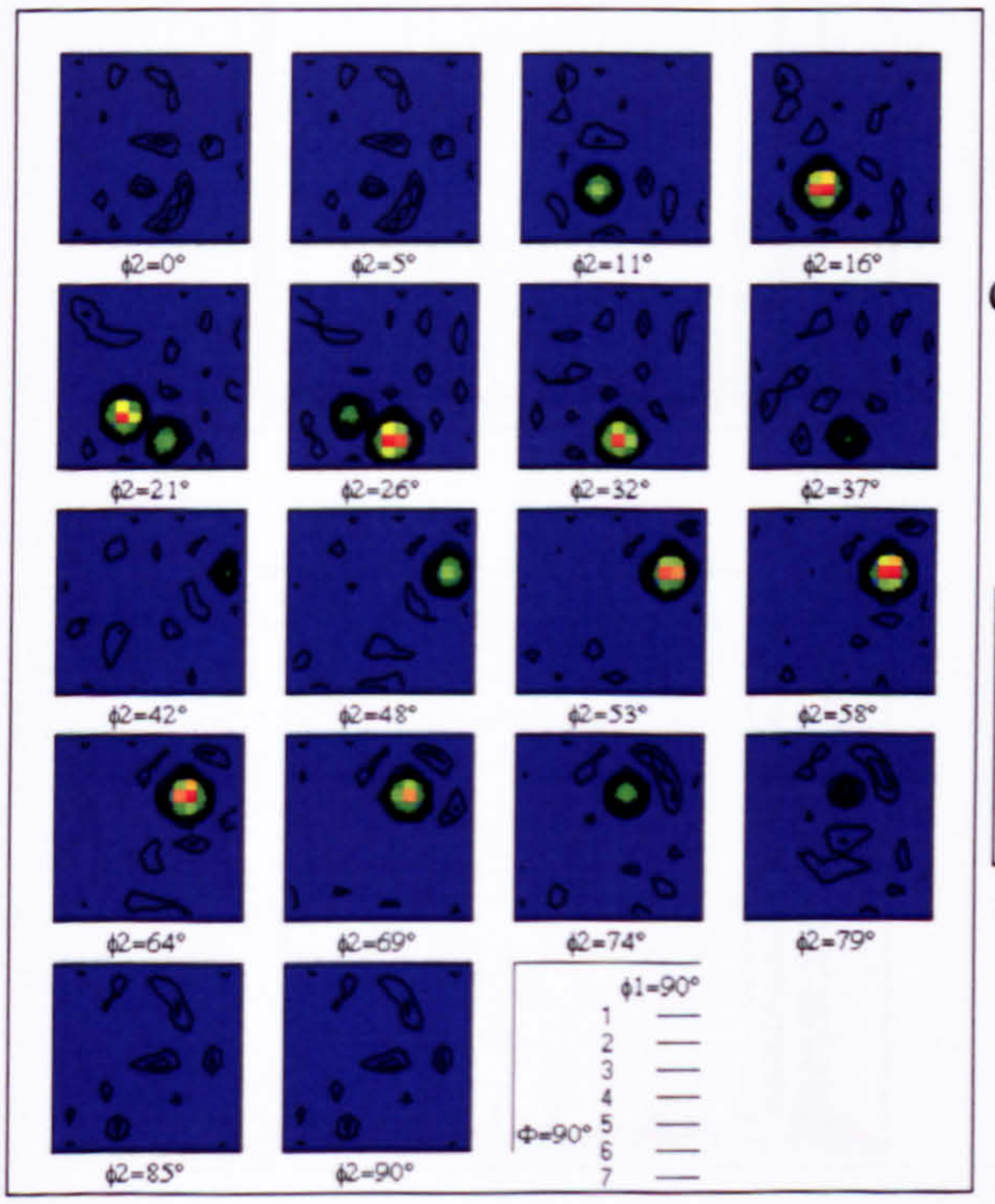

c

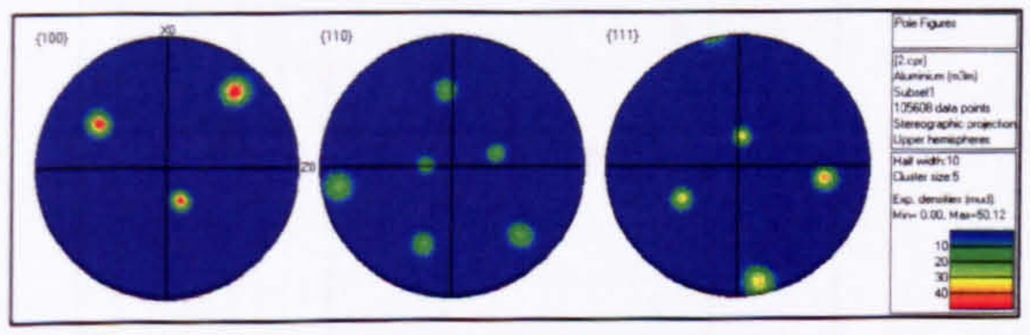

d

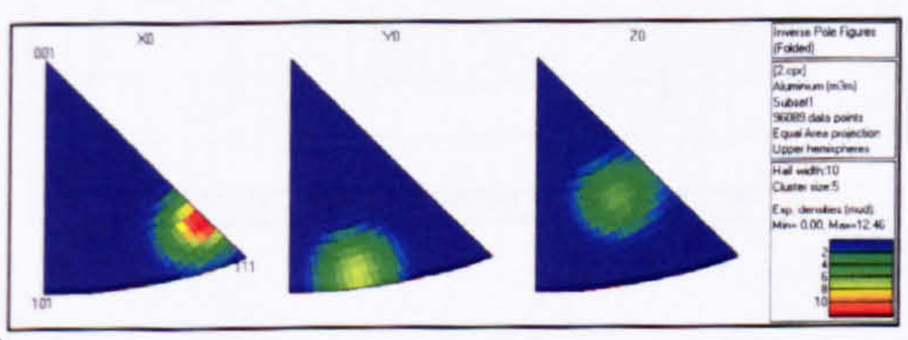

e

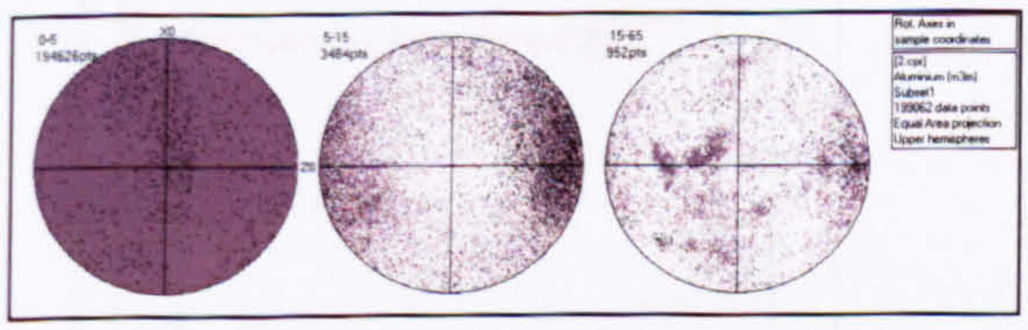

f

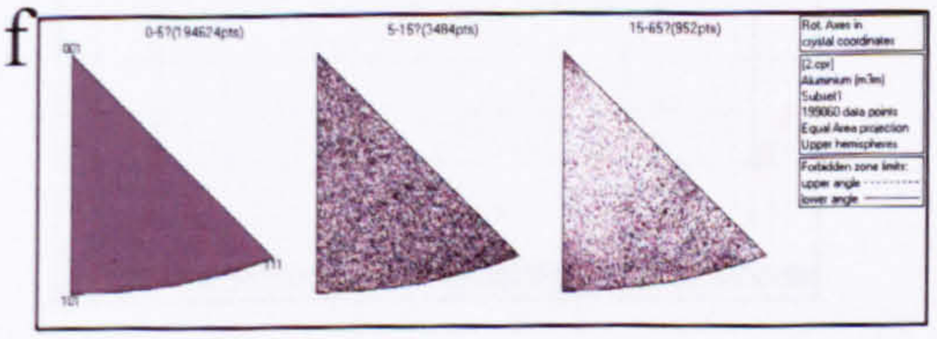

Fig. 5.140 S-orientated grain in the 6000 seconds delayed sample: (a) texture and boundary map, (b) ODF, (c) pole figures, (d) inverse pole figures, the distribution of misorientation axis vectors in (e) sample and (f) crystal lattice coordinates.

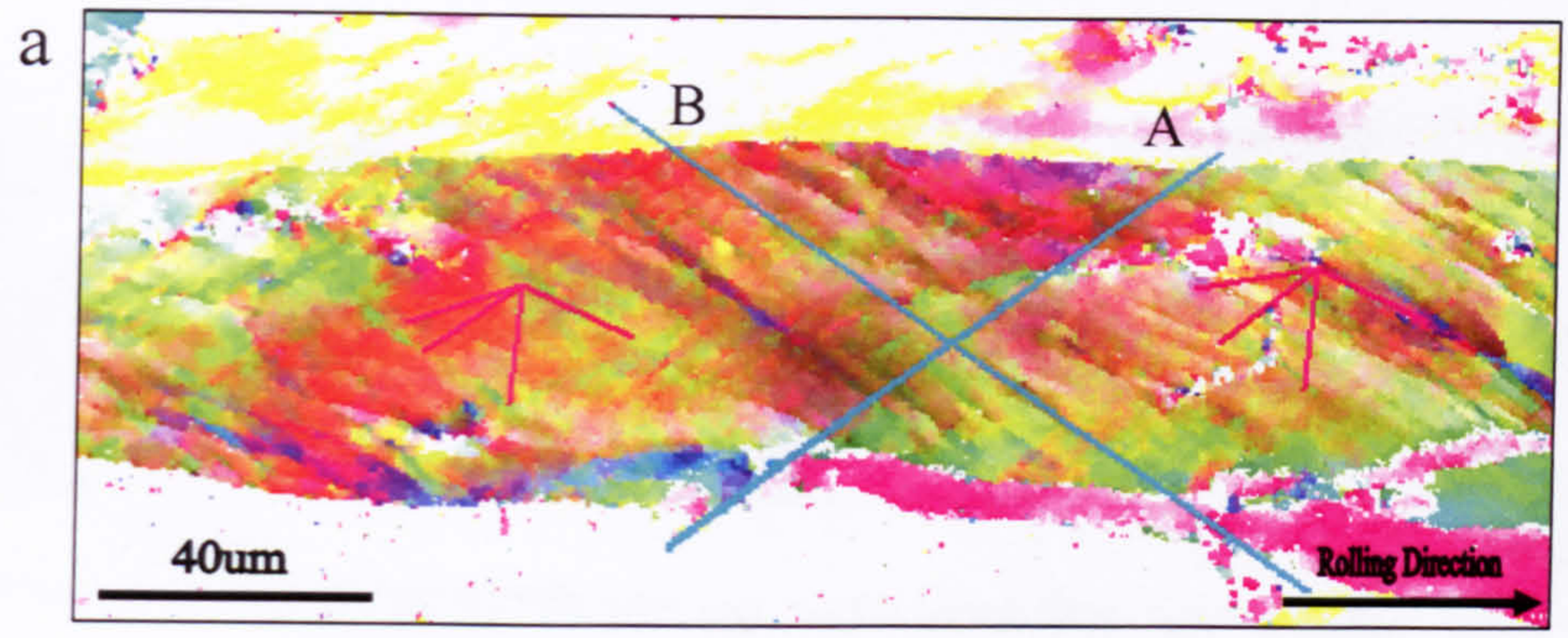

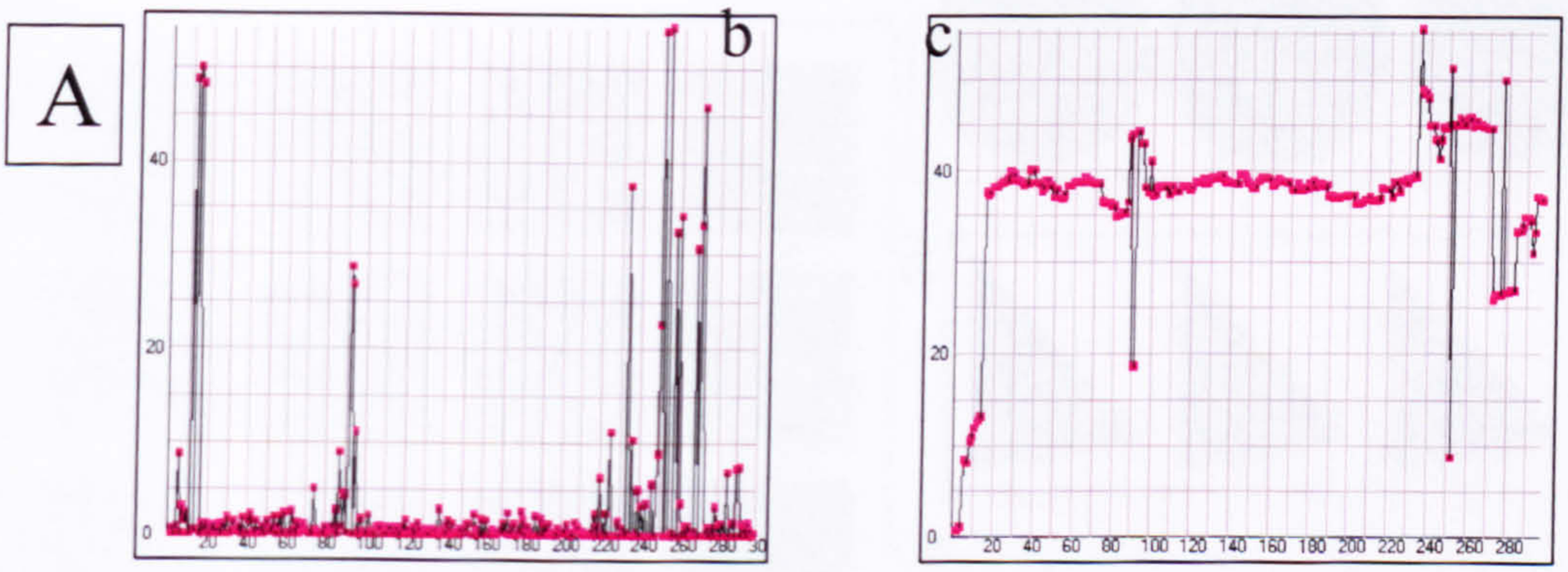

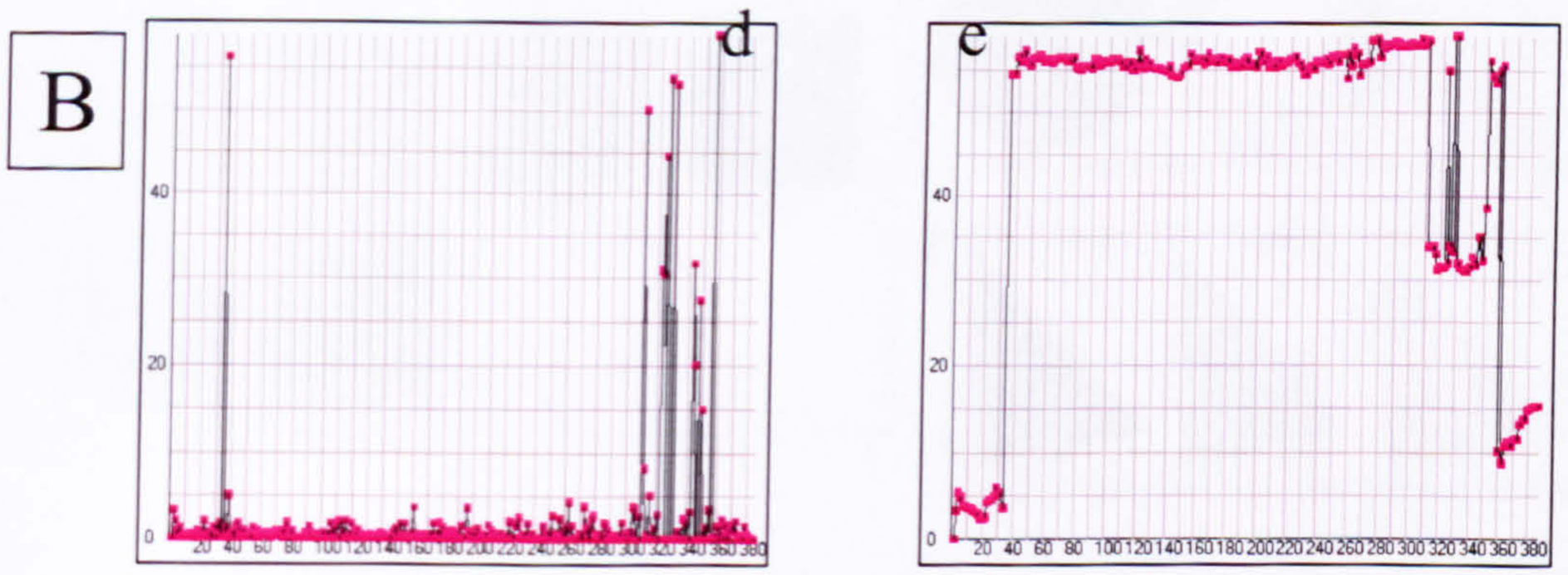

Fig. 5.141 S-orientated grain in the 6000 seconds delayed sample: (a) relative map, (b) (d) relative and (c) (e) cumulative misorientation distributions of line scans performed along A and B in (a).

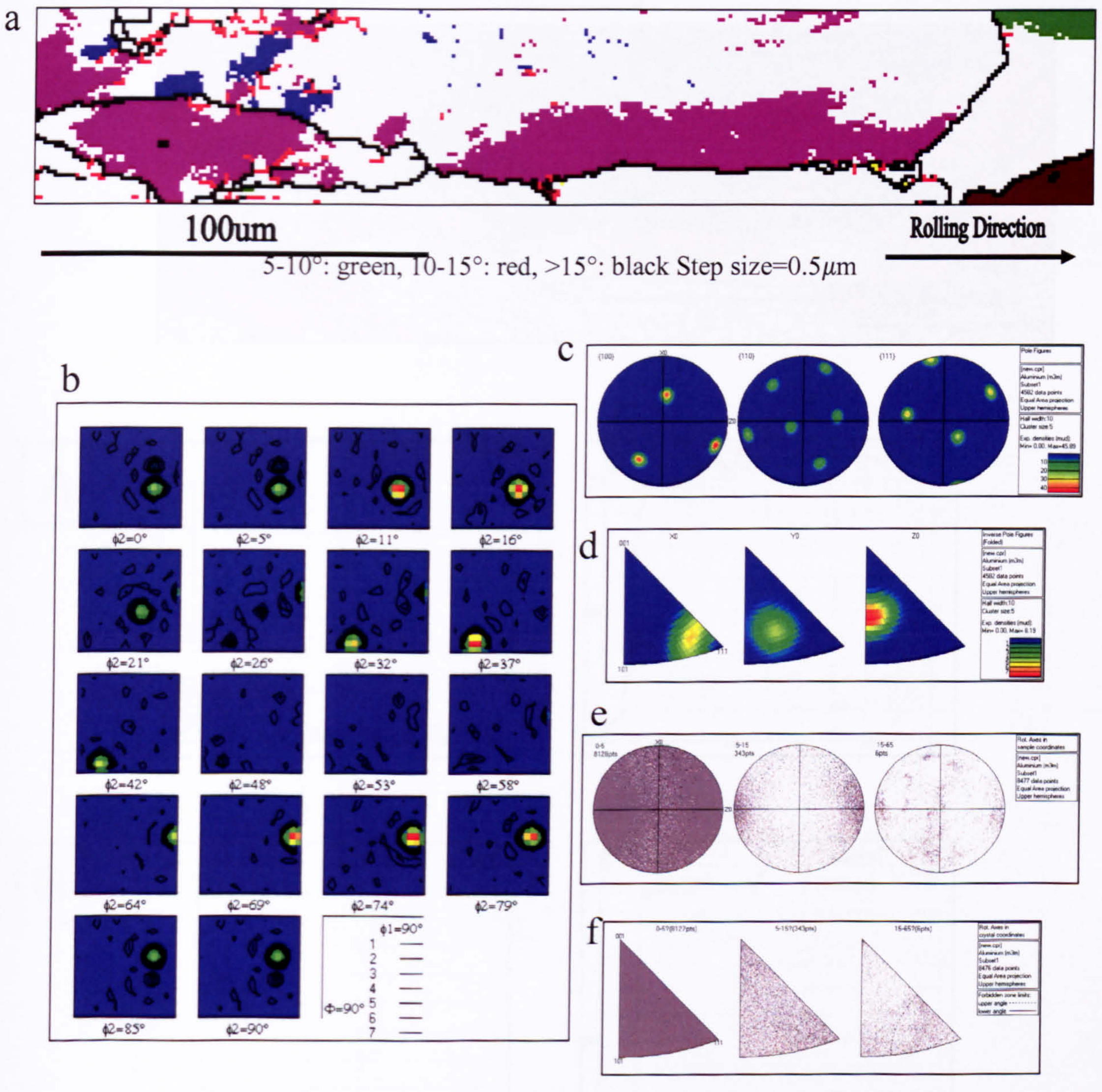

Fig. 5.142 P-orientated grain in the 6000 seconds delayed sample: (a) texture and boundary map, (b) ODF, (c) pole figures, (d) inverse pole figures, the distribution of misorientation axis vectors in (e) sample and (f) crystal lattice coordinates.

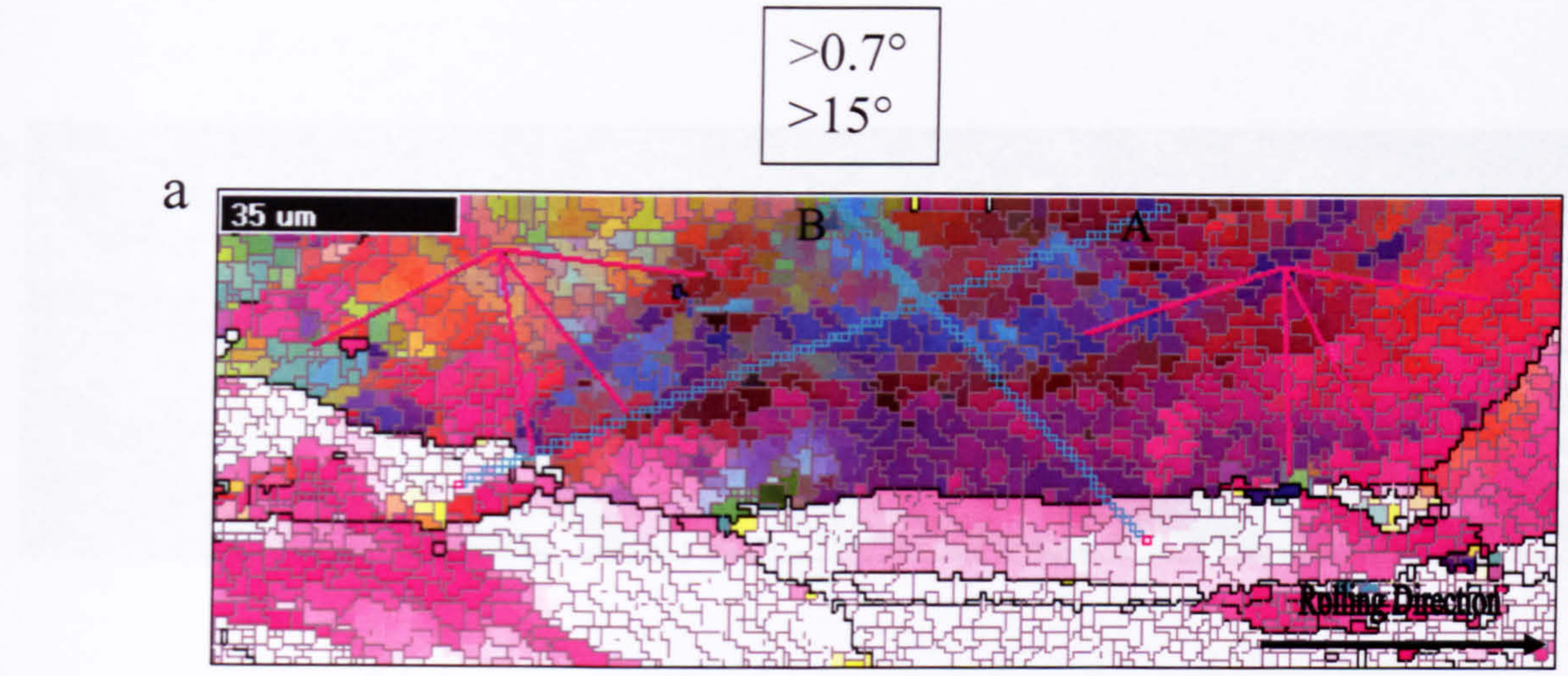

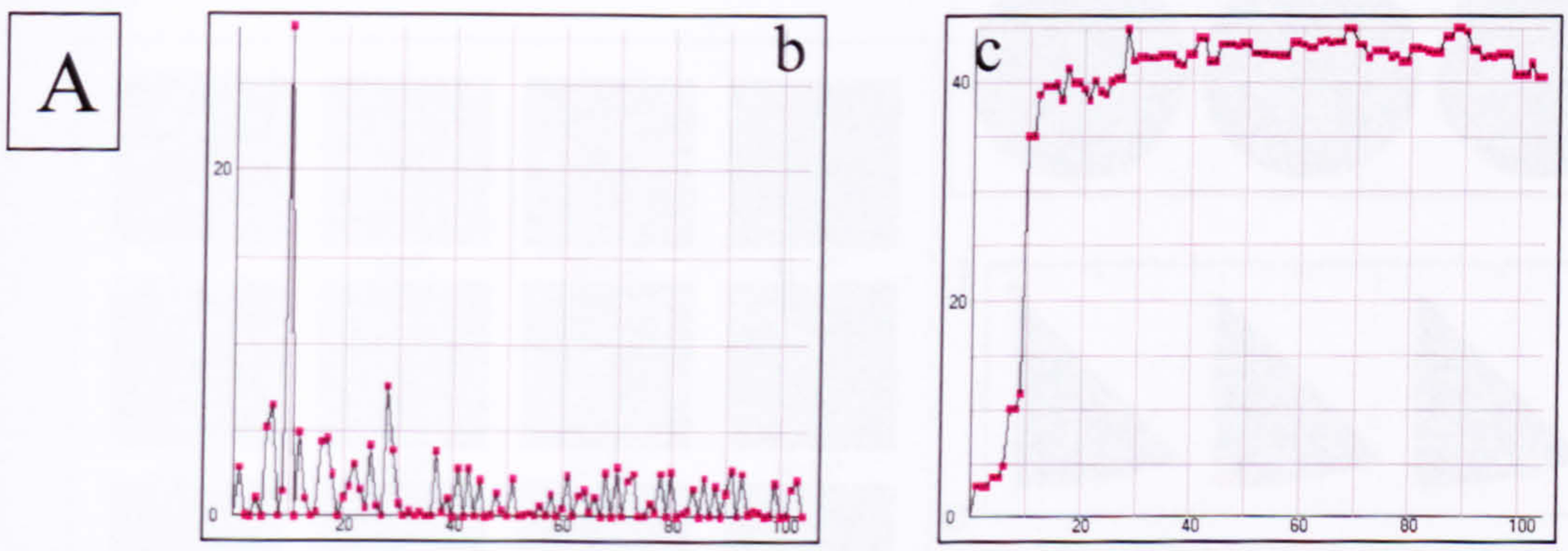

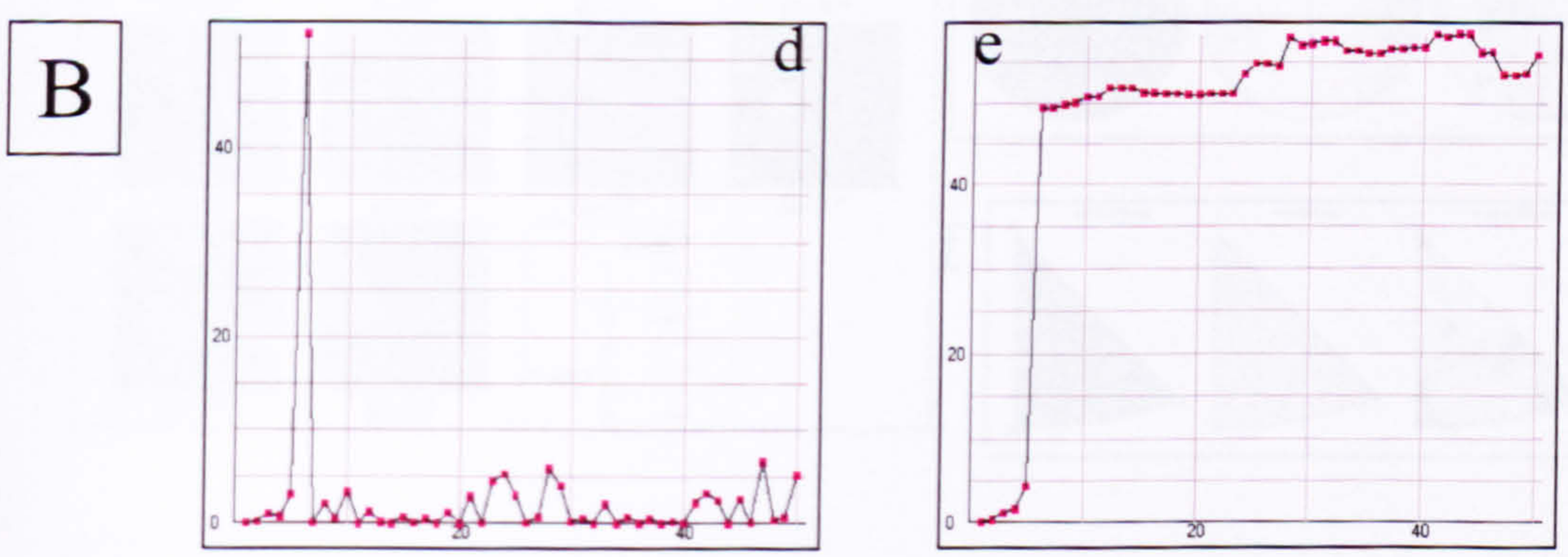

Fig. 5.143 P-orientated grain in the 6000 seconds delayed sample: (a) relative map, (b) (d) relative and (c) (e) cumulative misorientation distributions of line scans performed along A and B in (a).

a

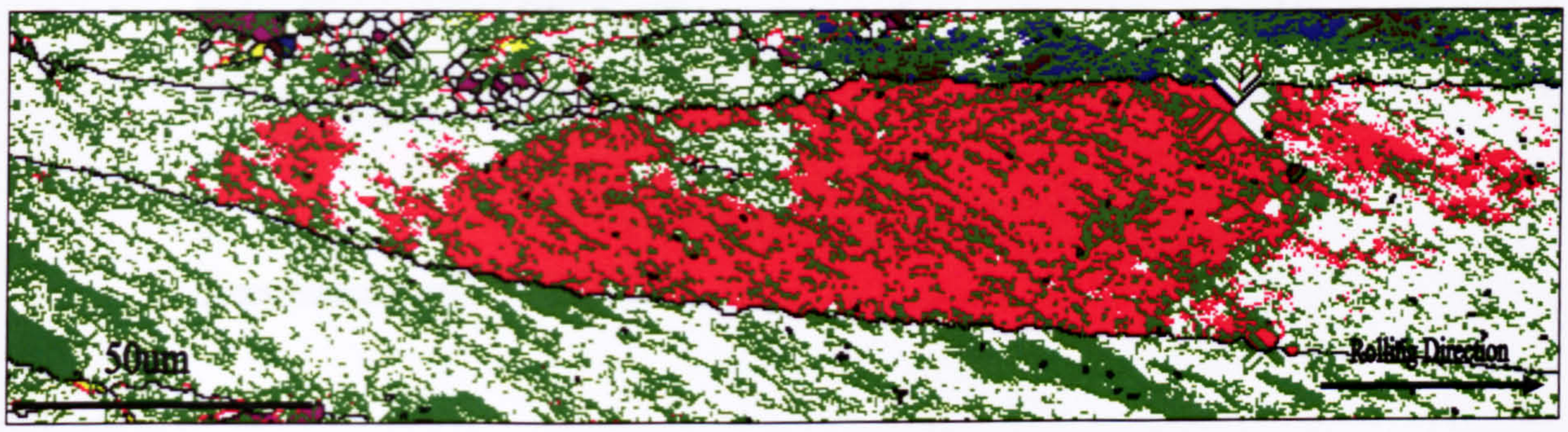

5-10°: green, 10-15°: red, >15°: black Step size=0.25μm

b

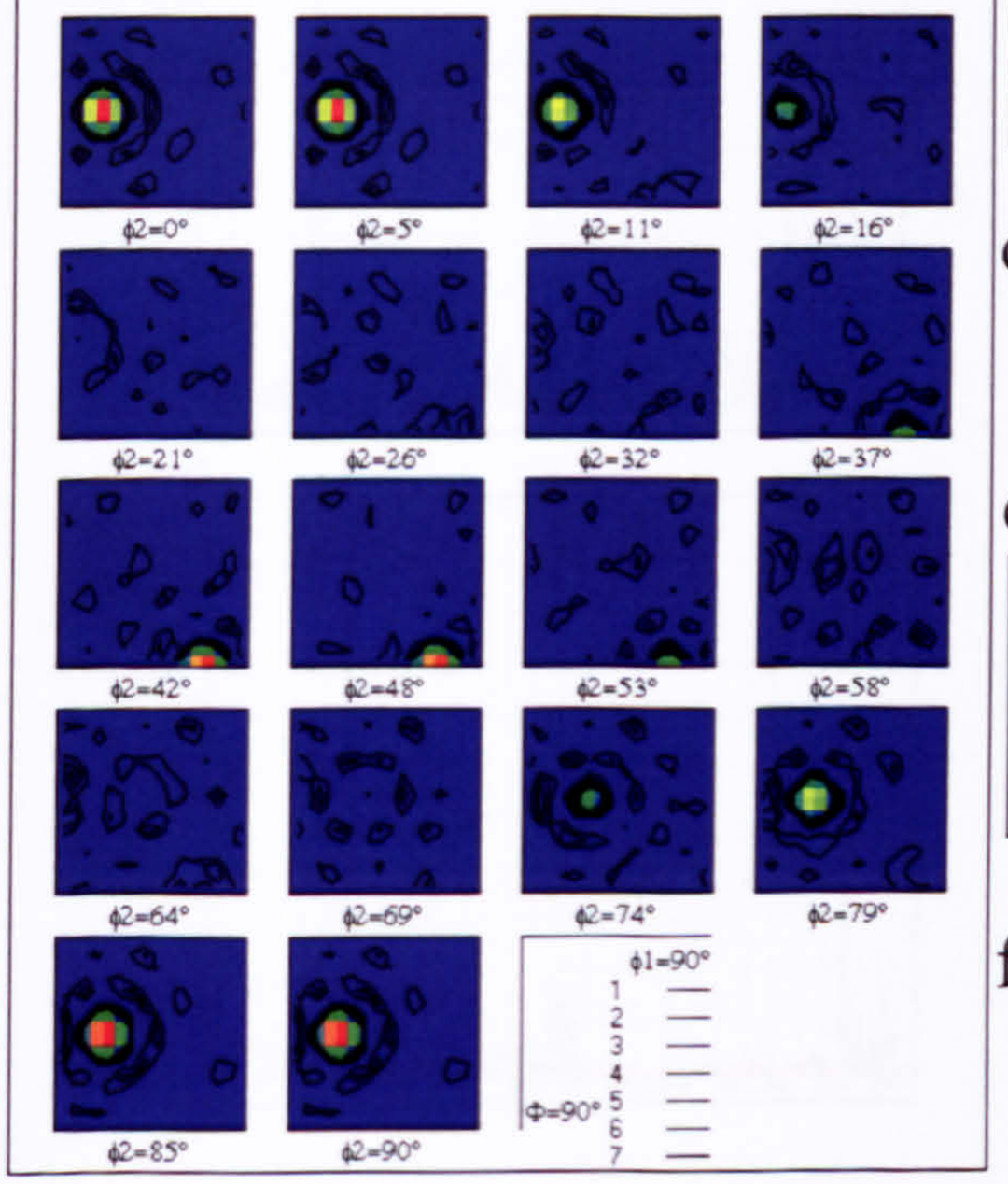

c

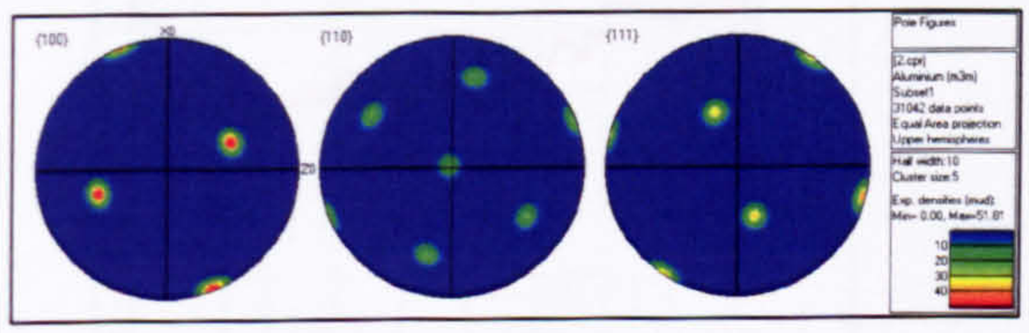

d

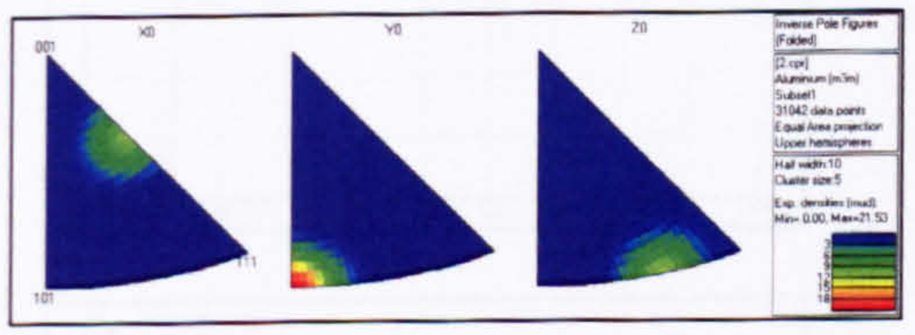

e

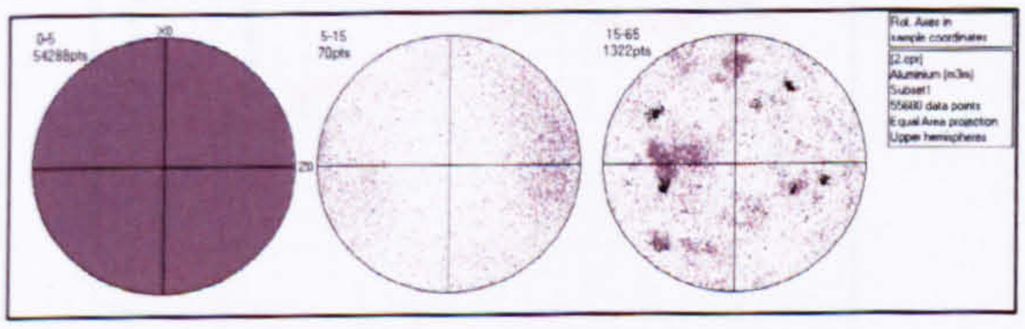

f

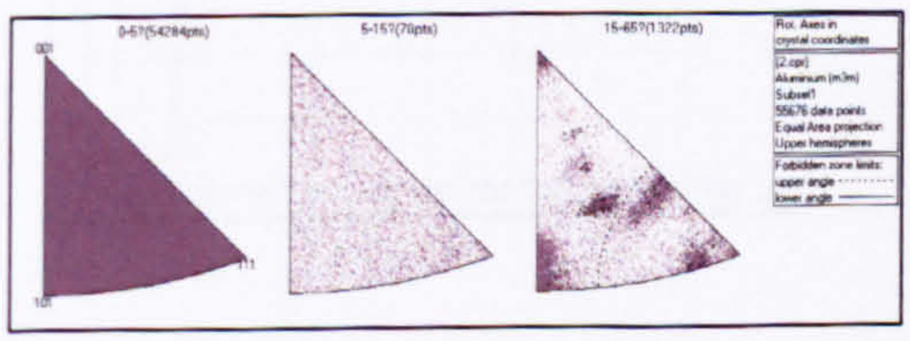

Fig. 5.144 Brass-orientated grain in the 6000 seconds delayed sample: (a) texture and boundary map, (b) ODF, (c) pole figures, (d) inverse pole figures, the distribution of misorientation axis vectors in (e) sample and (f) crystal lattice coordinates.

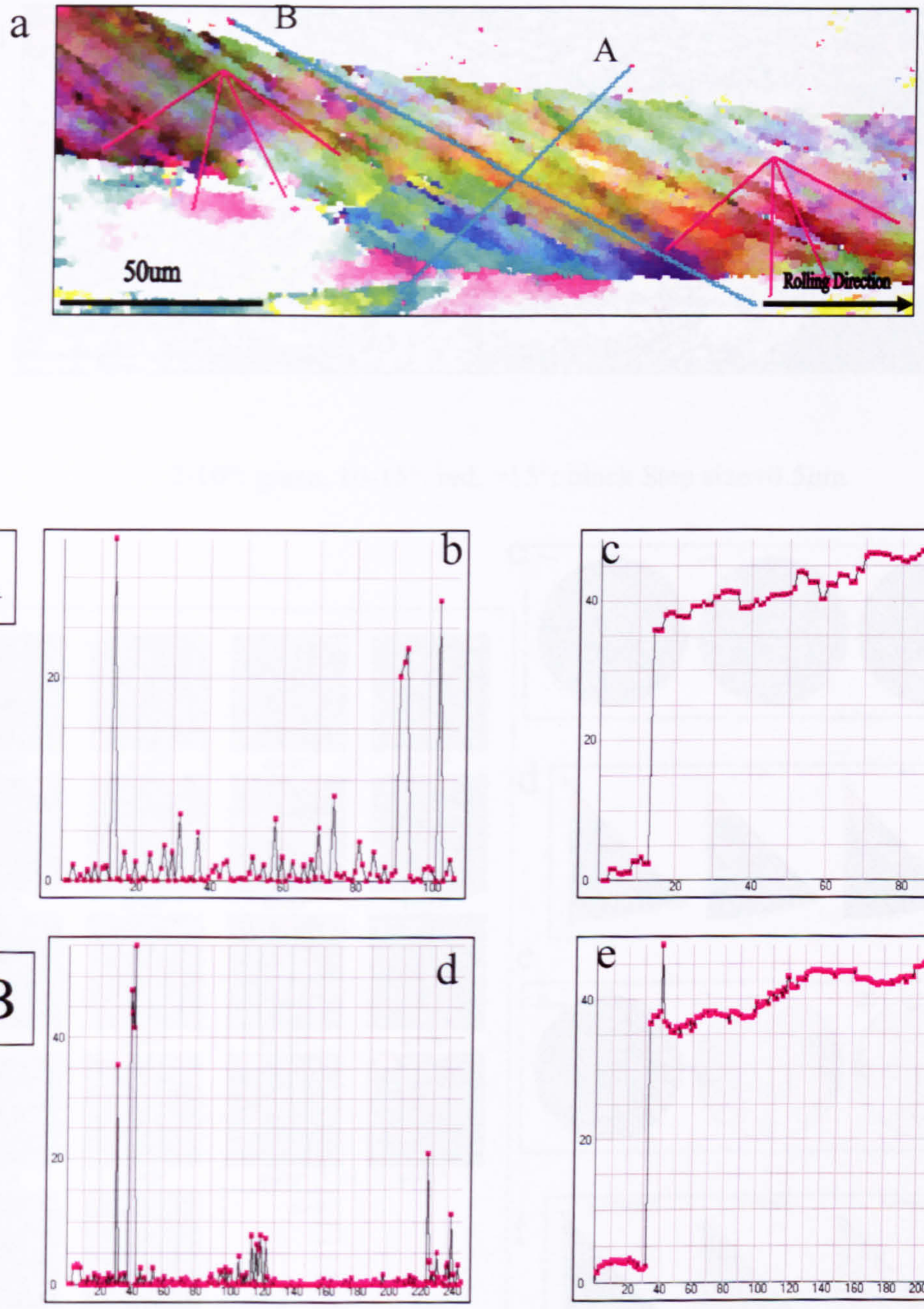

Fig. 5.145 Brass-orientated grain in the 6000 seconds delayed sample: (a) relative map, (b) (d) relative and (c) (e) cumulative misorientation distributions of line scans performed along A and B in (a).

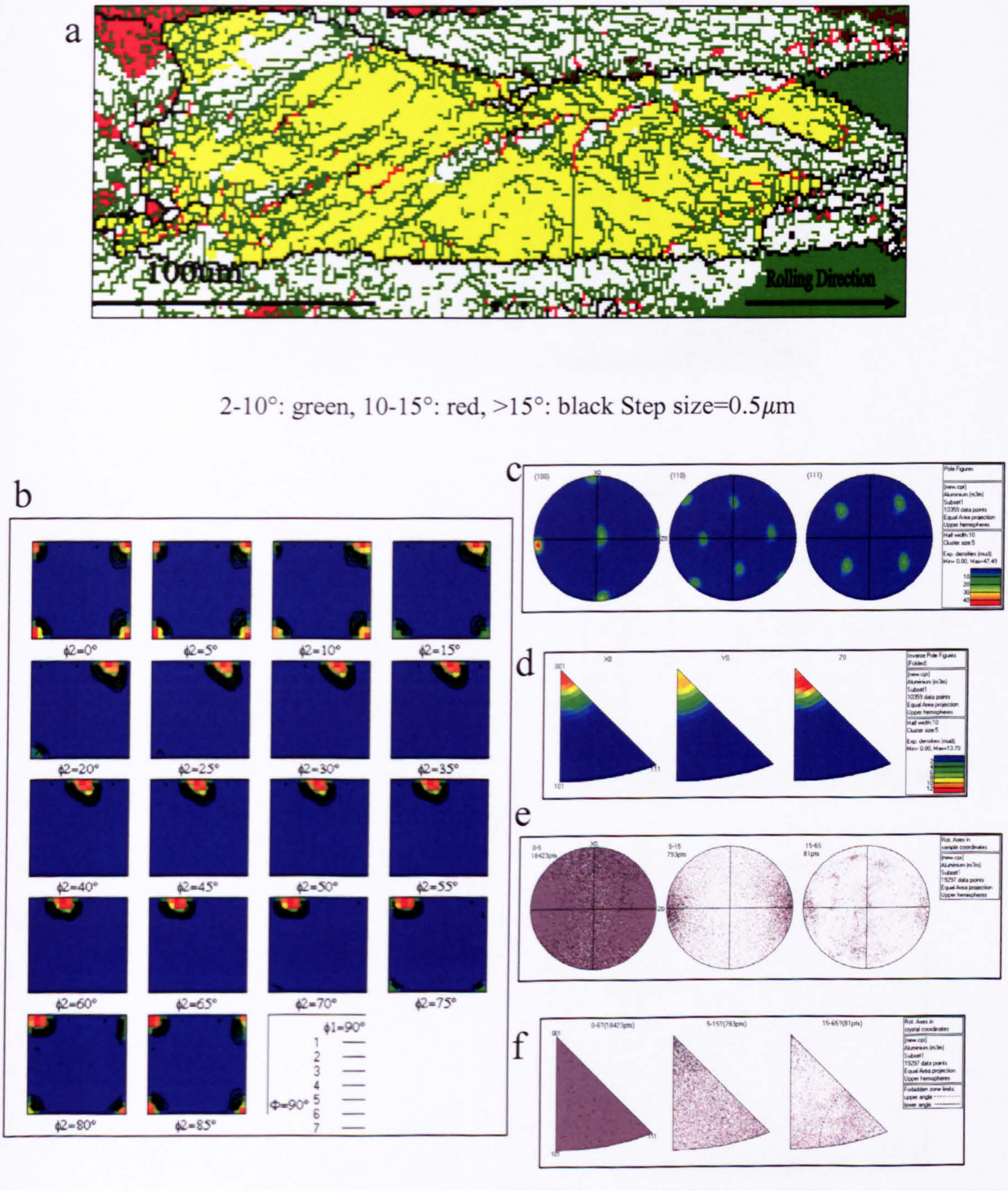

Fig. 5.146 Cube-orientated grain in the 6000 seconds delayed sample: (a) texture and boundary map, (b) ODF, (c) pole figures, (d) inverse pole figures, the distribution of misorientation axis vectors in (e) sample and (f) crystal lattice coordinates.

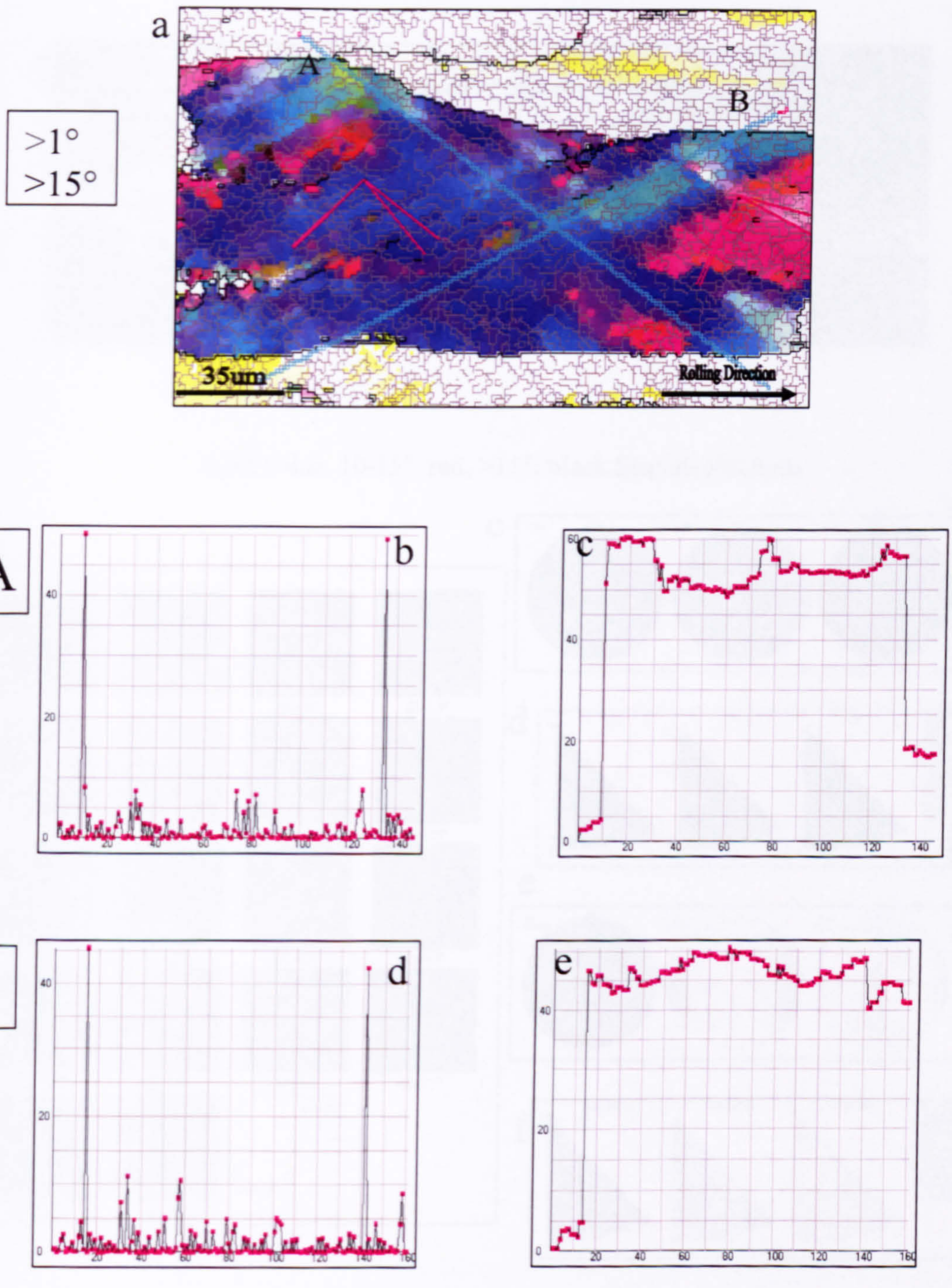

Fig. 5.147 Cube-orientated grain in the 6000 seconds delayed sample: (a) relative map, (b) (d) relative and (c) (e) cumulative misorientation distributions of line scans performed along A and B in (a).

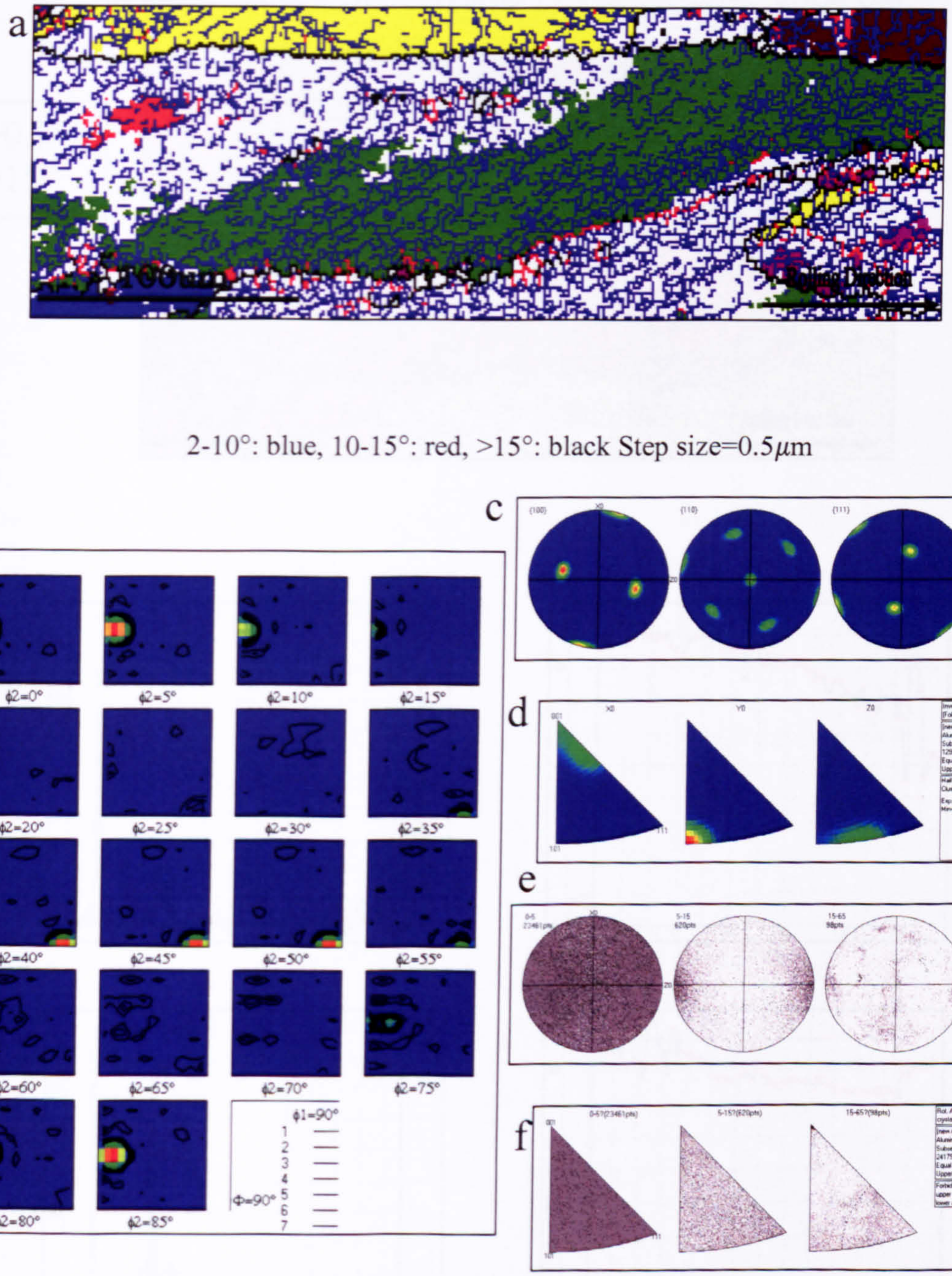

Fig. 5.148 Goss-orientated grain in the 6000 seconds delayed sample: (a) texture and boundary map, (b) ODF, (c) pole figures, (d) inverse pole figures, the distribution of misorientation axis vectors in (e) sample and (f) crystal lattice coordinates.

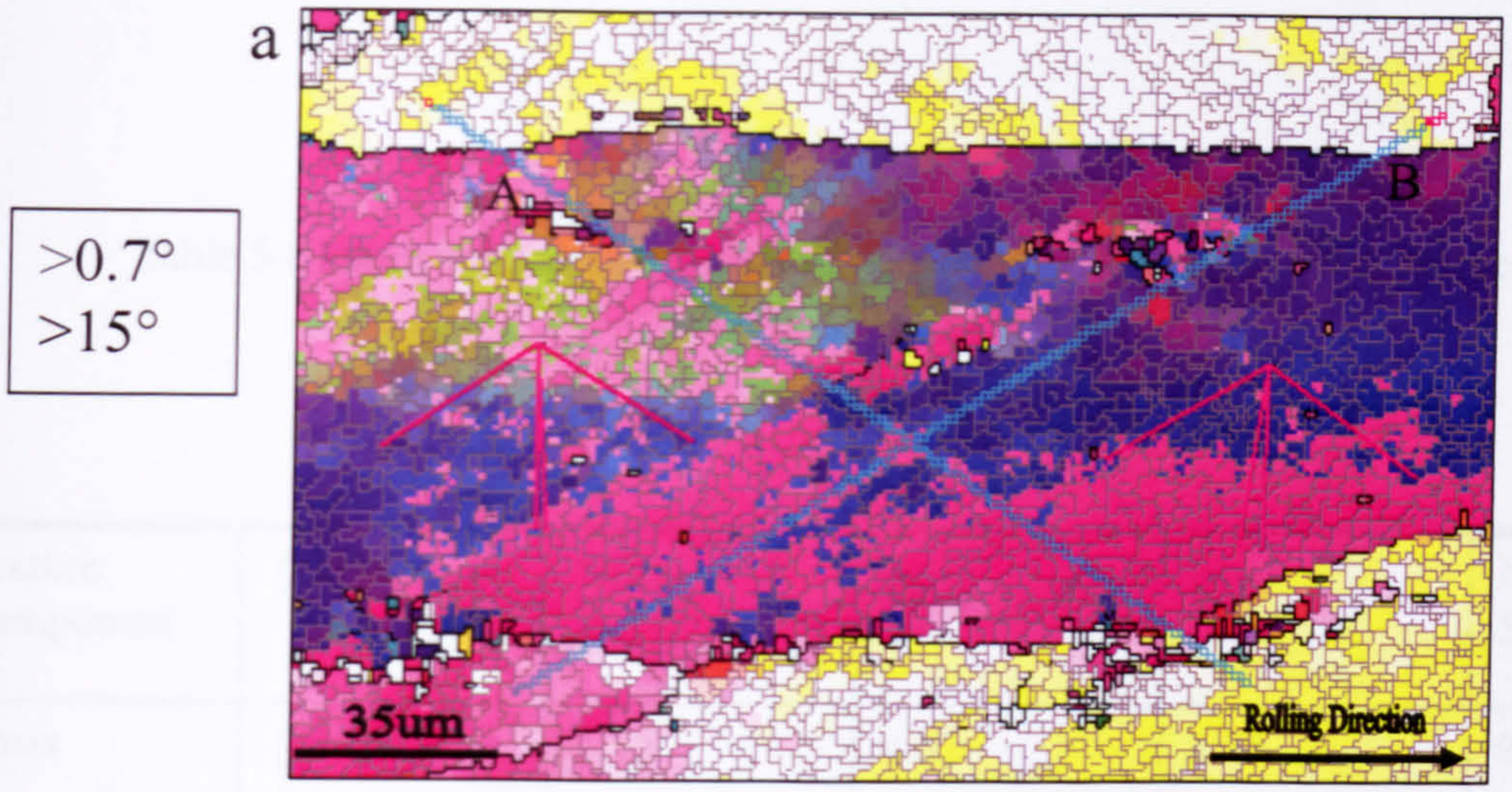

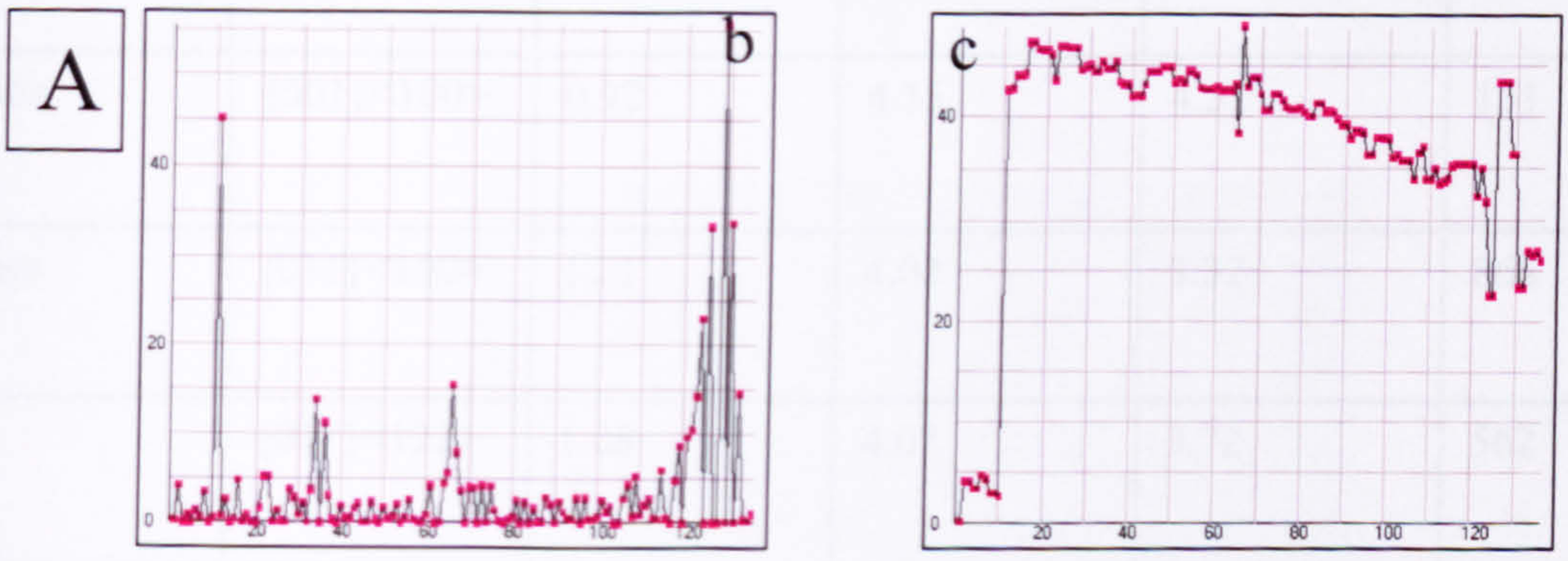

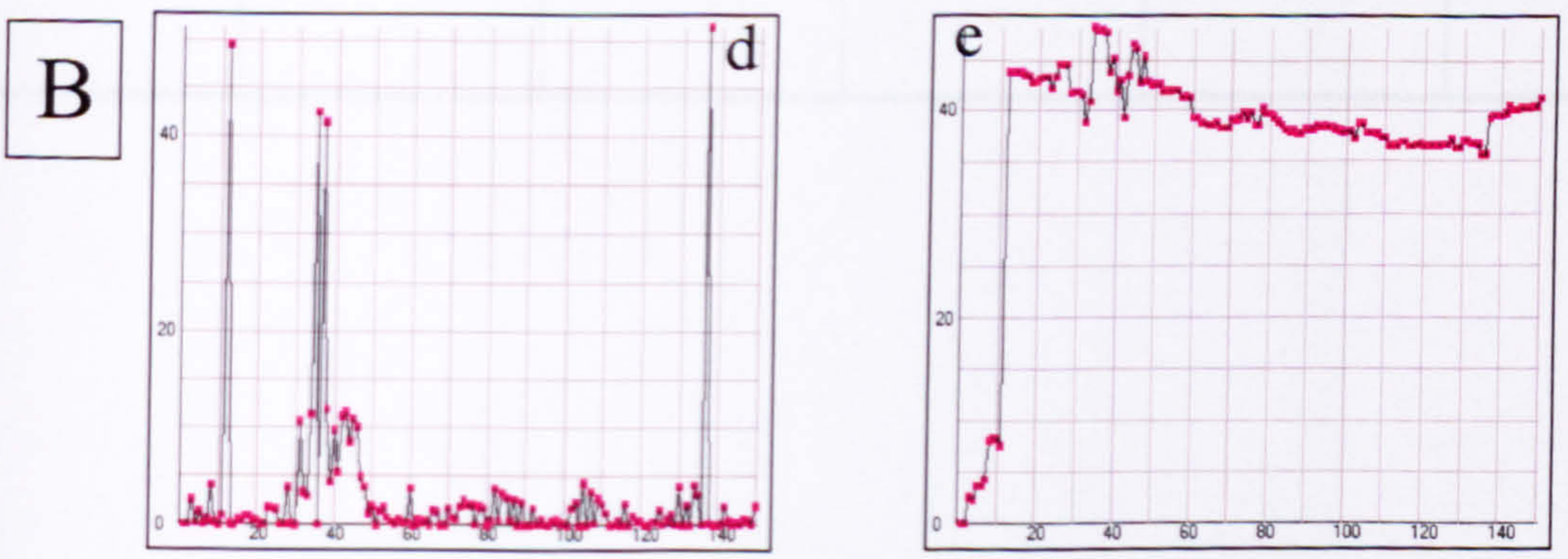

Fig. 5.149 Goss-orientated grain in the 6000 seconds delayed sample: (a) relative map, (b) (d) relative and (c) (e) cumulative misorientation distributions of line scans performed along A and B in (a).

Table 5.8 Mean subgrain size (D), misorientation angle (è) and Θ/d for the 6000 seconds delayed sample

Texture Component	{hkl}<uvw>	D(μm)	Θ(°)	Θ/d	Number of Subgrains
Brass	{011}<112>	1.15	4.32	3.75	969
Copper	{112}<111>	1.22	4.04	3.31	3272
Cube	{001}<100>	0.92	4.15	4.51	131
Goss	{011}<100>	1.21	4.02	3.32	868
P	{011}<122>	1.08	4.02	3.72	562
S	{123}<634>	1.27	4.04	3.18	3453

a

b

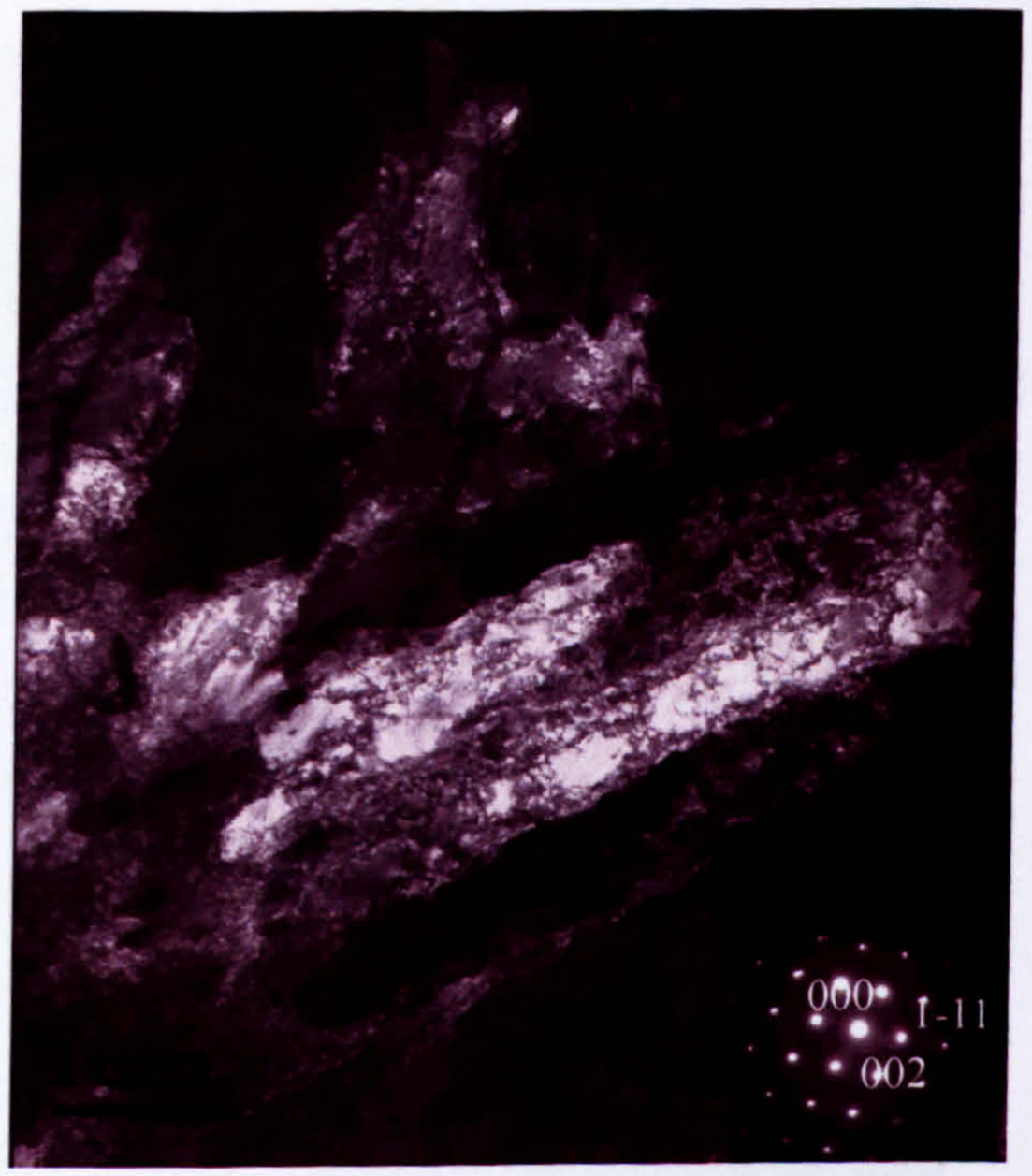

Fig. 5.150 TEM images after the 6000 seconds delayed deformation, shows a well-developed microbands structure bounded by the GNBs: (a) bright field image, (b) dark field image.

a

b

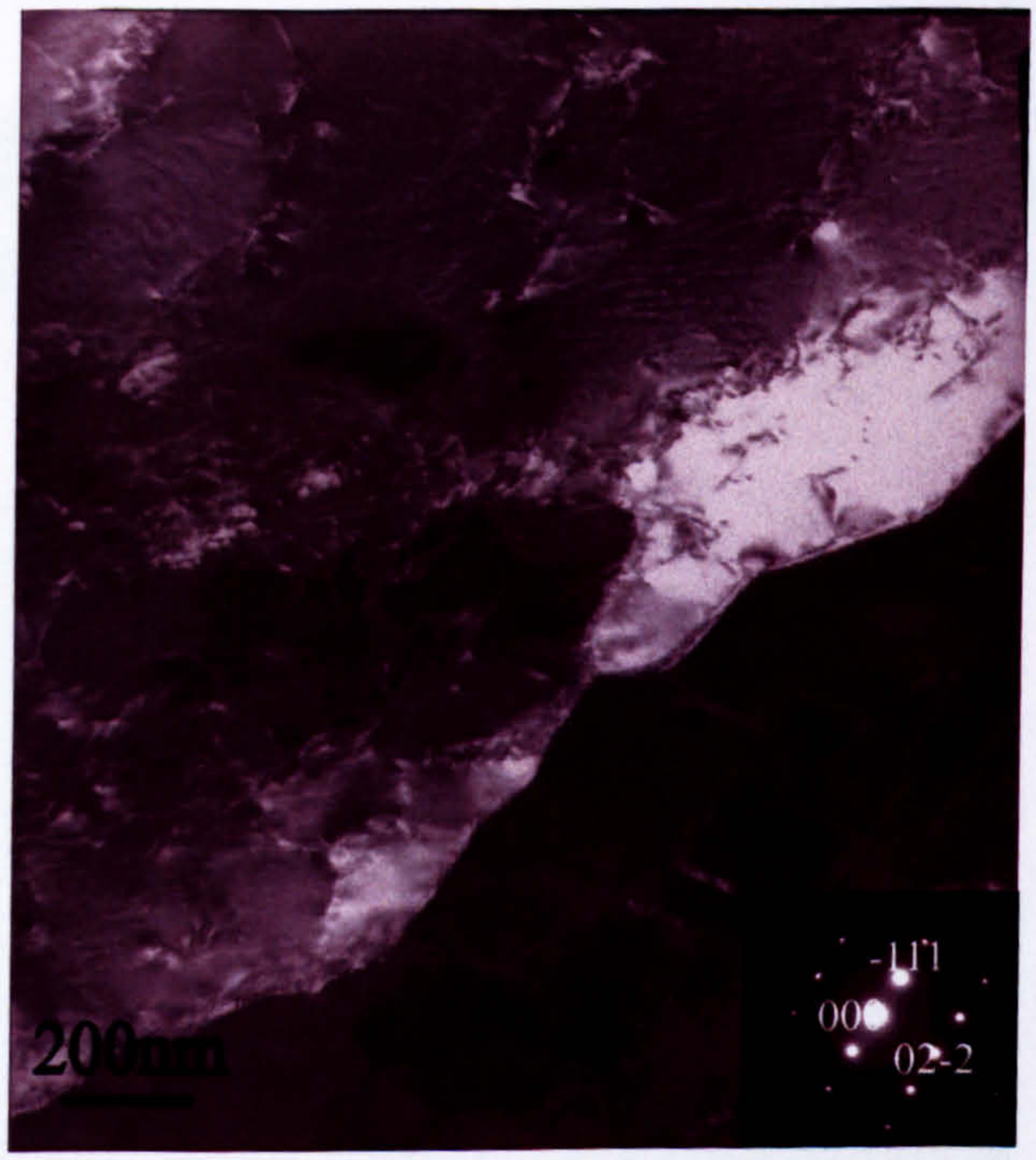

Fig. 5.151 TEM images after the 6000 seconds delayed deformation, shows the dense dislocation cells structure within the microbands: (a) bright field image, (b) dark field image.

a

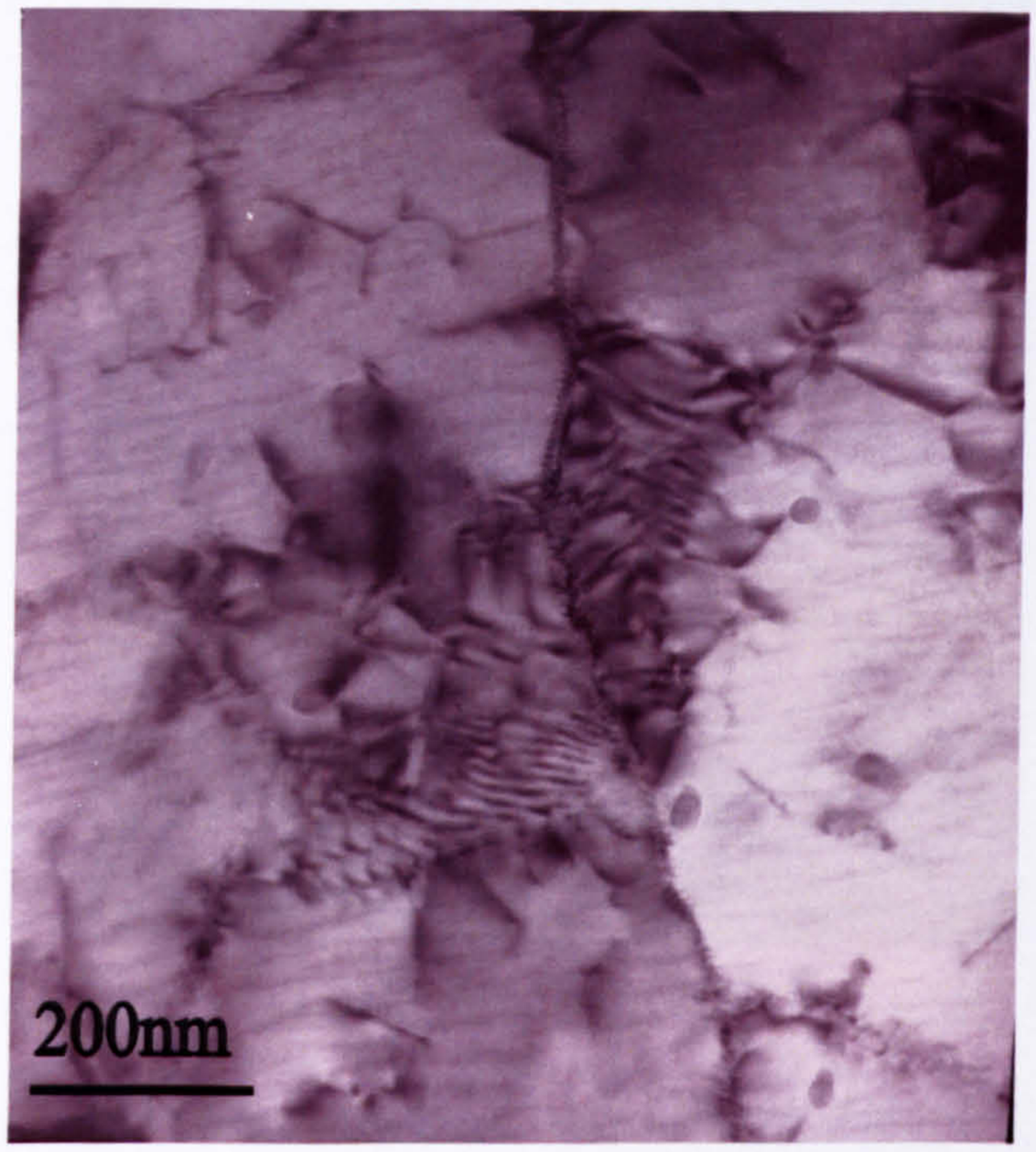

b

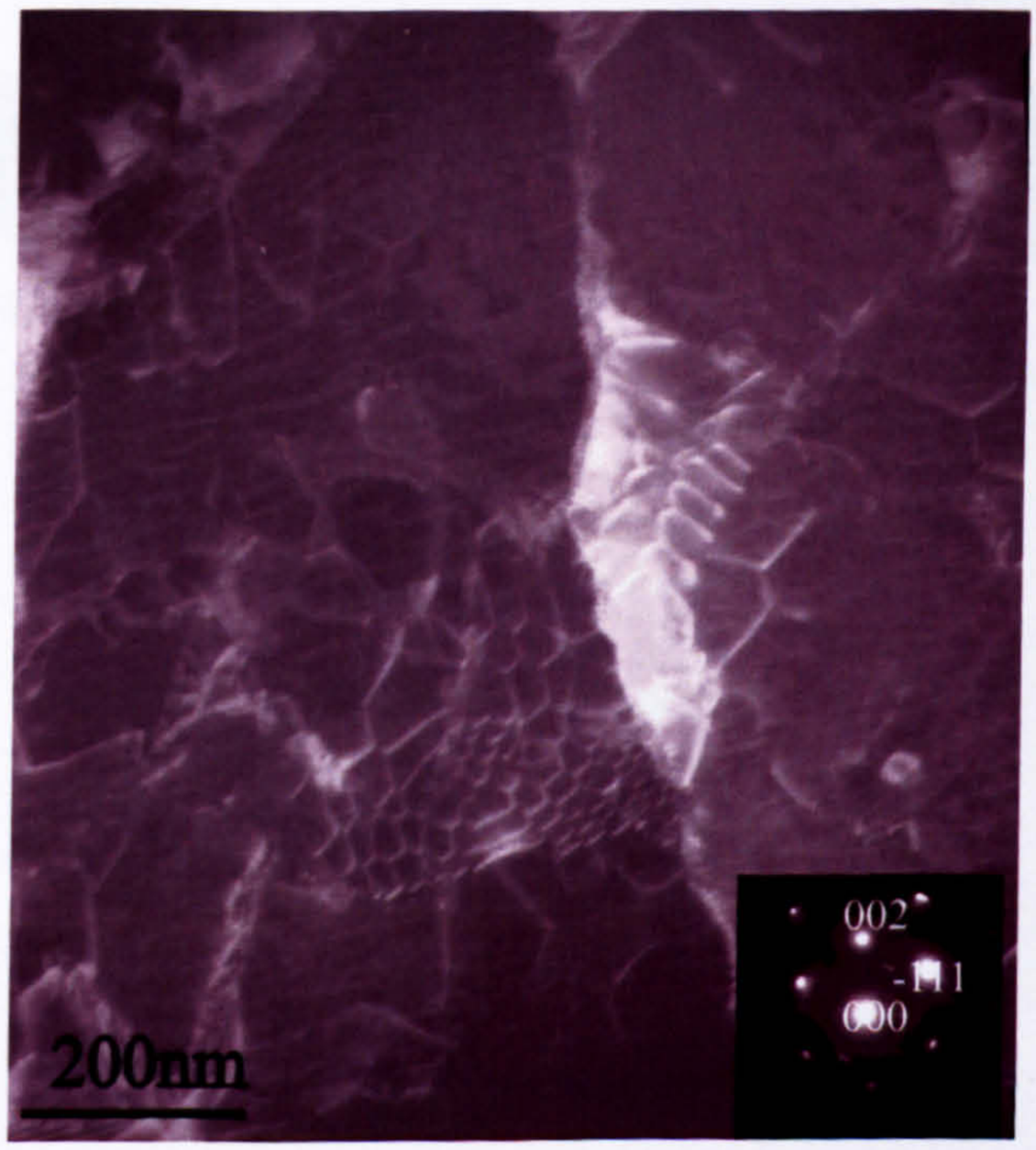

Fig. 5.152 TEM images after the 6000 seconds delayed deformation, show the network dislocation structure within the microbands: (a) bright field image, (b) dark field image.

a

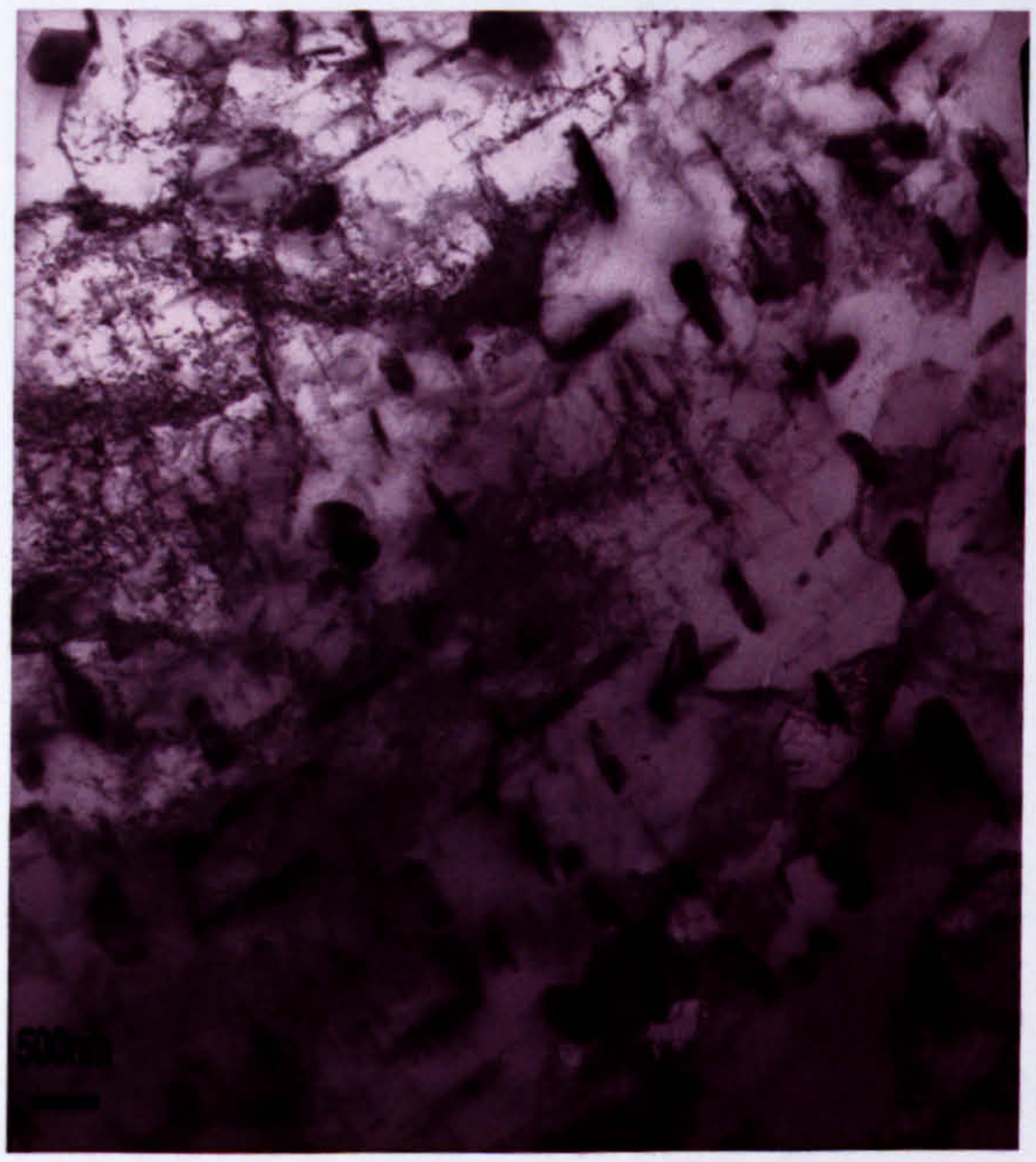

b

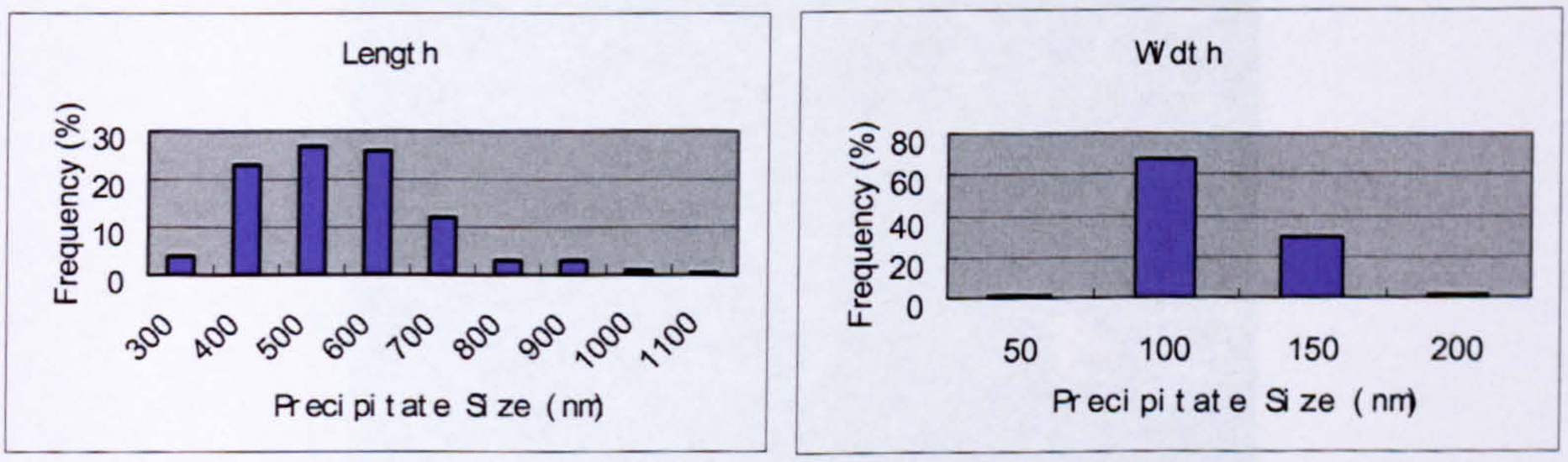

c

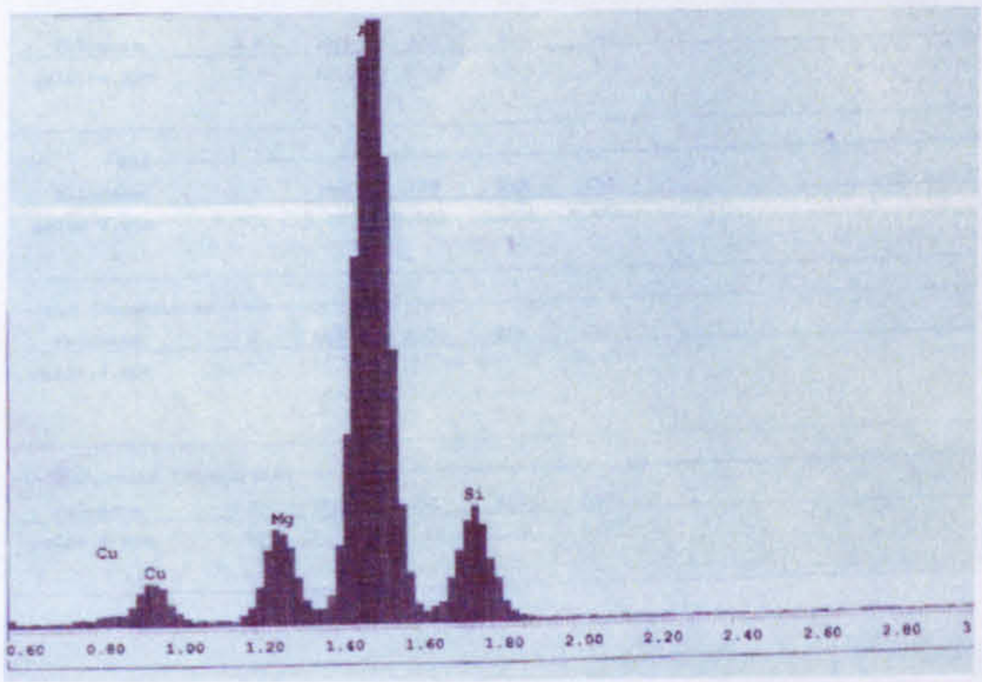

Fig. 5.153 Precipitate size analysis after the 6000 seconds delayed deformation: (a) TEM image, (b) particle size distribution, c) EDS spectrum.

a

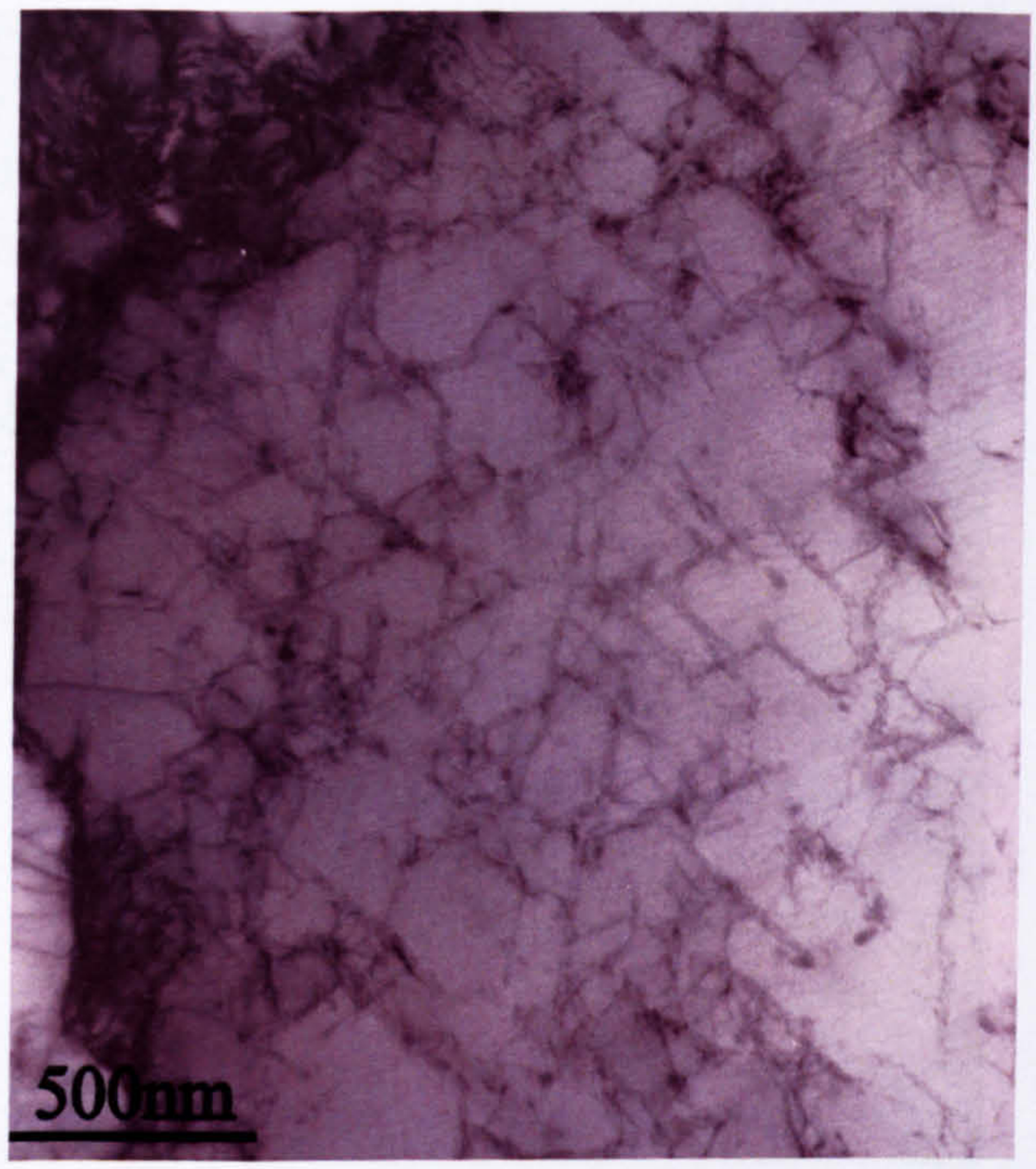

b

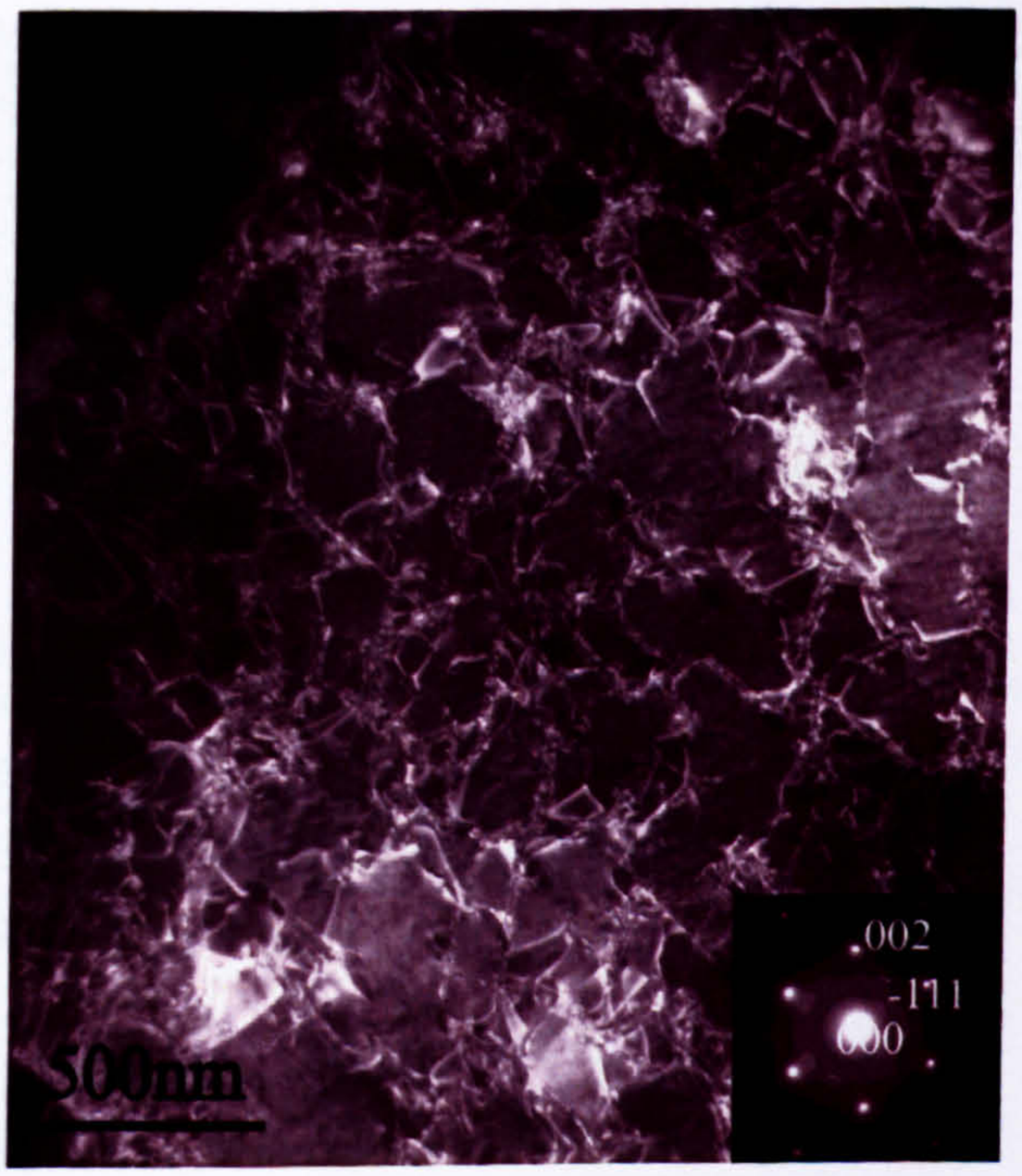

Fig. 5.154 TEM images after the 6000 seconds delayed deformation, shows the lath-shaped Q' phases formed on dislocations: (a) bright field image, (b) dark field image.

a

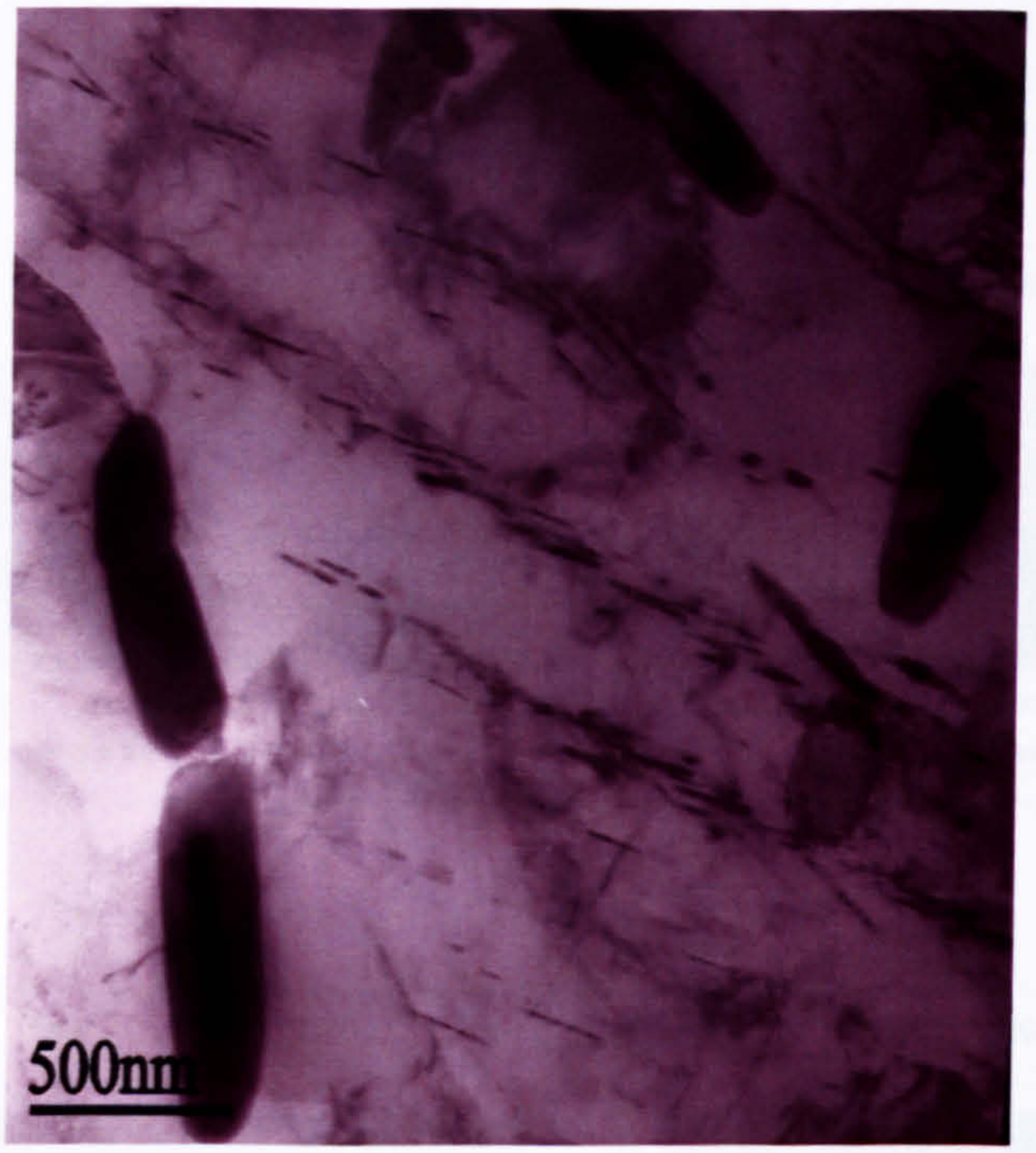

b

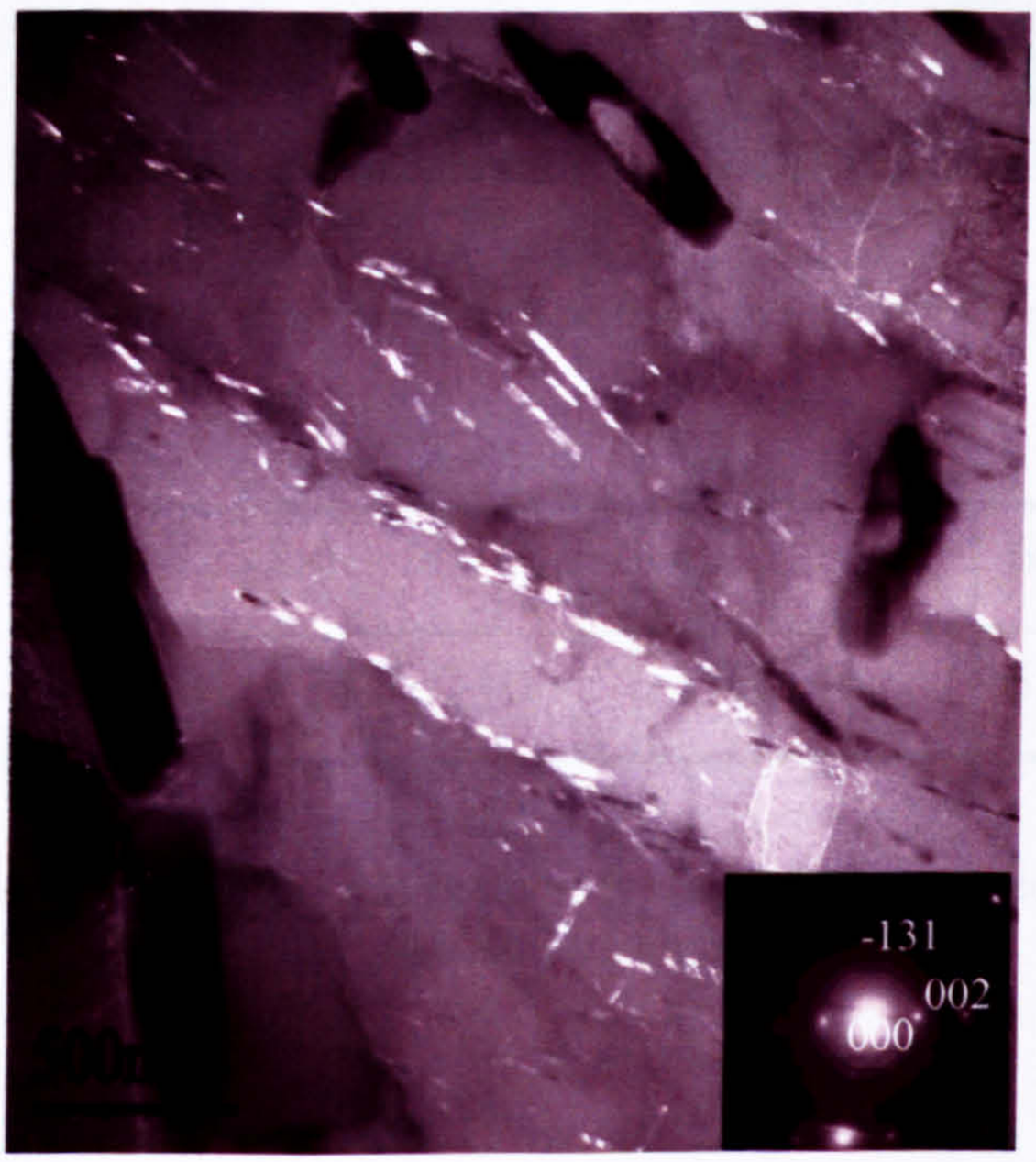

Fig. 5.155 TEM images after the 6000 seconds delayed deformation, shows the lath-shaped Q' phases formed on microband walls: (a) bright field image, (b) dark field image.

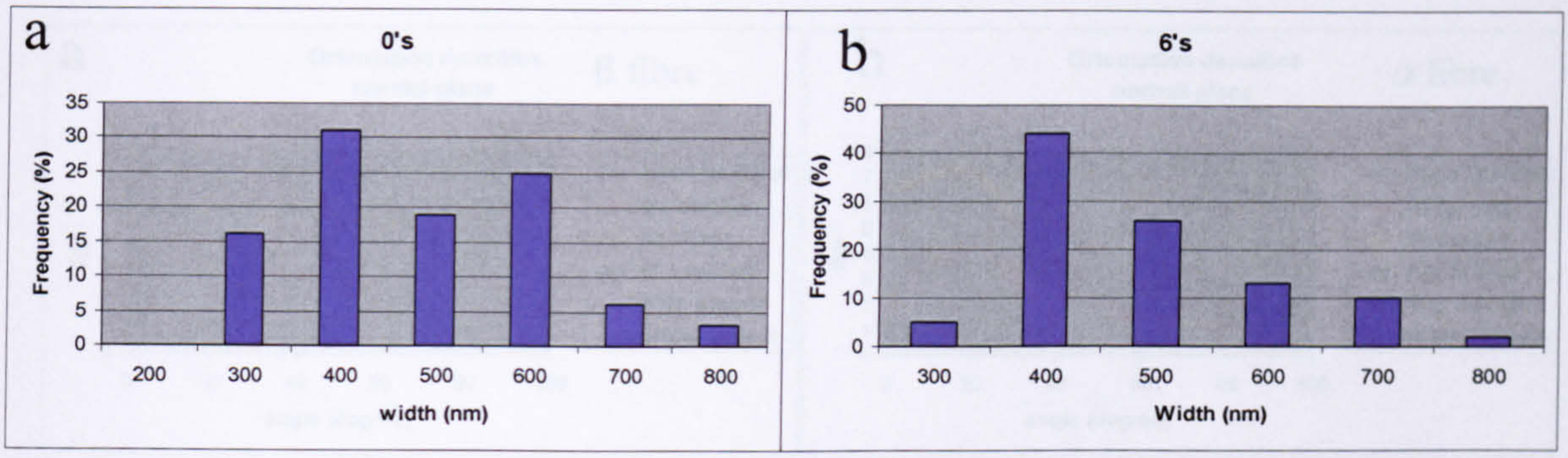

0	6	60	6000
400±130	390 ±110	350 ±46	520 ±240

Fig. 6.1 Microband width from TEM images: (a) 0 second, (b) 6 seconds, (c) 60 seconds, (d) 6000 seconds.

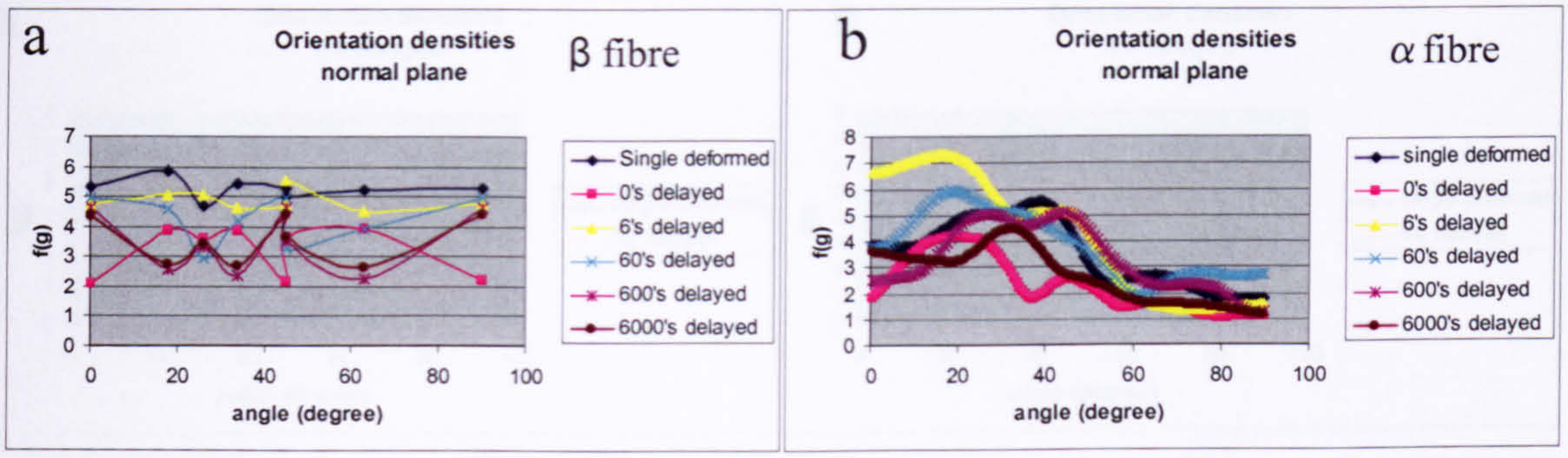

Fig. 6.2 Orientation density curve: (a) βfibre-normal plane, (b) α fibre-normal plane, (c) βfibre-transverse plane, (d) α fibre-transverse plane.

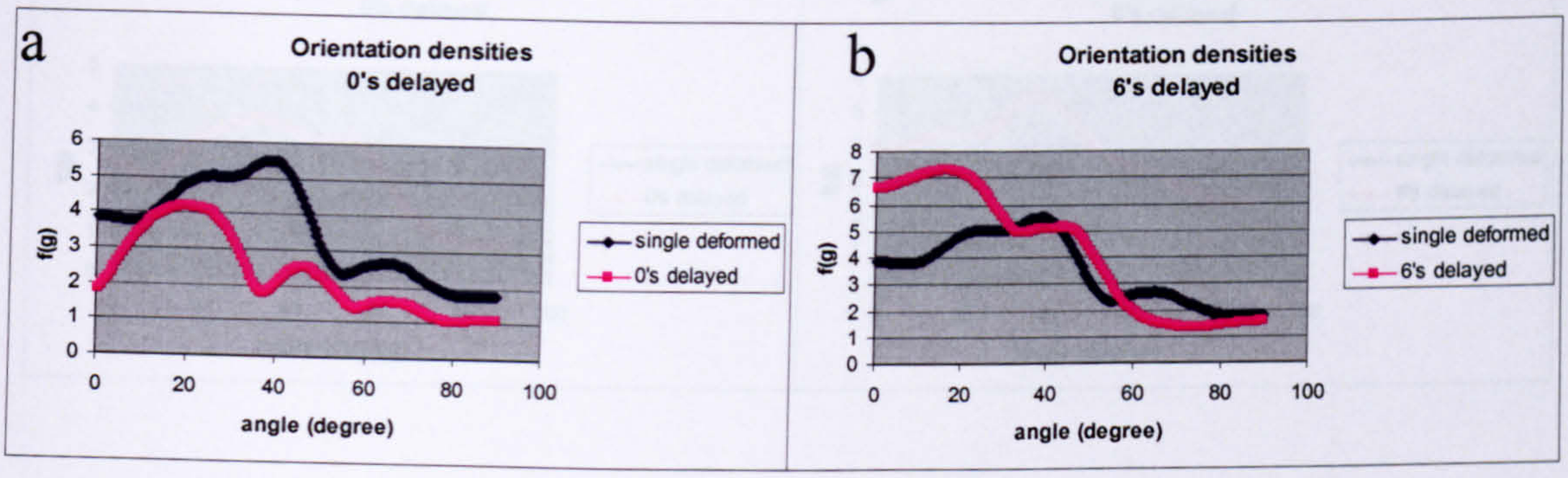

Fig. 6.3 Compare of the orientation density curve-α fibre (normal plane): (a) 0 second, (b) 6 seconds, (c) 60 seconds, (d) 600 seconds, (e) 6000seconds.

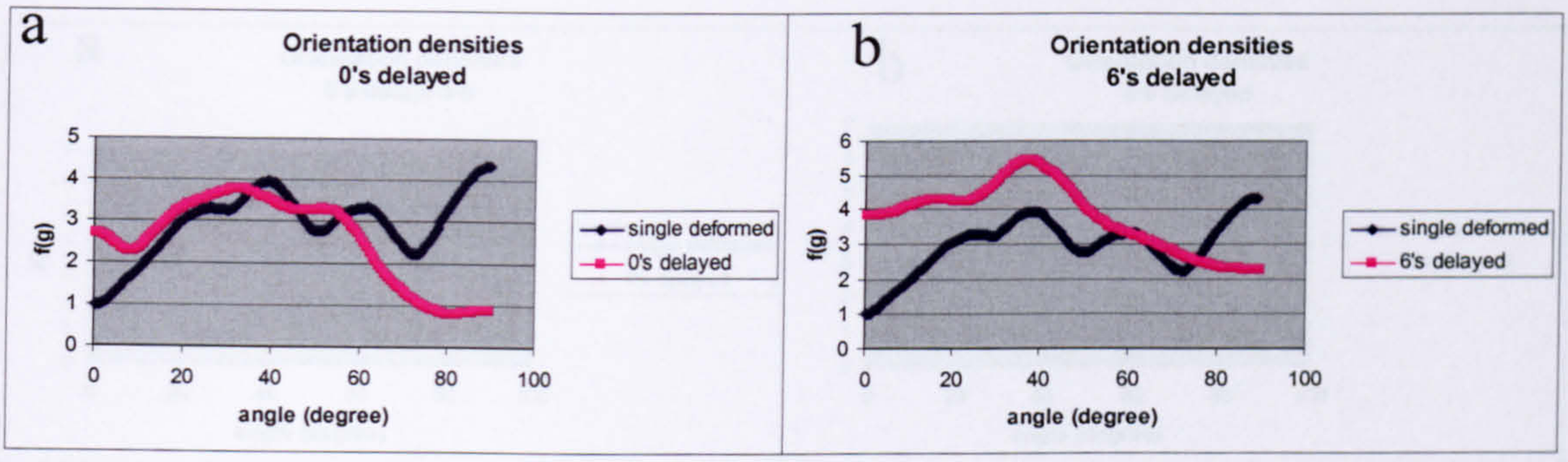

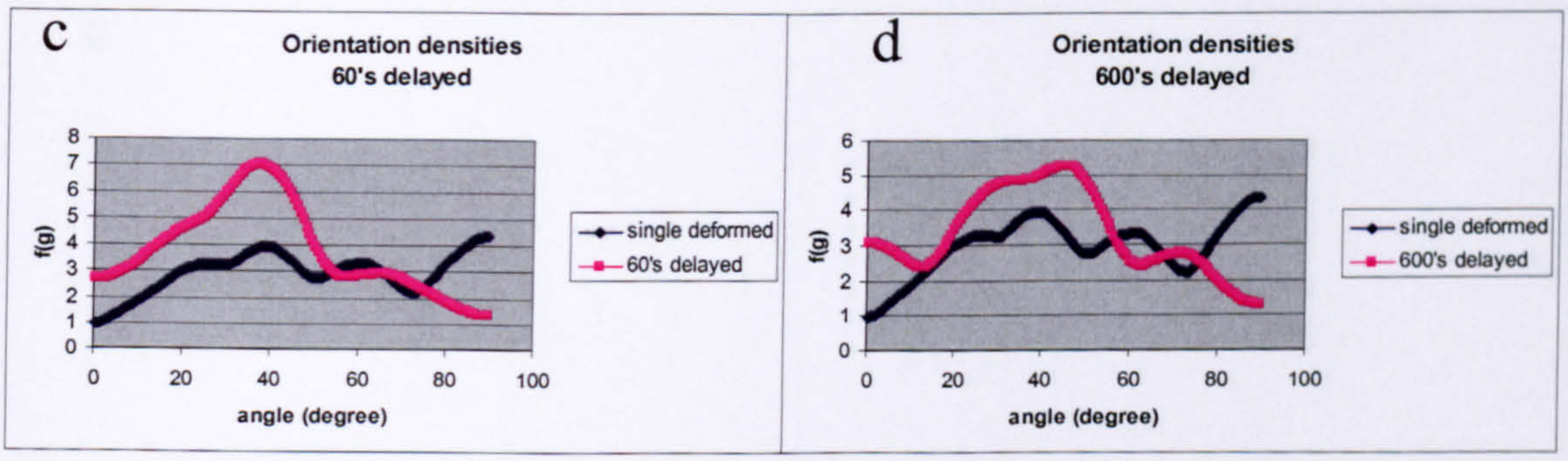

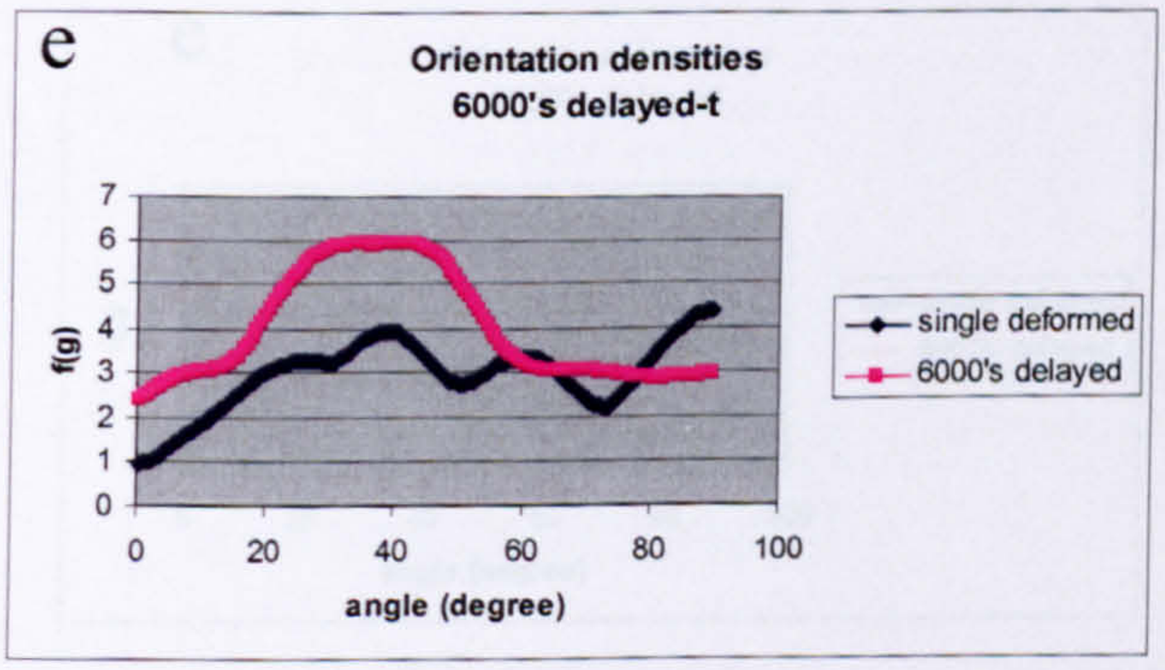

Fig. 6.4 Compare of the orientation density curve-α fibre (transverse plane): (a) 0 second, (b) 6 seconds, (c) 60 seconds, (d) 600 seconds, (e) 6000seconds.

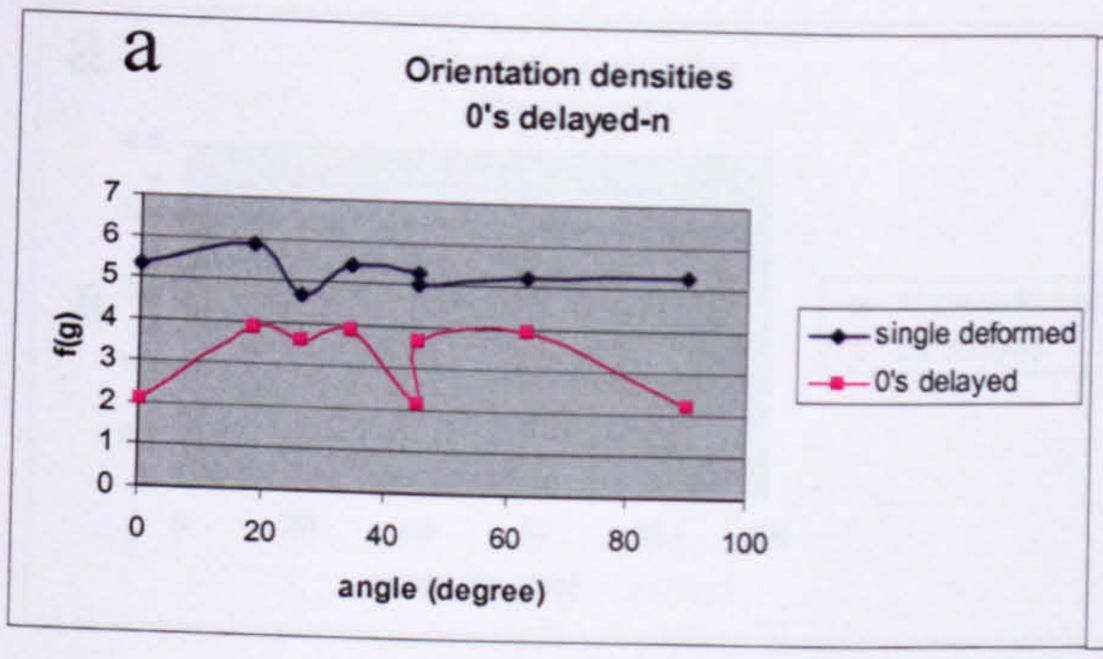

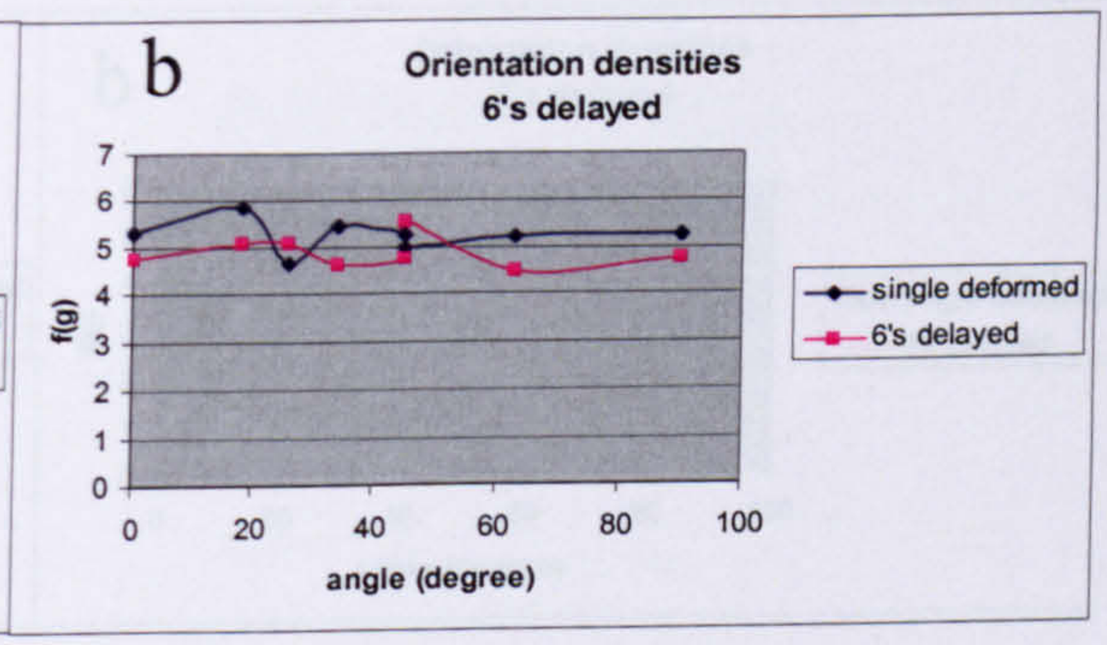

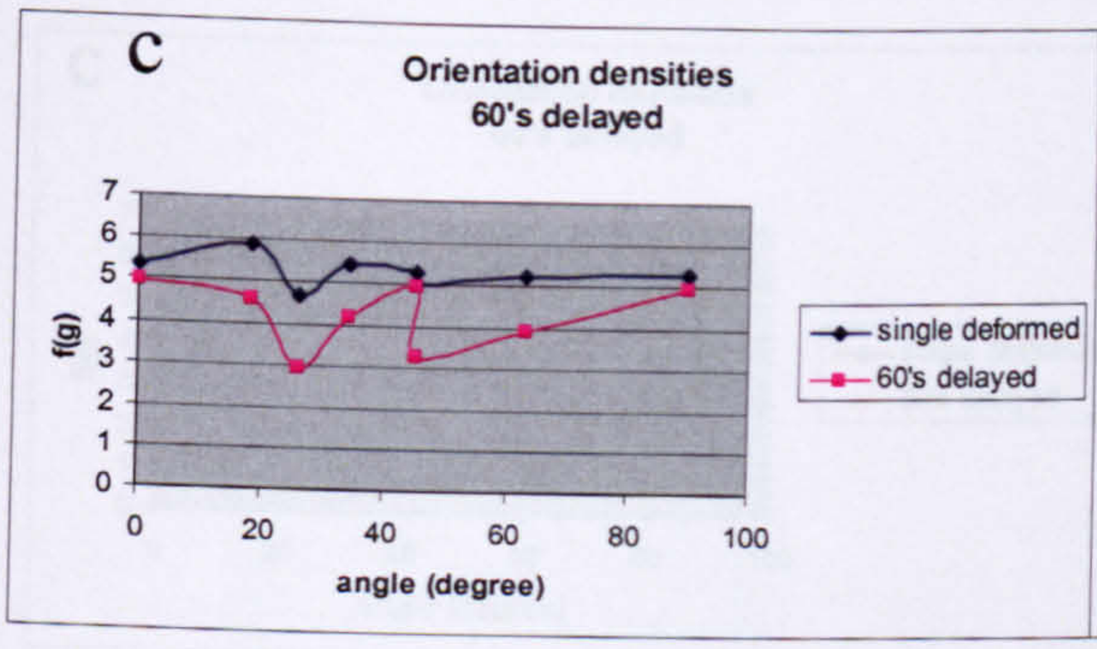

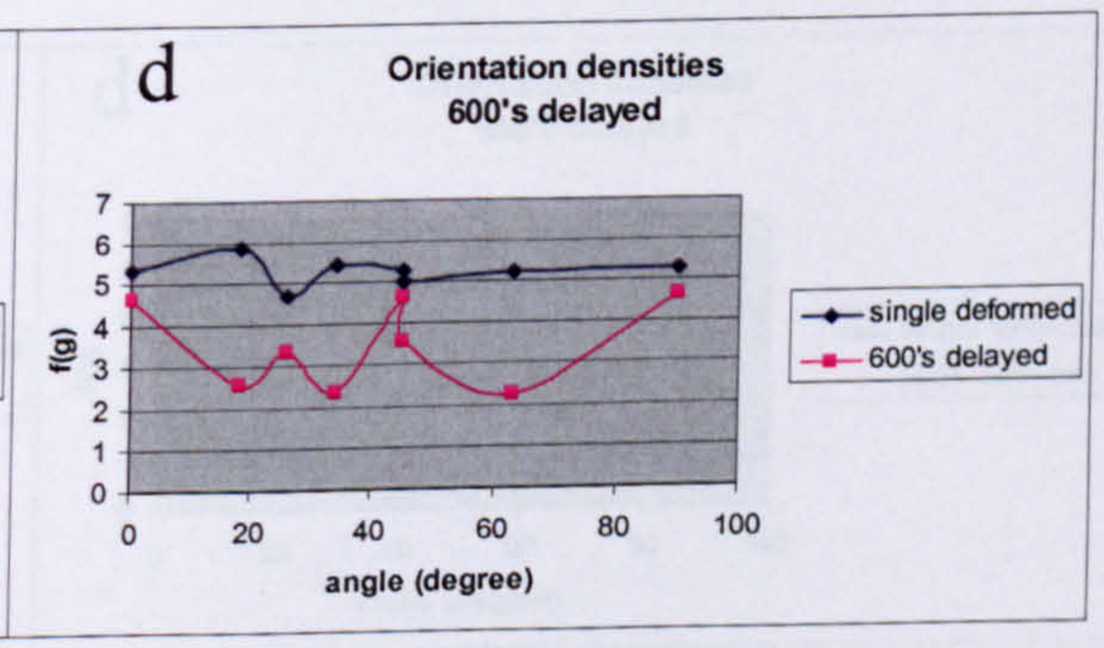

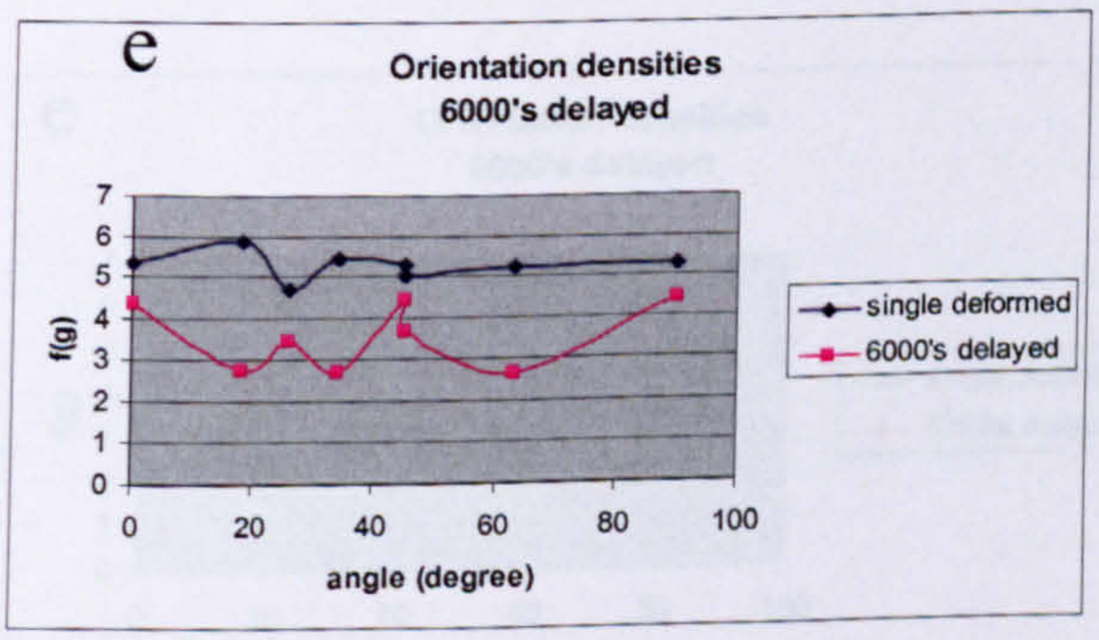

Fig. 6.5 Compare of the orientation density curve-β fibre (normal plane): (a) 0 second, (b) 6 seconds, (c) 60 seconds, (d) 600 seconds, (e) 6000seconds.

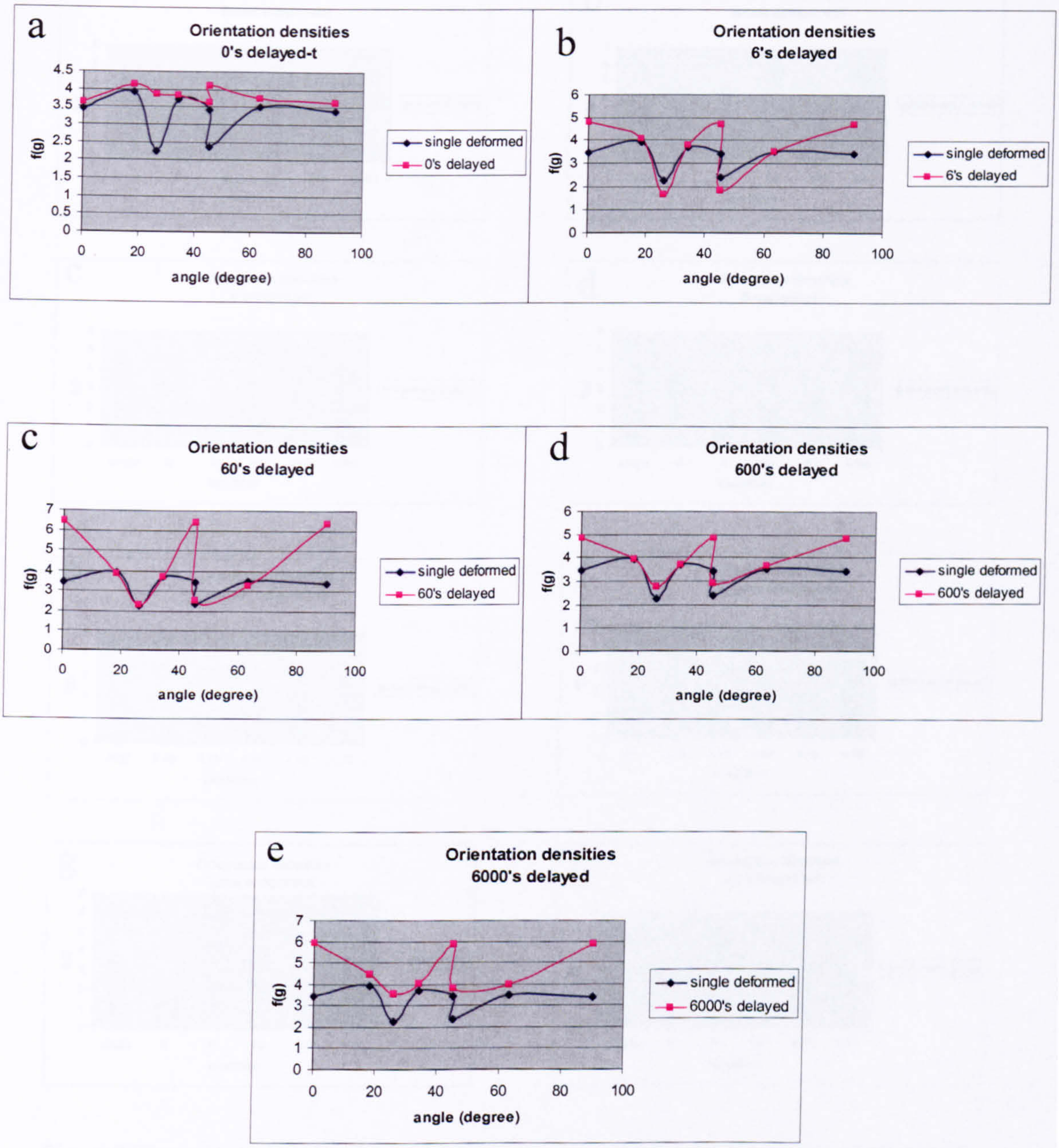

Fig. 6.6 Compare of the orientation density curve-β fibre (transverse plane): (a) 0 second, (b) 6 seconds, (c) 60 seconds, (d) 600 seconds, (e) 6000seconds.

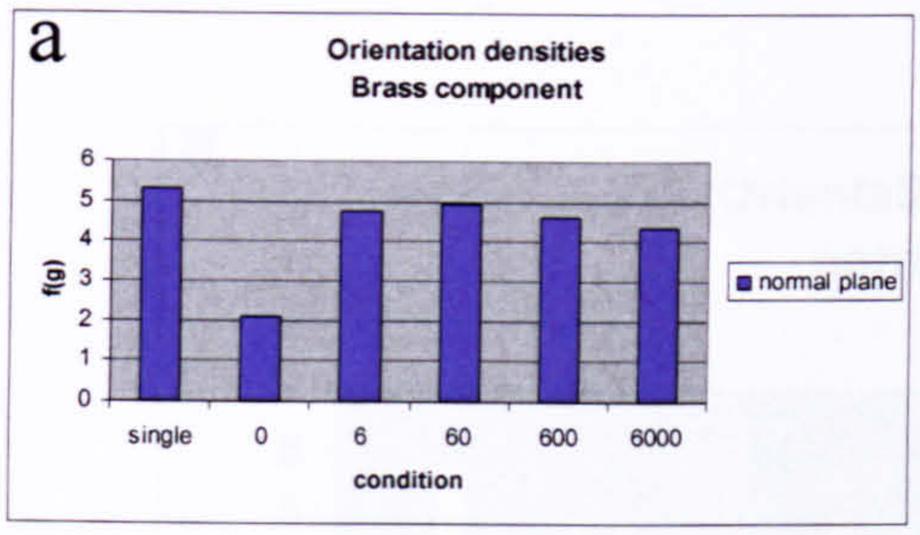

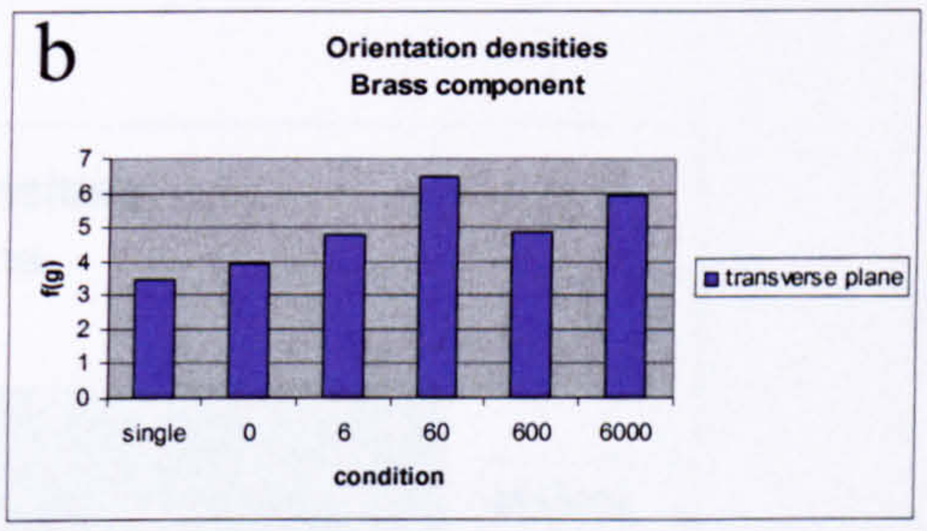

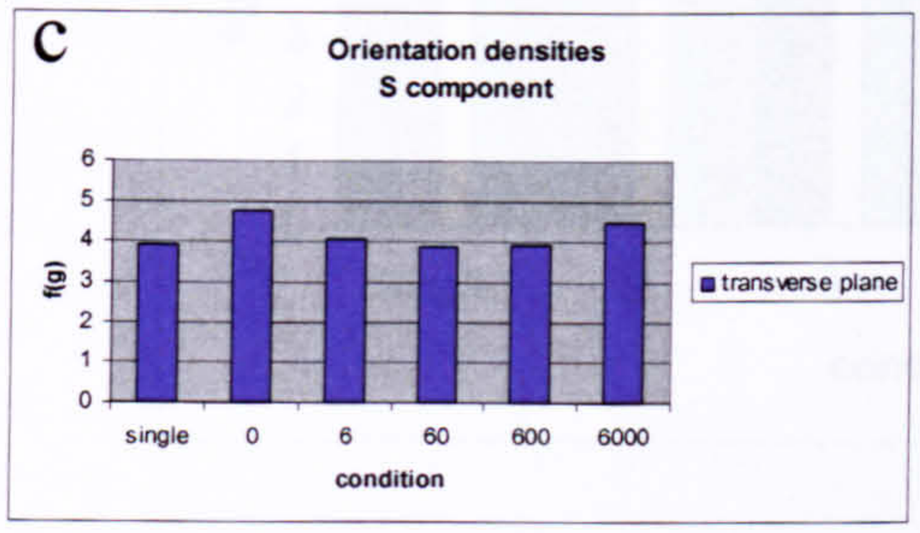

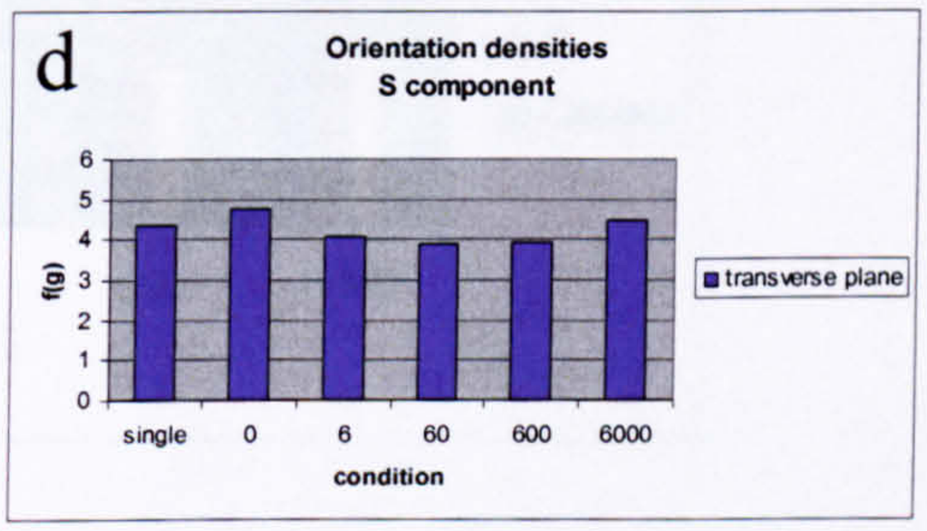

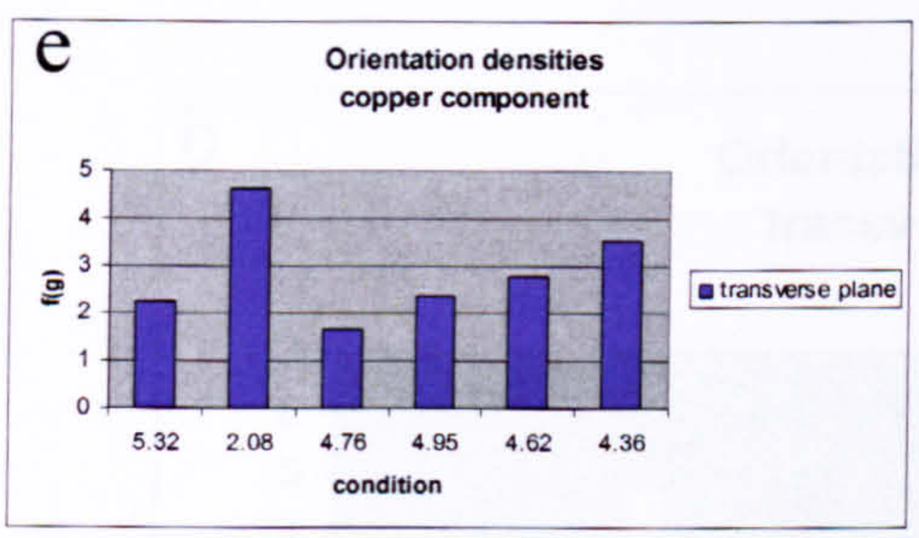

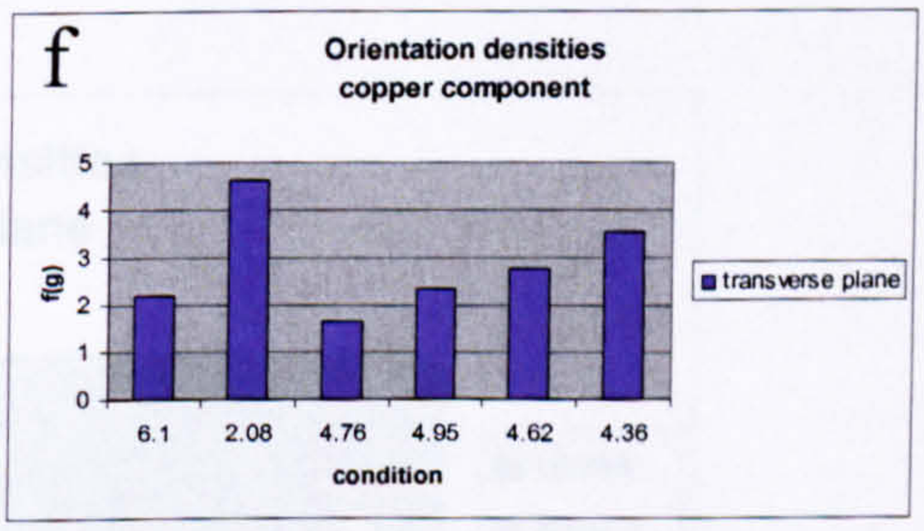

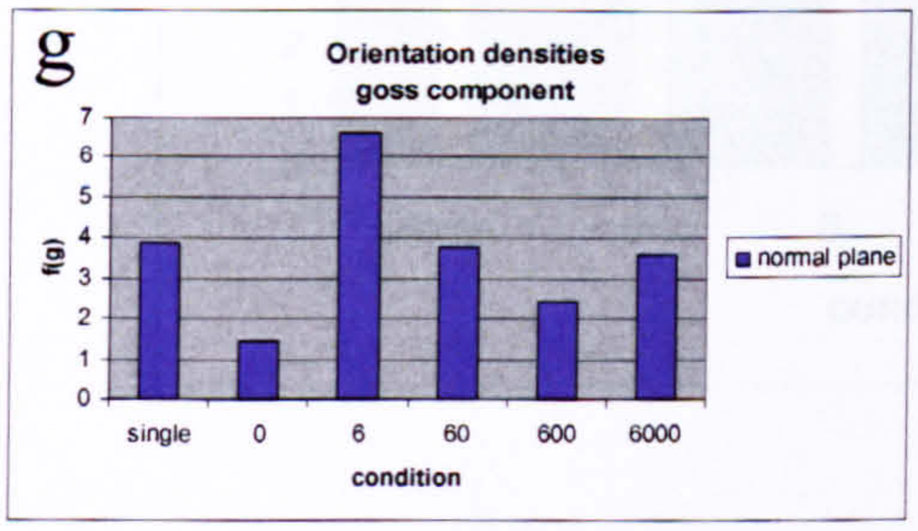

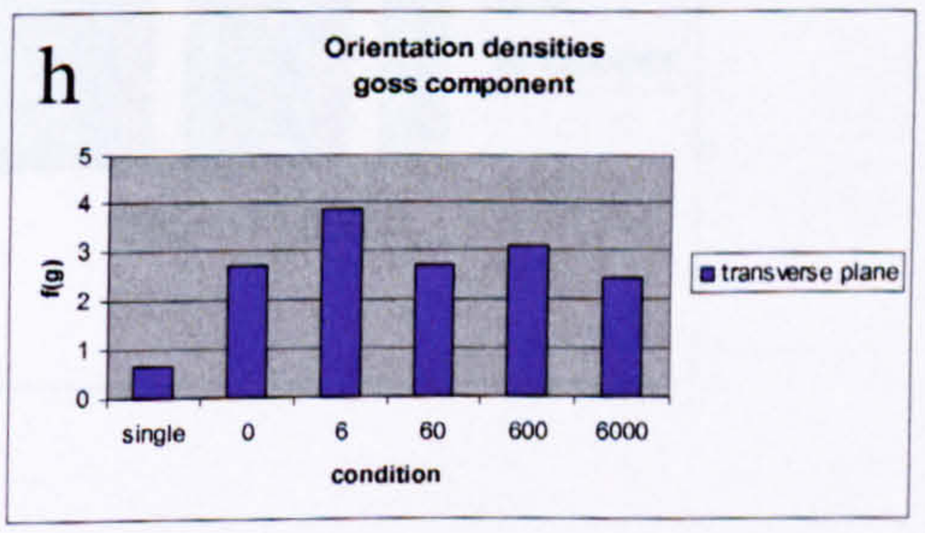

Fig. 6.7 The orientation density of texture components: (a) (b) Brass, (c) (d) S, (e) (f) Copper, (g) (h) Goss

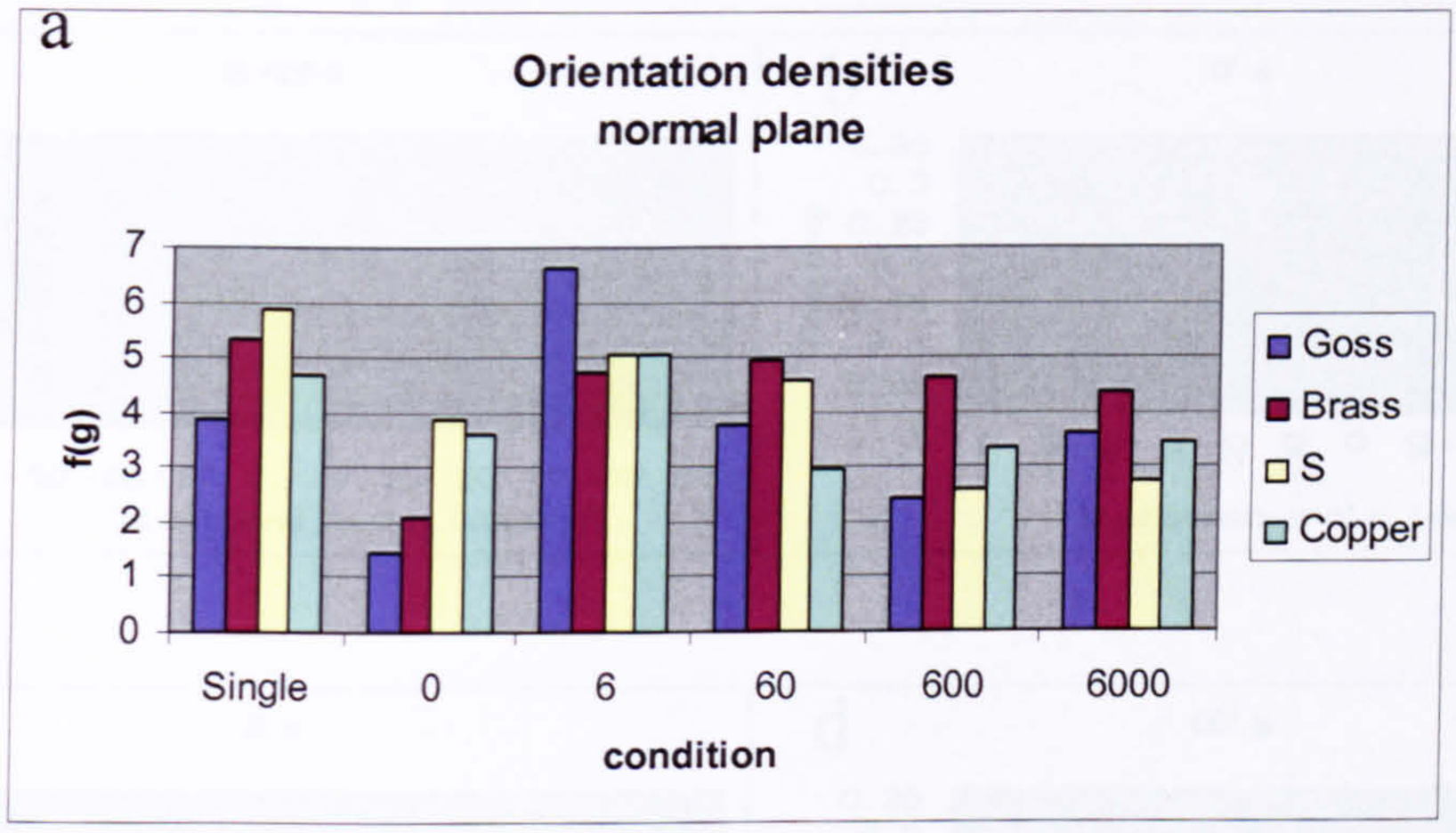

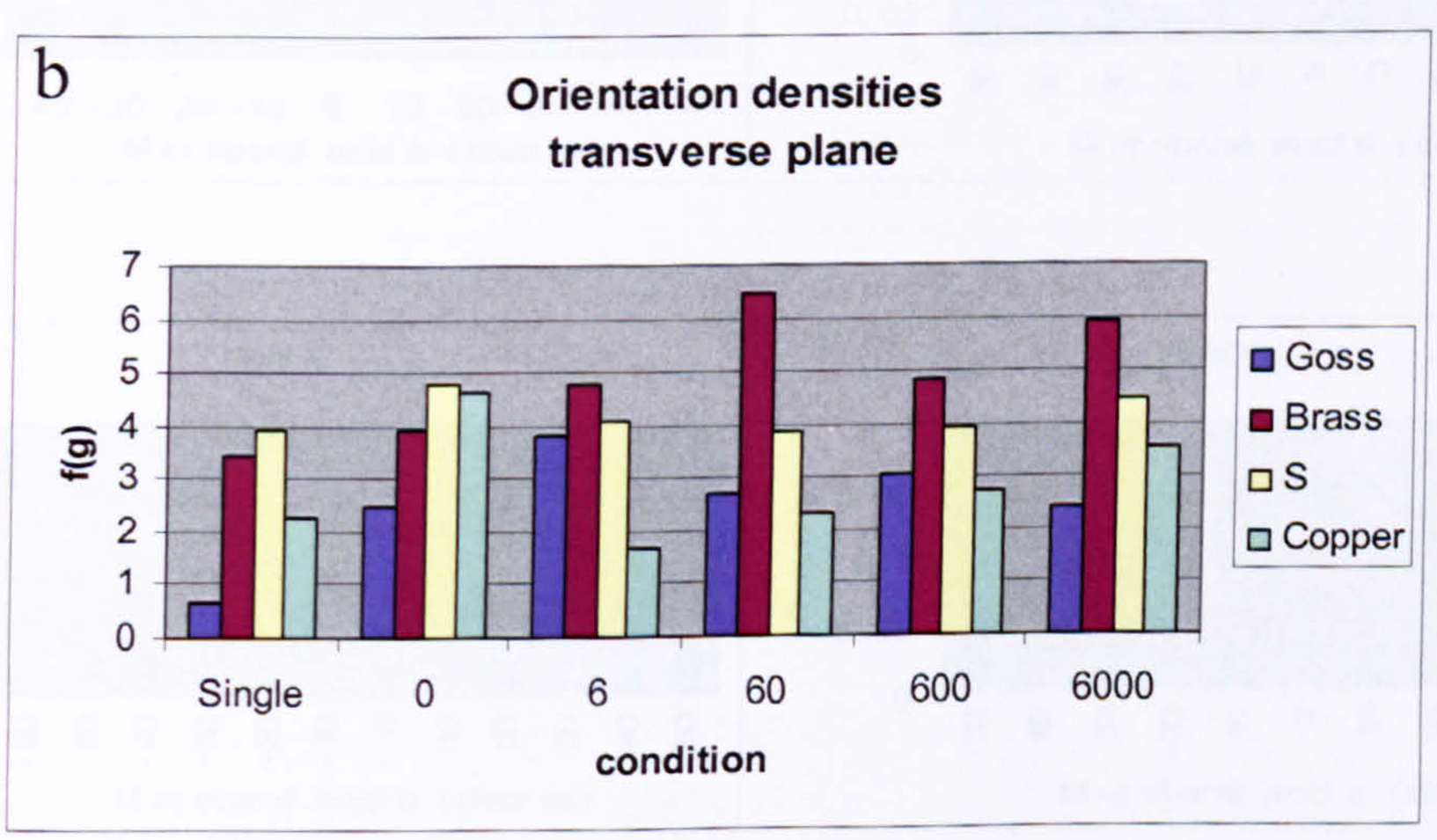

Fig. 6.8 Compare of the orientation density of the texture components: (a) normal plane, (b) transverse plane.

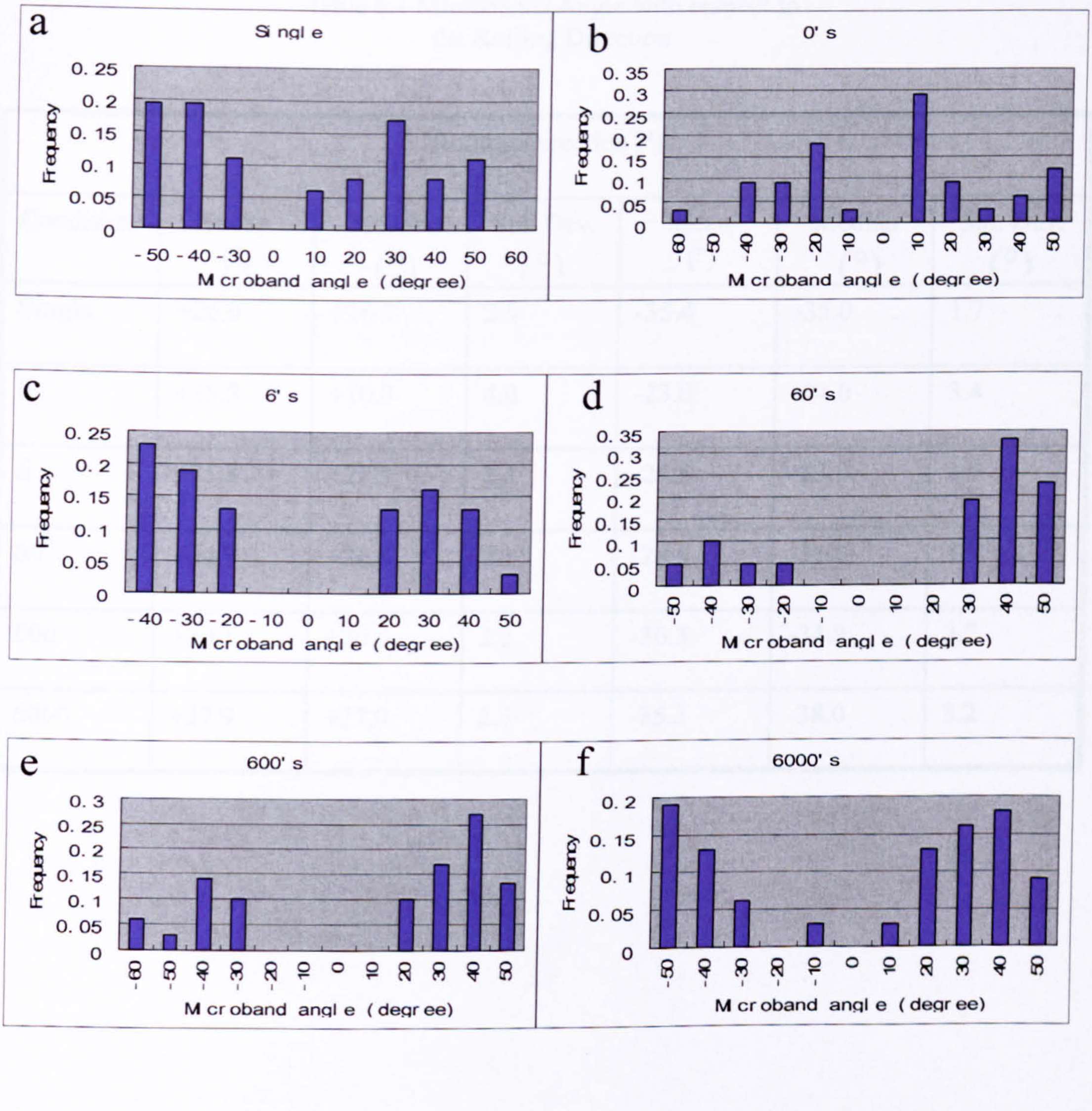

Fig. 6.9 Microband angle distribution from EBSD images. (a) Single deformed, (b) 0 second, (c) 6 seconds, (d) 60 seconds, (e) 600 seconds, (f) 6000seconds.

Table 6.1 Microbands Angle with respect to the Rolling Direction

Rolling Direction (°)						
Condition	Mean (°)	Median (°)	Std. Dev. (°)	Mean (°)	Median (°)	Std. Dev. (°)
Single	+26.0	+26.5	2.9	-35.4	-35.0	1.7
0	+15.3	+10.0	4.0	-23.0	-24.0	3.4
6	+25.8	+27.0	2.5	-25.8	-23.0	1.9
60	+34.3	+36.6	2.1	-28.9	-31.0	5.5
600	+30.1	+30.0	2.2	-36.3	-34.9	3.7
6000	+27.9	+27.0	2.5	-35.3	-38.0	3.2

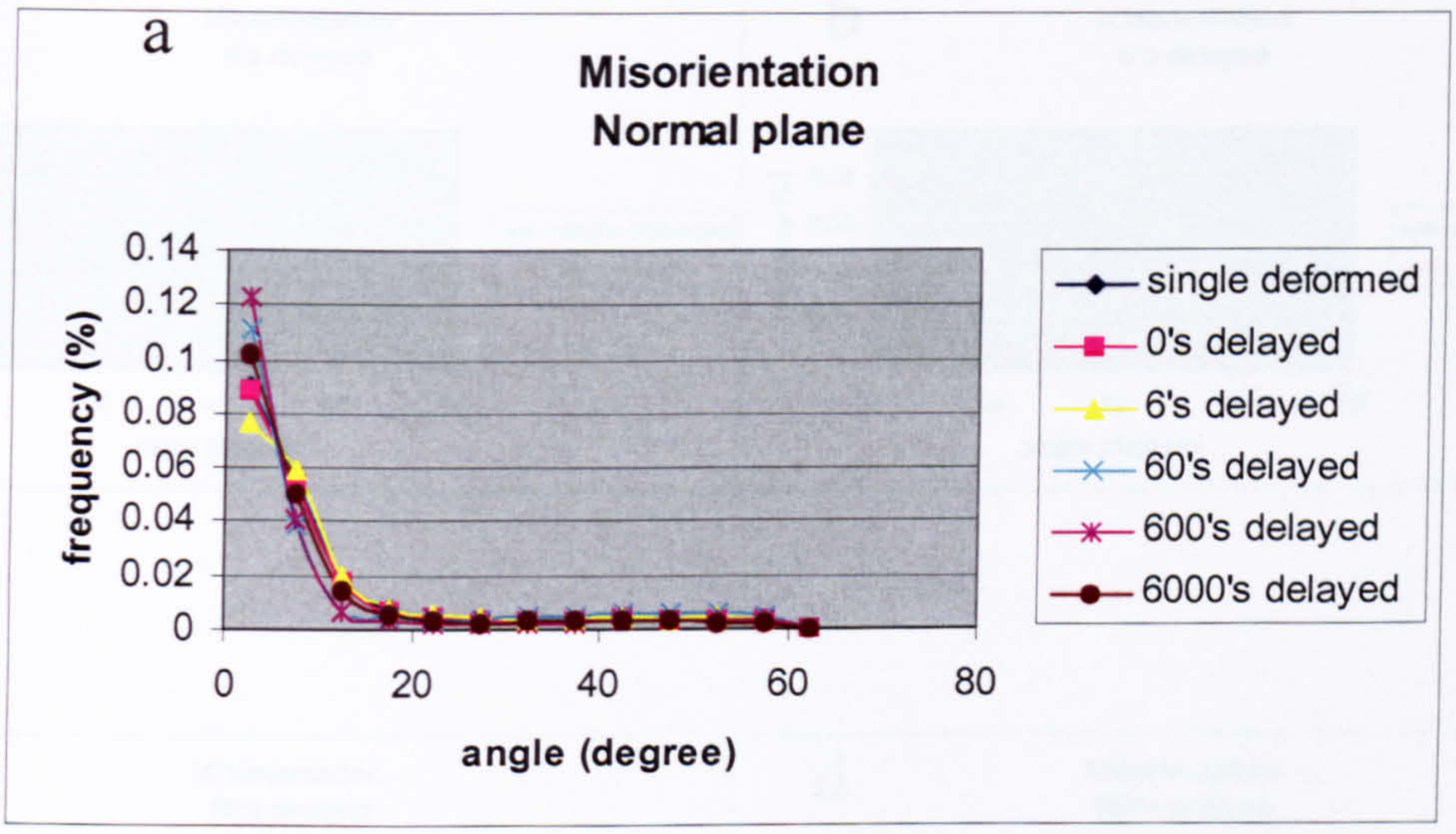

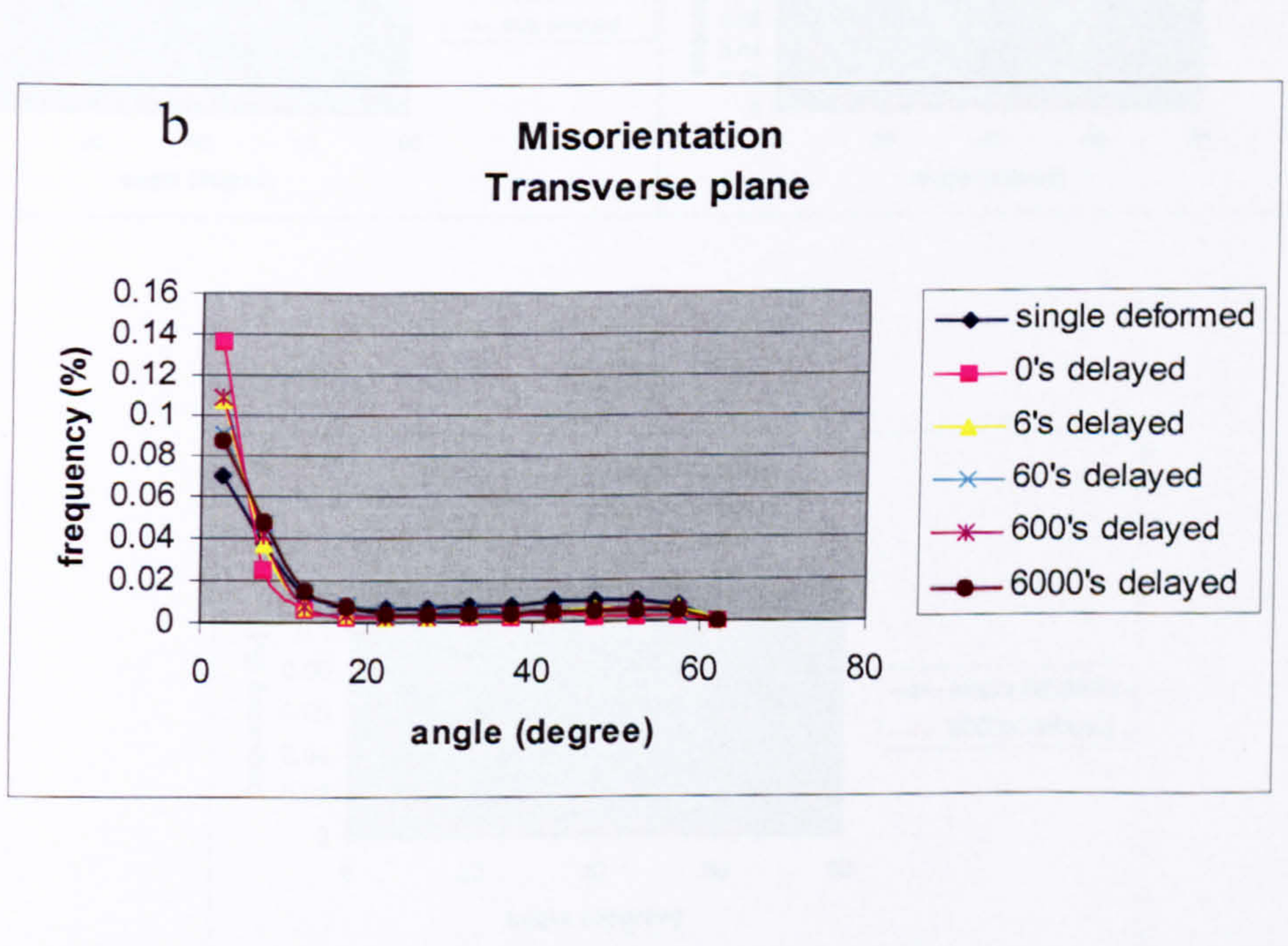

Fig. 6.10 Misorientation distribution curves: (a) normal plane, (b) transverse plane.

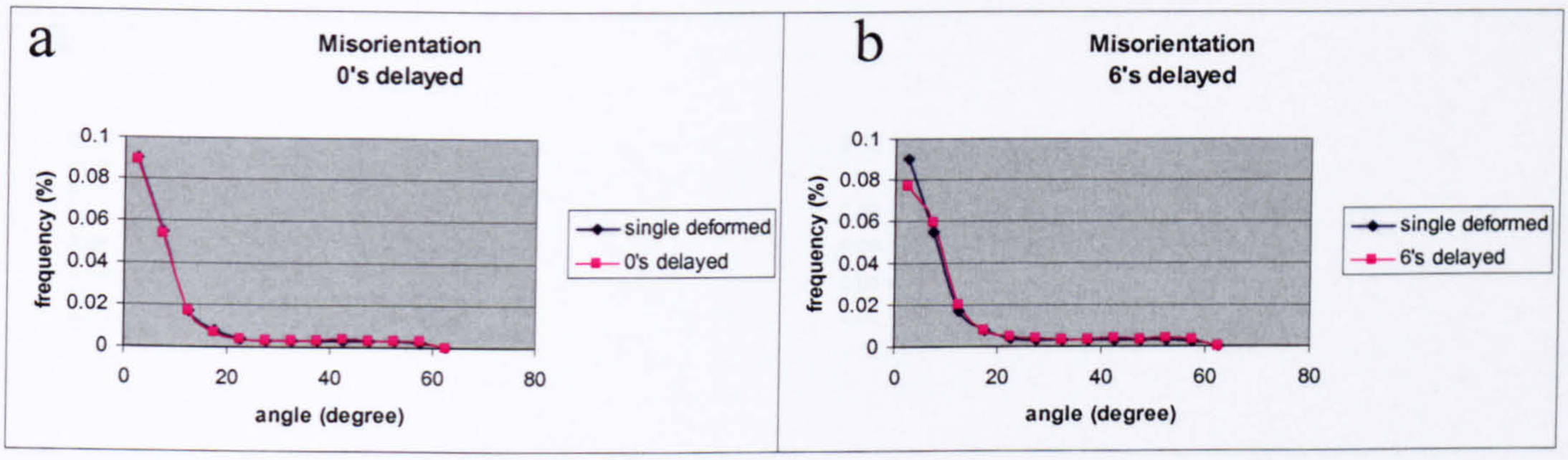

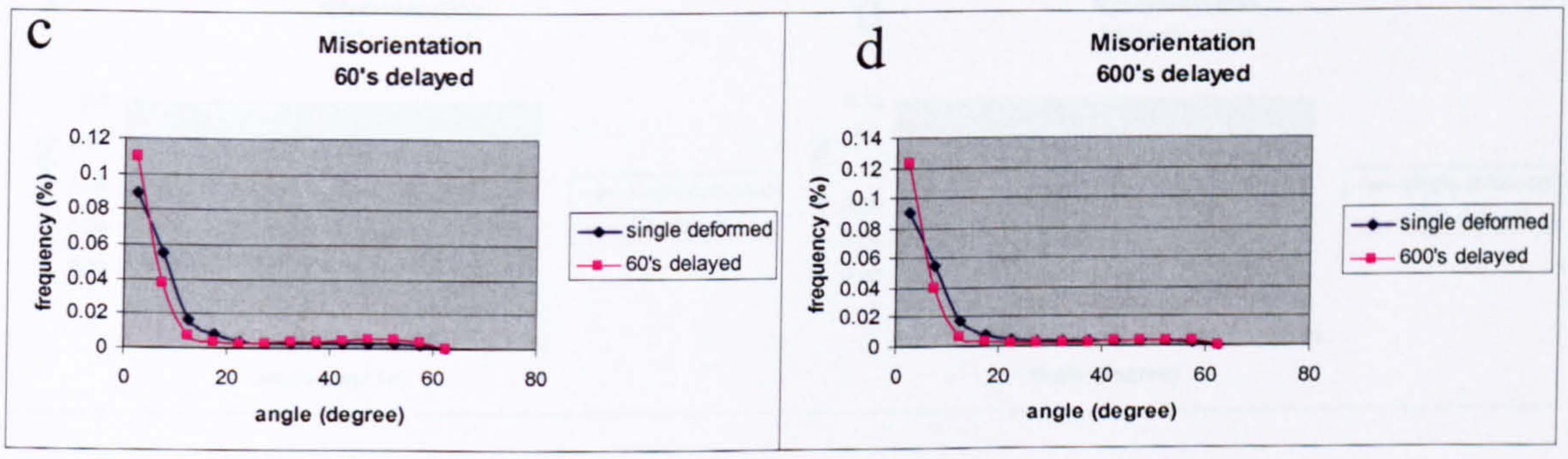

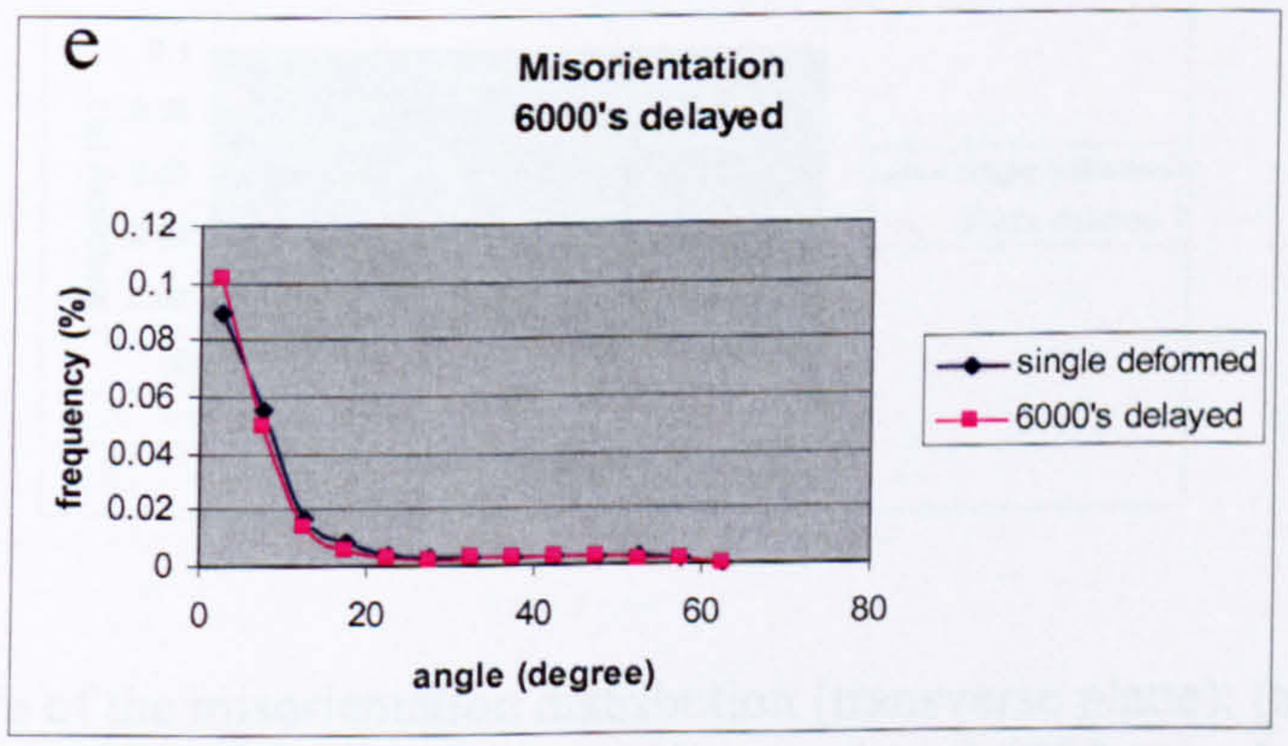

Fig. 6.11 Compare of the misorientation distribution (normal plane): (a) 0 second, (b) 6 seconds, (c) 60 seconds, (d) 600 seconds, (e) 6000seconds.

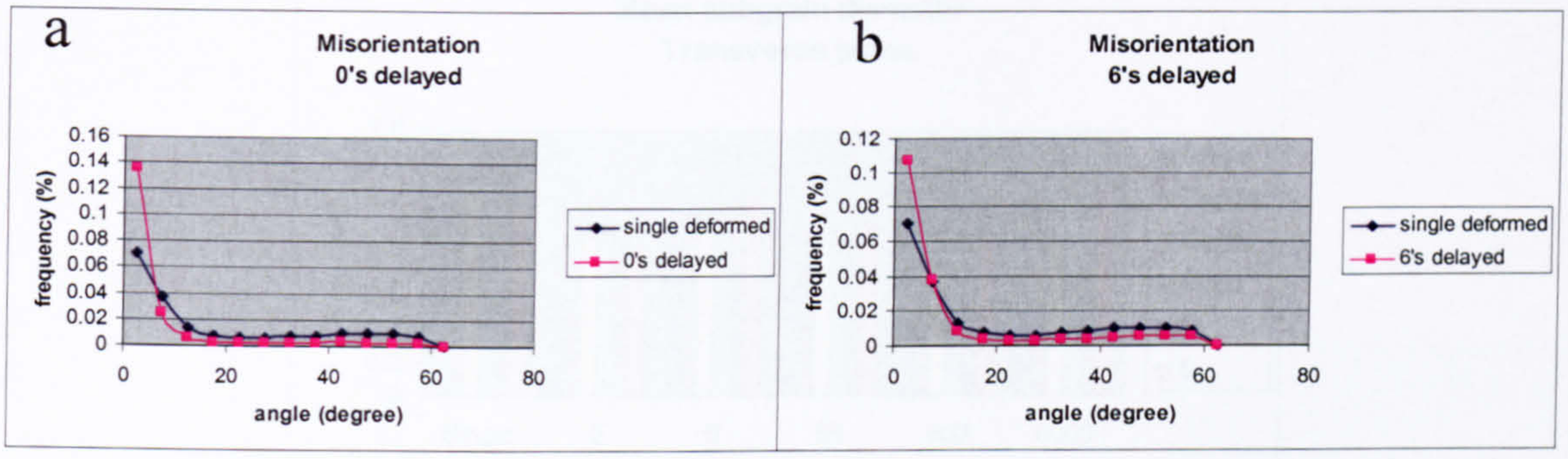

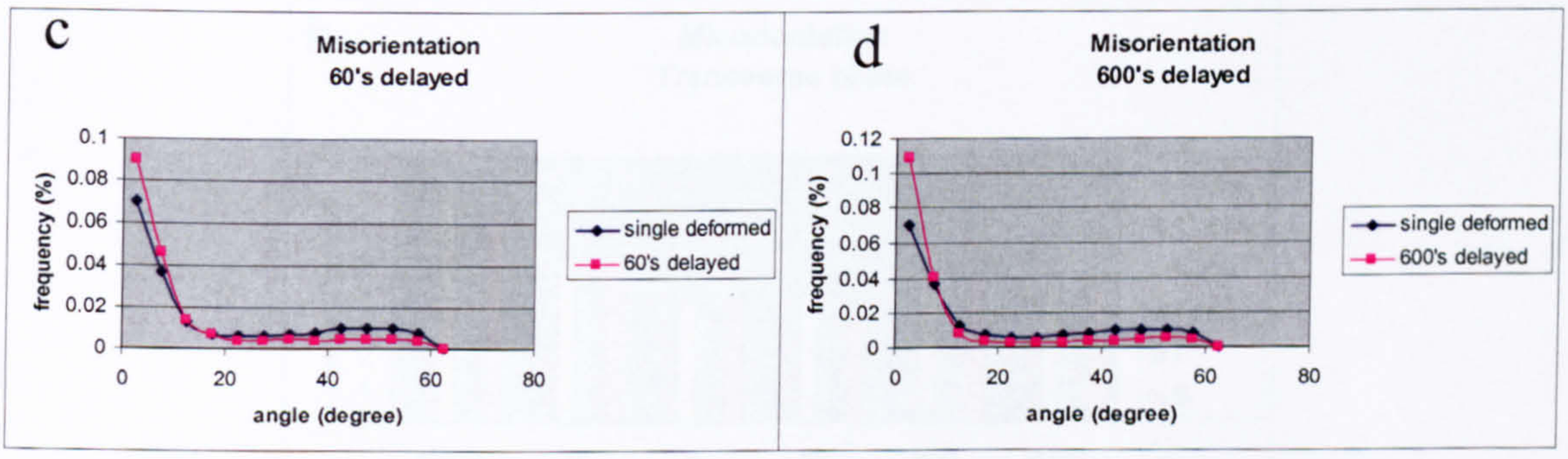

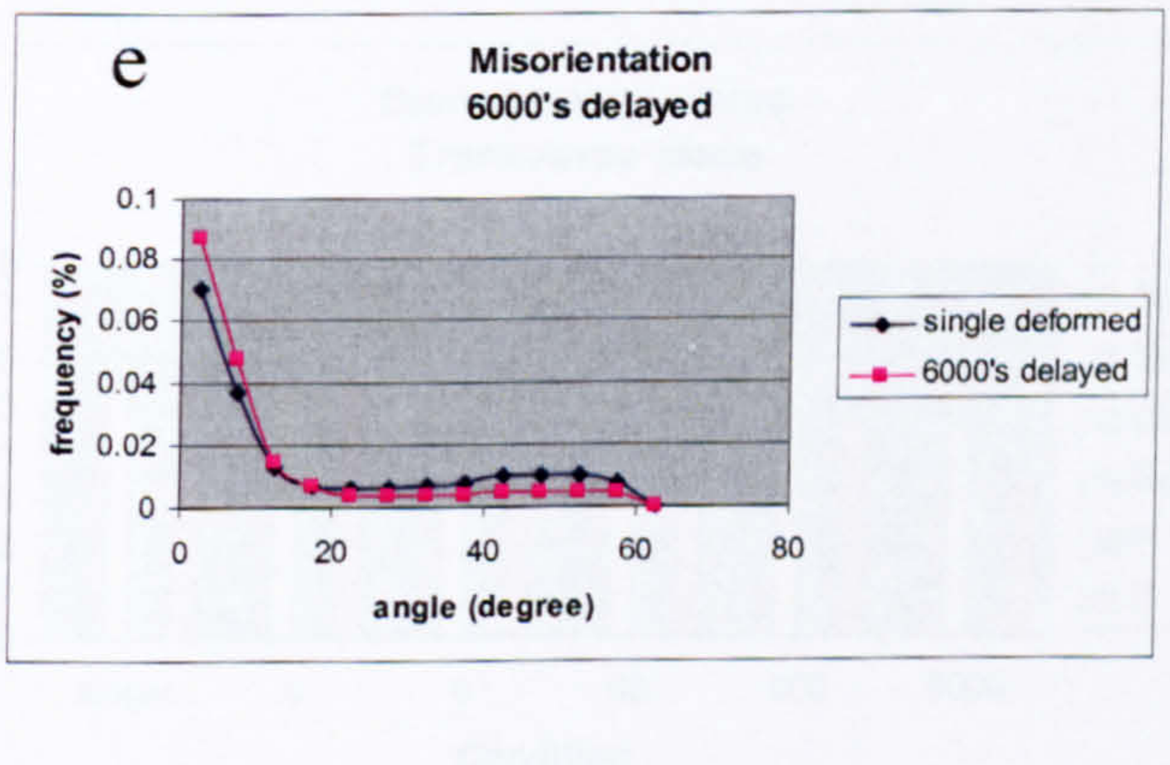

Fig. 6.12 Compare of the misorientation distribution (transverse plane): (a) 0 second, (b) 6 seconds, (c) 60 seconds, (d) 600 seconds, (e) 6000seconds.

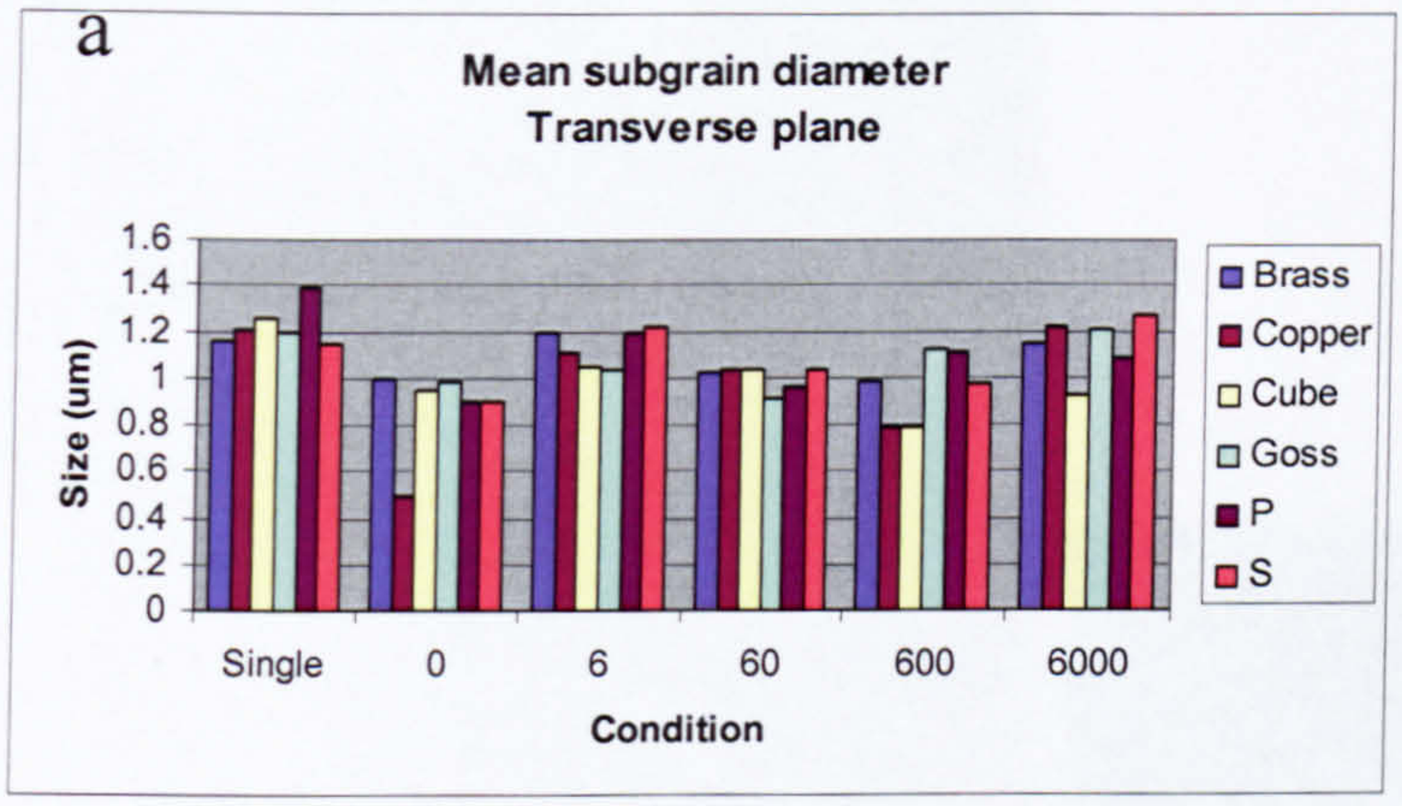

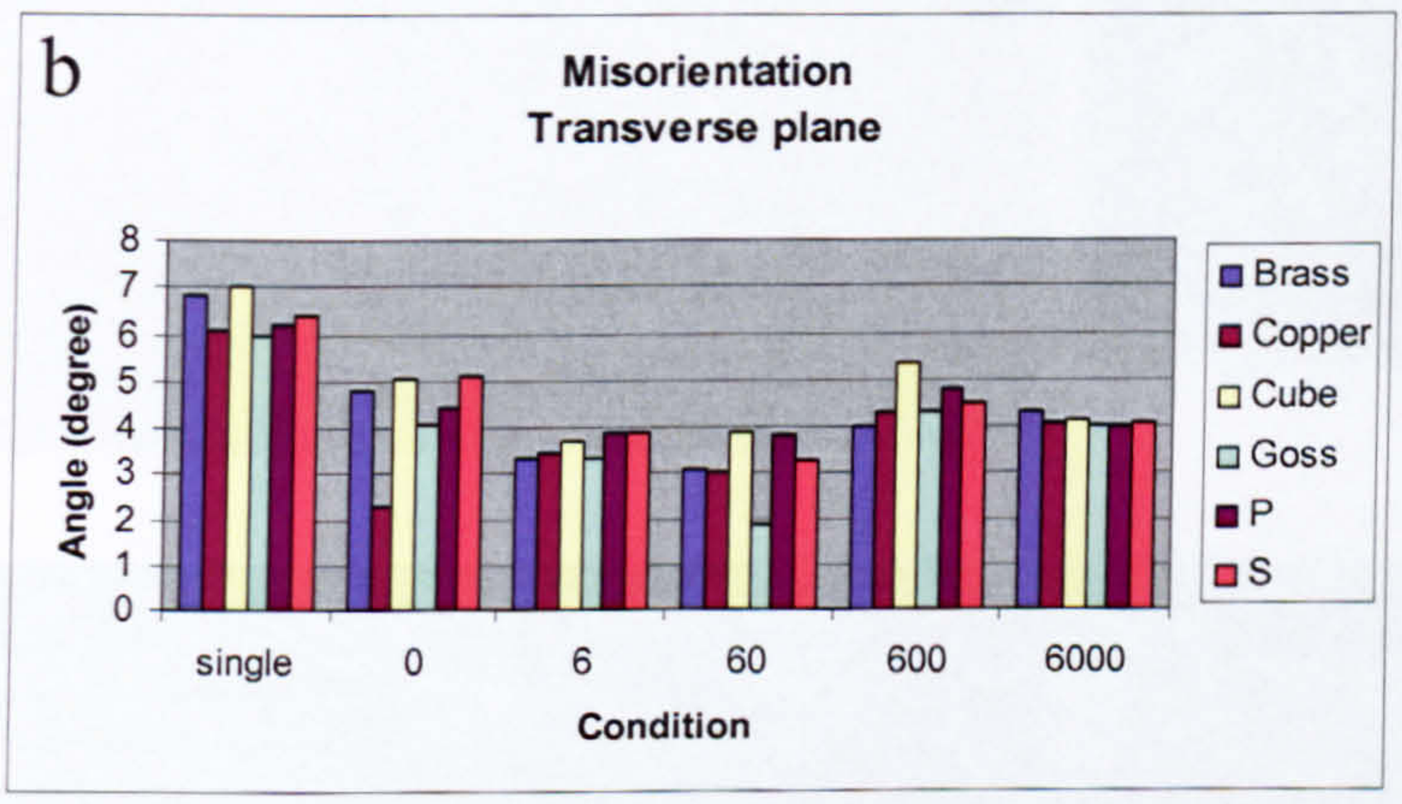

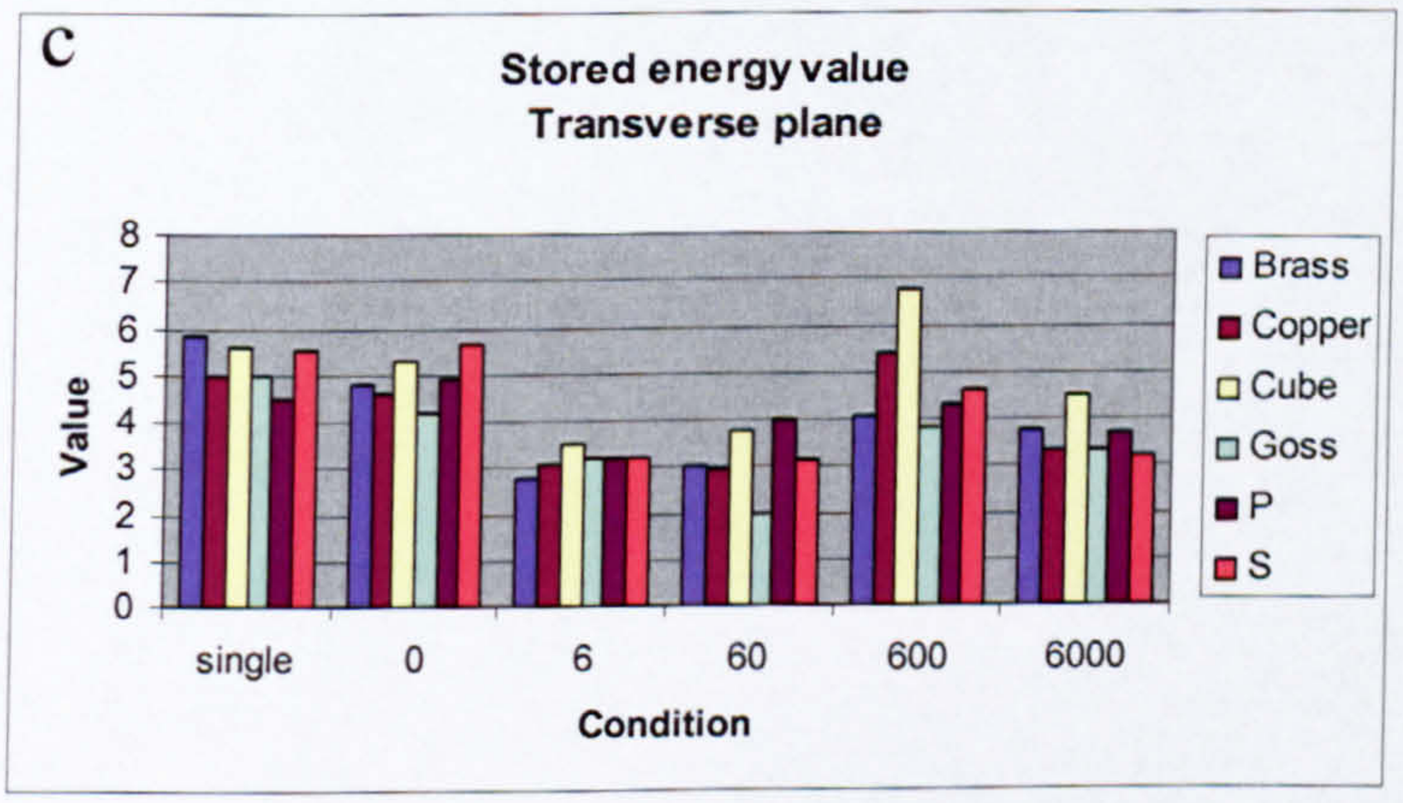

Fig. 6.13 Mean subgrain diameter, misorientation and stored energy: (a) mean subgrain diameter, (b) misorientation, (c) stored energy.

a

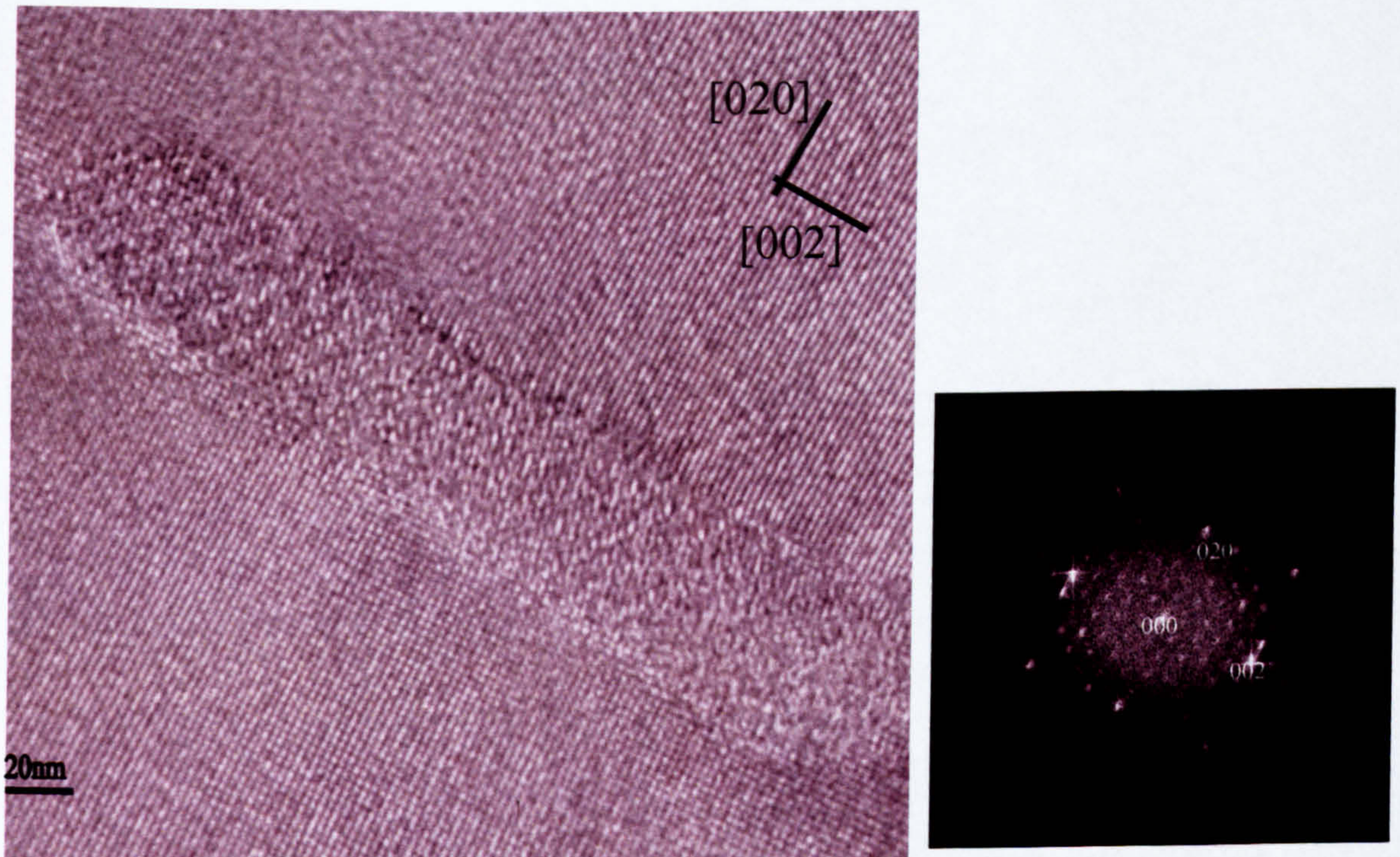

b

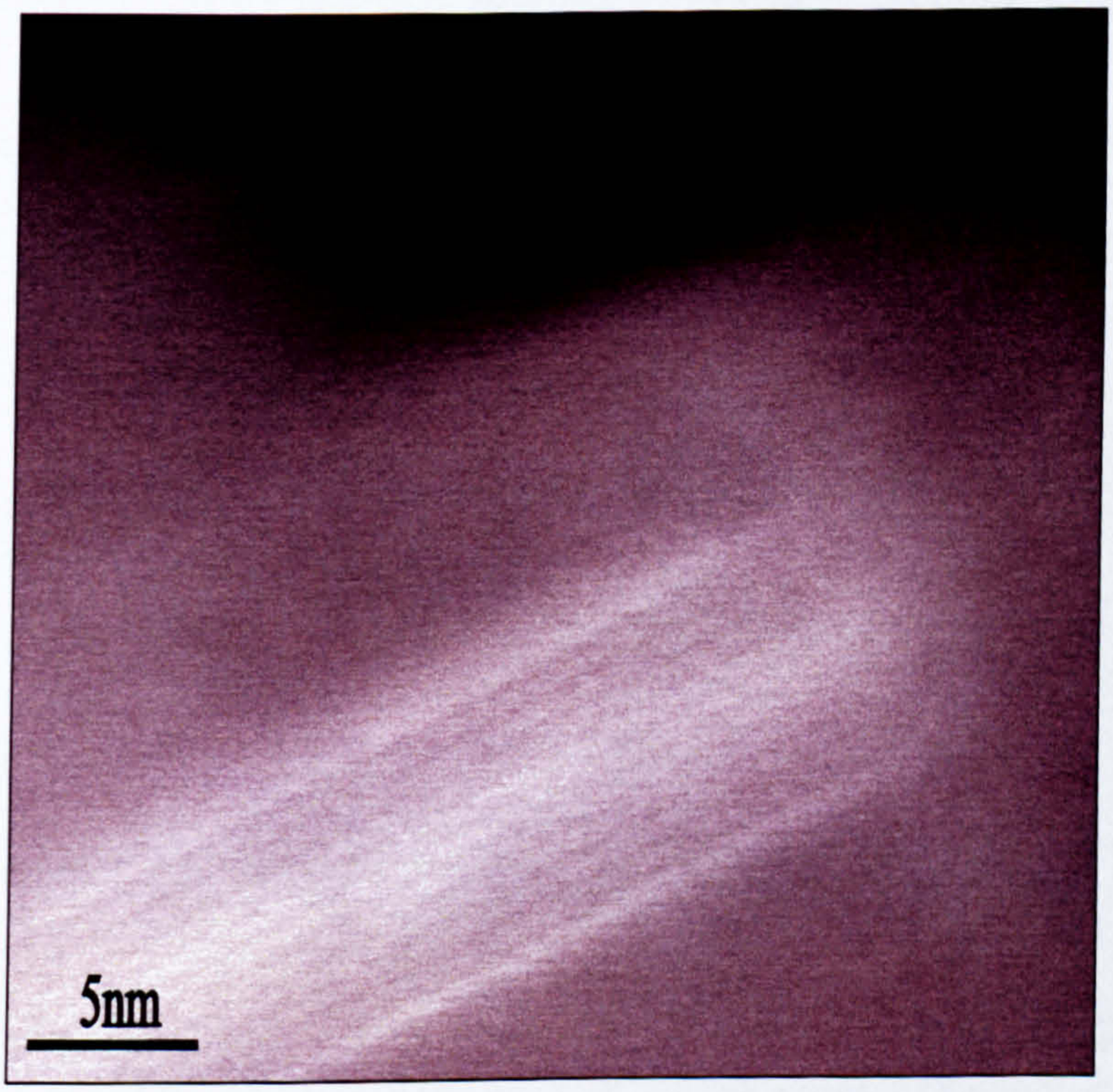

Fig. 6.14 Q' phase in the 60 seconds delayed sample: (a) HREM image, (b) HAADF STEM image.